

LEABHARLANN CHOLÁISTE NA TRÍONÓIDE, BAILE ÁTHA CLIATH | TRINITY COLLEGE LIBRARY DUBLIN
Ollscoil Átha Cliath | The University of Dublin

Terms and Conditions of Use of Digitised Theses from Trinity College Library Dublin

Copyright statement

All material supplied by Trinity College Library is protected by copyright (under the Copyright and Related Rights Act, 2000 as amended) and other relevant Intellectual Property Rights. By accessing and using a Digitised Thesis from Trinity College Library you acknowledge that all Intellectual Property Rights in any Works supplied are the sole and exclusive property of the copyright and/or other IPR holder. Specific copyright holders may not be explicitly identified. Use of materials from other sources within a thesis should not be construed as a claim over them.

A non-exclusive, non-transferable licence is hereby granted to those using or reproducing, in whole or in part, the material for valid purposes, providing the copyright owners are acknowledged using the normal conventions. Where specific permission to use material is required, this is identified and such permission must be sought from the copyright holder or agency cited.

Liability statement

By using a Digitised Thesis, I accept that Trinity College Dublin bears no legal responsibility for the accuracy, legality or comprehensiveness of materials contained within the thesis, and that Trinity College Dublin accepts no liability for indirect, consequential, or incidental, damages or losses arising from use of the thesis for whatever reason. Information located in a thesis may be subject to specific use constraints, details of which may not be explicitly described. It is the responsibility of potential and actual users to be aware of such constraints and to abide by them. By making use of material from a digitised thesis, you accept these copyright and disclaimer provisions. Where it is brought to the attention of Trinity College Library that there may be a breach of copyright or other restraint, it is the policy to withdraw or take down access to a thesis while the issue is being resolved.

Access Agreement

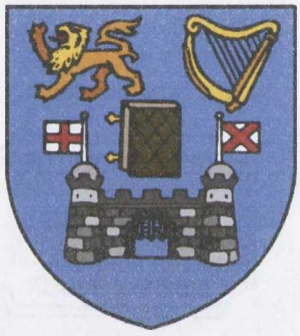
By using a Digitised Thesis from Trinity College Library you are bound by the following Terms & Conditions. Please read them carefully.

I have read and I understand the following statement: All material supplied via a Digitised Thesis from Trinity College Library is protected by copyright and other intellectual property rights, and duplication or sale of all or part of any of a thesis is not permitted, except that material may be duplicated by you for your research use or for educational purposes in electronic or print form providing the copyright owners are acknowledged using the normal conventions. You must obtain permission for any other use. Electronic or print copies may not be offered, whether for sale or otherwise to anyone. This copy has been supplied on the understanding that it is copyright material and that no quotation from the thesis may be published without proper acknowledgement.

Novel Lanthanide Luminescent Materials: Sensing in Solution and on Solid Surfaces

Laura Truman

October 2012



University of Dublin
Trinity College

Based on research carried out under the direction of
Prof. Thorfinnur Gunnlaugsson

A thesis submitted to the School of Chemistry, University of Dublin, Trinity College for the degree of Doctor of Philosophy

TRINITY COLLEGE
24 MAY 2013
LIBRARY DUBLIN

Thesis 9987

Declaration

This thesis is submitted for the degree of Doctor of Philosophy to the University of Dublin, Trinity College and has not been submitted before for any degree or examination to this or any other university. Other than where acknowledged, all work described herein is original and carried out by the author alone. Permission is granted so that the Library may lend or copy this thesis upon request. This permission covers only single copies made for study purposes, subject to normal conditions of acknowledgment.



L

Acknowledgements

First of all, I would like to thank my supervisor Prof. Thorri Gunnlaugsson for all his enthusiasm, guidance and support in my undergrad years and throughout my PhD.

Big thanks to all the staff members in the School of Chemistry, especially Dr. John O'Brien, Dr. Manuel Reuther and Dr. Martin Feeney for their help with characterisation, and to Dr. Neal Leddy in the CMA for all TEM imaging.

To all past members of the TG group, too many to list, and present group members; Emma, Oxana, Stevo, Jon, Miguel, Komala, Jenn, Joe, Esther, Fergus and Sachi, thanks for all the tea time chats, laughs, and support over the last four years. To Emma, thanks for being there since all the way back in 1st year undergrad as my (favourite) demonstrator! My amigo Miguel, thanks for all the footy chat and not putting up too much of a challenge in fantasy football league! Komala, thanks for being around for any advice and I'll miss sampling your amazing cooking at lunch time! Jenn, thanks for becoming one of the new members of the "pints" gang, couldn't have found a better fit for our group! Joe, for (trying) to keep us all on the straight and narrow with our grammar... and many other aspects, go raibh maith agat! Esther, I'll be calling in a favour you owe me very soon so be ready dude!! Fergus, try to leave the building (and yourself!) in one piece when you leave! And the newbies Sachi and Sam, hope you enjoy the rest of your time in the group! Also thanks to my favourite visiting students Stefano and Anna, was so much fun having you guys around!

Massive thanks to everyone that helped in the proof reading of this thesis, especially Oxana, Jon and Stevo. Oxana, keep up your adapted Irishness and hope our ways have rubbed off on you a bit, although Stevo probably doesn't! Thanks to Jon for all the help with the Langmuir work, and, more importantly, for teaching me the art of beer making! To Steve, I honestly don't know what I would have done without you over the last four years, other than eaten a lot less chocolate! Can't thank you enough for all the help you've given me in this Thesis and being there to answer the millions of questions I had, also can't believe you've put up with us "screaming blondes" for so long!
Also thanks to Rachel, who's been there for a coffee or chat when needed!

To my Med Chem family, Jeff, Brian and of course Dawn and Dave, thanks for putting up with me for the last eight years and counting!! As a wise man once said, "Friends are the family we choose ourselves", and I couldn't have chosen a better bunch of people. Dawn, from the very first day of college, trips to Regensburg and Australia, exam cramming sessions in your kitchen and some ripped jeans…thanks for all the memories, laughs and friendship. Dave, thanks for getting me through the undergrad years, "sharing" your lab reports with me, the walks to the "bus" stop after college, and for all the chats and advice over the last eight years…we might even be facebook friends some day! And to my girls Kim, Dee and Aoife, thanks for distracting me with a night out or cinema date from time to time. Never a dull moment with you guys, I just wish I could remember more of them!

Rob and Brian, my boys, thanks for your unbelievable support, the laughs, mad nights out and most importantly, friendship over the last four years. Brian, my fellow screaming blond and Bob, my pints buddy, the chats, laughs and our endless supply of funny stories with you guys made the tough days so much easier to get through!

To my fellow 4th years, Elaine and Swagata, thanks for being there for the last four years of my PhD, we've had our ups and downs but it made it easier having you guys with me! Elaine, what can I say, I wouldn't have been able to get through this year without my snuggle bunny by my side every step of the way, can't thank you enough and can't imagine going through this experience without you! Now bring on the Moët and celebrations!!

Finally, the biggest thank you has to go to my amazing family. From the beginning of my college years, I have had your constant support and encouragement, something I am truly grateful for. In appreciation, I would like to dedicate this thesis to you.

For My Family

"Ain't nothing' over 'til it's over"

Rocky Balboa

Abstract

This thesis entitled "Novel Lanthanide Luminescent Materials: Sensing in Solution and on Solid Surfaces" is divided into seven chapters. Chapter 1, the introduction, is divided into two sections. The first half introduces the field of luminescent sensing, with a brief description of some fluorescent based sensors previously developed. The unique photophysical properties that the lanthanide metal ions have to offer are next discussed as an advantage over fluorescent emitting sensors. A review on the advances of lanthanide based probes reported in the literature and within the Gunnlaugsson research group is presented. The remainder of Chapter 1 gives a brief introduction into gold nanoparticles (AuNPs), from their discovery to more recent advances such as functionalisation with lanthanides. A review of some recent AuNPs functionalised probes is also discussed. The Chapter concludes with a description of the research conducted in each of the subsequent Chapters.

Chapter 2 presents in detail the design, synthesis and photophysical evaluation of novel cyclen based Tb(III) and Eu(III) probes for functionalisation onto AuNPs. Both systems allow for the incorporation of an antenna moiety within their overall structures to allow for indirect excitation of the lanthanide metal. The effect of pH on the luminescent properties of these lanthanide complexes is investigated, with particular emphasis being placed on their response within the physiological pH window. A series of analyte studies on the Eu(III) complex demonstrate that anions such as acetate and phosphate and larger biomolecules such as terephthalic acid, malonic acid, AMP, ADP and ATP have a slight quenching effect on the Eu(III) emission. However, for the diketonates nta, tta and tfp, a significant enhancement of the lanthanide luminescence is observed. The functionalisation of the Ln(III) complexes onto the surface of AuNPs is investigated. Once functionalised and characterised the same photophysical investigations are carried out as for the complexes alone.

Chapter 3 begins by discussing the ability of NIR emitting systems to probe biological systems *in vivo*. The design and synthesis of a Yb(III) emissive ternary system is described in detail, followed by an investigation into the ability of the Yb(III) system to sense the biologically relevant metal ion Zn(II), in which it is discovered that the Yb(III) emission was switched on. The preference of the Yb(III) system for Zn(II) over a range of other metal ions is investigated. The formation of the ternary system with Zn(II) is fully reversible as a function of pH; an "on/off" system was established.

Chapter 4 details the synthesis and subsequent functionalisation of a Yb(III) complex onto gold nanoparticles. The external antenna tta is employed to form a ternary system on the AuNP surface and the ternary system is investigated for its ability to sense dopamine. However, the poor photostability of the tta antenna within the experimental conditions used

lead to the investigation of the XO antenna also being discussed. The pH dependency of the Yb(III) emission of the HQS-Yb(III) system on AuNPs, in particular its "on/off" behaviour, is investigated in detail that the Yb(III) emission from the AuNPs can be repeatedly switched "on/off" as a function of pH.

In Chapter 5, a series of Ln(III) complexes, possessing the amphiphilicity required to form Langmuir Blodgett films, are described. The synthesis of each derivative is discussed, in addition to their photophysical properties and ability to form Langmuir monolayers and Langmuir Blodgett films. Studies are presented which determine the stability, sensing ability and durability of the Ln(III) luminescent Langmuir Blodgett films once deposited onto quartz slides.

Chapter 6 discusses the attempted synthesis of a Tb(III) complex as a potential Hg(II) sensor. The various approaches taken toward the formation of the target molecule are described.

Finally, Chapter 7 outlines the experimental procedures used within this Thesis along with their full characterisation. Following this, literature references and Appendices are provided which provides spectroscopic and titration data to support work described in the main text.

Abbreviations

a.u.	arbitrary units
AcO^-	acetate ($CH_3CO_2^-$) anion
ADP	adenosine diphosphate
AMP	adenosine monophosphate
ATP	adenosine triphosphate
AuNP	gold nanoparticles
br	broad
BSA	bovine serum albumin
cyclen	1,4,7,10-tetraazacyclododecane
CD	circular dichrosim
d	doublet
δ	chemical shift
DIPEA	diisopropylethylamine
DLS	dynamic light scattering
DMAB	4-(dimethylamino)benzoic acid
DMAP	4-(N, N-dimethylamino)pyridine
DMF	dimethyl formamide
DMSO	dimethyl sulfoxide
DOTA	1,4,7,10-tetraazacyclododecane-1,4,7,10-tetraacetic acid
EDTA	ethylenediaminetetraacetic acid
Eq	equivalents
ES	electrospray
ESMS	electrospray mass spectrometry
ET	energy transfer
Et_3N	triethylamine
EtOAc	ethyl acetate
EtOH	ethanol
Hcy	homocysteine
HEPES	(4-(2-hydroxyethyl)-1-piperazineethanesulfonic acid
His	histidine
HPLC	high performance liquid chromatography
HRMS	high resolution mass spectrometry
hrs	hours

HSA	human serum albumin
I	intensity
IC	internal conversion
ICT	internal charge transfer
IR	infrared
ISC	intersystem crossing
J	coupling constant
K	rate constant
λ	wavelength
Ln(III)	lanthanides
Ln(III)*	lanthanide excited state
LOD	limits of detection
m	multiplet
MALDI-TOF	matrix assisted laser desorption ionisation - time of flight
MeCN	acetonitrile
MeOH	methanol
min	minute
MLCT	metal to ligand charge transfer
m.p.	melting point
MRI	magnetic resonance imaging
ms	milli ($\times 10^{-3}$) seconds
MS	mass spectrometry
m/z	mass charge ratio
NIR	near infrared
NMR	nuclear magnetic resonance
nm	nanometer
pdca	2,6-pyridinedicarboxylic acid
PET	photoinduced electron transfer
pH	$-\log[H_3O]^+$
Phe	phenylalanine
p*Ka*	$-\log[K_a]$ where K_a is the acidity constant
ppm	parts per million
pSer	phosphoserine
pThr	phosphothreonine
pTyr	phosphotyrosine

q	quartet
q	metal bound water molecules
RT	room temperature
s	singlet
SEM	scanning electron microscopy
SPR	surface plasmon resonance
t	triplet
τ	lifetime
TEAP	tetraethyl ammonium hydroxide
TEM	transmission electron microscopy
TGA	thermogravimetric analysis
TLC	thin layer chromatography
TMS	tetramethylsilane
TOAB	tetraoctlyammonium bromide
TRIS	tris(hydroxymethyl)aminomethane
Trp	tryptophan
Tyr	tyrosine
UV-vis	ultra violet-visible
μs	micro ($\times 10^{-6}$) seconds
μW	microwave irradiation

Contents

Chapter 1: Introduction

1. Introduction 1
1.1 Molecular Sensors 2
1.2 Fluorescence 2
1.2.1 Fluorescent Sensors 4
1.3 Lanthanide Metal Ions 6
1.3.1 Luminescent Properties of the Lanthanides 7
1.3.2 Lanthanide Luminescent Quenching 10
1.4 Macrocyclic Lanthanide Luminescent Complexes 11
1.5 Applications of Cyclen Based Lanthanide Complexes 14
1.5.1 pH Responsive Lanthanide Based Probes 14
1.5.2 Analyte Responsive Lanthanide Based Probes 18
1.5.3 Lanthanide Based Biological Imaging Probes 30
1.6 Gold Nanoparticles 34
1.6.1 **AuNPs**: Properties, Synthesis and Characterisation 35
1.6.2 **AuNP** Probes 37
1.7 Work Described within this Thesis 44

Chapter 2: Lanthanide Functionalised AuNPs for Potential Sensing Applications

2. Introduction 47
2.1 Design of Ligand **49** 48
2.2 Synthesis and Characterisation of Ligand **49** 49
2.3 Synthesis and Characterisation of Eu(III) and Tb(III) complexes of **49** 52
2.4 Photophysical Properties of **Eu·49** and **Tb·49** 54
2.5 Determination of Metal Bound Water Molecules for **Eu·49** and **Tb·49** 56
2.6 pH Response of Ligand **49** in Solution 59
2.6.1 Ground State Investigations 59
2.6.2 Singlet Excited State Investigations 60
2.7 pH Response of **Eu·49** in Solution 61
2.7.1 Ground State and Singlet Excited State Investigations 61
2.7.2 Eu(III) Excited State Investigations of **Eu·49** 62
2.8 pH Response of **Tb·49** in Solution 64
2.9 pH Response of **Eu·49**:**Tb·49** in Solution 65

2.10 Anion Titrations of **Eu·49** 67
2.10.1 Titrations with Antennae Containing the Diketonate Framework 72
2.11 Functionalisation of **AuNPs** with **Eu·49** 77
2.11.1 Modified Brust-Schiffrin Method 77
2.11.2 Citric Acid Method 78
2.12 Characterisation of **AuNP-Eu·49** 78
2.12.1 Dynamic Light Scattering Studies of **AuNP-Eu·49** 78
2.12.2 Transmission Electron Microscopy Studies of **AuNP-Eu·49** 80
2.13 Photophysical Properties of **AuNP-Eu·49** 82
2.14 pH Response of **AuNP-Eu·49** 84
2.15 Anion Titrations of **AuNP-Eu·49** 85
2.16 **AuNP-Tb·49** 89
2.16.1 Anion Titration of **AuNP-Tb·49** 93
2.17 **AuNP-Eu·49/Tb·49** 95
2.18 Conclusion 106

Chapter 3: Dual Emissive Lanthanide Probe for Zn(II) Sensing

3. Introduction 109
3.1 Design of **Yb·81-8-HQS** 113
3.2 Synthesis and Characterisation of **81** and **Yb·81** 115
3.3 Investigation of the Interaction of **8-HQS** with Cd(II), Mg(II) and Zn(II) 118
3.4 Formation and Photophysical Characterisation of **Yb·81-8-HQS** 120
3.5 Displacement Assay for the Detection of Zn(II) 125
3.5.1 Limit of Detection for the Sensing of Zn(II) 129
3.5.2 Zn(II) Sensing in the Presence of Biologically Relevant Anions 130
3.6 Reversibility of the Sensing Event 132
3.7 Interaction of **Yb·81-8-HQS** with Group I, II and d-Metal Ions 134
3.8 Interaction of **Yb·81-8-HQS** as a Function of pH 139
3.8.1 "On/Off" Switching of the NIR Emission as a Function of pH 142
3.9 Conclusion 144

Chapter 4: Switchable NIR emitting AuNPs

4. Introduction 147
4.1 Design of **AuNP-Yb·38** 151
4.2 Synthesis and Characterisation of Ligand **38** and **Yb·38** 153

4.3 Functionalisation of **AuNPs** with **Yb·38** 156
4.4 Formation and Photophysical Evaluation of **Yb·38-tta** and **AuNP-Yb·38-tta** 159
4.4.1 Formation of **Yb·38-tta** 159
4.4.2 Formation of **AuNP-Yb·38-tta** 160
4.5 Sensing of Dopamine 162
4.5.1 Sensing of Dopamine using **Yb·38-tta** 162
4.5.2 Sensing of Dopamine using **AuNP-Yb·38-tta** 163
4.6 Selectivity of **AuNP-Yb·38-tta** for Dopamine over Biologically Relevant Anions 165
4.7 Stability Study of **AuNP-Yb·38-tta** 168
4.8 **8-HQS** as an Antenna for the Sensing of Dopamine using **AuNP-Yb·38** 171
4.8.1 Formation of **AuNP-Yb·38-8-HQS** 171
4.8.2 Sensing of Dopamine using **AuNP-Yb·38-8-HQS** 174
4.9 Xylenol Orange as a Potential Antenna 175
4.10 Formation and Photophysical Evaluation of **Yb·38-XO** and **AuNP-Yb·38-XO** 176
4.10.1 Formation of **Yb·38-XO** 176
4.10.2 Formation of **AuNP-Yb·38-XO** 178
4.10.3 Determination of Quantum Yields for **Yb·38** and **AuNP-Yb·38** 180
4.11 pH Dependency of **XO**, **Yb·38-XO** and **AuNP-Yb·38-XO** 181
4.11.1 pH Dependency of **XO** 181
4.11.2 pH Dependency of **Yb·38-XO** 183
4.11.3 pH Dependency of **AuNP-Yb·38-XO** 187
4.12 Aluminium Sensing 190
4.13 Conclusion 193

Chapter 5: Lanthanide Based Langmuir Blodgett Films

5. Introduction 195
5.1 Design and Synthesis of **Eu·94** 202
5.1.1 Photophysical Characterisation of **Eu·94** 203
5.1.2 Langmuir Monolayer Formation of **Eu·94** 205
5.2 Design and Synthesis of **Ln·95/96** 206
5.3 Photophysical Characterisation of **Eu·95** and **Tb·95** 212
5.4 Langmuir Monolayer Formation of **Eu·95** and **Tb·95** 214
5.5 Photophysical Characterisation of **Eu·96** and **Tb·96** in Solution 215
5.6 Langmuir Studies of **Eu·96** and **Tb·96** 220
5.6.1 Langmuir Monolayer Formation of **Eu·96** and **Tb·96** 220

5.6.2 Investigating the Stability of Monolayer of **Eu·96** and **Tb·96** 221
5.6.3 LB Film Formation of **Eu·96** and **Tb·96** 222
5.7 Photophysical Properties of **Eu·96** and **Tb·96** LB films 223
5.8 Langmuir Film Formation of **Eu·96-nta** and **Tb·96-DMAB** 225
5.8.1 Langmuir Monolayer Formation of **Eu·96-nta** and **Tb·96-DMAB** 226
5.8.2 Stability of Monolayers of **Eu·96-nta** and **Tb·96-DMAB** 227
5.8.3 LB Film Formation of **Eu·96-nta** and **Tb·96-DMAB** 228
5.9 Photophysical Properties of **Eu·96-nta** and **Tb·96-DMAB** LB Films 228
5.10 "Off/On" Eu(III) Emission from a LB Film of **Eu·96**. 231
5.11 Investigation of Potential LOD for LB Film of **Eu·96** 232
5.12 Flow Test of LB Films 234
5.13 Scavenger Tests on LB Films of **Eu·96-nta** 236
5.13.1 Eu(III) Scavenger Test 237
5.13.2 Tb(III) Scavenger Test 238
5.14 Multilayer Deposition 241
5.14.1 Multilayer Deposition of **Eu·96-nta** 241
5.14.2 Multilayer Deposition of **Eu·96** 243
5.15 Dual Ln(III) Emission from a LB Film 244
5.16 Amino Acid Sensing using **Eu·96-nta** 247
5.16.1 Solution Studies 247
5.16.2 LB Film Studies 248
5.17 Conclusion 250

Chapter 6: Attempted Mercury Sensor Synthesis

6. Introduction 253
6.1 Retrosynthetic and Synthetic Pathway towards **Tb·104** 255
6.1.1 Photophysical Evaluation of **Tb·108** 258
6.2 Synthesis of Macrocycle **113** 260
6.3 Attempted Synthesis of **Tb·104** 261
6.4 Conclusion 262
Future Work 263

Chapter 7: Experimental

7. General Experimental Details 265

7.1 UV-vis Absorption and Luminescence Spectroscopy 266

7.2 Characterisation of the Surface-Modified **AuNPs** 266

7.3 Langmuir Film Measurements 266

7.4 General Synthetic Procedures 267

7.5 Experimental Details for Chapter 2 268

7.6 Experimental Details for Chapter 3 274

7.7 Experimental Details for Chapter 4 276

7.8 Experimental Details for Chapter 5 277

7.9 Experimental Details for Chapter 6 282

References 288

Appendices 295

Appendix 2 295

Appendix 3 308

Appendix 4 319

Appendix 5 328

Appendix 6 349

Publications 355

Chapter 1

Introduction

1. Introduction

There currently exists a real interest within the field of chemistry to design and investigate the properties of novel structurally defined supramolecular self-assemblies and functional nanostructures.[1] This area, known as supramolecular chemistry, is rapidly growing and involves investigations into new molecular systems. One of the main characteristics of a supramolecular structure is that it is held together by intermolecular forces, rather than bound covalently, so that formation of the architecture is a reversible process. The non-covalent interactions utilised in supramolecular assembly processes include: electrostatics, hydrogen bonding, π-π stacking interactions, van der Waals forces and hydrophobic or solvatophobic effects.[2] Such systems have been developed for various uses, including optical electronic devices[3], switches[4] and the sensing and imaging of biological analytes[5] to the monitoring of complex cellular biological processes.[6] The combination of supramolecular chemistry with nanostructures such as gold nanoparticles (**AuNPs**) in chemistry, biology, physics and medicine is becoming progressively important in modern science.[7,8]

Bearing this in mind, this thesis is focused on the design, development and evaluation of novel luminescent supramolecular architectures with applications towards biological analyte detection. The luminescence stems from the incorporation of a lanthanide (Ln(III)) metal ion into these systems. This Chapter will look to introduce a variety of topics discussed in this thesis, beginning with the concept of a supramolecular sensor, outlining fluorescent sensors and the drawbacks associated with them in biological systems. This leads to the introduction of the Ln(III), their unique photophysical properties and the advantages they have to offer. Ln(III) complexes span a wide range of sensing applications and a review of some principal and recent Ln(III) probes developed will be given, including examples from Gunnlaugsson and co-workers, as well as the groups of Parker, Pope, Faulkner, Bünzli, *etc.* all of whom have made key developments in the combination of the Ln(III) with supramolecular assemblies. The remainder of the chapter will present gold nanoparticles; their synthesis, functionalisation and characterisation. Most importantly, the functionalisation of **AuNPs** with organic supramolecular and biomolecular systems offers a novel type of functional hybrid nanomaterial, with the potential use in sensing of biological substrates. The final section encompasses some recent examples of **AuNP** probes, designed for a variety of sensing and biological applications.

1.1 Molecular Sensors

In recent years, great interest has been shown in the development of sensors within the field of supramolecular chemistry.[1] A molecule can be used as a sensor if it can report the presence of a guest by some physical means. Typically a supramolecular sensor is made up of a recognition site linked either directly to a signalling moiety or separated by a spacer unit as depicted by Figure 1.1.

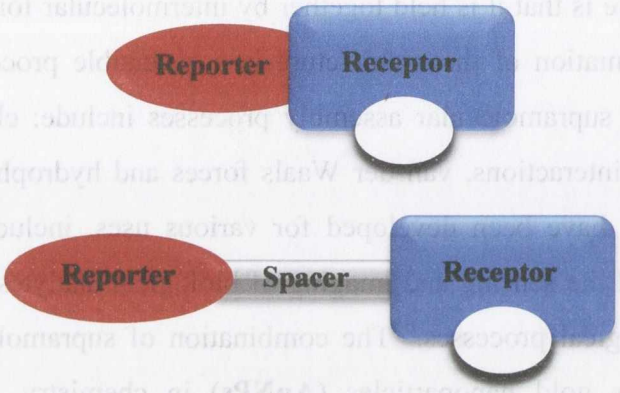


Figure 1.1: *Schematic representations of the basic components of supramolecular sensors.*

Sensors, where the reporter and the receptor molecule are integrated, involve a communication process in which an internal charge transfer (ICT) is required. However, in spaced systems, communication can occur *via* energy transfer (ET) between the two components and spacers are utilised to prevent any π-π and σ-π interactions between the two components.[9] The recognition moiety has defined structural features that enable selective and efficient binding of a guest/analyte such as ions and molecules. The signalling unit acts as a signal transducer, converting the recognition/binding event into an easily readable optical or spectroscopic response which could include a shift in an NMR signal, a colour change, or modification of luminescent properties. A common means of indication is through luminescent sensing, which has many advantages including the ability to detect analytes at low concentrations (in the order of 10^{-7} M and lower).[9]

1.2 Fluorescence

Luminescence is the term used to describe the emission of light from electronically excited species. The two main types of luminescence that occur are fluorescence and phosphorescence. Fluorescence is a light induced process that occurs in molecules known as fluorophores that generally contain polyaromatics or heterocyclic rings. It is a radiative process between states of the same spin multiplicity and is concerned with the singlet state only.

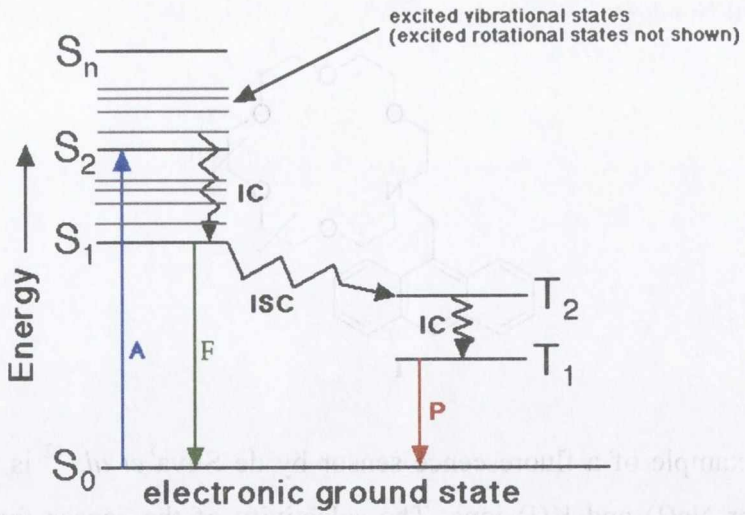


Figure 1.2: *Jablonski diagram illustrating the energy levels associated with fluorescence and phosphorescence, where A = photon absorbance, F = fluorescence, P = phosphorescence, S = singlet state, T = triplet state, IC = internal conversion, ISC = intersystem crossing.*[10]

The luminescence process is best illustrated by the Jablonski diagram shown in Figure 1.2.[10] When a molecule absorbs a photon of light an electron is excited from a singlet ground state, S_0, to a singlet excited state, S_n. The electron remains in its excited state vibrational level for a predetermined time, in the range of 1×10^{-5} to 10^{-8} seconds. The electron may then revert back to its ground state by emitting a photon of light, causing fluorescence. This is not the only method by which excited molecules return to their ground state. Other processes involve the spin allowed radiationless transitions between states of the same spin resulting in an internal conversion and vibrational deactivation of the excited state with only the release of heat (Equation 1.1). Spin forbidden radiationless transitions can also occur between excited states of different spin as shown in Equations 1.2 and 1.3, both resulting in an intersystem crossing and the release of heat.

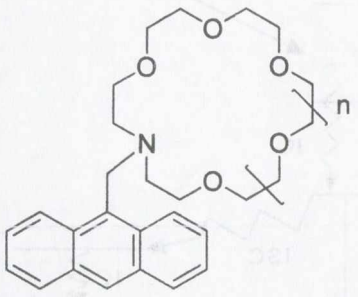
$$S_1 \rightarrow S_0 + \text{heat} \qquad \textbf{Equation 1.1}$$

$$S_1 \rightarrow T_1 + \text{heat} \qquad \textbf{Equation 1.2}$$

$$T_1 \rightarrow S_0 + \text{heat} \qquad \textbf{Equation 1.3}$$

In relation to sensing the most important process is the spin allowed singlet-singlet emission of photons giving rise to fluorescence. The field of fluorescent sensing has been extensively studied over the years, and as such some examples will be detailed in the following section.[11]

1.2.1 Fluorescent Sensors



1

An early example of a fluorescence sensor by de Silva *et al.* [12] is **1**, designed as an "off-on" sensor for Na(I) and K(I) ions. The selectivity of the sensor for Na(I) or K(I) is dependent on the type of crown ether. If n=0 the receptor is the molecule 1-aza-15-crown-5 and will bind Na(I) selectively. While if n=1 the receptor is 1-aza-16-crown-6, which confers selectivity to the binding of K(I). In the absence of these metal ions the anthracene fluorophore shows insignificant fluorescence due to photoinduced electron transfer (PET) from the lone pair on the nitrogen of the crown ether to the anthracene, quenching the fluorescent emission.

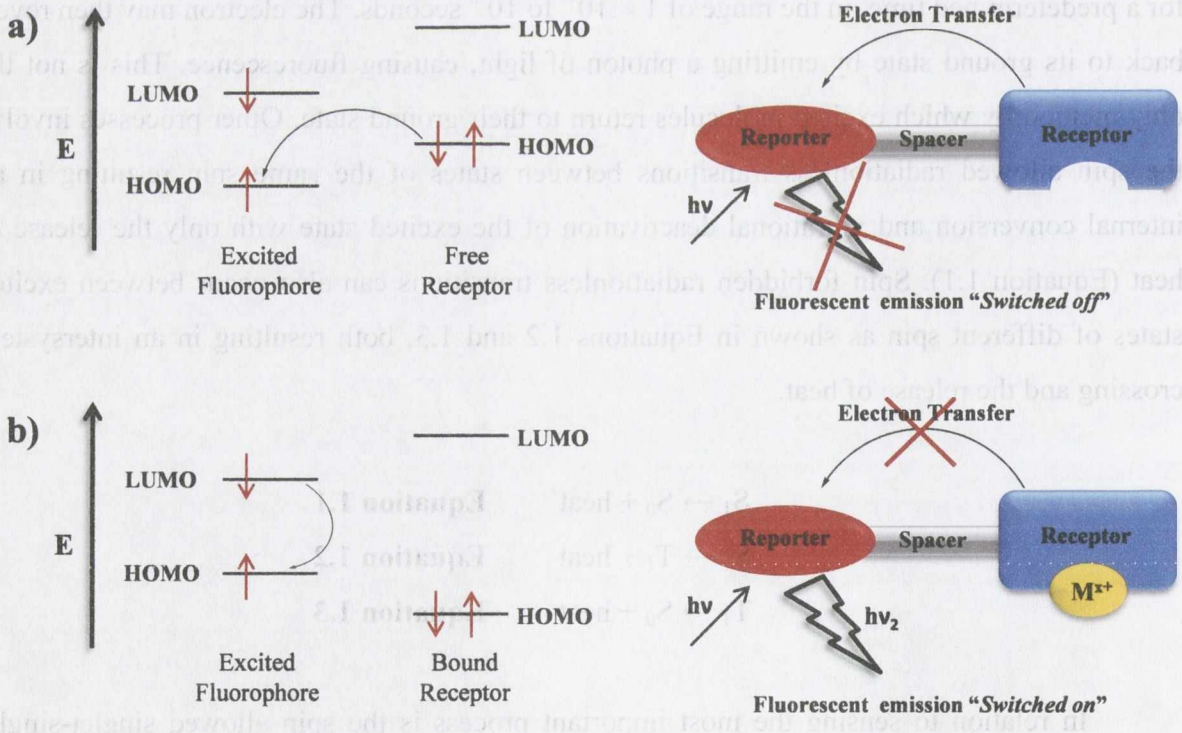
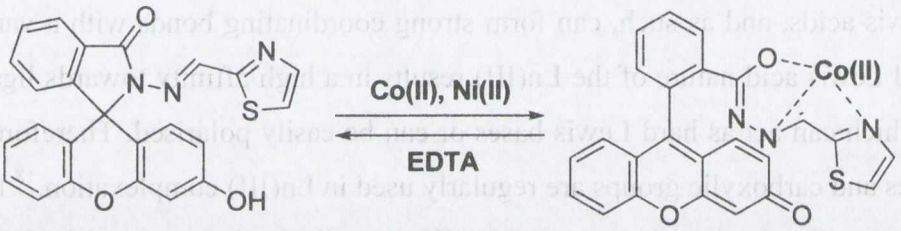


Figure 1.3: *Illustration of the PET signalling mechanism presented in example **1**; **a)** when the receptor is in the unbound state, electron transfer from the receptor's HOMO can occur, preventing fluorescence. **b)** When the receptor is bound to a substrate, its oxidation potential increases and electron transfer from the receptor's HOMO becomes thermodynamically unfeasible, resulting in the "switching on" of the fluorescence due to removal of the quenching pathway.*

In the presence of Na(I) or K(I) the oxidation potential of the receptor is increased and the receptor is unable to participate in electron transfer (ET) to the anthracenes excited state and emission is therefore observed. Illustration of the PET mechanism is shown in Figure 1.3.

A more recent example of a fluorescent sensor is **2**, shown in Scheme 1.1, a "turn on" sensor for the selective detection of cobalt and nickel ions in aqueous solution by Abebe *et al.*[13] Before the addition of either of the metal ions **2** was only weakly fluorescent in a DMSO-water (2% DMSO) solution and possessed almost no visible absorption, due to the predominance of the ring-closed spirolactam form. Upon the addition of Co(II) or Ni(II) the spirolactam ring was opened, allowing binding of Co(II) or Ni(II), causing a significant enhancement in the fluorescence emission of **2** and furthermore, a new absorbance peak at 500 nm was observed along with an instant colour change visible to the naked eye.



Minimal fluorescent — Highly fluorescent

2

Scheme 1.1: *Proposed binding mechanism responsible for the fluorescence changes of* ***2*** *upon the addition of Co(II) or Ni(II).*

In recent years, there has been a necessity for more advanced luminescent sensors bearing longer lived emission lifetimes which can be utilised for more efficient detection *in vivo.* Delayed emission of sensors *in vivo* is advantageous in that it can overcome the problematic signal-to-noise ratio caused by short lived background emission (autofluorescence) and light scattering from the surrounding biological environment.[14] The Ln(III) series possesses unique photophysical properties which enable them to overcome such difficulties and have thus been of special interest with regard to *in vivo* sensing. As this project focuses on the use of these metal ions, the following section will summarise the chemical, electronic and photophysical properties of these Ln(III) ions, focusing in particular on the Ln(III) ions Eu(III) and Tb(III).

1.3 Lanthanide Metal Ions

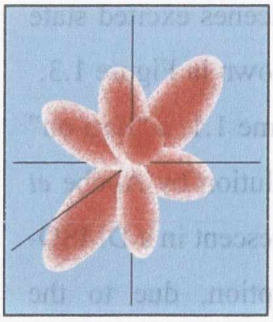


Figure 1.4: *4f Ln(III) configuration*

The lanthanides (Ln(III)) comprise the fifteen elements from lanthanum (La(III)) to lutetium (Lu(III)) in the *f*-block of the periodic table of elements. While the name lanthanide implies "rare earth", this is in fact misleading as the Ln(III) are abundant in nature.[15] The properties of the Ln(III), both physical and chemical are unique, giving rise to a growing interest in their use in the field of supramolecular chemistry.[16] They possess characteristic 4*f* open shell configurations and their most stable oxidation state is +3, particularly in water, with a [Xe]$4f^n$ configuration, as shown in Figure 1.4.[17] Due to the small and regular decrease in their atomic radii the Ln(III) also display close chemical resemblance across the periodic table; this is known as the Ln(III) contraction.[16] The Ln(III) ions have high charge density and high ionisation potentials, and can therefore be described as hard Lewis acids, and as such, can form strong coordinating bonds with a variety of ligands. The hard Lewis acid nature of the Ln(III) results in a high affinity towards ligands containing atoms which can act as hard Lewis bases or can be easily polarised. Therefore, combinations of amines and carboxylic groups are regularly used in Ln(III) complexation.[18] In order to fulfil the high coordination requirements of Ln(III), usually in the range of 9-12, ligands such as calixarenes, cyrptates, podands, macrocyclics and acyclics are often used.[19,20] One of the most popular ligand frameworks used in the complexation of Ln(III) is 1,4,7,10-tetraazacyclododecane, more commonly known as cyclen. By functionalising the cyclen framework with varying pendant arms containing amine or carboxylate groups, the Ln(III) can coordinate four nitrogen's of the cyclen and four carboxylate's/nitrogen's of the pendant arms, satisfying the Ln(III) demanding coordination environment. In recent years, the unique properties of the Ln(III) have resulted in their use in a growing number of applications.[21] For example, Ln(III) that emit in the visible region, terbium (Tb(III)), europium (Eu(III)), samarium (Sm(III)) and in the near-infrared (NIR) region; neodymium (Nd(III)), ytterbium (Yb(III)) and holmium (Ho(III)) have been increasingly used as diagnostic tools in biomedical analysis and as luminescent labels for fluoroimmunoassays.[22] As well as the unusual physical attributes of the Ln(III), they also possess unique photophysical properties that will be described hereafter.

1.3.1 Luminescent Properties of the Lanthanides

The Ln(III) have distinctive spectroscopic properties originating from the shielding of the 4*f* orbitals by the $5s^2$ and $5p^6$ orbitals. The majority of the Ln(III) are luminescent, emitting with characteristic narrow line-like emission bands with their excited state emission depending on how well their excited state(s) can be populated.[17] A major advantage in Ln(III) luminescence is their long lived excited states which are considerably longer than the majority of lifetimes exhibited by organic molecules (μs for Yb(III) and Nd(III) to ms for Eu(III) and Tb(III)). Ln(III) luminescence is also termed "delayed luminescence" because of this very useful property for probing biological systems *in vivo*. Such probes are based on a delay between the excitation of the molecule and the measurement of the Ln(III) luminescence, so that the shorter-lived autofluorescence and light scattering from the biological background decay to negligible levels (Figure 1.5a)[16] therefore enhancing the dependability of such detection.

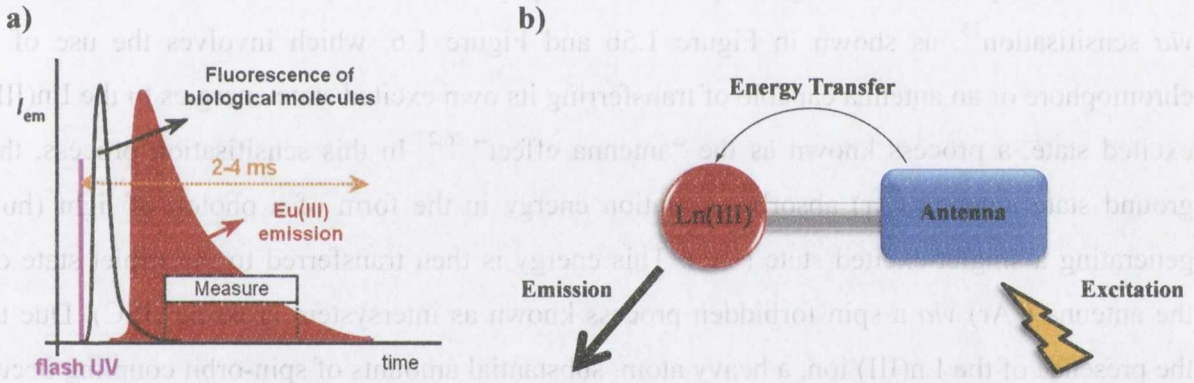


***Figure 1.5: a)** Ln(III) possess a long lived excited state which continues to emit long after biolological fluorescence has dispersed. **b)** Sensitisation process of Ln(III).*

With the advantages that arise from the photophysical properties of the Ln(III), there are also some disadvantages that need to be addressed in order to be able to design a ligand capable of overcoming these obstacles. One of the main drawbacks associated with Ln(III) luminescence *in vivo* is their Laporte-forbidden *f-f* transitions, which results in weak absorption and hence low extinction coefficients, less than 4 M^{-1} cm^{-1}.[23] Consequently, direct excitation of Ln(III) is not often efficient; unless an intense light source, such as a laser, is used.[24]

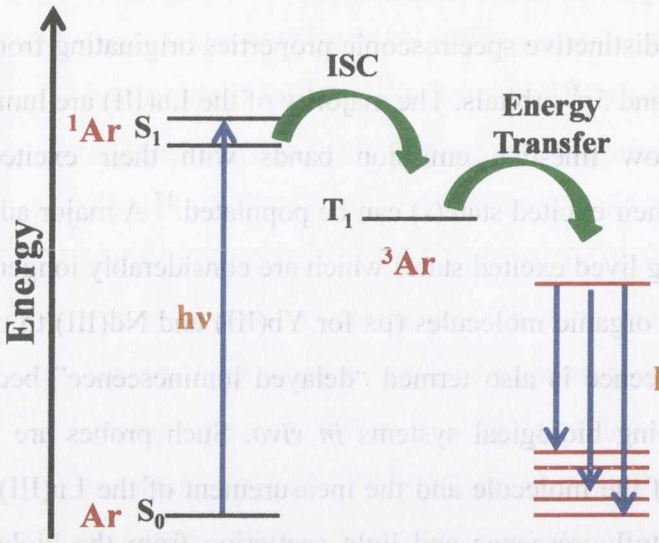


Figure 1.6: *Modified Jablonski diagram illustrating sensitisation of a Ln(III) ion by an antenna.*

One way of overcoming this problem is to populate the Ln(III) excited state indirectly *via* sensitisation[25], as shown in Figure 1.5b and Figure 1.6, which involves the use of a chromophore or an antenna capable of transferring its own excited state energies to the Ln(III) excited state, a process known as the "antenna effect".[26,27] In this sensitisation process, the ground state antenna (Ar) absorbs excitation energy in the form of a photon of light (hυ), generating a singlet-excited state (^{1}Ar). This energy is then transferred to the triplet state of the antenna (^{3}Ar) *via* a spin forbidden process known as intersystem crossing (ISC). Due to the presence of the Ln(III) ion, a heavy atom, substantial amounts of spin-orbit coupling occur which make this otherwise forbidden process possible. The excited state of the Ln(III), Ln(III)*, can now be populated from the antenna's triplet state through an intramolecular energy transfer process (EnT), provided that this triplet state lies at least 1700 cm^{-1} higher in energy than the Ln(III) excited state, therefore preventing any back energy transfer that would occur if the energy gap was smaller.[26,28] The excited state of the Ln(III) is now able to relax back down to the ground state, which, by the emission of light, results in the characteristic Ln(III) emission.[28] The Ln(III) Eu(III) and Tb(III) are the most frequently studied emissive Ln(III) ions and have their Ln(III)* states ($^5D_0$ and $^5D_4$) lying at 17200 cm^{-1} and 20500 cm^{-1}, respectively. Bipyridines, terpyridines, substituted phenyls and napthyl groups are preferred as chromophores as they possess excited states that lie 1700 cm^{-1} above these values.[20]

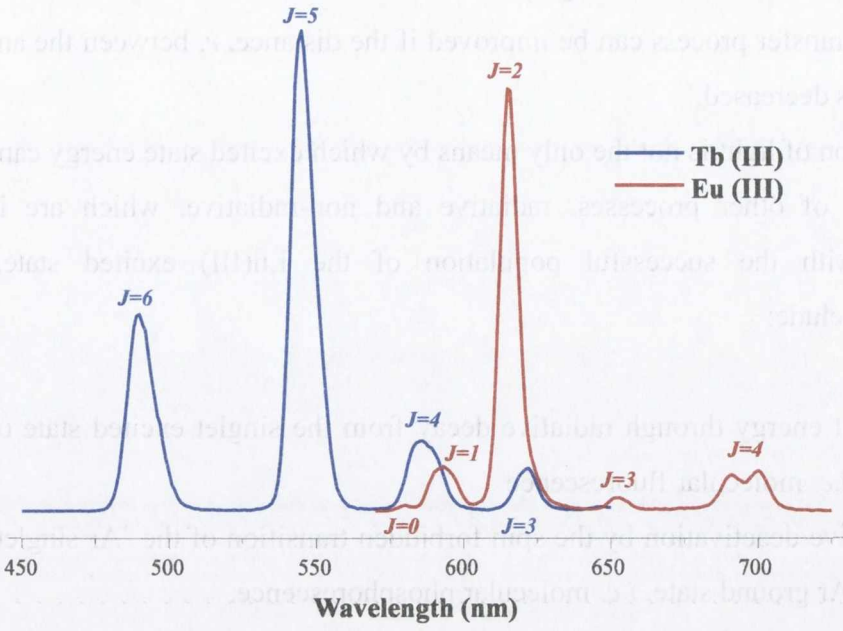


***Figure 1.7**: The characteristic Tb(III) $^5D_4 \rightarrow {}^7F_J$ and Eu(III) $^5D_0 \rightarrow {}^7F_J$ emission spectra that occur as a result of efficient Ln(III) sensitisation.*

Figure 1.7 shows the characteristic Eu(III) and Tb(III) spectra. In the case of the Eu(III) the five emission bands between 570-725 nm arise from the transitions $^5D_0$ to ^7F_J (J = 0, 1, 2, 3, 4) ground levels of the Eu(III) ion. For Tb(III), there are four emission bands between 450-650 nm resulting from the transitions from the $^5D_4$ emissive state to the ^7F_J (J = 6, 5, 4, 3) ground levels. Splitting of these bands can occur due to the loss of degeneracy of the J levels. This fine structure is dependent on the Ln(III) complex under study and the symmetry of the coordination environment.

There are two mechanisms that are used to describe the intramolecular energy transfer (EnT) that occurs from the triplet state of the antenna (^{3}Ar) to the Ln(III) excited state (Ln(III)*); the Förster energy transfer mechanism[29] and the Dexter mechanism.[30] The Förster mechanism is also known as a dipole-dipole mechanism and involves the coupling of the dipole moment associated with the ^{3}Ar excited state of the sensitising antenna and the dipole moment of the 4*f* orbitals of the Ln(III) ion. This energy transfer occurs through space and is r^{-6} distance dependence, where r is the distance between the metal ion and the excited antenna. Subsequently, by minimising the distance between the metal ion and the excited antenna the energy transfer process can be made more efficient. Alternatively, the Dexter exchange mechanism is described as a non-radiative energy transfer process which involves a double electron exchange between the excited state of the antenna and the Ln(III) metal ion. This process requires efficient orbital overlap between the donor (antenna) and acceptor (Ln(III))

species and is known as a short range process. In the case of both mechanisms the efficiency of the energy transfer process can be improved if the distance, *r*, between the antenna and the Ln(III) metal is decreased.

Emission of light is not the only means by which excited state energy can be lost; there are a number of other processes, radiative and non-radiative, which are in continuous competition with the successful population of the Ln(III) excited state.[20,26,31] Other mechanisms include:

- Loss of energy through radiative decay from the singlet excited state of the antenna (^{1}Ar), *i.e.* molecular fluorescence.
- Radiative deactivation by the spin forbidden transition of the ^{3}Ar singlet excited state to the Ar ground state, *i.e.* molecular phosphorescence.
- Non-radiative decay by collisions and vibrational interactions with the surrounding molecules[16].
- Back energy transfer to the triplet state (T_1) of the antenna or the vibrational interactions of the Ln(III) excited state ($Ln(III)^*$) with surrounding molecules such as water; also known as quenching.[15]

Of all these factors, the non-radiative quenching process is the most significant process when it comes to determining the Ln(III) luminescence quantum yield. This non-radiative deactivation can occur through vibrational modes on the condition that their energy is matching the energy gap between the ground and excited state of the Ln(III) ion.[32] When studying the Ln(III) in aqueous solution the principal quenching process is through first and second coordination sphere O-H stretching vibrations of the surrounding water molecules. Along with O-H vibrations, quenching by other high frequency vibrations such as N-H and even C-H oscillators, is also of vital concern and will be discussed in more detail in the following section.

1.3.2 Lanthanide Luminescent Quenching

One of the principle deactivation pathways by which Ln(III) luminescence can be quenched is the vibrational quenching by metal bound water molecules. Studies into this process also found that the number of O-H oscillators, or metal bound water molecules (*q*) were proportional to the rate of luminescence quenching. This quenching process of Ln(III) luminescence involves vibrational energy transfer of coordinated or diffusing O-H, N-H and even C-H oscillators. An empirical formula to quantify the amount of coordinating water

molecules directly attached to the Ln(III) metal centre (q value) was developed by Horrocks *et al.*,[33] for a range of Eu(III) complexes. It was developed on the hypothesis that, when the Eu(III) complex is in deuterated water, the O-D oscillators contribute minimally to the deactivation process of the Ln(III) excited state and that all other quenching processes are the same in H_2O and D_2O.[34] Therefore the q value of a Eu(III) complex can be determined by the difference in the luminescent lifetimes (τ) of the Ln(III) excited state in H_2O and D_2O. This formula was modified by Parker *et al.*, [35] who took into account the deactivation by N-H oscillators in addition to O-H oscillators to give Equations 1.4 and 1.5 for Eu(III) and Tb(III), respectively.

$$q^{Eu(III)} = A[(1/\tau_{H2O}-1/\tau_{D2O})-0.25-0.075x] \pm 0.5 \qquad \textbf{Equation 1.4}$$

$$q^{Tb(III)} = A[(1/\tau_{H2O}-1/\tau_{D2O})-0.06] \pm 0.5 \qquad \textbf{Equation 1.5}$$

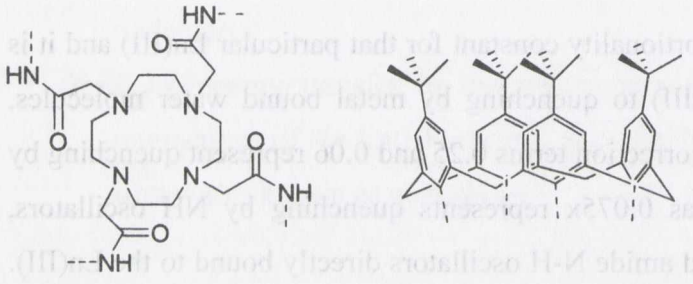
The term A in each equation is the proportionality constant for that particular Ln(III) and it is a measure of the sensitivity of the Ln(III) to quenching by metal bound water molecules, where $A^{Eu(III)} = 1.2$ and $A^{Tb(III)} = 5$. The correction terms 0.25 and 0.06 represent quenching by second sphere water molecules, whereas 0.075x represents quenching by NH oscillators, where x is the number of carbonyl-bound amide N-H oscillators directly bound to the Ln(III). Further studies into these equations by Supkowki *et al.*[36] lead to the incorporation of a smaller error of ± 0.5 being achieved, however this refinement was only appropriate for Ln(III) complexes with a greater number of metal bound water molecules (>5).

In order to minimise the vibration induced deactivation process, the design of responsive Ln(III) complexes usually incorporates thermodynamically and kinetically stable polydentate ligands in order to shield the Ln(III) from solvent coordination and fulfil the high coordination requirement of the Ln(III) ion.[17,21,37,38] Removal of the solvent coordinated to the Ln(III) metal centre will give rise to an increase in the Ln(III) emission. The next sections will detail some examples of acyclic and macrocyclic ligands employed in Ln(III) complexation and their various functions.

1.4 Macrocyclic Lanthanide Luminescent Complexes

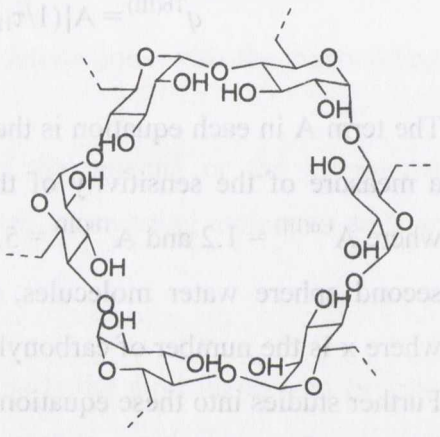
Due to their size similarity, Ln(III) ions have the capability to displace Ca(II), and as such are extremely toxic to biological systems.[37,39] For these ions to be used in biological *in vivo* sensing, they must be encapsulated by thermodynamically and kinetically stable ligands which in turn form stable complexes.[40] This can be achieved by devising ligands that are suitable for encapsulation of the Ln(III) and can satisfy the Ln(III) high coordination

requirement, hence shielding it from any solvent coordination that may give rise to quenching of the Ln(III) emission. One important condition of the ligand design is that it should include several "hard" donor atoms to bind to satisfy the polarising, hard nature of the Ln(III) ions. A macrocycle has these donor atoms arranged in fixed positions so that there is a preorganised cavity of diameter that is well suited to the binding of Ln(III) ions, for example, within the four N macrocycle of the cyclen framework. This type of organised macrocyclic system guarantees the minimum amount of reorganisation energy upon complexation, as the conformation of the free and bound ligand are relatively similar.[16,21] Less rigid and slightly more flexible frameworks have also been investigated as a new generation of chelating macrocycles.



3

4

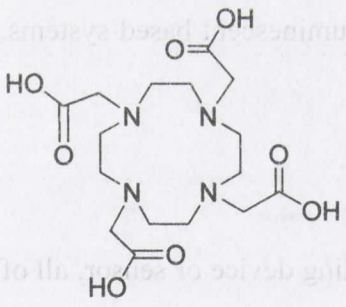


5

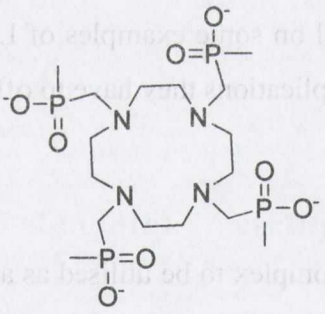
Such types of systems include cyclen (**3**), calixarene (**4**) and cyclodextrin (**5**) derivatives, all of which contain functionalised pendant arms, capable of encompassing the Ln(III) metal centre through reorganisation of the ligand system. The energy involved in this reorganisation upon complexation of the Ln(III) metal is offset by the enthalpy gain accompanying the strong metal-ligand interaction. In other words, the complexation results in a decrease in the number of metal bound water molecules, generating a positive entropy change favourable to the complexation process.[21]

The aza-macrocycle 1,4,7,10-tetraazacyclododecane offers a good platform to form efficient luminescent Ln(III) complexes through the functionalisation of the ring nitrogen atoms with groups that contain hard donor atoms. For example, the tetra-substituted cyclen ligand **6** possessing four coordinating carboxylates can provide eight atoms capable of binding to the Ln(III) and form kinetically inert and thermodynamically stable 1:1 Ln(III) complexes.[41] The ability to functionalise the ring nitrogens of cyclen also provides the possibility to easily incorporate aromatic chromophores as sensitisers for the Ln(III), hence giving rise to responsive Ln(III) luminescent sensors. [42]

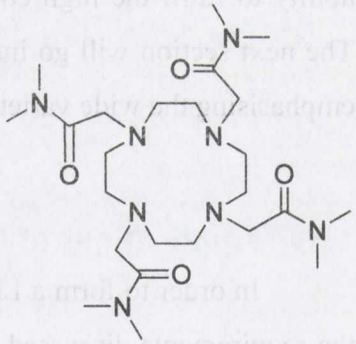
The ligands **6-8** shown below are all based on the cyclen framework and are therefore perfect candidates to form stable Ln(III) complexes. These three examples demonstrate that a variety of pendant arm groups can be utilised in the functionalisation of the macrocyclic ring; the groups most frequently used being carboxylates[43] (**6**), phosphinates[41] (**7**) and amides[44] (**8**). Ln(III) complexes of ligand **6**, 1,4,7,10-tetraazacyclododecane-1,4,7,10-tetraacetic acid (DOTA) have been studied since the 1980s and the very first Eu(III) crystal structure was solved by Spirlet *et al.*[45] in 1984. The DOTA ligand is most commonly complexed with the Ln(III) Gd(III) to form the magnetic resonance imaging (MRI) contrast agent Dotarem; $[Gd(DOTA)H_2O]^-$.[37] Dotarem is ideal to be used *in vivo* as its high thermodynamic stability constant K_{GdL} (10) guarantees that dissociation of the Gd(III) metal ion from the ligand does not occur.[46,47] Should the Gd(III) metal ion dissociate and be released into the body it would cause major disturbance as its similar size to Ca(II) ions could lead to the replacement of Ca(II) by Gd(III) in proteins.[39] With the Gd(III) metal ion released from the cyclen, this leaves the cyclen ligand with a free macrocyclic cavity which could potentially bind to metal ions present in the body. Parker *et al.*[48,49] investigated the ability of cyclen with appended amide arms (**8**) to bind to biologically relevant cations such Li(I), Mg(II) and Ca(II) and found that **8** selectively bound to Ca(II) due to its tendency to form octadentate complexes.



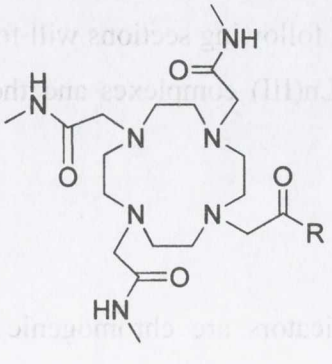
6



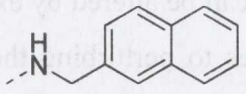
7



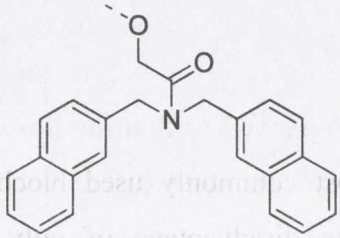
8



R=



9



10

The ligands **6-8** have all been shown to form stable complexes with Ln(III), however, none of them contain a sensitising chromophore to allow for indirect excitation of the Ln(III) ion and hence this limits the luminescence studies unless there is an external chromophore added. Ligands **9** and **10** were developed by Beeby *et al.*[27] and both possess aromatic chromophores in one of their pendant arms making it possible to obtain Ln(III) centred luminescence. In the case of the Eu(III) complex of **9** it was observed that the napthyl group did serve as an antenna chromophore for Eu(III), but the quantum yields for the metal emission were low (0.12% in MeOH and 0.19% in MeCN).[50] It was expected that the Eu(III) emission from the complex of **10** would be much more intense than that of **9** as it emits strongly at 400 nm, overlapping with the Eu(III) absorption band at 397 nm. However, this was not the case and the fluorescence emission intensity was reduced. The authors proposed that the reason for the decrease in intensity was that the ET quenching pathway was too fast relative to excimer formation and subsequent energy transfer to the metal.

Numerous Ln(III) sensing systems containing macrocyclic ligands similar to those described above have also been designed which take advantage of luminescent Ln(III) as signalling moieties by the incorporation of one or more aromatic systems into the pendant arms.[20,51] These ligands have been extensively studied as receptors for Ln(III) due to their ability to fulfil the high coordination requirement and entirely enclose the metal ion centre. The next section will go into detail on some examples of Ln(III) luminescent based systems, emphasising the wide variety of applications they have to offer.

1.5 Applications of Cyclen Based Lanthanide Complexes

In order to form a Ln(III) complex to be utilised as a signalling device or sensor, all of the requirements discussed in previous sections must be taken into account, and moreover, it is of vital importance to be able to detect any changes in the photophysical properties of the complexes. There are various different approaches through which the emission properties of Ln(III) complexes can be altered by external sources. The following sections will focus on the different approaches to perturbing the emission of the Ln(III) complexes and the resulting applications.

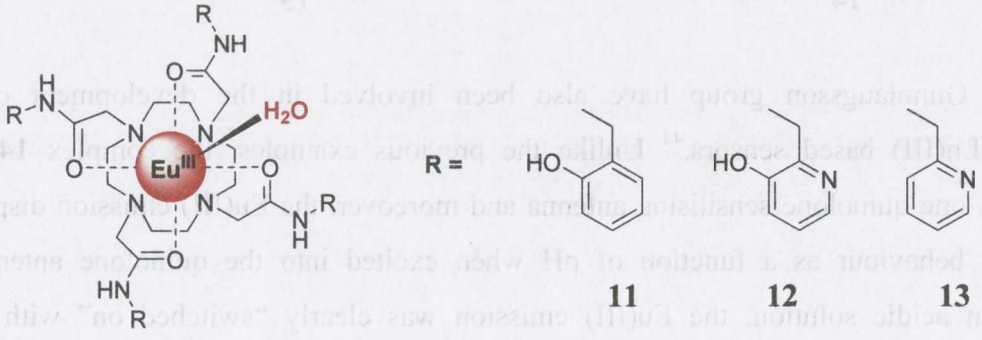
1.5.1 pH Responsive Lanthanide Based Probes

The most commonly used biochemical pH indicators are chromogenic indicators which have the disadvantage of only utilising the lower, visible wavelengths of the electromagnetic spectrum.[52] There has been a growing need for pH probes that exhibit higher

pH sensitivity over a wider wavelength range which has led to the development of a large array of Ln(III) based luminescent systems, that can be used in situations where indicator concentration or visual observation may be limited.[22] This is often the case when investigating intracellular pH and Ln(III) based probes have the potential to monitor diverse physiological and pathological processes.[22,53]

For a luminescent pH probe to be employed for cellular application, a number of factors must be taken into account in its design. Foremost, the complex must be cell permeable, kinetically stable and non-toxic to biological tissues, and in addition it should possess a large Stokes shift in order to minimise autofluorescence from the surrounding biological environment. It should be excited at wavelengths above 340 nm and must be capable of signifying changes in the emission of the complex.[53]

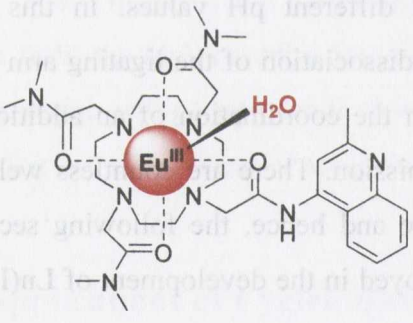
The design of luminescent Ln(III) based pH sensors can be approached in two ways. Firstly, the Ln(III) complex can be designed such that the protonation or deprotonation of the incorporated antenna moiety will modulate the energy transfer process from its singlet excited state to the Ln(III) excited state and hence result in an increase or decrease in the resulting Ln(III) emission.[54] Alternatively, the process could take advantage of the coordination environment (q value) surrounding the Ln(III) at different pH values. In this method, protonation of the chelating pendant arms results in dissociation of the ligating arm from the Ln(III) metal centre and furthermore, this results in the coordination of an additional H_2O molecule, culminating in the decrease in Ln(III) emission. There are countless well studied examples of both types of methods in the literature and hence, the following section will describe some relevant cyclen based examples employed in the development of Ln(III) based pH sensors.



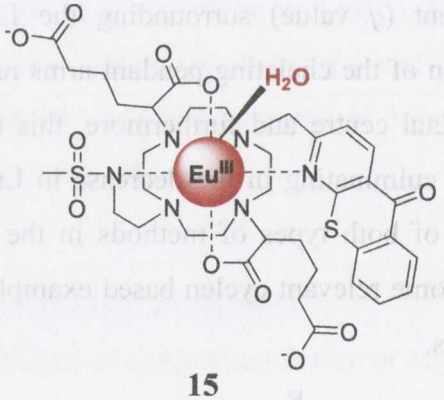
11 **12** **13**

In 2003, Woods and Sherry reported a series of DOTA-tetraamide cyclen complexes **11-13**, some of which contained extended phenol or pyridine substituent antennae, enabling efficient sensitisation of the Eu(III) metal centre.[55] In order to investigate the ability of these complexes to act as pH responsive emission probes the pH response of the Eu(III) complexes were studied by luminescence spectroscopy and NMR techniques.

The luminescence studies involved the emission spectra of **11-13** being recorded as a function of pH after excitation into the aryl chromophore at 397 nm. The most intense emission bands observed were the $J = 1$ and $J = 2$ bands centred at 594 nm and 613 nm, respectively. It was observed that the ratio of the relative intensities of these bands varied over a pH range of 2-10. At low pH the emission of the 594 nm band was much more intense than at 613 nm. Increasing the pH slightly caused an increase in the emission at 613 nm relative to that at 594 nm, and at pH 4 the emission intensities were equal. Further basification intensified the emission at 613 nm with a concomitant increase in the luminescent lifetime also being obtained. The $^5D_0 \rightarrow {}^7F_2$ transition, corresponding to the Eu(III) emission at 613 nm, is considered hypersensitive to the coordination environment around the Eu(III) metal centre and as such, any changes to the coordination environment as a result of altering the pH will be reflected by changes to this transition. The pH sensitivity of I_{613}:I_{594} ratio presents the opportunity of using this system as a ratiomeric pH probe without the need to determine the concentration of the probe. Moreover, it was ascertained that by varying the antenna moiety used the effective pH range to be investigated could be fine-tuned to a specific section of the pH range.



14



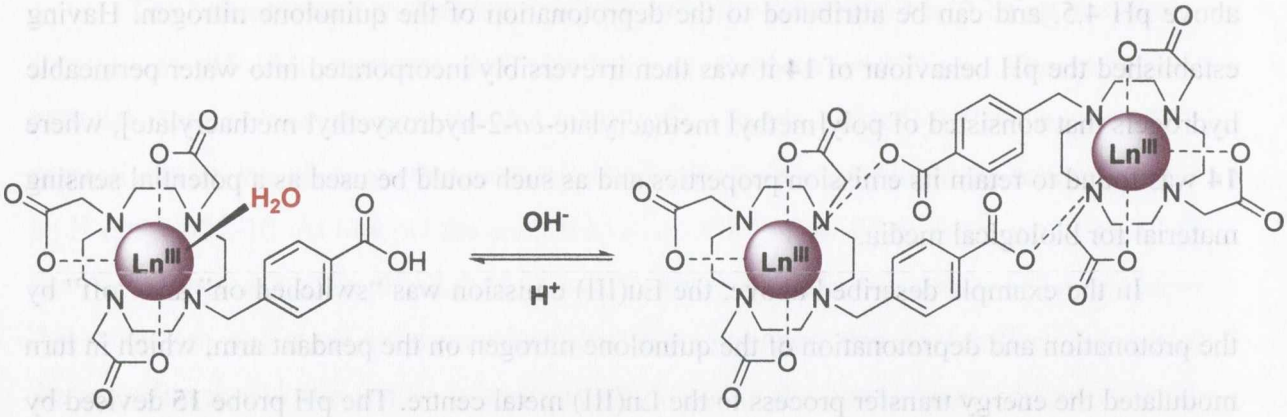
15

The Gunnlaugsson group have also been involved in the development of pH responsive Ln(III) based sensors.[44] Unlike the previous examples, the complex **14** only incorporates one quinolone sensitising antenna and moreover, the Eu(III) emission displayed an "on/off" behaviour as a function of pH when excited into the quinolone antenna at 330 nm.[54] In acidic solution, the Eu(III) emission was clearly "switched on" with large enhancements in the $J = 0$-4 emission bands. Reaching more basic pH caused a decrease in the Eu(III) emission output that became completely quenched above pH 9. Adjusting the pH back to acidic levels switched back "on" the Eu(III) emission and this luminescence switching effect was found to be fully reversible. The pK_a value was determined by potentiometric measurements to be 5.93, which accounts for the sudden decrease in the Eu(III) emission

above pH 4.5, and can be attributed to the deprotonation of the quinolone nitrogen. Having established the pH behaviour of **14** it was then irreversibly incorporated into water permeable hydrogels that consisted of poly[methyl methacrylate-*co*-2-hydroxyethyl methacrylate], where **14** was found to retain its emission properties and as such could be used as a potential sensing material for biological media.

In the example described above, the Eu(III) emission was "switched on" and "off" by the protonation and deprotonation of the quinolone nitrogen on the pendant arm, which in turn modulated the energy transfer process to the Ln(III) metal centre. The pH probe **15** devised by Parker and co-workers[53] envisaged a different approach, whereby in addition to an efficient azathioxanthone sensitiser, a pH dependant alkyl sulphonamide moiety was also attached as a separate pendant arm. The "switching on" and "off" of the Eu(III) emission operated on the basis that the coordination number of the Eu(III) metal centre fluctuated from 8 in basic media to 7 at more acidic pH, where protonation of the chelating nitrogen of the sulphonamide would result in dissociation from the Eu(III) metal centre, modulating directly the energy transfer as well as the Eu(III) coordination environment. Changes in the Eu(III) emission of **15** were investigated as a function of pH and there were reversible changes observed in the splitting of the $J = 1$, 2 and 4 bands as a result of this protonation process. Basification from pH 4.5 to 8 causes an 80% change in the intensity ratios of the 680 nm ($J = 4$ band) and 587 nm ($J = 1$ band). Confocal fluorescence microscopy imaging revealed fast uptake of the compound **15** into mouse embryonic fibroblast (NIH 3T3) cells and that the distribution was localised within protein-rich regions of the nucleous. The complex **15** shows great promise to function as a ratiometric pH probe for living cells and biological media.

The below Ln(III) compound, Scheme 1.2 was developed by Faulkner *et al.*[43] as a pH dependent self-assembly dimetallic Ln(III) complex. At neutral and high pH values, the hydration state of the molecule was found to be different than that at basic pH. At pH 2 the Eu(III) complex possesses a q value of 2, while moving toward neutral pH the carboxylate group becomes deprotonated and can act as a bridging ligand and displace water from a neighbouring Eu(III) complex. This process is confirmed by following the luminescence spectrum of **16** at pH 2 and pH 8, where the emission at pH 2 was much less intense due to the presence of an extra coordinating water molecule. Further evidence for the formation of the dimetallic species was the change in the relative intensities of the Eu(III) emission bands at 595 nm and 616 nm, indicating a change in the local environment of the Ln(III) metal centre. This self-association and resulting change in the luminescence offers the possibility of **16** to be utilised as a ratiometric pH probe with the advantage that the concentration of the compound does not need to be known.



16

***Scheme 1.2:** pH driven self-assembly of **16**.*

All of the above examples have described Ln(III) based cyclen compounds that display substantial changes in their photophysical properties such as excited state lifetimes, emission intensity or Ln(III) coordination environment, upon adjustment of their environment. While this area of Ln(III) based sensing is still being explored, another field that has been actively researched in recent years is the response of Ln(III) complexes to cations and anions such that a recognition event occurs between the Ln(III) and the ion that causes a measurable change in the photophysical properties of the Ln(III).[1] The next section will illustrate examples of these systems.

1.5.2 Analyte Responsive Lanthanide Based Probes

The modulation of Ln(III) metal-centred luminescence by an external analyte can occur through three main mechanisms as described schematically in Figure 1.8 below, redrawn from [16].

Firstly, the analyte may bind directly to the Ln(III) metal centre. This process is illustrated in Figure 1.8a whereby any metal bound water molecules that are quenching the Ln(III) luminescence are displaced by the reversible binding of the external analyte. Hence, Ln(III) emission intensity would be expected to be enhanced. The second mechanism, b, depicts that the analyte may bind to the ligand and that this guest inclusion results in changes in the analyte properties that in turn alter the effectiveness of the sensitisation to the Ln(III) metal centre. Finally, in the case of c, the analyte itself is used as the sensitising moiety and upon its addition there is sufficient energy transfer to the Ln(III) metal centre causing a "switching on" of the Ln(III) luminescence.

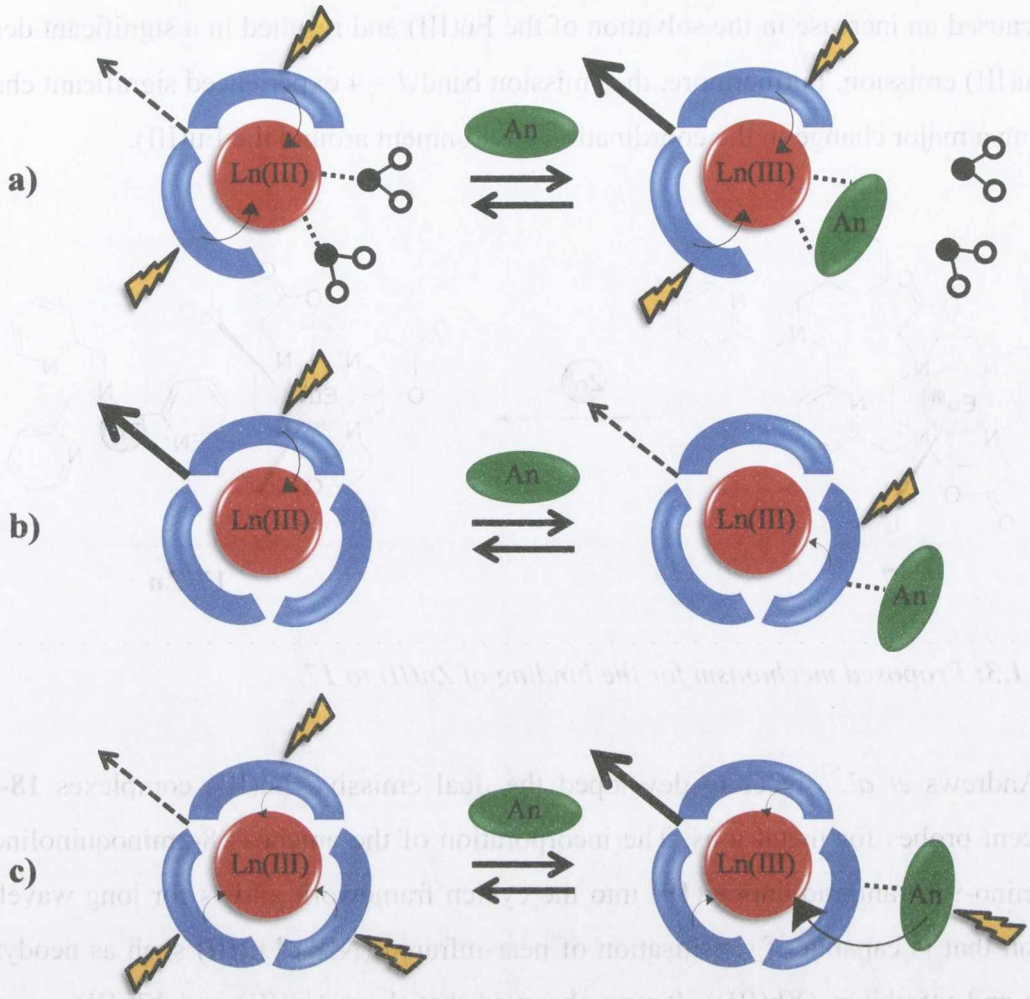
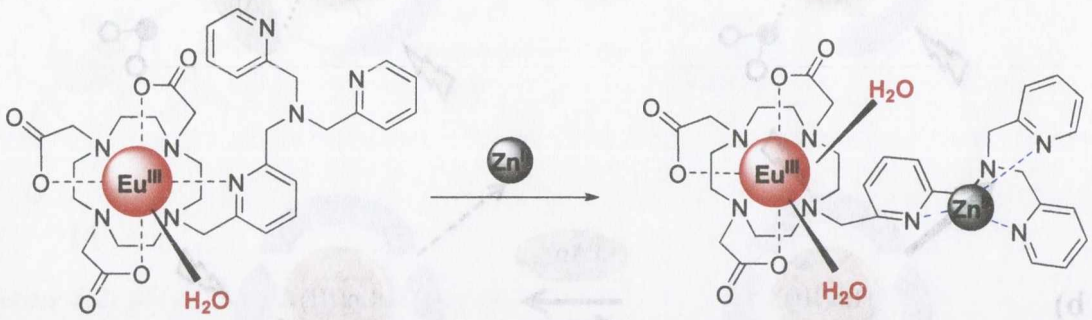


Figure 1.8: *The three main mechanisms through which the Ln(III) emission can be modulated.*

The following examples, based on these mechanisms, will examine how the luminescent properties of the Ln(III) have been applied to the development of selective Ln(III) sensors.

Sensors for zinc are of growing interest as the metal ion Zn(II) is vital for human growth and development and more recently, has been shown to be connected with neuronal degenerative conditions such as Alzheimer's disease. Pope *et al.*[56] developed a cyclen based Eu(III) complex (**17**), Scheme 1.3, for potential in vivo sensing of Zn(II), incorporating a bis-picolyl unit to selectively bind Zn(II) over other biologically relevant metal ions such as Mg(II) and Ca(II). The luminescence studies on **17** were all carried out in aqueous solutions of simulated biological environment at pH 7.4 (140 mM NaCl, 4 mM KCl, 1.16 mM $MgCl_2$ and 2.3 mM $CaCl_2$). For the free complex the authors presume that the bridging pyridyl unit is coordinating to the Eu(III) metal centre, and that efficient sensitisation can occur. Upon addition of Zn(III) the pyridyl unit detaches itself from the Eu(III) centre in order to accommodate encapsulation of the Zn(III), Scheme 1.3. Removal of one of the coordinating

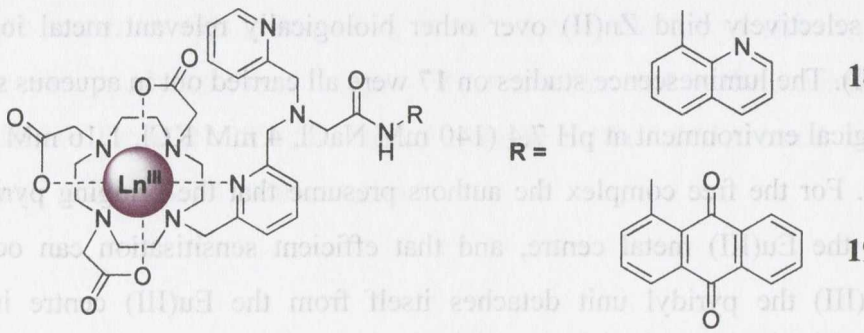
centres caused an increase in the solvation of the Eu(III) and resulted in a significant decrease in the Eu(III) emission. Furthermore, the emission band $J = 4$ experienced significant changes, suggesting a major change in the coordination environment around the Eu(III).



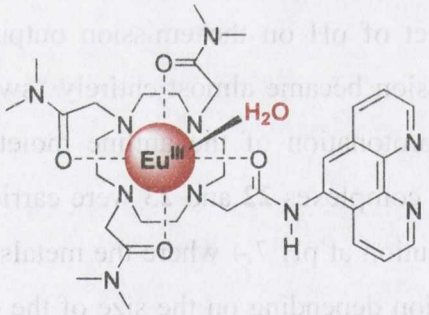
17 **17-Zn**

Scheme 1.3: *Proposed mechanism for the binding of Zn(II) to* ***17****.*

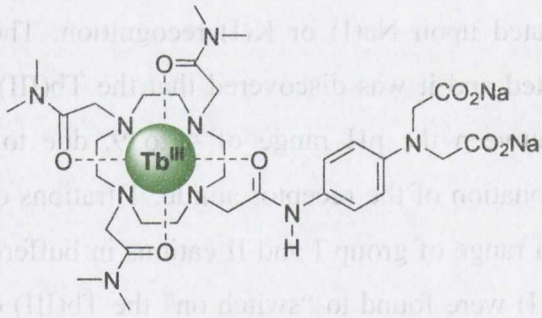
Andrews *et al.*[57] recently developed the dual emissive Ln(III) complexes **18-19** as luminescent probes for metal ions. The incorporation of the antennas 8-aminoquinoline (**18**) and 1-amino-9,10-anthraquinone (**19**) into the cyclen framework allows for long wavelength absorption that is capable of sensitisation of near-infrared (NIR) Ln(III) such as neodymium (Nd(III)) and ytterbium (Yb(III)). It was observed that these Nd(III) and Yb(III) complexes displayed dual emission upon excitation at 355 nm; with both the NIR Ln(III) emission and ligand centred fluorescence being observed. The effect of the d-block metal di-cations Cu(II), Zn(II), Cd(II) and Hg(II) on the emission properties of the Eu(III) analogues of **18** and **19** was examined in buffered pH 7.4 solution. It was discovered that the addition of Cu(II) gave rise to the greatest changes, quenching the pyridyl, anthraquinone, quinolone and Eu(III) emission bands. In contrast, the addition of Hg(II) caused a slight enhancement in the anthraquinone and quinolone emission with a concomitant decrease in the pyridine fluorescence. Moreover, a change in the relative ratio of the Eu(III) $^5D_0 \rightarrow {}^7F_J$ transitions is indicative of a change in the coordination environment of the Eu(III) metal centre.



The Gunnlaugsson group have also been involved in developing cyclen based Ln(III) complexes for the recognition of d-block metal ions. These metals are of significance in environmental and biomedical monitoring[57]; where free Cu(II) can disrupt various biological processes and Hg(II) is well known for its toxicity to humans.[58] The Eu(III) complex **20** is a cationic tri-amide cyclen based system to which a 1,10–phenanthroline (*phen*) ligand was conjugating.[59] The *phen* ligand plays a dual role, functioning as the sensitising chromophore for the Eu(III) metal centre and also as the receptor moiety for Cu(II). The addition of Cu(II) to an aqueous buffered solution of **20** at pH 7.4 caused a "switching off" of the Eu(III) emission bands, an effect that was not observed by group I and II transition metals such as Fe(II), Co(II) and Zn(II). Notably, the addition of EDTA to a solution of **20**-Cu(II) resulted in the Eu(III) emission being switched back "on", denoting that the Cu(II) detection by **20** was a reversible process. The authors also investigated the stoichiometry of the interaction and by plotting the emission changes as a function of equivalents of Cu(II) it was evident that the emission became fully quenched after the addition of *ca.* 0.35 equivalents of Cu(II). Jobs plot method of analysis of these results indicated the formation of a tetranuclear species, where the Cu(II) ion is coordinating to three **20** complexes.



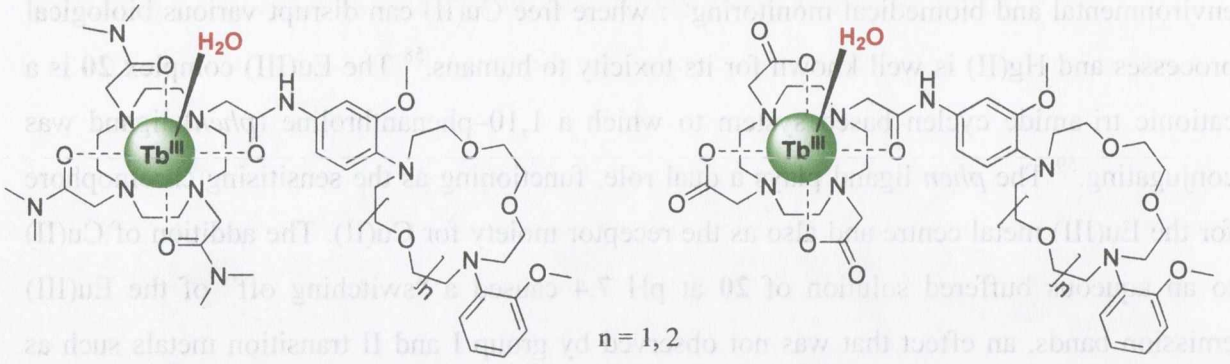
20



21

Compound **21** was reported by McMahon *et al.*[60] to detect the metal ions Cu(II) and Hg(II). This was the first example utilising Ln(III) luminescence for the detection of Hg(II). The design of the complex incorporated a phenyl iminodiacetate antenna as the receptor whereby the Cu(II) and Hg(II) bind to the iminodiacetate moiety which in turn modulates the energy transfer process from the phenyl ring to the Tb(III) metal centre and a decrease of 65% and 40% in the Tb(III) emission was observed for Cu(II) and Hg(II), respectively. When the emission response to other biologically relevant metal ions such as Zn(II), Ca(II) and Mg(II) was studied, very minor changes were observed, signifying that **21** shows high sensitivity and selectivity for Cu(II) and Hg(II). Although it was possible that the photophysical properties of the Tb(III) complex could be perturbed by protonation of the aniline moiety as well as

deprotonation of the secondary amine, the Tb(III) was shown to be pH independent over the physiological pH window.

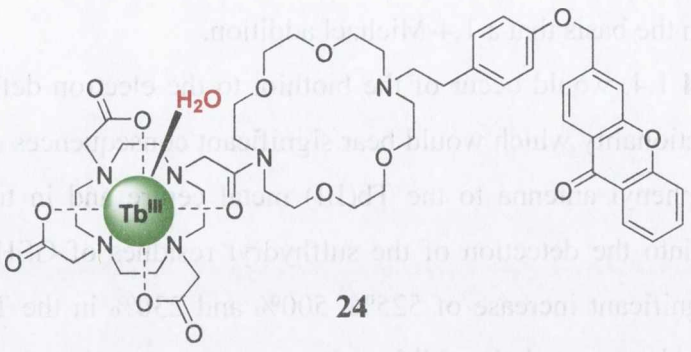


22 **23**

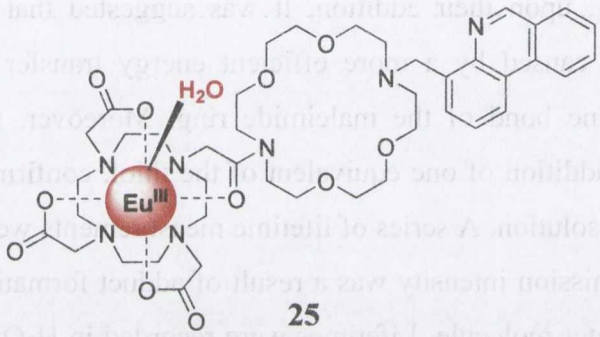
The sensing of alkali metals such as Na(I) and K(I) is of great importance as these metals have relevance in conditions such as hypertension, stroke and cardiovascular disease. Tb(III) complexes **22** and **23** have been developed by Gunnlaugsson *et al.*[23,61] incorporating either a diaza-15-crown-5 ether or a diaza-18-crown-6 ether for the selective recognition of Na(I) and K(I) ions. The crown ether moiety was linked to the main cyclen framework *via* a phenyl moiety, which allows for efficient sensitisation of the Tb(III). The aromatic crown ether also functions as an antenna for the sensitisation of the Tb(III) whereby the emission was modulated upon Na(I) or K(I) recognition. The effect of pH on the emission output was evaluated and it was discovered that the Tb(III) emission became almost entirely "switched off" between the pH range of 4 to 9, due to the protonation of the aniline moiety and deprotonation of the receptor amide. Titrations on the complexes **22** and **23** were carried out using a range of group I and II cations in buffered solution at pH 7.4 where the metals Na(I) and K(I) were found to "switch on" the Tb(III) emission depending on the size of the crown ether used; the smaller 15-crown-5 macrocycle showed selectivity for the smaller Na(I) ion whereas the larger 18-crown-6 macrocycle favoured the larger K(I) ion.

It is crucial in biomedical diagnosis to be able to selectively sense K(I) as disparities in serum and extracellular K(I) levels have been linked to hypertension, stroke and seizures.[62] Difficulties associated with measuring K(I) (3.5-5.3 mM) levels are due to the large excess of Na(I) (135-148 mM) also present. To address these complications associated with K(I) detection Pierre and co-workers designed the Tb(III) complex **24** containing a diaza-18-crown-6 moiety linked to an azaxanthone antenna.[63,64] Without K(I) present, **Tb·24** was only weakly emissive due to the large separation between the Tb(III) metal centre and the sensitising antenna. Upon addition of K(I) to the macrocycle a cation-π interaction with the aryl ether is favoured, and consequently the conformation of the complex was altered so that the antenna is considerably closer to the Tb(III) cyclen complex. This conformational change

facilitates more efficient energy transfer from the azaxanthone antenna to the Tb(III) excited state and hence the Tb(III) emission is "switched on". Moreover, this effect was not observed upon the addition of Na(I), Li(I), Mg(I) and Ca(I), with the complex **24** detecting K(I) with a 93-, 260-, 105- and 61-fold selectivity respectively.



24

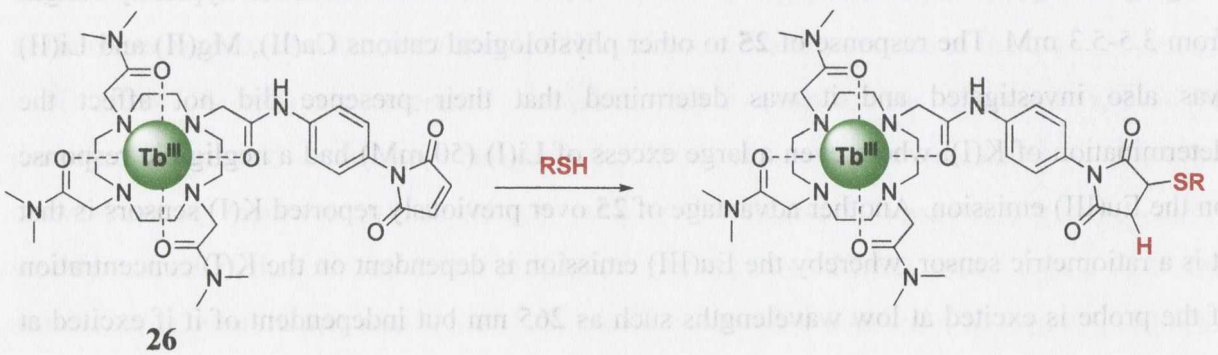


25

This design was further improved on by Pierre and co-workers, who developed **Eu·25**, a Eu(III) probe for the ratiometric detection of potassium in water.[65] This complex encompasses a Eu(III) metal centre for improved stability in biological media attached to a diaza-18-crown-6 receptor and a phenanathridine antenna. The antenna is conjugated to the crown ether in the 4 position *via* a methylene spacer which enables it to coordinate to the potassium once encapsulated within the crown ether. This added coordination effect gave rise to a high binding affinity of 26 ± 0.8 μM^{-1}, which enabled detection of K(I) in concentrations as low as 0-10 mM in water at physiological pH. This renders the complex **25** ideal for the imaging of K(I) in the extracellular environment, where its concentration typically ranges from 3.5-5.3 mM. The response of **25** to other physiological cations Ca(II), Mg(II) and Li(II) was also investigated and it was determined that their presence did not affect the determination of K(I), where even a large excess of Li(I) (50 mM) had a negligible response on the Eu(III) emission. Another advantage of **25** over previously reported K(I) sensors is that it is a ratiometric sensor, whereby the Eu(III) emission is dependent on the K(I) concentration if the probe is excited at low wavelengths such as 265 nm but independent of it if excited at 400 nm, a consequence of such is a more accurate determination of the level of K(I) in solutions.

McMahon *et al.*[66] reported the thiol sensor **26** for selective detection of biothiols, which has become an active area of research in recent years due to the strong link between intracellular thiols and a range of well-known diseases, including cancer, liver damage, cardiovascular disease and AIDS.[67,68] Cysteine (Cys), homocysteine (Hcy) and glutathione (GSH) are all potential thiol containing targets that are associated with the above conditions. **26** was designed on the basis that a 1,4-Michael addition,

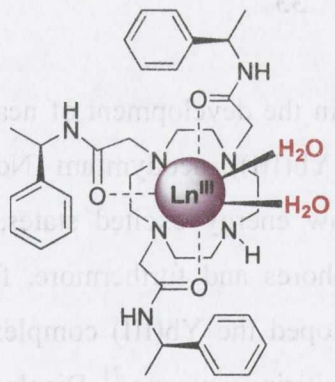
Scheme 1.4 1.4, would occur of the biothiol to the electron deficient alkene bond of the maleimide functionality which would bear significant consequences on the energy transfer process from the phenyl antenna to the Tb(III) metal centre and in turn effect the Tb(III) emission. Studies into the detection of the sulfhydryl residues of GSH, Cys and Hcy were carried out and significant increase of 525%, 500% and 230% in the Tb(III) emission were observed, respectively, upon their addition. It was suggested that the enhancement in the Tb(III) emission was caused by a more efficient energy transfer process occurring upon saturation of the alkene bond of the maleimide ring. Moreover, the increase in emission levelled off after the addition of one equivalent of the thiol, confirming the formation of the 1:1 **26**:RSH adduct in solution. A series of lifetime measurements were undertaken to confirm that the increase in emission intensity was a result of adduct formation and not displacement of the metal bound water molecule. Lifetimes were recorded in H_2O and D_2O in the presence and absence of GSH, Cys and Hcy molecules and it was discovered that even in high excess of GSH, Cys and Hcy, the *q* value remained the same; hence, the hydration state of **26** did not change upon reduction of the malemide unit. Selectivity studies verified negligible modulation in the Tb(III) emission by all other non-thiol based amino acids, confirming the 1,4-Michael addition detection mechanism at the maleimide site was discriminative for sufhydryl based molecules only. Another major observation in the analysis of **26** was that it was able to distinguish GSH from its disulphide GSSH form. Titrations showed that even in the presence of a high excess of GSSH, no substantial increase in the luminescence properties of **26** was observed; a discovery which highlights its potential to be used in cellular studies.



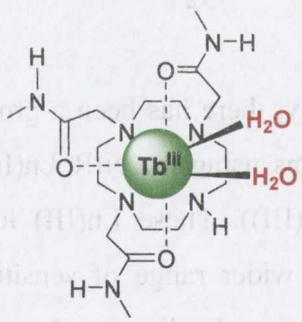
26

Scheme 1.4: *1,4-Michael addition of RSH to the maleimide functionality of the thiol probe* ***26****.*

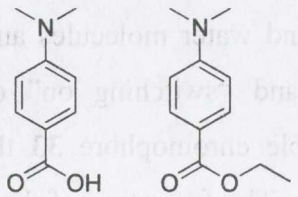
Another approach in the sensing of analytes involves the use of coordinatively unsaturated systems that upon analyte binding cause displacement of the metal bound water molecules, resulting in subsequent modulation of the Ln(III) emission. One example of this type is the Eu(III) and Tb(III) complexes of **27**, designed by Parker and co-workers.[69,70] Without any external analyte present, the complexes **Eu·27** and **Tb·27** display only very weak Ln(III) emission, due to the presence of the two metal bound water molecules. Displacement of these water molecules by anions would be signalled by an increase in the emission intensity, excited state lifetimes and q values of the complexes. The authors reported investigations into the study of the reversible binding of common bioactive oxyanions in aqueous solution to the cationic Ln(III) centre. When the anions I^-, Br^-, Cl^- and NO_3^- were studied it was discovered that the excited state lifetimes remained unchanged. In contrast, the anions F^-, acetate and sulphate were in competition in binding to the Ln(III) with the metal bound water molecule, which resulted in displacement of one water molecule. Most notably, the addition of hydrogencarbonate and carbonate caused displacement of both water molecules, resulting in a large change in the excited state lifetime values. It was suggested that a chelating adduct was forming between **27-Eu** and HCO_3^-/CO_3^{2-} with evidence for this provided by a marked change in the hypersensitive $J = 2$ transition at 618 nm which is known to be particularly sensitive to the coordination environment around the Ln(III) metal centre.



27

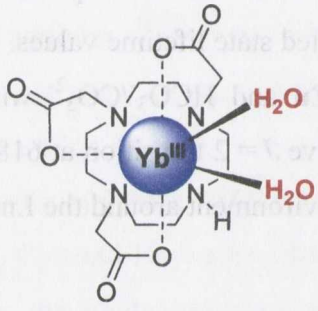


28

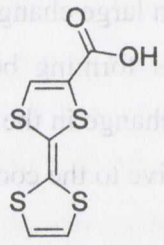


29 **30** **31**

A similar approach was also undertaken by Gunnlaugsson *et al.*[14] in the development of complex **28**. This complex contains no antenna moiety directly bound to the Tb(III) centre, instead the aromatic carboxylate analytes **29** and **31** would act as the sensitising antenna. Prior to the addition of these analytes, the complex **28** is "photophysically silent", however upon anion binding the two metal bound water molecules are displaced and a ternary complex is formed. Efficient population of the Tb(III) excited state can then occur *via* indirect excitation of the benzylic antenna, causing a "switching on" effect of the Tb(III) emission. Excited state lifetime measurements are in agreement with the formation of this self-assembly whereby the *q* value of the complex decreases from two to zero, indicating that chelation of the carboxylate to the Tb(III) centre *via* the formation of a four-member bidentate ring chelate. This binding process was verified by photophysical evaluation of the ester analogue, **30**, upon addition to **28** where no displacement of the water molecules took place, and consequently, there was no modulation in the Tb(III) emission or lifetimes of the complex.

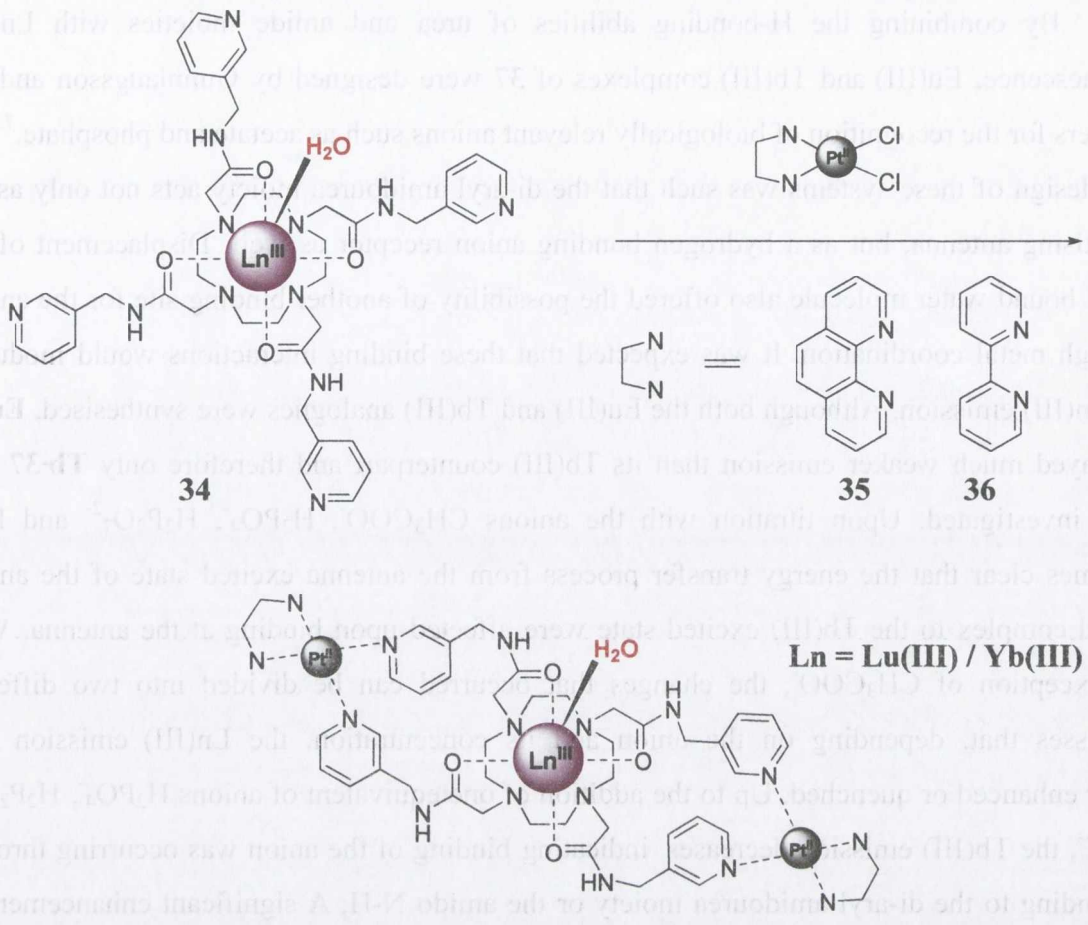


32



33

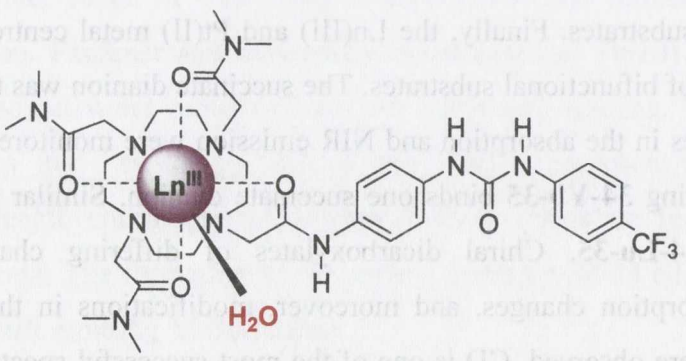
More recently, there has been a growing interest in the development of near-infrared (NIR) Ln(III) systems using the NIR Ln(III) ytterbium (Yb(III)), neodymium (Nd(III)) and praseodymium (Pm(III)). These Ln(III) ions possess low energy excited states, enabling compatibity with a wider range of sensitising chromophores and furthermore, facilitating grater tissue penetration. Faulkner and co-workers developed the Yb(III) complex **32**, that possesses two metal bound water molecules and no sensitising antenna.[71] Displacement of these water molecules and "switching on" of the Yb(III) emission was achieved by coordination of the visible chromophore **33** through the carboxylate functionality of the tetrathiafulvalene antenna. The formation of the ternary complex **32-33** allowed for efficient energy transfer to the NIR emitting Yb(III) metal.



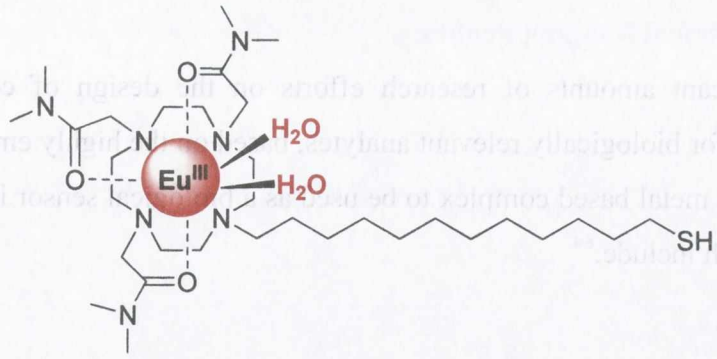
Scheme 1.5: *Coordination of Pt(II) complexes to* ***34****.*

Tsukube and co-workers combined a Ln(III) based cyclen complex with a chromophoric platinum complex yielding the mixed metal receptor system **Ln·34**, capable of forming 1:1 complexes with dicarboxylates.[72] This complex possesses several features that assist in its ability to effectively bind bifunctional substrates. These include an unsaturated Ln(III) coordination environment containing one metal bound water molecule capable of metal dissociation; the Pt(II) coordinating complexes **35-36**, Scheme 1.5, can act as potential binding sites for substrates. Finally, the Ln(III) and Pt(II) metal centres permit chain-length selective binding of bifunctional substrates. The succinate dianion was titrated against **34-Yb-35** and the changes in the absorption and NIR emission were monitored, with changes in the absorption indicating **34-Yb-35** binds one succinate dianion. Similar spectral changes were also seen for **34-Lu-35**. Chiral dicarboxylates of differing chain lengths displayed characteristic absorption changes, and moreover, modifications in their circular dichroism (CD) spectrum were observed. CD is one of the most successful spectroscopic techniques in determining the absolute configuration of substrates. The authors have succeeded in the development of a new type of CD chirality probes and the CD response observed is dependent on the chain length and chirality of the dicarboxylate substrate in question.

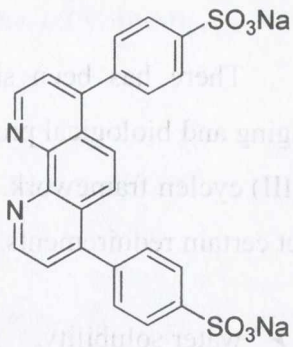
By combining the H-bonding abilities of urea and amide moieties with Ln(III) luminescence, Eu(III) and Tb(III) complexes of **37** were designed by Gunnlaugsson and co-workers for the recognition of biologically relevant anions such as acetate and phosphate.[73] The design of these systems was such that the di-aryl amidourea moiety acts not only as the sensitising antenna, but as a hydrogen bonding anion receptor as well. Displacement of the metal bound water molecule also offered the possibility of another binding site for the anions through metal coordination. It was expected that these binding interactions would modulate the Ln(III) emission. Although both the Eu(III) and Tb(III) analogues were synthesised, **Eu·37** displayed much weaker emission than its Tb(III) counterpart and therefore only **Tb·37** was fully investigated. Upon titration with the anions CH_3COO^-, $H_2PO_4^-$, $H_2P_2O_7^{2-}$ and F^- it becomes clear that the energy transfer process from the antenna excited state of the anion-bound complex to the Tb(III) excited state were affected upon binding at the antenna. With the exception of CH_3COO^-, the changes that occurred can be divided into two different processes that, depending on the anion and its concentration, the Ln(III) emission was either enhanced or quenched. Up to the addition of one equivalent of anions $H_2PO_4^-$, $H_2P_2O_7^{2-}$ and F^-, the Tb(III) emission decreases, indicating binding of the anion was occurring through H-bonding to the di-aryl amidourea moiety or the amido N-H. A significant enhancement in the Tb(III) emission intensity was observed at higher anion concentrations, which was attributed to direct binding of the anions to the metal centre. In the case of CH_3COO^-, the Tb(III) emission intensity was quenched by *ca.* 56% indicating that the binding only occurred through hydrogen bonding and not through metal coordination. In summary, it was established that the complex **37-Tb** could bind anions *via* multiple binding interactions involving hydrogen binding, which resulted in a decrease in the Tb(III) emission and direct metal coordination, causing enhancements in the Tb(III) emission.



37



38



39

Complex **38** was developed as a luminescent Ln(III) sensor for the detection of *d*-metal ions by means of a displacement assay.[74] The Eu(III) complex **38** possesses two metal bound water molecules and no sensitising antenna, giving rise to very weak Eu(III) luminescence (λ_{ex} = 278 nm). The external antenna 4,7-diphenyl-1,10-phenanthroline-disulfonate, BPS (**39**) was chosen as it is a known Eu(III) sensitiser and moreover, it has been recognised for its selective colourimetric sensing of Fe(II).[75,76] First, the formation of the 1:1 ternary complex **38**-BPS was observed in buffered pH 7.4 solution by monitoring the evolution of the Eu(III) emission, which was found to have reached a maximum after the addition of one equivalent of BPS. The photophysical properties of **38**-BPS was then evaluated in the presence of a number of metal (II) cations such as Ca, Cd, Co, Cu, Fe, Mg, Ni and Zn. The addition of Fe(II) caused a significant decrease in the Eu(III) emission before reaching a plateau at *ca.* 0.33 equivalents, indicating displacement of the BPS from **38** and the formation of a BPS Fe(II) complex in a 3:1 stoichiometry. The addition of metal ions of similar affinity to Fe(II) such as Co(II), Cu(II) and Ni(II) caused a comparable decrease in the Eu(III) emission. However, only very minor changes were observed in the absorption spectrum. The authors also demonstrated the sensing ability of **38**-BPS for Fe(II) in the presence of various anions including carbonate, lactate, citrate and phosphate, and no considerable changes in the absorption or fluorescence were detected, while the Eu(III) emission experienced minor decreases (5-10%) in intensity. The complex **38**-BPS has been shown to give both good selectivity and effective sensitivity for Fe(II) in competitive media, and was the first example of a Ln(III) luminescent displacement assay for biologically active *d*-metal cations.

As discussed previously, Ln(III) complexes can be highly luminescent and exhibit excited state lifetimes in the millisecond range which enables them to overcome autofluorescence from biological measurement and hence detect biomolecules. It is therefore obvious that Ln(III) complexes appear promising for cellular imaging and other biological applications, some examples of which will be discussed in the following section.

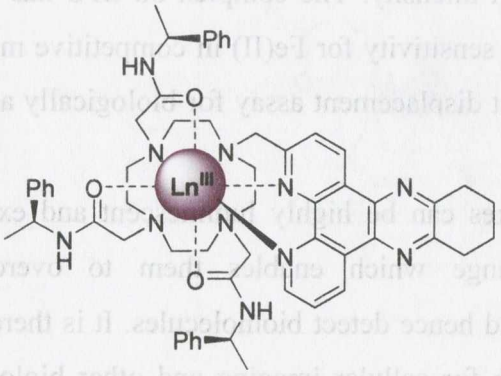
1.5.3 Lanthanide Based Biological Imaging Probes

There has been significant amounts of research efforts on the design of cellular imaging and biological probes, for biologically relevant analytes, based on the highly emissive Ln(III) cyclen framework. For a metal based complex to be used as a biological sensor it must meet certain requirements, which include:[64]

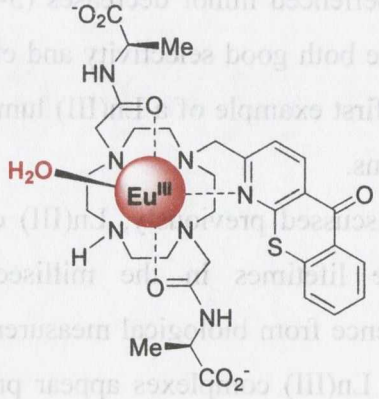
- water solubility,
- high selectivity for the target substrate in question,
- reversible binding of the substrate for real time measurements,
- high thermodynamic and kinetic stability,
- low toxicity and
- high cell permeability.

The Parker research group has been involved in the development of Ln(III) complexes for the purpose of biological probing.[77,78] One such example is the complex **40**, where the Eu(III), Tb(III) and Yb(III) complexes were synthesised and investigated for their potential to enantioselectively bind to human serum albumin (HSA).[79,80] In this case, the NMR technique of saturation transfer difference (STD) was employed to investigate if these complexes bind to the protein. STD allows the detection of transient binding of small molecule ligands to macromolecular receptors, *i.e.* proteins and can be used to determine which part of the complex is responsible for binding to the protein, since the most strongly interacting groups of the complex will show stronger STD effect and requires the use of a diamagnetic ion Yb(III). Both the *SSS*- and *RRR*-isomers were studied and it was discovered that the *SSS*-isomer associates selectively with the HSA compared to the *RRR*-enantiomer, and moreover, the drug site II of the protein was identified as directly interacting with the complex **40**, principally through the phenyl methyl pendant arms and the aromatic region of the chromophore.

Complex **41** was also developed by Parker and co-workers for use in a Eu(III)



40



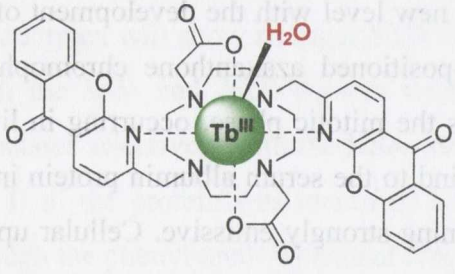
41

luminescence assay for the analysis of citrate in biological fluids.[81,82] Citrate detection is of importance as the levels of citrate are significantly reduced in prostate cancer tissue, and hence it can be used as a viable diagnostic marker for prostate cancer.[83] Preliminary studies carried out ascertained that lactate was the main interferent in the sensing of citrate. However, the selectivity for citrate over lactate was found to be 89:1, which should minimise interference from variable sample lactate concentrations. Eu(III) emission profiles in differing concentrations of citrate (0.08 and 0.45 mM) revealed considerable changes in the ratio of the intensity of the various emission bands, in particular, the intensity of the hypersensitive $J = 2$ transition was increased relative to the $J = 1$ transition at higher citrate concentrations. These modifications in the intensity ratios were associated with the selective and reversible binding of citrate to the Eu(III) metal centre, which occurs through the formation of a 5-membered ring chelate of the citrate molecule in a similar manner to that previously shown. The authors discovered that, owing to the markedly different Eu(III) emission spectra, they were able to distinguish the **41**-citrate adduct from that of the corresponding carbonate, lactate and phosphate ternary complexes. Enzymatic assays, based on the activity of citrate lyase, were undertaken and were found to verify the citrate concentrations obtained using the Eu(III) luminescence assay. The luminescence analytical method developed had two clear advantages over enzymatic studies; firstly, it took less time (ten minutes) to complete than the enzymatic study, which took three hours in total and secondly, it required smaller sample amounts and fewer preparation steps.

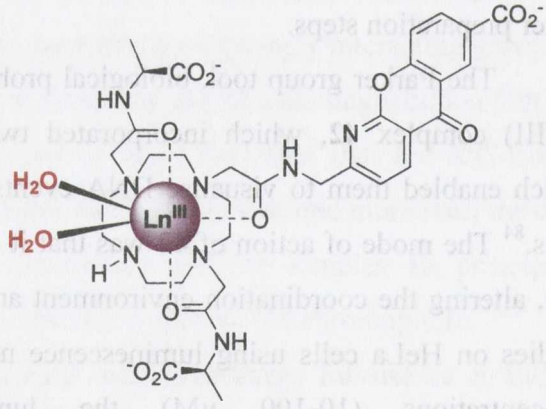
The Parker group took biological probing to a new level with the development of the Tb(III) complex **42**, which incorporated two *trans*-positioned azaxanthone chromophores which enabled them to visualise DNA events such as the mitotic phase, occurring in living cells.[84] The mode of action of **42** was that it would bind to the serum albumin protein in the cell, altering the coordination environment and remaining strongly emissive. Cellular uptake studies on HeLa cells using luminescence microscopy demonstrated that at relatively high concentrations (10-100 μM) the luminescent staining was consistent with endosomal/liposomal distribution, whereas at much lower concentrations (<1 μM), less than 10% of the observed cells were stained. It was concluded from these studies that the pattern of staining, along with the type of nuclear localisation profile, was consistent with cells going through division in the 'M' phase of the mitotic cycle. Furthermore, the low toxicity value (IC_{50} > 400 μM) was estimated for complex **42**. Higher resolution luminescence studies allowed the authors to follow the lifetime of a single cell stained with **42** in a cell growth medium at five minute intervals. The evolution of the cell cycle from prophase to metaphase was clearly witnessed; however the investigation was discontinued after an hour due to the

phototoxicity associated with the intensity of the laser source used. Future work involved investigating the use of less intense irradiation to avoid this phototoxicity.

In comparison to **42**, **43**, also developed by Parker and co-workers, acts within the mitochondrial region of living cells to signal changes in bicarbonate levels.[85] The amide-linked azaxanthone sensitising moiety was incorporated into the Eu(III) complex as it had been previously demonstrated to promote uptake and staining of the probe in the mitochondria of cells.[78] *In vitro* studies were carried out where the changes in the Ln(III) emission were monitored as a function of various biological analytes, including bicarbonate, HSA, citrate, lactate and phosphate. The largest changes were observed upon the addition of bicarbonate, where the ratio of the $J = 1$:$J = 2$ band changes from 2:1 to >4:1 upon addition of the bicarbonate and displacement of the water molecules. The addition of HSA (20 μM) to **43** gave rise to reduction in Eu(III) emission in conjunction with a spectral change, with the former being attributed to the quenching of the azaxanthone triplet state by a charge transfer process from the electron rich residues in the protein. Cellular incubation studies using various cell lines, accompanied by co-localisation studies verified localisation of **42** within the mitochondrial region of the cells. The percentage of CO_2 in the incubation centre was altered and the Eu(III) emission was found to increase with increasing pCO_2, which the authors suggest may be attributed to a rise in the steady state bicarbonate concentration.



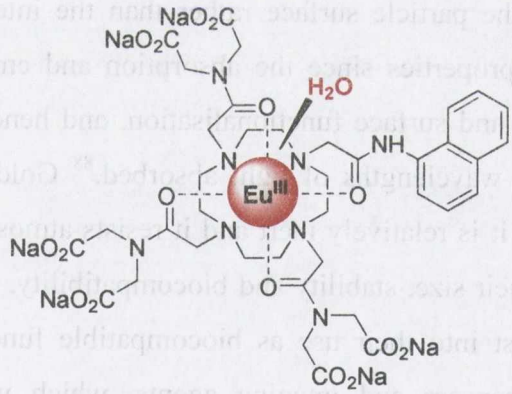
42



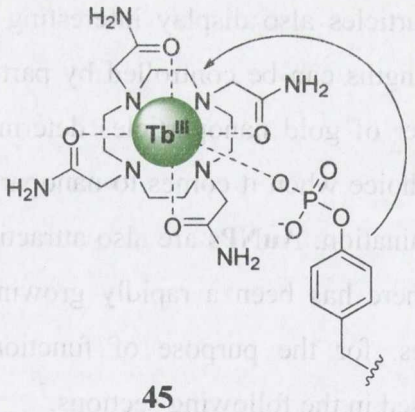
43

Ln(III) based biological probes have also been developed within the Gunnlaugsson group. The Eu(III) complex **44**, studied by Mc Mahon *et al.*[86] incorporates a naphthalene antenna, capable of Eu(III) sensitisation and three iminodiacetate moieties, for the binding of the exposed Ca(II) in microdamaged bone samples. Before examining **44** as a contrast imaging agent, its luminescence behaviour was investigated as a function of pH and in the presence of other metal ions, which results from the former showed that Eu(III) emission was

"switched on" within the physiological pH range and "switched off" in acidic conditions below pH 5 and basic media above pH 8. The metal ion studies involving selective group I, II and *d*-metal ions were carried out. The metal ions Ca(II), Mg(II), Cd(II) and Zn(II) caused no changes in the Eu(III) emission whereas Cu(II), Hg(II), Fe(II), Co(II) and Ni(II) caused a minor reduction in the Eu(III) emission intensity. Luminescent solid state bone studies were carried out to evaluate the effectiveness of **44** as an imaging agent for microcrack damaged bone. The Eu(III) emission spectra were recorded on scratched and smooth surfaces of the bone over various time periods, with significantly larger emission intensities being observed within the scratched region. To ensure that chelation to the Ca(II) in the damaged bone region was occurring through the iminodiacetate moieties, analysis of the corresponding esters were also carried out; the results from which confirmed no significant interaction of the iminodiacetate functionalities with the bone's structure in their ester form. The next imaging technique employed was confocal fluorescence laser scanning microscopy. A 28-fold enhancement in the Eu(III) emission intensity was observed in the microscratched region in comparison to the healthy bone sample. In agreement with the solid state studies, the ester analogue showed no significant contrast between damaged and healthy bone samples.



44



45

The Tb(III) complex **45** was designed by Komiyama and co-workers for the purpose of selectively detecting phosphotyrosine (pTyr) in the presence of various phosphorylated amino acids. Tyrosine functions as a receiver of phosphate groups that are transferred by way of protein kinases, a process that is central in cellular regulation. With pTyr accounting for less than 1% of the total phosphorylated amino acids in humans, selective detection of it is difficult leading to a relatively poor understanding of its role in cellular biology. The detection of pTyr was achieved using complex **45**, which bound through its phosphate group, displacing the single metal bound water molecule. Additionally, the distance between the Tb(III) centre

and the phenyl ring is short enough to facilitate energy transfer to the Tb(III) centre, resulting in a significant increase in the Tb(III) emission. There is selectivity towards pTyr over the nonphosphorylated Tyr as it has no phoshate group capable of binding to the Tb(III) centre and furthermore, no emission enhancement will be observed in the presence of other phosphorylated amino acids such as pSer and pThr as they possess no antenna capable of Ln(III) sensitisation.

When it comes to the selective sensing of biological molecules, the incorporation of sensors, such as those described above, onto solid surfaces such as nanomaterials is highly desirable as larger structures are often favoured over smaller molecules. Previously, such nanostructures have included gold nanoparticles (**AuNPs**) and nanotubes.[7] This is a new and an exciting area within the field of supramolecular chemistry and provides an additional application element to such sensors.

1.6 Gold Nanoparticles

Nanoparticles are particles with size in the range of 1-100 nm in at least one of three dimensions. They have large surface area per unit volume and display vast morphological diversity.[7] The unique physical, chemical and biological properties of nanoparticles stem from the presence of a high fraction of atoms on the particle surface rather than the interior.[87] Nanoparticles also display interesting optical properties since the absorption and emission wavelengths can be controlled by particle size and surface functionalisation, and hence, the diameter of gold nanoparticles determines the wavelengths of light absorbed.[88] Gold is an ideal choice when it comes to nanoparticles as it is relatively inert and it resists atmospheric contamination. **AuNPs** are also attractive for their size, stability and biocompatibility, and as such there has been a rapidly growing interest into their use as biocompatible functional surfaces, for the purpose of functionalised sensors and imaging agents, which will be discussed in the following sections.[7]

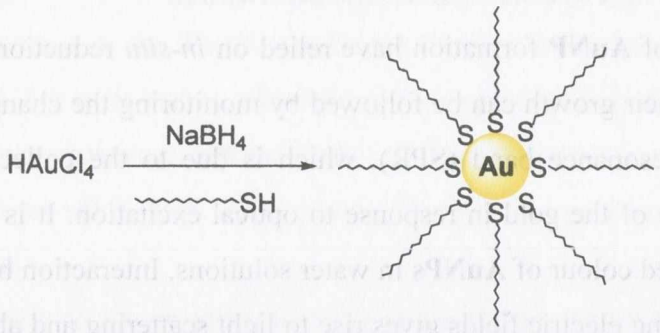
AuNPs have been investigated for a long period of time.[7] Colloidal gold has been used for centuries to make ruby glass and in the colouring of ceramics. The first reported preparation of pure colloidal gold was by Michael Faraday in 1857, which he described as 'activated gold'.[89] He used phosphorus to reduce a solution of gold chloride and was the first to recognise that the colour was due to the minute size of the gold particles. Further development led to Turkevich *et al.* producing spherical **AuNPs**,[90] and, by 1973 Frens was able to control the average particle size.[91]

1.6.1 AuNPs: Properties, Synthesis and Characterisation

Most methods of **AuNP** formation have relied on *in-situ* reduction of Au(III) salt *via* chemical means, and their growth can be followed by monitoring the change in absorbance of the surface plasmon resonance band (SPR), which is due to the collective oscillations of electrons at the surface of the gold in response to optical excitation. It is this SPR band that gives rise to the deep red colour of **AuNPs** in water solutions. Interaction between the incident light and these oscillating electric fields gives rise to light scattering and absorption and hence the optical properties of **AuNPs** can be monitored by UV-vis absorption spectroscopy. The SPR is sensitive to shape and so is constantly changing as the **AuNPs** are being formed.[92] When the SPR no longer changes it is presumed that all of the gold has been consumed to form **AuNPs**. This SPR band usually occurs with a λ_{max} between 520-530 nm for **AuNPs** that are between 5-20 nm in diameter in size, with 5 nm **AuNPs** having their SPR band at 520 nm whereas larger 20 nm **AuNPs** have a λ_{max} at *ca.* 530 nm. The number of atoms in **AuNPs** can be calculated from the radius of the **AuNP** atoms and clusters as determined by TEM analysis.[93] For example Pikramenou and co-workers determined that **AuNP** clusters with a radius of 6.5 nm consisted of 106 801 gold atoms *per* **NP**. [93]

In general, well known preparation methods of **AuNPs** involve the nucleation and growth of gold clusters from the reduction of a gold salt, such as ($HAuCl_4 \cdot H_2O$) with an attempt to control the size and shape of the **AuNPs** produced.[94] In addition to a reducing agent, the use of a stabilising agent is also essential that can either be adsorbed or chemically bound to the surface of the **AuNPs**. This stabilising agent (also known as a surfactant) is usually charged, ensuring that the equally charged **AuNPs** repel each other, prevent aggregation and remain stable in solution.

One of the most commonly used methods of **AuNP** synthesis is the so called 'citrate method' developed by Turkevich *et al.*[95] which involves the simultaneous reduction and stabilisation of the **AuNPs** in aqueous solution using sodium citrate and gives rise to **AuNPs** with an average diameter of *ca.* 20 nm. An important aspect of this technique is the ability to tune the size of the **AuNP** based on the gold/citrate ratio used; higher ratios of citrate produce smaller **AuNPs** owing to increased stabilisation. Although the citrate acts as a stabiliser for the **AuNPs**, it can readily be displaced by ligands possessing a higher affinity for **AuNPs**, such as thiol containing ligands, and as such this method prepares suitable precursor **AuNPs** to valuable **AuNP**-based systems.



Scheme 1.6: *Formation of **AuNPs** coated with organic shells by reduction of Au(III) in the presence of thiols.*

Another well-established method for the synthesis of **AuNPs** is the so called 'Brust-Schiffrin method', which was the first procedure that yielded thermally stable and air-stable **AuNPs** of reduced dispersity and controlled size (ranging from 1.5-5.2 nm in diameter). In comparison to the 'citrate method' the 'Brust method' requires the use of a two phase aqueous/organic solvent system, where in an aqueous solution, hydrogen tetrachloroaurate is mixed with an organic solution of tetraoctylammonium bromide (TOAB) in toluene. The TOAB acts as a transfer agent and by means of surfactant stabilisation, transfers the gold into the organic solution from the aqueous environment. Once stabilised within the organic layer, the gold is reduced by the addition of sodium borohydride ($NaBH_4$) and **AuNPs** are formed. Subsequent stabilisation of these nanoparticles can be achieved through various approaches, Scheme 1.6.

Following the successful synthesis, the **AuNPs** are left encased by a shell of stabilising molecules which can be replaced by other stabiliser molecules or ligands in a ligand exchange reaction, in a similar manner to that seen in the citrate method. It is well established that thiol moieties bind with high affinity to the surface of **AuNPs** due to the soft character of both gold and sulphur, hence thiol containing ligands are commonly used in such a ligand exchange. The properties of **AuNPs** are governed by the ligand attached to its surface. For example, water soluble **AuNPs** can be transferred to organic solution by the addition of a hydrophobic surfactant. In this sense, by altering the surfactant molecule it is possible to adjust the surface properties of the particles.

Caruso *et al.*[96] demonstrated complete transfer of **AuNPs** across the phase boundary by ligand exchange using 4-dimethylaminopyridine (DMAP), replacing the need for covalent interactions in the stablisiation process.[97] It was found that the transferred particles were stable after six months and the authors have stated that they expected them to be indefinitely stable. As discussed above, the most successful methods in stabilising **AuNPs** involves the use of thiol based ligands. However, a variety of alternative methods have recently been developed

that involve the use of reducing agents and stabilisers including polystyrene[98], triphenyl phosphine[99], amino acids[100], polyelectrolytes[101] and certain biomolecules.[94]

With the field of functionalised **AuNPs** ever growing, the ability to fully and accurately characterise these particles both in solution and in the solid state has become of tremendous importance. Characterisation of the **AuNPs** in solution is achieved by UV-vis absorption spectroscopy of the **AuNP** suspensions, as the SPR band is a well-studied characteristic of **AuNPs**, as discussed above. If the **AuNPs** are disperse in solution the SPR band will be a single, defined peak, however if aggregation of the **AuNPs** is occurring this band will become red shifted and may broaden with the occurrence of one or more peaks. Information regarding the size, concentration and aggregation of the **AuNPs** is critical in the study of these particles and UV-vis absorption spectra is one method in which to analyse these properties.

Dynamic light scattering (DLS) is a technique that also uses **AuNP** solutions for the determination of characteristics such as zeta potential and hydrodynamic radius from the diffusion coefficients of solutions of the nanoparticles. In this technique the sample is illuminated by a laser source, and the intensity of resulting light fluctuates at a rate that is proportional to the size of molecules in solution.[102] For investigations into the solid state of **AuNPs**, and imaging of the gold core, transmission electron microscopy (TEM) is employed, a microscopy technique whereby a beam of electrons is transmitted through an ultra-thin sample of **AuNPs**, interacting with them as they pass through. An image is formed from the interaction of the electrons transmitted through the **AuNPs**, which is magnified and focused onto an imaging device, such as a fluorescent screen.

As previously discussed, a significant feature of **AuNPs** is their ability to be functionalised with organic molecules. The combination of the biocompatible nature of the **AuNPs** with the intrinsic functionalities of organic and biomolecular systems offers a novel type of functional hybrid nanomaterial, with the potential use in sensing of biological substrates and as a novel method of drug delivery.[103,104] Examples of such will be discussed in the following section.

1.6.2 AuNP Probes

As discussed above, the optical properties of **AuNPs** differ depending on their size, shape, degree of aggregation and the characteristics of the organic shells on their surface.[94,105] This unusual optical variation has led to **AuNPs** being extensively investigated as probes for sensing and imaging for a variety of analytes including heavy metallic cations,[106] nucleic acids, proteins[107] and cells[108] *etc.*

Frequently encountered heavy metal cations such as Pb(II), Cr(II), Hg(II) and Ag(I) are known to be hazardous to the environment and also to public health when present in minute quantities in drinking water. Pb(II) is considered as being especially detrimental to human health, even causing mental retardation in children. Lin *et al.*[109] developed a **AuNP** based sensor for Pb(II), surface bifunctionalised with ([15]crown-5)$CH_2O(CH_2)_4SH$ (15C5) and thioctic acid (TA). In the absence of Pb(II), hydrogen bonding occurs between the carboxylic acid residues causing aggregation of the **AuNPs** as depicted in Figure 1.9 and the resulting solution was blue in colour. The Pb(II) has a high affinity for the 15C5 crown ether and TA moieties and the positive charge of the metal cation when bound causes electroststic repulsions between the **AuNPs**, leading to a very fast aggregation to dispersion transformation in conjunction with a blue to red change in the solution colour. Control experiments were carried out to prove the proposed mechanism of action by the carboxylic and crown ether moieties. To remove the effect of the carboxylic acid, **AuNPs** were synthesised containing a crown ether thiol with a twelve carbon spacer group instead of a four carbon one, so that the carboxylic acid moieties were encased within the organic shell. In 90% methanol the solution appears red, indicating interparticle hydrogen bonding by the carboxylic acid moieties is responsible for the aggregation that occurs. **AuNPs** were also synthesised without the crown ether moiety attached and upon the addition of Pb(II) no coordination and hence, no change in colour is observed, indicating no dispersion has occurred upon addition of the Pb(II). These findings confirm that both the carboxylic acid and crown ether moieties were essential in the sensing of Pb(II).

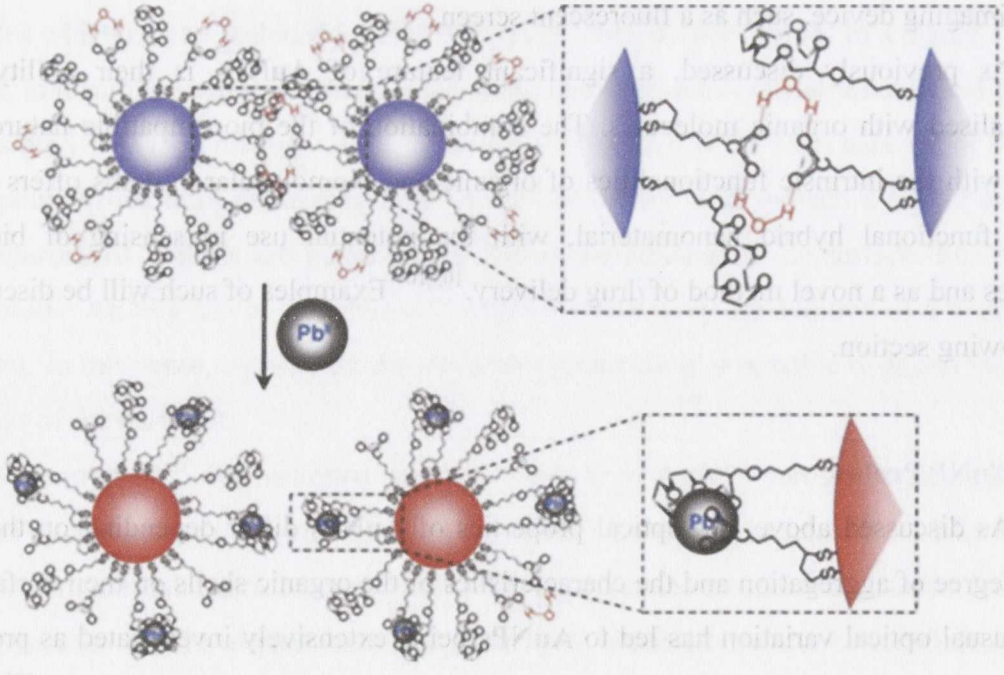


Figure 1.9: *Proposed mechanism of action for the recognition of Pb(II) by functionalised* ***AuNPs*** *in a methanol/water* solution.

The authors investigated the selectivity of this system towards other metal cations by measuring the relative amounts of aggregation and dispersion of the **AuNP** system with increasing concentrations of different metal cations, including Na(I), Cs(I), Ca(II), Ni(II), Zn(II), Cd(II), Hg(II) and Fe(II). They discovered that the ratio of aggregated:dispersed **AuNPs** rises sharply over a narrow range between 0.25 and 2.5 μM. In contrast, it is relatively unaffected by other metals at 100-fold higher concentration levels. Furthermore, the high extinction coefficient of the **AuNPs**, and the distinct colour changes observed permits the detection of Pb(II) at concentrations as low as 1 μM using the naked eye.

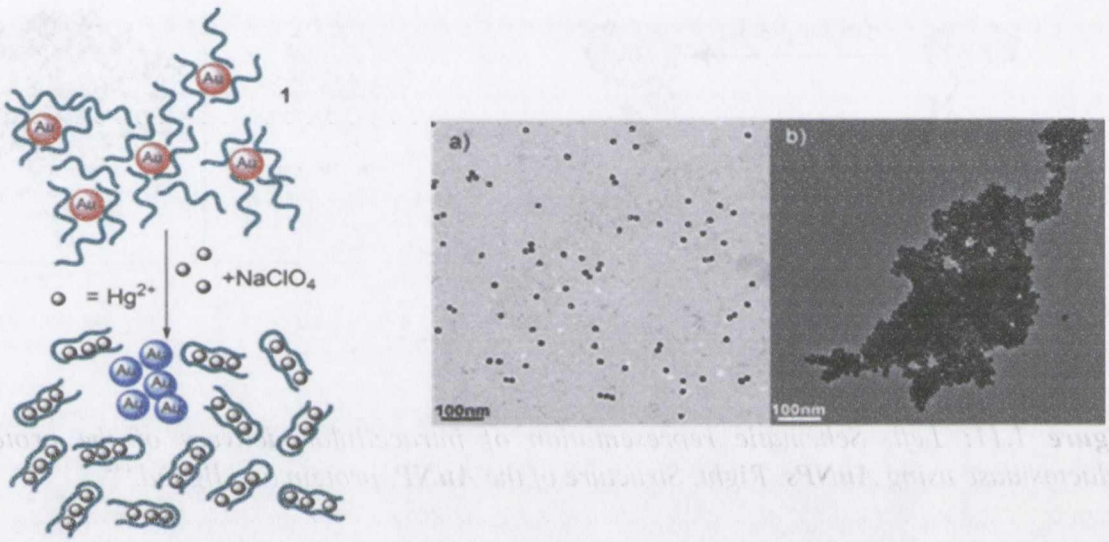


Figure 1.10: *Left. Hg(II) simulated aggregation of* ***AuNPs*** *Right. TEM images of a) dispersed* ***AuNPs*** *stabilised by* $NaClO_4$ *and b) aggregated* ***AuNPs*** *in the presence of Hg(II).*

The detection of Hg(II) is vital as mercury ions contribute extensively to environmental damage and can cause severe medical complications, leading to brain damage and other chronic diseases. Consequently, the analysis and detection of Hg(II) in water, food resources and in human fluids such as saliva is of significant diagnostic value. Recently, polymer DNA complexes have been utilised in the fluorescence detection of Hg(II) due to their ability to orientate into a 'hairpin' structure surrounding the Hg(II) metal ions. Li *et al.*[110] demonstrate the sensing of Hg(II) by optical methods based on the formation of **AuNP** aggregates the hairpin Hg(II)-bis-thymine complex. The system, depicted in Figure 1.10, shows that **AuNPs** coated with nucleic acid are stable and disperse in solution, even in the presence of excess $NaClO_4$ salt, giving rise to the TEM image a) in Figure 1.10. Addition of Hg(II) causes formation of the hairpin structure of the nucleic acid through complexation of Hg(II) with the T sites of the nucleic acid, which as a result is removed from the **AuNPs**. As the destabilising salt $NaClO_4$ is already present in solution, the **AuNPs** undergo aggregation in

concert with a colour change from red to blue. The aggregation was evident from the TEM images obtained (Figure 1.10b)) and also can be followed by UV-vis absorption spectroscopy, whereby higher concentrations of Hg(II) causes the SPR band to be red-shifted, along with a decrease in emission. Selectivity for Hg(II) was proven by screening other metal ions, which, with the exception of Pb(II), give rise to insignificant changes in comparison to those observed for Hg(II). Any interaction with Pb(II) was masked by the addition of 2,6-pyridinedicarboxylic acid (pdca) to the system. The concentration limit of detection of this **AuNP** system for Hg(II) was found to be 10 nM.

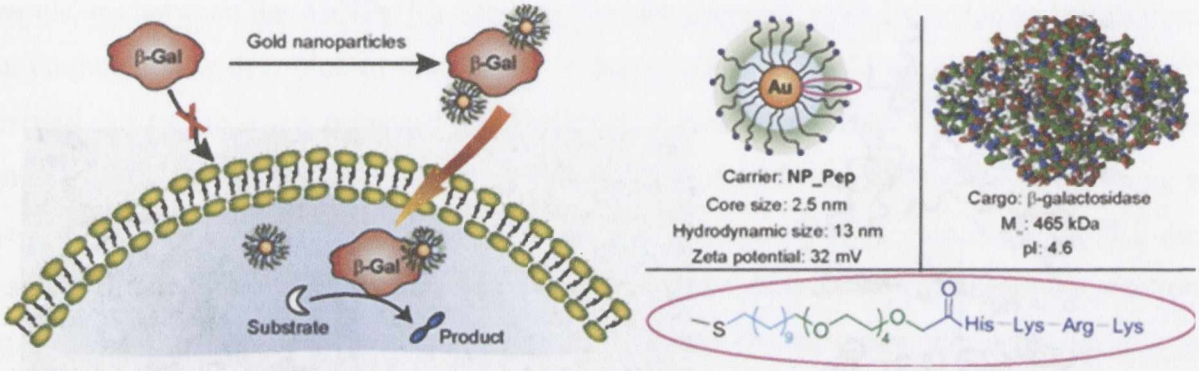


Figure 1.11: *Left. Schematic representation of intracellular delivery of the protein β-galactosidase using **AuNPs**. Right. Structure of the **AuNP**, protein and ligand.*[112]

Owing to their narrow size distribution and excellent biocompatibility, **AuNPs** have the potential to function as *in vivo* carriers of probes or substrates.[111] Rotello and co-workers have taken advantage of this potential and designed a **AuNP** system capable of intracellular delivery of the membrane impermeable enzyme β-galactosidase (β-gal).[112] **AuNPs** of diameter *ca.* 2.5 nm were synthesised and coated with a peptide incorporating operational regions; first a long alkyl chain providing stability to the core, tethered with a thiol group permitting attachment to the **AuNPs**, the next section consists of a chain of tetraethylene glycol (TEG) which prevents nonspecific interactions with biomolecules and denaturation, and finally the peripheral peptide tags function as a recognition unit (Figure 1.11). The peptide sequence used incorporated arginine, lysine and histidine residues; lysine coated **AuNPs** have been previously shown to be water stable[113] and His residues are known to assist endosomal escape of cargo.[114] Complexation of the **AuNPs** with β-gal was monitored by fluorescence, which was quenched due to the gold core and its cellular delivery monitored using FITC- β-gal as a fluorescent probe. HeLa cells were treated with the **AuNP**-β-gal system and green fluorescence was detected. To ensure the fluorescence was intracellular, confocal laser

scanning microscope (CLSM) studies were carried out and fluorescence was observed in the perinuclear regions of the cells, signifying protein internalisation. Having established that the β-gal enters the cells, the next, possibly most important test was to investigate if it retained its bioactivity. HeLa cells were incubated with **AuNP**-β-gal and then treated with X-gal, a colourless substrate for β-gal that upon enzymatic hydrolysis turns blue. Indeed, blue precipitates were observed inside those cells containing **AuNP**-β-gal, signifying preservation of enzymatic activity after delivery. Toxicity studies revealed no cell death after 24 hours of transfection. The efficienct delivery of β-gal and lack of toxicity reveals the potential for therapeutic applications of this strategy.

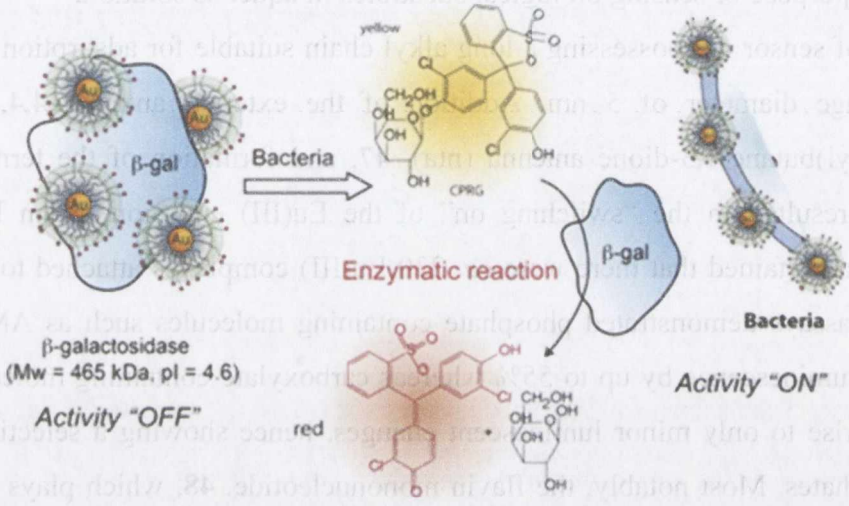
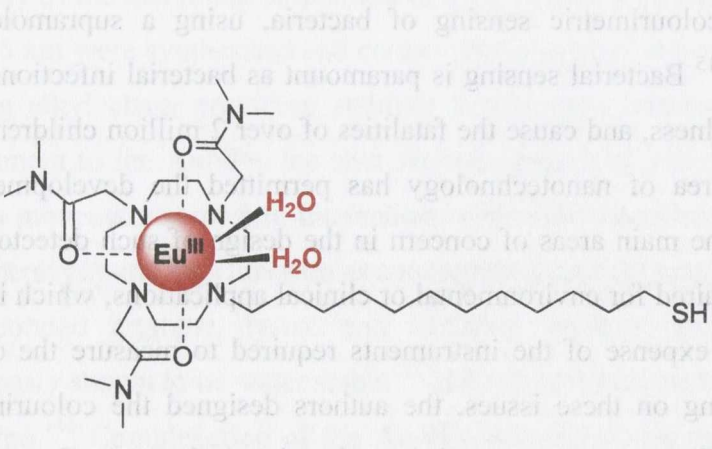


Figure 1.12: *The colourimetric sensing of bacteria, showing the relative sizes of the 2 nm core diameter* ***AuNPs*** *and β-gal.*

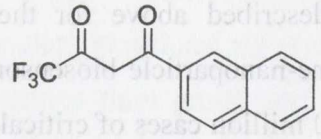
The Rotello group were also responsible for the development of a system similar to that described above for the colourimetric sensing of bacteria, using a supramolecular enzyme-nanoparticle biosensor.[115] Bacterial sensing is paramount as bacterial infections lead to 300 million cases of critical illness, and cause the fatalities of over 2 million children each year.[116] The ever developing area of nanotechnology has permitted the development of enhanced pathogen detection. The main areas of concern in the design of such detectors are the limit of detection (LOD) required for environmental or clinical applications, which is 10^4-10^2 cells/mL and secondly, the expense of the instruments required to measure the output should not be too high. Focusing on these issues, the authors designed the colourimetric sensor depicted in Figure 1.12. The sensor possessed three functional elements; first a β-gal enzyme to provide signal amplification, a chlorophenol red β-D-galactopyranoside (CPRG), a chromogenic substrate that produces a colourimetric response and finally, a cationic **AuNP** that binds reversibly to β-gal, inhibiting it without denaturation. To provide further

biocompatibility and stability, the **AuNPs** were functionalised with quaternary ammonium ligands. The resulting cationic nature of the **AuNPs** binds the anionic surfaces of the bacteria such as *Escherichia coli* (*E-coli*), resulting in displacement of β-gal, which is now free to convert the CPRG substrate from yellow to red, affording a colourimetric response. Having established the effectiveness of this bacterial sensing system, the authors next explored the application of their design to a test strip format which showed changes could be visually detected at concentrations of 10^4 bacteria/mL. The authors state that work is currently on going to improve the sensitivity of detection and also develop dual detection strategies.

Gunnlaugsson *et al.* were the first to combine **AuNPs** with the unique properties of the Ln(III) for the purpose of sensing biological substrates in aqueous solution.[117,118] This resulted in the design of sensor **46**, possessing a long alkyl chain suitable for adsorption onto **AuNPs** with an average diameter of 5 nm. Addition of the external antenna 4,4,4-trifluoro-1-(naphthalen-2-yl)butane-1,3-dione antenna (nta), **47**, and formation of the ternary complex **AuNP-46**-nta resulted in the "switching on" of the Eu(III) emission. From luminescence studies it was ascertained that there were *ca.* 230 Eu(III) complexes attached to each **AuNP**. Displacement assays demonstrated phosphate containing molecules such as AMP and ADP quenched the luminescence by up to 55% whereas carboxylate containing molecules such as creatine gave rise to only minor luminescent changes, hence showing a selective behaviour towards phosphates. Most notably, the flavin mononucleotide, **48**, which plays a key role in many biological processes such as electron transfer, oxidation and dehydrogenation processes, was found to be the only anion studied that was capable of efficiently displacing nta from **AuNP-46**-nta. This action resulted in an almost complete quenching of the Eu(III) emission caused by the formation of **AuNP-46-48**.



46



47



48

Building on this work, Comby *et al.*[107] used the same **AuNP** system to exploit the interactions with the protein bovine serum albumin (BSA), which is often used as a protein concentration standard. As in the previous example, **AuNP-46** is not luminescent due to the absence of a sensitising chromophore (and the presence of two metal bound water molecules). Addition of the external antenna **nta** formed the luminescent system **AuNP-46-nta**, characterised by the appearance of the Eu(III) emission bands between 570-720 nm upon excitation at 330 nm. The photophysical properties of **AuNP-46**-nta were investigated at physiological pH in the presence of BSA. The Eu(III) was found to be almost completely quenched upon the addition of *ca.* 150 equivalents of BSA. In order to determine the origin of the quenching, excitation spectra were recorded and binding constants for the systems **AuNP-46**-nta and **46**-nta were determined, neither of which supported the theory that displacement of nta by BSA was occurring, and that there was in fact an interaction taking place between nta and BSA on the surface of the **AuNP**, Figure 1.13. Analysis of the binding constant determined from the **AuNP-46**-nta-BSA indicated that the **AuNP-46**-nta system can act as an accurate reporter for the binding interaction of small molecules with proteins. The interaction of the "switched off" system, **AuNP-46**-nta-BSA, with other drugs and toxins was investigated. A "switch on" effect of the Eu(III) was observed upon the addition of the competitive drug ibuprofen while the anticoagulant warfarin had the contrary effect. This system exhibits the highly successful biosensing system using a combination of the unique properties that **AuNPs** and Ln(III) have to offer.

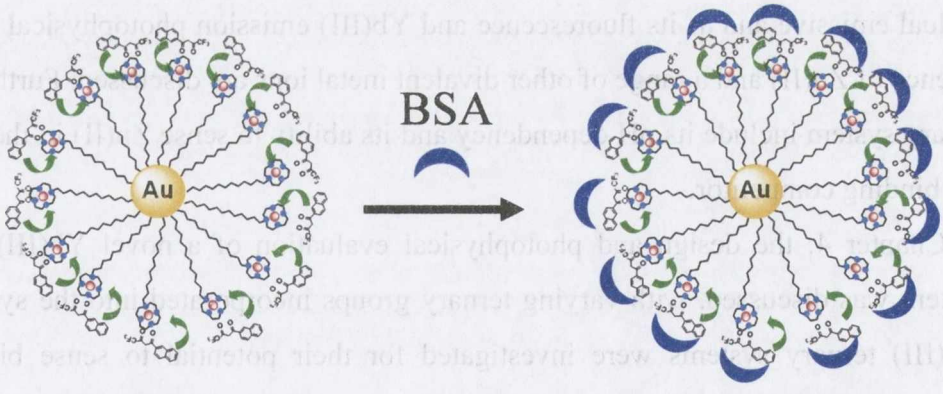


Figure 1.13: *Schematic representation of* ***AuNP-46-nta*** *and* ***AuNP-46-nta-BSA****.*

Bearing the above examples in mind, it is clear that the combination of Ln(III) and **AuNPs** is novel and extremely beneficial for the purpose of sensing biological analytes, and research is beginning to concentrate on investigation into functionalised **AuNP** for biological

applications. This project focuses on the design and development of such Ln(III) luminescent **AuNPs** and the exploration of such systems and their sensing abilities.

1.7 Work Described within this Thesis

The overall aim of this thesis is to build on previous work carried out within the Gunnlaugsson group by the design and synthesis of functional Ln(III) luminescent probes, both on and off the surface of **AuNPs**, with applications varying from the sensing of biologically important molecules to the immobilisation of such probes for material based applications. All systems described in this thesis will be based on the skeletal framework of the cyclen macrocycle, with modifications in the choice of Ln(III) and pendant arms, which will differ depending on the application required.

In Chapter 2, the design, synthesis and photophysical evaluation of a novel Ln(III) luminescent system is described before attachment of the complex onto the surface of **AuNPs** by means of the pendant arm terminating in a thiol group. Photophysical studies of the Ln(III) complex and corresponding water soluble **AuNP** Ln(III) system investigated include the determination of lifetimes and metal bound water molecules, pH dependency of these systems and analyte titrations to probe their sensing ability. Furthermore, studies into dual Ln(III) systems on **AuNPs** is also discussed.

In Chapter 3, the design of a NIR emitting Yb(III) ternary system arising from self-assembly in aqueous solution for the purpose of Zn(II) sensing is discussed. The ternary system is dual emissive and as its fluorescence and Yb(III) emission photophysical properties in the presence of Zn(II) and a range of other divalent metal ions are discussed. Further studies on the ternary system include its pH dependency and its ability to sense Zn(II) in the presence of a Zn(II) binding competitor.

In Chapter 4, the design and photophysical evaluation of a novel Yb(III) complex **AuNP** system was discussed, with varying ternary groups incorporated into the system. The **AuNP** Yb(III) ternary systems were investigated for their potential to sense biologically relevant molecules. The pH dependency of one of these ternary systems, including its "on/off" Yb(III) emission behaviour as a function of pH, was investigated in great detail.

In Chapter 5, work described focuses on the development of Ln(III) complexes suitable for the formation of Langmuir monolayers and subsequent Langmuir Blodgett (LB) film deposition onto quartz slides. These LB films were investigated fully photophysically and compared to that of the complexes in solution. The stability of the LB films was determined, along with a series of studies and tests aimed to examine the durability of the LB films in relation to their Ln(III) luminescence output.

In Chapter 6, the attempted synthesis of a Ln(III) complex for the purpose of mercury sensing will be discussed.

Finally, in Chapter 7, general experimental procedures are outlined and the synthesis and characterisation of each of the compounds is detailed.

Chapter 2

Lanthanide Functionalised AuNPs for Potential Sensing Applications

2. Introduction

The development of sensing devices that offer a luminescent output is ever active in the field of supramolecular chemistry. Among the countless sensors designed to date, substantial amounts have incorporated luminescent Ln(III) within their structure. Ln(III) possess unique and advantageous properties as was discussed in Chapter 1, such as line-like emission bands and long-lived excited states, of which the latter can be taken advantage of in the utilisation of time-resolved luminescence spectroscopy.[21] In concert with their benefits, there are also certain drawbacks that need to be taken into account when using Ln(III) ions. Free Ln(III) is toxic *in vivo* owing to their size similarity with Ca(II) and furthermore, their luminescence can be quenched by protic solvents *via* non-vibrational decay through the O-H oscillators. In order to overcome these drawbacks and employ Ln(III) *in vivo*, thermodynamically and kinetically stable complexes of the Ln(III) are essential, which can be attained through the incorporation of these ions into organic ligands. Cyclen (1,4,7,10-tetraazacyclododecane) derivatives are commonly used as ligands for Ln(III) ions due to their stability and ability to be easily functionalised.[119] Another major drawback related to the Ln(III) is that they have very low extinction coefficients, which leads to inefficient direct excitation.[120] This problem can be overcome by means of indirect excitation; whereby the excited state of the Ln(III) can be populated by energy transfer from the triplet excited state of an external antenna, giving rise to sensitised Ln(III) luminescence.[23,121] This can be accomplished by different approaches; firstly by coordination of the chromophore directly to the Ln(III) metal centre and secondly, by incorporation of the antenna into a macrocyclic framework, such as cyclen, through functionalisation of the macrocyclic ligand. A highly appealing feature of macrocyclic Ln(III) sensors is that selective analyte sensing can be achieved through modulation of the chromophore or simply by the number of chromophores attached. Subsequent addition of an analyte to the Ln(III) complex alters the Ln(III) emission output. In recent times, the field of sensing has begun to exploit nanomaterials as a platform for which to attach the sensors.[122]

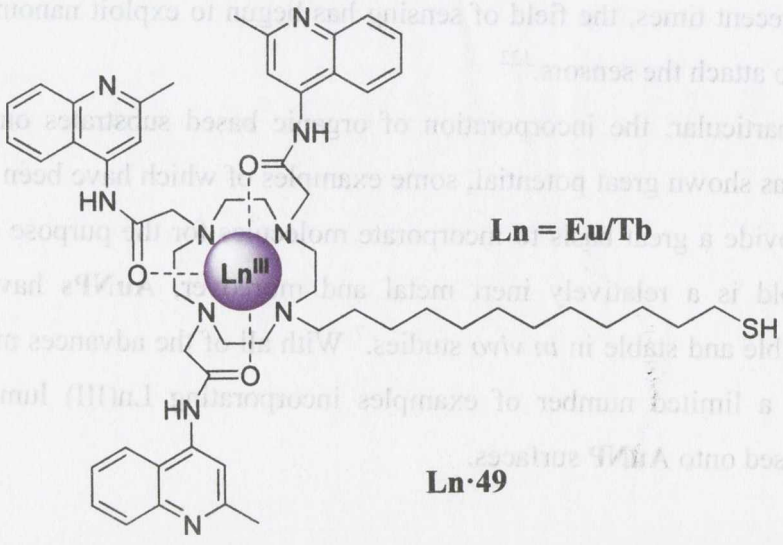
In particular, the incorporation of organic based substrates onto gold nanoparticles (**AuNPs**) has shown great potential, some examples of which have been detailed in Chapter 1. **AuNPs** provide a great basis to incorporate molecules for the purpose of sensing analytes *in vivo* as gold is a relatively inert metal and moreover, **AuNPs** have been shown to be biocompatible and stable in *in vivo* studies.[7] With all of the advances made in this area, there have been a limited number of examples incorporating Ln(III) luminescent architectures functionalised onto **AuNP** surfaces.

Keeping the above points in mind, and building on previous work reported by Gunnlaugsson and co-workers[117] the aim of this project was to develop a Ln(III) based luminescent sensor using the cyclen framework and modify its pendant arms to ensure suitability for both the sensing of substrates and attachment to **AuNPs**. The main areas which will be addressed in the design of such molecules will be:

- The ability to overcome short-lived biological background emission.
- pH independent nature within the physiological range.
- Efficient sensitisation of the Ln(III).
- Efficient sensing of biologically relevant substrates and signalling of their presence.
- Ability to attach to **AuNPs**.

2.1 Design of Ligand 49

The aim of this Chapter was to develop **Ln·49** for the purpose of forming Ln(III) luminescent **AuNPs** capable of sensing biological analytes such as acetate and ATP. The synthesis of **49** is shown in Scheme 2.2. The cyclen framework will be functionalised with suitable pendant arms so that the high coordination requirements of the Ln(III) are fulfilled, leaving the minimum number of metal bound water molecules. The main Ln(III) chosen for this project was Eu(III), due to its reduced sensitivity to oxygen quenching in comparison to Tb(III), however the Tb(III) complex of the ligand was investigated to a lesser extent. The quinaldine moiety **52** was chosen as a suitable antenna for the system due to the fact that its photophysical properties are such that efficient Eu(III) sensitisation can occur.[123] Another important reason for the choice of the quinaldine antenna was that our previous work had shown that these Ln(III) complexes possess little dependence on pH within the physiological pH range.[54,124]



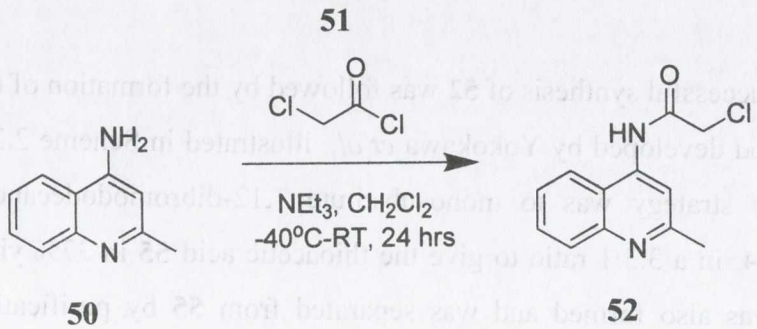
Ln·49

Ligand **49** is able to provide seven potential coordination sites for the Ln(III) ions; four nitrogens of the cyclen ring and three additional oxygen atoms of the amide based pendant arms. The remaining two coordination sites will be occupied by solvent molecules, in this case H_2O. It was envisaged that displacement of these water molecules could occur through the addition of external coordinating ligands which would in turn give rise to an enhancement in the Eu(III) emission. The remaining cyclen amine would be utilized to attach an alkyl thiol chain necessary for adsorption of the cyclen-Ln(III) complex onto the surface of the **AuNPs**. As previously published work by the Gunnlaugsson group has shown that the incorporation of a twelve carbon chain between the **AuNP** surface and the Ln(III) metal centre limits the quenching of the Ln(III) luminescence, the same chain was incorporated into this ligand.[117,125] The carbon chain was terminated with a thiol group; sulfur being a "soft" element has a high affinity for the "soft" nature of the **AuNPs** and as such was ideal to bind the Ln(III) complex to the surface of the **AuNP**.

The following sections will include a detailed description of the synthesis and characterisation of ligand **49** and the corresponding Eu(III) and Tb(III) complexes, **Eu·49** and **Tb·49**, followed by a photophysical evaluation of these complexes and finally their attachment and properties once attached to **AuNPs**.

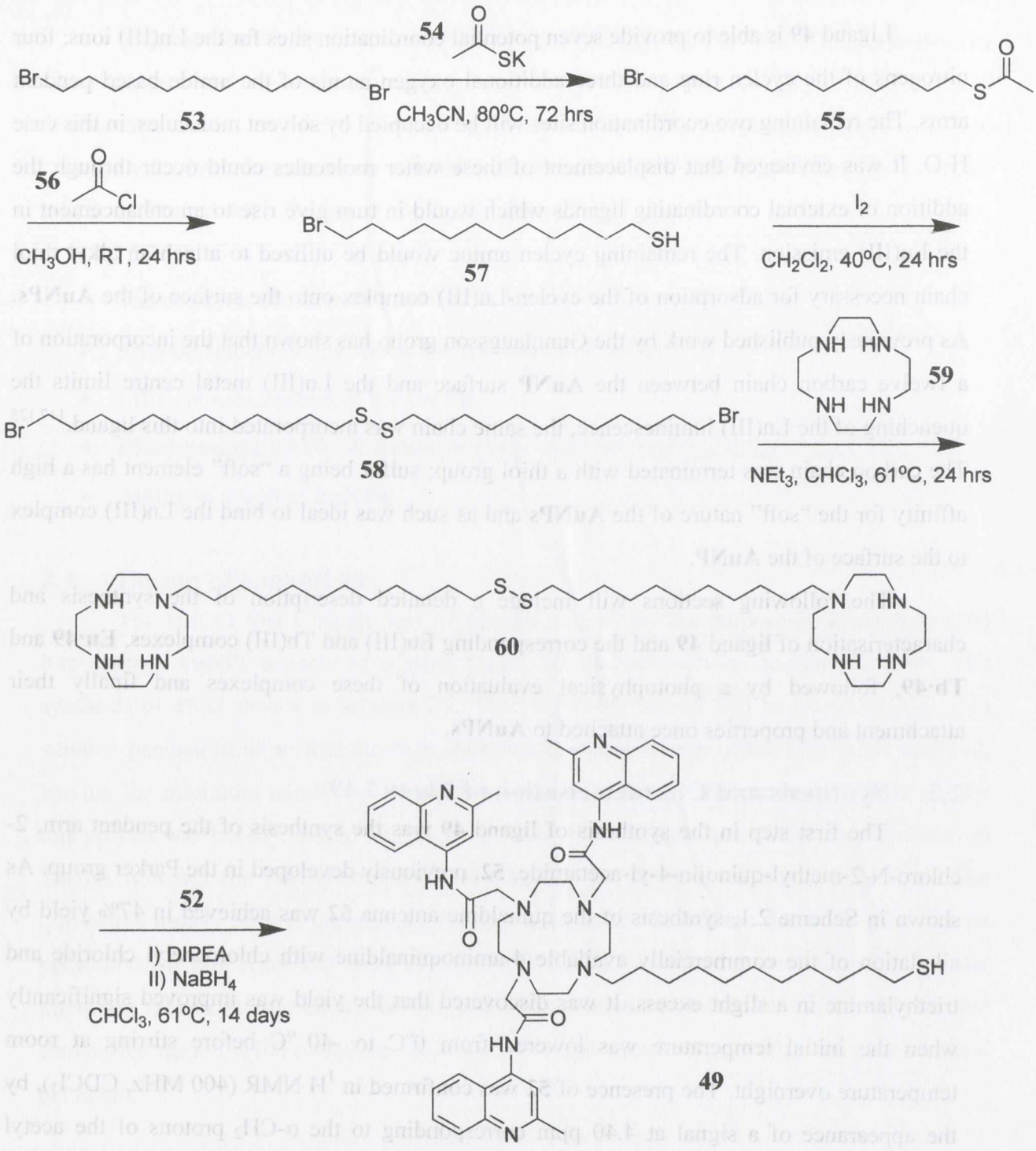
2.2 Synthesis and Characterisation of Ligand 49

The first step in the synthesis of ligand **49** was the synthesis of the pendant arm, 2-chloro-N-2-methyl-quinolin-4-yl-acetamide, **52**, previously developed in the Parker group. As shown in Scheme 2.1, synthesis of the quinaldine antenna **52** was achieved in 47% yield by alkylation of the commercially available 4-aminoquinaldine with chloroacetyl chloride and triethylamine in a slight excess. It was discovered that the yield was improved significantly when the initial temperature was lowered from 0°C to -40 °C before stirring at room temperature overnight. The presence of **52** was confirmed in ^{1}H NMR (400 MHz, $CDCl_3$), by the appearance of a signal at 4.40 ppm corresponding to the α-CH_2 protons of the acetyl chloride and a broad singlet of one NH at 9.23 ppm.



50 **52**

Scheme 2.1: *Synthetic pathway for* ***52****.*



Scheme 2.2: *Synthetic pathway for ligand* ***49****.*

The successful synthesis of **52** was followed by the formation of the disulfide chain **58**, using a method developed by Yokokawa *et al.*, illustrated in Scheme 2.2.[126] The first stage of this synthetic strategy was to monosubstitute 1,12-dibromododecane **53** with potassium thioacetate, **54**, in a 3.3:1 ratio to give the thioacetic acid **55** in 37% yield. The disubstituted by-product was also formed and was separated from **55** by purification using an alumina column chromatography (gradient elution 100:0 – 95:5 hexane:ethyl acetate). The ^{1}H NMR

spectrum (400 MHz, $CDCl_3$) was in agreement with previously published literature data.[126] The acyl group of **55** was then cleaved in the presence of an excess acetyl chloride, **56** to yield the thiol **57** in 98% yield. The ^1H NMR spectrum (400 MHz, $CDCl_3$) confirmed the successful reaction, while the ^{13}C DEPT-135 NMR spectrum (100 MHz, $CDCl_3$) confirmed the presence of only CH_2 carbons. Oxidative disulfide bond formation was achieved through the addition of iodine to **57** to give **58** in 48% yield. The next step which involved the formation of **60** required the monoalkylation of cyclen by **58**. Gunnlaugsson *et al.*[127] developed a novel method for the mono-alkylation of cyclen in a single synthetic step. This synthesis involved the use of 1 equivalent of **58**, 8 equivalents of cyclen and 2.4 equivalents of triethylamine, yielding **60** in 77% yield. Analysis of the ^1H NMR spectrum (400 MHz, $CDCl_3$) shows a multiplet intergrating to 32 protons between 2.94 and 2.61 ppm, characteristic of cyclen protons. The final step involved the alkylation of **60** with **52**. The reaction was carried out under reflux in $CHCl_3$ in the presence of 3.5 equivalents of diisopropylethylamine (DIPEA) and after 14 days formation of **49** was observed by mass spectrometry; 966.5744 $[M + H]^+$. Purification to remove any unreacted starting material and any other side products (such as di- or tri-substituted **60**) was achieved through an acid-base extraction work up followed by precipitation out of diethyl ether to give **49** in *ca.* 14% yield, the ^1H NMR of which is shown below in Figure 2.1. The reaction was repeated with a variety of solvents (MeOH, EtOH, MeCN, THF) and bases (KI/K_2CO_3, Cs_2CO_3, NEt_3) however, none had any significant effect on improving the yield of this transformation.

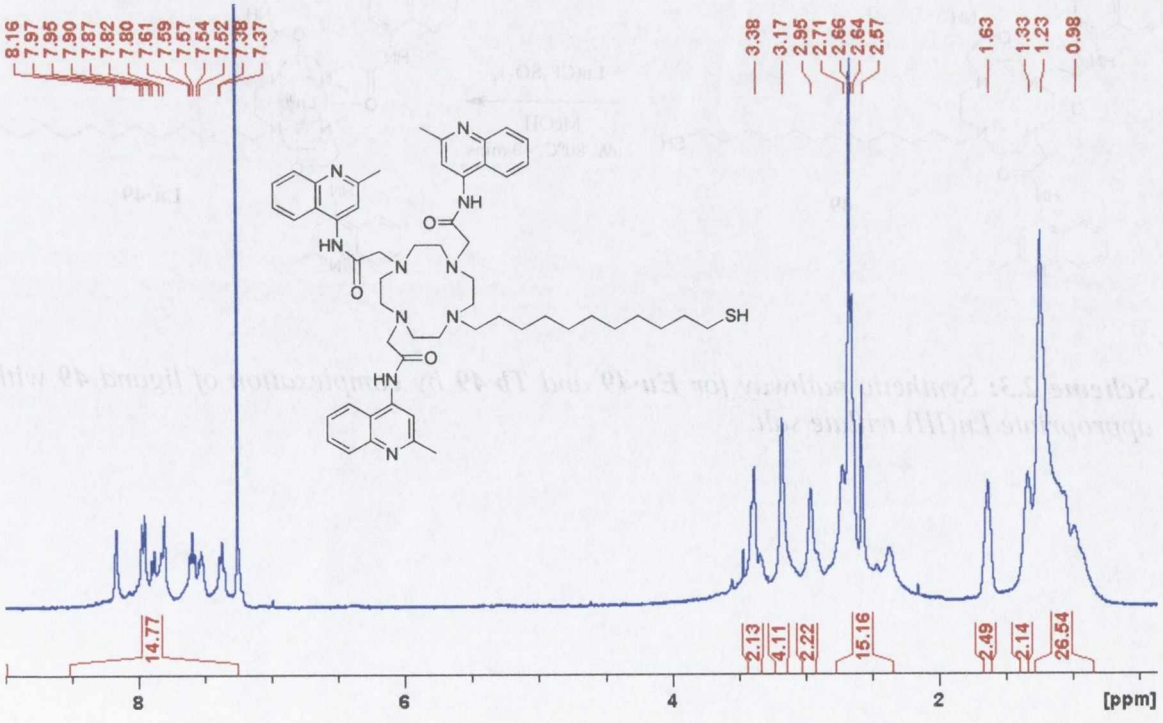
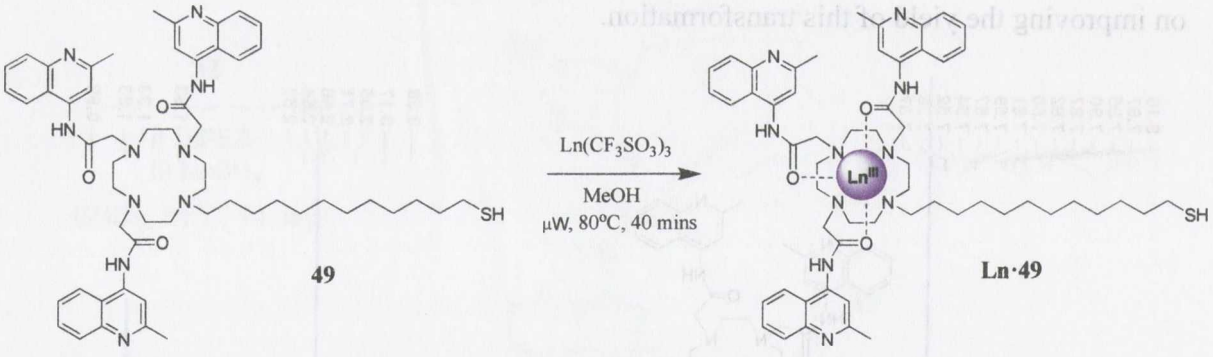


Figure 2.1: *The ^1H NMR spectrum (400 MHz, $CDCl_3$) of ligand **49**.*

In the ^{1}H NMR spectrum (400 MHz, $CDCl_3$), shown in Figure 2.1, the downfield signals at 10.09 ppm and 9.25 ppm, with a combined integration of 3 can be assigned to the three amide protons. The presence of two environments around the cyclen cavity gives rise to a multiplet of peaks in the aromatic region between 8.16 ppm and 7.37 ppm that correspond to the 15 aromatic protons of the quinaldine antenna arms. The signals ranging from 3.38-2.57 ppm include the 16 protons of the cyclen and the majority of the CH_2 protons of the long alkyl chain can be found in the large multiplet spanning 1.33-0.98 ppm. ^{13}C NMR, IR and elemental analysis were also used to fully characterise ligand **49**, the full characterisation of which, and all other precursor compounds can be found in the experimental section of Chapter 7.

2.3 Synthesis and Characterisation of Eu(III) and Tb(III) complexes of 49

The Eu(III) and Tb(III) complexes of **49** were obtained by reacting ligand **49** with 1 equivalent of either Eu(III) triflate ($Eu(CF_3SO_3)_3$) or Tb(III) triflate ($Tb(CF_3SO_3)_3$), Scheme 2.3, in a small volume of MeOH (*ca.* 5 mL) under microwave irradiation for 40 minutes. Precipitation of the product from the MeOH solution into a large volume of diethyl ether, followed by filtration gave **Eu·49** and **Tb·49** as beige solids in 90% and 86% yield, respectively.



Scheme 2.3: *Synthetic pathway for* ***Eu·49*** *and* ***Tb·49*** *by complexation of ligand* ***49*** *with the appropriate Ln(III) triflate salt.*

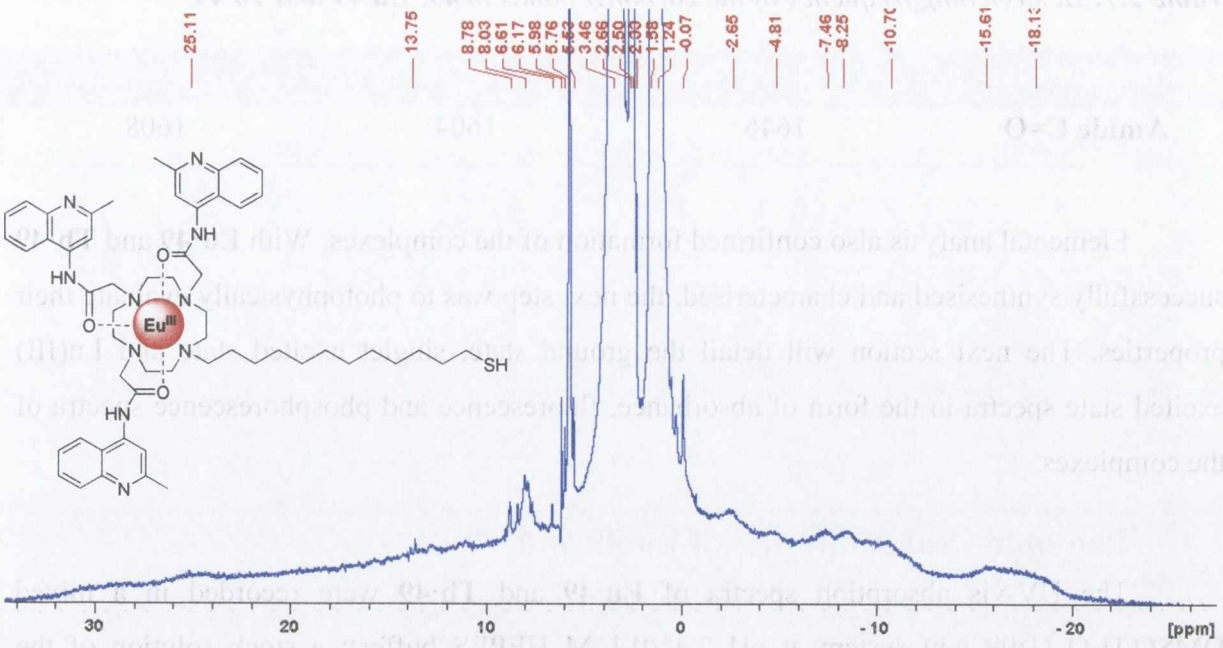


Figure 2.2: *^{1}H NMR (400 MHz, DMSO-d_6) of* ***Eu·49****.*

The Ln(III) ions are paramagnetic by nature and as a result, any protons in close proximity to the Ln(III) metal centre will be affected by the presence of unpaired *f* electrons, and hence, their nuclear spins will experience more efficient relaxation resulting in a broadening and shifting effect of their ^{1}H NMR resonances.[128] The ^{1}H NMR (400 MHz, DMSO-d_6) of **Eu·49** showed the characteristic Eu(III) shifted axial and equatorial cyclen protons, in the range of -18 to 25 ppm (Figure 2.2), verifying successful complexation of the Ln(III) within the cyclen cavity. The ^{1}H NMR spectrum of **Tb·49** is shown in the Appendix A2.1 and shows a similar shifting of the resonances.

Another important method of characterisation of the Ln(III) complexes is IR spectroscopy. Once complexed, the amide carbonyl bonds coordinate to the Ln(III) metal centre, causing a shift in the electron density and this effect was observed as a shifting in the IR stretching frequency of the carbonyl bands and hence, further evidence was provided of the successful formation of the Ln(III) complexes. The carbonyl signals were shifted downfield from 1646 cm^{-1} to 1604 cm^{-1}, verifying that they were involved in the coordination of the Eu(III) ion, thus weakening the carbonyl stretching and hence resulting in a peak at a lower wavenumber. A summary of the shifts in the frequency of the carbonyl band for **Eu·49** and **Tb·49** is detailed below in Table 2.1.

Table 2.1: *IR stretching frequency of the carbonyl bands in* ***49****,* ***Eu·49*** *and* ***Tb·49****.*

IR Frequency (cm^{-1})	Ligand 49	Eu·49	Tb·49
Amide C=O	1646	1604	1608

Elemental analysis also confirmed formation of the complexes. With **Eu·49** and **Tb·49** successfully synthesised and characterised, the next step was to photophysically evaluate their properties. The next section will detail the ground state, singlet excited state and Ln(III) excited state spectra in the form of absorbance, fluorescence and phosphorescence spectra of the complexes.

2.4 Photophysical Properties of Eu·49 and Tb·49

The UV-vis absorption spectra of **Eu·49** and **Tb·49** were recorded in a mixed DMSO/H_2O (1:99 *v/v*) system at pH 7.4 (0.1 M HEPES buffer); a stock solution of the respective **Ln·49** was prepared in DMSO and diluted into HEPES such that the concentration of DMSO in the cuvette was 1% overall. The absorption maximum π-π* band was centred at 318 nm, accompanied by a slight shoulder at 330 nm. Excitation into the main band at 318 nm produces the fluorescence emission spectrum, possessing a λ_{max} at 355 nm and two minor shoulders at 345 nm and 370 nm. Both the absorbance and fluorescence are shown below in Figure 2.3. Sensitisation of the Ln(III) metal centre by the antenna was confirmed by the excitation spectra (Appendix A2.2) which closely matched the absorption spectrum of **Eu·49** and **Tb·49**.

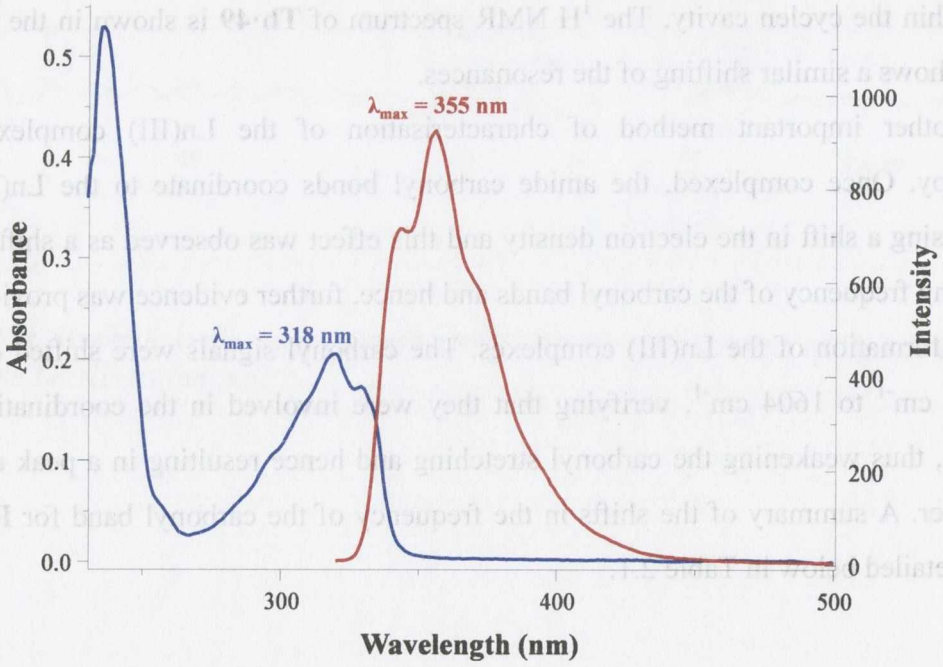


Figure 2.3: *The UV-vis absorption (-) and the fluorescence emission (λ_{ex} = 318 nm) spectra (-) of* ***Eu·49*** *and* ***Tb·49*** *in a mixed DMSO:H_2O (1:99 v/v) solution.*

The design of **Eu·49** and **Tb·49** was such that the Eu(III) and Tb(III) ion would be indirectly excited by the covalently attached quinaldine antenna, which would transfer its energy, *via* the triplet state, to the $^5D_0$ state of the Eu(III) and $^5D_4$ state of the Tb(III) and hence, Ln(III) emission would be observed. The metal centred emission spectra of **Eu·49** and **Tb·49** was recorded in a mixed DMSO/H_2O (1:99 *v/v*) system by exciting the solution at 318 nm (max absorbance of the antenna, λ_{max}) confirming that energy transfer from the antenna had occurred. Figure 2.4 shows the Eu(III) and Tb(III) emissions resulting from the transitions from the $^5D_0$ state to the ^7F_J state of the Eu(III) ion where $J = 0$ (577 nm), 1 (591 nm), 2 (616 nm), 3 (651 nm), 4 (split; 690 and 699 nm) and the $^5D_4$ to the ^7F_J state of the Tb(III) ion where $J = 6$ (490 nm), 5 (545 nm), 4 (585 nm), 3 (620 nm).

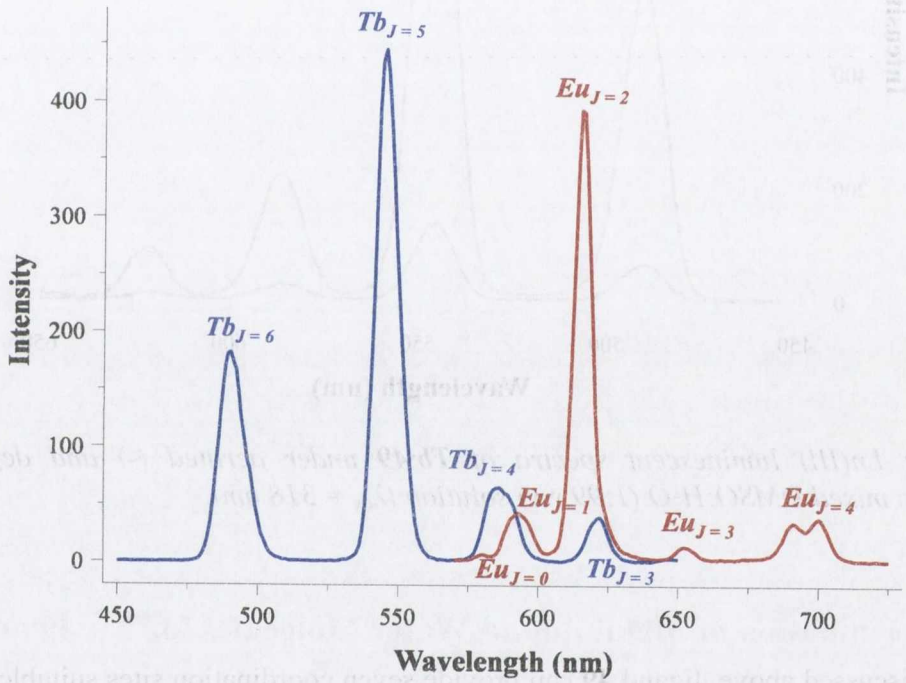


Figure 2.4: *Ln(III) luminescent spectra of* ***Eu·49*** *(-) and* ***Tb·49*** *(-) in a mixed DMSO:H_2O (1:99 v/v) solution (λ_{ex} = 318 nm).*

In the case of **Tb·49**, it was important to examine the effect that oxygen had on the photophysical properties of the Tb(III) complex. This was not necessary for **Eu·49**, as the energy gap between Eu(III) and the triplet state of the antenna is large enough such that back energy transfer, and therefore Ln(III) quenching, is prevented.[77] However, the energy of the Tb(III) excited state and the triplet state of the napthyl containing chromophores were both in the region of *ca.* 20000 cm^{-1}, enabling back transfer to occur.[27] While it has little direct effect on the excited state of Tb(III), the triplet state of the quinaldine chromophore can be subjected to rapid quenching by molecular oxygen. This, combined with the small energy gap between the emissive Tb(III) and antenna triplet state causes back energy transfer to occur, will give

rise to quenched Tb(III) emission. To investigate this, the luminescence of a solution of **Tb·49** was measured, before being degassed by bubbling argon through it for five minutes. A 7 fold enhancement was observed in the Tb(III) emission of the degassed solution of **Tb·49**, as illustrated in Figure 2.5.

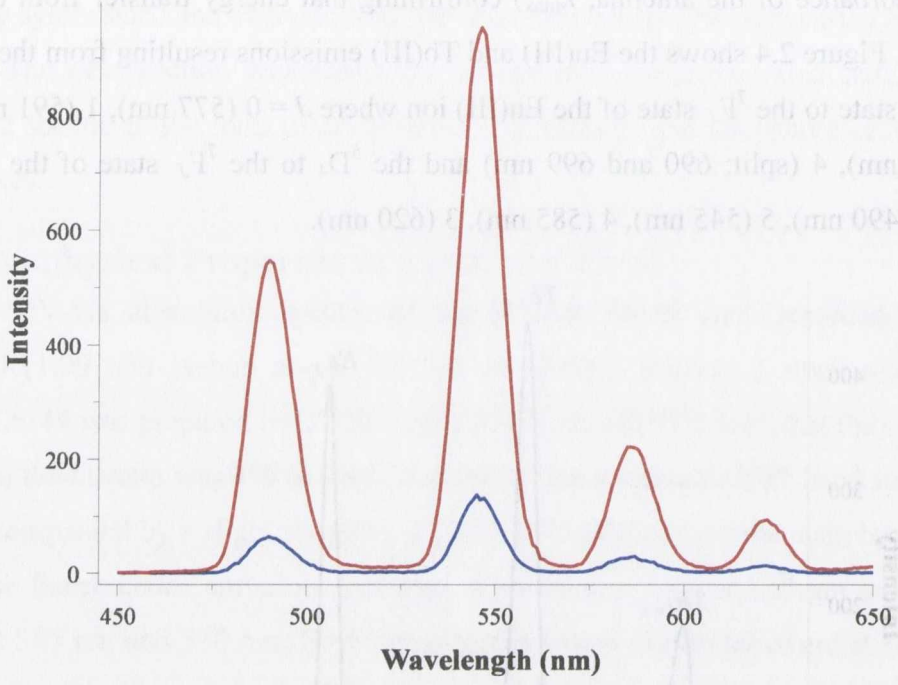


Figure 2.5: *Ln(III) luminescent spectra of* ***Tb·49*** *under aerated (-) and degassed (-) conditions in mixed DMSO:H_2O (1:99 v/v) solution (λ_{ex} = 318 nm).*

2.5 Determination of Metal Bound Water Molecules for Eu·49 and Tb·49

As discussed above, ligand **49** can provide seven coordination sites suitable for Ln(III) complexation. Eu(III) and Tb(III) generally have a coordination number of nine, hence it would be expected that two solvent molecules fulfil the coordination demand in the case of **Eu·49** and **Tb·49** in water; this is referred to as the hydration state or the *q* value. In order to investigate the hydration state (*q*), the excited state lifetimes of **Eu·49** and **Tb·49** were measured in a mixed DMSO/H_2O (1:99 *v/v*) system (τ_{H2O}) and a mixed DMSO d_6/D_2O (1:99 *v/v*) system (τ_{D2O}) by excitation of the antenna at 318 nm. The value of *q* was then determined using the Horrocks modified equation developed by Parker *et al.* as discussed in Section 1.3.2.[35,129] As mentioned in Chapter 1, Ln(III) luminescence quenching involves vibrational energy transfer by coordinated or diffusing O-H oscillators, which is reduced upon replacement by O-D oscillators resulting in longer excited state lifetimes in D_2O.

By recording the excited state exponential decay of the Eu(III) and Tb(III) centred emission with respect to time, lifetimes of **Eu·49** and **Tb·49** were obtained. The luminescence decay obtained for **Eu·49**, shown in Figure 2.6 was fit to a mono exponential decay, giving lifetimes of 0.653 ± 0.1 ms and 1.561 ± 0.1 ms, in H_2O and D_2O, respectively, resulting in a q value of 0.86 ± 0.5 being obtained from calculations. A summary of all the q values obtained are shown in Table 2.2.

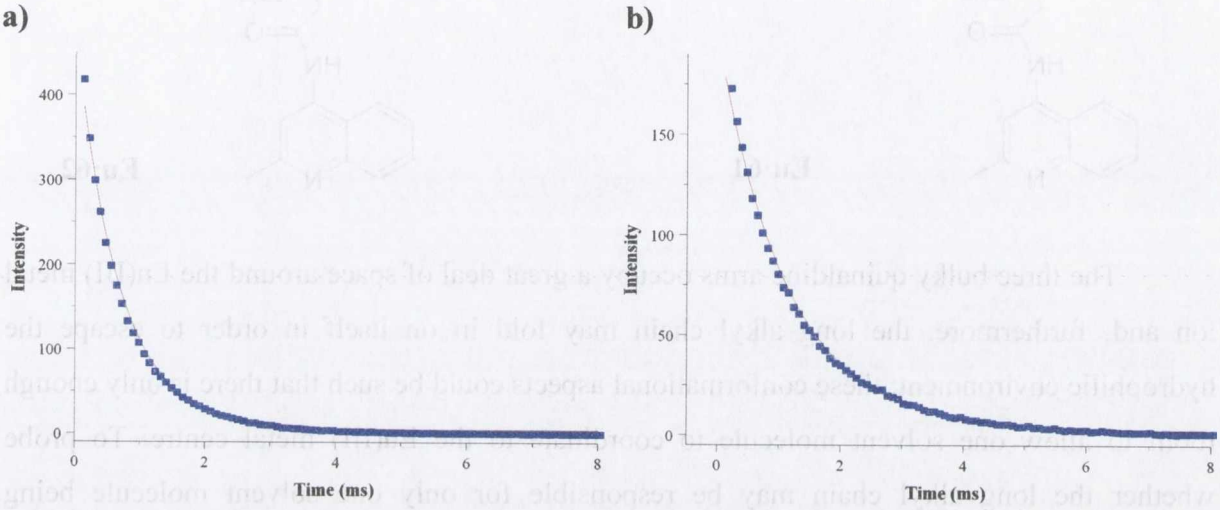
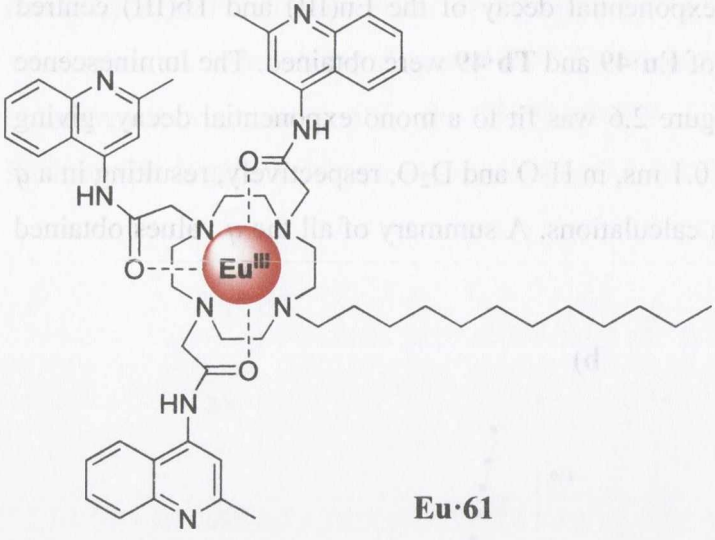
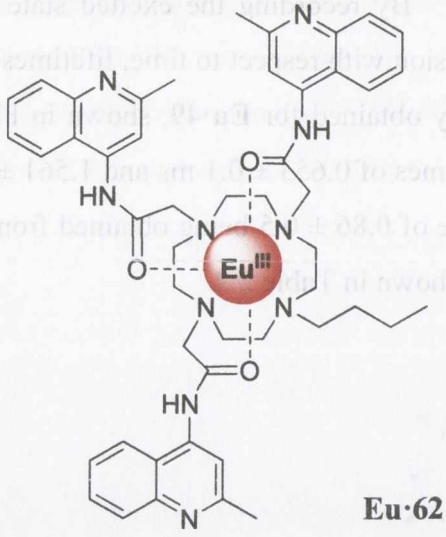


Figure 2.6: *Luminescence decay of the complex* ***Eu·49*** *fit to a monoexponential decay in a* ***a)*** *mixed DMSO:H_2O (1:99 v/v) solution and* ***b)*** *mixed DMSO-D_6:D_2O(1:99 v/v) solution (λ_{ex} = 318 nm).*

Eu(III) ions usually possess a total coordination number of nine, and so obtaining a q value of *ca.* 1 (Table 2.2) instead of 2 for **Eu·49** was thus unexpected. A possible explanation for this was that the –SH of the alkyl chain was coordinating to the Eu(III), leaving only one vacant coordination site to be filled by a solvent molecule. To investigate this hypothesis complex **Eu·61** was synthesised which contained a methyl group instead of a thiol group at the end of the alkyl chain. Ligand **61** was synthesised in a similar manner to **49** as discussed in Section 2.2, cyclen was monoalkylated with bromododecane followed by alkylation with three equivalents of the quinaldine antenna and finally complexation with $Eu(CF_3SO_3)_3$ which gave **Eu·61** in 86% yield. Again, a q value of 1, Appendix A2.3, was obtained instead of the expected value of 2. With the –SH now ruled out as coordinating to the Eu(III), another feasible explanation could be that the configuration of the complex in solvent is such that it was preventing a solvent molecule from binding.[42]



Eu·61



Eu·62

The three bulky quinaldine arms occupy a great deal of space around the Ln(III) metal ion and, furthermore, the long alkyl chain may fold in on itself in order to escape the hydrophilic environment; these conformational aspects could be such that there is only enough room to allow one solvent molecule to coordinate to the Eu(III) metal centre. To probe whether the long alkyl chain may be responsible for only one solvent molecule being observed, complex **Eu·62** was synthesised with a four carbon chain from bromobutane, in the same manner as **Eu·61**, instead of a twelve carbon one, and upon investigation, a q value of 2 was obtained, Appendix A2.4. From these results it can be concluded that the long alkyl chain was in fact preventing a solvent molecule from binding to the metal centre.

Table 2.2: *Lifetime studies for* ***Eu·49****,* ***Eu·61*** *and* ***Eu·62*** *at neutral pH, each number is an average of 6 measurements all agreeing to within 5% of each other with an error of ± 0.01.*

Complex	τ_{H2O} (ms)	τ_{D2O} (ms)	k_{H2O} (ms^{-1})	k_{D2O} (ms^{-1})	q (± 0.5)
Eu·49	0.65	1.56	1.53	0.64	0.86
Eu·61	0.46	1.24	2.19	0.68	1.12
Eu·62	0.36	1.20	2.53	0.82	1.99
Tb·49(dg)	0.53	0.63	1.87	1.55	1.10

For the case of **Tb·49**, the excited state decay was best fitted to double exponential instead of single exponential, Appendix A2.5. However once the solutions were degassed by bubbling argon through them for several minutes, a single exponential fit was observed, Appendix A2.6, with lifetimes of 0.534 ms and 0.627 ms in H_2O and D_2O, respectively, resulting in a q value of 1.10 ± 0.50 being obtained from calculations. This result is in agreement with that obtained for **Eu·49**; there is one water molecule coordinated to the Ln(III) metal centre.

2.6 pH Response of Ligand 49 in Solution

A requirement of a biological sensor is independent behaviour at physiological pH. Therefore studies were carried out to determine the behaviour of both the ligand **49** and its corresponding complex **Eu·49** over a pH range from 2-12 by observing the changes in the UV-vis absorption and fluorescence spectrum as a function of pH. It was apparent that the ground state of the ligand and complex would be greatly perturbed by pH due to possible protonation of the quinaldine nitrogen as well as potential deprotonation of the secondary amide. All pH measurements reported were fully reproducible.

2.6.1 Ground State Investigations

Firstly, the effect of pH on the ground state of the ligand was analysed in a mixed DMSO/H_2O (1:99 *v/v*) solution in the presence of tetraethylammonium perchlorate (TEAP) (*I* = 0.1 M) to maintain a constant ionic strength. In acidic conditions, the ligand displays a maximum band in the absorption spectrum at 315 nm which upon basification was considerably hypochromically and hypsochromically shifted, leading to formation of a new band centred at 300 nm (Figure 2.7). A significant decrease in the absorbance at 300 nm was particularly observed within the pH window of 3.0-6.5. This change was most likely due to the deprotonation of the quinaldine nitrogen.[54] From these changes, a pK_a of 5.35 ± 0.10 was determined using the standard formula for the calculation of ground state, Equation 2.1.[130]

$$pK_a\,(S_0) = pH - \log \frac{(Abs_{AH} - Abs_A)}{(Abs_{AH} - Abs_{A^-})} \qquad \textbf{Equation 2.1}$$

Abs_{AH}, Abs_A and Abs_{A^-} are the absorbance's of the protonated species, the absorbance of each solution and the absorbance of the deprotonated species, respectively. The determined p*Ka* value was in good agreement with that of ligand **14** (5.71 ± 0.10), discussed in the introduction, which possessed one quinaldine chromophore and three acetamide arms. After pH 7, the absorbance reached a plateau, indicating the deprotonation of the remaining nitrogens: the secondary amide and the cyclen nitrogens had no detectable effect on the spectroscopic properties of the ligands ground state. The same trend followed when plotting the changes in absorbance at different wavelengths (Appendix A2.7). Furthermore, not all spectra passed through the isosbestic points at 273 nm and 292 nm indicating the presence of more than one species in equilibrium in solution. The changes observed were found to be reversible on back titration from pH 12-2.

The next section will investigate the spectroscopic properties of the singlet excited state of ligand **49** as a function of pH.

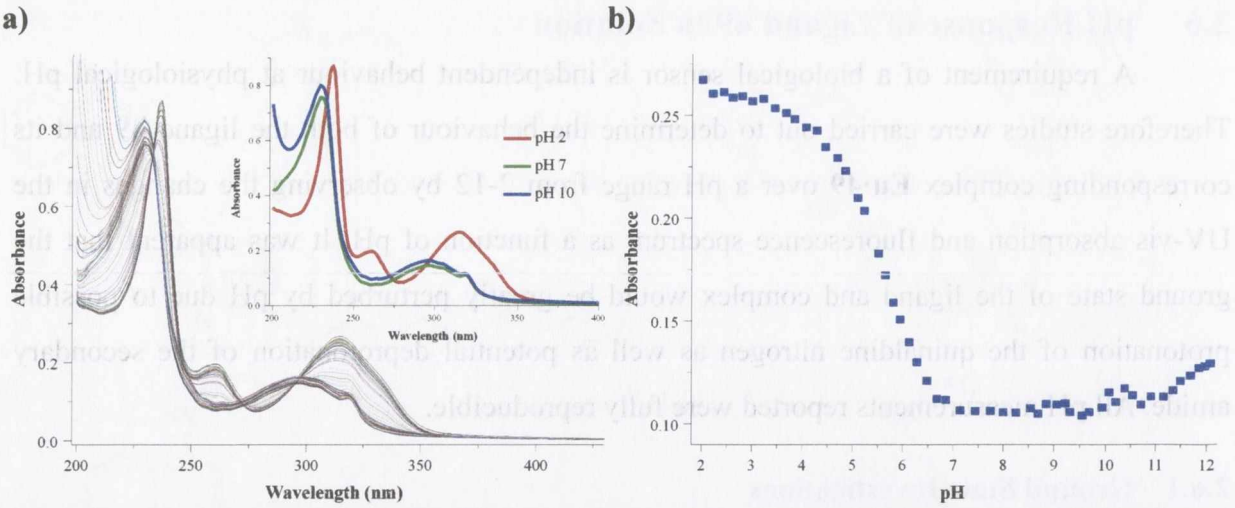


Figure 2.7: a) *Changes in the UV-vis absorption spectra of ligand* ***49*** *as a function of pH in a mixed DMSO:H_2O (1:99 v/v) solution [I = 0.1 M TEAP]. Inset: The UV-vis absorption spectra recorded at various pH.* ***b)*** *Changes in the absorbance at 315 nm as a function of pH.*

2.6.2 Singlet Excited State Investigations

The changes in the fluorescence emission spectra of ligand **49** were investigated as a function of pH in a mixed DMSO/H_2O (1:99 *v/v*) solution in the presence of TEAP (*I* = 0.1 M). Upon excitation at 318 nm, in acidic solution, pH 2.0-4.5 a band centred at 375 nm was observed with two shoulders at 342 nm and 359 nm. Between pH 4.5-7.0 the band at 375 nm was hypochromically shifted and upon basification beyond pH 7; further changes were observed, with a significant hyperchromic and hypsochromic shift being observed with the formation of a new band centred at 370 nm. These latter changes were followed with a simultaneous loss of the hyperfine structure (Figure 2.8).

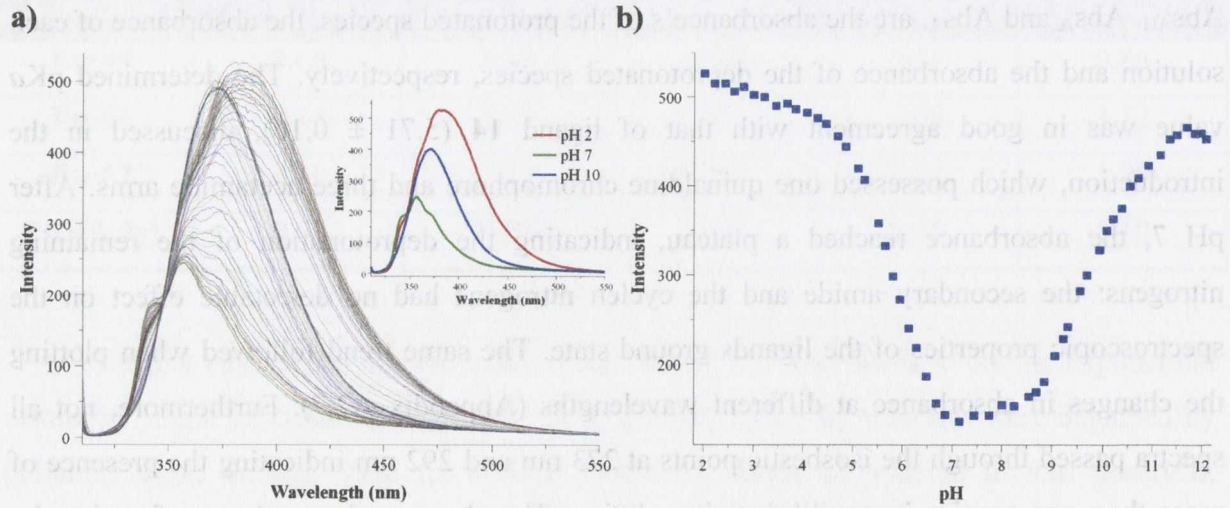


Figure 2.8: a) *Changes in the fluorescence emission (λ_{ex} = 318 nm) spectra of ligand* ***49*** *as a function of pH in a mixed DMSO:H_2O (1:99 v/v) solution [I = 0.1 M TEAP]. Inset: The fluorescence emission spectra recorded at various pH.* ***b)*** *Changes in the fluorescence at 381 nm as a function of pH.*

The changes at the various wavelengths were plotted against pH and a number of sigmoidal curves were obtained that when fitted using Origin 7.5® gave pK_a values of 5.43 ± 0.10 (quinaldine nitrogen) and 8.67 ± 0.10 (secondary amide). In the same manner as the UV-vis absorption changes, the fluorescence changes were found to be fully reversible.

2.7 pH Response of Eu·49 in Solution

With the pK_a's of the ligand determined, the same set of experiments, UV-vis absorption and fluorescence pH titrations were also carried out on **Eu·49**, as described in the next section.

2.7.1 Ground State and Singlet Excited State Investigations

In the same manner as described above, the UV-vis absorption and fluorescence spectra were recorded at different pH ranging from 2-12, in the presence of TEAP (I = 0.1 M). The results obtained were similar to those from the ligand pH titrations.

As shown in Figure 2.9a the absorption spectrum displayed a main band at 318 nm with a shoulder at 330 nm in acidic solution and upon basification to pH 7, a considerable hypochromic and hypsochromic shift occurred in the band centred at 300 nm, which was assigned to the π-π* transition of the ligand. The formation of a pseudo-isosbestic point was observed at *ca.* 303 nm indicating the presence of two or more species in solution. The changes in absorbance at 318 nm and 330 nm were plotted as a function of pH and fitted to a sigmoidal curve using Origin 7.5®. A pK_a of 9.66 ± 0.10 was obtained, which was assigned to deprotonation of the secondary amide and differs slightly from that of **Eu·14** (8.77 ± 0.10).

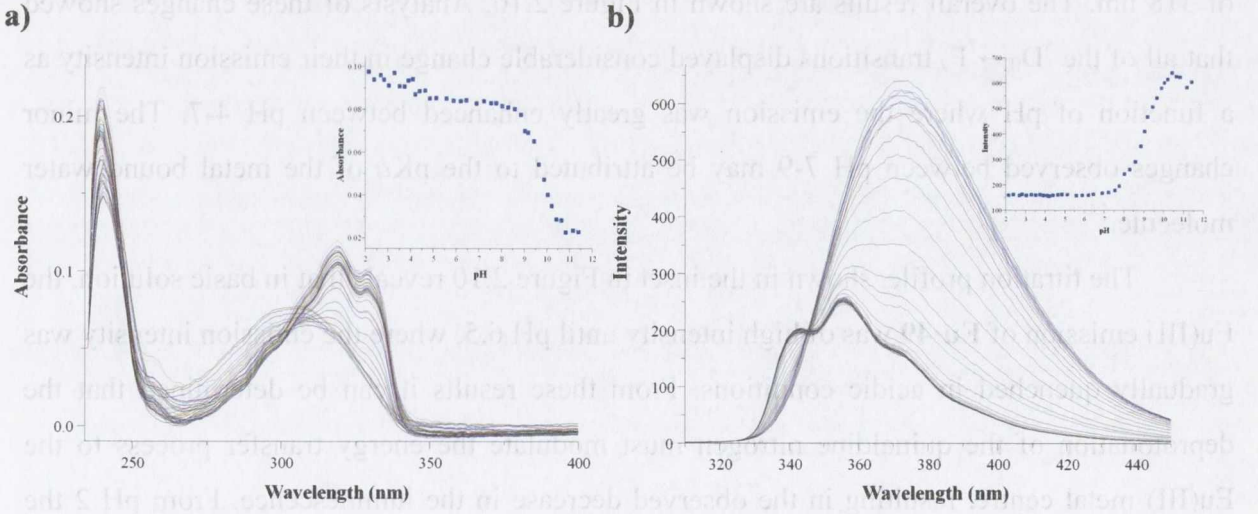


Figure 2.9: a) *Changes in the UV-vis absorption spectra of* ***Eu·49*** *as a function of pH in a mixed DMSO:H_2O (1:99 v/v) solution [I = 0.1 M TEAP]. Inset: Changes in the absorbance at 318 nm as a function of pH.* ***b)*** *Changes in the fluorescence emission (λ_{ex} = 318 nm) spectra of* ***Eu·49*** *as a function of pH in a mixed DMSO:H_2O (1:99 v/v) solution [I = 0.1 M TEAP]. Inset: Changes in the fluorescence at 370 nm as a function of pH.*

It is of importance to note that all major changes in the absorbance occurred between pH 8.5-11.0, with the absorption remaining relatively constant over the physiological pH range, as shown in the inset in Figure 2.9a.

The fluorescence emission of **Eu·49** was also investigated as a function of pH in TEAP (I = 0.1 M) upon excitation at 318 nm. In acidic solution a band was centred at 354 nm accompanied by two shoulders at 342 nm and 368 nm. Upon basification there was a significant hyperchromic and bathochromic shift to the band centred at 370 nm (Figure 2.9b). The changes at 341 nm and 370 nm were plotted as a function of pH to give sigmoidal curves. The pK_a calculated for the singlet excited state using Equation 2.1 was 9.38 ± 0.20, similar to that recorded for the ground state and also assigned to be deprotonation of the secondary amide (pK_a for **14** 9.47 ± 0.10). Again the results confirmed the presence of a large physiological pH window between pH 5-8, in which the fluorescence emission remained pH independent.

With the pH behaviour of the ground and singlet excited state of **Eu·49** investigated, both sets of results, demonstrating that these states did not undergo any modifications within the physiological pH range and any major changes that did occur over the pH range 2-12 were attributed to deprotonation of the secondary amide. Following this, the Eu(III) luminescent emission was also studied as a function of pH, as described in the following section.

2.7.2 Eu(III) Excited State Investigations of Eu·49

The Eu(III) complex **Eu·49** was studied in terms of its Ln(III) luminescence with respect to pH in aqueous solution using TEAP (I = 0.1 M) and using an excitation wavelength of 318 nm. The overall results are shown in Figure 2.10. Analysis of these changes showed that all of the $^5D_0 \rightarrow {}^7F_J$ transitions displayed considerable change in their emission intensity as a function of pH where the emission was greatly enhanced between pH 4-7. The minor changes observed between pH 7-9 may be attributed to the pK_a of the metal bound water molecule.[54]

The titration profile, shown in the inset in Figure 2.10 reveals that in basic solution, the Eu(III) emission of **Eu·49** was of high intensity until pH 6.5, where the emission intensity was gradually quenched in acidic conditions. From these results it can be determined that the deprotonation of the quinaldine nitrogen must modulate the energy transfer process to the Eu(III) metal centre, resulting in the observed decrease in the luminescence. From pH 2 the phosphorescence behaviour became irreversible and remained quenched upon titration back to pH 12, possibly due to dissociation of the Eu(III) ion from the macrocyclic cavity at very acidic pH. The same changes were observed upon plotting the Eu(III) emission at different wavelengths against pH. Moreover, the Eu(III) emission changes as a function of pH

contradicted those observed for other Eu(III) complexes (**14**) possessing the same antenna.[54,123]

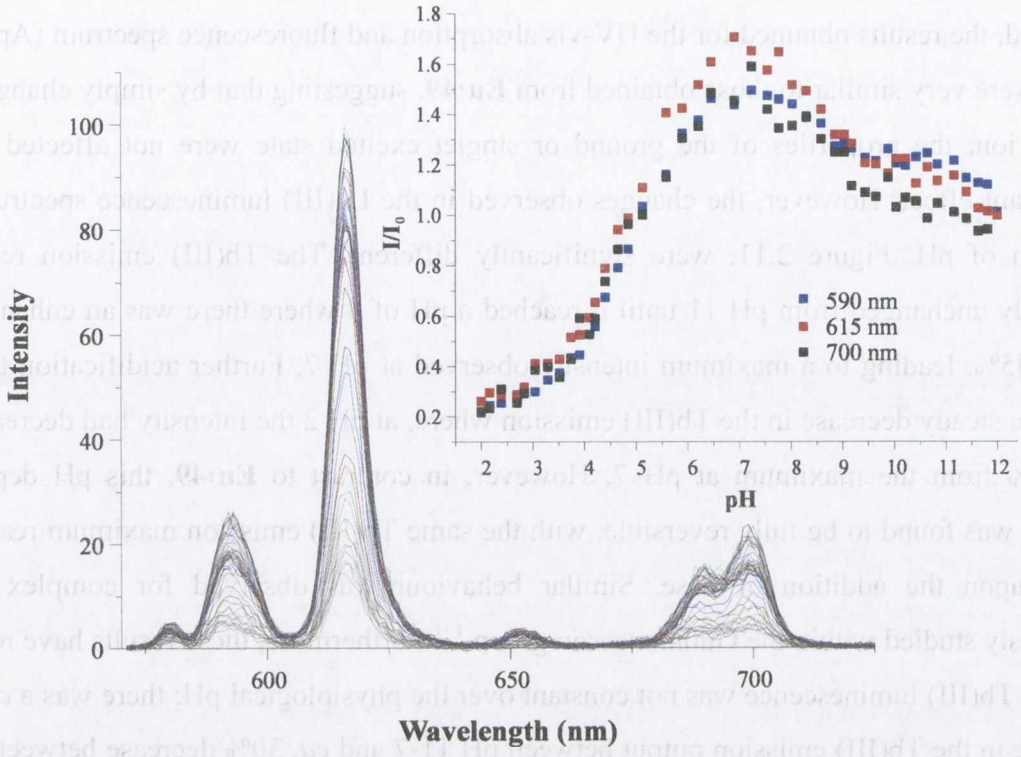


Figure 2.10: *The Eu(III) luminescence response of* ***Eu·49*** *(λ_{ex} = 318 nm) as a function of pH in a mixed DMSO:H_2O (1:99 v/v) solution [I = 0.1 M TEAP]. Inset: Changes in the Eu(III) emission intensity at 592 nm (J = 1), 615 nm (J = 2) and 700 nm (J = 4) as a function of pH.*

One observation made from the pH titration results was that between pH 2 and 8 no substantial change was observed in the absorbance of **Eu·49**, whereas a decrease in the luminescence was observed, leading us to conclude that the functionality being deprotonated in this pH range effects the energy transfer process to the metal centre alone.

Luminescent enhancement in basic media highlights the ability of the antenna to populate the Eu(III) excited state by sensitisation, and that this process was highly pH dependent. Furthermore, the luminescence switching was not fully reversible; the addition of acid below pH 4 quenched the emission which could not be switched on again with the subsequent addition of base (pH 8-12). However, from the pH titrations it can be concluded that **Eu·49** was stable at physiological pH, confirming its suitability for the sensing of biological substrates. The next stage in investigating **Eu·49** was to probe its ability to sense anions through displacement of its metal bound water molecule and hence, increasing the Eu(III) luminescence.

2.8 pH Response of Tb·49 in Solution

In the same method as described for **Eu·49**, the UV-vis absorption, fluorescence and phosphorescence spectra of **Tb·49** were recorded at different pH ranging from 2-12. As expected, the results obtained for the UV-vis absorption and fluorescence spectrum (Appendix A2.8) were very similar to those obtained from **Eu·49**, suggesting that by simply changing the Ln(III) ion, the properties of the ground or singlet excited state were not affected to any significant effect. However, the changes observed in the Ln(III) luminescence spectrum as a function of pH, Figure 2.11, were significantly different. The Tb(III) emission remained relatively unchanged from pH 11 until it reached a pH of 8 where there was an enhancement of *ca.* 45%, leading to a maximum intensity observed at pH 7. Further acidification to pH 2 caused a steady decrease in the Tb(III) emission where, at pH 2 the intensity had decreased by *ca.* 65% from the maximum at pH 7. However, in contrast to **Eu·49**, this pH dependent process was found to be fully reversible, with the same Tb(III) emission maximum reached at pH 7 upon the addition of base. Similar behaviour was observed for complex **Tb·14** previously studied within the Gunnlaugsson group.[131] Furthermore, these results have revealed that the Tb(III) luminescence was not constant over the physiological pH; there was a *ca.* 30% increase in the Tb(III) emission output between pH 11-7 and *ca.* 30% decrease between pH 7-5. It is of vital importance that a biological sensing agent possesses pH independent behaviour at biological pH and for this reason it was decided that only the complex **Eu·49** would be studied for its anion sensing ability.

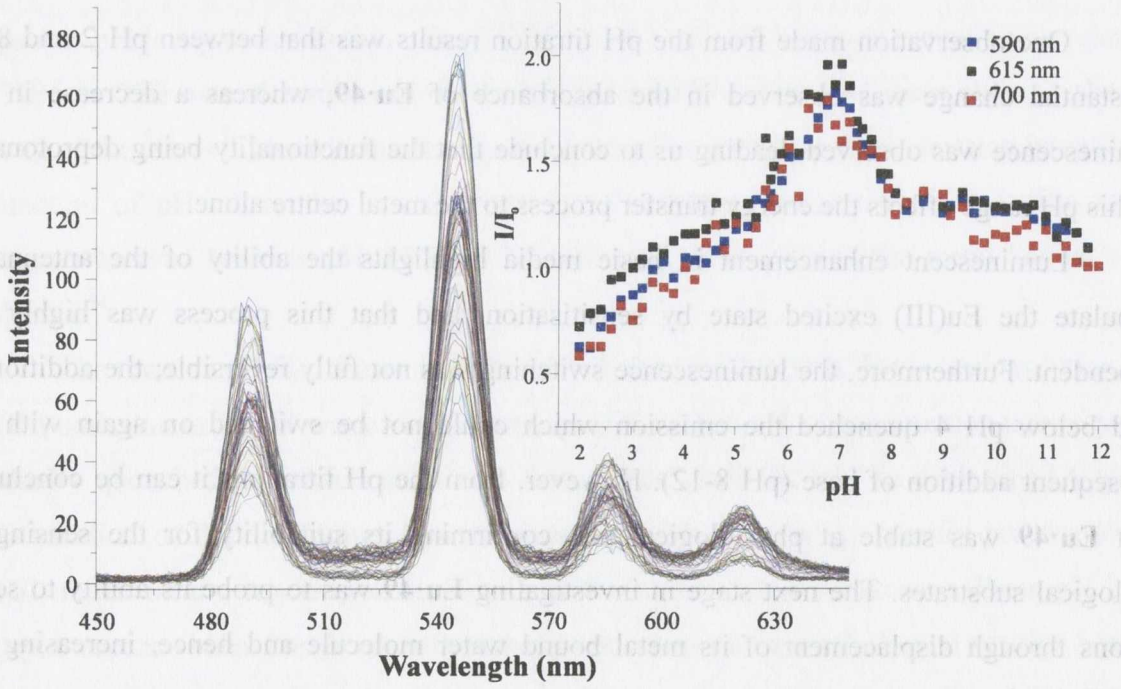


Figure 2.11: *The Tb(III) luminescence response of* ***Tb·49*** *(λ_{ex} = 318 nm) as a function of pH in a mixed DMSO:H_2O (1:99 v/v) solution [I = 0.1 M TEAP]. Inset: Changes in the Tb(III) emission intensity at 490 nm (J = 6), 545 nm (J = 5) and 585 nm (J = 4) as a function of pH.*

2.9 pH Response of Eu·49:Tb·49 in Solution

In a similar manner as for **Eu·49** and **Tb·49**, the UV-vis absorption, fluorescence and phosphorescence spectra of a solution containing a 50:50 mixture of **Eu·49:Tb·49** were recorded as a function of pH, in a mixed DMSO/H_2O (1:99 *v/v*) solution with TEAP (I = 0.1 M) to maintain a constant ionic strength. The results obtained for the UV-vis absorption and fluorescence studies (Figure 2.12a and b) were very similar to those obtained from pH titrations of both **Eu·49** and **Tb·49**, indicating that the presence of both Ln(III) ions did not change the properties of the ground or excited state of the quinaldine antenna.

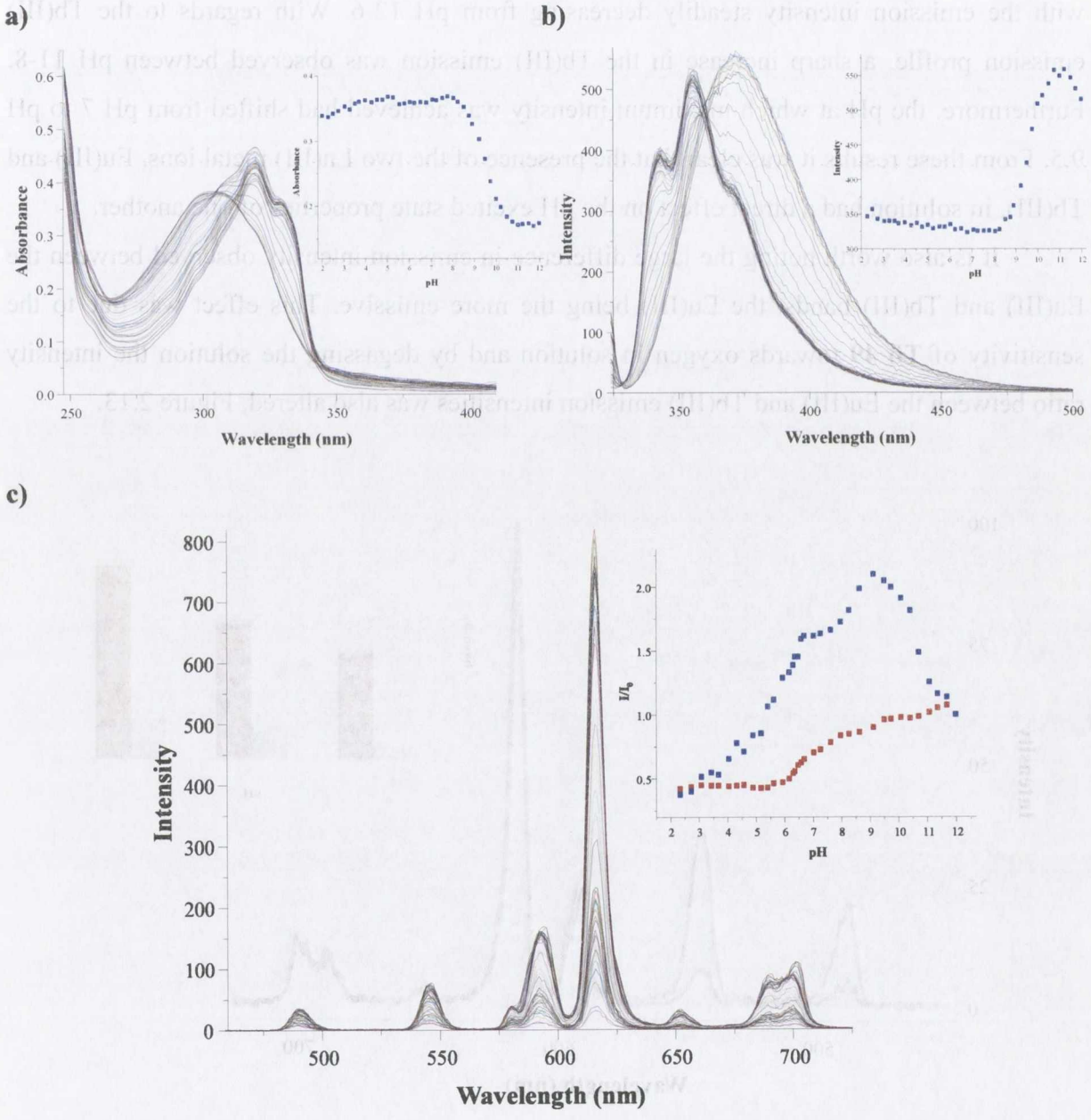


Figure 2.12: a) *Changes in the UV-vis absorption spectra of a 1:1 mixture of* ***Eu·49:Tb·49*** *as a function of pH. Inset: Changes in the absorbance at 330 nm as a function of pH.* ***b)*** *Changes in the fluorescence emission (λ_{ex} = 318 nm) spectra of* ***Eu·49:Tb·49*** *as a function of pH. Inset: Changes in the fluorescence at 370 nm as a function of pH.* ***c)*** *The Eu(III) and Tb(III) luminescence response of* ***Eu·49:Tb·49*** *(λ_{ex} = 318 nm). Inset: Changes in the normalised Eu(III) and Tb(III) emission intensity at 615 nm and 545 nm, respectively, as a function of pH.*

Investigation into the phosphorescence emission of **Eu·49**:**Tb·49** as a function of pH upon excitation into 318 nm lead to the spectra shown in Figure 2.12c. The results showed that there were slight deviations from the trends observed in the Ln(III) emission of the individual complexes, **Eu·49** and **Tb·49**, as a function of pH. As was observed with **Eu·49**, the Eu(III), emission was seen to be quenched at acidic pH, however it remains quenched until pH 6, by which the emission had almost reached its maximum and had started to stabilise for **Eu·49**.

Moreover, changes in the Eu(III) emission did occur over the physiological pH range, with the emission intensity steadily decreasing from pH 12-6. With regards to the Tb(III) emission profile, a sharp increase in the Tb(III) emission was observed between pH 11-8. Furthermore, the pH at which maximum intensity was achieved had shifted from pH 7 to pH 9.5. From these results it was clear that the presence of the two Ln(III) metal ions, Eu(III) and Tb(III), in solution had a direct effect on the pH excited state properties of one another.

It is also worth noting the large difference in emission intensity observed between the Eu(III) and Tb(III) bands, the Eu(III) being the more emissive. This effect was due to the sensitivity of **Tb·49** towards oxygen in solution and by degassing the solution the intensity ratio between the Eu(III) and Tb(III) emission intensities was also altered, Figure 2.13.

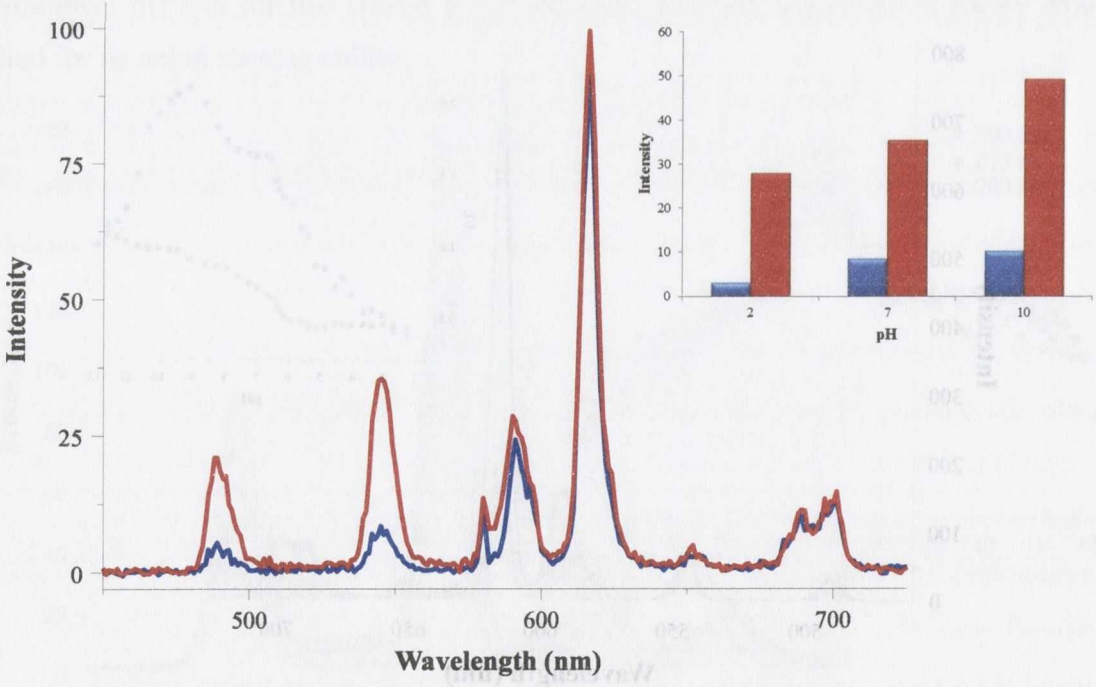


Figure 2.13: *The Eu(III) and Tb(III) luminescence response of* ***Eu·49***:***Tb·49*** *(λ_{ex} = 318 nm) at pH 7 in a mixed DMSO:H_2O (1:99 v/v) solution [I = 0.1 M TEAP] in gassed (-) and degassed (-) solutions. Inset: Changes in the Tb(III) emission intensity at 545 nm at pH 2, 7 and 10 in gassed (blue) and degassed (red) solutions.*

2.10 Anion Titrations of Eu·49

As discussed in the introduction to this Chapter, the aim of this project was to develop a luminescent sensor, capable of sensing biological analytes through displacement of the metal bound water molecules. During the photophysical evaluation of **Eu·49** as outlined above, it was determined from the luminescence lifetime measurements that the complex possessed only one metal bound water molecule and not two as had been anticipated (Section 2.5).

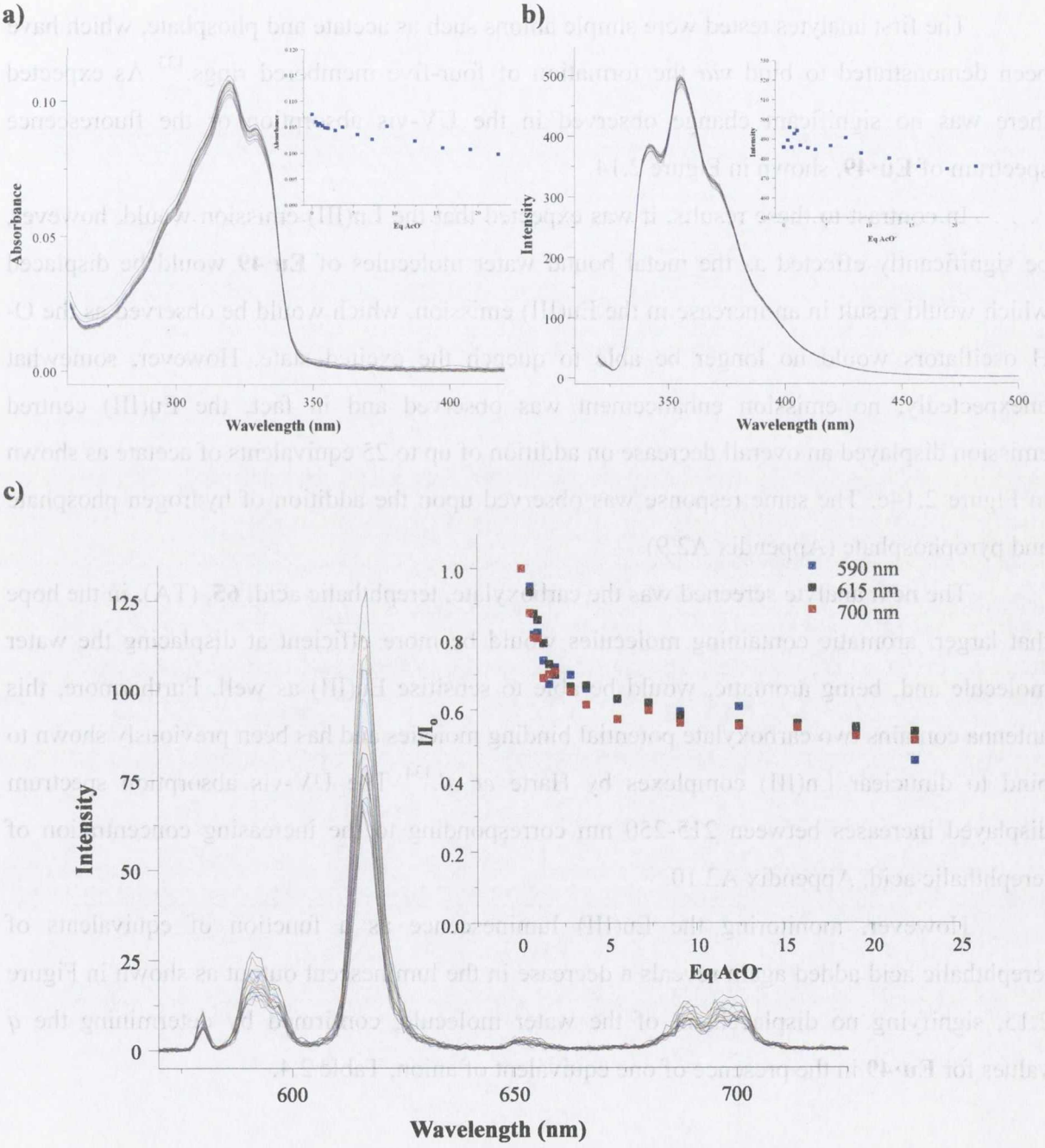


Figure 2.14: *Changes in the* ***a)*** *UV-vis absorption spectra* ***b)*** *fluorescence spectra (λ_{ex} = 318 nm) and* ***c)*** *Eu(III) emission of* ***Eu·49*** *(1 × 10^{-5} M) as a function of equivalents of AcO^- at pH 7.4 in 0.1 M HEPES. Insets: Changes in the* ***a)*** *absorbance at 318 nm and* ***b)*** *fluorescence at 355 nm and* ***c)*** *Eu(III) emission at 592, 615 and 700 upon the addition of AcO^- (0-25 equivalents).*

In theory, the addition of analytes to the complex could cause displacement of this metal bound water molecule, giving rise to the formation of a nine-coordinate complex and an enhancement in the Eu(III) emission upon excitation of the quinaldine antenna as the quenching effect of the water molecule would be removed. Analytes containing carboxylates, phosphates and diketonates were chosen for investigation as they all exhibit strong binding affinities towards Ln(III) metal ions.[132] All titrations were carried out in a buffered pH 7.4 environment (0.1 M HEPES) and were fully reproducible.

The first analytes tested were simple anions such as acetate and phosphate, which have been demonstrated to bind *via* the formation of four-five membered rings.[133] As expected there was no significant change observed in the UV-vis absorption or the fluorescence spectrum of **Eu·49**, shown in Figure 2.14.

In contrast to these results, it was expected that the Ln(III) emission would, however, be significantly effected as the metal bound water molecules of **Eu·49** would be displaced which would result in an increase in the Eu(III) emission, which would be observed as the O-H oscillators would no longer be able to quench the excited state. However, somewhat unexpectedly, no emission enhancement was observed and in fact, the Eu(III) centred emission displayed an overall decrease on addition of up to 25 equivalents of acetate as shown in Figure 2.14c. The same response was observed upon the addition of hydrogen phosphate and pyrophosphate (Appendix A2.9).

The next analyte screened was the carboxylate, terephthalic acid, **65**, (TA), in the hope that larger, aromatic containing molecules would be more efficient at displacing the water molecule and, being aromatic, would be able to sensitise Eu(III) as well. Furthermore, this antenna contains two carboxylate potential binding moieties and has been previously shown to bind to dinuclear Ln(III) complexes by Harte *et al.*[134] The UV-vis absorption spectrum displayed increases between 215-250 nm corresponding to the increasing concentration of terephthalic acid, Appendix A2.10.

However, monitoring the Eu(III) luminescence as a function of equivalents of terephthalic acid added again reveals a decrease in the luminescent output as shown in Figure 2.15, signifying no displacement of the water molecule, confirmed by determining the q values for **Eu·49** in the presence of one equivalent of anion, Table 2.4.

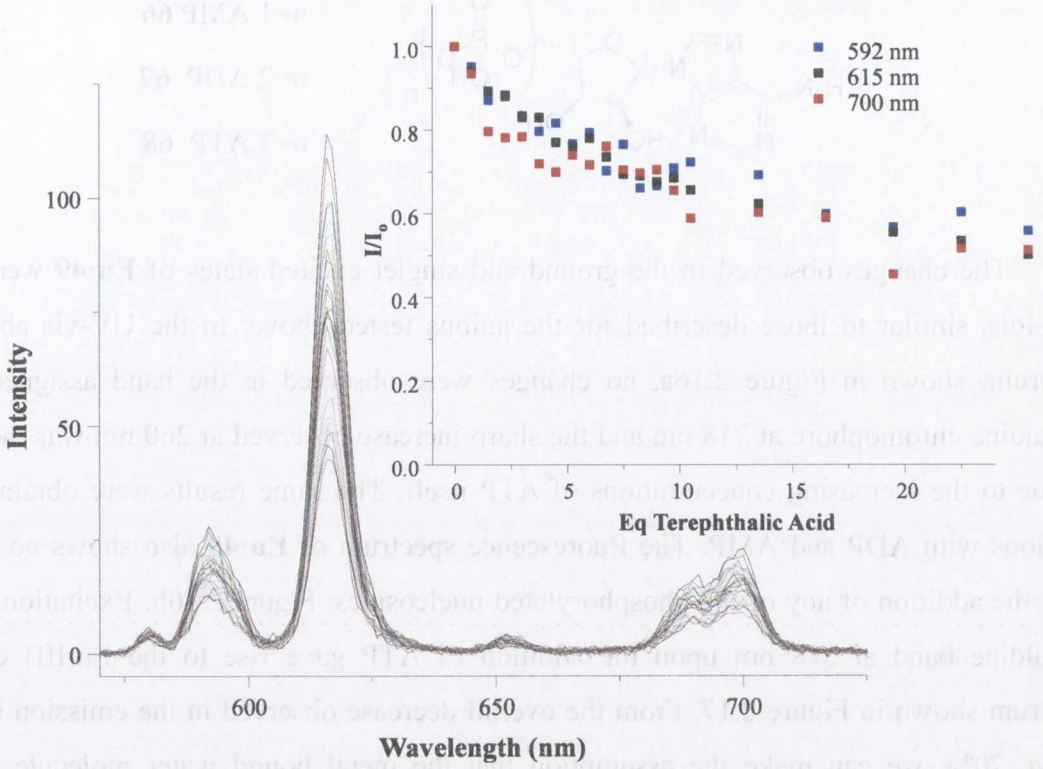
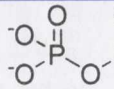
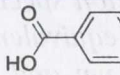
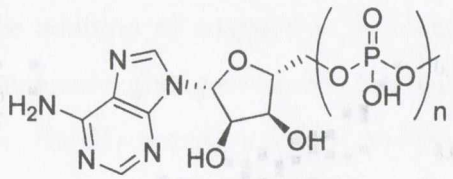


Figure 2.15: *The Eu(III) luminescence response (λ_{ex} = 318 nm) of* ***Eu·49*** *(1×10^{-5} M) as a function of equivalents of terephthalic acid at pH 7.4 in 0.1 M HEPES. Inset: Changes in the phosphorescence at 615 nm upon the addition of terephthalic acid (0-25 equivalents).*

Table 2.3 gives a summary of the anions studied thus far, and the overall effect they had on the Eu(III) emission. Larger biomolecules AMP (**66**), ADP (**67**) and ATP (**68**), containing one, two and three phosphate groups, respectively, were also studied as potential analytes for **Eu·49**, with the idea that the phosphate groups would be capable of displacing the metal bound water molecule.

Table 2.3: *Anion titrations of* ***Eu·49*** *buffered at pH 7.4 (0.1 M HEPES) and their effect on the Eu(III) luminescence.*

Anion Titrated	Structure	Effect on luminescence
AcO^-	 **63**	↓ 21 %
$HP_2O_7^{3-}$	 **64**	↓ 30 %
Terephthalic acid	 **65**	↓ 46 %



n=1 AMP **66**

n=2 ADP **67**

n=3 ATP **68**

The changes observed in the ground and singlet excited states of **Eu·49** were on all occasions similar to those described for the anions tested above. In the UV-vis absorption spectrum, shown in Figure 2.16a, no changes were observed in the band assigned to the quinaldine chromophore at 318 nm and the sharp increase observed at 260 nm was thought to be due to the increasing concentrations of ATP itself. The same results were obtained from titrations with ADP and AMP. The fluorescence spectrum of **Eu·49** also shows no changes upon the addition of any of the phosphorylated nucleosides, Figure 2.16b. Excitation into the quinaldine band at 318 nm upon the addition of ATP gave rise to the Eu(III) emission spectrum shown in Figure 2.17. From the overall decrease observed in the emission intensity by *ca.* 70%, we can make the assumption that the metal bound water molecule was not displaced by ATP. Again, the exact same effect was seen upon the addition of AMP and ADP (Appendix A2.11 and A2.12) which both display a decrease in Eu(III) emission by *ca.* 70%, concluding that the nucleosides were not efficient at either binding to or sensitising **Eu·49**.

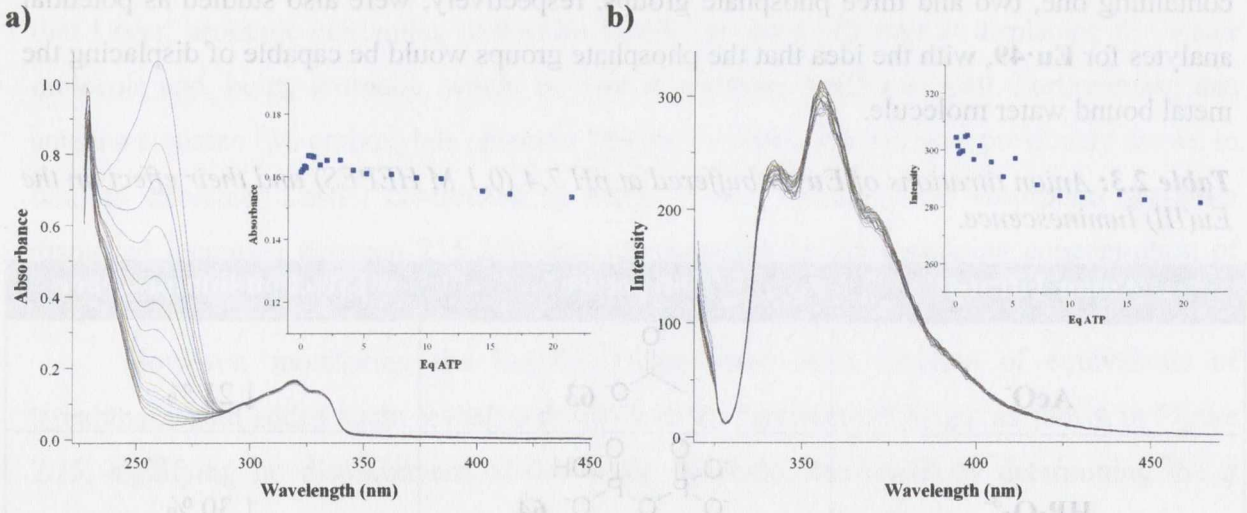


Figure 2.16: *Changes in the* ***a)*** *UV-vis absorption spectra and* ***b)*** *fluorescence spectra (λ_{ex} = 318 nm) of* ***Eu·49*** *(1×10^{-5} M) as a function of equivalents of ATP at pH 7.4 in 0.1 M HEPES. Insets: Changes in the* ***a)*** *absorbance at 318 nm and* ***b)*** *fluorescence at 355 nm upon the addition of ATP (0-25 equivalents).*

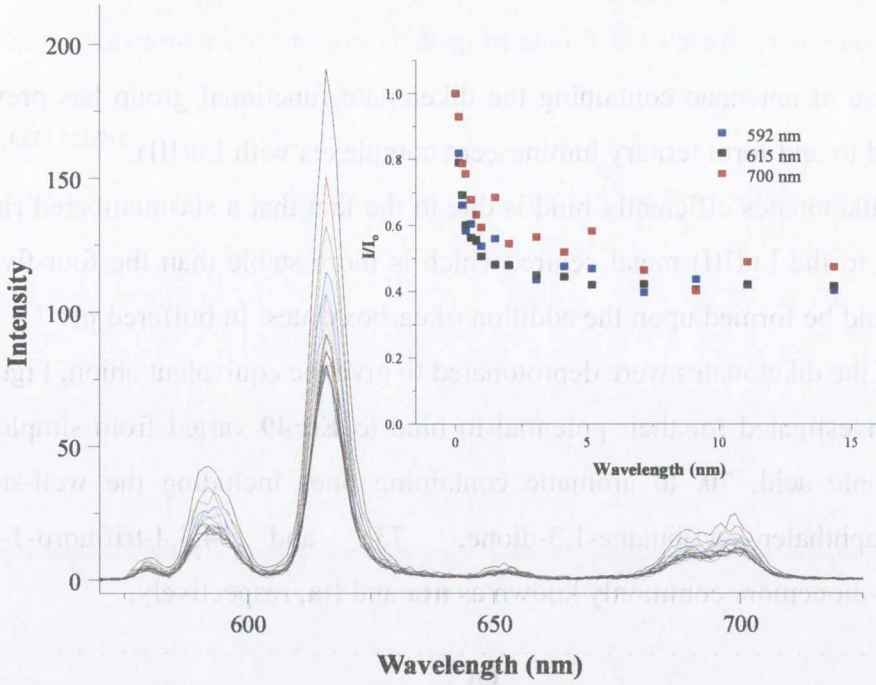


Figure 2.17: *The Eu(III) luminescence response (λ_{ex} = 318 nm) of* ***Eu·49*** *(1×10^{-5} M) as a function of equivalents of ATP at pH 7.4 in 0.1 M HEPES. Inset: Changes in the phosphorescence at 592, 615 and 700 nm upon the addition of ATP (0-15 equivalents).*

To provide further proof that there was no displacement of the water molecule occurring, lifetimes of **Eu·49** were obtained in the presence of one equivalent of each of the analytes studied thus far with a summary of all the *q* values obtained shown in Table 2.4. The excited state lifetimes of **Eu·49** were measured in a mixed DMSO/H_2O (1:99 *v/v*) system (τ_{H2O}) and a mixed DMSO-d_6/D_2O (1:99 *v/v*) system (τ_{D2O}) by indirect excitation of the antenna at 318 nm. The value of *q* was then determined using the Horrocks modified equation developed by Parker *et al.* as discussed in Section 1.3.2.[35,129] In each case, a *q* value of 1 was obtained, verifying that there was still one water molecule attached to **Eu·49** in the presence of the analytes.

Table 2.4: *Lifetime studies for* ***Eu·49****, with one equivalent of analyte added, at neutral pH, each number is an average of 6 measurements all agreeing to within 5 % of each other with an error of ± 0.01.*

	τ_{H2O}(ms)	τ_{D2O}(ms)	k_{H2O}(ms^{-1})	k_{D2O}(ms^{-1})	*q* (± 0.5)
Eu·49	0.65	1.56	1.53	0.64	0.9
+ AMP	0.56	1.00	1.77	0.99	0.7
+ ADP	0.56	1.08	1.78	0.91	0.8
+ ATP	0.63	1.35	1.56	0.74	0.7
+ AcO^-	0.58	1.15	1.70	0.87	0.8
+ $H_2PO_4^-$	0.53	1.07	1.77	0.93	0.9
+ TA	0.55	1.11	1.73	0.90	0.9

2.10.1 Titrations with Antennae Containing the Diketonate Framework

The use of antennae containing the diketonate functional group has previously been shown to bind to and form ternary luminescent complexes with Ln(III).[117,125,132,135] One of the reasons that diketonates efficiently bind is due to the fact that a six-membered ring is formed upon binding to the Ln(III) metal centre, which is more stable than the four-five membered rings that would be formed upon the addition of carboxylates. In buffered pH 7.4 solutions the H_α protons of the diketonates were deprotonated to give the equivalent anion, Figure 2.18. The diketonates investigated for their potential to bind to **Eu·49** varied from simple diketonates such as malonic acid, **70**, to aromatic containing ones including the well-studied 4,4,4-trifluoro-1-(naphthalen-2-yl)butane-1,3-dione, **73**, and 4,4,4-trifluoro-1-(thiophen-2-yl)butane-1,3-dionemore commonly known as **nta** and **tta**, respectively.

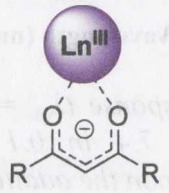
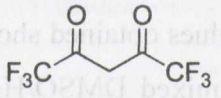
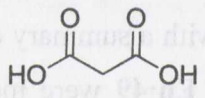


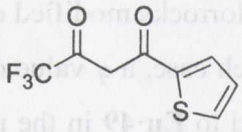
Figure 2.18: *Illustration of the six-membered ring formed between Ln(III) and diketonate containing molecules.*



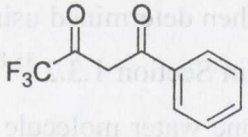
69



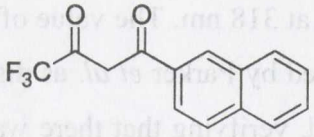
70



71



72



73

The trends observed from titrations involving the analytes containing no chromophore, **69-70**, were in keeping with what had been observed in the previous titrations. There was little or no change detected in the UV-vis absorption or fluorescence spectrum of **Eu·49**, indicating that the addition of the diketonates had no observable effect on the ground or singlet excited state of **Eu·49**. In contrast, the Eu(III) emission displayed a decrease in intensity in the case of Malonic acid, Figure 2.19, Appendix A2.13, again indicating that no displacement of the metal bound water molecule was occurring. The excited state lifetimes of **Eu·49** with one equivalent of **69-70** were measured in a mixed DMSO/H_2O (1:99 *v/v*) system (τ_{H2O}) and a mixed DMSO-d_6/D_2O (1:99 *v/v*) system (τ_{D2O}) by indirect excitation of Eu(III) at 318 nm. In each case, a q value of 1 was obtained, confirming the presence of one water molecule attached to **Eu·49**.

The next group of analytes studied possessed both the diketonate moiety, capable of binding to Ln(III) *via* the formation of a six membered ring, and an aromatic group which could efficiently sensitise the Eu(III) metal centre. The diketonates in question were 4,4,4-trifluoro-1-(thiophen-2-yl)butane-1,3-dione, **71** (**tta**), 4,4,4-trifluoro-1-phenylbutane-1,3-dione, **72** (**tfp**), 4,4,4-trifluoro-1-(naphthalen-2-yl)butane-1,3-dione **73** (**nta**). The presence of an aromatic group implies that the UV-vis absorption spectrum will be affected upon the addition of **tta**, **tfp** and **nta**.

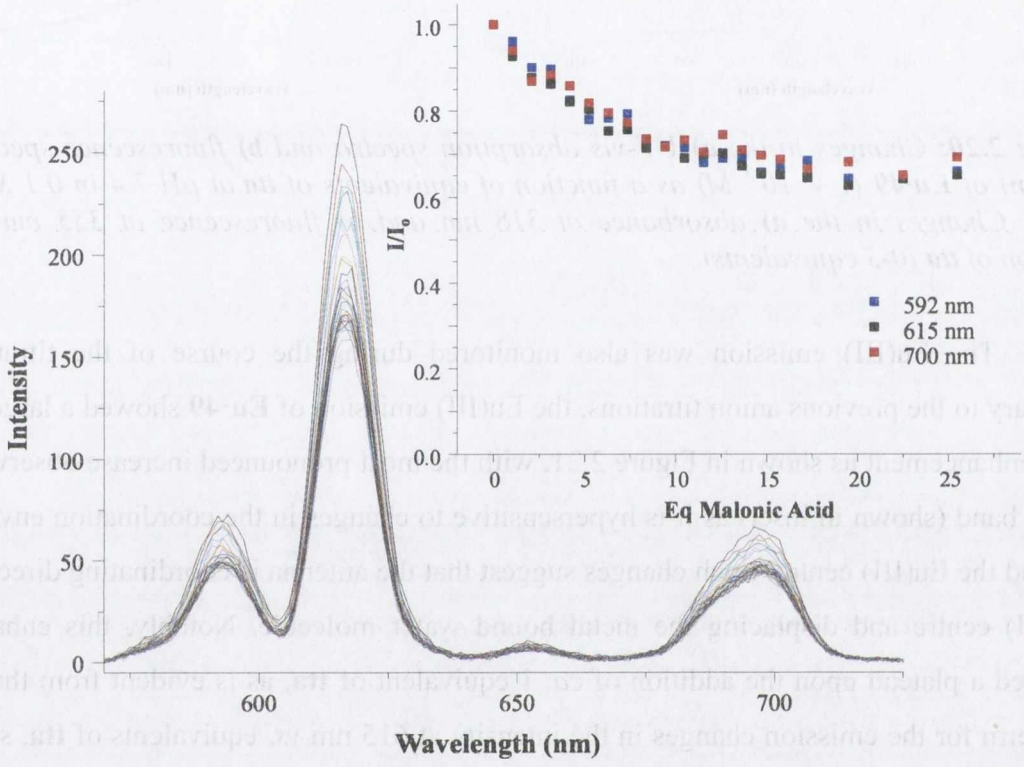


Figure 2.19: *The Eu(III) luminescence response (λ_{ex} = 318 nm) of* ***Eu·49*** *(1×10^{-5} M) as a function of equivalents of Malonic Acid at pH 7.4 in 0.1 M HEPES. Inset: Changes in the phosphorescence at 615 nm upon the addition of Malonic Acid (0-25 equivalents).*

The changes in the UV-vis absorption spectrum for the titration of **Eu·49** with **tta**, shown in Figure 2.20a, display a consecutive increase in the absorbance band centred at 330-340 nm. This rise can be attributed to the increasing concentration of **tta** in solution as the UV-vis absorption spectrum of **tta** contains a band at 340 nm (Appendix A2.14). The changes in absorbance at 245 nm and 350 nm can be accredited to the $S_0 \rightarrow {}^1\pi\pi^*$ and the $S_0 \rightarrow {}^3n\pi^*$ transitions, respectively. Excitation into 318 nm gave rise to the fluorescence emission spectrum shown in Figure 2.20b, which was significantly quenched upon the addition of **tta**. The UV-vis absorption and fluorescence spectra of **Eu·49** upon titration with **nta** and **tfp** are shown in Appendix A2.16 and A2.17, respectively, and display similar changes to those described above for **tta**.

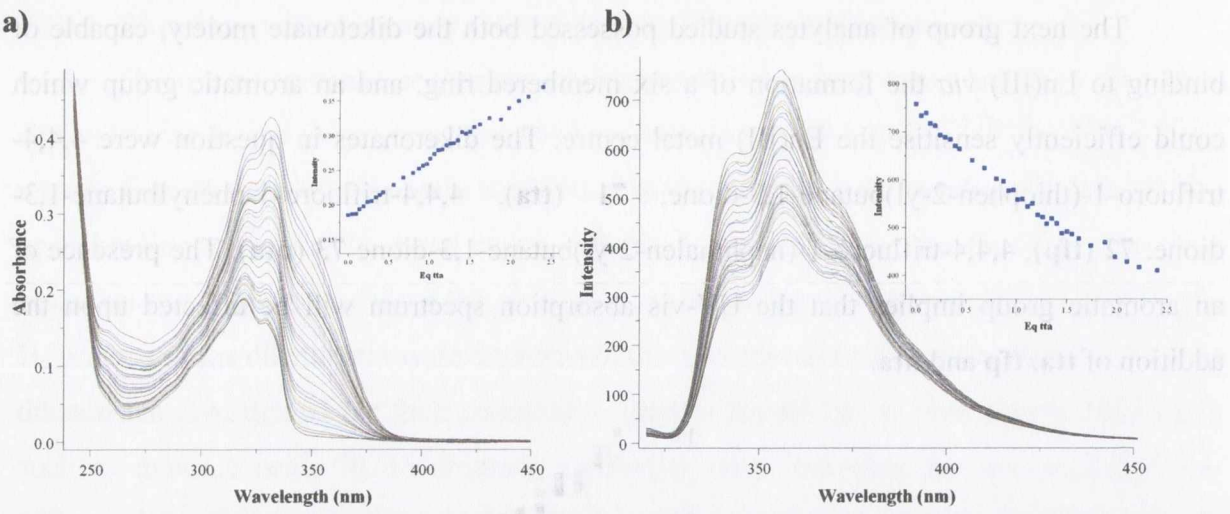


Figure 2.20: *Changes in the* ***a)*** *UV-vis absorption spectra and* ***b)*** *fluorescence spectra (λ_{ex} = 318 nm) of* ***Eu·49*** *(1×10^{-5} M) as a function of equivalents of* ***tta*** *at pH 7.4 in 0.1 M HEPES. Insets: Changes in the* ***a)*** *absorbance at 318 nm and* ***b)*** *fluorescence at 355 nm upon the addition of* ***tta*** *(0-3 equivalents).*

The Eu(III) emission was also monitored during the course of the titration and, contrary to the previous anion titrations, the Eu(III) emission of **Eu·49** showed a large, *ca.* 30-fold enhancement as shown in Figure 2.21, with the most pronounced increase observed in the $J = 2$ band (shown in inset) as it is hypersensitive to changes in the coordination environment around the Eu(III) centre. Such changes suggest that the antenna is coordinating directly to the Eu(III) centre and displacing the metal bound water molecule. Notably, this enhancement reached a plateau upon the addition of *ca.* 1 equivalent of **tta**, as is evident from the binding isotherm for the emission changes in the intensity at 615 nm *vs.* equivalents of **tta**, signifying the formation of a 1:1 ternary complex between **Eu·49** and **tta**. The same trend and simultaneous formation of a 1:1 ternary complex were also obtained from titrations of **Eu·49** with **tfp** and **nta** respectively (see Appendix A2.18, A2.19 and A2.20). Sensitisation of the Eu(III) metal centre was ascertained by recording excitation spectra before and after the addition of **tta**, Appendix A2.15. Before the addition of **tta**, it matches closely the absorption spectrum of **Eu·49**. However, after forming the ternary complex **Eu·49-tta**, the excitation spectra suggests that the Eu(III) emission is arising from both the antenna and the added **tta**.

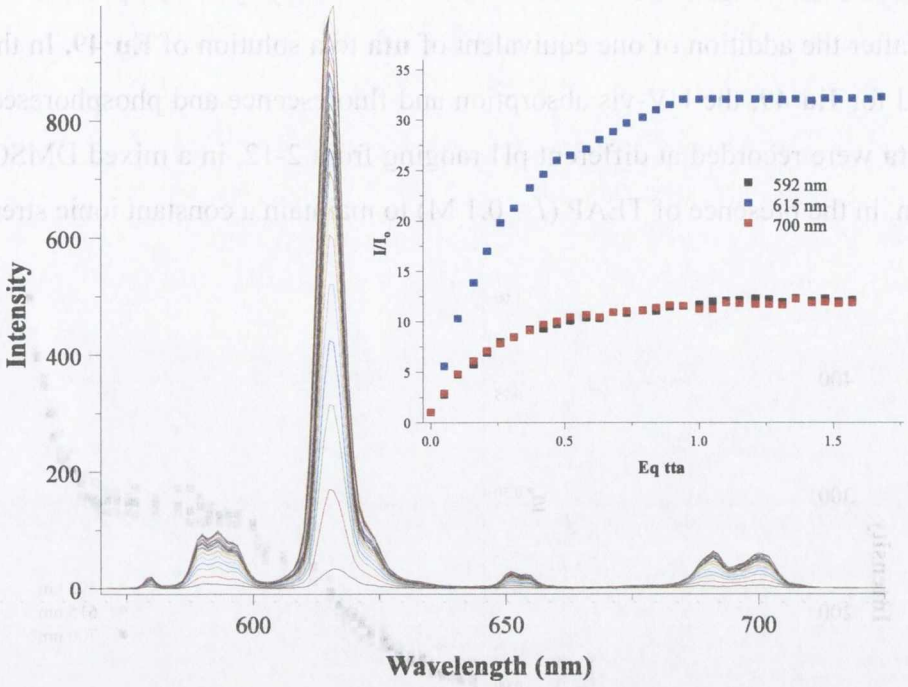


Figure 2.21: *The Eu(III) luminescence response (λ_{ex} = 318 nm) of* ***Eu·49*** *(1×10^{-5} M) as a function of equivalents of* ***tta*** *at pH 7.4 in 0.1 M HEPES. Inset: Changes in the Eu(III) emission at 592, 615 and 700 nm upon the addition of* ***tta*** *(0-2 equivalents).*

The q values were determined for **Eu·49** in the presence of one equivalent of **tta**, **nta** and **tfp** to confirm that the addition of the diketonates had indeed displaced the metal bound water molecule. The excited state lifetimes were measured in a mixed DMSO/H_2O (1:99 *v/v*) system (τ_{H2O}) and a mixed DMSO-d_6/D_2O (1:99 *v/v*) system (τ_{D2O}) by excitation at 318 nm of the antenna. The value of q was then determined using Horrocks modified equation developed by Parker *et al.* (Section 1.3.2).[35,129] In each case, a q value of 0 was obtained, Table 2.5, verifying that displacement of the water molecules had occurred, and furthermore, the lifetimes observed were all longer than that of the complex on its own and best fit to a single exponential decay.

Table 2.5: *Lifetime studies for* ***Eu·49****, with one equivalent of diketonate added at neutral pH, each number is an average of 6 measurements all agreeing to within 5% of each other with an error of ± 0.01.*

Eu·49	τ_{H2O} (ms)	τ_{D2O} (ms)	k_{H2O} (ms^{-1})	K_{D2O} (ms^{-1})	q (±0.5)
+ nta	0.80	0.96	1.25	1.02	0
+ tta	0.77	0.86	1.22	1.16	0
+ tfp	0.79	0.92	1.24	1.09	0

To further investigate the formation of the 1:1 ternary system, a pH titration study was carried out after the addition of one equivalent of **nta** to a solution of **Eu·49.** In the same way as described for **Eu·49**, the UV-vis absorption and fluorescence and phosphorescence spectra of **Eu·49-nta** were recorded at different pH ranging from 2-12, in a mixed DMSO/H_2O (1:99 *v/v*) solution, in the presence of TEAP (I = 0.1 M) to maintain a constant ionic strength.

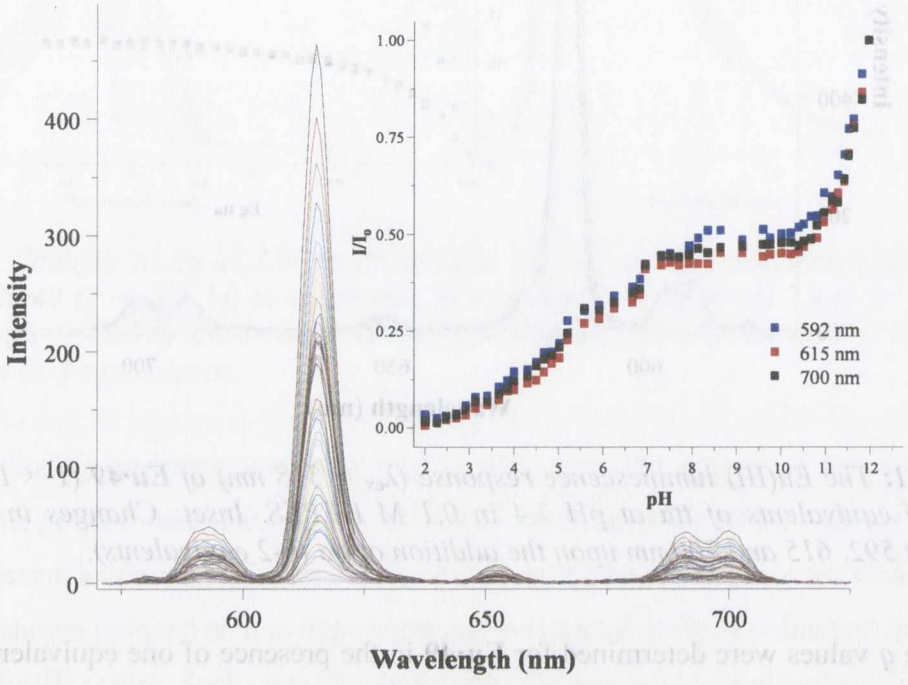


Figure 2.22: *The Eu(III) luminescence response of* ***Eu·49-nta*** *(λ_{ex} = 318 nm) as a function of pH in a mixed DMSO:H_2O (1:99 v/v) solution [I = 0.1 M TEAP]. Inset: Changes in the Eu(III) emission intensity at 592, 615 and 700 nm as a function of pH.*

The results from this investigation demonstrate that the changes in the ground and singlet excited state mirror those of the complex alone as a function of pH (Appendix 2.21), *i.e.* the addition of the external antenna **nta** did not affect the pH behaviour of **Eu·49**. The Eu(III) emission of the ternary system **Eu·49-nta** was next examined using an excitation wavelength of 318 nm and the overall results are shown in Figure 2.22. A considerable difference was observed in the trend in the Ln(III) luminescence spectrum, signifying the Eu(III) emission of the self-assembly that was highly pH dependent.

With **Eu·49** shown to be a physiological pH stable sensor and the ternary **Eu·49-nta/tta/tfp** system studied, synthesis of the Eu(III) functionalised **AuNPs** was next undertaken. The following section will describe the different methods employed in the synthesis of **AuNPs** followed by functionalisation with **Eu·49**.

2.11 Functionalisation of AuNPs with Eu·49

The synthesis of **AuNPs** can be achieved using various methods described in the literature.[136] Once synthesised, the functionalisation of **AuNPs** by surface modification allows for the introduction of many diverse functionalities onto the **AuNP** surface. Two different methods will be discussed in the following sections; the Brust-Schiffrin two-phase method and the citric acid method. Given that we wanted water soluble functionalised **AuNPs**, such methods were ideally suited for the proposed formation of **AuNP-Eu·49**.

2.11.1 Modified Brust-Schiffrin Method

The first attempt used a modified version of the Brust-Schiffrin two-phase method which reports the formation of **AuNPs** with an average diameter of 5 nm.[137] Full description of the method is given in Chapter 7. This procedure involves mixing an aqueous solution of hydrogen tetrachloroaurate [Au(III)], 0.025 M with a solution of tetraoctylammonium bromide [TOAB], 0.026 M in toluene and the two phase mixture was vigorously stirred until all the gold had been transferred into the organic layer. It was then reduced to Au(II) with the addition of the reducing agent sodium borohydride [$NaBH_4$], 0.003 M, Figure 2.23, where the organic phase was seen to rapidly change colour from orange to purple after vigorous stirring, indicating the formation of the colloidal species.



$HAuCl_4 \cdot 3H_2O$ in water | + TOAB in toluene | + $NaBH_4$ in water

Figure 2.23: *Reduction of Au(III) to Au(II) using the Brust-Schiffrin two-phase method.*

The resulting reduced **AuNPs** in the toluene layer were separated from the water layer using a separating funnel and washed with H_2O, acid (0.1 M HCl) and base (0.1 M NaOH). In order to exchange the TOAB stabiliser on the surface with **Eu·49**, a solution of **Eu·49** in a mixed DMSO/H_2O (1:99 *v/v*) solution (*ca.* 1×10^{-4} M) was stirred vigorously overnight with **AuNP** in toluene (*ca.* 1×10^{-2} M). The initially pale yellow aqueous solution turned a deep

purple colour confirming phase transfer of the **AuNPs** from the toluene layer to the aqueous layer. The aqueous layer was separated and any unbound **Eu·49** was removed using sephadex G15 column chromatography with NaCl (0.05 M) as the eluent. A purple **AuNP** band was observed moving down the column, with any unbound complex remaining at the top of the column. The **AuNP-Eu·49** were characterised using UV-vis absorption spectroscopy, dynamic light scattering (DLS) and transmission electron microscopy (TEM) techniques, details of which are described in the following sections. The resulting water-soluble **AuNP-Eu·49** were found to be stable for many months when kept at room temperatures in aqueous solution.

2.11.2 Citric Acid Method

The second method used for the synthesis of **AuNPs** was the citric acid method, which involves only the use of aqueous solution and not a mixed organic-aqueous one such as that described above. Moreover, it is known to give larger particles than the Brust-Schiffrin method of *ca.* 20-40 nm in diameter.[138] A small amount of hydrogen tetrachloroaurate (0.04 g) was dissolved in a large volume of Millipore water (300 mL) to give a *ca.* 3×10^{-4} M solution. The yellow coloured solution was heated, and once at boiling point a solution (4×10^{-2} M) of citric acid in Millipore water (10 mL) was added and the mixture refluxed at 110°C for a further 20 minutes, over which time the solution turned from pale yellow to a deep red signifying the formation of the colloidal species in aqueous solution. Formation of the **AuNPs** was confirmed by the UV-vis absorption spectrum which shows the appearance of the characteristic surface plasmon resonance (SPR) band at *ca.* 520 nm. Functionalisation was achieved by stirring a solution of **Eu·49** with the citric acid stabilised **AuNPs**. However, continual monitoring of the UV-vis absorption spectrum revealed the gradual aggregation of the **AuNPs** in solution and for this reason, the principal method of **AuNP** synthesis carried out for the remainder of this Thesis will be the modified Brust-Schiffrin method.

2.12 Characterisation of AuNP-Eu·49

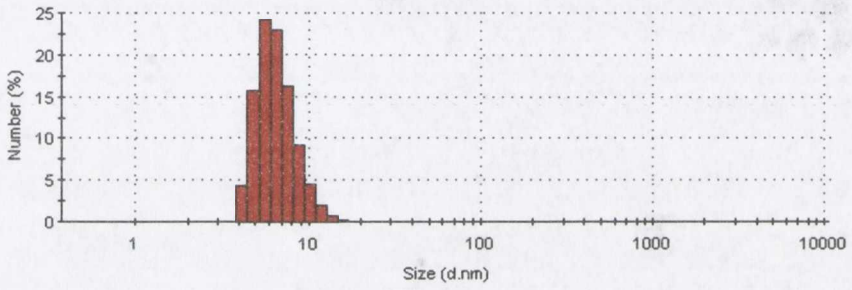
2.12.1 Dynamic Light Scattering Studies of AuNP-Eu·49

In order to obtain an approximate size of the diameter of the **AuNP** conjugate species **AuNP-Eu·49**, dynamic light scattering (DLS) measurements were carried out using a Malvern Zetasizer Instrument. DLS is a non-invasive technique used to determine the size distribution profile of small particles in suspension or polymers in solution.[139] One condition of this technique is that the particles in question must be undergoing Brownian motion, induced by the bombardment of solvent molecules in the sample that themselves are in motion. These particles are illuminated by a laser source; the intensity of the resulting

scattered light fluctuates at a rate that is proportional to the size of the molecules in the solution. The diameter that is measured by DLS takes into account not only the particle "core", but also anything that is bound to its surface; this is referred to as the hydrodynamic diameter and represents how a particle diffuses within a fluid.

DLS measurements were carried out on filtered samples of **AuNP-Eu·49** and gave hydrodynamic diameter readings of 6.66 ± 1.40 nm for the **AuNPs** synthesised by the modified Brust-Schiffrin method and 54.11 ± 4.80 nm for the **AuNPs** synthesised by the citric acid method, the size distribution graphs being shown in Figure 2.24.

a)



b)

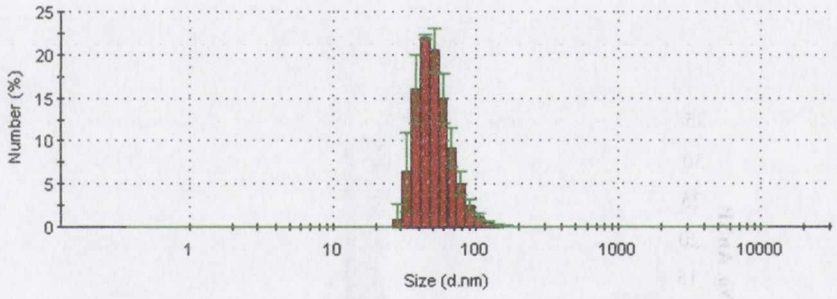


Figure 2.24: *Particle size distribution plots as determined from DLS analysis for* ***AuNP-Eu·49*** *synthesised by* ***a)*** *modified Brust-Schiffrin method and* ***b)*** *citric acid method.*

The results of the hydrodynamic diameter range of the **AuNPs** is in keeping with previously reported **AuNPs** synthesised according to similar procedures.[108,117,137,138] Furthermore, the DLS data also illustrates a very narrow size distribution of **AuNPs** indicating no agglomeration of the **AuNPs** has occurred in solution. This information suggests successful formation of **AuNP-Eu·49**. Further characterisation of the **AuNPs** was carried out using TEM measurements, the results of which will be discussed in the following section.

2.12.2 Transmission Electron Microscopy Studies of AuNP-Eu·49

Further characterisation was achieved from transmission electron microscopy (TEM) measurements, a technique in which a beam of electrons is transmitted through a thin sample of the **AuNP** solution, interacting with the **AuNPs** as they pass through creating an image from the interaction. The images recorded from the Brust method showed the existence of monodisperse nanoparticles with diameter ranging from 4-15 nm as shown in Figure 2.25.

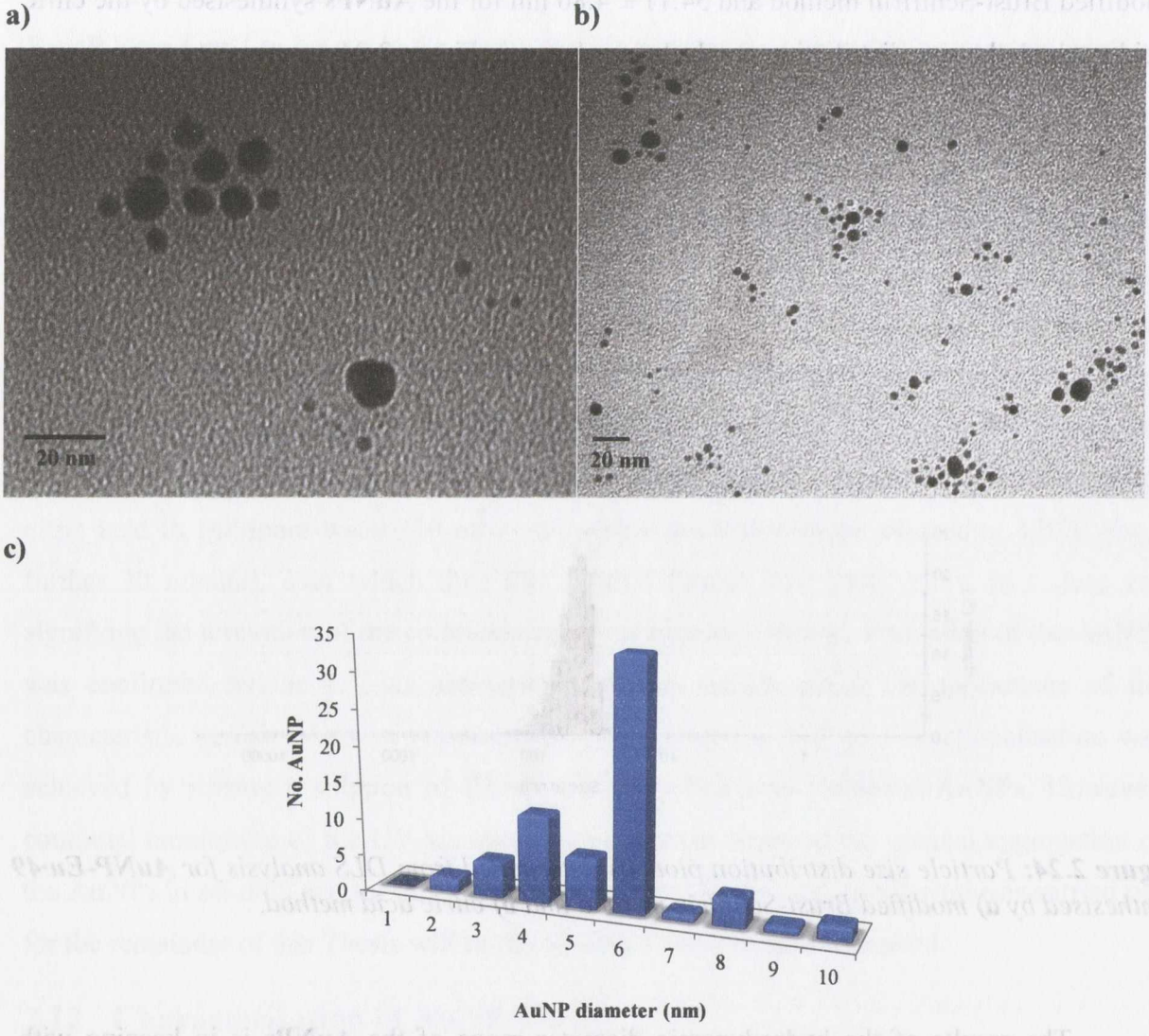


Figure 2.25: *TEM images of **AuNP-Eu·49** synthesised by the Brust method after deposition on copper grids showing: **a)** close-up image and **b)** a larger field view. **c)** The corresponding particle size distribution calculated from the TEM data.*

From these images it was clear that formation of the desired species **AuNP-Eu·49** was achieved. Particle size distribution was calculated by the measurement of *ca.* 100 particles in a field of view for each sample, and shows that the majority of **AuNPs** possess an average diameter of 6 nm, in keeping with that observed from DLS measurements. The images recorded from the citric acid method also showed the existence of monodisperse nanoparticles; however, the diameter had a significantly larger range of 30-60 nm, with the average diameter being 40 nm, as shown in Figure 2.26. Again, these results correlate well with results obtained from the DLS measurements discussed in the previous section. Furthermore, DLS and TEM of number of different batches of **AuNP-Eu·49** were obtained and were all found to agree within ± 1.8 and ± 1.3 nm for DLS and TEM, respectively.

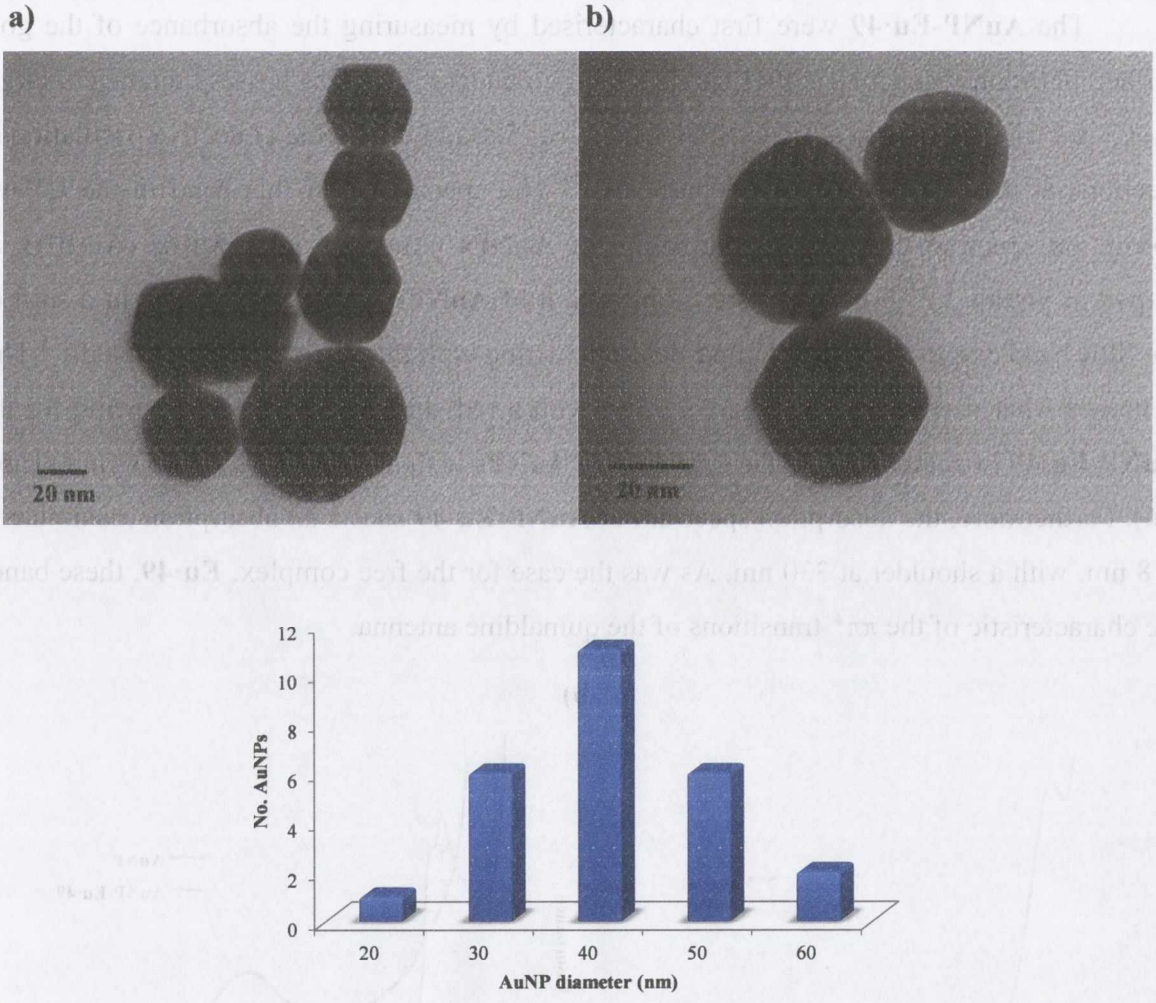


Figure 2.26: *TEM images of* ***AuNP-Eu·49*** *synthesised by the citric acid method after deposition on copper grids showing:* ***a)*** *and* ***b)*** *close up image.* ***c)*** *The corresponding particle size distribution calculated from the TEM data.*

In addition to DLS and TEM, further information regarding **AuNP-Eu·49** can be obtained using UV-vis spectroscopy, which is commonly utilised in the characterisation of the relationship between **AuNP** particle size and its optical properties as it is known that the size of **AuNPs** play a crucial role in their optical response.[105] Bearing this in mind, an investigation

into the photophysical properties of **AuNP-Eu·49** was undertaken, which will be discussed in the following section.

2.13 Photophysical Properties of AuNP-Eu·49

With **Eu·49** attached onto the **AuNPs**, the photophysical properties (absorption, fluorescence, phosphorescence spectra and lifetimes) of the functionalised nanoparticles could be investigated. As the **AuNPs** synthesised by the citric acid method were large and not fully stable in aqueous solution, they were not be fully investigated. Only a brief description of their photophysical properties is given herein and all spectra shown in the Appendix. Hence, the main focus will be on the **AuNPs** synthesised according to the modified Brust-Schiffrin method.

The **AuNP-Eu·49** were first characterised by measuring the absorbance of the gold surface plasmon resonance (SPR) band. Metallic nanoparticles that possess diameters larger than 3 nm usually display a broad SPR band at *ca.* 520 nm due to the collective oscillation of electrons at the surface of the nanoparticles.[140] The appearance of this band in the UV-vis absorption spectrum denotes the formation of **AuNPs** (Au(0)) from $HAuCl_4$ (Au(III)), as shown in Figure 2.27a. Furthermore, stabilisation of **AuNPs** with **Eu·49** results in a shift of the SPR band due to the strong ligand field interacting with the surface electron cloud.[141] This is indeed what was observed (Figure 2.27b), with a red shift of *ca.* 10 nm occurring for the **AuNP-Eu·49** in comparison to the unstabilised **AuNPs** with an average λ_{max} at 533 nm (Table 2.6). Furthermore, the absorption spectrum of **AuNP-Eu·49** shows an absorption maximum at 318 nm, with a shoulder at 330 nm. As was the case for the free complex, **Eu·49**, these bands are characteristic of the $\pi\pi^*$ transitions of the quinaldine antenna.

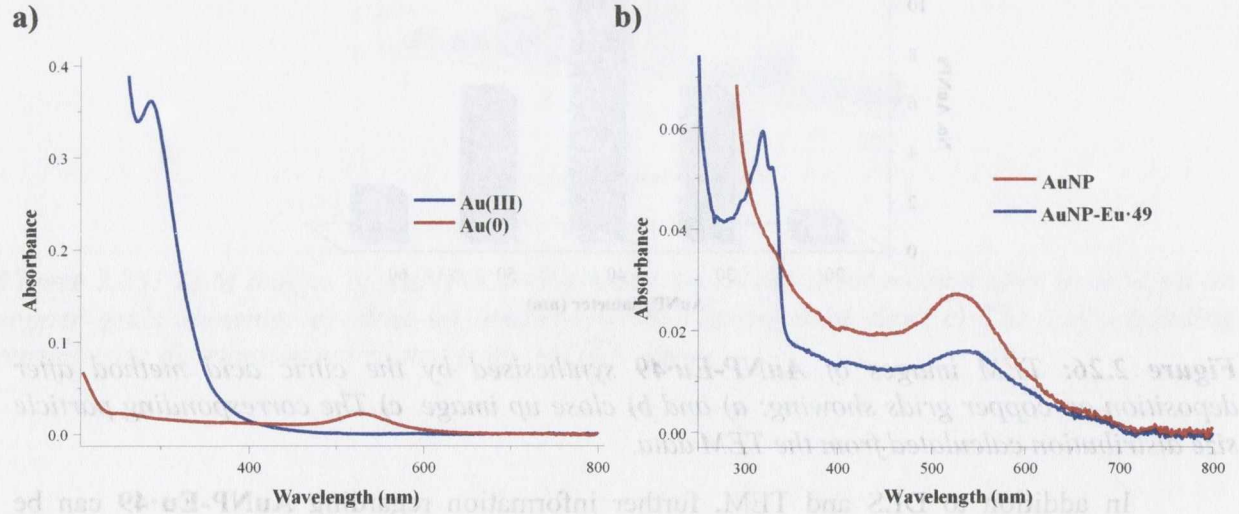


***Figure 2.27: a)** Appearance of the SPR band in the UV-vis absorption spectrum upon reduction of Au(III) to Au(0). **b)** Shift of the SPR band by ca. 10 nm upon functionalisation of the **AuNPs** with **Eu·49**.*

Table 2.6: *Absorption maxima of different samples of* ***AuNP-Eu·49****.*

Sample	λ_{max} (nm)
1	535
2	537
3	531
4	528
5	534

The UV-vis absorption spectrum of the citric acid **AuNPs** before and after functionalisation with **Eu·49** is shown in Appendix A2.22, where a shift of *ca.* 5 nm was observed in the SPR band.

In the same manner as the unbound complex, excitation into the main absorption band of **AuNP-Eu·49** at 318 nm produced a fluorescence emission spectrum, possessing a λ_{max} at 355 nm and two minor shoulders at 345 nm and 370 nm, shown in Figure 2.28a. Figure 2.28b shows the Eu(III) emission resulting from the transitions from the $^5D_0$ state to the ^7F_J state of the Eu(III) ion where J = 0 (577 nm), 1 (591 nm), 2 (616 nm), 3 (651 nm), 4 (split; 690 nm and 699 nm). There was a small amount of quenching observed in the Eu(III) compared to that of the unbound complex. Such behaviour can be attributed to the deactivation of the excited state of **Eu·49** when bound to the **AuNPs**. The fluorescence and phosphorescence spectra for the citric acid method **AuNPs** were found to be almost identical to those below.

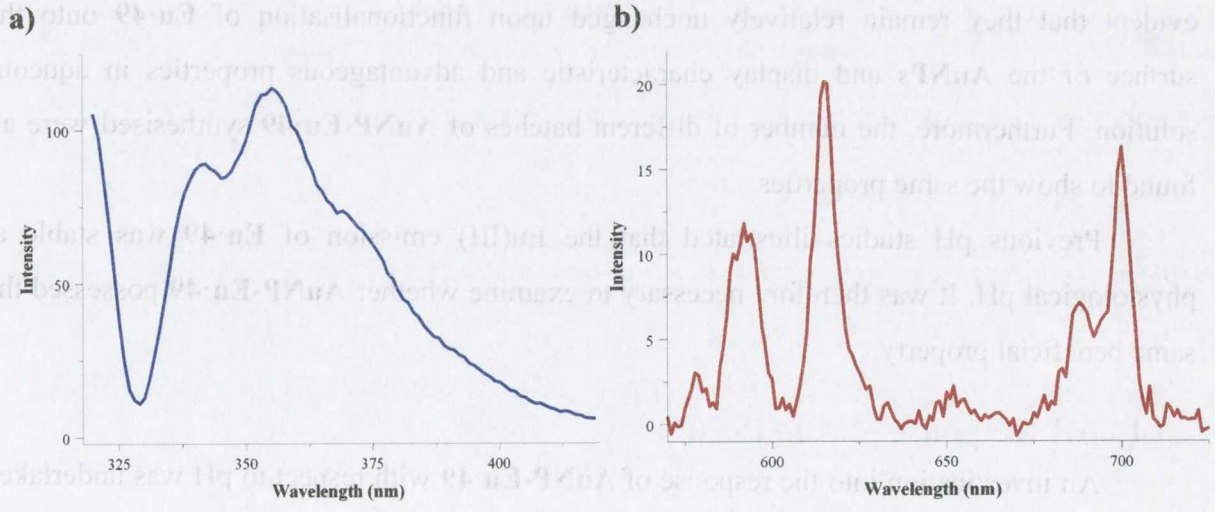


Figure 2.28: ***a)*** *Fluorescence spectrum and* ***b)*** *Eu(III) emission spectrum of* ***AuNP-Eu·49*** *in aqueous solution (λ_{ex} = 318 nm).*

In order to further investigate the excited state properties of **AuNP-Eu·49**, excited state lifetime measurements were recorded in buffered pH 7.4 solution (HEPES 0.1 M). Indirect excitation at 318 nm afforded the decay profile illustrated in Figure 2.29, which was

best fit to a monoexponential decay to give a lifetime of $\tau = 0.44 \pm 0.01$ ms. The observed decrease in the lifetime of **AuNP-Eu·49** in comparison to the unbound complex **Eu·49** ($\tau = 0.65 \pm 0.01$ ms) can be attributed to quenching as a consequence of attachment to the **AuNP** surface, in keeping with the reduced emission of the Eu(III) emission spectrum.

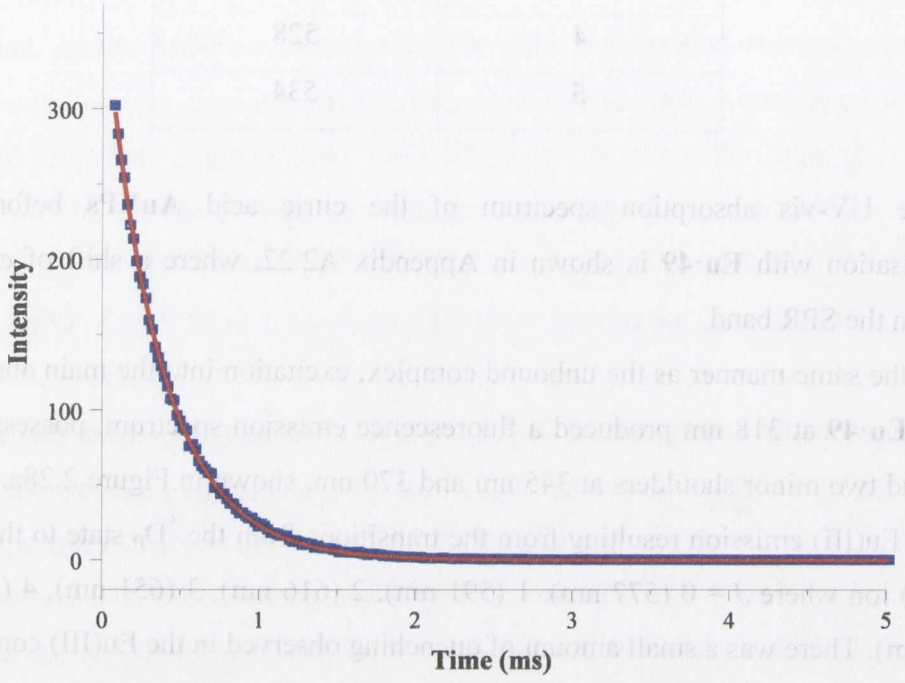


Figure 2.29: *Luminescence decay of **AuNP-Eu·49** fit to a monoexponential decay in aqueous solution (λ_{ex} = 318 nm).*

In summary, having investigated the photophysical properties of **AuNP-Eu·49** it was evident that they remain relatively unchanged upon functionalisation of **Eu·49** onto the surface of the **AuNPs** and display characteristic and advantageous properties in aqueous solution. Furthermore, the number of different batches of **AuNP-Eu·49** synthesised were all found to show the same properties.

Previous pH studies illustrated that the Eu(III) emission of **Eu·49** was stable at physiological pH. It was therefore necessary to examine whether **AuNP-Eu·49** possessed the same beneficial property.

2.14 pH Response of AuNP-Eu·49

An investigation into the response of **AuNP-Eu·49** with respect to pH was undertaken in a similar manner to that of **Eu·49**, as described in this Chapter, Section 2.7. Firstly, the effect of pH on the ground state and singlet excited state of **AuNP-Eu·49** was analysed in H_2O in the presence of tetraethylammonium perchlorate (TEAP) (I = 0.1 M). Changes observed in the UV-vis absorption spectrum and fluorescence spectrum were identical to those observed for the unbound complex **Eu·49**. The changes in the Eu(III) emission intensity as a

function of pH were analogous to those obtained for the unbound complex, and are shown in Figure 2.30; **AuNP-Eu·49** showed stability over the physiological pH range. The only observable difference was in the quality of the spectra obtained, in which the Eu(III) emission bands were rather broad and the splitting of the bands, such as $J = 4$, was not seen. This was due to the different parameters used in order to obtain relatively intense Eu(III) emission spectra so as to accommodate for the quenching effect of the **AuNPs** on the Eu(III) emission.

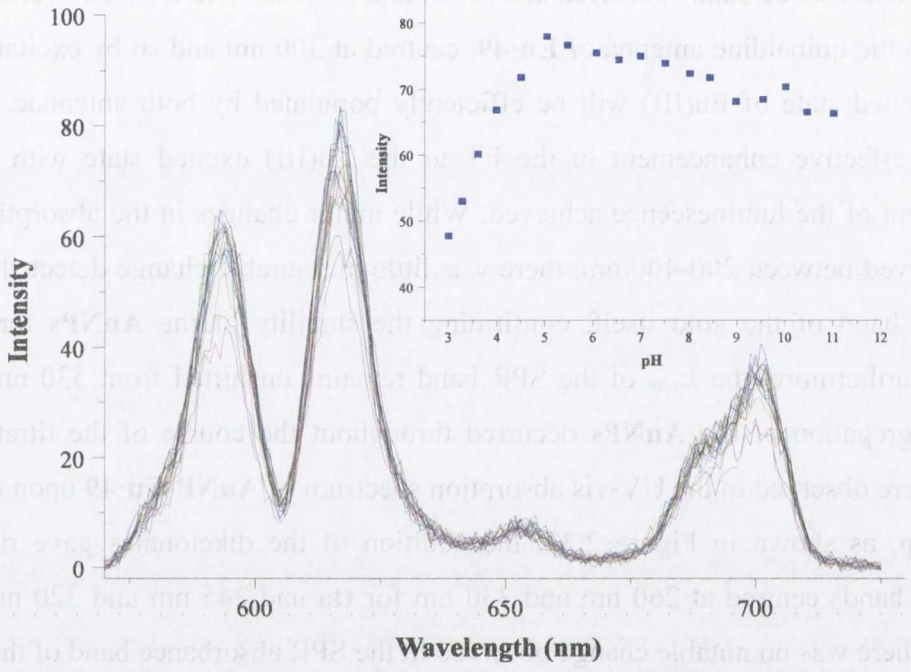


Figure 2.30: *Changes in the Eu(III) luminescence response of* ***AuNP-Eu·49*** *(λ_{ex} = 318 nm) as a function of pH in aqueous solution [I = 0.1 M TEAP]. Inset: Eu(III) emission intensity at 615 nm as a function of pH.*

With the pH behaviour, and hence photostability within the physiological pH range, of **Eu·49** remaining unchanged upon attachment to **AuNPs**; we next needed to establish whether the functionalised **AuNPs**, **AuNP-Eu·49** behaved in a similar way to the unbound complex **Eu·49**; *i.e.* to determine if the luminescence can be switched on by the addition of the external antenna through anion titrations.

2.15 Anion Titrations of AuNP-Eu·49

The sensing ability of the unbound complex **Eu·49** by displacement of the metal bound water molecule has previously been discussed in this Chapter, the results of which established that only the aromatic containing diketonates **nta**, **tta** and **tfp** had the ability to displace the metal bound water molecule and bind to the Eu(III) metal centre, hence enhancing the Eu(III) emission. Consequently, titrations were carried out on **AuNP-Eu·49** in buffered solutions pH 7.4, 0.1 M HEPES, in the presence of increasing amounts of the diketonates **nta**, **tta** and **tfp** (0-160 equivalents) and the ground, singlet excited and triplet

excited state of **AuNP-Eu·49** were monitored. The concentration of **AuNP-Eu·49** was determined by using the extinction coefficient (ε_{318} = 27039 M^{-1} cm^{-1}) previously established for **Eu·49**. Similar results were obtained for all three titrations, of which the **nta** titration will be discussed in detail, while the other two titrations plots will be shown in the Appendix.

The overall changes in the UV-vis absorption spectrum of **AuNP-Eu·49** upon titration with **nta** are shown in Figure 2.31. As was observed for the complex alone, the appearance of two strong absorbance bands occurred at 245 nm and 330 nm. These bands overlap with those assigned to the quinaldine antenna of **Eu·49**, centred at 300 nm and so by excitation into 318 nm the excited state of Eu(III) will be efficiently populated by both antennae. This should ensure an effective enhancement in the ET to the Eu(III) excited state with concomitant enhancement of the luminescence achieved. While major changes in the absorption spectrum were observed between 200-400 nm, there was little measurable change detected for the SPR absorption band of the gold itself, confirming the stability of the **AuNPs** throughout the titration. Furthermore, the λ_{max} of the SPR band remains unshifted from 530 nm, signifying that no aggregation of the **AuNPs** occurred throughout the course of the titration. Similar changes were observed in the UV-vis absorption spectrum of **AuNP-Eu·49** upon titration with **tta** and **tfp**, as shown in Figure 2.32; the addition of the diketonates gave rise to strong absorption bands centred at 260 nm and 330 nm for **tta** and 245 nm and 320 nm for **tfp**. In each case there was no notable change observed in the SPR absorbance band of the **AuNPs**.

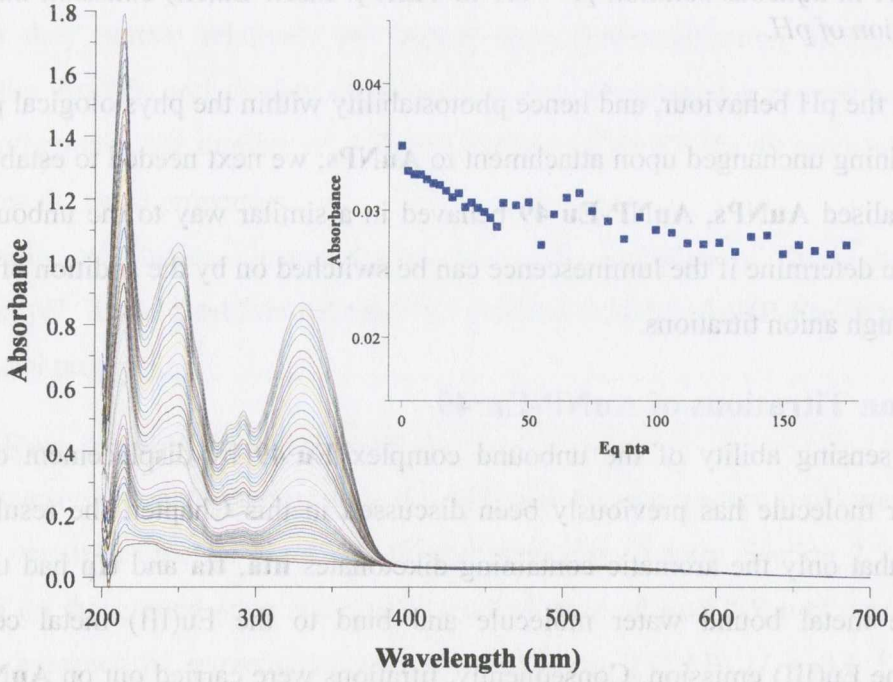


Figure 2.31: *Changes in UV-vis absorption spectrum of* ***AuNP-Eu·49*** *(λ_{ex} = 318 nm) (1 × 10^{-7} M) as a function of added equivalents of* ***nta*** *at pH 7.4 in 0.1 M HEPES. Inset: Corresponding changes in the SPR band at 534 nm.*

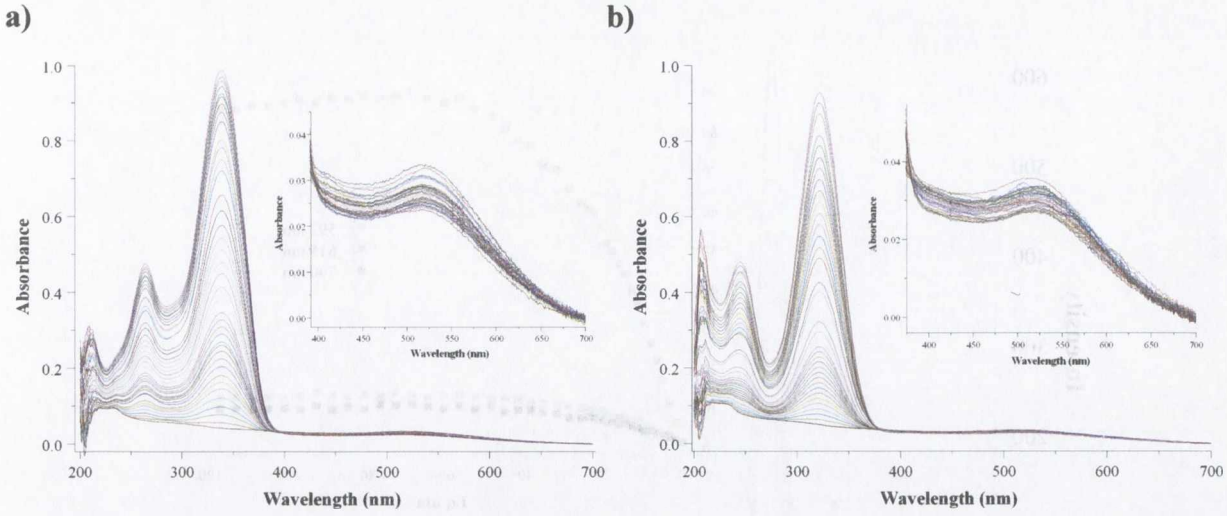


Figure 2.32: *Changes in the UV-vis absorption spectra of* ***AuNP-Eu·49*** *(1×10^{-7} M) as a function of equivalents of* ***a) tta*** *and* ***b) tfp*** *at pH 7.4 in 0.1 M HEPES. Insets: Changes in the SPR band.*

The changes in the singlet excited state of **AuNP-Eu·49** were also monitored upon the addition of **nta**, and the overall changes are shown in Figure 2.33 and Appendix A2.23. There was *ca.* 40% decrease observed in the fluorescence emission intensity of **AuNP-Eu·49** at 370 nm, which is characteristic of the $\pi\pi^*$ deactivation of the quinaldine moiety, with a concomitant 27 fold increase in the fluorescence band at 450 nm, attributed to the **nta** itself. Similar fluorescence changes were observed upon the addition of **tta** and **tfp** to **AuNP-Eu·49** under identical conditions. These results were in agreement with similar systems previously studied within the Gunnlaugsson group.[142]

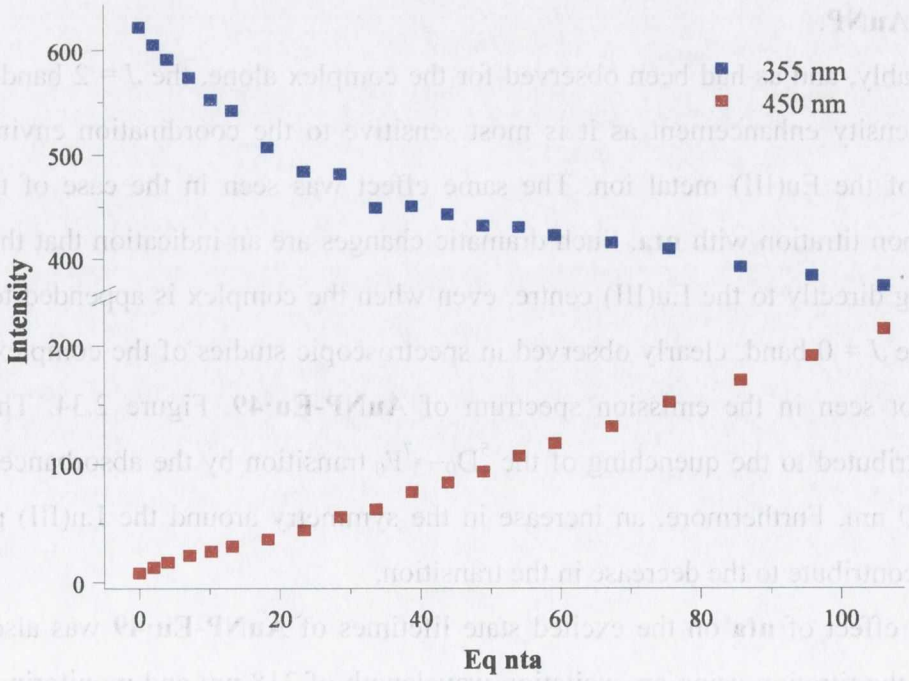


Figure 2.33: *Changes in fluorescence spectrum of* ***AuNP-Eu·49*** *at 355 nm and 450 nm (λ_{ex} = 318 nm) (1×10^{-7} M) as a function of equivalents of* ***nta*** *at pH 7.4 in 0.1 M HEPES.*

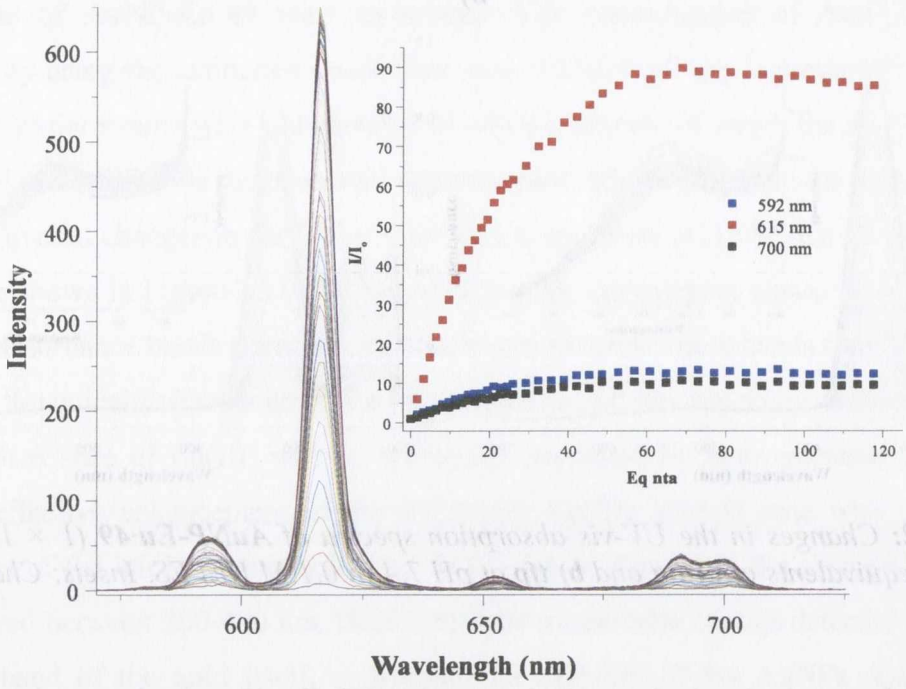


Figure 2.34: *The Eu(III) luminescence response (λ_{ex} = 318 nm) of* ***AuNP-Eu·49*** *(1 × 10^{-7} M) as a function of equivalents of* ***nta*** *at pH 7.4 in 0.1 M HEPES. Inset: Changes in the normalised Eu(III) emission at 615 nm upon the addition of* ***nta*** *(0-180 equivalents).*

As expected, large enhancements were observed in the Eu(III) ^7F_J (J = 0-4) emission bands upon the addition of **nta**, with maximum intensity occurring after addition of *ca.* 60 ± 10 equivalents of the antenna, as shown in Figure 2.34. Considering it has been established that **Eu·49** formed a 1:1 ternary complex with **nta**, a plateau initiating after the addition of 60 equivalents might be taken as an indication that *ca.* 60 ± 10 **Eu·49** complexes were attached to an average **AuNP**.

Notably, and as had been observed for the complex alone, the J = 2 band showed the greatest intensity enhancement as it is most sensitive to the coordination environment and symmetry of the Eu(III) metal ion. The same effect was seen in the case of the unbound complex upon titration with **nta**. Such dramatic changes are an indication that the antenna is coordinating directly to the Eu(III) centre, even when the complex is appended to the **AuNP** surface. The J = 0 band, clearly observed in spectroscopic studies of the complex alone, was however not seen in the emission spectrum of **AuNP-Eu·49**, Figure 2.34. This could be possibly attributed to the quenching of the $^5D_0 \rightarrow {}^7F_0$ transition by the absorbance of the SPR band at 520 nm. Furthermore, an increase in the symmetry around the Ln(III) metal centre could also contribute to the decrease in the transition.

The effect of **nta** on the excited state lifetimes of **AuNP-Eu·49** was also monitored throughout the titration using an excitation wavelength of 318 nm and monitoring the Eu(III) emission at 615 nm in the presence of varying concentrations of **nta**. These measurements

were best fit to a monoexponential decay; *i.e.* there was one species present in solution (Appendix A2.24). The lifetimes observed, shown in Table 2.7 were lower than that of the complex alone (0.65 ± 0.01 ms), possibly due to the quenching effect on the Eu(III) from the **AuNP** surface, and remained unchanged throughout the titration. A possible explanation for this could be that the lifetimes observed are only from the highly emissive ternary complexes on the **AuNPs** and the emission from the non-ternary complexes cannot be observed.

Table 2.7: *Lifetime studies for* ***AuNP-Eu·49-nta*** *with increasing equivalents of* ***nta*** *at pH 7.4 with an error of ± 0.01.*

AuNP-Eu·49	τ_{H2O}
+ 1 eq **nta**	**0.37**
+ 15 eq **nta**	**0.37**
+ 30 eq **nta**	**0.37**
+ 50 eq **nta**	**0.37**
+ 80 eq **nta**	**0.37**

The results from the analysis of the photophysical properties of **AuNP-Eu·49** have shown it to retain most of the properties of the unbound complex **Eu·49** upon attachment to the **AuNP** surface. With such success attained, we decided to extend the functionalisation of the **AuNPs** to incorporate **Tb·49** to form **AuNP-Tb·49**.

2.16 AuNP-Tb·49

The **AuNPs** were synthesised and functionalised in the same manner as described above for **AuNP-Eu·49**; using the Brust-Schiffrin method. Exchanging the TOAB stabiliser on the surface with **Tb·49**, was achieved by stirring a solution of **Tb·49** in a mixed DMSO/H_2O (1:99 *v/v*) solution of *ca.* 1×10^{-4} M vigorously overnight with the **AuNP** solution in toluene (*ca.* 1×10^{-2} M). The aqueous layer turned from a pale yellow to a deep purple colour, verifying that the phase transfer of **AuNPs** from toluene to the aqueous layer had occurred. Purification of **AuNP-Tb·49** was achieved using sephadex G15 column chromatography with NaCl (0.05 M) as the eluent. **AuNP-Tb·49** were found to be fully water soluble and stable for many months when kept at room temperatures in aqueous solution. The **AuNP-Tb·49** were characterised using TEM and DLS techniques. The DLS measurements were carried out on filtered samples of **AuNP-Tb·49** and gave hydrodynamic diameter readings of 10.95 nm, as shown in Figure 2.35c. The TEM images recorded showed the existence of monodisperse nanoparticles with diameters ranging from 5-15 nm as shown in Figure 2.35a and b.

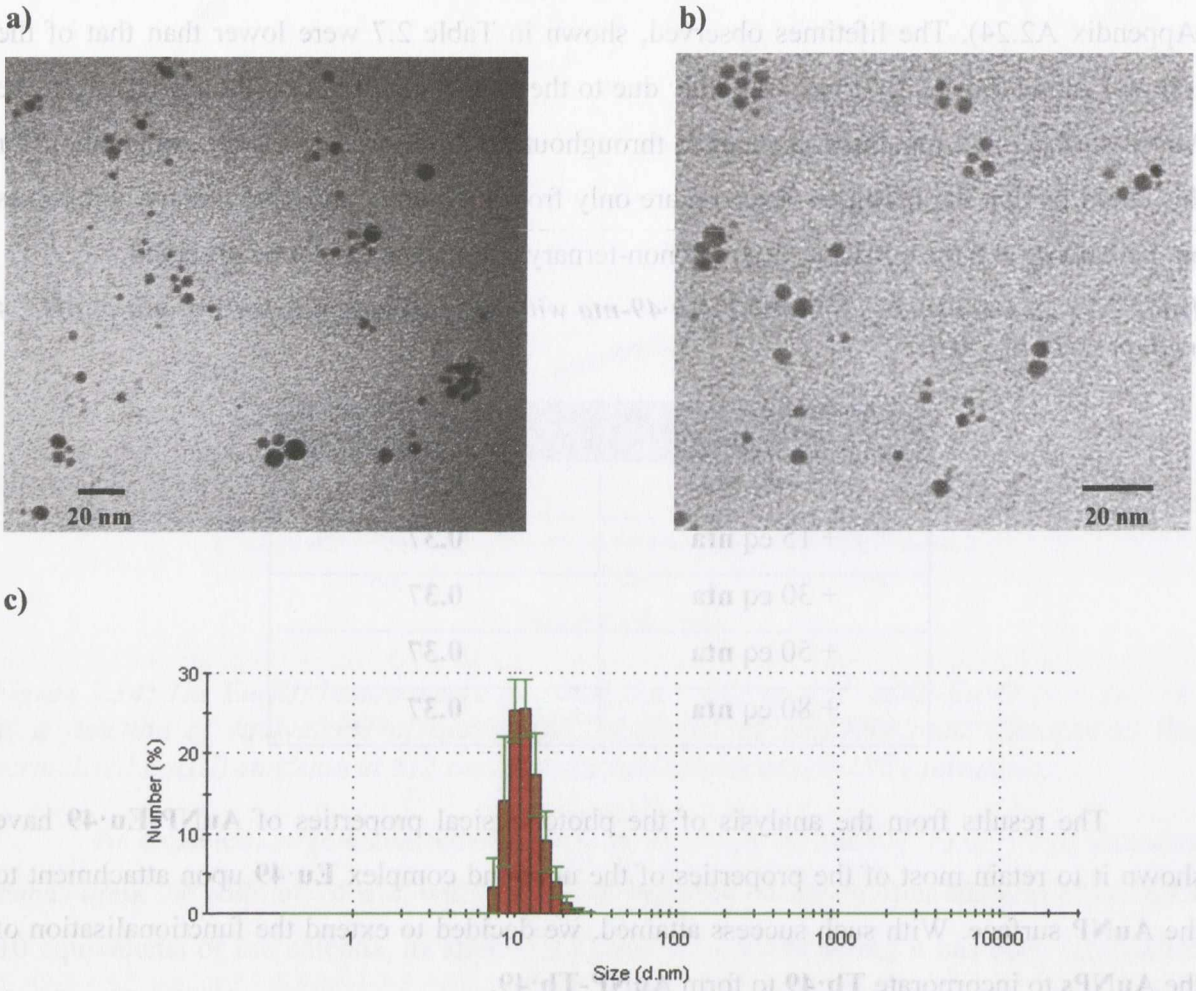


***Figure 2.35: a)** and **b)** TEM images of **AuNP-Tb·49** synthesised by a modified Brust-Schiffrin method after deposition on copper grids showing close up image. **c)** Particle size distribution plots as determined from DLS analysis for **AuNP-Tb·49**.*

The **AuNP-Tb·49** were also characterised using UV-vis absorption spectroscopy, in which the absorbance of the gold SPR band was recorded. The reduction of Au(III) to Au(0), and hence the formation of **AuNPs** was confirmed by the appearance of this band in the UV-vis absorption spectrum. The addition of **Tb·49** to stabilise the **AuNPs** and form **AuNP-Tb·49** can be seen by a bathochromic shift of the SPR band from 527 nm to 535 nm as a result of the strong ligand field interacting with the surface electron cloud.[141] The UV-vis absorption spectra of the unstabilised and **AuNPs** functionalised with **Tb·49** was shown in Figure 2.36a. Furthermore, the absorption spectrum of **AuNP-Tb·49** again shows the distinctive absorption maximum centred at 318 nm, with a slight shoulder at 330 nm. By exciting into the main absorption band at 318 nm, a fluorescence emission spectrum which was identical to that of the unbound complex, possessing a λ_{max} at 355 nm and two lesser shoulders observed at 342 nm and 370 nm, was observed (Figure 2.36b).

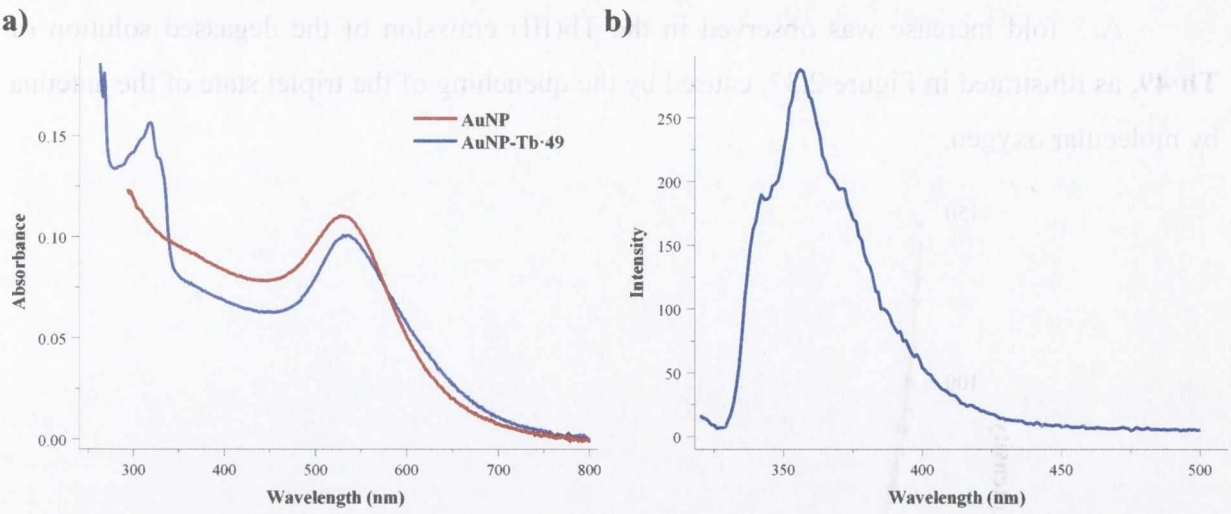


Figure 2.36: *a) UV-vis absorption spectrum of* ***AuNP*** *and* ***AuNP-Tb·49****. b) Fluorescence emission spectrum of* ***AuNP-Tb·49*** *in aqueous solution (λ_{ex} = 318 nm).*

The Tb(III) emission spectrum of **AuNP-Tb·49** was recorded to ensure that sensitisation of the Ln(III) metal centre could still be achieved once the complex **Tb·49** was attached to the **AuNP** surface. Figure 2.37 illustrates the Tb(III) emission resulting from the transitions from the $^5D_4$ state to the ^7F_J state of the Tb(III) ion where J = 6 (490 nm), 5 (545 nm), 4 (585 nm), 3 (620 nm). The quenching observed in the Tb(III) emission compared to that of the unbound complex was due to the deactivation of the excited state of **Tb·49** when bound to the **AuNPs**. Similar to that carried out for **Tb·49**, the effect that oxygen had on **AuNP-Tb·49** was examined. The luminescence of **AuNP-Tb·49** was measured before being degassed by carefully bubbling argon through it for five minutes.

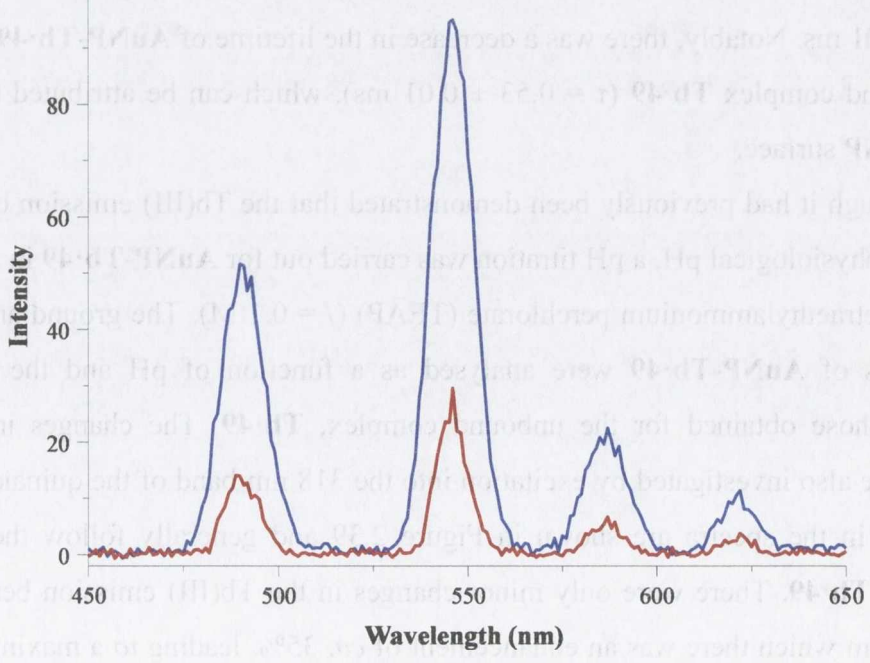


Figure 2.37: *Ln(III) luminescent spectra of* ***AuNP-Tb·49*** *under aerated (-) and degassed (-) conditions in aqueous solution (λ_{ex} = 318 nm).*

A 3 fold increase was observed in the Tb(III) emission of the degassed solution of **Tb·49**, as illustrated in Figure 2.37, caused by the quenching of the triplet state of the antenna by molecular oxygen.

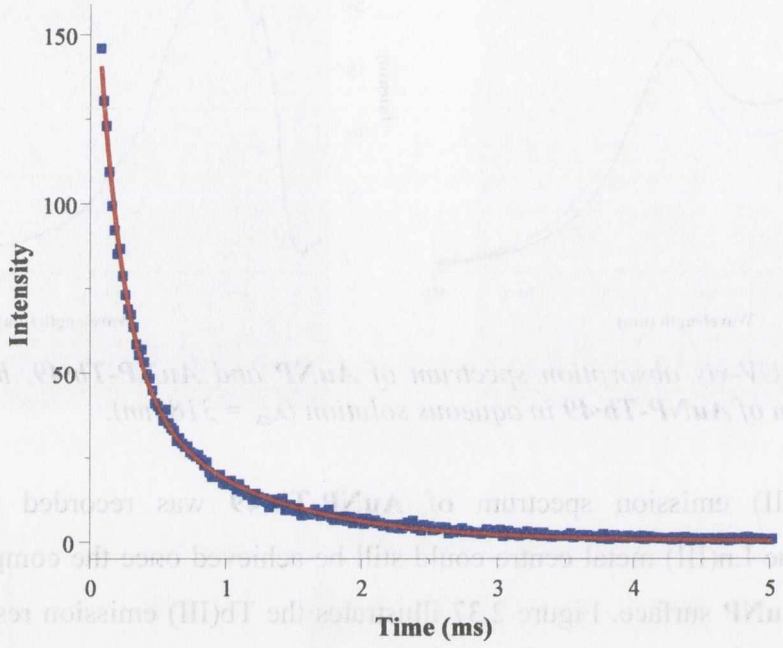


Figure 2.38: *Luminescence decay of **AuNP-Tb·49** fit to a monoexponential decay in aqueous degassed solution (λ_{ex} = 318 nm).*

In order to further investigate the excited state properties of **AuNP-Tb·49**, excited state lifetime measurements were recorded in degassed buffered pH 7.4 solution (HEPES 0.1 M). By indirect excitation of the antenna at 318 nm the luminescence decay shown in Figure 2.38 was obtained, which when fit to a monoexponential decay gave a lifetime value of $\tau = 0.38 \pm 0.01$ ms. Notably, there was a decrease in the lifetime of **AuNP-Tb·49** with respect to the unbound complex **Tb·49** ($\tau = 0.53 \pm 0.01$ ms), which can be attributed to quenching from the **AuNP** surface.

Although it had previously been demonstrated that the Tb(III) emission of **Tb·49** was not stable at physiological pH, a pH titration was carried out for **AuNP-Tb·49** in H_2O with the presence of tetraethylammonium perchlorate (TEAP) (I = 0.1 M). The ground and the singlet excited states of **AuNP-Tb·49** were analysed as a function of pH and the results were identical to those obtained for the unbound complex, **Tb·49**. The changes in the Tb(III) emission were also investigated by excitation into the 318 nm band of the quinaldine antenna. The changes in the spectra are shown in Figure 2.39 and generally follow the same trend observed for **Tb·49**. There were only minor changes in the Tb(III) emission between pH 11 and pH 8, from which there was an enhancement of *ca.* 35%, leading to a maximum intensity at pH 7. Acidification to very low pH (2) caused a steady decrease of the intensity by 70%.

The changes were found to be fully reversible upon back titration from pH 2-11. Overall, the results were in keeping to those obtained from the pH titration of **Tb·49**, and we can conclude that neither **Tb·49** nor **AuNP-Tb·49** showed stable Tb(III) emission across the physiological pH range.

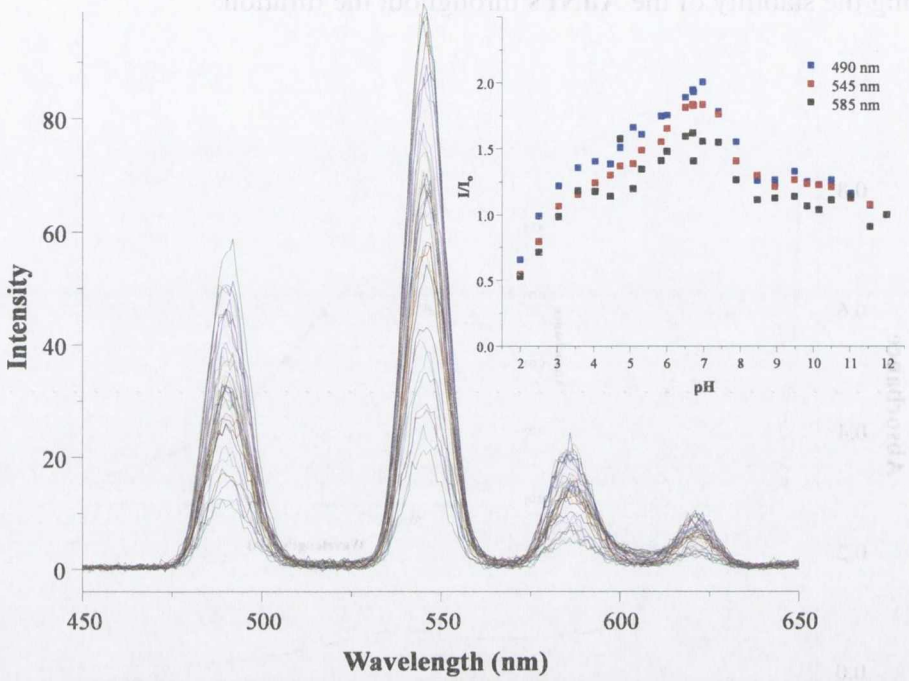
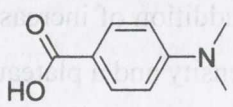


Figure 2.39: *Changes in the Tb(III) luminescence response of **AuNP-Tb·49** (λ_{ex} = 318 nm) as a function of pH in aqueous solution [I = 0.1 M TEAP]. Inset: Tb(III) emission intensity at 490, 545 and 585 nm as a function of pH.*

2.16.1 Anion Titration of AuNP-Tb·49

The sensing ability of **AuNP-Tb·49** was investigated by the addition of 4-(dimethylamino)benzoic acid, **DMAB** (**74**), which is known for its ability to sensitise Tb(III).[134] The titration was carried out on **AuNP-Tb·49** in buffered solution pH 7.4, 0.1 M HEPES, in the presence of increasing amounts of the **DMAB** (0-110 equivalents) and the ground, singlet excited and the Ln(III) excited state of **AuNP-Tb·49** were monitored. The concentration of **AuNP-Tb·49** was determined by using the extinction coefficient previously established for **Tb·49** (ε_{318} = 27048 M^{-1} cm^{-1}).



74

The changes in the UV-vis absorption spectrum of **AuNP-Tb·49** upon titration with **DMAB** were shown in Figure 2.40. A strong absorbance band occurs overlapping with that of the quinaldine chromophore, centred at 300 nm, as a result of increasing concentrations of **DMAB**. Excitation into 318 nm means that energy transfer should occur from both the

quinaldine antenna and the external chromophore **DMAB**, which should lead to a significant increase in the Tb(III) emission. In a similar manner to that observed for **AuNP-Eu·49**, major changes in the UV-vis absorption spectrum only occurred between 200-400 nm due to the addition of the antenna, with very little change detected in the **AuNP** SPR absorption band, again verifying the stability of the **AuNPs** throughout the titration.

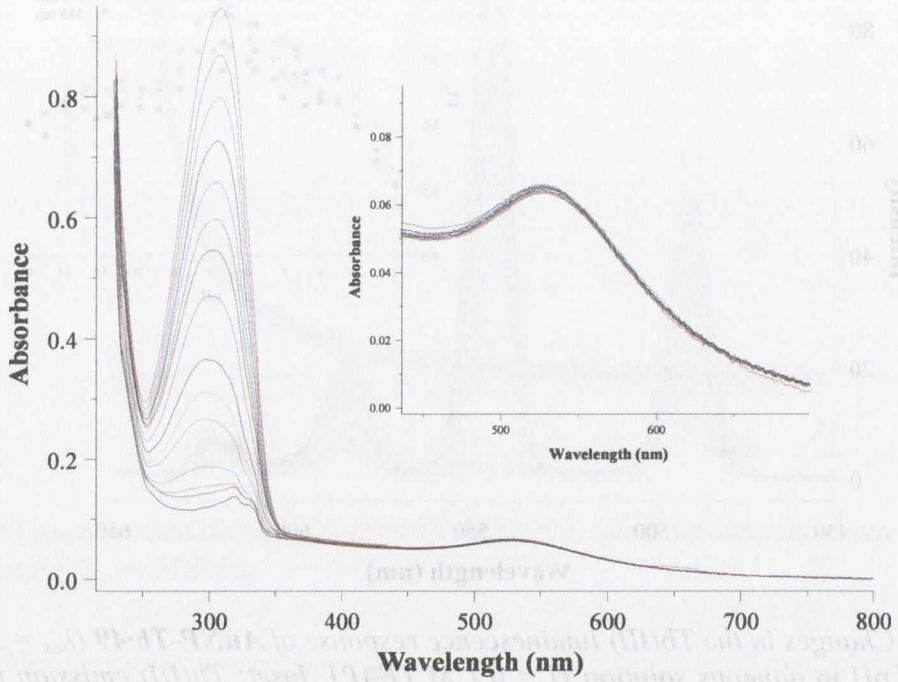


Figure 2.40: *Changes in UV-vis absorption spectrum of **AuNP-Tb·49** (1×10^{-7} M) as a function of equivalents of **DMAB** at pH 7.4 in 0.1 M HEPES. Inset: Changes in the SPR band.*

The changes in the singlet excited state of **AuNP-Tb·49** were also examined upon the addition of **DMAB**, and the overall changes are shown Appendix A2.25. Here *ca.* 60% decrease, characteristic of the π-π^* deactivation of the quinaldine moiety, was observed in the fluorescence emission intensity of **AuNP-Tb·49** at 370 nm. This behaviour was consistent with the fluorescence changes observed when **AuNP-Eu·49** was titrated with the diketonates, **nta**, **tta** and **tfp**.

In monitoring the Tb(III) emission, a considerable enhancement was observed in the ^7F_J (J = 6-3) emission bands upon the addition of increasing equivalents of **DMAB**, as shown in Figure 2.41. Maximum emission intensity and a plateau begins to occur after the addition of *ca.* 60 ± 10 equivalents of **DMAB**, signifying that the *ca.* 60 ± 10 **Tb·49** complexes attached to the surface of the **AuNP** have each formed a 1:1 highly emissive ternary complex with **DMAB**, and furthermore, displacement of the metal bound water molecule has occurred.

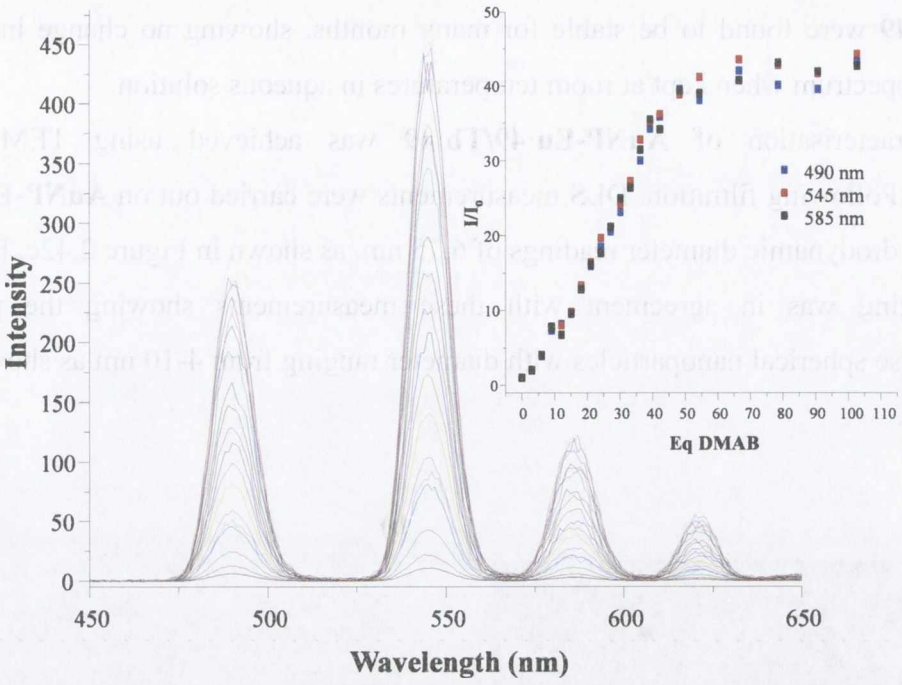


Figure 2.41: *The Tb(III) luminescence response (λ_{ex} = 318 nm) of* ***AuNP-Tb·49*** *(1 × 10^{-7} M) as a function of equivalents of* ***DMAB*** *at pH 7.4 in 0.1 M HEPES. Inset: Changes in the emission at 545 nm upon the addition of* ***DMAB*** *(0-110 equivalents).*

Although the Tb(III) emission of **AuNP-Tb·49** was not stable over the physiological pH, in buffered pH 7.4 solution it has been shown that it was capable of functioning as a supramolecular sensing system in aqueous solution.

This behaviour highlights the fact that **Tb·49** functions efficiently as a sensor on the surface of **AuNPs** and its emission can be enhanced by the addition of a suitable antenna. Bearing this in mind, it was decided to combine both Eu(III) and Tb(III) emission on the surface of **AuNPs**. The following section will discuss this dual emissive system, its photophysical properties, pH dependency and anion sensing ability.

2.17 AuNP-Eu·49/Tb·49

The **AuNPs** were synthesised and functionalised using the same Brust-Schiffrin method as described for both **AuNP-Eu·49** and **AuNP-Tb·49**. Functionalisation was achieved by exchange of the TOAB stabiliser on the surface of the toluene solubilised **AuNPs** (*ca.* 1 × 10^{-2} M) with a 50:50 solution of **Eu·49:Tb·49** in a mixed DMSO/H_2O (1:99 *v/v*) solution of *ca.* 1 × 10^{-4} M. The organic and aqueous solutions were mixed together and stirred vigorously overnight. Once allowed to settle the deep purple colour of the aqueous layer was observed, signifying complete phase transfer of the **AuNPs** from the toluene layer to the aqueous layer containing **Eu·49:Tb·49**. The resulting water solubilised **AuNPs** were purified in the same manner as both **AuNP-Eu·49** and **AuNP-Tb·49**, using sephadex G15 column chromatography with NaCl (0.05 M) as the mobile phase. The resulting **AuNPs**, **AuNP-**

Eu·49/Tb·49 were found to be stable for many months, showing no change in the UV-vis absorption spectrum when kept at room temperatures in aqueous solution.

Characterisation of **AuNP-Eu·49/Tb·49** was achieved using TEM and DLS techniques. Following filtration, DLS measurements were carried out on **AuNP-Eu·49/Tb·49** and gave hydrodynamic diameter readings of 6.75 nm, as shown in Figure 2.42c. Furthermore, TEM imaging was in agreement with these measurements showing the presence of monodisperse spherical nanoparticles with diameter ranging from 4-10 nm as shown in Figure 2.42a and b.

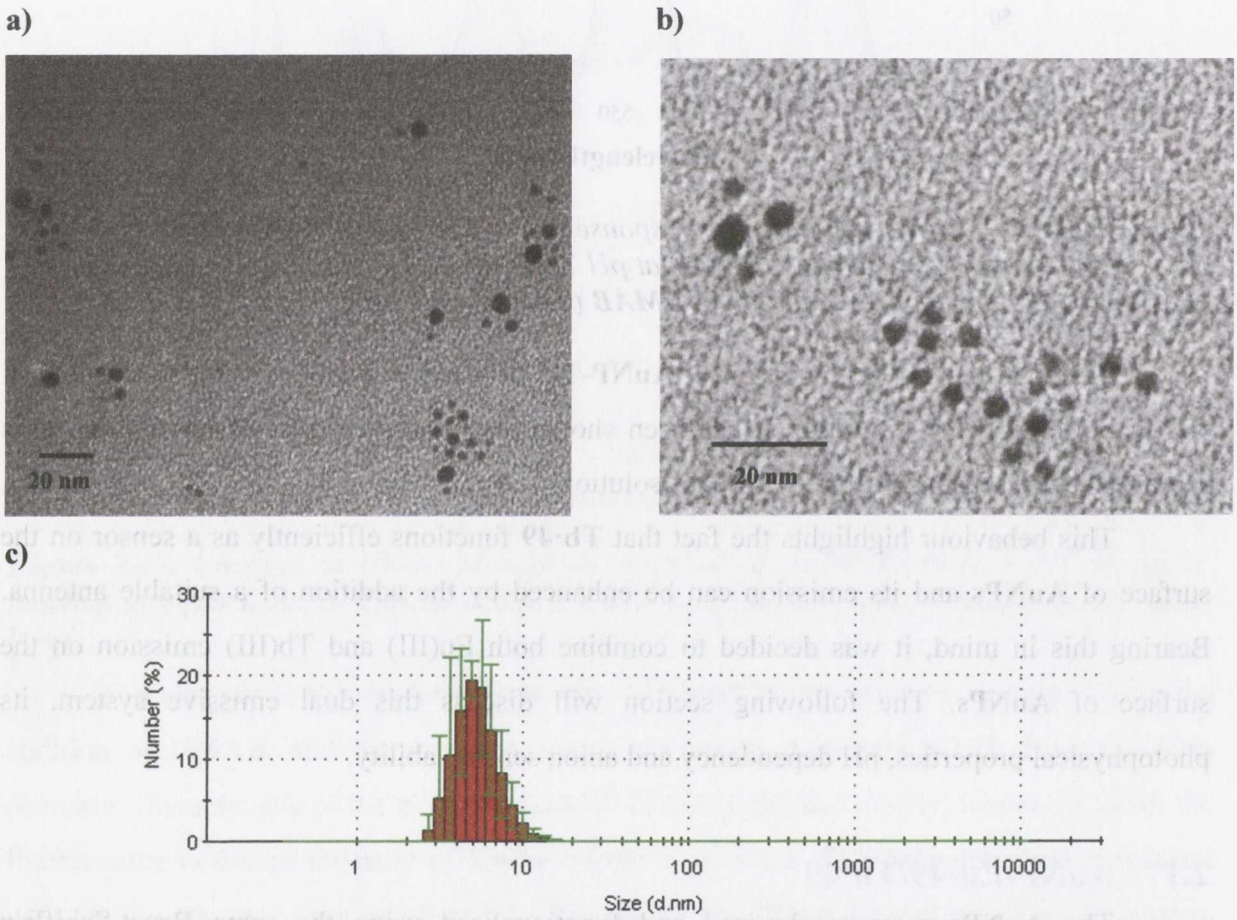


Figure 2.42: a) and b) TEM images of AuNP-Eu·49/Tb·49 synthesised by a modified Brust-Schiffrin method after deposition on copper grids showing close-up image. c) Particle size distribution plots as determined from DLS analysis for AuNP-Eu·49/Tb·49.

AuNP-Eu·49/Tb·49 were also characterised using UV-vis absorption spectroscopy. Before functionalisation, the reduction of Au(III) to Au(0), with concomitant appearance of the characteristic **AuNP** SPR band, was clearly observed in the UV-vis absorption spectrum as shown in Figure 2.43a, signifying the formation of **AuNPs**. Adsorption of **Eu·49/Tb·49** onto the **AuNP** surface caused a red shift in the SPR maximum of *ca.* 6 nm, which was

indicative of **AuNP** surface functionalisation. Moreover, between 280 nm and 340 nm, and with a maximum at 318 nm, the distinctive absorption of the quinaldine antenna occurs.

The singlet excited state of **AuNP-Eu·49/Tb·49** was investigated by excitation into the main absorption band at 318 nm, yielding the fluorescence emission spectrum shown in Figure 2.43. An emission maximum occurred at 355 nm, with two slight shoulders at 342 nm and 370 nm. As in the case of **AuNP-Eu·49** and **AuNP-Tb·49**, the fluorescence spectrum was identical to that of both unbound complexes.

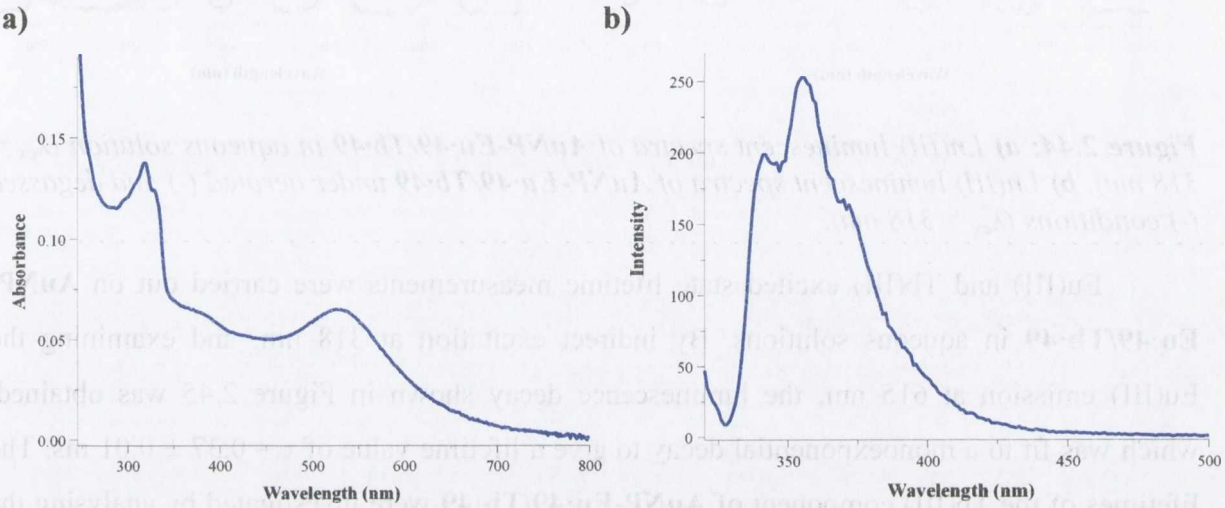


***Figure 2.43: a)** UV-vis absorption spectrum of **AuNP-Eu·49/Tb·49**. **b)** Fluorescence emission spectrum of **AuNP-Eu·49/Tb·49** in aqueous solution (λ_{ex} = 318 nm).*

The phosphorescence spectrum of **AuNP-Eu·49/Tb·49** was obtained using an excitation wavelength of 318 nm, and is shown in Figure 2.44a. As expected, emission from both Eu(III) and Tb(III) metal centres was observed, resulting from the transitions from the $^5D_0$ state to the ^7F_J state of the Eu(III) ion where J = 0-4 and the $^5D_4$ to the ^7F_J state of the Tb(III) ion where J = 6-3, where overlapping occurs between the J = 3-4 bands of Tb(III) and J = 1-2 bands of Eu(III). Quenching of the Ln(III) excited state was clearly observed due to deactivation of **Eu·49** and **Tb·49** once absorbed onto the **AuNP** surface.

The effect of oxygen on **AuNP-Eu·49/Tb·49** was examined by measuring the phosphorescence of a solution of **AuNP-Eu·49/Tb·49** before and after being degassed with argon. A 6 fold increase was observed in the Tb(III) emission of the degassed solution, as illustrated in Figure 2.44b, in comparison little change occurred in the Eu(III) centred emission.

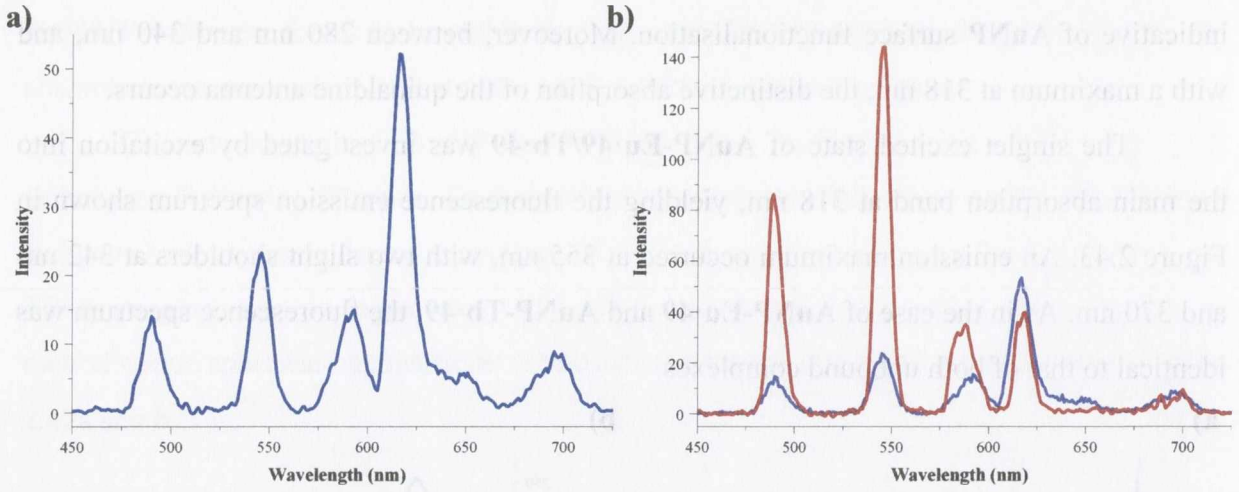


Figure 2.44: a) *Ln(III) luminescent spectra of* ***AuNP-Eu·49/Tb·49*** *in aqueous solution (λ_{ex} = 318 nm).* ***b)*** *Ln(III) luminescent spectra of* ***AuNP-Eu·49/Tb·49*** *under aerated (-) and degassed (-) conditions (λ_{ex} = 318 nm).*

Eu(III) and Tb(III) excited state lifetime measurements were carried out on **AuNP-Eu·49/Tb·49** in aqueous solutions. By indirect excitation at 318 nm, and examining the Eu(III) emission at 615 nm, the luminescence decay shown in Figure 2.45 was obtained, which was fit to a monoexponential decay to give a lifetime value of $\tau = 0.37 \pm 0.01$ ms. The lifetimes of the Tb(III) component of **AuNP-Eu·49/Tb·49** were investigated by analysing the emission output at 545 nm, under degassed conditions. The luminescence decay curve obtained was also best fit to monoexponential decay and a lifetime value of $\tau = 0.28 \pm 0.01$ ms was obtained. Again, a decrease in the lifetime value from that of the unbound complexes, **Eu·49** and **Tb·49** was observed which can be attributed to quenching from the **AuNP** surface.

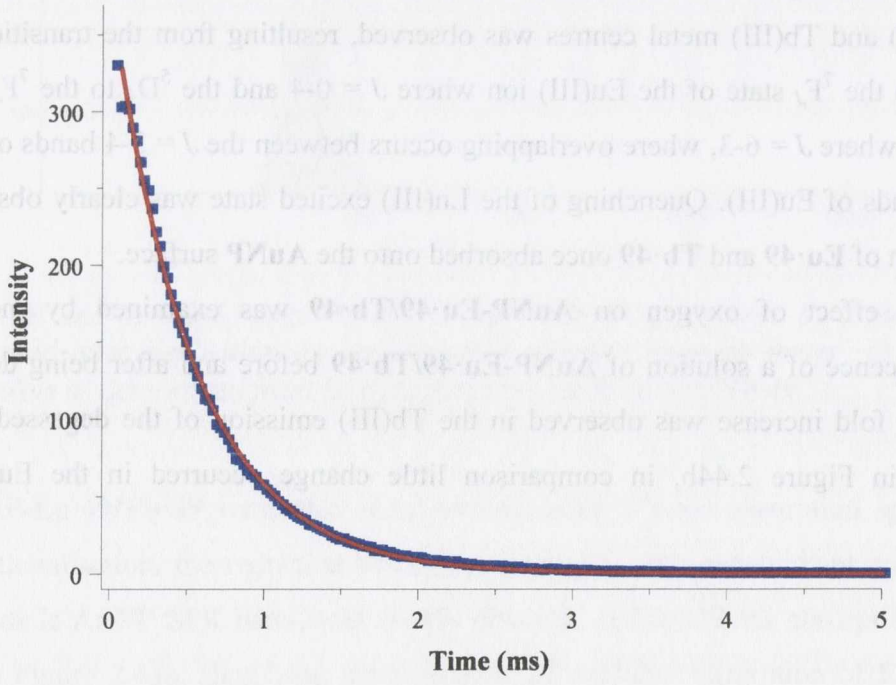


Figure 2.45: *Luminescence decay of* ***AuNP-Eu·49/Tb·49*** *fit to monoexponential decay in aqueous degassed solution (λ_{ex} = 318 nm, λ_{em} = 615 nm).*

Having established the photophysical properties of **AuNP-Eu·49/Tb·49**, its pH behaviour was next examined and compared to that of the 50:50 mixture of **Eu·49/Tb·49** previously studied. A pH titration was carried out on **AuNP-Eu·49/Tb·49** in H_2O with the presence of tetraethylammonium perchlorate (TEAP) ($I = 0.1$ M).

Firstly, the ground and singlet excited state of **AuNP-Eu·49/Tb·49** were analysed as a function of pH and the results were found to be identical to those obtained for the unbound complexes, **Eu·49** and **Tb·49** and the functionalised **AuNP** systems, **AuNP-Eu·49** and **AuNP-Tb·49**. By excitation into the 318 nm band of the quinaldine chromophore, the alterations in the Eu(III) and Tb(III) emission were monitored as a function of pH, as depicted in Figure 2.46.

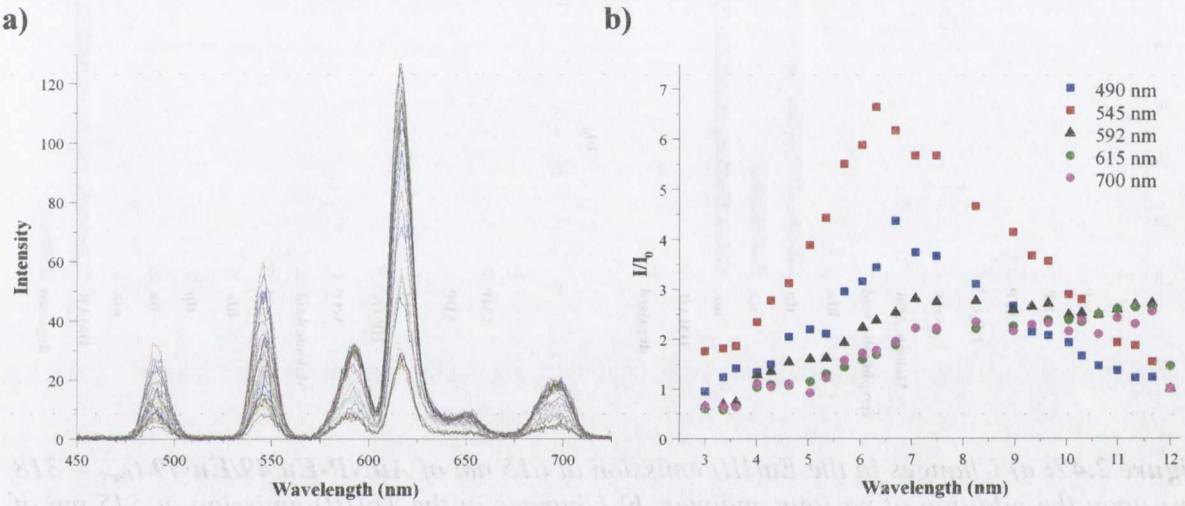


Figure 2.46: ***a)*** *Changes in the Eu(III) and Tb(III) luminescence response of* ***AuNP-Eu·49/Eu·49*** *as a function of pH in aqueous solution (λ_{ex} = 318 nm) [I = 0.1 M TEAP].* ***b)*** *Eu(III) and Tb(III) emission intensity at various wavelengths, as a function of pH.*

With regard to the Eu(III) emission, the changes observed at 615 nm were comparable to those observed for both **Eu·49** and **AuNP-Eu·49**; with the emission being "switched off" in acidic pH and "switched on" between physiological and basic pH. In the case of the Tb(III) emission, the trend observed was the same, however a more drastic increase and decrease was observed in the emission intensity at 545 nm from the maximum at pH 7. Where only minor changes were observed in the Tb(III) emission between pH 11 and pH 8, there was a large increase of 73% in intensity until the maximum at pH 7 was reached, from which further acidification to pH 2 caused a significant decrease where the intensity was reduced to 16% of that of the maximum.

These results denote that although both Ln(III) metal centres were in close proximity to one another, their general photophysical properties remained unchanged. Bearing this in mind, we next set out to determine the sensing ability of this dual emissive system.

AuNP-Eu·49/Tb·49 was firstly screened for its ability to sense a range of biologically important analytes. 60 equivalents of each of the analytes was added to a buffered pH 7.4 (0.1 M HEPES) solution of **AuNP-Eu·49/Tb·49**, and the corresponding emission intensity of Eu(III) at 615 nm and Tb(III) at 545 nm was monitored. The results of this screening test are depicted in the bar charts shown in Figure 2.47. As had been observed before for **Eu·49**, the addition of simple anions such as acetate and phosphate caused no major perturbations of either the Eu(III) or Tb(III) emission bands. In a similar manner, terephthalic ATP, ADP and AMP caused no observable change in either the Eu(III) or Tb(III) emission.

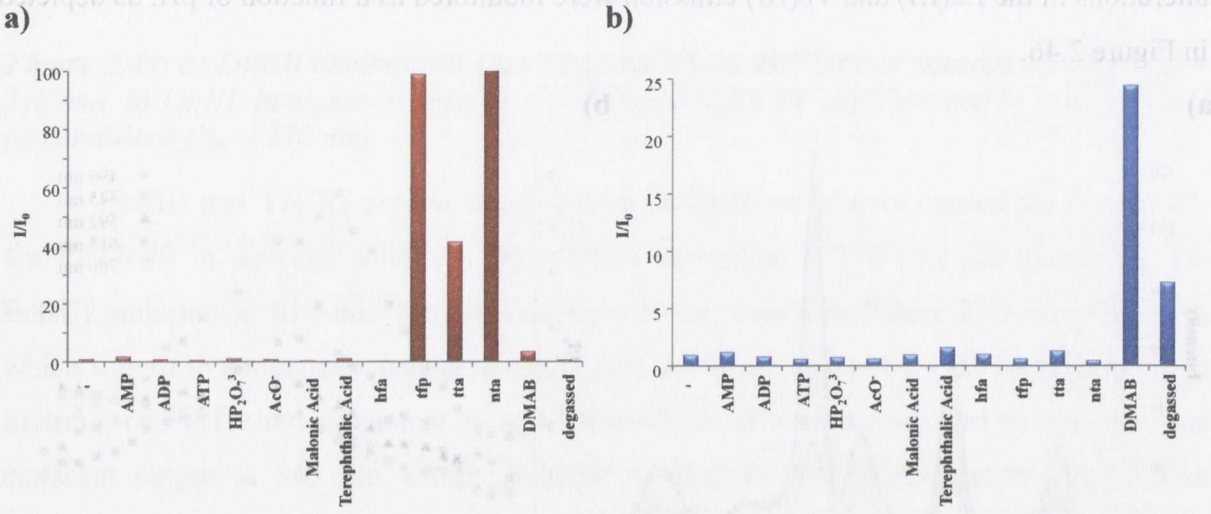


***Figure 2.47: a)** Changes in the Eu(III) emission at 615 nm of **AuNP-Eu·49/Eu·49** (λ_{ex} = 318 nm) upon the addition of various analytes. **b)** Changes in the Tb(III) emission at 545 nm of **AuNP-Eu·49/Eu·49** (λ_{ex} = 318 nm) upon the addition of various analytes.*

The next analytes chosen to test were the diketonates malonic acid, **hfa**, **tfp**, **nta** and **tta** (**69-73**), which have previously been shown to form stable six-membered ring complexes with Ln(III) metal ions.[117,125,132,135] The addition of the diketonates not containing antennae, malonic acid and **hfa**, both gave rise to negligible changes in both the Eu(III) or the Tb(III) emission. This was also the case for **Eu·49**, suggesting that no displacement of the metal bound water molecule was occurring. As expected, the diketonates **tfp**, **nta** and **tta** demonstrated efficient Eu(III) sensitisation enhancement. Furthermore, these had also caused displacement of the water molecule producing a large increase in the Eu(III) emission of **AuNP-Eu·49/Tb·49**, where no such enhancement was observed for the Tb(III) emission. Hence, while these antennae were capable of sensitising the excited state of the Eu(III), they were not able to do the same for Tb(III) and so we can selectively "switch on" the Eu(III) emission while the Tb(III) emission remains "switched off".

In order to turn on the Tb(III) emission of **AuNP-Eu·49/Tb·49**, the antenna **DMAB** was chosen as it proved to be sufficient in sensitising Tb(III) when the system **AuNP-Tb·49**

was investigated. Addition of *ca.* 60 equivalents of **DMAB** indeed showed this to be the case as the addition caused a 32 fold increase in the Tb(III) emission, while only a minor increase of less than 50% was detected for the Eu(III) emission. Hence, this demonstrates a selective "switching on" of the Tb(III) emission while the Eu(III) emission remains quenched.

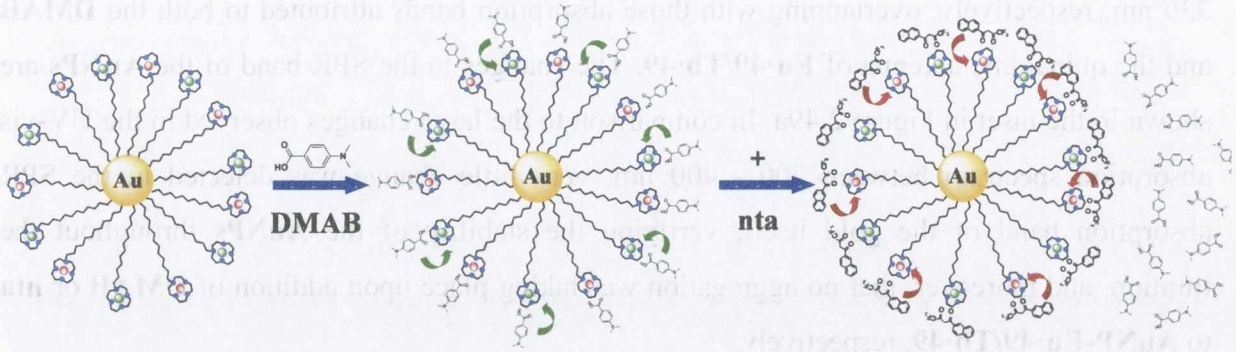


Figure 2.48: *Schematic representation of the switching on of the Tb(III) and Eu(III) emission by the addition of* ***DMAB*** *and* ***nta*** *to* ***AuNP-Eu·49/Tb·49****.*

The effect of oxygen on the system was also investigated as an input into the system **AuNP-Eu·49/Tb·49**. By bubbling argon through the solution, the Tb(III) emission increases 6 fold while the Eu(III) emission remains unchanged. This screening test of the dual emissive system **AuNP-Eu·49/Tb·49** illustrates the logic behaviour of the Eu(III) and Tb(III) emission and its ability to be "switched on and off" depending on the input into the system, which can range from the addition of different analytes to the presence or absence of oxygen in solution. This was expanded to a full titration of **AuNP-Eu·49/Tb·49** using the antennae **DMAB** and **nta** which would switch on the Tb(III) and Eu(III) emission, respectively. First, addition of **DMAB** would selectively "switch on" the Tb(III) emission, followed by the addition of **nta**, "switching on" the Eu(III) emission, as depicted in Figure 2.48.

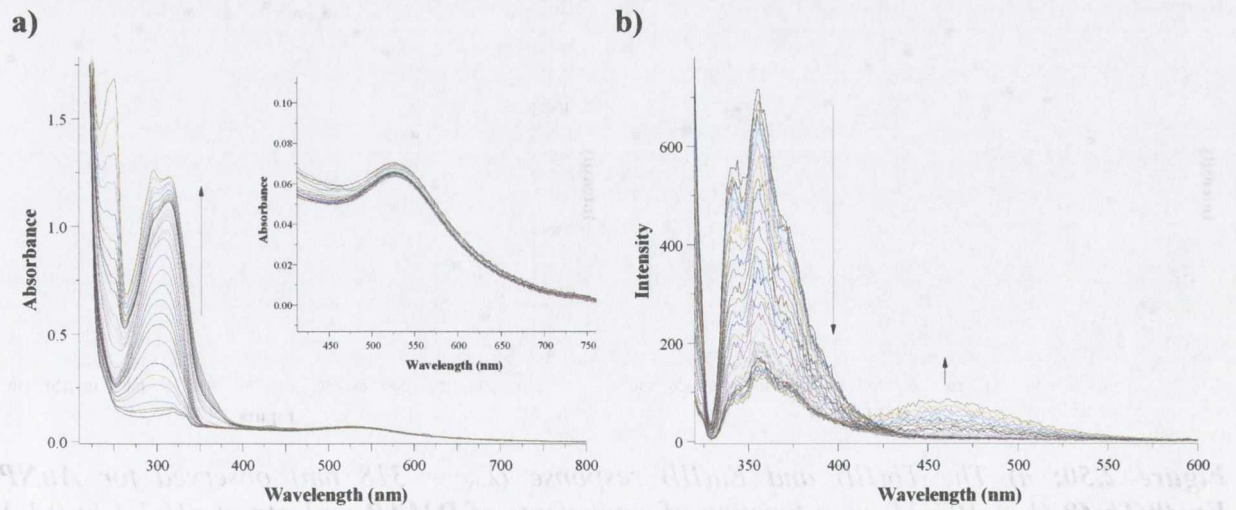


Figure 2.49: ***a)*** *Changes in UV-vis absorption spectrum of* ***AuNP-Eu·49/Tb·49*** *(1×10^{-7} M) as a function of equivalents of* ***DMAB*** *and* ***nta*** *at pH 7.4 in 0.1 M HEPES. Inset: Changes in the SPR band.* ***b)*** *The fluorescence response (λ_{ex} = 318 nm) of* ***AuNP-Eu·49/Tb·49*** *as a function of equivalents of* ***DMAB*** *and* ***nta*** *at pH 7.4 in 0.1 M HEPES.*

The changes in the UV-vis absorption spectrum of **AuNP-Eu·49/Tb·49** upon titration with **DMAB** and **nta** are shown in Figure 2.49a. The addition of **DMAB** to the solution resulted in a strong absorbance band centred at 300 nm. This was followed by the addition of **nta**, which as previously shown, gives rise to two absorbance bands occurring at 245 nm and 330 nm, respectively, overlapping with those absorption bands attributed to both the **DMAB** and the quinaldine antenna of **Eu·49/Tb·49**. The changes in the SPR band of the **AuNPs** are shown in the inset in Figure 2.49a. In comparison to the large changes observed in the UV-vis absorption spectrum between 200 - 400 nm, very little change was detected in the SPR absorption band of the gold itself, verifying the stability of the **AuNPs** throughout the titration, and moreover, that no aggregation was taking place upon addition of **DMAB** or **nta** to **AuNP-Eu·49/Tb·49**, respectively.

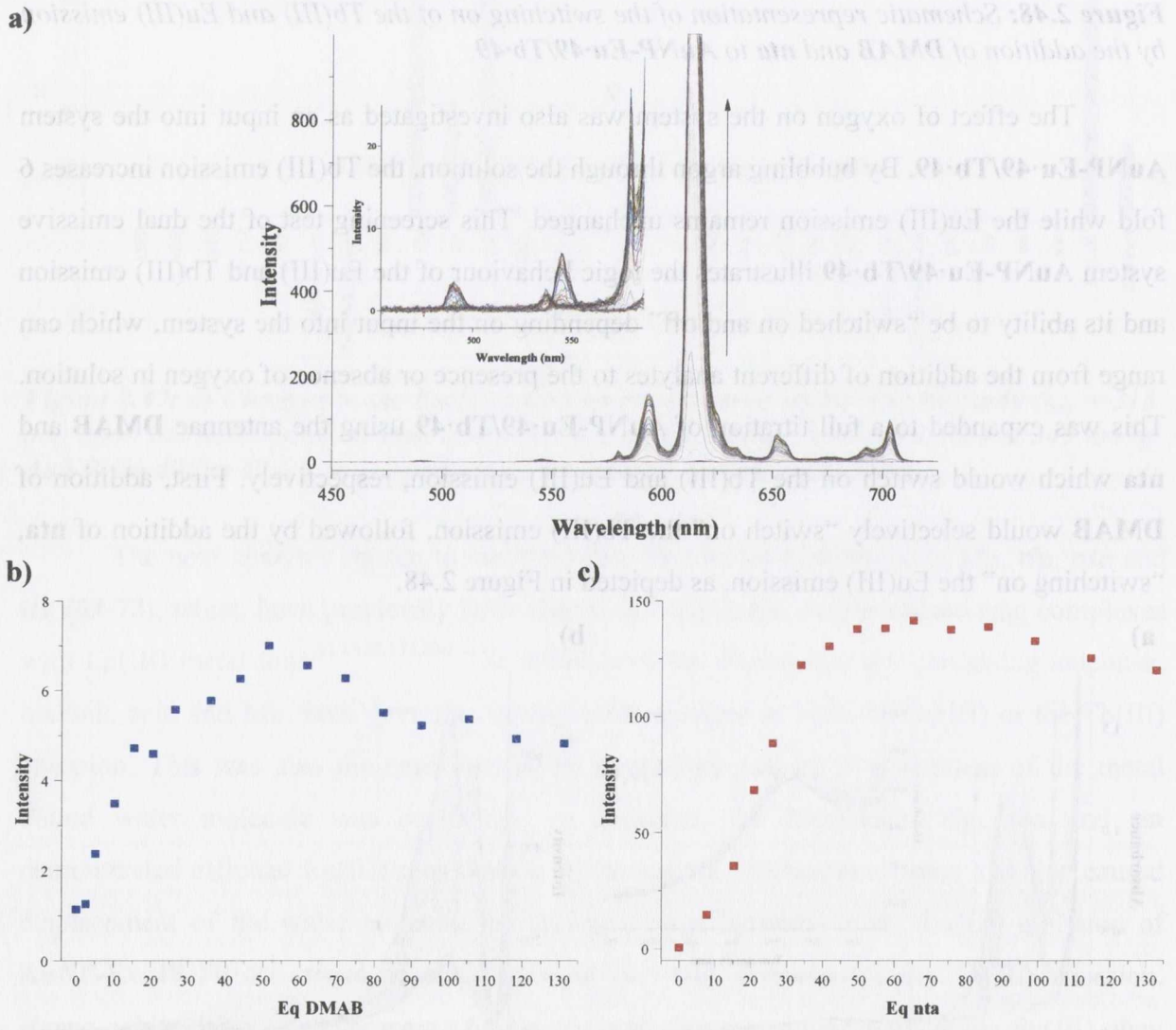


Figure 2.50: a) *The Tb(III) and Eu(III) response (λ_{ex} = 318 nm) observed for* ***AuNP-Eu·49/Tb·49*** *(1×10^{-7} M) as a function of equivalents of* ***DMAB*** *and* ***nta*** *at pH 7.4 in 0.1 M HEPES.* ***b)*** *Changes in the Tb(III) emission at 545 nm upon the addition of* ***DMAB*** *(0-130 equivalents).* ***c)*** *Changes in the Eu(III) emission at 592 nm upon the addition of* ***nta*** *(0-130 equivalents).*

The changes in the singlet excited state of **AuNP-Eu·49/Tb·49** were also investigated upon the addition of **DMAB** and **nta**, and the overall changes are shown in Figure 2.49b, where an initial decrease of *ca.* 60% was observed in the fluorescence centred emission at 355 nm caused by the addition of **DMAB**. This decrease was extended by a further 15% when increasing amounts of **nta** were added to the solution. Simultaneously, a 9 fold increase occurs in the emission band centred at 450 nm, which was attributed to the **nta** itself. These changes in both the ground and singlet excited state were in agreement with the results obtained when studying the mono emissive systems **AuNP-Eu·49** and **AuNP-Tb·49**.

The Ln(III) excited state of **AuNP-Eu·49/Tb·49** was next investigated as a function of equivalents of **DMAB** and **nta** using an excitation wavelength of 318 nm. Initially, addition of **DMAB** resulted in an enhancement in the Tb(III) emission of the ^7F_J (J = 6-3) emission bands as shown in Figure 2.50a. In the case of **AuNP-Tb·49**, a plateau was reached at *ca.* 60 equivalents of **DMAB** added, indicating *ca.* 60 complexes per **AuNP**. It could therefore be expected that a 50:50 mixture of **Eu·49:Tb·49** on the surface of the AuNPs would result in a Tb(III) emission intensity maximum occurring after the addition of *ca.* 30 equivalents of **DMAB**. However, this was not the case, and the plateau was still observed at *ca.* 60 equivalents, Figure 2.50b. A possible explanation for this was that although the **DMAB** is not an efficient sensitiser for Eu(III), it was still capable of binding to the Eu(III) metal centre and as such, was not selectively binding to the Tb(III) metal centre. This means that only when every Ln(III) (Eu(III) and Tb(III)) around the **AuNP** has bound to a **DMAB** molecule, will maximum Tb(III) emission intensity be achieved.

Once the plateau had been reached, increasing amounts of **nta** were added to the **AuNP-Eu·49/Tb·49-DMAB** system, in order to displace **DMAB** from the Ln(III) metal centres, "switching off" the Tb(III) emission and hence, "switching on" the Eu(III) emission. A large enhancement in Eu(III) ^7F_J (J = 0-4) emission bands was observed, as shown in Figure 2.50a, which caused the most intense band at 615 nm to reach saturation, and as such the J = 1 band was monitored throughout the titration. The plot of Eu(III) intensity *vs.* equivalents of **nta** added is shown in Figure 2.50c and follows the same trend as described above; a maximum intensity, and plateau was only reached after the addition of *ca.* 60 equivalents of **nta**. Again, the **nta** can bind to, but not efficiently sensitise Tb(III) and it was only after the addition of *ca.* 60 equivalents of **nta** that all the **DMAB** molecules were displaced from the Eu(III) and Tb(III) metal centres, Tb(III) emission was "switched off" and maximum Eu(III) emission intensity was reached and **AuNP-Eu·49/Tb·49-nta** was formed.

The reverse titration, whereby **nta** was added to **AuNP-Eu·49/Tb·49**, followed by the addition of **DMAB** was also carried out in buffered pH 7.4 solution (0.1 M HEPES). The

changes in the UV-vis absorption and fluorescence spectra were identical to those shown in Figure 2.49. In the phosphorescence spectrum, increasing amounts of **nta** to the solution gave rise to significant enhancements in the Eu(III) emission bands, Appendix A2.26, which reached a plateau after the addition of *ca.* 60 equivalents of **nta**. Subsequent addition of **DMAB** to **AuNP-Eu·49/Tb·49-nta** caused no observable change in the Tb(III) emission, which remained relatively low in comparison to the Eu(III) emission. Diketonates such as **nta** form six-membered rings with Ln(III) metal ions which possess enhanced stability over the four-membered ring formed between Ln(III) and carboxylate of **DMAB**. Addition of **DMAB** to **AuNP-Eu·49/Tb·49-nta** cannot displace the **nta** from the Ln(III) metal centre, which favours the formation of the ternary complex that procedures a six-membered ring, and as such, no enhancement in the Tb(III) emission was observed and the Eu(III) emission remained "switched on".

In order to ascertain whether there was in fact a 50:50 mixture of **Eu·49/Tb·49** on the surface of the **AuNPs**, simultaneous titrations were carried out on **AuNP-Eu·49/Tb·49-nta**, **AuNP-Eu·49** and **AuNP-Tb·49** using **DMAB** and **nta**. For each of the titrations, the same experimental conditions were used so that any changes in Ln(III) emission intensity occurring was a direct result of the amount of Ln(III) present on the **AuNP** surface. The results of these titrations are shown below in Figure 2.51.

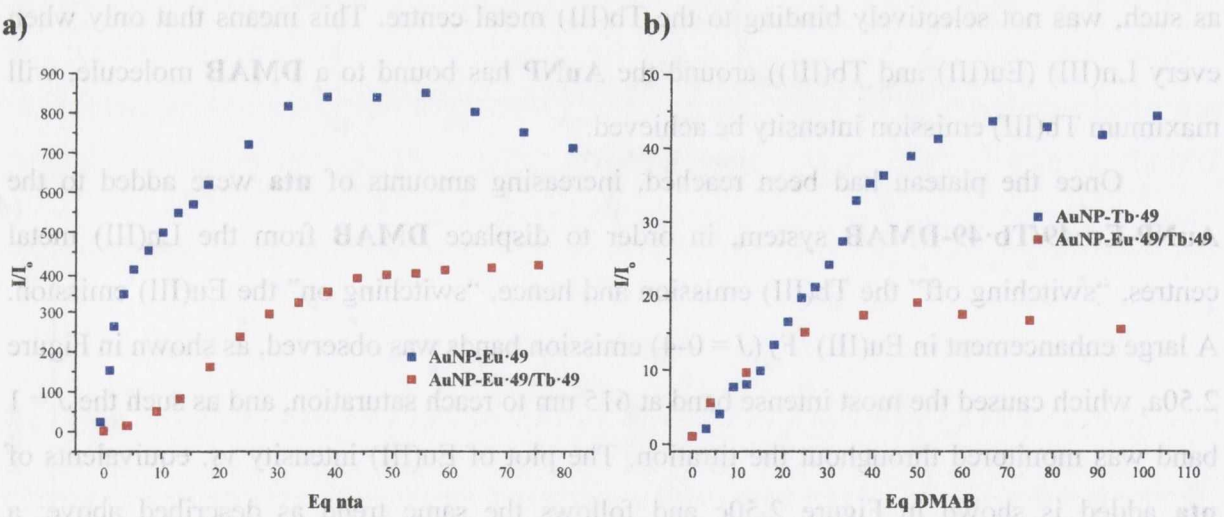


Figure 2.51: a) *Relative emission intensity at 615 nm as a function of equivalents of* ***nta*** *for* ***AuNP-Eu·49*** *and* ***AuNP-Eu·49/Tb·49*** *(λ_{ex} = 318 nm) (1 × 10^{-7} M) at pH 7.4 in 0.1 M HEPES.* ***b)*** *Relative emission intensity at 545 nm as a function of equivalents of* ***DMAB*** *for* ***AuNP-Tb·49*** *and* ***AuNP-Eu·49/Tb·49*** *(λ_{ex} = 318 nm) (1 × 10^{-7} M) at pH 7.4 in 0.1 M HEPES.*

Figure 2.51a shows the normalised emission intensity at 615 nm of **AuNP-Eu·49** and **AuNP-Eu·49/Tb·49-nta** as a function of equivalents of added **nta**. In both cases, a plateau was reached after the addition of *ca.* 60 equivalents. However, the difference between the two

titrations was the maximum intensity value that was reached at *ca.* 60 equivalents; the Eu(III) intensity at 615 nm was twice as intense for **AuNP-Eu·49** than for the dual emissive system **AuNP-Eu·49/Tb·49**. This implies that there was twice as much Eu(III) present in **AuNP-Eu·49** than in **AuNP-Eu·49/Tb·49**, confirming our assumption that there was a 50:50 mixture of Eu(III) and Tb(III) present on the **AuNP** surface.

The same result was obtained when investigating the Tb(III) emission intensity of **AuNP-Tb·49** and **AuNP-Eu·49/Tb·49** as a function of **DMAB** added, Figure 2.51b. A plateau and maximum Tb(III) emission occurred after the addition of *ca.* 60 equivalents, of which the intensity of **AuNP-Eu·49/Tb·49** was half that of **AuNP-Tb·49**, again indicating that there was a 50:50 mixture of **Eu·49** and **Tb·49** on the **AuNPs**.

The results presented in this section have detailed a water soluble dual Ln(III) emissive system on **AuNPs**, the Eu(III) and Tb(III) emission of which can be "switched on" or "off" depending on the input into the system, as depicted in the Table 2.8 below, where 0 indicates that the Ln(III) emission was very low or totally "switched off "and 1 indicating it was enhanced or "switched on".

Table 2.8: *Various inputs into the system* ***AuNP-Eu·49/Tb·49*** *and the effect they have on the Eu(III) and Tb(III) emission.*

Input	Eu(III)	Tb(III)
-	0	0
nta	1	0
DMAB	0	1
DMAB + nta	1	0
nta + DMAB	1	0
degassed	0	1

2.18 Conclusion

The initial study discussed in this Chapter dealt with the design, synthesis and photophysical evaluation of novel cyclen based Ln(III) complexes, sensitisation of which was achieved through the incorporation of a quinaldine antenna unit into the cyclen framework. Moreover, the attachment of a long alkyl chain, terminated by a thiol group, was essential to this design in order to enable absorption onto the surface of **AuNPs**.

The first section of this Chapter focuses on the investigation into the complexes **Eu·49** and **Tb·49**. Eu(III) and Tb(III) emission was achieved through excitation at 318 nm, by which sufficient energy transfer can occur from the triplet excited state of the quinaldine antenna to the excited state of the Eu(III) and Tb(III) metal ions, resulting in Ln(III) metal centred emission. An investigation into the number of metal bound water molecules was carried out. The coordination environment around the Ln(III) metal centre of **Eu·49** and **Tb·49** suggested that each complex would possess two metal bound water molecules; $q = 2$. This was not found to be the case. By recording the exponential decay of the Eu(III) and Tb(III) luminescence with respect to time, lifetimes of **Eu·49** and **Tb·49** were measured and as a q value of 1 was obtained. To probe this result, complexes **Eu·61** and **Eu·62** were synthesised, possessing a twelve carbon and a four carbon chain, respectively. **Eu·61** was found to have a q value of 1 and **Eu·62**, $q = 2$. From the short chain possessing two water molecules we could conclude that the long alkyl chain must be overlapping on itself to escape the hydrophilic environment and as such, there was only enough space to allow one water molecule to bind to the Ln(III) metal centre. The effect of oxygen on **Tb·49** showed the sensitivity of the Tb(III) emission to the presence of oxygen, where in degassed solutions, a 7 fold increase was observed in the Tb(III) emission intensity.

Extensive pH studies were carried out on the complexes **Eu·49** and **Tb·49**, where changes in the ground, singlet excited and Eu(III) and Tb(III) excited states were monitored as a function of pH. For **Eu·49**, the Eu(III) emission was found to be quenched in acidic pH and most importantly, the Eu(III) emission showed stability over the physiological pH range. A rather different trend was observed for **Tb·49**, where a maximum emission occurred at pH 7 followed by a significant decrease in Tb(III) emission intensity as the solution was adjusted to either acidic or basic pH. A pH study on a 50:50 solution of **Eu·49:Tb·49** was also carried out and the trends observed in the Ln(III) emission changes were identical to those of the individual complexes. As **Tb·49** did not show stability over the physiological pH range, it was decided to carry out anion titrations using **Eu·49** only.

Titrations were undertaken to establish the sensing ability of **Eu·49** using different biologically relevant analytes, ranging from simple anions such as acetate and phosphate to

larger biomolecules such as ATP. Sensing of the analytes would occur through displacement of the metal bound water molecule and hence, an increase in the Eu(III) emission would be observed. No such increase was observed in the case of most of the analytes tested and q values confirmed that the metal bound water molecule had not been displaced. The next set of molecules tested were diketonates, which have been shown to bind to Ln(III) through the formation of a stable six membered ring between the diketonate and the Ln(III) metal centre. It was discovered that only the aromatic containing diketonates (**nta**, **tta**, **tfp**) bound to **Eu·49**, causing a substantial increase in the Eu(III) centred luminescence, which reached maximum emission intensity and a plateau after the addition of 1 equivalent of diketonate. Moreover, q values of 0 confirmed the formation of the 1:1 ternary complex **Eu·49-nta/tta/tfp**.

Having established the photophysical and pH properties and anion binding ability of **Eu·49**, a subsequent description of the synthesis and functionalisation of **AuNPs** was given, yielding the **Ln-AuNP** conjugates **AuNP-Eu·49**, **AuNP-Tb·49** and the dual emissive system **AuNP-Eu·49/Tb·49**. The procedure described for the synthesis of the **AuNPs** is a modified Brust-Schriffin method that involves direct functionalisation of the **AuNPs** with the Ln(III) complexes, yielding water soluble **Ln-AuNPs** with an average diameter of 10 nm.

The photophysical properties of all three systems were evaluated and it was determined that attachment onto the **AuNP** surface did not change the photophysical properties; only the intensity of the Ln(III) was effected, which experienced a quenching effect attributable to the proximity of the Ln(III) metal centre to the gold surface. Investigation into the pH dependence of the **AuNP** systems revealed the same pH profiles as the unbound complexes; **AuNP-Eu·49** remained stable at physiological pH and **AuNP-Tb·49** displayed maximum intensity at pH 7.

In addition to their pH dependency, **AuNP-Eu·49**, **AuNP-Tb·49** and **AuNP-Eu·49/Tb·49** were evaluated for their ability to function as analyte sensors. The addition of the diketonates **nta**, **tta** and **tfp** caused a large increase in the Eu(III) emission intensity which reached a plateau after the addition of *ca.* 60 equivalents of diketonate added. Considering a 1:1 ternary complex was formed between each complex and diketonate on the surface of the **AuNP**, we can conclude that there were *ca.* 60 Ln(III) complexes per **AuNP**. The same behaviour was observed when **AuNP-Tb·49** was titrated against the Tb(III) sensitising carboxylate **DMAB**. The Tb(III) emission intensity began to level off by the addition of *ca.* 60 equivalents of **DMAB**, again verifying the presence of *ca.* 60 complexes per **AuNP**.

Analogous titration studies were carried out on the dual emissive system **AuNP-Eu·49/Tb·49**. Addition of **nta** and **DMAB** to this system resulted in an increase in the respective Eu(III) and Tb(III) emission that was half the intensity reached in the mono

emissive systems **AuNP-Eu·49** and **AuNP-Tb·49**, confirming that there was in fact a 50:50 mixture of **Eu·49** and **Tb·49** present on the surface of the gold, and the Eu(III) and Tb(III) emission of which can be individually modulated depending on the input into the system.

The work presented here, thus, represents the development of a novel dual emissive Ln(III) based **AuNP** system, for sensing purposes in aqueous solution, by the formation of ternary complexes with Ln(III) on the surface of the **AuNPs**.

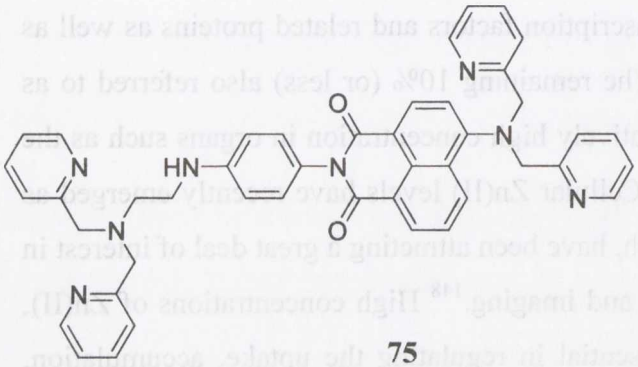
Chapter 3

Dual Emissive Lanthanide Probe for Zn(II) Sensing

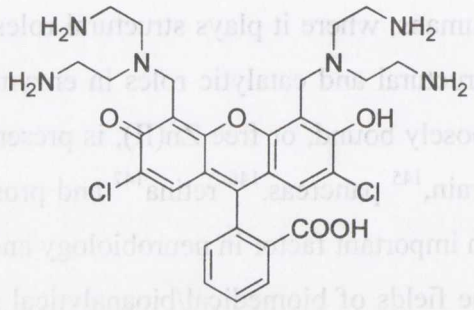
3. Introduction

There are a growing number of diseases which have been identified as originating from metal imbalance occurring within cells and/or tissues. Therefore, the identification and quantification of metal ions in their native physiological environment is of great current interest.[143] Divalent zinc (Zn(II)), is the second most abundant metal ion after iron (Fe(II), Fe(III)), among transition metal ions in the human body. It exists in both tightly bound and mobile forms; its highest concentrations occurring in the brain. The former comprises the so-called static Zn(II) pool; which represents more than 90% of the total amount of Zn(II) in humans, where it plays structural roles in transcription factors and related proteins as well as structural and catalytic roles in enzymes.[144] The remaining 10% (or less) also referred to as loosely bound, or free Zn(II), is present at relatively high concentration in organs such as the brain,[145] pancreas,[146] retina[147] and prostate.[83] Cellular Zn(II) levels have recently emerged as an important factor in neurobiology and as such, have been attracting a great deal of interest in the fields of biomedical/bioanalytical sensing and imaging.[148] High concentrations of Zn(II), together with its mobility in the brain, is essential in regulating the uptake, accumulation, trafficking and efflux of Zn(II) homeostasis, which is the tendency of a system, especially the physiological system of higher animals, to maintain internal stability by regulating properties such as temperature or pH. Abnormal zinc homeostasis has been linked to a growing number of diseases, including different types of cancer as well as neurodegenerative disorders characteristic of both Alzheimer's and Parkinson's diseases.[149,150] Alzheimer's disease is characterised by the extracellular accumulation of amyloid-β and the intracellular accumulation of tau, a microtubule-associated protein. In cases of advanced Alzheimer's disease, Zn(II) levels within brain tissue are remarkably increased, which correlates with high levels of amyloid-β42. It has been suggested that there are two phases of abnormal Zn(II) homeostasis which occur in the brain and result in enhanced levels of Zn(II). Phase I is an early stage, in which Zn(II) uptake is inhibited, giving rise to increased extracellular Zn(II) levels including amyloid-β deposition. A later phase is thought to inhibit the export of Zn(II), also causing increased Zn(II) concentrations. One of the therapeutic developments in the treatment of Alzheimer's disease based on this metal hypothesis was the use of Clioquinol, which possesses a moderate affinity for Zn(II).[151] It binds Zn(II) and causes displacement of Zn(II) from the low-affinity metal binding sites of amyloid-β, reversing amyloid-β oligomerization. Clioquinol reached phase II clinical trials, in which a drop in the rate of cognitive decline was observed in patients with Alzheimer's disease, caused by a decrease in the levels of plasma amyloid-β42.

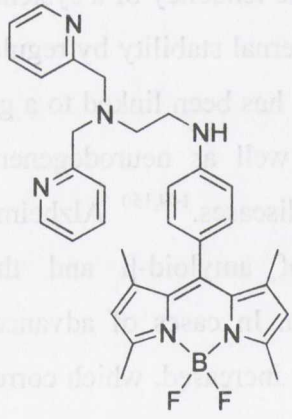
The growing contributions of abnormal zinc homeostasis to neurophysiology and neuropathology, and hence the importance of Zn(II) concentrations in neuronal disorders, have prompted the design and development of numerous fluorescent sensors for the detection of Zn(II) in biological samples.[152] These fluorescent probes are usually of similar design and consist of a chelating unit able to coordinate Zn(II), typically iminodiacetate, di(2-picolyl)amine or quinoline moieties that has been further functionalized with an organic dye such as naphthalimide, **75**,[10] rhodamine, **76**,[153] boron-dipyrromethene (BODIPY), **77**,[154] or anthracene, **78**.[155]



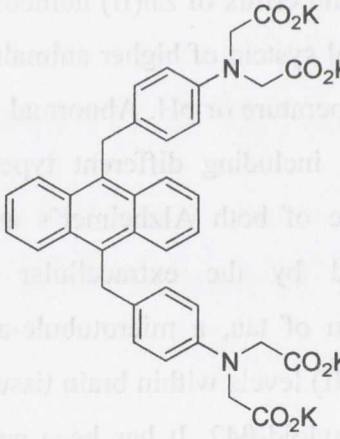
75



76



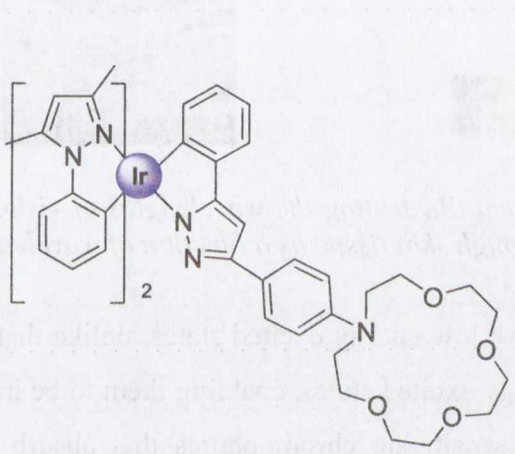
77



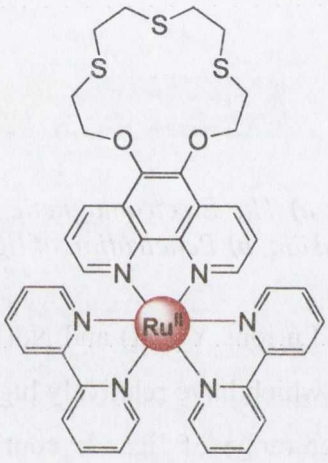
78

For example, the 4-amino-1,8-naphthalimide substituted compound, **75** was designed by Wang *et al.*[156] as a Cu(II) and Zn(II) sensor. In the absence of the metal cations, considerable internal charge transfer (ICT) as well as photoinduced electron transfer (PET) occurring from the receptors to the naphthalimide excited state occurs, resulting in a shifting of the UV-vis absorption spectrum and significant fluorescence quenching. Addition of Zn(II) and Cu(II) alters these processes and hence modulates the UV-vis absorption and fluorescence spectra.

The development of such probes is particularly advantageous since, contrary to the early detection using histochemical procedures, spectroscopic techniques such as fluorescence imaging offer a relatively non-invasive approach. Recently, there has been growing development in the use of phosphorescent heavy-metal complexes such as Pt(II), Ru(II), Re(I), Ir(III), Cu(I), Au(I) and Os(II) to replace fluorescent chemosensors, due to the advantageous photophysical properties that heavy metal complexes have to offer, such as long wavelength emission and relatively long-lived emission (μs range).[157] The Ir(III) compound **79** designed by Ho *et al.*,[158] incorporating an aza-crown receptor, functions as a highly sensitive phosphorescence sensor for Ca(II), whereas complex **80**, developed by Li *et al.*[159] shows selectivity towards Hg(II) ions due to the presence of sulfur atoms in the macrocycle framework.



79



80

In addition to transition metal complexes, luminescent lanthanide (Ln(III)) based systems have also been concurrently investigated for the detection of divalent cations such as Zn(II)[56,160] and for the sensing of other transition metal and group I and II metal ions,[60] due to the advantageous properties of Ln(III) ions including easily recognisable line-like emission spectra, long excited-state lifetimes (μs to ms range) and large Stokes shifts upon ligand excitation.

As discussed in the Introduction, Section 1.5, there has been a great focus in recent years on the development of biological probes incorporating visibly emitting Ln(III) such as Eu(III) and Tb(III), emitting with red and green emission, respectively.[34] However, biological tissues are not transparent, absorbing most of the visible light, Figure 3.1, and thus a growing interest was observed in the use of NIR emitting Ln(III) complexes, such as Ytterbium (Yb(III)) and Neodymium (Nd(III)), and their potential for non-invasive *in vivo* imaging and probing for biological interactions due to their long emission wavelengths, ranging from between 900 nm and 1400 nm.[161,162] Ln(III) ions possessing emission in this range are

appealing for probing biological interactions because of the low autofluorescence and biological tissues are transparent in this spectral range. Hence, they can penetrate through skin tissue, as depicted in Figure 3.1b. Their use as a tool for *in vivo* imaging could help in the early detection of cancer and tumours, provide application in luminescent immunoassays, as well as the examination of deeper skin tissues as biological tissues have very low absorption coefficients above 700 nm.[163]

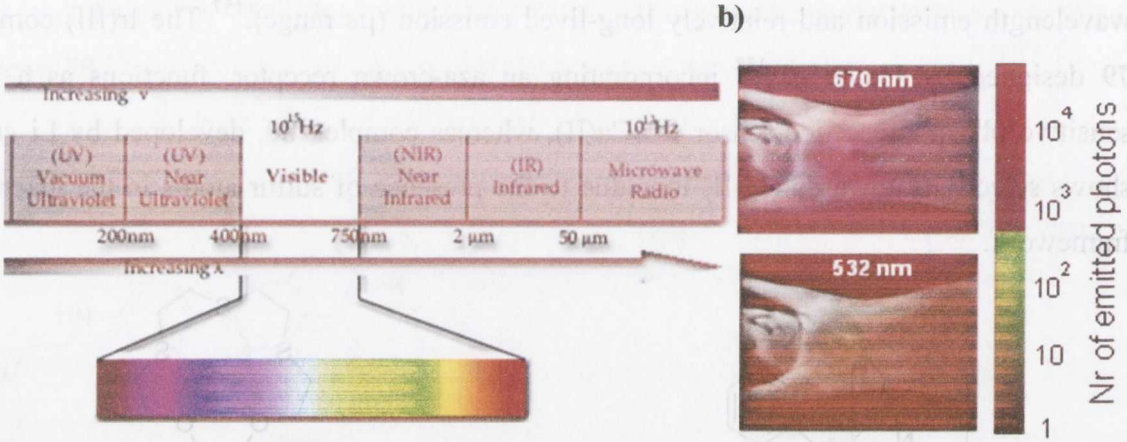
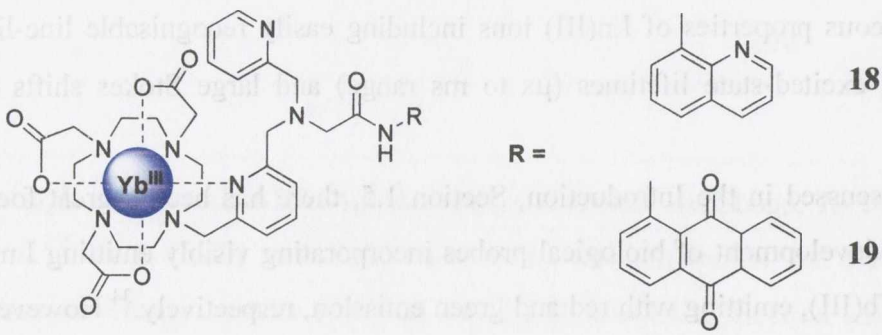


Figure 3.1: a) *The Electromagnetic Spectrum illustrating the wavelengths of visible and NIR Ln(III) emission.* ***b)*** *Penetration of light through skin tissue as a function of wavelength.*

The Ln ions Yb(III) and Nd(III) have low energy excited states, unlike that of Eu(III) and Tb(III) which have relatively high energy excited states, enabling them to be incorporated into a wider range of ligands containing sensitising chromophores that absorb within the visible region, and hence, deeper tissue penetration can be achieved. Moreover, further incentive for designing NIR emitting probes over visible emitting ones is that the former has the ability to be excited using visible light, whereas the UV light needed to excite the latter, may cause damage to biological molecules and the surrounding biological environment.[15]

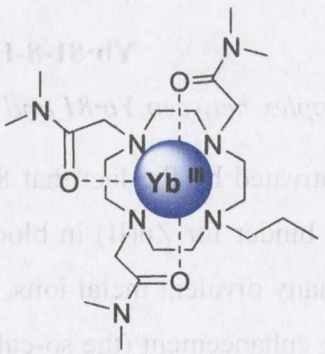


Bearing these advantageous properties in mind, many advances have been made in the in the area of cyclen based complexes as NIR emitting sensors. One such example developed by Pope and co-workers involved the incorporation of a secondary binding site component for targeting metal cations along with antenna capable of NIR Ln(III) sensitisation.[57] Unlike the

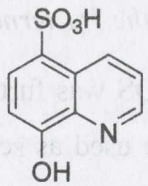
Eu(III) complex of **18** and **19** previously mentioned in the Introduction, the Nd(III) and Yb(III) complexes of **18** and **19** demonstrated dual emission; visible, ligand-centred fluorescence together with NIR Ln(III) emission. The Yb(III) emission was found to be dramatically enhanced upon the addition of Hg(II).

3.1 Design of Yb·81-8-HQS

The majority of visible-emitting Ln(III) based Zn(II) sensors developed to date have been based on a similar fluorescent probe design to that described above, mainly consisting of a Zn(II) chelating unit linked to a fluorophore, in this case, a Ln(III) complex. The design of the complex in this Chapter is different to this approach and instead relies on the formation of a luminescent ternary complex and subsequent dissociation as a response to the sensing event. This approach, which takes advantage of the displacement of the sensitising antenna from the Ln(III) centre, upon Zn(II) binding has previously been used for the sensing of anions and biologically relevant molecules in our laboratory.[125] However, we demonstrated that a slight modification in the design, for instance, by carefully selecting the sensitising antenna forming the ternary complex with the Ln(III) unit, allowed the transformation of the system from an anion into a *d*-metal ion sensor. Following this design, the first example of Ln(III) luminescent displacement assay for the sensing of metal cations was developed in the Gunnlaugsson group, where the red-emitting ternary complex formed between 4,7-diphenyl-1,10-phenanthroline-disulfonate and a Eu(III) cyclen complex was applied for the sensing of Fe(II) in competitive media at physiological pH.[74] Here we extend this approach to the sensing of Zn(II).



Yb·81

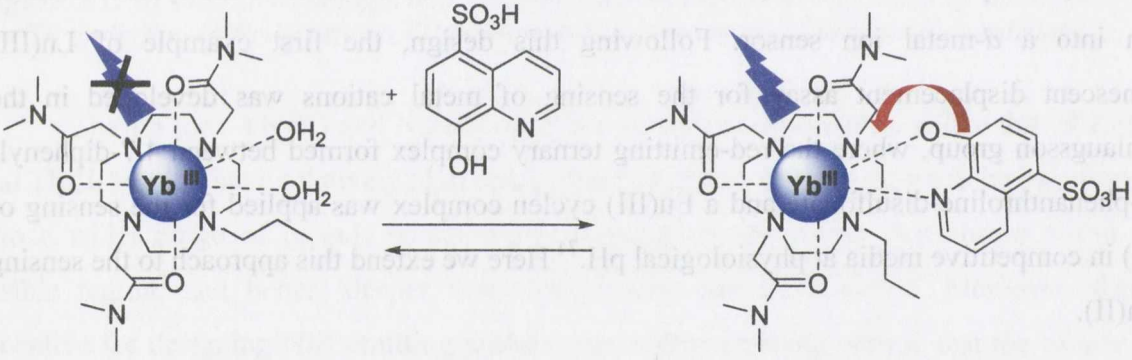


8-HQS
82

The work described in this Chapter was carried out in collaboration with Dr. Steve Comby, Dr. Oxana Kotova and Sarah Tuck, a fourth year undergraduate student, where we evaluated the ability of a novel NIR-emitting ternary system formed between the non-emissive Yb(III) cyclen complex, **Yb·81**, and the 8-hydroxyquinoline-5-sulfonic acid, **82**, (**8-HQS**) antenna for the detection of Zn(II) in aqueous buffered solution at physiological pH. As

mentioned in Chapter 2, the cyclen framework was chosen to incorporate the NIR emitting Yb(III) as it is known to form kinetically and thermodynamically stable complexes with Ln(III). Three of the four N-H sites on the cyclen would be functionalised with simple acetamide arms, giving an overall 7-membered coordination environment, with an additional short alkyl chain occupying the fourth position merely to avoid the presence of N-H oscillators in the first coordination sphere of the Ln(III) ion, as they are known to be efficient luminescence quenchers. This leaves also a vacancy for an additional coordination which is achieved by **8-HQS**.

In our design the **8-HQS** antenna was selected first of all for its ability to strongly bind Ln(III) ions and efficiently sensitise their emission in the NIR range. Hence, the sensitisation of the Yb(III) excited state is achieved within this sensing system. Indeed, the low-lying singlet and triplet excited states of 8-hydroxyquinoline (8-HQ) and its sulfonated derivatives, used as a single ligand or as a building block in larger architectures, make them perfectly well-suited for the sensitisation of NIR-emitting Ln(III) ions, including Yb(III), as depicted in Scheme 3.1.[164-166]



Yb·81 **8-HQS** **Yb·81-8-HQS**

Scheme 3.1: *Formation of the 1:1 ternary complex between* ***Yb·81*** *and* ***8-HQS****.*

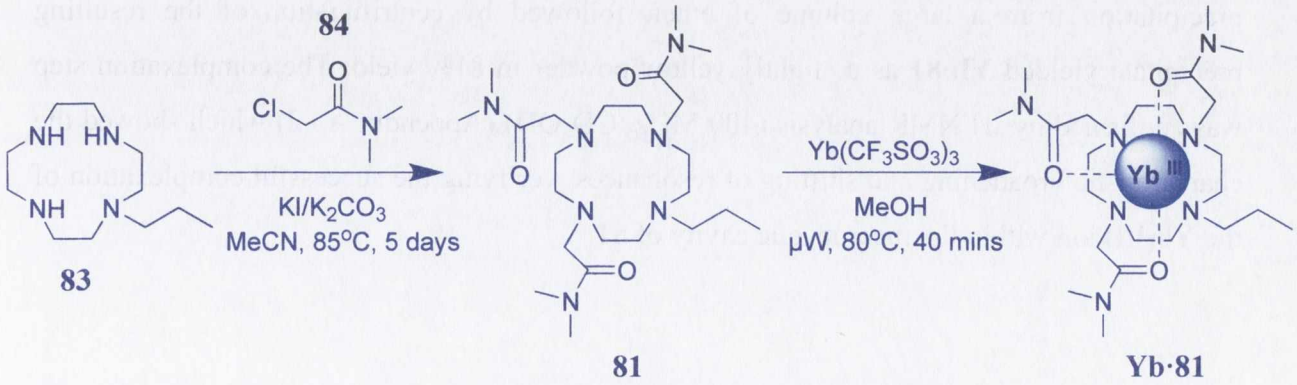
The choice of **8-HQS** was further motivated by the fact that 8-HQ is one of the first fluorescent indicators to be used as selective binder for Zn(II) in blood plasma and urine.[167] While 8-HQ formed stable complexes with many divalent metal ions, only binding of Zn(II), Ca(II) and Mg(II) led to a strong fluorescence enhancement (the so-called chelation-enhanced fluorescence, CHEF), with Zn(II) exhibiting the highest binding affinity.[168] Sulfonation of 8-HQ to obtain **8-HQS** was performed to ensure good water solubility, being aware that the introduction of the sulfonate group in *para* of the hydroxyl moiety had in the past not significantly affected the binding ability to Zn(II).

Using our system, we foresaw that the Yb(III) emission of **Yb·81-8-HQS** could be modulated or "switched off" through the displacement of the **8-HQS** antenna in the presence of Zn(II). The former, in the absence of antenna, is expected to be completely "switched off"

in the NIR region, while the newly formed Zn(II) chelate displayed sizeable emission ("switch on" effect) in the visible region, providing two luminescence signals in completely different ranges of the electromagnetic spectrum. The Zn(II) induced displacement would be reflected in the Yb(III)-centred NIR emission upon formation of **Yb·81** and Zn(**8-HQS**)$_x$ (x = 1-2). The self-assembly of the luminescent ternary complex, **Yb·81-8-HQS**, was first investigated in aqueous solution monitoring the evolution of the UV-vis absorption, fluorescence and Yb(III)-centred emission spectra and the stability constant of the resulting complex formed in solution was then determined using nonlinear regression analysis. The ability of the system to be applied in luminescent displacement assays for the detection of Zn(II) in aqueous solution has been assessed and the influence of the pH as well as other biologically relevant cations and anions was evaluated. Finally, the system, namely the sensing event involving the dissociation of the ternary complex in the presence of Zn(II), was shown to be completely reversible upon addition of EDTA.

3.2 Synthesis and Characterisation of 81 and Yb·81

The cyclen unit used in **Yb·81** was formed in a few step synthesis. The synthesis of **Yb·81**, shown in Scheme 3.2, began with a mono alkylation of 1,4,7,10-tetraazacyclododecane (cyclen) with 1-bromopropane using a 4-fold excess of cyclen according to the method developed by Gunnlaugsson and co-workers.[169] This afforded the compound **83** in 87% yield. The ^{1}H NMR spectrum (400 MHz, $CDCl_3$) showed the presence of a triplet at 0.81 ppm corresponding to the terminal CH_3 protons of the alkyl and a quartet (1.40 ppm) and triplet (2.28 ppm) representing the CH_2 protons of the alkyl chain. The alkylation of the remaining 3 amines of **Yb·81** was achieved under reflux in acetonitrile by reacting 3.1 equivalents of 2-chloro-*N,N*-dimethylacetamide, **84**, with **83** in the presence of K_2CO_3 and KI. After 5 days the formation of **81** was observed by mass spectrometry; 470.3818 $[M + H]^+$.



***Scheme 3.2**: Synthesis of ligand **81** and corresponding complex **Yb·81**.*

Purification of **81** to remove any excess dimethyl arm was achieved using column chromatography on neutral alumina eluting with CH_2Cl_2:MeOH using a gradient of 100:0 to 80:20. The ligand **81** was obtained as a white solid in 61% yield. The triplet and the quartet resonances assigned to the terminal carbons of the alkyl chain are still clearly visible in the ^1H NMR spectrum (400 MHz, $CDCl_3$) as shown in Figure 3.2. The remaining protons however, corresponding to the CH_2 protons of the alkyl chain, the 16 CH_2 protons of cyclen and the CH_2 and two CH_3 groups of the dimethylacetamide arms, are undistinguishable from one another and appear as a very broad multiplet which extends from 1.98 ppm to 3.39 ppm. The ^{13}C spectrum (100 MHz, $CDCl_3$) of ligand **81** can be found in Appendix A3.1.

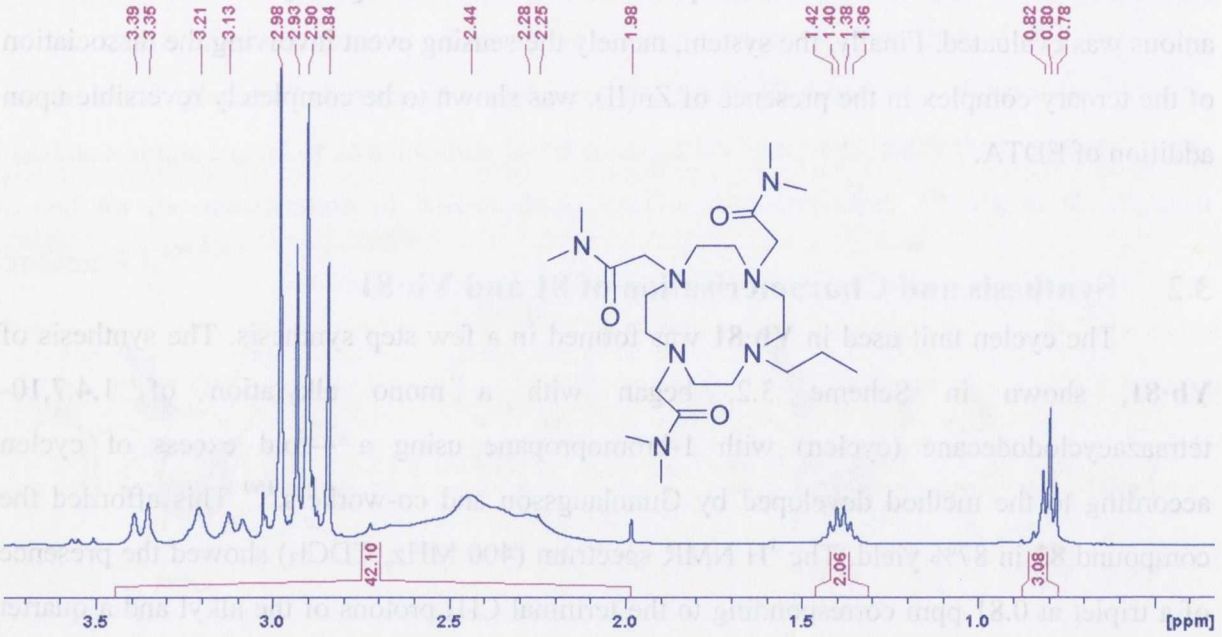


Figure 3.2: *The ^1H NMR spectrum (400 MHz, $CDCl_3$) of ligand **81**.*

The Yb(III) complex of **81** was formed by microwave irradiation for 40 minutes in a small volume (5 mL) of methanol with 1 equivalent of $Yb(CF_3SO_3)_3$. Purification by precipitation from a large volume of ether, followed by centrifugation of the resulting precipitate yielded **Yb·81** as a slightly yellow powder in 81% yield. The complexation step was confirmed by ^1H NMR analysis (400 MHz, CD_3OD) (Appendix A3.2) which showed the characteristic broadening and shifting of resonances, verifying the successful complexation of the Yb(III) ion within the macrocyclic cavity of **81**.

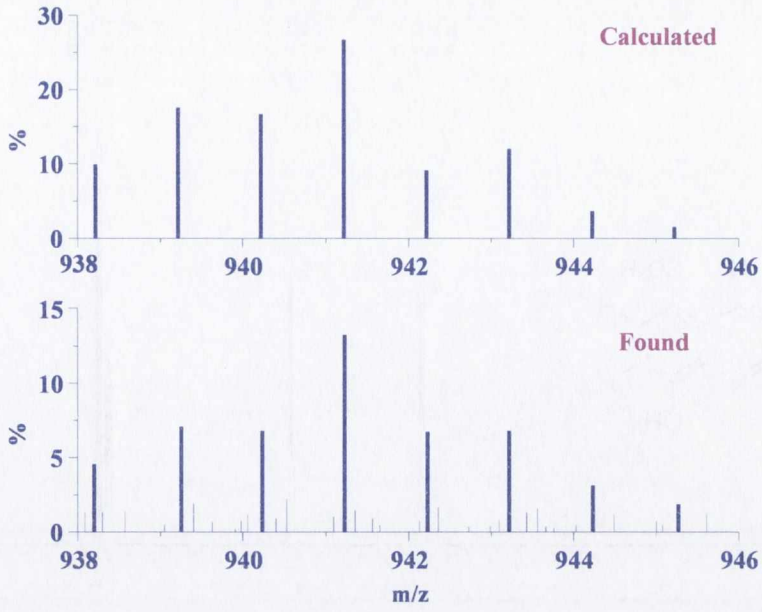
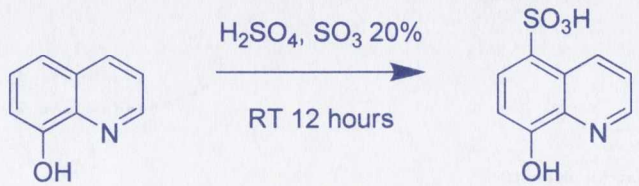


Figure 3.3: *The MALDI mass spectrum of* ***Yb·81*** *displaying the expected isotopic distribution pattern for the* $[\mathbf{Yb{\cdot}81} + 2CF_3SO_3^-]^+$ *species.*

IR spectroscopy was also employed to characterise the complex **Yb·81**. In comparison to the ligand **81**, the carbonyl bond of the complex was found to have shifted by 20 wavenumbers from 1644 cm^{-1} to 1624 cm^{-1} upon binding to the Yb(III) metal centre. The final method of characterisation used for **Yb·81** was mass spectrometry. The spectrum in Figure 3.3 showed a variety of peaks, representing the *m/z* of the complex with varying number of triflate counter ions. The observed mass spectrum matched the expected isotopic distribution of the calculated species.

The synthesis of 8-hydroxylquinoline-5-sulfonic acid (**8-HQS**), was achieved following literature procedure by stirring 8-hydroxyquinoline in a minimum amount of oleum solution (H_2SO_4, SO_3 20%) overnight.[170] The mixture was poured over ice, affording a precipitate that was collected by filtration and washed with cold water yielding the desired product, **8-HQS** as a yellow powder in quantitative yield. The ^1H NMR spectrum (400 MHz, DMSO-d_6) as shown in Figure 3.4 clearly reveals the presence of the 5 aromatic proton signals and a broad singlet corresponding to the OH at 12.12 ppm.



85 **82**

Scheme 3.3: *Synthesis of ligand antenna* ***8-HQS, 82.***

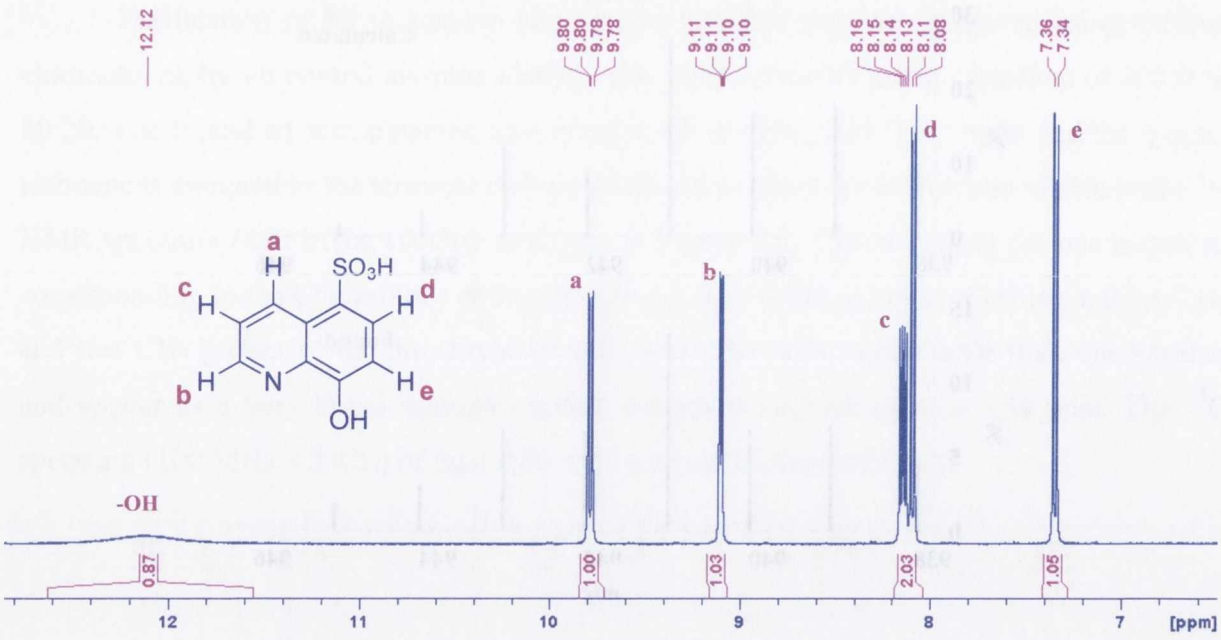


Figure 3.4: *The ^{1}H NMR spectrum (400 MHz, DMSO-d_6) of* ***8-HQS****.*

3.3 Investigation of the Interaction of 8-HQS with Cd(II), Mg(II) and Zn(II)

Before formation of the ternary system **Yb·81-8-HQS**, the antenna itself, **8-HQS** was investigated for its ability to sense the divalent cationic metals Cd(II), Mg(II) and Zn(II). All titrations of **8-HQS** (5×10^{-5} M) were carried out in HEPES buffered solution at pH 7.4 and were shown to be fully reproducible. The titration of **8-HQS** with Zn(II) will be discussed with results from titrations with Mg(II) and Cd(II) referred to and the spectra shown in the Appendix.

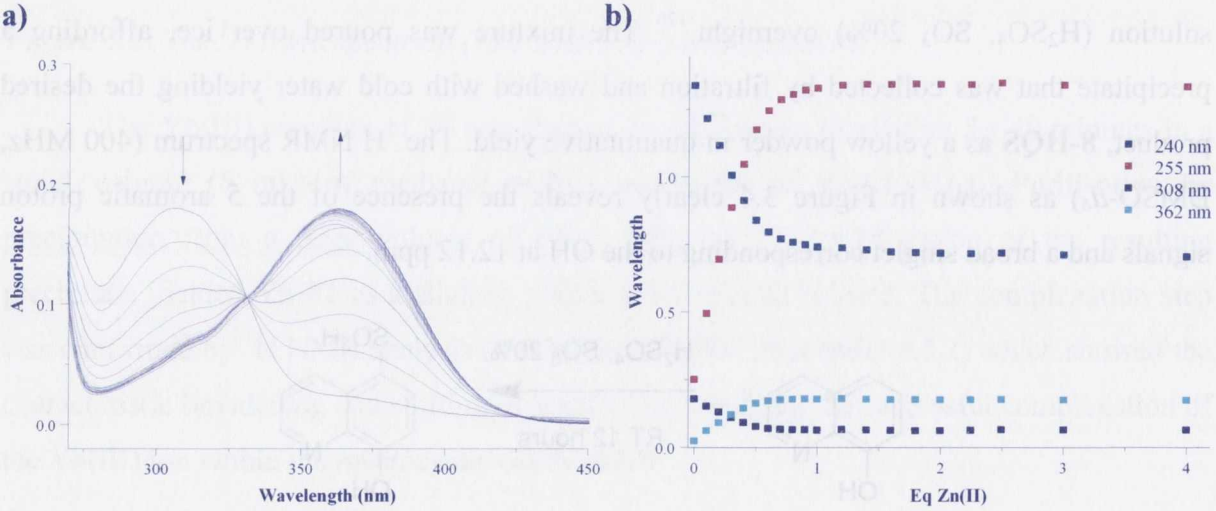


Figure 3.5: ***a)*** *Changes in the UV-vis absorption spectrum of* ***8-HQS*** *as a function of equivalents of Zn(II) added at pH 7.4 in HEPES buffered solution.* ***b)*** *Changes in the absorbance at 240 nm, 255 nm, 308 nm and 362 nm upon the addition of Zn(II).*

Before the addition of the metals, the UV-vis absorption spectrum of **8-HQS** displays two main absorption bands centred at 240 nm and 310 nm, which can be assigned to the $\pi \rightarrow \pi^*$ and $n \rightarrow \pi^*$ transitions of the chromophore, respectively. Addition of Zn(II) in the form of $Zn(ClO_4)_2$ results in a hypochromic shift of these bands detected with concomitant appearance and hyperchromic shift of absorbance bands centred at 255 nm and 360 nm, as shown in Figure 3.5. These changes were accompanied by the appearance of three distinct isosbestic points, located at 243 nm, 268 nm and 330 nm, respectively, which confirmed the binding of Zn(II) to **8-HQS**, and moreover, indicates the presence of a single species in solution. Similar results were obtained in the UV-vis absorption spectrum upon titration of **8-HQS** with Cd(II) and Mg(II) and are shown in Appendix A3.3 and A3.4. While the changes associated with the addition of Cd(II) were almost identical as those for Zn(II), the resulting changes upon addition of Mg(II) (although they followed the same trend) were much less pronounced.

The small changes in the UV-vis absorbance spectrum of **8-HQS** were detected upon the addition of 40 equivalents of Mg(II), and thus it was decided to investigate whether the addition of Zn(II) would still give rise to changes in the spectrum. As shown in Figure 3.6, the presence of Zn(II) still affects the ground state of **8-HQS** even in the presence of *ca.* 40 equivalents of Mg(II). The changes in the fluorescence emission of **8-HQS** were also monitored upon addition of Zn(II). In the absence of any metal, the fluorescence emission was found to be effectively quenched. However, upon the addition of Zn(II) the emission was greatly enhanced (*ca.* 68 fold enhancement), Figure 3.7a. This "switching on" of the fluorescence could be visually observed under a UV-visible lamp to the naked eye as shown in Figure 3.7b.

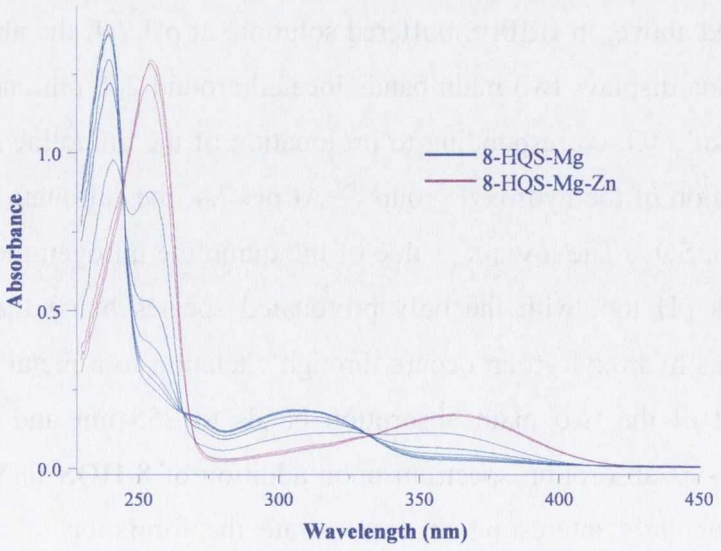


Figure 3.6: *The changes in the UV-vis absorption spectrum of* ***8-HQS-Mg*** *as a function of equivalents of Zn(II) added at pH 7.4 in HEPES buffered solution.*

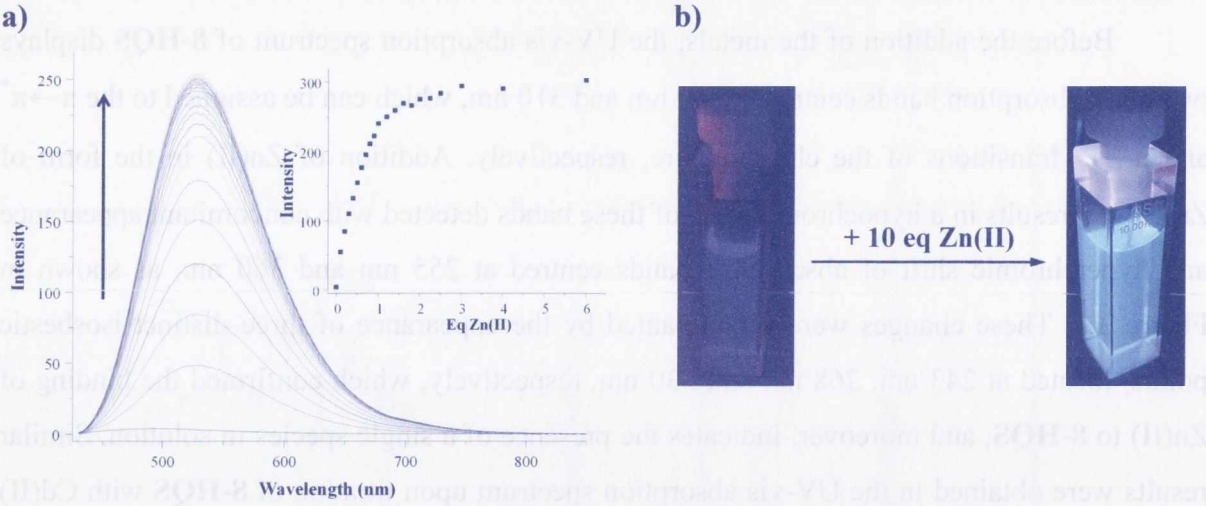


Figure 3.7: a) *Changes in the fluorescence emission spectrum of* ***8-HQS*** *as a function of equivalents of Zn(II) added at pH 7.4 in HEPES buffered solution. Inset: Changes in the fluorescence at 527 nm upon the addition of Zn(II).* ***b)*** *Fluorescence response of* ***8-HQS*** *in the presence of Zn(II) under a UV-visible lamp (λ_{ex} = 365 nm).*

Again, the addition of Zn(II) and Cd(II) cause similar enhancement in the fluorescence emission which appears to level off after the addition of 2 equivalents of metal, as shown in Appendix A3.5. In contrast, the changes observed upon titration with Mg(II) show a linear increase in the fluorescence emission that does not level off even after the addition of over 10 equivalents. These results are as expected from the binding constants of **8-HQS** with the different metal ions; the larger value being observed with Zn(II).[171] Having verified that the presence of Zn(II) effects both the ground and singlet excited state of **8-HQS**, and with both components of the desired ternary complex synthesised and characterised, the next stage involved the formation of **Yb·81-8-HQS** in aqueous solution.

3.4 Formation and Photophysical Characterisation of Yb·81-8-HQS

As mentioned above, in HEPES buffered solution, at pH 7.4, the absorption spectrum of the **8-HQS** antenna displays two main bands located around 240 nm and 310 nm. **8-HQS** possess pK_a values of 3.93, corresponding to protonation of the quinoline nitrogen and 8.42, revealing deprotonation of the hydroxyl group.[165] At pH 7.4, the sulfonate group exists as its corresponding anion, SO_3^-. The low pK_a value of the quinoline nitrogen means that it will be deprotonated at this pH too, with the only protonated species being the hydroxyl group. Deprotonation of this hydroxyl group occurs through chelation to a metal ion, resulting in a significant red shift of the two main absorption bands to 255 nm and 356 nm which is observed in the UV-vis absorption spectrum upon addition of **8-HQS** to **Yb·81**, Figure 3.8. This feature is particularly interesting to demonstrate the formation of a ternary complex between **Yb·81** and **8-HQS** as the position of the main absorption bands allow differentiating between free and bound antenna in solution.

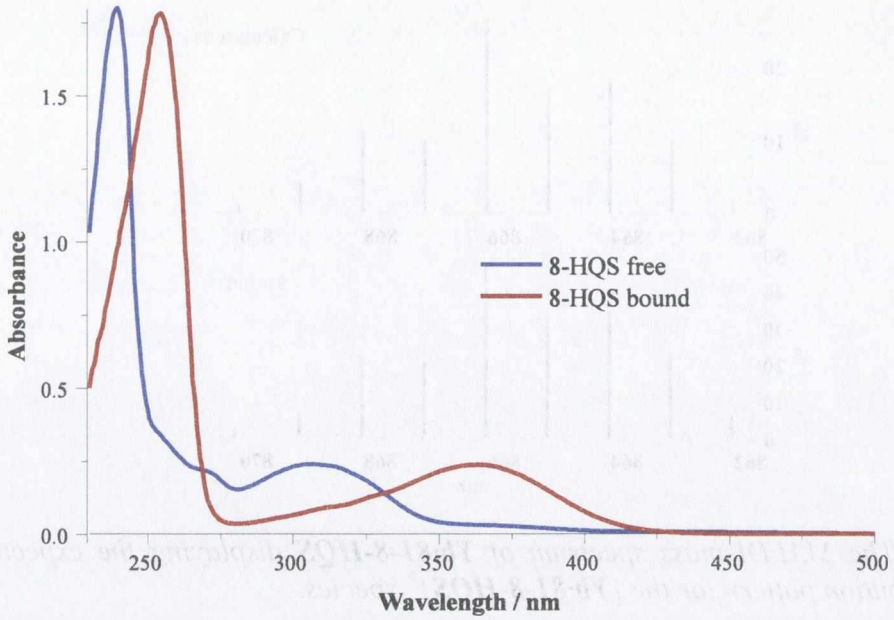


Figure 3.8: *Changes in the UV-vis absorption spectrum of* ***8-HQS*** *upon complexation to* ***Yb·81*** *at pH 7.4 in HEPES buffered solution.*

The UV-vis absorption spectrum of **Yb·81** showed substantial changes upon titration with **8-HQS** in HEPES buffered solution at pH 7.4 and is shown in Figure 3.9a. The appearance of absorption bands between 240 nm and 365 nm was a direct result of increasing concentrations of **8-HQS** added. The 255 nm and 365 nm absorption bands, which are characteristic of the Yb(III) bound form, increased considerably between 0 and 1 equivalents of **8-HQS** added, while increasing to a far lesser extent at more than 1 equivalent, Figure 3.9b, indicating the formation of the 1:1 ternary complex, **Yb·81-8-HQS**, between **Yb·81** and **8-HQS** in buffered solution. Concomitantly, the absorption bands at 240 nm and 310 nm show the opposite trend, with the increase of these bands being much larger after 1 equivalent of **8-HQS** added, due to the increasing concentration of the unbound form of **8-HQS** in solution.

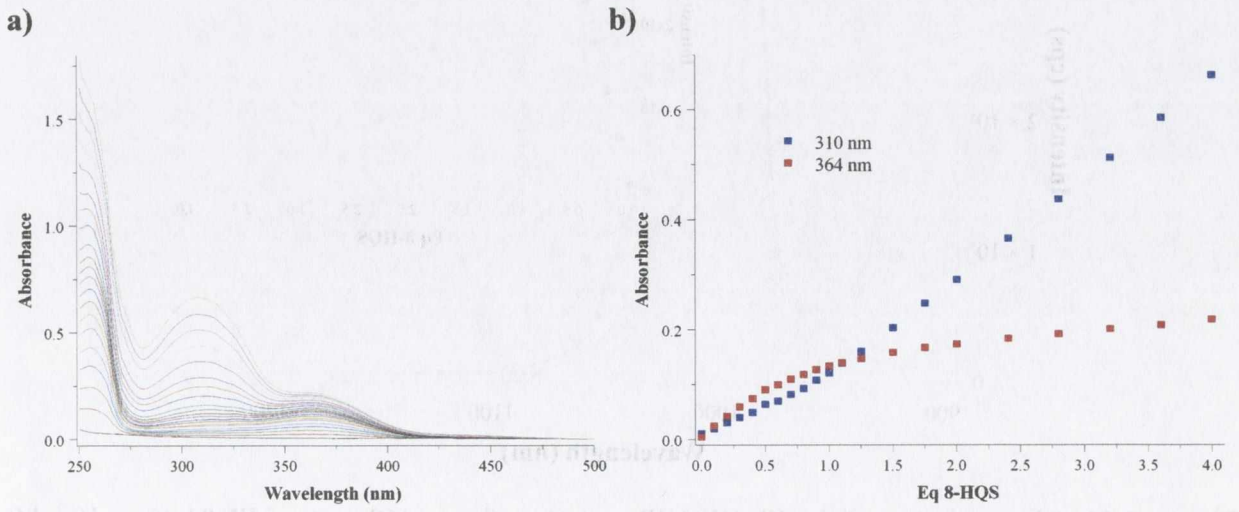


Figure 3.9: a) *Changes in the UV-vis absorption spectrum of* ***Yb·81*** *(5×10^{-5} M) as a function of equivalents of* ***8-HQS*** *added at pH 7.4 in HEPES buffered solution.* ***b)*** *Changes in the absorbance at 310 nm and 364 nm upon the addition of* ***8-HQS****.*

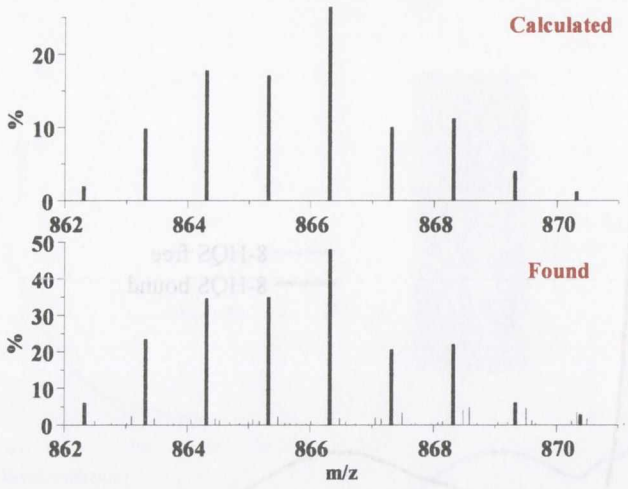


Figure 3.10: *The MALDI mass spectrum of* ***Yb·81-8-HQS*** *displaying the expected Yb(III) isotopic distribution pattern for the* ***[Yb·81-8-HQS]***$^{+}$ *species.*

Further evidence of the ternary complex formation, **Yb·81-8-HQS** was ascertained by mass spectrometry as shown in Figure 3.10. A solution of **Yb·81** in the presence of 1.2 equivalents of **8-HQS** were prepared and analysed using MALDI-MS. Examination of this solution revealed the presence of a single charged species at *m/z* = 866.3179, which corresponds to **[Yb·81-8-HQS]**$^{+}$ of which the isotopic distributions are shown to be in agreement with theoretical simulations. In addition, the formation of the ternary complex *in situ* **Yb·81-8-HQS** was demonstrated by monitoring the appearance of Yb(III)-centred emission throughout the titration, Figure 3.11.

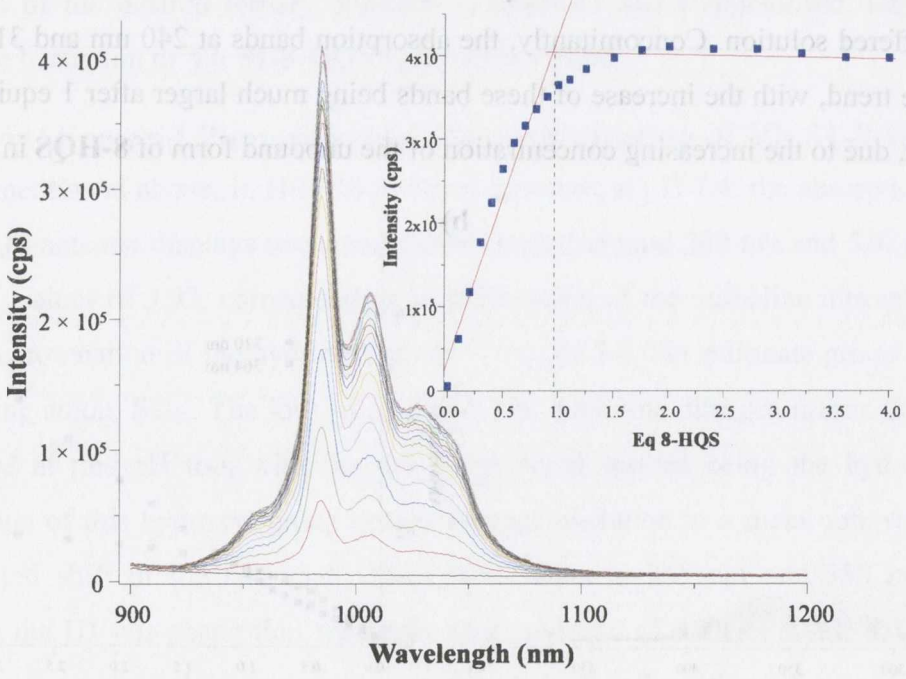


Figure 3.11: *The evolution of the Yb(III) NIR emission (λ_{ex} = 360 nm) of* ***Yb·81*** *(5 × 10^{-5} M) upon the addition of* ***8-HQS*** *at pH 7.4 in HEPES buffered solution. Inset: Changes in the NIR emission at 985 nm as a function of equivalents of* ***8-HQS****.*

In the absence of **8-HQS**, the Yb(III) metal centred emission of **Yb·81** was not observed. The addition of **8-HQS** and the formation of **Yb·81-8-HQS** resulted in characteristic Yb(III) NIR luminescence arising from the $^2F_{5/2} \rightarrow {}^2F_{7/2}$ transitions upon excitation into the **8-HQS** antenna at 360 nm. The emission can be described as "switched on" in the wavelength range of 920-1100 nm, with a sharp main component being observed at 985 nm and broader components at longer wavelengths due, in part, to the occurrence of vibronic transitions. The changes observed in the NIR emission at the maximum 985 nm, as shown in Figure 3.11, begin to plateau around the addition of one equivalent of **8-HQS**, confirming the formation of the 1:1 ternary complex **Yb·81-8-HQS**.

The 1:1 ternary complex formation of **Yb·81-8-HQS** was further established by measuring the lifetimes of the Yb($^2F_{5/2}$) excited state of **Yb·81** in the presence of one equivalent of **8-HQS**. Using the empirical equation reported by Faulkner and co-workers[172] the hydration state or q value for **Yb·81** was determined from the lifetimes measured in H_2O (3.4 μs) and D_2O (6.1 μs) and found to be 0, indicating the absence of any metal bound water molecules and hence, establishing the presence of the 1:1 ternary complex **Yb·81-8-HQS**.

The changes in the UV-visible absorption and Yb(III) emission were analysed by Dr. Steve Comby using the non-linear regression analysis program SPECFIT, Figure 3.12 from which the binding constant for the formation of **Yb·81-8-HQS** was determined as log K_{11} = 5.5 ± 0.3.

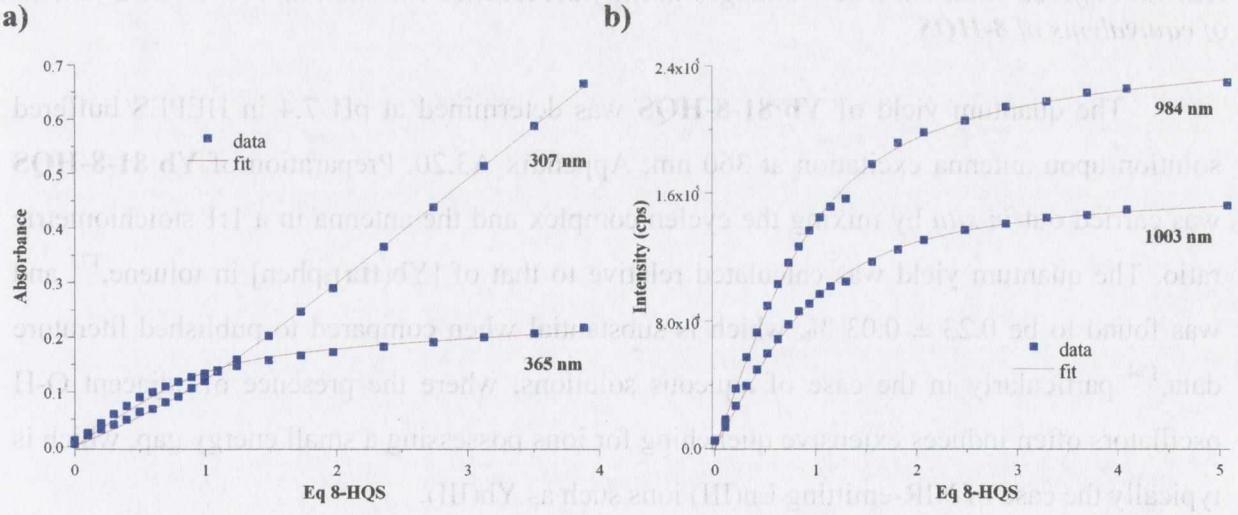


Figure 3.12: *Experimental binding isotherms at different* ***a)*** *absorption and* ***b)*** *emission wavelengths for the titration of* ***Yb·81*** *with* ***8-HQS*** *at pH 7.4 in HEPES buffered solution and their corresponding fits using SPECFIT (-).*

Energy transfer from the **8-HQS** antenna to the Yb(III) ion and thus sensitization of the NIR luminescence was confirmed by recording the excitation spectra which closely match the absorption spectra as depicted in Figure 3.13a. It is important to note that the two main

bands observed in the excitation spectrum are located around 255 nm and 360 nm, which match the absorbance of the bound form of **8-HQS** and not that of the unbound form, indicating that any excess of **8-HQS** added to the solution after the formation of the ternary complex **Yb·81-8-HQS** (*i.e.* any amount after the addition of one equivalent of **8-HQS**) would not contribute to the sensitisation process as shown in the inset of Figure 3.11 and that energy transfer to the Yb(III) metal centre only occurs from those antennae that are covalently bound to the Ln(III) ion.

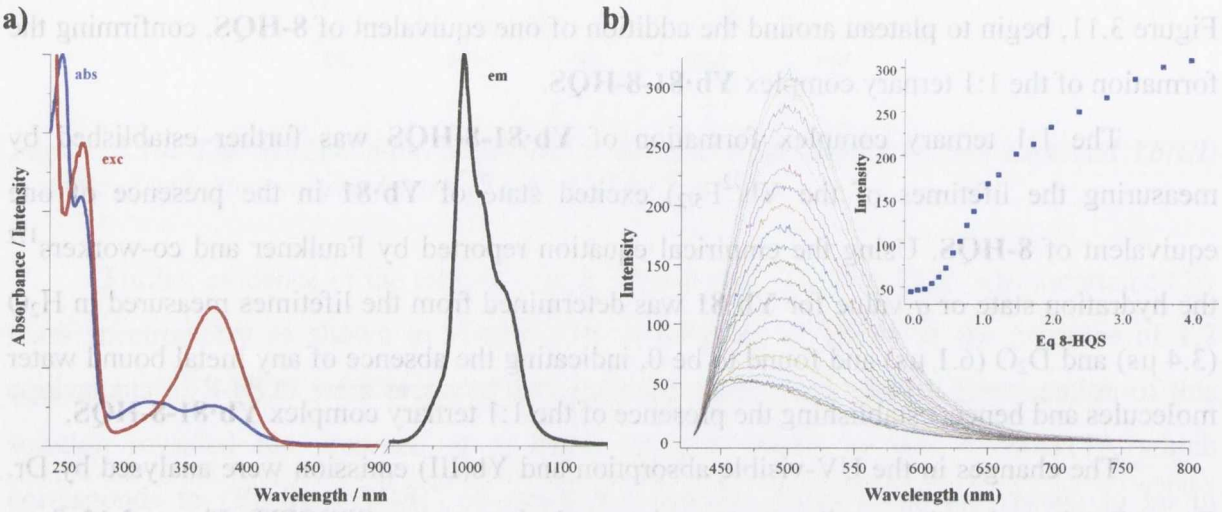


Figure 3.13: ***a)*** *Absorption, emission (λ_{ex} = 360 nm) and excitation (λ_{em} = 985 nm) spectra of* ***Yb·81-8-HQS*** *at pH 7.4 in HEPES buffered solution.* ***b)*** *The evolution of the* ***8-HQS*** *antenna fluorescence (λ_{ex} = 360 nm) of* ***Yb·81*** *(5×10^{-5} M) upon the addition of* ***8-HQS*** *at pH 7.4 in HEPES buffered solution. Inset: Changes in the fluorescence emission at 497 nm as a function of equivalents of* ***8-HQS****.*

The quantum yield of **Yb·81-8-HQS** was determined at pH 7.4 in HEPES buffered solution upon antenna excitation at 360 nm, Appendix A3.20. Preparation of **Yb·81-8-HQS** was carried out *in situ* by mixing the cyclen complex and the antenna in a 1:1 stoichiometric ratio. The quantum yield was calculated relative to that of [Yb(**tta**)$_3$phen] in toluene,[173] and was found to be 0.23 ± 0.03 %, which is substantial when compared to published literature data,[174] particularly in the case of aqueous solutions, where the presence of adjacent O-H oscillators often induces extensive quenching for ions possessing a small energy gap, which is typically the case of NIR-emitting Ln(III) ions such as Yb(III).

Despite this relatively high quantum yield, it must be highlighted that some ligand-centred fluorescence was observed in the visible range (*ca.* 495 nm), as a result of **8-HQS** binding to the Yb(III) centre, as shown in Figure 3.13b. The fluorescence emission spectrum showed a 6 fold enhancement upon the addition of up to 4 equivalents of **8-HQS**. Furthermore, it undergoes a hypsochromic shift from 365 nm to 310 nm. The presence of both

ligand and metal centred emission indicates that even if the sensitisation is significant, the energy transfer from the antenna to the Ln(III) ion is not complete.

3.5 Displacement Assay for the Detection of Zn(II)

Having determined that the formation of the ternary complex **Yb·81-8-HQS** occurs, we next evaluated its ability to act as a luminescent sensor for Zn(II) by the addition of $Zn(ClO_4)_2$ to a solution of **Yb·81-8-HQS** at pH 7.4 in HEPES buffered solution.

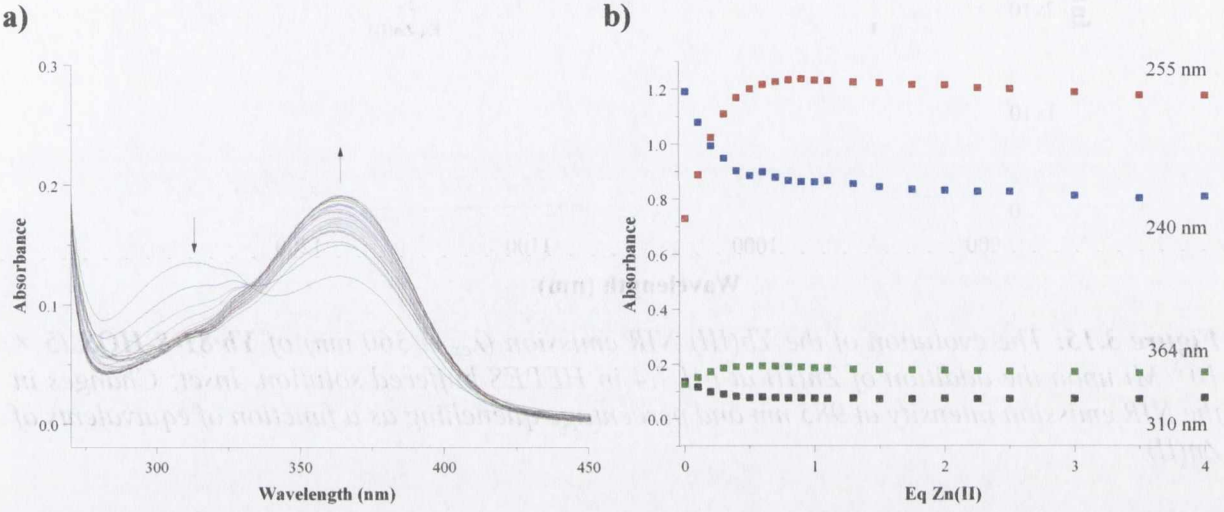


***Figure 3.14: a)** Changes in the UV-vis absorption spectrum of **Yb·81-8-HQS** (5×10^{-5} M) as a function of equivalents of Zn(II) added at pH 7.4 in HEPES buffered solution. **b)** Changes in the absorbance at 240 nm, 255 nm, 310 nm and 364 nm upon the addition of Zn(II).*

The ground state spectroscopic properties of **Yb·81-8-HQS** were first examined upon the addition of Zn(II). The changes observed are shown in Figure 3.14 and are similar to those observed in the titration of **8-HQS** against Zn(II). Before the addition of Zn(II); the UV-vis absorption spectrum of **Yb·81-8-HQS** displays two main absorption bands centred at 240 nm and 310 nm. Upon addition of Zn(II) these bands underwent a 2 fold hypochromic shift which also gave rise to the formation of new absorption bands centred at 255nm (+ 70%) and 364 nm (+ 50%) and the formation of three pseudo-isosbestic points were observed at 244 nm, 266 nm and 332 nm.

The NIR emission spectrum showed significant changes in the $^2F_{5/2} \rightarrow {}^2F_{7/2}$ transitions of the Yb(III) metal centre upon addition of Zn(II). As displayed in Figure 3.15, the addition of 0→4 equivalents of Zn(II) resulted in a 95% quenching in the Yb(III) emission. However, as can be seen from the inset in Figure 3.15, the NIR emission was quenched by *ca.* 80% within the addition of one equivalent of Zn(II). This was due to the displacement of the **8-HQS** antenna from the Yb(III) centre, which results in the dissociation of the luminescent **Yb·81-8-HQS** ternary complex and formation of $Zn(\mathbf{8\text{-}HQS})_x$ (x = 1,2) chelates.

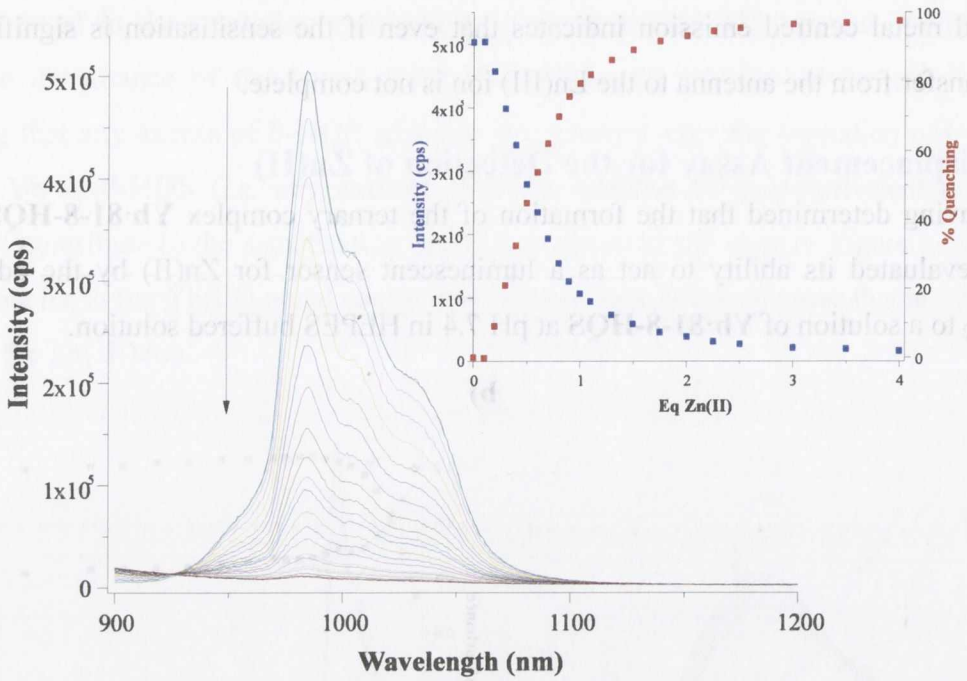


Figure 3.15: *The evolution of the Yb(III) NIR emission (λ_{ex} = 360 nm) of* ***Yb·81-8-HQS*** *(5 × 10^{-5} M) upon the addition of Zn(II) at pH 7.4 in HEPES buffered solution. Inset: Changes in the NIR emission intensity at 985 nm and percentage quenching as a function of equivalents of Zn(II).*

This was indeed found to be the case with appearance of an intense and broad green fluorescence emission band centred at 529 nm, as shown in Figure 3.16a, which was characteristic of the formation of Zn(II) chelates with **8-HQS**. This demonstrates that the formation of the **8-HQS** metal chelates, **8-HQS-Zn**, prevents the photoinduced charge transfer from the oxygen atom to the pyridinium ring, which, in the free **8-HQS**, accompanies tautomerization and leads to fluorescence quenching, Figure 3.17.[175]

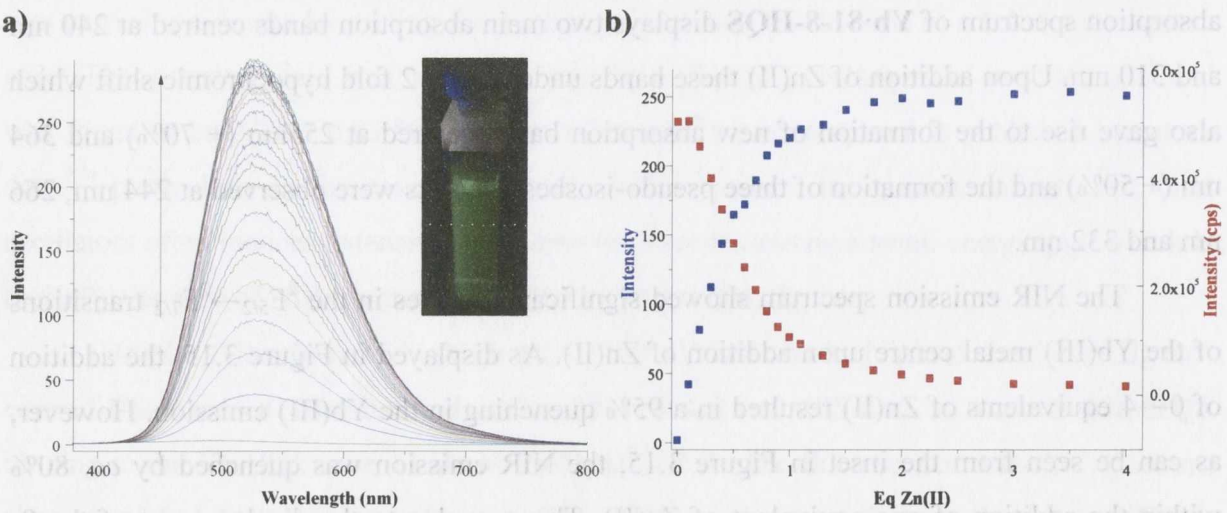


Figure 3.16: ***a)*** *Changes in the fluorescence spectrum of* ***Yb·81-8-HQS*** *as a function of equivalents of Zn(II) added at pH 7.4 in HEPES buffered solution. Inset: Fluorescence response of* ***Yb·81-8-HQS*** *with Zn(II) under a UV-visible lamp (λ_{ex} = 365 nm).* ***b)*** *Changes in the fluorescence at 528 nm and concomitant quenching of Yb(III) emission.*

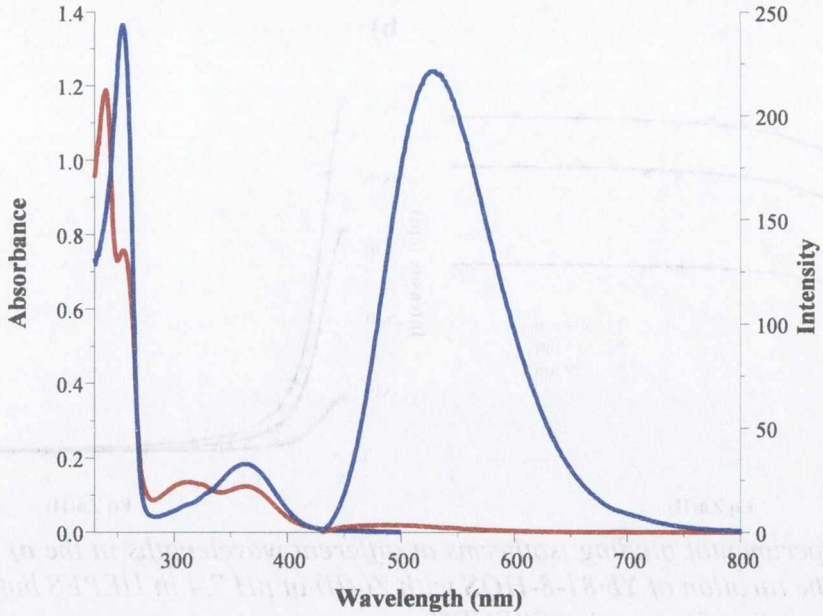


Figure 3.17: *Absorption and visible emission (λ_{ex} = 360 nm) spectra of* ***Yb·81-8-HQS*** *(5×10^{-5} M) pH 7.4 in HEPES buffered solution in the absence (-) and presence (-) of one equivalent of Zn(II).*

Since the **8-HQS** fluorescence enhancement arises purely from its chelation to Zn(II), it was expected that the NIR emission quenching should correspond to the mirror image of the enhancement in the visible region. This was in fact found to be the case as demonstrated in Figure 3.17. In the same way that the majority of the quenching of the Yb(III) emission occurs between the addition of 0 and 1 equivalents of Zn(II), the enhancement in the fluorescence emission occurs predominately over the same range. The addition of Zn(II) simultaneously quenched the NIR emission and gave rise to enhancement in visible fluorescence.

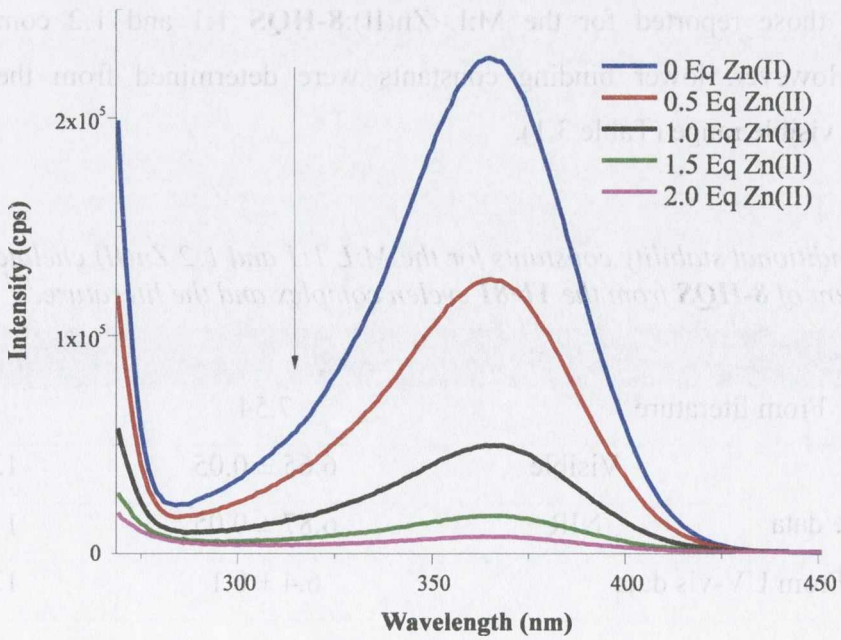


Figure 3.18: *The excitation spectrum (λ_{em} = 985 nm) of* ***Yb·81-8-HQS*** *(5×10^{-5} M) pH 7.4 in HEPES buffered solution upon titration with Zn(II).*

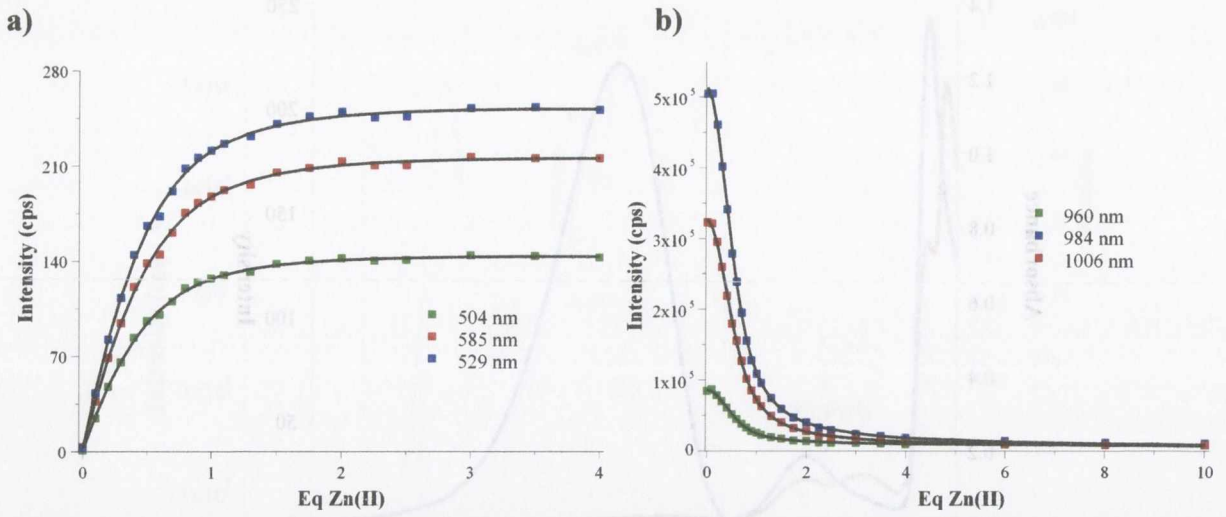


Figure 3.19: *Experimental binding isotherms at different wavelengths in the* ***a)*** *visible and* ***b)*** *NIR ranges for the titration of* ***Yb·81-8-HQS*** *with Zn(II) at pH 7.4 in HEPES buffered solution and their corresponding fits (-) using SPECFIT.*

To further confirm that the loss of the NIR Yb(III) centred emission was due to antenna displacement, the excitation spectrum was monitored at 985 nm ($^2F_{5/2} \rightarrow {}^2F_{7/2}$ transition), Figure 3.18, and the absence of any changes in the spectrum, signifies that no other quenching or sensitisation mechanisms are taking place during the titration.

The emission data obtained from both the visible and NIR ranges were fit using the non-linear regression analysis programme SPECFIT by Dr. Steve Comby in order to determine the conditional stability constants for the formation of Zn(II) chelates with **8-HQS**. Figure 3.19 shows the experimental binding isotherms and the corresponding fits at different wavelengths as a function of equivalents of Zn(II), with the stability constants determined for **Zn-8-HQS** (M:L) shown in Table 3.1 below. The binding constants obtained correspond adequately to those reported for the M:L Zn(II):**8-HQS** 1:1 and 1:2 complexes in the literature.[171] However, lower binding constants were determined from the fluorescence changes in the visible range (Table 3.1).

Table 3.1: *Conditional stability constants for the M:L 1:1 and 1:2 Zn(II) chelates formed after the displacement of* ***8-HQS*** *from the* ***Yb·81*** *cyclen complex and the literature.*[171]

Zn-8-HQS		log $K_{1:1}$	log $\beta_{1:2}$
From literature		7.54	14.32
From Fluorescence data	Visible	6.65 ± 0.05	12.0 ± 0.2
	NIR	6.87 ± 0.05	11.7 ± 0.1
From UV-vis data		6.4 ± 0.1	12.5 ± 0.2

3.5.1 Limit of Detection for the Sensing of Zn(II)

Previously discussed studies on Zn(II) sensing using **Yb·81-8-HQS** were carried out using a 5×10^{-5} M concentration of the sensor and 0 to 0.10 equivalents of Zn(II).

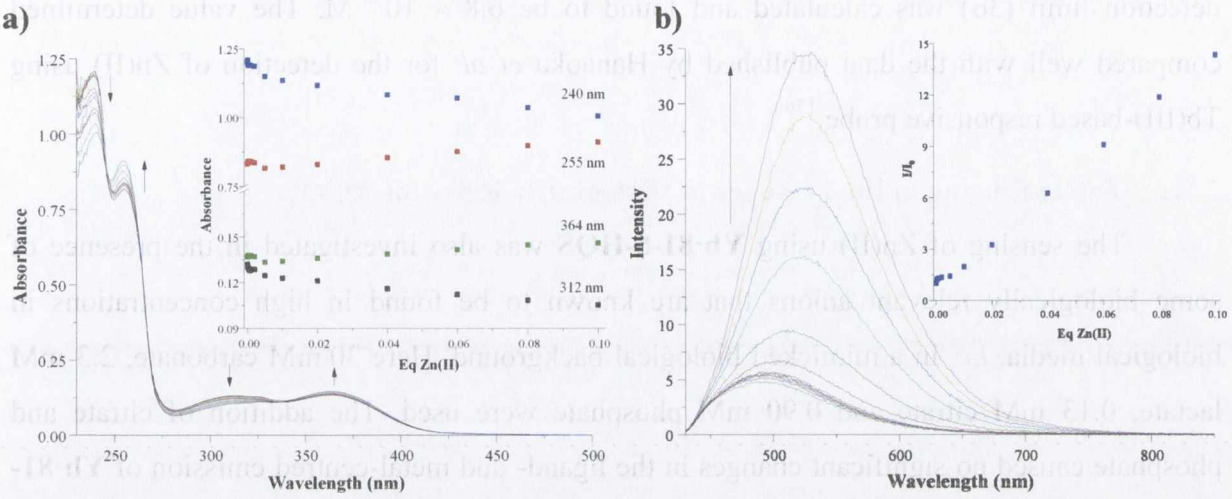


Figure 3.20: *a) UV-vis absorption spectrum and* ***b)*** *fluorescence spectrum changes during the limit of detection study of the ability of* ***Yb·81-8-HQS*** *to sense Zn(II) at pH 7.4 in HEPES buffered solution. Insets: Changes in the* ***a)*** *absorbance at 240 nm, 255 nm, 310 nm and 364 nm and* ***b)*** *fluorescence at 526 nm as a function of equivalents of Zn(II).*

It was necessary to monitor any modulation in the sensing ability of **Yb·81-8-HQS** as the equivalents of Zn(II) were decreased. The study involved adding smaller equivalents of a solution of $Zn(ClO_4)_2$; 0.005 to 0.10, to **Yb·81-8-HQS**. Even with only minor amounts of Zn(II) added, changes were still clearly observable in the UV-vis absorption and fluorescence spectrum, as shown in Figure 3.20, where a 20% hypochromicity occurred for the absorbance band at 312 nm and a significant 7-fold increase in the fluorescence was observed in concert with a bathochromic shift to a maximum at 525 nm.

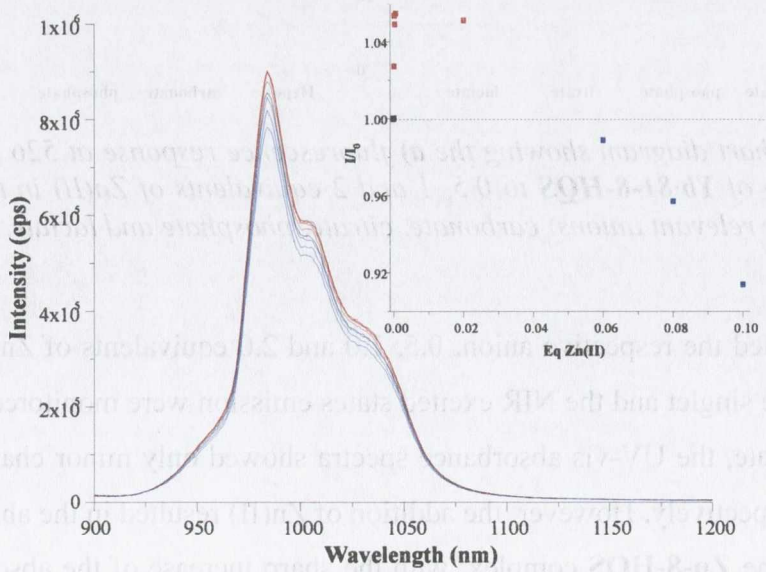


Figure 3.21: *NIR emission changes during the limit of detection study of the ability of* ***Yb·81-8-HQS*** *to sense Zn(II) at pH 7.4 in HEPES buffered solution. Inset: Changes in the NIR emission at 985 nm as a function of equivalents of Zn(II).*

Upon excitation of the **8-HQS** antenna at 360 nm, the NIR emission quenching of **Yb·81-8-HQS** (5×10^{-5} M) at pH 7.4 in HEPES buffered solution, Figure 3.21, shows a linear relationship within the Zn(II) concentration range of 0 to 4.5×10^{-5} M ($R^2 = 0.983$). The detection limit (3σ) was calculated and found to be 6.8×10^{-6} M. The value determined compared well with the data published by Hanaoka *et al.* for the detection of Zn(II) using Tb(III)-based responsive probe.[176]

3.5.2 Zn(II) Sensing in the Presence of Biologically Relevant Anions

The sensing of Zn(II) using **Yb·81-8-HQS** was also investigated in the presence of some biologically relevant anions that are known to be found in high concentrations in biological media, *i.e.* in a mimicked biological background. Here 30 mM carbonate, 2.3 mM lactate, 0.13 mM citrate and 0.90 mM phosphate were used. The addition of citrate and phosphate caused no significant changes in the ligand- and metal-centred emission of **Yb·81-8-HQS**. However, carbonate and lactate did give rise to enhanced quenching in the Yb(III)-centred emission. The results of this biological anion screening test are summarised below in Figure 3.22.

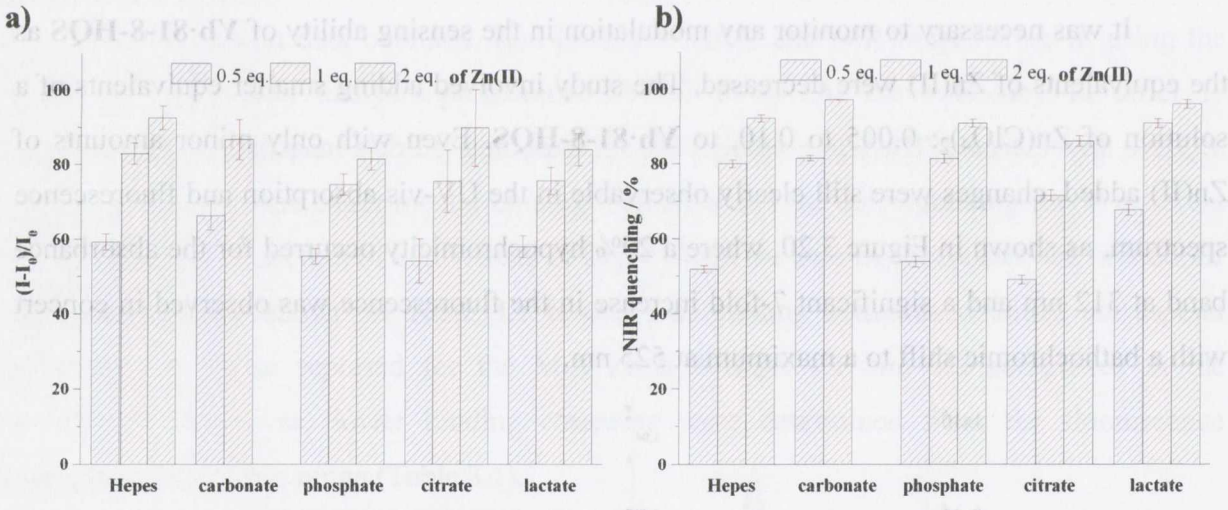


Figure 3.22: *Bar chart diagram showing the* ***a)*** *fluorescence response at 526 nm and* ***b)*** *NIR emission quenching of* ***Yb·81-8-HQS*** *to 0.5, 1 and 2 equivalents of Zn(II) in the presence of various biologically relevant anions: carbonate, citrate, phosphate and lactate.*

Having added the respective anion, 0.5, 1.0 and 2.0 equivalents of Zn(II) were added and the ground, the singlet and the NIR excited states emission were monitored. In the case of citrate and phosphate, the UV-vis absorbance spectra showed only minor changes, Appendix A3.7 and A3.8, respectively. However, the addition of Zn(II) resulted in the absorption spectra characteristic for the **Zn-8-HQS** complex, with the sharp increase of the absorption bands at 255 nm and 364 nm. Although more pronounced changes occur in the UV-vis absorption

spectrum upon the addition of lactate and carbonate, Appendix A3.9 and A3.10, the consecutive addition of Zn(II) still results in the spectra characteristic for **Zn-8-HQS**.

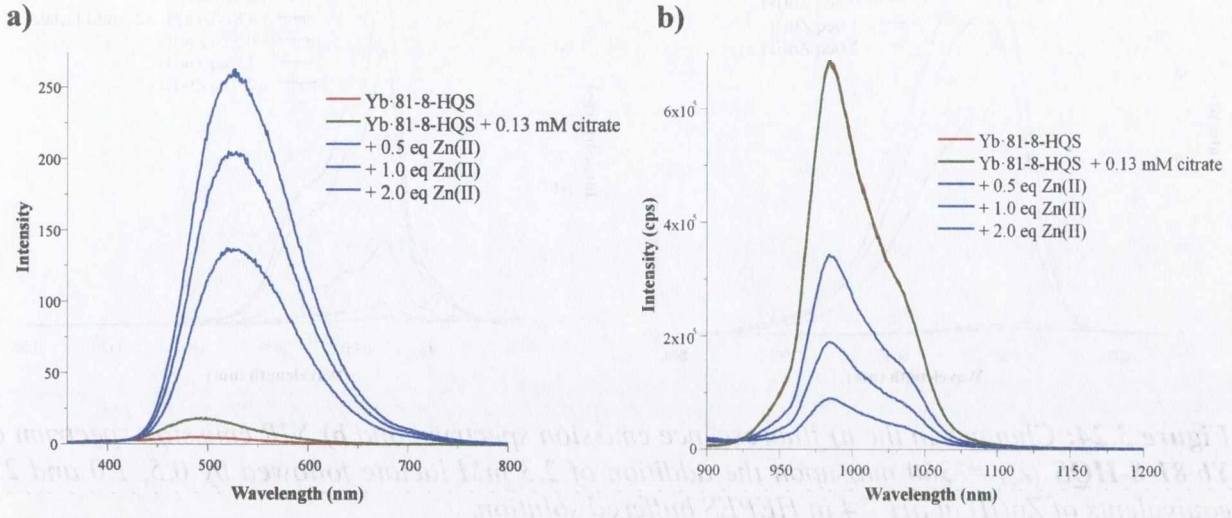


Figure 3.23: *Changes in the* ***a)*** *fluorescence emission spectrum and* ***b)*** *NIR emission spectrum of* ***Yb·81-8-HQS*** *(λ_{ex} = 360 nm) upon the addition of 0.13 mM citrate followed by the addition of 0.5, 1.0 and 2.0 equivalents of Zn(II) at pH 7.4 in HEPES buffered solution.*

The singlet excited state emission of **Yb·81-8-HQS** was only slightly enhanced upon addition of 0.13 mM citrate, 2.3 mM lactate, 0.90 mM phosphate and 30 mM carbonate; Figure 3.23a, Figure 3.24a and Appendix 3.11a and 3.12a, respectively. It was evident that neither anion interfered with the **Zn-8-HQS** binding process as the fluorescence, upon addition of Zn(II), was greatly enhanced, similar to that seen before for the **Zn-8-HQS** complex.

For the Yb(III) centred emission, no measurable changes were detected upon the addition of citrate or phosphate, Figure 3.23b, and Appendix A3.11b, respectively. Further addition of Zn(II) caused the expected quenching of the Yb(III) emission; confirming that the presence of citrate or phosphate did not interfere in the dissociation of **8-HQS** from the metal centre of **Yb·81**. The added anions carbonate and lactate did give rise to some quenching of the NIR emission, which was more pronounced for carbonate, with *ca.* 4 fold decrease in the emission intensity, Figure 3.24b and Appendix A3.12b. This quenching was somewhat expected, as at such a high concentration, competition between the anion and **8-HQS** to bind to **Yb·81** cyclen complex exists.

It was established that the sensing of Zn(II) by the ternary complex **Yb·81-8-HQS** was efficient in the presence of these anions, at high biological concentrations. The interaction of **Yb·81-8-HQS** with a range of transition and alkali metal ions will be discussed in the following section.

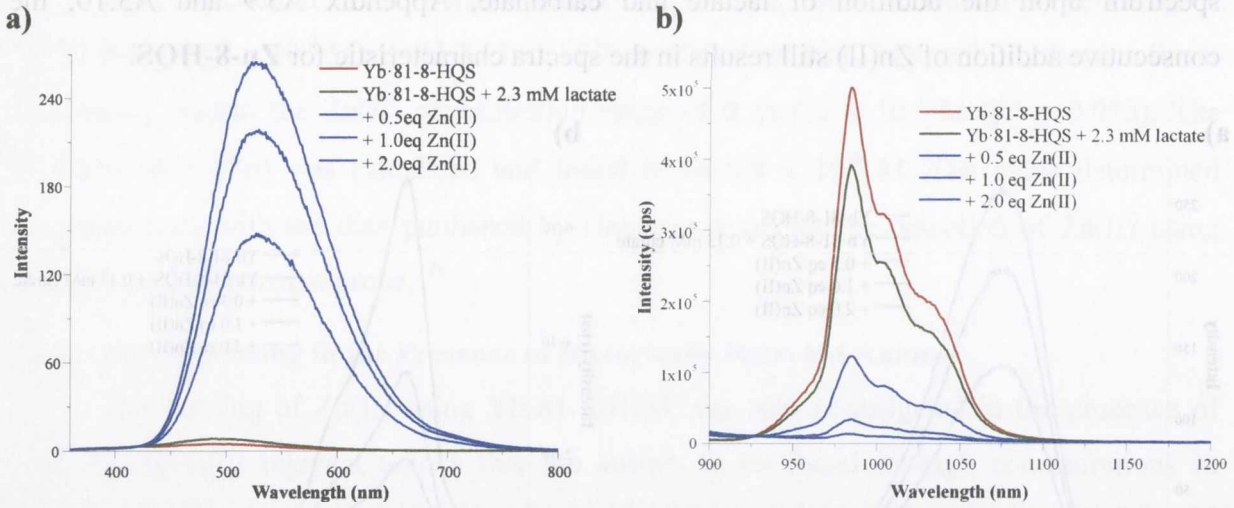


Figure 3.24: *Changes in the* ***a)*** *fluorescence emission spectrum and* ***b)*** *NIR emission spectrum of* ***Yb·81-8-HQS*** *(λ_{ex} = 360 nm) upon the addition of 2.3 mM lactate followed by 0.5, 1.0 and 2.0 equivalents of Zn(II) at pH 7.4 in HEPES buffered solution.*

3.6 Reversibility of the Sensing Event

As previously demonstrated, it is advantageous for the formation of the ternary complex to be fully reversible as a function of pH. Moreover, it was also important to ascertain whether the sensing event involving Zn(II) could also be reversible, and as such would allow for multiple detections. To investigate the reversibility, titrations involving the use of ethylenediaminetetraacetic acid (EDTA) were carried out. EDTA was used as it is a hexadentate ligand that is known for its ability to bind to metal ions such as Ca(II), Fe(II) and Zn(II).

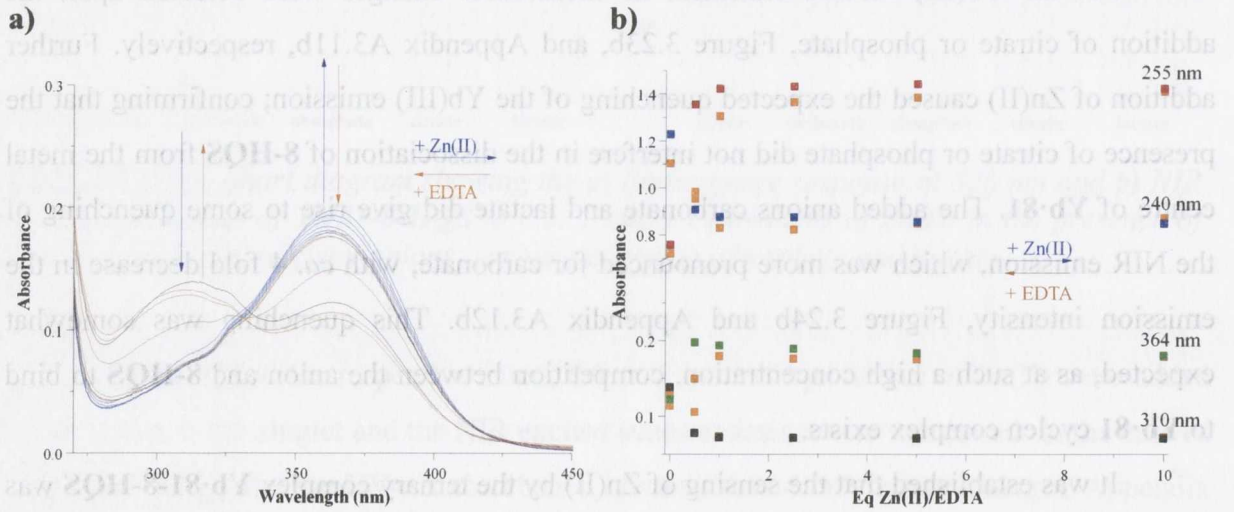


Figure 3.25: ***a)*** *Changes in the UV-vis absorption spectrum of* ***Yb·81-8-HQS*** *(5×10^{-5} M) upon titration with Zn(II) followed by the addition of EDTA at pH 7.4 in HEPES buffered solution.* ***b)*** *Reversibility of the "off/on" switching behaviour of the Yb(III) centred upon the addition of EDTA.*

In order to prove the reversibility of the ternary system, **Yb·81-8-HQS**, towards the addition of Zn(II), a solution of **Yb·81-8-HQS** at pH 7.4 in HEPES buffered solution was first titrated with increasing amounts of Zn(II), from 0 to 10 equivalents. This was followed by the addition of EDTA, also in increasing amounts from 0 to 10 equivalents. The changes in the ground state are shown in Figure 3.25. As expected, upon addition of Zn(II) to **Yb·81-8-HQS**, formation of **8-HQS-Zn** resulted in an appearance of the UV-vis absorption band centred at 364 nm with a concomitant decrease in the band centred at 310 nm. At this stage up to 10 equivalents of EDTA were added and the above changes were shown to be fully reversed; the band at centred 364 nm experienced a hypochromic shift while the band centred at 310 nm was enhanced, indicating the reformation of **Yb·81-8-HQS**. This demonstrated that EDTA was able to mop up and bind any excess Zn(II) present in solution and hence, the antenna was free to associate with **Yb·81** giving rise to the formation of the sensing system.

The effects on the singlet excited state and Yb(III) excited state of **Yb·81-8-HQS** were also examined and the results were in agreement with previous titrations, where the addition of Zn(II) caused a significant enhancement in the fluorescence emission, as shown in Figure 3.26a. The addition of EDTA reversed these changes, signifying the reformation of the less emissive **Yb·81-8-HQS** ternary complex. Similarly, the NIR emission saw the expected decrease in emission intensity upon the addition of Zn(II) as the **8-HQS** antenna, which was reversed upon the addition of up to 10 equivalents of EDTA, where a complete recovery of the metal-centred NIR emission was observed, shown in Figure 3.26b. The reversibility of the sensing ability of **Yb·81-8-HQS** is particularly advantageous and interesting as it would allow for both direct and indirect determination of the Zn(II) concentration in addition to opening the possibility of multisampling detection.

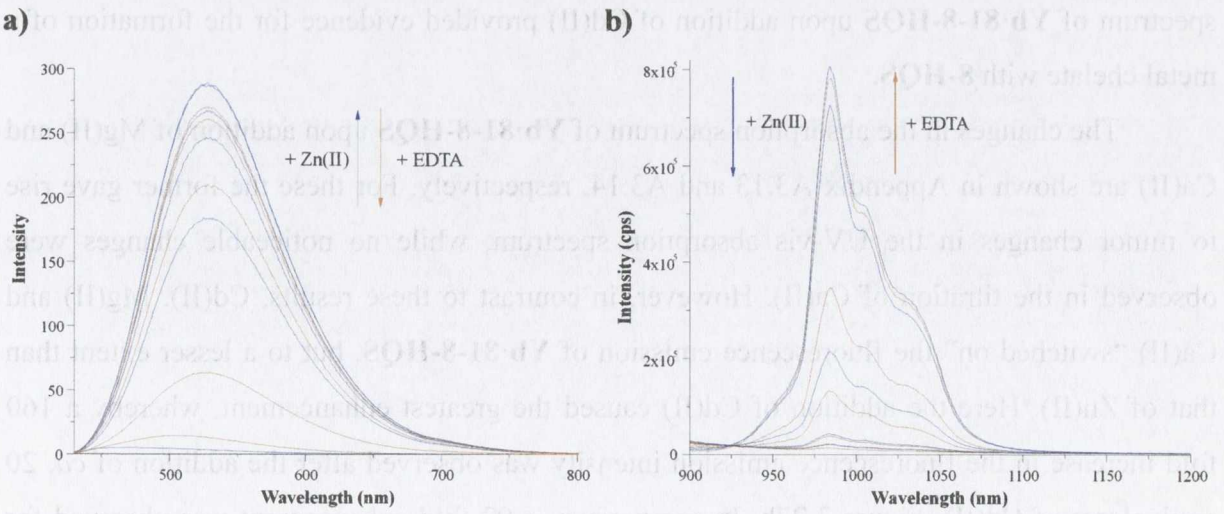


Figure 3.26: *Evolution of the* ***a)*** *fluorescence and* ***b)*** *NIR emission of* ***Yb·81-8-HQS*** *(5×10^{-5} M) upon titration with Zn(II) (-), 0→10 equivalents, followed by the addition of EDTA (-), 0→10 equivalents, at pH 7.4 in HEPES buffered solution.*

3.7 Interaction of Yb·81-8-HQS with Group I, II and d-Metal Ions

The Zn(II) selectivity was next examined by evaluating the luminescence and absorption dependence of **Yb·81-8-HQS** towards transition metal ions such as Cd(II), Co(II), Ni(II) and Cu(II) as well as the alkali metal ions Ca(II) and Mg(II) at pH 7.4 in HEPES buffered solutions. During a screening test, Section 3.3, it was noticed that Cd(II) gave rise to a similar response as that seen for Zn(II) above and so it was investigated in more detail.

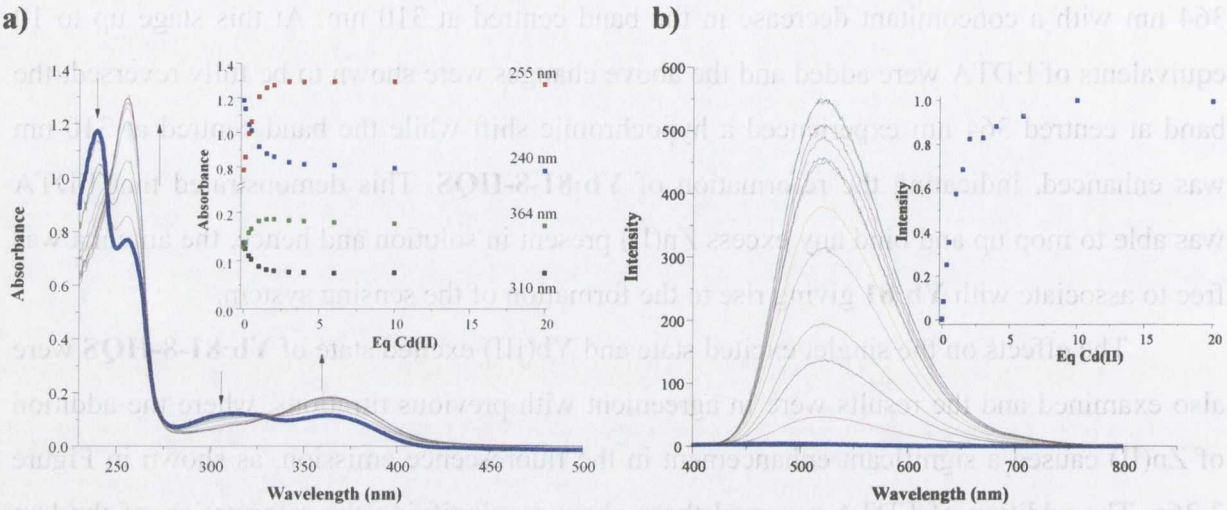


Figure 3.27: *Changes in the* ***a)*** *UV-vis absorption spectrum and* ***b)*** *fluorescence emission spectrum of* ***Yb·81-8-HQS*** *(λ_{ex} = 360 nm) upon the addition of Cd(II) at pH 7.4 in HEPES buffered solution. Insets: Changes in the* ***a)*** *absorbance at 240 nm, 255 nm, 310 nm and 364 nm and* ***b)*** *fluorescence at 527 nm upon the addition of Cd(II).*

The changes observed in the ground state upon addition of Cd(II) were similar to those observed for Zn(II), whereby the bands centred at 255 nm and 364 nm undergo a hyperchromic shift with a concomitant decrease in the absorption bands at 240 nm and 310 nm, Figure 3.27a. As for Zn(II), the evolution of a new band in the UV-visible absorption spectrum of **Yb·81-8-HQS** upon addition of Cd(II) provided evidence for the formation of a metal chelate with **8-HQS**.

The changes in the absorption spectrum of **Yb·81-8-HQS** upon addition of Mg(II) and Ca(II) are shown in Appendix A3.13 and A3.14, respectively. For these the former gave rise to minor changes in the UV-vis absorption spectrum, while no noticeable changes were observed in the titration of Ca(II). However, in contrast to these results, Cd(II), Mg(II) and Ca(II) "switched on" the fluorescence emission of **Yb·81-8-HQS**, but to a lesser extent than that of Zn(II). Here the addition of Cd(II) caused the greatest enhancement, whereby a 160 fold increase in the fluorescence emission intensity was observed after the addition of *ca.* 20 equivalents of Cd(II), Figure 3.27b. In comparison, a 93 fold enhancement was observed for Mg(II), Appendix A3.15, while a lower 14 fold enhancement was observed in response to the addition of Ca(II), Appendix A3.16.

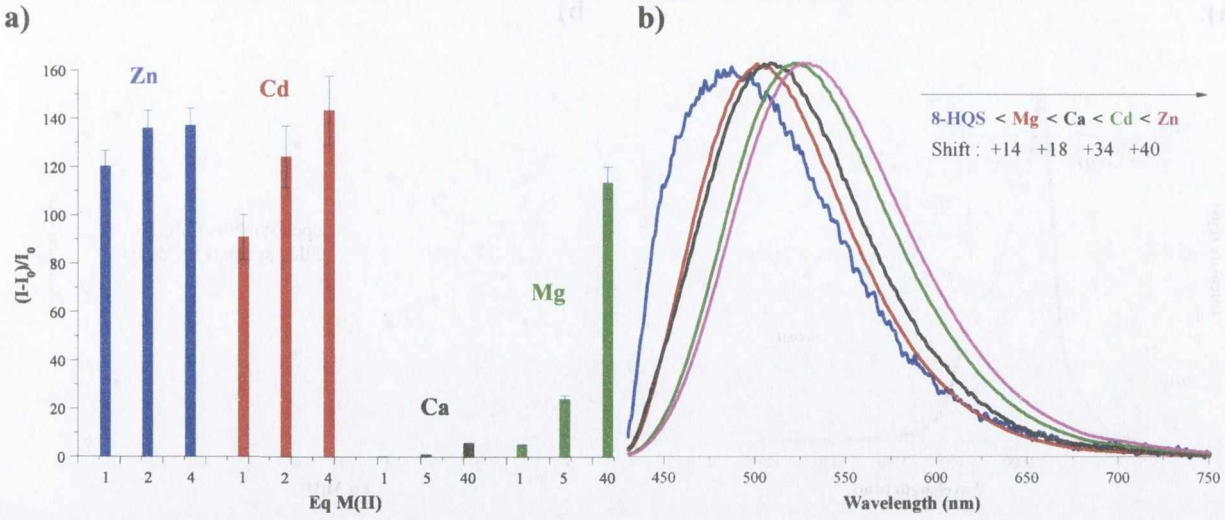


Figure 3.28: a) *Bar chart representing the ligand centred emission enhancement upon addition of M(II).* ***b)*** *Normalised fluorescence spectra (λ_{ex} = 360 nm) of* ***Yb·81-8-HQS*** *(5×10^{-5} M) at pH 7.4 in HEPES buffered solution and the corresponding red shift observed in the absence and presence of 1 equivalent of Zn(II) or Cd(II) and 40 equivalents of Ca(II) or Mg(II).*

In addition to these enhancements for Zn(II), Figure 3.28a, the **8-HQS** fluorescence maximum was also slightly less red-shifted upon binding to Cd(II), Ca(II) and Mg(II), with, for Cd(II) a maximum at 524 nm compared to 530 nm for Zn(II), Figure 3.28b.

Similarly the NIR emission was monitored during these titrations, Figure 3.29. While the addition of each of these metal ions, resulted in different extents of quenching in the NIR signal, only Cd(II) gave rise to an enhancement of the ligand-centred fluorescence after the addition of *ca.* 1 equivalent. This demonstrates the advantage of having a dual emissive probe in displacement assays, which allows for the differentiation of Zn(II) and Cd(II) from other transition metal ions as chelation of the two aforementioned ions to the **8-HQS** antenna selectively enhanced the ligand-centred fluorescence, while simultaneously quenching the metal-centred NIR emission.

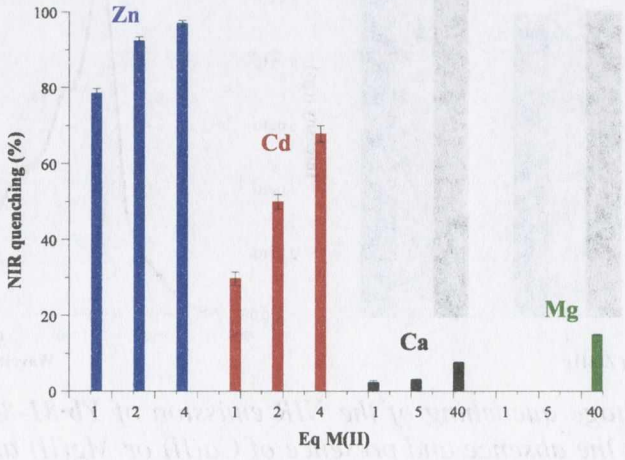


Figure 3.29: *Bar chart diagram representing the metal centred NIR emission quenching upon addition of M(II).*

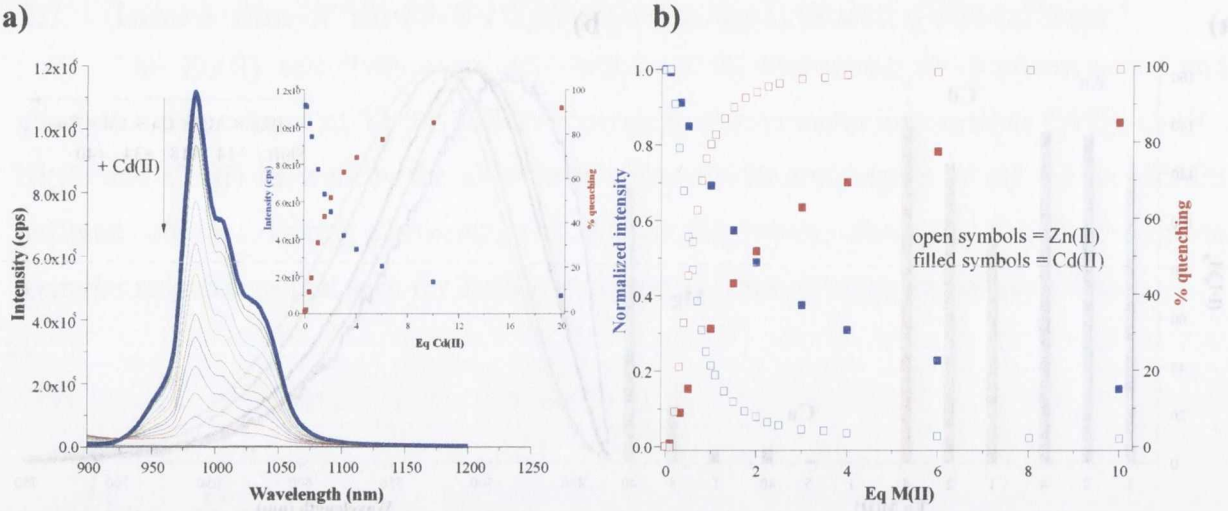


Figure 3.30: a) *Changes in the Yb(III) NIR emission (λ_{ex} = 360 nm) of* ***Yb·81-8-HQS*** *(5×10^{-5} M) upon the addition of Cd(II) at pH 7.4 in HEPES buffered solution. Inset: Changes in the NIR emission intensity at 984 nm and percentage quenching as a function of equivalents of* ***8-HQS****.* ***b)*** *Changes in the NIR emission normalised intensities of* ***Yb·81-8-HQS*** *at 984 nm (blue squares) and the percentage quenching (red squares) as a function of equivalents of Zn(II) or Cd(II).*

Although the addition of Cd(II) did give rise to a marked decrease in the NIR emission intensity, it was not to the same extent as that caused by Zn(II), Figure 3.29.. As can be seen in Figure 3.30, over 10 equivalents of Cd(II) were required to quench 90% of the emission, whereas only 1.5 equivalents of Zn(II) were required to attain the same degree of quenching. These results altogether are in good agreement with the stability constants for the formation of the different **8-HQS** metal chelates, with the constants determined for Zn(II) being one order of magnitude larger than the ones for Cd(II).[171]

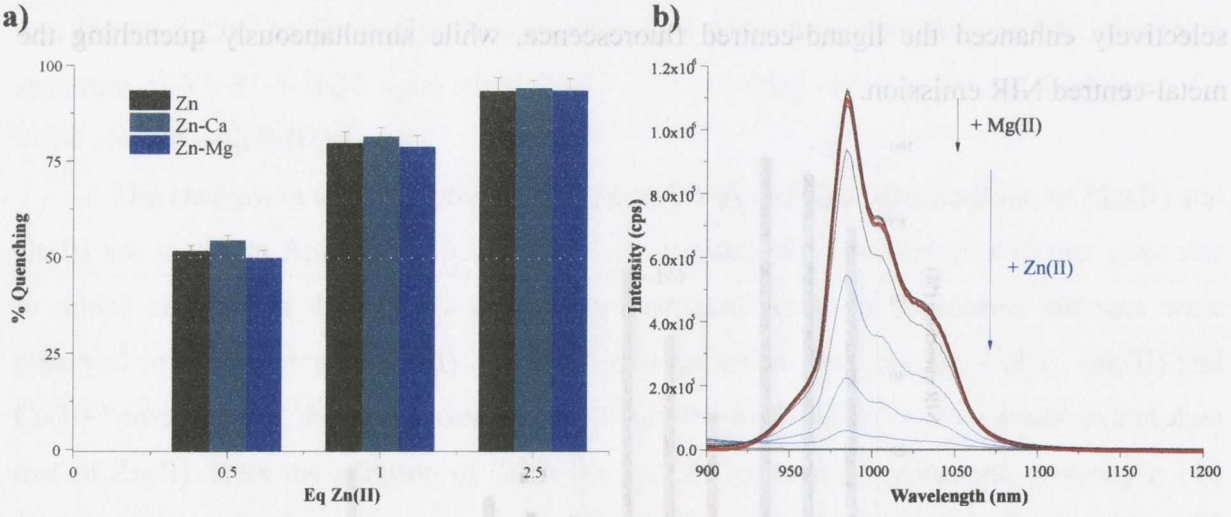


Figure 3.31: a) *Percentage quenching of the NIR emission of* ***Yb·81-8-HQS*** *observed upon the addition of Zn(II) in the absence and presence of Ca(II) or Mg(II) at a concentration of 2 mM.* ***b)*** *NIR emission spectrum (λ_{ex} = 360 nm) of* ***Yb·81-8-HQS*** *(5×10^{-5} M) upon the addition of Mg(II) followed by Zn(II) at pH 7.4 in HEPES buffered solution.*

To evaluate the Zn(II) sensing ability of the ternary system **Yb·81-8-HQS** in the presence of the biologically abundant cations such as Ca(II) and Mg(II), 2 mM concentrations of Ca(II) and Mg(II) were added to a solution of **Yb·81-8-HQS**, followed by increasing equivalents of Zn(II). The results obtained from examining the Yb(III) emission response are summarised by the bar chart in Figure 3.31a, and illustrate that the presence of Ca(II) or Mg(II) in solution did not affect the detection of Zn(II), even though some quenching of the NIR emission occurred at high concentrations of these ions prior to Zn(II) addition (< 8% for Ca(II), Appendix A3.17 and 15% for Mg(II), Figure 3.31b). However, the sequential addition of Zn(II) to **Yb·81-8-HQS-Ca/Mg** still resulted in a significant quenching the NIR Yb(III) centred emission, that are fully comparable to the changes observed in the absence of Ca(II) and Mg(II).

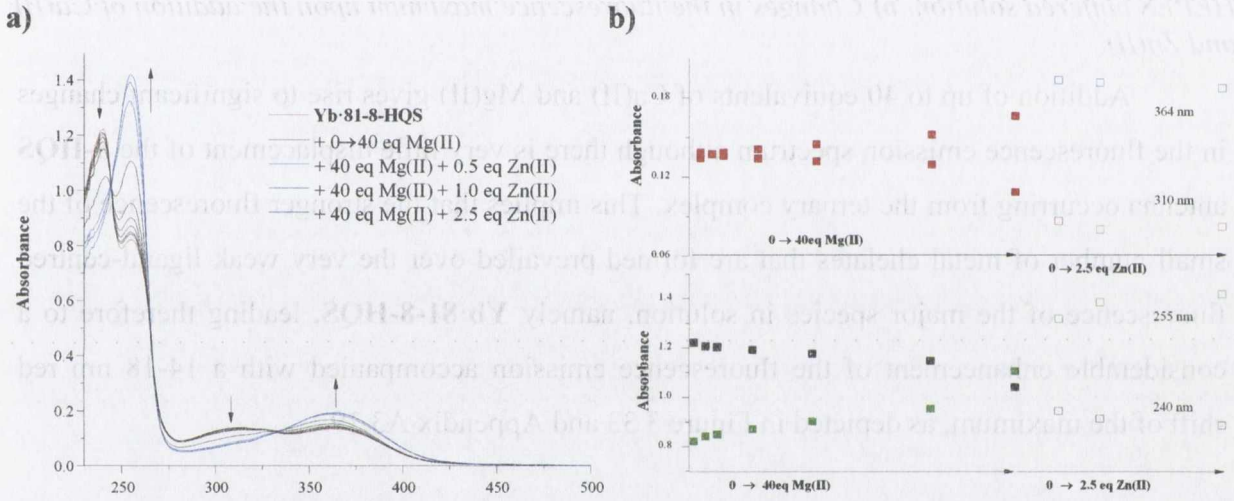


Figure 3.32: a) *Changes in the UV-vis absorption spectrum of* ***Yb·81-8-HQS*** *as a function of equivalents of Mg(II) followed by the addition of Zn(II) at pH 7.4 in HEPES buffered solution.* ***b)*** *Changes in the absorbance at 240 nm, 255 nm, 308 nm and 362 nm upon the addition of Mg(II) and Zn(II).*

The partial displacement of the **8-HQS** antenna that occurs after the addition of *ca.* 40 equivalents of alkali metal ions such as Ca(II) and Mg(II) has been previously confirmed by monitoring the changes observed in both UV-visible absorption and ligand-centred fluorescence spectra. From these results it was discovered that only a small percentage of the antenna, **8-HQS**, was displaced from the ternary system **Yb·81-8-HQS** in the presence of high concentrations (2 mM) of Ca(II) and Mg(II). Minor changes occur in the UV-vis absorption spectrum of **Yb·81-8-HQS**, however, the addition of Zn(II) to the solution causes further drastic changes that result in a UV-vis absorption spectra identical to that of **8-HQS-Zn**, Figure 3.32, Appendix A3.18, verifying the formation of **8-HQS-Zn**, even in the presence of a large excess of Ca(II) or Mg(II) in solution.

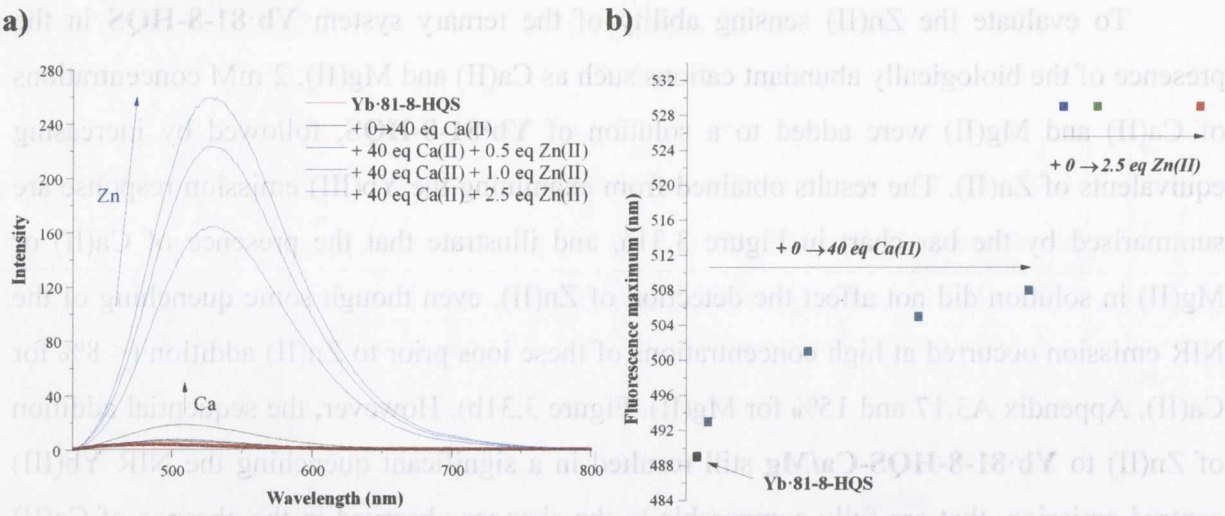


Figure 3.33: a) *Changes in the fluorescence emission spectrum (λ_{ex} = 360 nm) of* ***Yb·81-8-HQS*** *as a function of equivalents of Ca(II) followed by the addition of Zn(II) at pH 7.4 in HEPES buffered solution.* ***b)*** *Changes in the fluorescence maximum upon the addition of Ca(II) and Zn(II).*

Addition of up to 40 equivalents of Ca(II) and Mg(II) gives rise to significant changes in the fluorescence emission spectrum although there is very little displacement of the **8-HQS** antenna occurring from the ternary complex. This implies that the stronger fluorescence of the small number of metal chelates that are formed prevailed over the very weak ligand-centred fluorescence of the major species in solution, namely **Yb·81-8-HQS**, leading therefore to a considerable enhancement of the fluorescence emission accompanied with a 14-18 nm red shift of the maximum, as depicted in Figure 3.33 and Appendix A3.19.

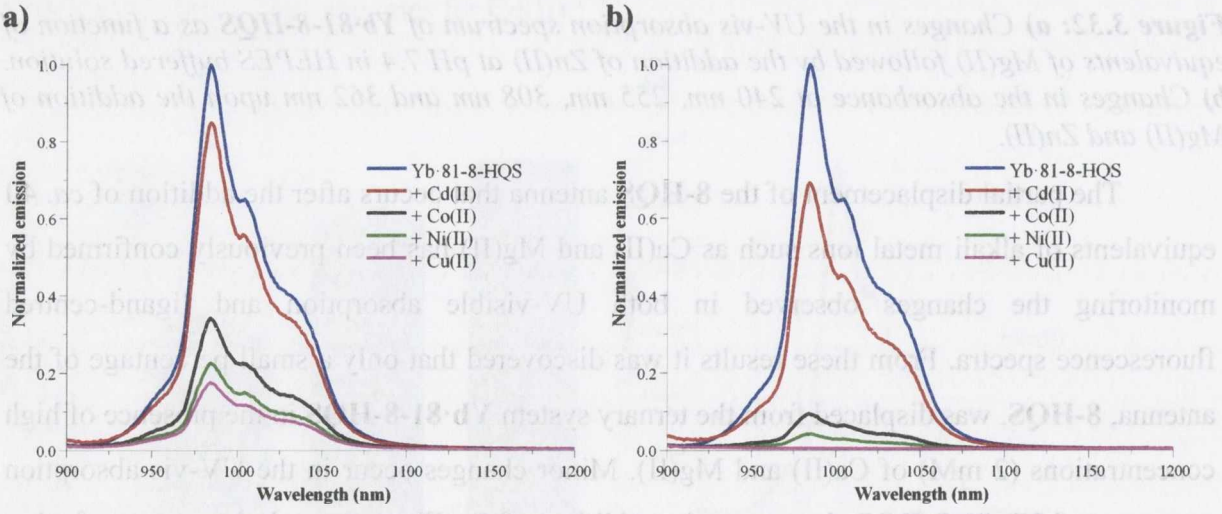


Figure 3.34: *Changes in the NIR emission spectrum (λ_{ex} = 360 nm) of* ***Yb·81-8-HQS*** *in the absence and presence of various transition metal ions at a concentration of* ***a)*** *25 μM and* ***b)*** *50 μM at pH 7.4 in HEPES buffered solution..*

The addition of Zn(II) to the solution, and subsequent formation of the highly fluorescent complex **8-HQS-Zn** results in a substantial increase in the fluorescence emission intensity, and, as in the case of the UV-vis absorption spectrum, the final fluorescence spectrum obtained after the addition of 2.5 equivalents of Zn(II), is of comparable emission intensity and maximum value to that of **8-HQS-Zn**.

The selectivity of **Yb·81-8-HQS** towards Zn(II) over Co(II), Ni(II) and Cu(II), was also investigated. The effect of the addition of 25 μM and 50 μM of these metal ions on the NIR Yb(III) centred emission of **Yb·81-8-HQS** is shown in Figure 3.34. For these significant quenching in the Yb(III) emission was observed. Cu(II) caused the greatest quenching, whereby the NIR emission signal was almost fully quenched after the addition of 50 μM of Cu(II). Unlike the alkali metal ions investigated previously, the addition of Co(II), Ni(II) and Cu(II) to a solution of **Yb·81-8-HQS** also resulted in a decrease in the ligand centred fluorescence, as shown in Figure 3.35, where all the transition metals gave rise to the same amount of quenching. Although Cu(II), Ni(II) and Co(II) interfered to some degree with the detection of Zn(II) in aqueous solution, it has to be stressed that these metal ions are not present in micromolar concentrations in typical biological samples and therefore should not limit the use of our system in a variety of applications.

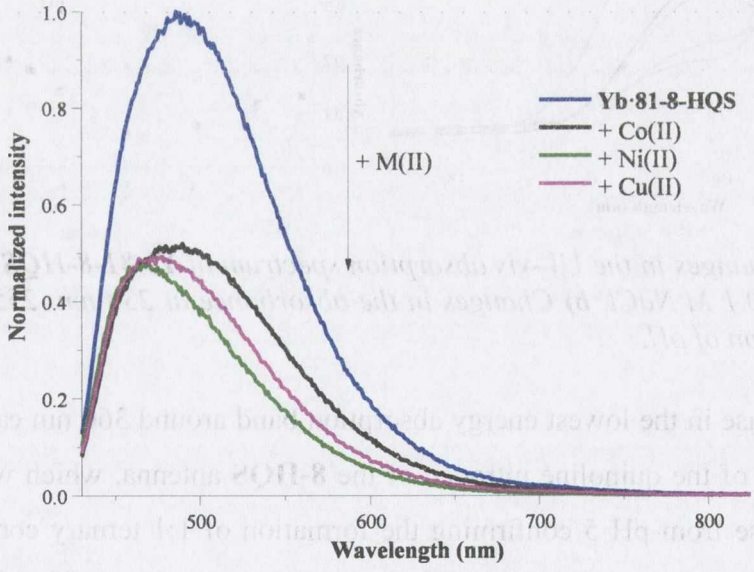


Figure 3.35: *Fluorescence emission response of* ***Yb·81-8-HQS*** *in the presence of Co(II), Ni(II) and Cu(II).*

3.8 Interaction of Yb·81-8-HQS as a Function of pH

Having demonstrated the sensing ability of **Yb·81-8-HQS** for Zn(II) in buffered solution, it was important to investigate its behaviour as a function of pH. For this purpose, the UV-vis absorption and emission spectra of a 50 μM solution of **Yb·81** in the presence of one equivalent of **8-HQS** were monitored as a function of pH within the pH range of 2 to 10. It

was foreseen that the ground state, the singlet state and Yb(III) centred emission would be greatly perturbed by pH due to the presence of possible protonation and deprotonation sites such as the nitrogen of the aromatic quinoline and the appended hydroxyl group.

Firstly, the effect of pH on the ground state of the ternary complex **Yb·81-8-HQS** was analysed in aqueous solution in the presence of 0.1 M NaCl to maintain a constant ionic strength. In acidic conditions, the complex displays a sharp absorption band with a maximum at 255 nm and another broad absorption band with a maximum centred at 355 nm and a slight shoulder at 315 nm, Figure 3.36. Basification to pH 5 caused a hypochromic shift of the absorption bands at 255 nm and 355 nm with the concomitant appearance of absorption bands centred at 238 nm and 308 nm. Further basification to pH 10 results in the hyperchromic shift and the reappearance of the bands centred at 255 nm and 360 nm, respectively. The changes in the absorption at 255 nm, 238 nm, 308 nm and 360 nm are shown in Figure 3.36b.

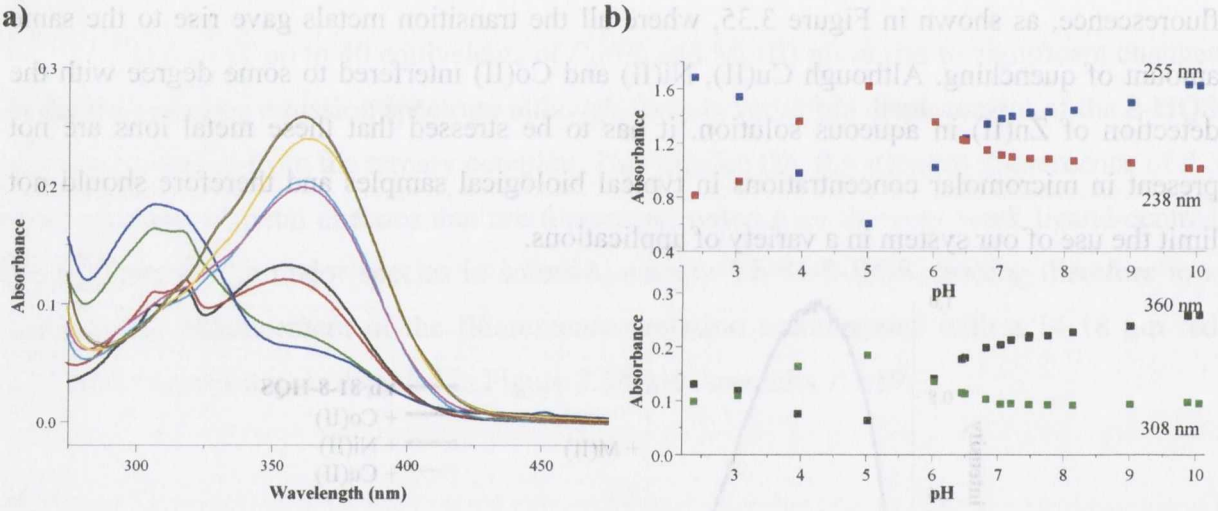


***Figure 3.36: a)** Changes in the UV-vis absorption spectrum of **Yb·81-8-HQS** (5×10^{-5} M) as a function of pH in 0.1 M NaCl. **b)** Changes in the absorbance at 238 nm, 255 nm, 308 nm and 360 nm as a function of pH.*

The decrease in the lowest energy absorption band around 360 nm can be attributed to the deprotonation of the quinoline nitrogen of the **8-HQS** antenna, which was followed by a significant increase from pH 5 confirming the formation of 1:1 ternary complex between **8-HQS** and **Yb·81**. The change in the absorption at higher pH confirmed that the ternary complex was not dissociating as the ratio between the bands at 360 nm and 308 nm remained unchanged throughout these pHs.

The changes in the fluorescence emission spectrum of **Yb·81-8-HQS** were also monitored during these titrations. As anticipated, the intensity in the fluorescence emission remained relatively weak throughout the titration. Below pH 4, the fluorescence emission was particularly weak, with a band centred at 475 nm, Figure 3.37. Adjustment to pH 5 resulted in

a 2 fold increase in emission intensity, which is most likely due to the binding of **8-HQS** to the Yb(III) cyclen complex. This was accompanied with a significant red shift in the intensity maximum to 495 nm. Further basification gave rise to *ca.* 15-25% decrease in the emission intensity between pH 5 and pH 8, which was attributed to the increasing efficiency in the NIR sensitization by the **8-HQS** antenna. This decrease was followed by a substantial enhancement in the **8-HQS** fluorescence by the antenna before pHs of 8-10 due to the less efficient sensitization of the metal-centred NIR emission.

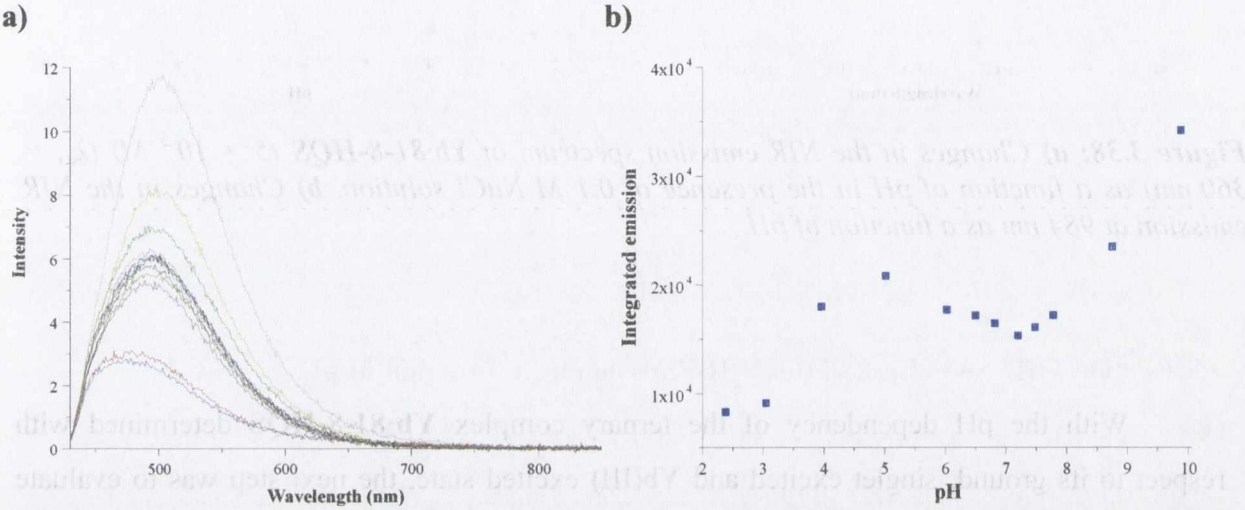


Figure 3.37: ***a)*** *Changes in the fluorescence spectrum of* ***Yb·81-8-HQS*** *(5×10^{-5} M) (λ_{ex} = 360 nm) as a function of pH in 0.1 M NaCl.* ***b)*** *Changes in the fluorescence emission integrals.*

The NIR emission intensity at the Yb(III) centre was examined as a function of pH upon excitation of **Yb·81-8-HQS** at 360 nm and the results are shown in Figure 3.38. In acidic media below pH 4 very little or no NIR emission was observed. An explanation for this behaviour is the fact that the quinoline nitrogen has a pK_a of 3.93[165] and as such the antenna is protonated below pH 4, therefore preventing the **8-HQS** from binding to the Yb(III) metal centre. Adjusting the pH to more alkaline values caused the NIR emission to be "switched on". For this pH titration the maximum emission intensity was reached at *ca.* pH 7.5 with a 40 fold enhancement being observed when adjusting the pH from pH 4 to pH 7.5. After pH 7.5 the intensity at 984 nm remained unchanged upon further basification to pH 9, after which the emission decreased in intensity. This is possibly due to modulations in the Yb(III) coordination environment or the detrimental effects of basic pH on the sensitisation process. Most notably, these results show that the Yb(III) emission was at its maximum within the physiological pH window of 7-7.5.

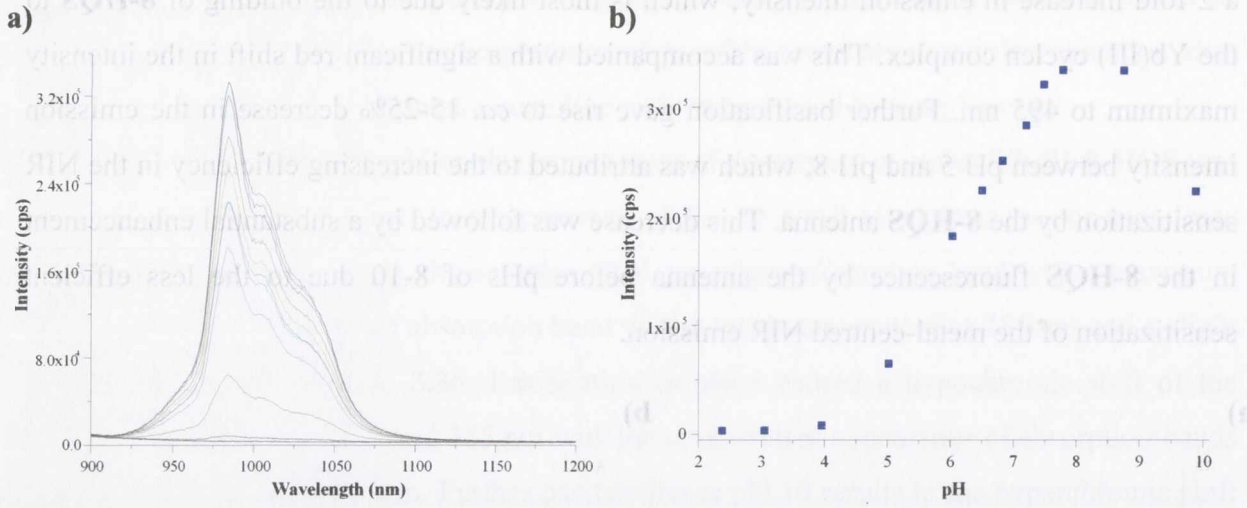


Figure 3.38: a) *Changes in the NIR emission spectrum of* ***Yb·81-8-HQS*** *(5×10^{-5} M) (λ_{ex} = 360 nm) as a function of pH in the presence of 0.1 M NaCl solution.* ***b)*** *Changes in the NIR emission at 984 nm as a function of pH.*

3.8.1 "On/Off" Switching of the NIR Emission as a Function of pH

With the pH dependency of the ternary complex **Yb·81-8-HQS** determined with respect to its ground, singlet excited and Yb(III) excited state, the next step was to evaluate the reversibility of these changes as a function of pH. The changes in the UV-vis absorption spectrum of **Yb·81-8-HQS** were first investigated and the overall results are illustrated below in Figure 3.39a.

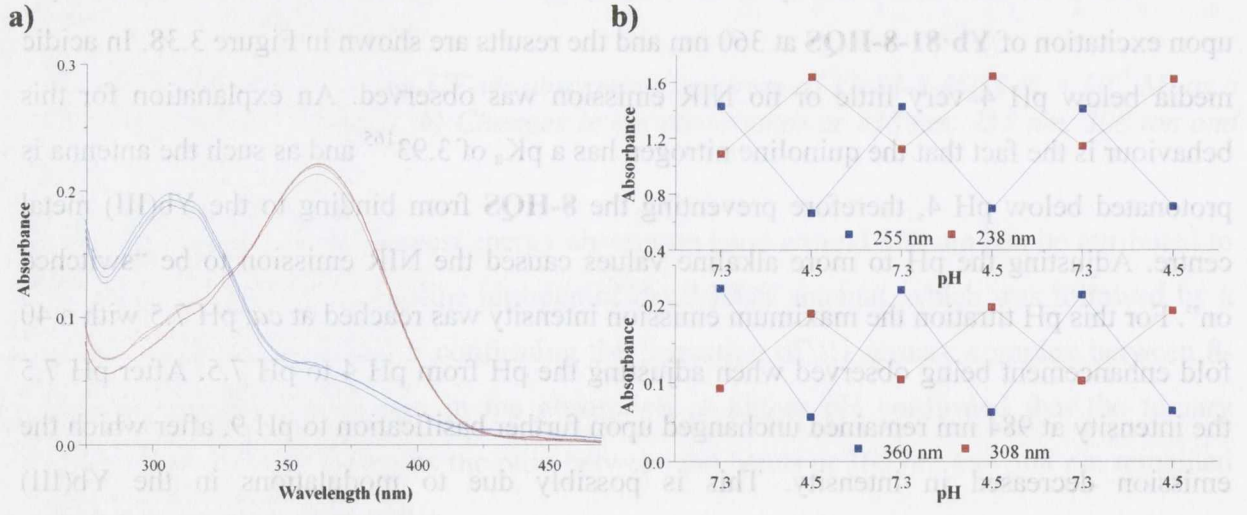


Figure 3.39: a) *Reversible changes in the UV-vis absorption spectrum of* ***Yb·81-8-HQS*** *(5×10^{-5} M) at pH 4.5 (-) and 7.3 (-) in 0.1 M NaCl.* ***b)*** *Reversibility of the UV-vis absorption at 238 nm, 255 nm, 308 nm and 360 nm between pH 4.5 and pH 7.3.*

At pH 7.3 the UV-vis absorption spectrum displays a band with a maximum at 360 nm. Acidification to pH 4.5 resulted in a substantially different spectrum obtained whereby the band at 360 nm was hypochromically shifted with concomitant increase in the band at 308 nm. Adjusting the pH to 7.3 reversed these spectral changes, and the band centred at 360 nm reappeared. The same trend was seen at lower wavelengths. These results demonstrate full reversibility and that the self-assembly between the antenna and the Yb(III) complex is, as a function of pH, reversible and this reversibility was investigated further over a number of cycles. The behaviour was found to be fully reversible; shown in Figure 3.39b.

The fluorescence emission graphs shown in Figure 3.40 are confirmation that by adjusting the pH several times from pH 7.3 to pH 4.5, the formation of the ternary complex was not affected and the fluorescence could be repeatedly "switched off" and on as desired without any loss of signal observed. This was found to be the case when two different excitation wavelengths of 257 nm and 360 nm were used; however the intensity difference between the off and on state was more extreme when the excitation wavelength of 257 nm was used.

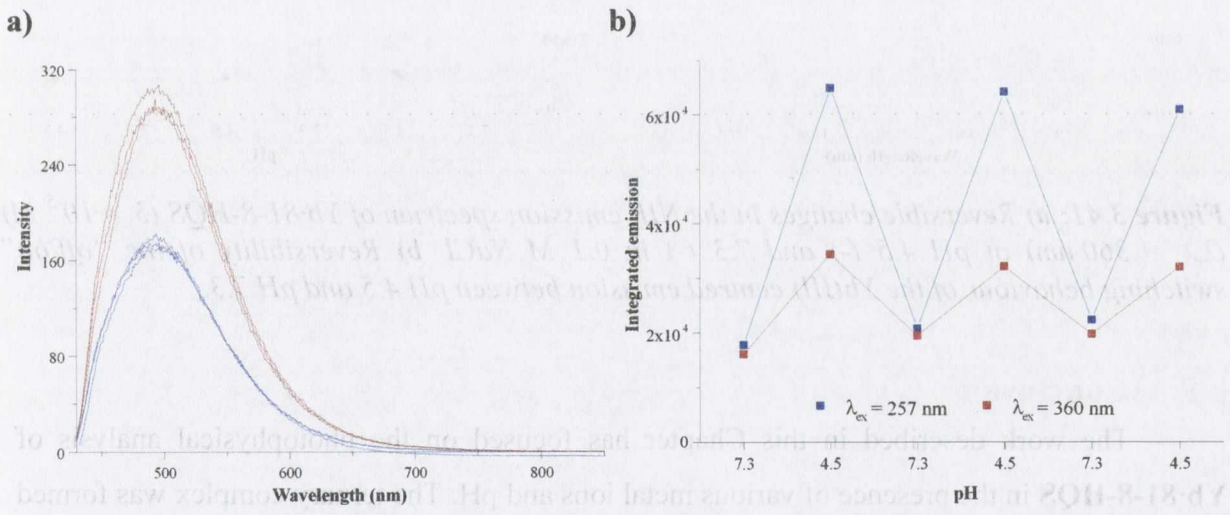


Figure 3.40: a) *Reversible changes in the fluorescence emission spectrum of* ***Yb·81-8-HQS*** *(5 × 10^{-5} M) (λ_{ex} = 360 nm) at pH 4.5 (-) and 7.3 (-) in 0.1 M NaCl.* ***b)*** *Reversibility of the "on/off" switching behaviour of the ligand centred fluorescence between pH 4.5 and pH 7.3.*

The reversibility of the system was further corroborated by monitoring the changes observed in the NIR emission of **Yb·81-8-HQS**. As depicted in Figure 3.41, the Yb(III) emission displayed maximum emission at neutral pH (pH 7.3) and was significantly quenched when the pH was adjusted to 4.5. Readjusting the pH back to pH 7.3 resulted in the recovery of the NIR emission. Concurrent pH jumps from pH 7.3 to pH 4.5, again did not appear to disturb the formation of the ternary complex and the NIR signal could be "switched on" and "off" without any loss in signal.

Determining the behaviour of the system **Yb·81-8-HQS** over the entire pH range is essential, especially if it is to be utilised as an *in vitro* sensor for the detection of Zn(II). Notably, at physiological pH the NIR emission was at its maximum and therefore a maximum difference will be obtained between the intensities of the "on" and "off" states upon the addition of Zn(II). Furthermore, it can be concluded that the UV-vis absorption, fluorescence and Yb(III) centred NIR emission spectrum were identical within the experimental error, to the previous measurement performed at that particular pH, and more importantly, that the formation of the ternary complex, **Yb·81-8-HQS**, was fully reversible as a function of pH.

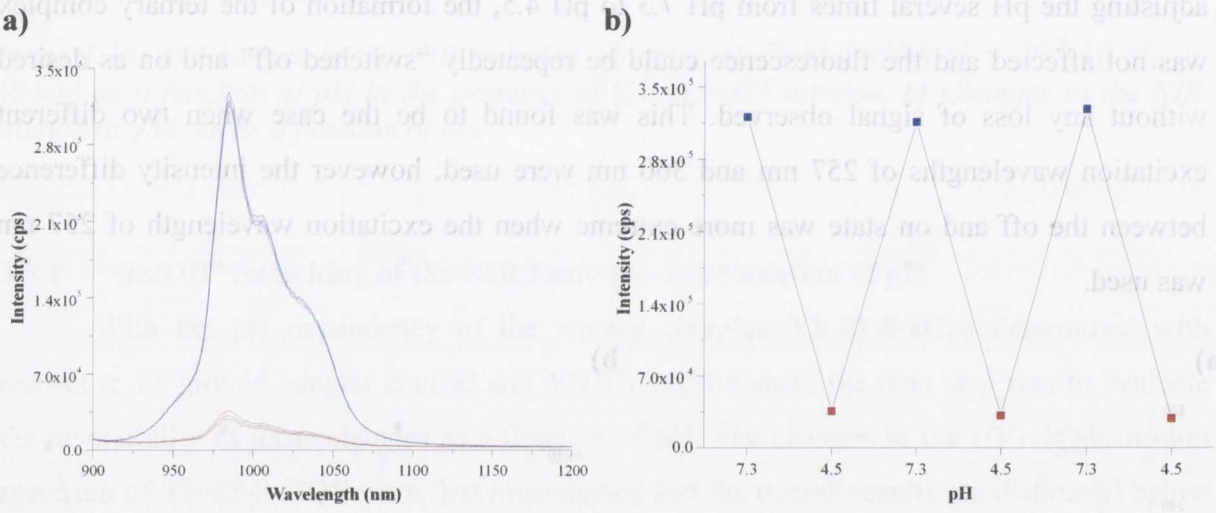


Figure 3.41: a) *Reversible changes in the NIR emission spectrum of Yb·81-8-HQS (5×10^{-5} M) (λ_{ex} = 360 nm) at pH 4.5 (-) and 7.3 (-) in 0.1 M NaCl.* ***b)*** *Reversibility of the "off/on" switching behaviour of the Yb(III) centred emission between pH 4.5 and pH 7.3.*

3.9 Conclusion

The work described in this Chapter has focused on the photophysical analysis of **Yb·81-8-HQS** in the presence of various metal ions and pH. The ternary complex was formed through the self-assembly process between the **Yb·81** cyclen complex and the sensitising 8-hydroxyquinoline antenna, **8-HQS** which was shown to be fully reversible.

The antenna **8-HQS** was chosen as it is known to sensitise the NIR emission of Yb(III) and because of its ability to bind to Zn(II) metal ions. The antenna on its own was investigated for its ability to bind to several divalent metal ions, in aqueous solution at physiological pH, such as Cd(II), Mg(II) and Zn(II). Significant changes were observed in the UV-vis absorption and fluorescent spectra upon the addition of Cd(II) and Zn(II) while minor changes occurred in the case of Mg(II). Notably, the addition of Zn(II) gave rise to a highly green luminescent **8-HQS-Zn** species; the fluorescence of which was clearly observable to the naked eye under a UV lamp.

It was demonstrated that **8-HQS** can bind to **Yb·81**, a cyclen based Yb(III) complex possessing three acetamide arms and a 4 carbon alkyl chain. Titration of **8-HQS** into a solution of **Yb·81** resulted in the "switching on" of the NIR Yb(III) centred emission, signifying the formation of the ternary complex **Yb·81-8-HQS** in a 1:1 stoichiometric ratio with a log *K* of 5.5 ± 0.3. The hydration state or *q* value for **Yb·81** was determined from the lifetimes measured in H_2O (3.4 μs) and D_2O (6.1 μs) and found to be 0, indicating the absence of any metal bound water molecules and hence, establishing the presence of the 1:1 ternary complex **Yb·81-8-HQS**. This resulting complex displayed substantial Yb(III) NIR centred emission upon excitation into the absorption band of the **8-HQS** antenna at 360 nm with a quantum yield of $Q = 0.23 \pm 0.03$. Monitoring the excitation spectrum of this system, at the maximum Yb(III) emission intensity at *ca.* 985 nm, verified energy transfer and hence, sensitisation of **Yb·81** by **8-HQS** when covalently bound to **Yb·81**.

The photophysical properties **Yb·81-8-HQS** were further investigated in aqueous solution at physiological pH in the presence of Zn(II) and other biologically relevant metal ions. It was discovered that addition of Zn(II) "switched off" the Yb(III) metal centred emission. However this was accompanied by a significant enhancement in the ligand-centred (visible) fluorescence. These changes signify the displacement of the **8-HQS** from the Yb(III) metal centre and concomitant formation of a highly luminescent Zn(II) chelates with **8-HQS**. A limit of detection of 6.8 μM for Zn(II) at pH 7.4 was demonstrated and furthermore, it was shown that the presence of biologically relevant anions such as citrate, carbonate, phosphate and lactate, had only a slight effect on the metal centred emission, while not influencing the ligand centred emission to a great extent.

An investigation was carried out which involved the addition of the known Zn(II) chelator EDTA to a solution of **Yb·81-8-HQS** to which Zn(II) has already been added. The NIR emission was recovered with concomitant quenching of the ligand centred fluorescence. This reversibility of the response of the ternary system to the presence of Zn(II) is important and presents the opportunities for multiple detection analysis

The system was also tested for its ability to sense a range of divalent alkali and transition metal ions such as Cd(II), Ca(II), Mg(II), Co(II), Ni(II) and Cu(II). The presence of Ca(II) and Mg(II) caused no measurable change in the photophysical properties of **Yb·81-8-HQS**, even at concentration as high as 2 mM. However, it was shown that the transition metal ions Ni(II), Co(II) and Cu(II), all gave rise to quenching in the NIR emission, however none caused enhancement in the ligand centred fluorescence, as had been seen for Zn(II). These findings were noteworthy as they emphasise the importance of a dual emissive probe which emits at different wavelength ranges of the electromagnetic spectrum, and can distinguish

between Zn(II) and other divalent transition metal ions as well as within two different time frames.

Finally, the effect of pH on the system was also investigated and the results concluded that the formation of the ternary complex was a fully reversible process. Here, an "on/off" reversible system was established for the NIR emission between pH 7 and pH 4.5.

Overall, this Chapter has detailed the evaluation of a novel near-infrared (NIR) emissive Ln(III)-based zinc sensor that arises from the self-assembly in aqueous solution between the non-emissive unsaturated Yb(III) cyclen complex, **Yb·81**, and the sulfonated 8-hydroxyquinoline (**8-HQS**) antenna; a process that was shown to be fully reversible.

Chapter 4

Switchable NIR Emitting AuNPs

4. Introduction

Dopamine is an excitatory neurotransmitter of the central nervous system, where it carries out a large number of crucial functions in the body, such as movement control and moreover, it plays an important role in bridging the central nervous system and immune systems. It is only found to be present in a small number of brain cells and is dispersed among four of the major tracts in the brain; the substantia nigra (involved in the fine tuning of movement), the hypothalamus (involved in the control of hormones) and two tracts of the mesolimbocortial system (involved in organised thought process and which is associated with the disordered thought characteristic of schizophrenia). Modified immune functions arise from changes that can occur in the expression of dopamine receptors and their signalling pathways, which is associated with disorders such as Parkinson's disease and schizophrenia.[177] These findings suggest that dopamine is involved in an immunoregulatory role, and hence drugs which target dopamine receptors and its signalling pathways may prove beneficial for the treatment of diseases where dopamine induced altered immunity play a pathogenic role.

Parkinson's disease is a common neurological movement dysfunction in the brain and is the second most common neurodegenerative disorder of adults, after Alzheimer's disease. Parkinson's disease is characterised by the slowing of voluntary movements (bradykinesia), rigidity, loss of reflexes and occasionally behavioural manifestations. The pathophysiology behind Parkinson's disease is that it is caused by a progressive dopamine deficiency (Figure 4.1) due to a loss of more than 75% of dopaminergic neurons in the brain which in turn leads to an imbalance in the activities of dopamine and acetylcholine, a small excitatory neurotransmitter involved in the process of learning and memory.

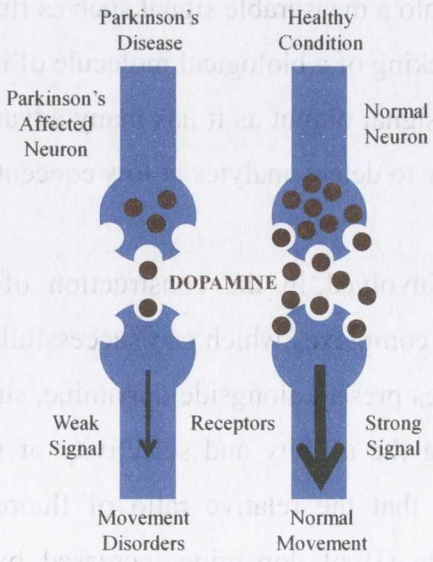


Figure 4.1: *Illustration of dopamine levels in a normal and Parkinson's affected neuron.*

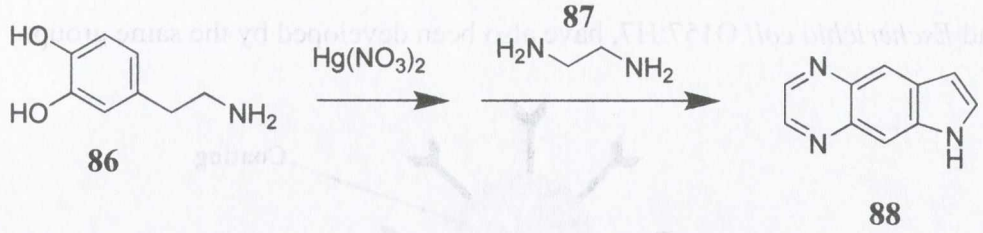
In contrast to Parkinson's disease, where there is a decreased level of dopamine, schizophrenia is associated with the excessive neurotransmission of dopamine in the central nervous system.[178,179] The common feature of both diseases is that there is an abnormal level of dopamine present, and hence, the detection of dopamine levels is essential in the diagnosis of such diseases.

Recently, there has been a growing interest in monitoring biologically important molecules, such as dopamine, that are involved in central processes in the body.[180]

One approach taken in the literature has been the detection of dopamine by electrochemical means due to the electrochemically active (oxidisable) nature of dopamine.[181,182] This method offers a simple, selective and environmentally friendly method for the detection of dopamine. One challenge associated with this method is the high levels of the electronically active biological molecule, ascorbic acid (0.2-0.5 mM) present alongside the relatively low levels of dopamine (10^{-8}-10^{-7} M) in physiological samples.[183] Zhang and co-workers investigated the sensing ability of a layer by layer assembly of an Os(II) polymer on hydrophilic carbon nanotubes towards dopamine.[183] They found that the linear sweep voltammetry peak current density of the coated carbon nanotubes was increased by 7.3 and 3.9 times in response to 10 μM and 50 μM solutions of dopamine, respectively, with a limit of detection determined to be 0.05 μM. This novel carbon nanotube electrode approach has the potential to be developed as an ideal biosensor for the direct and *in situ* detection of dopamine levels.

While most examples rely on the electrochemical detection of dopamine, much attention has focused on the development of biosensors, consisting of a recognition site capable of sensing the target, and a signalling moiety that acts as a signal transducer, converting the sensing event into a measurable signal such as fluorescence output, all of which can allow for the real time tracking of a biological molecule of interest. Fluorescence emission response is a popular chosen signal output as it has many advantages such as high sensitivity and selectivity, with the ability to detect analytes at low concentrations (in the order of 10^{-7} M and lower).[11]

Liew *et al.*[184] were involved in the construction of dopamine sensors by using fluorescent ribonucleopeptide complexes which can successfully discriminate dopamine from other catecholamine derivatives present alongside dopamine, such as norepinephrine, tyrosine and epinephrine. Investigating the affinity and selectivity of the isolated ribonucleopeptide receptors, they demonstrated that the relative ratio of fluorescence intensity (I/I_0) in the absence (I_0) and the presence (I) of dopamine increased by 2 fold as well as showing selectivity for dopamine over other catecholamines.



Scheme 4.1: *Formation of fluorescent product* ***88*** *from dopamine.*

Wang *et al.*[185] developed a method for the fluorimetric determination of dopamine using ethylene diamine as the fluorigenic reagent. As shown in Scheme 4.1, dopamine, **86**, was oxidised by mercury (II) nitrate, and the oxidation product condensed with ethylene diamine, **87**, to give the presumed fluorescent quinoxaline derivative product **88**. Measurement of the fluorescence of **88** in urine samples provided a linear relationship between the fluorescence intensity and the concentration of dopamine with a detection range of 0.02-0.6 μM; a range that is 2-3 times lower than that of other fluorimetry techniques.

The drawback associated with fluorescence detection *in vivo* is that interference can be caused by the short lived background emission (autofluorescence) and light scattering from the surrounding biological environment.[14] A somewhat less investigated method of dopamine detection is the use of Ln(III), NIR emitting Ln(III) and **AuNPs** which can overcome the drawbacks associated with fluorescent detection. As previously discussed in the Chapter 1, the use of Ln(III) in biological probing applications has proved extremely beneficial over fluorescent probes due to the long lived excited state lifetimes and sharp line like emission the Ln(III) possess.

The combination of Ln(III) with nanomaterials such as **AuNPs** for the purpose of biological sensing is highly desirable. Recently, there has been a growing advancement in the area of Ln(III)-doped nanomaterials, known as upconverted nanoparticles (UCNPs), which, when functionalised with Ln(III) that can be excited with NIR light where biological tissues are transparent.[186] Moreover, these UCNPs possess low cytotoxicity[187] and high photostability, rendering them very attractive for use in bio-imaging applications, the variety of applications is shown below in Figure 4.2.[188] Biological imaging applications involving UCNPs, as investigated by Wang *et al.*[189] established that Yb(III) and Er(III) coated NPs conjugated with antibody, can be used for highly specific staining and imaging of HeLa cells with antigen expressed on the cell membrane. Another example devoleped by Niedbala *et al.*[190] consisted of an assay for the simultaneous detection of amphetamine, methamphetamine, phencyclidine, and opiates in saliva by using multicolour UCNPs doped with Yb(III) and

Er(III). Preliminary assays that use up-converting phosphor labels, including tests for drugs of abuse and *Escherichia coli* O157:H7, have also been developed by the same group.

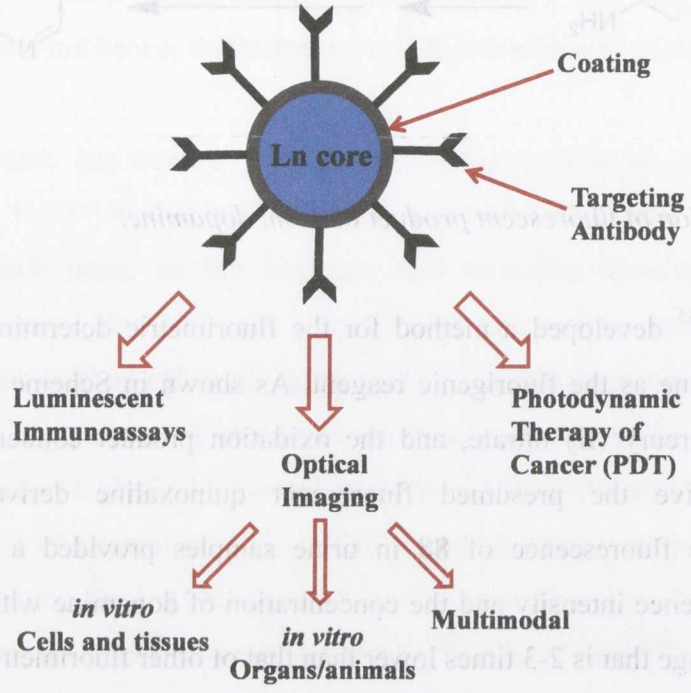


Figure 4.2: *Illustration of the many bio-analytical and bio-medical applications of NIR Ln(III)-containing upconverted nanoparticles. Redrawn from* [188].

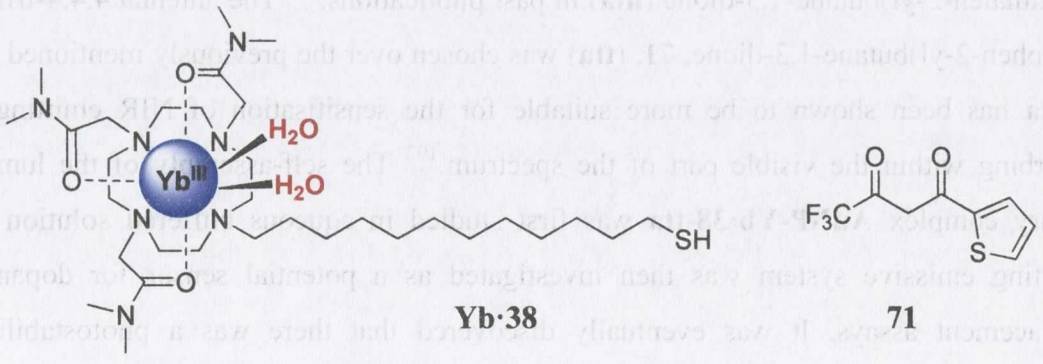
As well as UCNPs, functionalised **AuNPs** have attracted great interest in biological applications, particularly as sensing systems due to their known stability, size- and shape-dependant properties and biocompatibility.[7] The combination of **AuNPs** and Ln(III) for the purpose of luminescent sensing in aqueous solution has been recently investigated, the first example of such being a Eu(III)-cyclen **AuNP** system developed for the sensing of phosphate anions.[117,118] Recently these systems have been further developed to exploit the interaction with the protein bovine serum albumin (BSA) for potential biomedical sensing and imaging applications.[107] However, due to low extinction coefficient, it is necessary to populate the Ln(III) excited state by sensitising antennae. Ln(III) such as Nd(III) and Yb(III) emit in the near-infrared (NIR) range, within the emission window of 840-1400 nm, and are particularly attractive for use in probing biological interactions, due to increased tissues transparency and reduced interferences from biological matter autofluorescence, resulting in deeper penetration into biological tissue.[162] Moreover, unlike the sensitisation of ions such as Eu(III) and Tb(III), the NIR Ln(III) excited states can be achieved through the use of visibly absorbing organic antennae.[191] However, and to the best of our knowledge, the unique combination of **AuNPs** and NIR emitting Ln(III) for sensing applications has not yet been explored to date, and will be the basis for the research discussed in this Chapter. The work described in this Chapter was

carried out in collaboration with Dr. Steve Comby, a senior postdoctoral fellow in the TG research group.

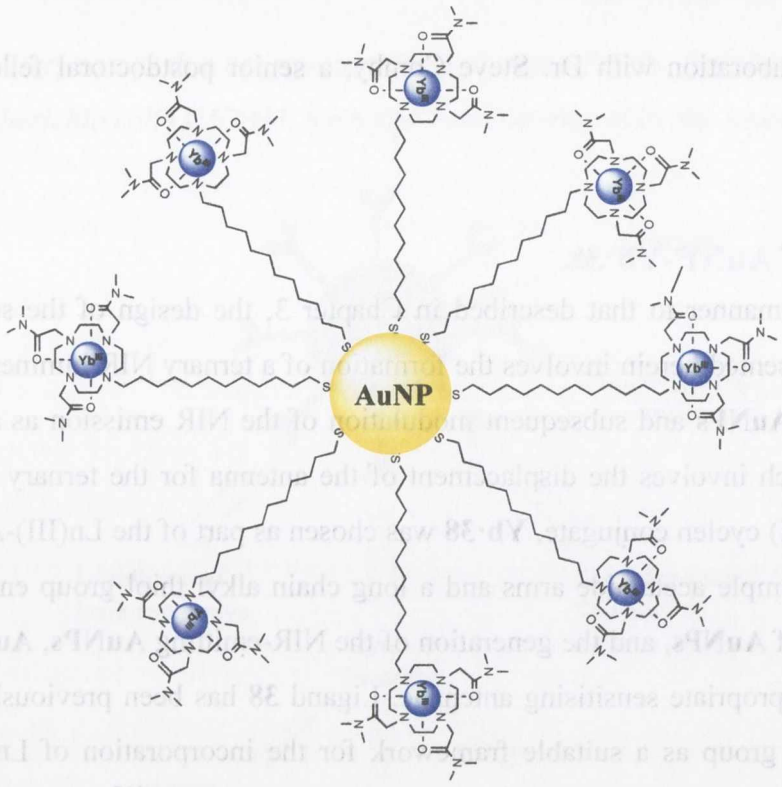
4.1 Design of AuNP-Yb·38

In a similar manner to that described in Chapter 3, the design of the sensing system developed and presented herein involves the formation of a ternary NIR luminescent complex on the surface of **AuNPs** and subsequent modulation of the NIR emission as a result of the sensing event which involves the displacement of the antenna for the ternary complex. The macrocyclic Yb(III) cyclen conjugate, **Yb·38** was chosen as part of the Ln(III)-**AuNP** system, possessing three simple acetamide arms and a long chain alkyl thiol group enabling surface functionalisation of **AuNPs**, and the generation of the NIR-emitting **AuNPs**, **AuNP-Yb·38**, in the presence of appropriate sensitising antennae. Ligand **38** has been previously used within the Gunnlaugsson group as a suitable framework for the incorporation of Ln(III) ions and moreover, has been shown to successfully be adsorbed onto **AuNPs**.[117] A twelve carbon chain was chosen in order to minimise the quenching of the Ln(III) luminescence from the **AuNP** surface.

The Yb(III) complex **Yb·38** was designed as a coordinatively unsaturated cationic complex; where the Yb(III) ion is bound to the four amines of the cyclen framework and the three carbonyl oxygen atoms of the acetamide arms giving rise to a strong Lewis acid character. The high coordination demand of Yb(III) suggests that two metal bound water molecules would be coordinated to **Yb·38** in aqueous solution, however it was not possible to determine the number of water molecules directly bound to the Yb(III) centre due to the low emission intensity of **Yb·38**.



Yb·38 **71**



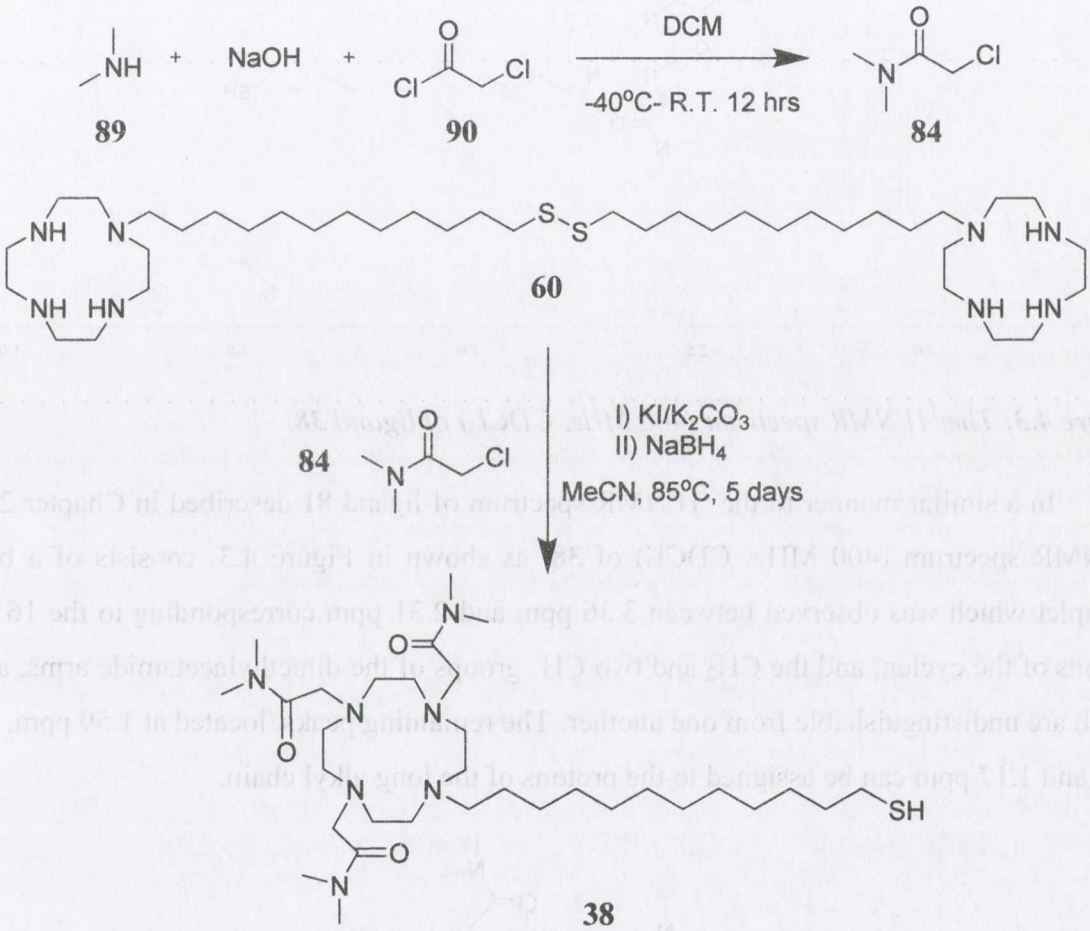
AuNP-Yb·38

In the absence of any sensitising antenna, there was no significant Yb(III) emission observable from either the complex **Yb·38**, or the corresponding **AuNP** system, **AuNP-Yb·38**. Hence, the *q* value could not be determined directly for this complex using luminescent techniques. As in our previous examples, it was anticipated that the Ln(III) emission could be "switched on" upon displacement of these metal bound water molecules by a suitable coordinating antenna (which upon excitation can populate the emissive states of Yb(III)). Excitation of Ln(III) by an external antenna is a well-known phenomenon, which we had demonstrated previously using **Eu·38** and the β-diketone antenna 4,4,4-trifluoro-1-(naphthalen-2-yl)butane-1,3-dione (**nta**) in past publications.[117] The antenna 4,4,4-trifluoro-1-(thiophen-2-yl)butane-1,3-dione, **71**, (**tta**) was chosen over the previously mentioned antenna, as **tta** has been shown to be more suitable for the sensitisation of NIR emitting Ln(III) absorbing within the visible part of the spectrum.[192] The self-assembly of the luminescent ternary complex **AuNP-Yb·38-tta** was first studied in aqueous buffered solution and the resulting emissive system was then investigated as a potential sensor for dopamine *via* displacement assays. It was eventually discovered that there was a photostability issue associated with the ternary complex **Yb·38-tta** within the experimental conditions used; however, the titrations involved will still be discussed.

This Chapter details synthesis and application of **Yb·38**, a macrocyclic Yb(III) cyclen conjugate, that can be used for surface functionalization of **AuNPs**, and moreover, the generation of NIR-emitting **AuNPs**, **AuNP-Yb·38**, in the presence of appropriate antennae.

4.2 Synthesis and Characterisation of Ligand 38 and Yb·38

The synthesis of ligand **38** has previously been reported by the Gunnlaugsson group and consequently will only be briefly discussed here.[117] The synthesis of the dimethyl acetamide arm, **84**, was achieved by dissolving dimethylamine, **89**, and sodium hydroxide in DCM, which was cooled to -40°C in a liquid N_2/ethanol ice bath before adding in dropwise a solution of chloroacetyl chloride, **90**, in DCM. The mixture was then stirred at room temperature overnight, followed by an aqueous acid workup. The ^{1}H NMR spectrum (400 MHz, $CDCl_3$), Appendix A4.1, consisted of only three singlet peaks; one at 4.02 ppm, corresponding to the two protons of the CH_2 moiety and two singlets at 3.01 ppm and 2.98 ppm, each intergrating for the three protons of the methyl groups.



Scheme 4.2: *Synthesis of ligand **38**.*

The synthesis of the disulphide bridged cyclen moiety, **60**, has been described in Chapter 2. The final step towards achieving ligand **38** involved the alkylation of the remaining three free amine groups of **60** with 2-chloro-*N,N*-dimethylacetamide, **84**. This was accomplished over a 5 day reflux in acetonitrile under an inert atmosphere by reacting **60** with **84** in the presence of 3.1 equivalents of potassium carbonate and potassium iodide. Once the desired ligand had been observed by ES^+ mass spectrometry; 621.4873 $[M]^+$, sodium

borohydride ($NaBH_4$) was added to the reaction mixture to reduce the disulfide bond to the corresponding thiol. Purification of **38** to remove any unreacted arm or mono or di-substituted ligand was achieved through column chromatography on an automated column machine using alumina and eluting with DCM:MeOH (100:0-80:20). Ligand **38** was obtained as an orange oil in 48% yield.

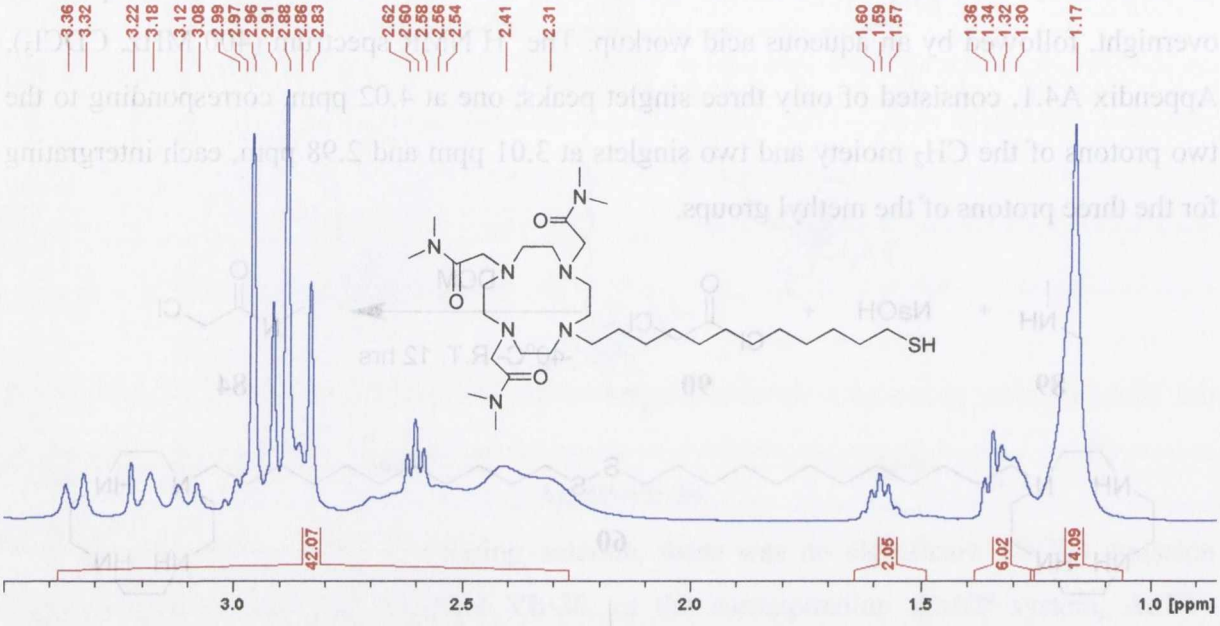
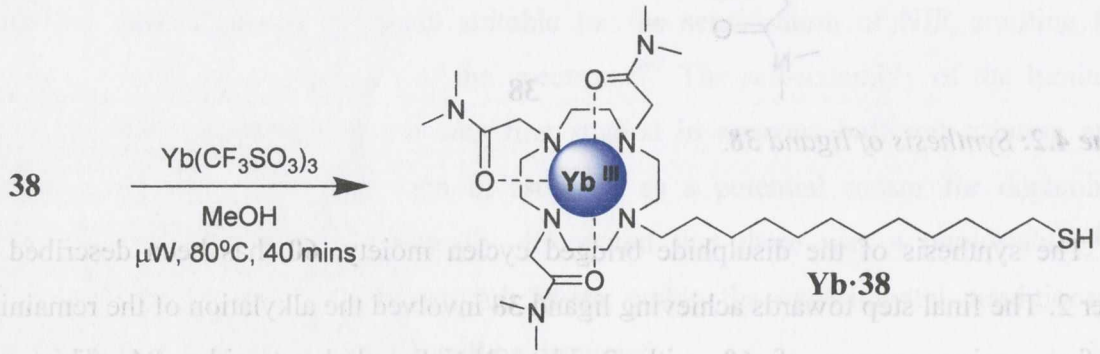


Figure 4.3: *The ^1H NMR spectrum (400 MHz, $CDCl_3$) of ligand **38**.*

In a similar manner to the ^1H NMR spectrum of ligand **81** described in Chapter 2, the ^1H NMR spectrum (400 MHz, $CDCl_3$) of **38**, as shown in Figure 4.3, consists of a broad multiplet which was observed between 3.36 ppm and 2.31 ppm corresponding to the 16 CH_2 protons of the cyclen, and the CH_2 and two CH_3 groups of the dimethylacetamide arms, all of which are undistinguishable from one another. The remaining peaks, located at 1.59 ppm, 1.34 ppm and 1.17 ppm can be assigned to the protons of the long alkyl chain.



Scheme 4.3: *Synthesis of **Yb·38** by complexation of ligand **38** with one equivalent of $Yb(CF_3SO_3)_3$.*

The corresponding Yb(III) complex **Yb·38** was formed by microwave irradiation of ligand **38** in a small volume (5 mL) of MeOH for 40 minutes in the presence of one equivalent of $Yb(CF_3SO_3)_3$. Precipitation of the product from the methanol solution into a large volume of ether afforded **Yb·38** as a yellow powder in 74% yield. Similar to what was observed for all other cyclen based Ln(III) complexes described within this Thesis, the ^1H NMR spectrum (400 MHz, CD_3CN) of **Yb·38** displayed the characteristic broadening and Ln(III) induced shifting of signals, indicating successful complexation of the Yb(III) ion within the macrocyclic cyclen cavity of **38**. Such interaction, as shown in Figure 4.4 resulted in proton resonances being shifted over a total spectral range of *ca.* 30 ppm, from 4.91 ppm to -22.33 ppm.

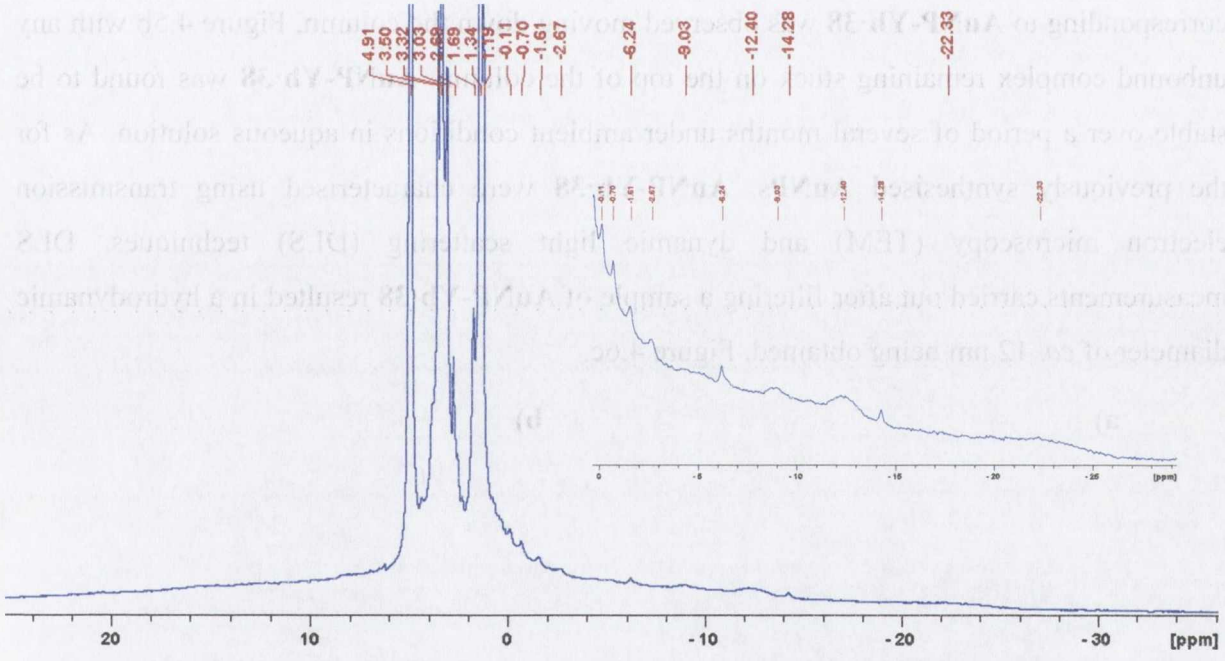


Figure 4.4: *The ^1H NMR spectrum (400 MHz, CD_3CN) of* ***Yb·38****. Inset: Zoomed in area from 0 ppm to -25 ppm.*

Evidence that the complexation of the Yb(III) metal ion was achieved through IR spectroscopy, which showed significant shifting in the carbonyl stretching frequencies from 1644 cm^{-1} to 1626 cm^{-1} indicating heptadentate coordination with the Yb(III) metal centre locate within the cyclen cavity. Elemental analysis also confirmed successful complexation.

With the complex synthesised and fully characterised, the next step was to attach it to the surface of **AuNPs**, the synthesis and method of which will be discussed in the following section.

4.3 Functionalisation of AuNPs with Yb·38

The synthesis of the surface functionalised **AuNPs**, **AuNP-Yb·38** was achieved using a modified two-phase Brust method[137] which has been described in detail in Chapter 2. The resulting toluene solubilised **AuNPs** were transferred into aqueous phase by direct ligand exchange with no need for intermediate DMAP stabilised **AuNPs**; a *ca.* 1×10^{-4} M concentration in aqueous solution of **Yb·38** and a *ca.* 1×10^{-7} M solution of **AuNPs** in toluene were stirred vigorously together with the addition of $NaBH_4$ (1.5 equivalents) to ensure no oxidation of the S-H bond of **Yb·38** was occurring. After twelve hours, complete transfer of the **AuNP-Yb·38** into water was achieved, as shown in Figure 4.5a, where the deep purple colour of the **AuNPs** can be observed in the bottom aqueous layer.

Purification of the resulting **AuNP-Yb·38** was achieved using sephadex G15 column chromatography, by using aqueous NaCl (0.05 M) solution as an eluent. A purple band corresponding to **AuNP-Yb·38** was observed moving down the column, Figure 4.5b with any unbound complex remaining stuck on the top of the column. **AuNP-Yb·38** was found to be stable over a period of several months under ambient conditions in aqueous solution. As for the previously synthesised **AuNPs**, **AuNP-Yb·38** were characterised using transmission electron microscopy (TEM) and dynamic light scattering (DLS) techniques. DLS measurements carried out after filtering a sample of **AuNP-Yb·38** resulted in a hydrodynamic diameter of *ca.* 12 nm being obtained, Figure 4.6c.

a) **b)**

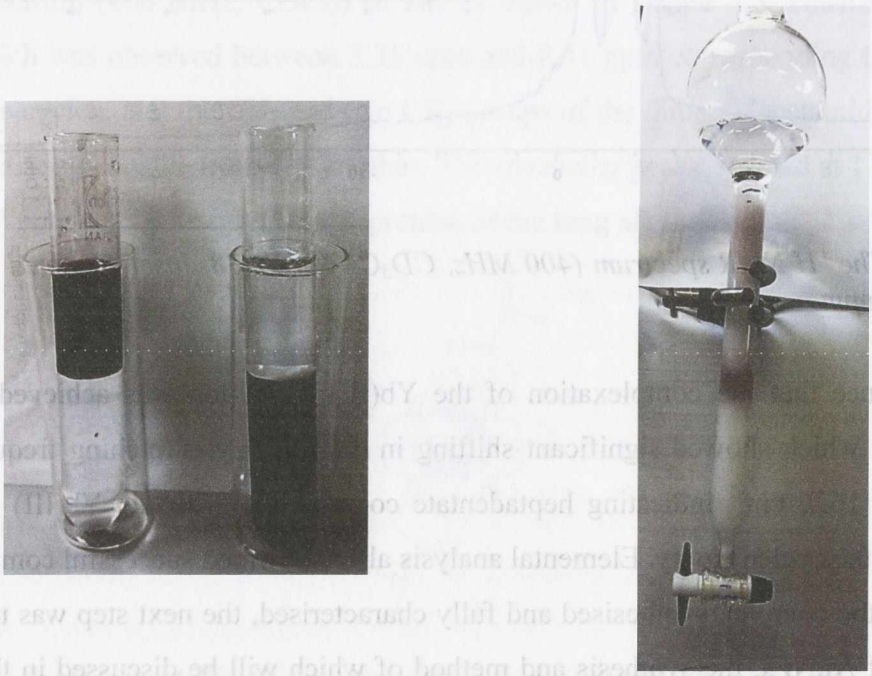


Figure 4.5: ***a)*** *Complete transfer of* ***AuNPs*** *from toluene layer (top) to aqueous layer (bottom) of* ***Yb·38*** *after stirring overnight.* ***b)*** *Purification of* ***AuNPs*** *by gel chromatography using a G-15 Sephadex column.*

TEM images were recorded after deposition of **AuNP-Yb·38** on copper grids and showed the existence of monodisperse nanoparticles with an average core diameter of *ca.* 8 nm, Figure 4.6a-b. **AuNP-Yb·38** was also characterised using UV-vis absorption spectroscopy. The reduction of Au(III) to Au(0), and hence the formation of **AuNPs** was monitored by the appearance of the SPR band at 517 nm in the UV-vis absorption spectrum in water. Stabilisation by functionalisation with **Yb·38** can be verified by the bathochromic shift of the surface plasmon resonance (SPR) band from 517 nm to 523 nm, shown in Figure 4.7 as a result of the strong ligand field interacting with the surface electron cloud.[141]

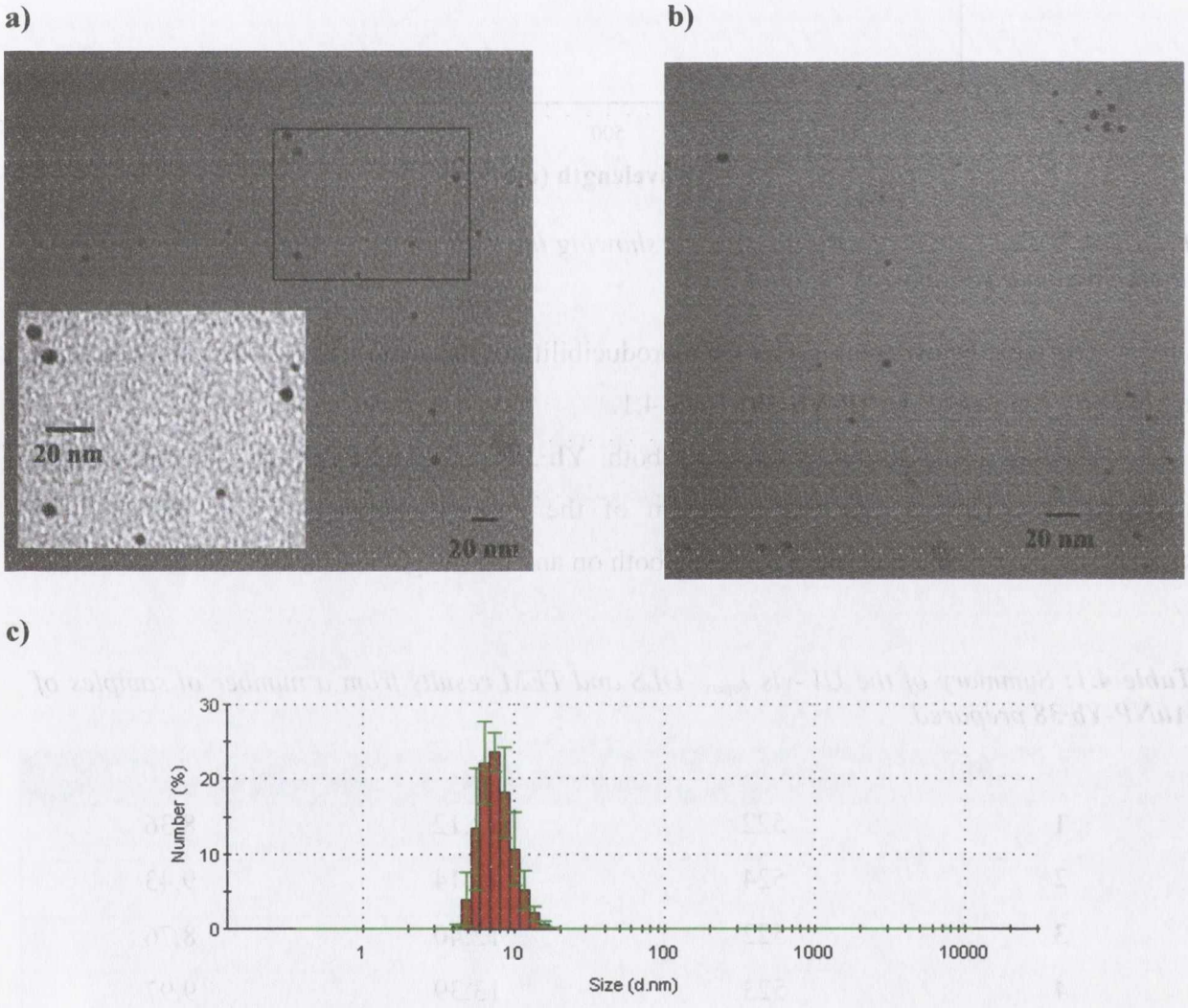


***Figure 4.6: a)** and **b)** TEM images of **AuNP-Yb·38** synthesised by a modified Brust-Schiffrin method after deposition on copper grids. Inset: close up image. **c)** Particle size distribution in solution as determined from DLS analysis for **AuNP-Yb·38** in water.*

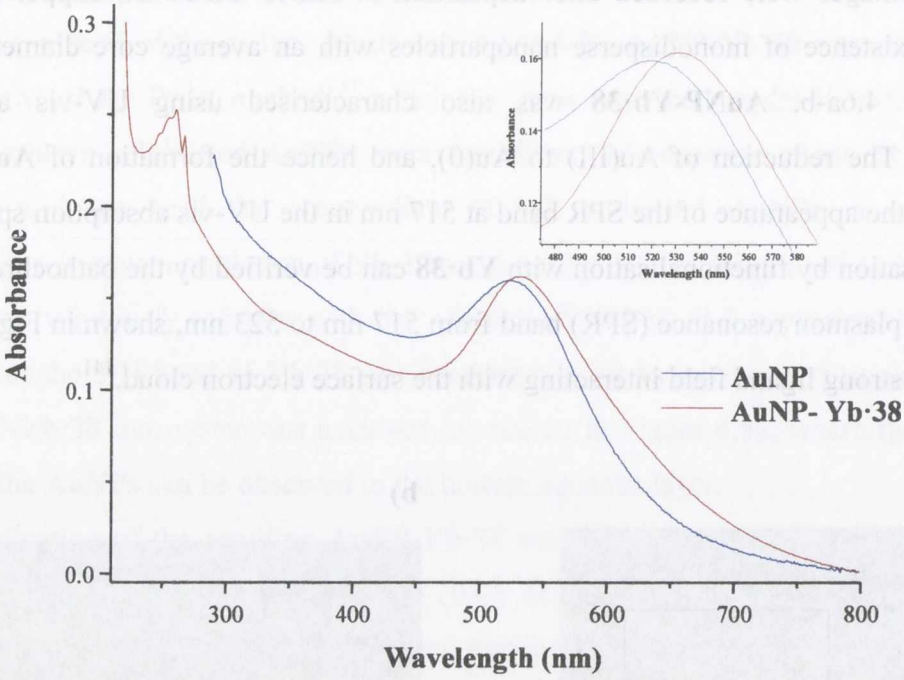


Figure 4.7: *The UV-vis absorption spectra showing the shift in the SPR band of the* ***AuNPs*** *upon functionalisation with* ***Yb·38*** *in water.*

The table below summarises the reproducibility of the same size **AuNPs** achieved for a number of samples of **AuNP-Yb·38**; Table 4.1.

Having successfully synthesised both **Yb·38** and **AuNP-Yb·38**, the next stage involved investigation into the formation of the ternary complex system between the complexes and the antenna **tta**, **Yb·38-tta**, both on and off the gold surface.

Table 4.1: *Summary of the UV-vis* λ_{max}*, DLS and TEM results from a number of samples of* ***AuNP-Yb·38*** *prepared.*

Sample	λ_{max} (nm)	DLS (nm)	TEM (nm)
1	522	12.12	8.36
2	524	13.14	9.43
3	522	12.40	8.76
4	523	13.39	9.97

4.4 Formation and Photophysical Evaluation of Yb·38-tta and AuNP-Yb·38-tta

4.4.1 Formation of Yb·38-tta

The formation of the ternary system **Yb·38-tta** was firstly studied using the free complex. The titration of **Yb·38** with **tta** was carried out in 0.1 M HEPES buffer solution at pH 7.4 with a constant ionic strength (NaCl, 0.1 M). Throughout the titration the changes in the UV-vis absorption spectrum and in the NIR centred emission were monitored.

The UV-vis absorption spectrum, Figure 4.8 showed substantial changes upon titration with **tta**. Having no chromophore, **Yb·38** displayed no major absorption bands before the addition of **tta**. The appearance of absorption bands at 260 nm and 340 nm were a direct result of increasing concentration of **tta** in solution. Simultaneously, the formation of the ternary complex **Yb·38-tta** was also followed by monitoring the evolution of the NIR Yb(III)-centred emission throughout the titration as **tta** is known to be an efficient sensitiser for NIR-emitting Ln(III) ions.[173] In the absence of **tta**, the Yb(III) centred emission of **Yb·38** was found to be very weak, which can be attributed to the fact that there was no chromophore incorporated into its structure in addition to the presence of two metal bound water molecules. Following the excitation of the **tta** absorption band at 340 nm, characteristic Yb(III) emission in the 900-1200 nm range occurred, arising from the $^2F_{5/2} \rightarrow {}^2F_{7/2}$ transition, confirming that sensitised NIR emission had indeed occurred, Figure 4.9.

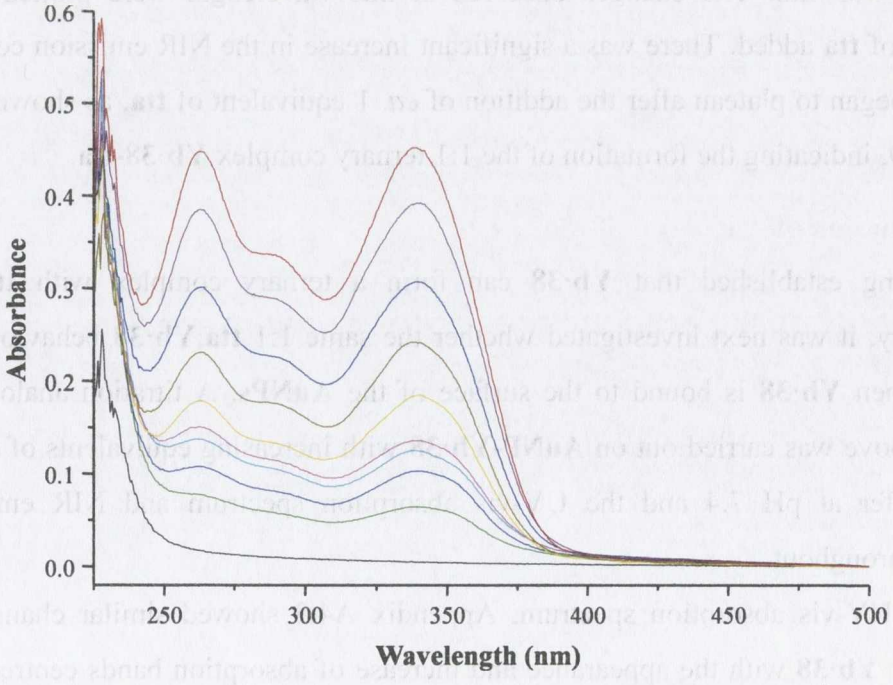


Figure 4.8: *Changes in the UV-vis absorption spectrum of* ***Yb·38*** *(1.2×10^{-5} M) as a function of added equivalents of* ***tta*** *at pH 7.4 in 0.1 M HEPES buffer.*

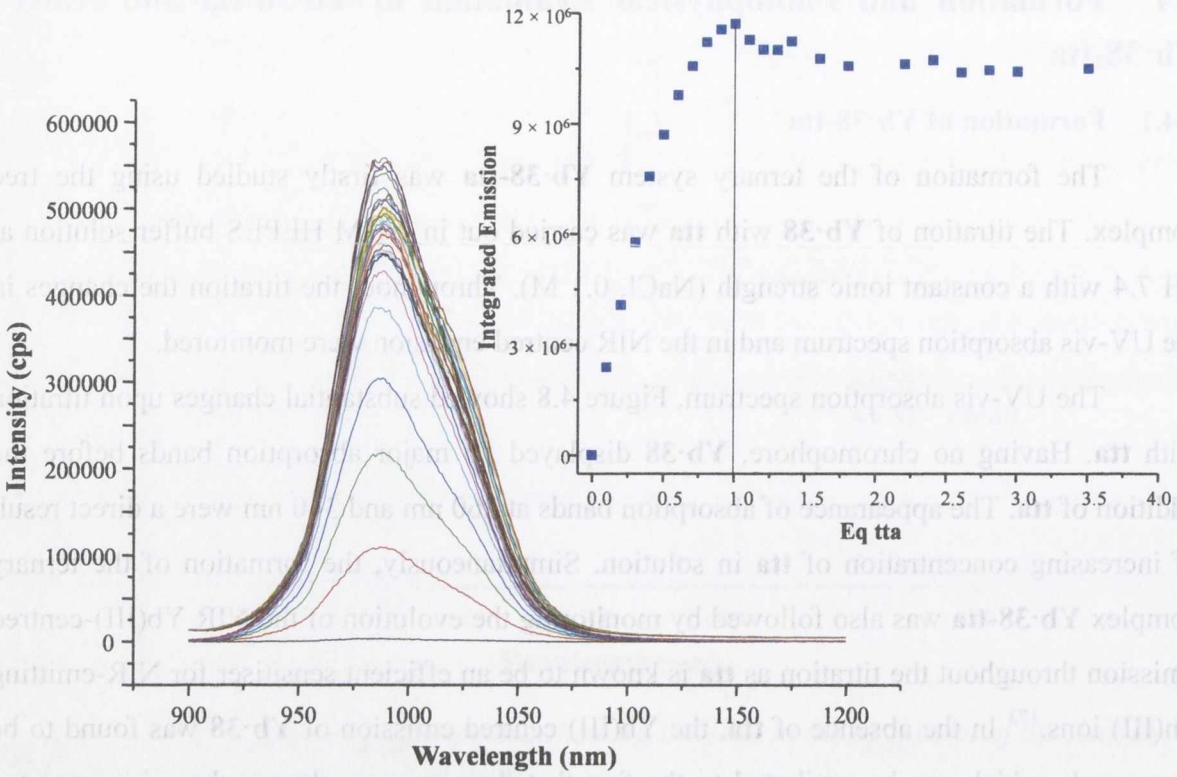


Figure 4.9: *The evolution of the Yb(III) NIR emission of* ***Yb·38*** *(1.2×10^{-5} M) (λ_{ex} = 340 nm) as a function of equivalents of* ***tta*** *added at pH 7.4 in 0.1 M HEPES buffer. Inset: Changes in the integrated emission as a function of added equivalents of* ***tta****.*

The NIR emission was "switched on" by the addition of **tta**, with maximum emission observed at 985 nm. The changes observed at this wavelength were plotted against the equivalents of **tta** added. There was a significant increase in the NIR emission centred at 985 nm, which began to plateau after the addition of *ca.* 1 equivalent of **tta**, as shown in the inset in Figure 4.9, indicating the formation of the 1:1 ternary complex **Yb·38-tta**.

4.4.2 Formation of AuNP-Yb·38-tta

Having established that **Yb·38** can form a ternary complex with **tta** in a 1:1 stoichiometry, it was next investigated whether the same 1:1 **tta**:**Yb·38** behaviour would be observed when **Yb·38** is bound to the surface of the **AuNPs**. A titration analogous to that described above was carried out on **AuNP-Yb·38** with increasing equivalents of **tta** in 0.1 M HEPES buffer at pH 7.4 and the UV-vis absorption spectrum and NIR emission were monitored throughout.

The UV-vis absorption spectrum, Appendix A4.3 showed similar changes to those observed for **Yb·38** with the appearance and increase of absorption bands centred at 260 nm and 340 nm being attributed to the increasing concentration of **tta** in solution

As expected, in the absence of **tta** there was no NIR emission signal observed due to the lack of sensitising antenna bound to the Yb(III) metal centre. Addition of **tta**, using an

excitation wavelength of 340 nm causes a large increase in the Yb(III) emission bands, with maximum intensity occurring at the addition of *ca.* 120 ± 10 equivalents of antenna, Figure 4.10, found to be reproducible over several titrations. Considering it has been established that the complex **Yb·38** forms a 1:1 ternary system with the diketonate **tta**, a plateau initiating after the addition of 120 equivalents indicated the attachment of *ca.* 120 ± 10 **Yb·38** complexes per **AuNP**. This was in agreement with our previous results obtained for **AuNP-Eu·38** using **nta** as the sensitising antenna.[107]

It was also worth noting that although the exact same settings were used for both titrations of **tta** against **Yb·38** and **AuNP-Yb·38**, the maximum Yb(III) emission intensity reached for **Yb·38** was *ca.* 15 times higher than that reached for **AuNP-Yb·38**, with the difference in intensity being attributed to the quenching effect of the **AuNP** surface on the Yb(III) luminescence.

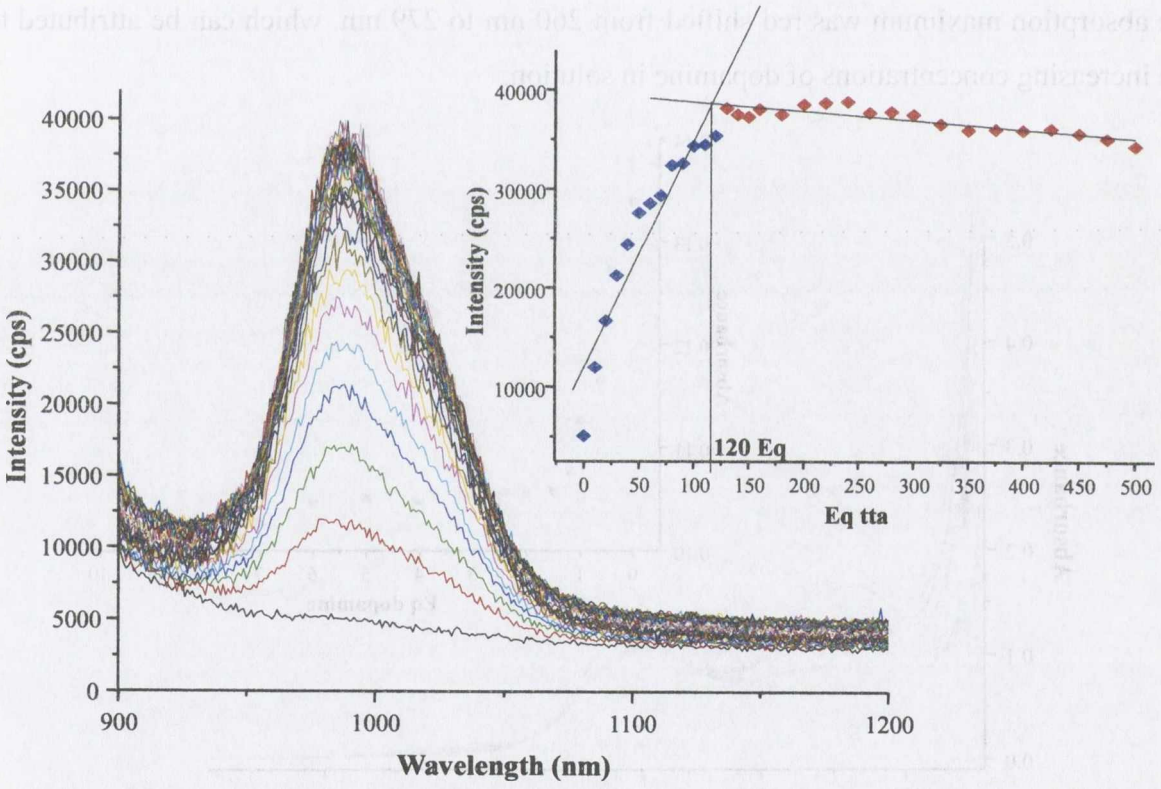


Figure 4.10: *Changes in the Yb(III) NIR emission of* ***AuNP-Yb·38*** *(1 × 10^{-7} M) (λ_{ex} = 340 nm) as a function of equivalents of* ***tta*** *added at pH 7.4 in 0.1 M HEPES. Inset: Changes in the emission intensity at 985 nm as a function of equivalents of* ***tta****.*

4.5 Sensing of Dopamine

4.5.1 Sensing of Dopamine using Yb·38-tta

Having determined that the formation of the ternary complex **Yb·38-tta** occurs in aqueous solution, both off and on the **AuNP** surface, we next evaluated its ability to act as a sensor for dopamine through modulation of the Yb(III) metal centred emission *via* a displacement assay. Titrations were carried out involving the addition of increasing equivalents of dopamine to a 1:1 solution of the ternary complex **Yb·38-tta** at pH 7.4 in 0.1 M HEPES buffer.

The changes observed in the UV-vis absorption spectrum of **Yb·38-tta** upon the addition of dopamine are shown below in Figure 4.11. A hypochromic shift of the UV-vis absorption band centred at 339 nm occurs which shows no further changes after the addition of one equivalent of dopamine, shown as inset in Figure 4.11. Concurrently, the band centred at 260 nm undergoes a hyperchromic shift that does not appear to level off and furthermore, the absorption maximum was red shifted from 260 nm to 279 nm, which can be attributed to the increasing concentrations of dopamine in solution.

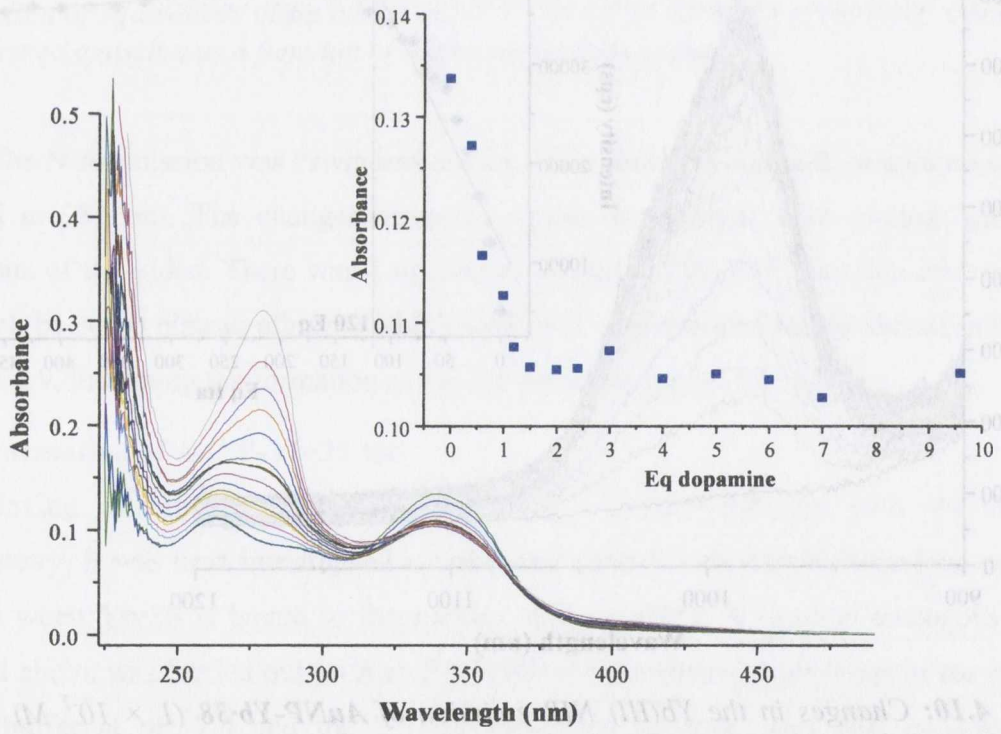


Figure 4.11: *Changes in the UV-vis absorption spectrum of* ***Yb·38-tta*** *(1×10^{-5} M) as a function of equivalents of dopamine added at pH 7.4 in 0.1 M HEPES. Inset: Changes in the absorbance at 339 nm as a function of equivalents of dopamine.*

The NIR emission spectrum displayed significant changes in the $^2F_{5/2} \rightarrow {}^2F_{7/2}$ transition of the Yb(III) metal centre upon the addition of dopamine. Before the addition of dopamine **Yb·38-tta** exhibited a relatively strong NIR emission signal with a maximum centred at

985 nm, as shown in Figure 4.12, upon excitation at 340 nm. The addition of dopamine into the system resulted in a significant quenching (*ca.* 70%) in the Yb(III) luminescence after the addition of 2 equivalents of dopamine, with further addition of up to 10 equivalents of dopamine resulting in almost complete quenching of the signal, shown as inset in Figure 4.12.

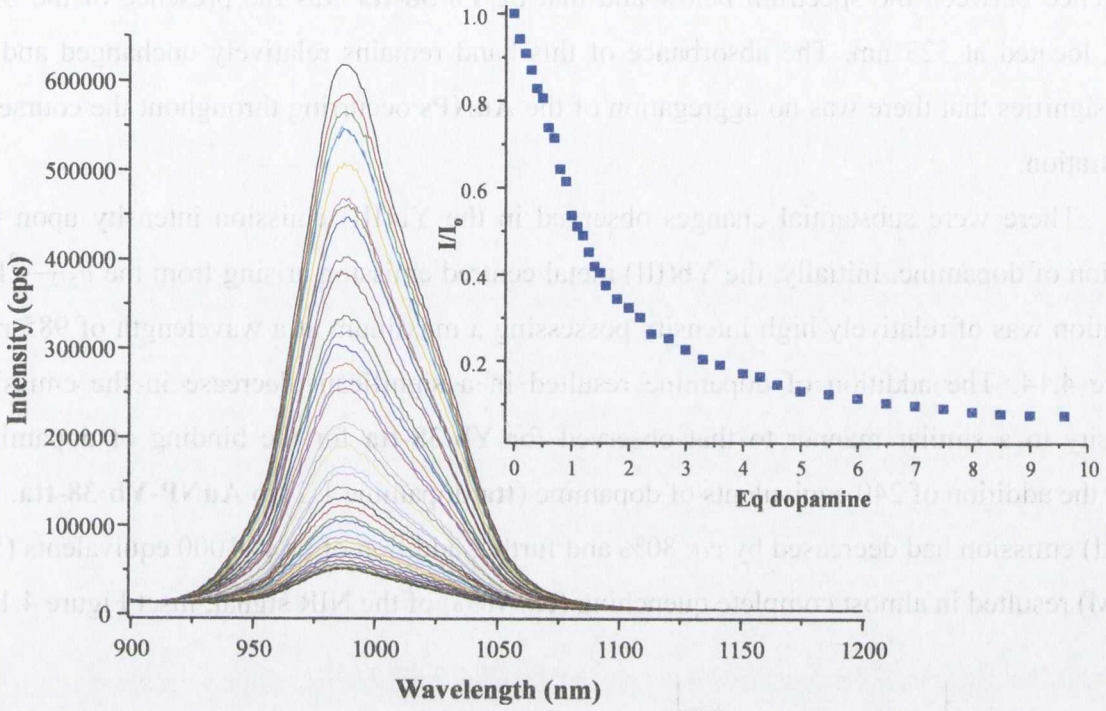


Figure 4.12: *Changes in the Yb(III) NIR emission of* ***Yb·38-tta*** *(1×10^{-5} M) (λ_{ex} = 340 nm) as a function of equivalents of dopamine added at pH 7.4 in 0.1 M HEPES. Inset: Changes in the normalised emission intensity (I/I_o, where I_o = intensity in the absence of dopamine) at 985 nm as a function of equivalents of dopamine.*

It was postulated that the changes occurring in the NIR emission spectrum could be due to dopamine interacting with the **tta** bound to the Yb(III) metal centre in such a manner that it is detrimental to the energy transfer process from the **tta** antenna to the Yb(III) metal centre and hence, gives rise to the decrease in intensity that was observed. Alternatively, dopamine could be causing the displacement of the **tta** from the Yb(III) metal centre and binding itself, which would also account for the dramatic decrease in emission intensity observed as dopamine is not known as an efficient sensitiser for NIR Ln(III) ions.

The sensing ability of the ternary complex **Yb·38-tta** once bound to the surface of **AuNPs** was also investigated, with the results described in the following section.

4.5.2 Sensing of Dopamine using AuNP-Yb·38-tta

An analogous titration was carried out using **AuNP-Yb·38-tta** at a concentration of two fold magnitude lower than the free complex. The changes observed in the UV-vis absorption spectrum of **AuNP-Yb·38-tta** upon titration with dopamine are shown below in

Figure 4.13, and are comparable to the changes observed in the investigation of the simple ternary complex, **Yb·38-tta**, as a function of dopamine. A hypochromic shift in the band at 337 nm occurs in concert with the appearance of a strong absorption band centred at 279 nm, the latter being attributed to increasing concentrations of dopamine in solution. The significant difference between the spectrum below and that of **Yb·38-tta** was the presence of the SPR band, located at 523 nm. The absorbance of this band remains relatively unchanged and as such signifies that there was no aggregation of the **AuNPs** occurring throughout the course of the titration.

There were substantial changes observed in the Yb(III) emission intensity upon the addition of dopamine. Initially, the Yb(III) metal centred emission arising from the $F_{5/2} \rightarrow {}^2F_{7/2}$ transition was of relatively high intensity possessing a maximum at a wavelength of 985 nm, Figure 4.14. The addition of dopamine resulted in a significant decrease in the emission intensity in a similar manner to that observed for **Yb·38-tta** for the binding of dopamine. After the addition of 240 equivalents of dopamine (**tta**:dopamine 1:2) to **AuNP-Yb·38-tta**, the Yb(III) emission had decreased by *ca.* 80% and further addition of up to 1000 equivalents (5×10^{-4} M) resulted in almost complete quenching (*ca.* 98%) of the NIR signal, inset Figure 4.14.

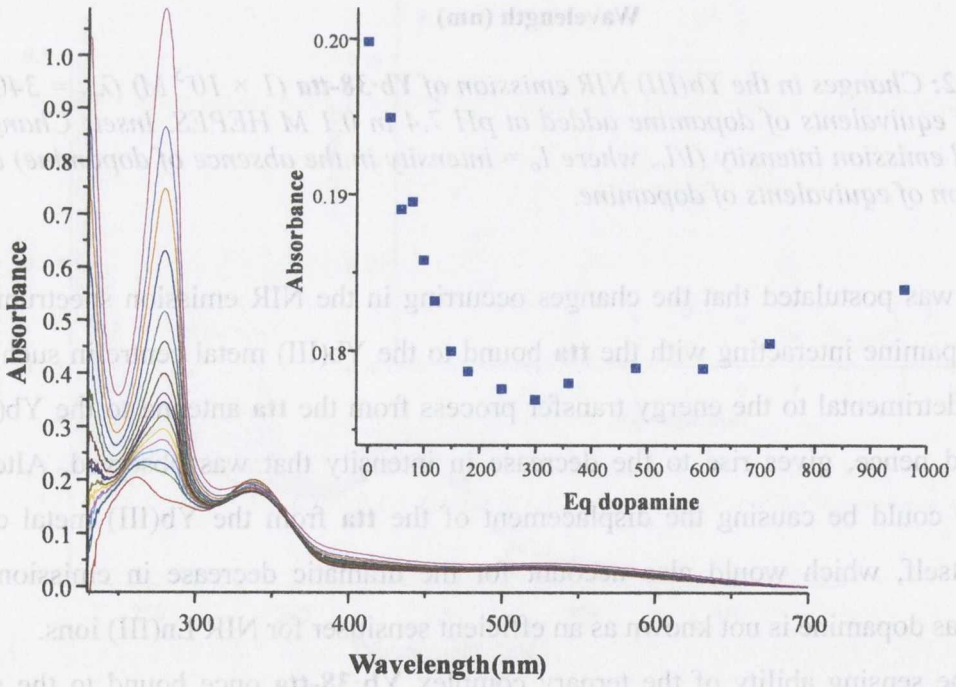


Figure 4.13: *Changes in the UV-vis absorption spectrum of* ***AuNP-Yb·38-tta*** *(1×10^{-7} M) as a function of equivalents of dopamine added at pH 7.4 in 0.1 M HEPES. Inset: Changes in the absorbance at 337 nm as a function of equivalents of dopamine.*

The system **AuNP-Yb·38-tta** has thus far proven to be capable of sensing dopamine through the modulation of the Yb(III) centred emission. It was next important to investigate whether the sensing event was selective for dopamine over other biologically relevant anions that are present alongside dopamine in the body. The following section will examine the effects that different biological anions have on the Yb(III)-centred emission of **AuNP-Yb·38-tta** and compare their quenching ability to that of dopamine. The substrates that will be investigated are ascorbate, citrate, carbonate and phosphate.

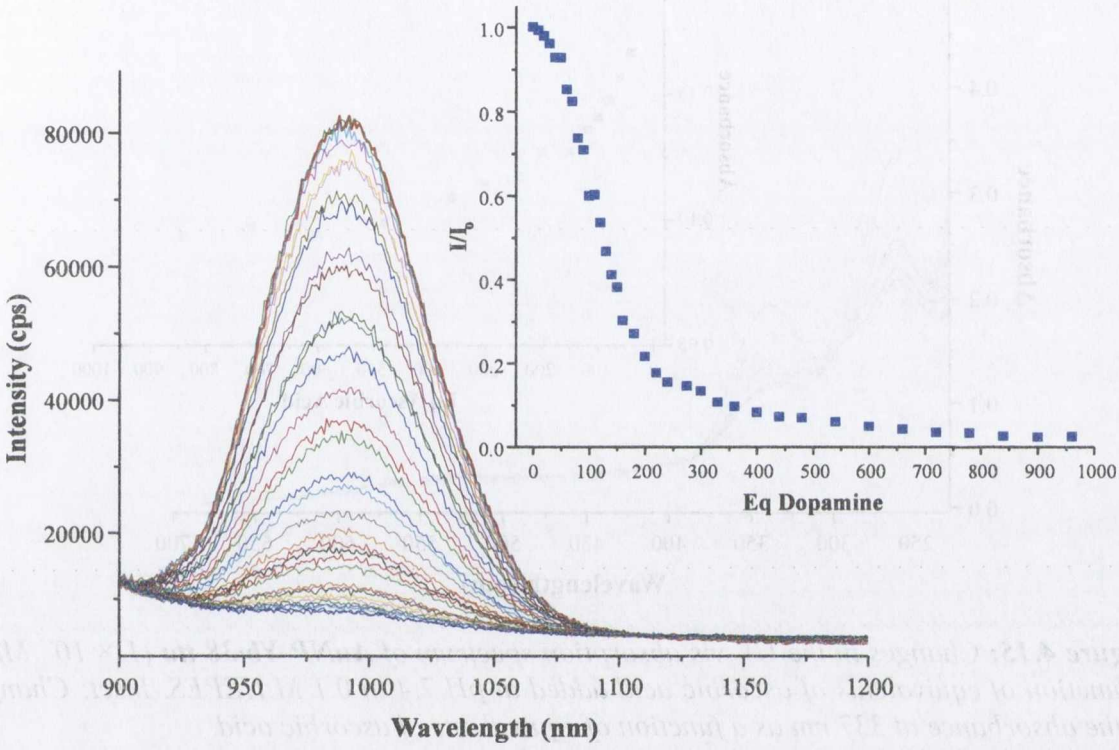


Figure 4.14: *Changes in the Yb(III) NIR emission of* ***AuNP-Yb·38-tta*** *(1×10^{-7} M) (λ_{ex} = 340 nm) as a function of equivalents of dopamine added at pH 7.4 in 0.1 M HEPES. Inset: Changes in the normalised emission intensity (I/I_0) at 985 nm as a function of equivalents of dopamine (5×10^{-6} M → 1×10^{-4} M).*

4.6 Selectivity of AuNP-Yb·38-tta for Dopamine over Biologically Relevant Anions

Ascorbic acid is a powerful antioxidant which coexists with dopamine in biological samples, and is a vital component in human diet. A common method of sensing dopamine and ascorbic acid is by electrochemical techniques using carbon coated electrodes.[193] However, due to their similar oxidation potentials it is often very difficult to differentiate between them.[194] Therefore, the development of a sensitive and selective biosensor that can discriminate between the two is highly desirable. Bearing this in mind, a titration was undertaken to determine the effect of ascorbic acid on the NIR emission of **AuNP-Yb·38-tta**, and how the effect differs to that of dopamine.

The changes in the UV-vis absorption spectrum of **AuNP-Yb·38-tta** due to the addition of ascorbic acid are shown in Figure 4.15. There was a 2 fold decrease in the absorption maximum at 337 nm; inset Figure 4.15, with concomitant hyperchromic shift of the absorbance band centred at *ca.* 260 nm, associated with increasing concentrations of ascorbic acid. As in the case of dopamine, no change in the SPR band was observed.

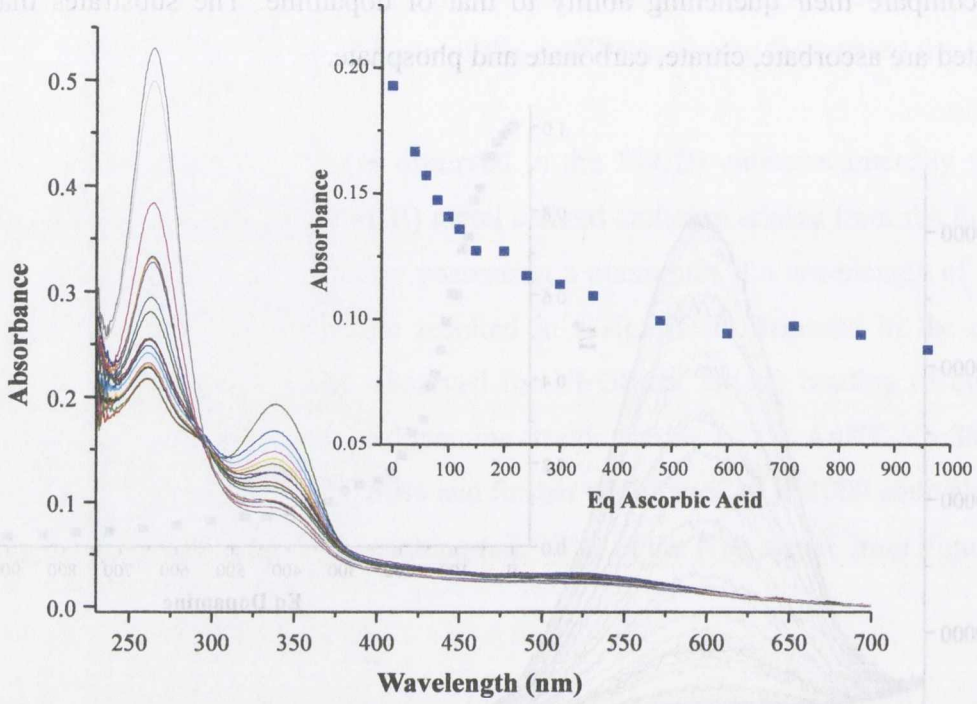


Figure 4.15: *Changes in the UV-vis absorption spectrum of* ***AuNP-Yb·38-tta*** *(1×10^{-7} M) as a function of equivalents of ascorbic acid added at pH 7.4 in 0.1 M HEPES. Inset: Changes in the absorbance at 337 nm as a function of equivalents of ascorbic acid.*

In monitoring the Yb(III) emission as a function of equivalents of ascorbic acid added it was discovered that although the NIR emission was somewhat quenched, it was quenched significantly less than it had been upon the addition of dopamine, Figure 4.16. After the addition of *ca.* 200 equivalents of ascorbic acid the Yb(III) emission intensity at 985 nm had decreased by *ca.* 40%; inset Figure 4.16. In comparison, the addition of the same equivalents of dopamine gave rise to double the decrease (80%) of the emission intensity, indicating that even though the presence of ascorbic acid, modulations in the Yb(III) of **AuNP-Yb·38-tta** would still occur, allowing for the selective sensing of dopamine over other biologically relevant analytes.

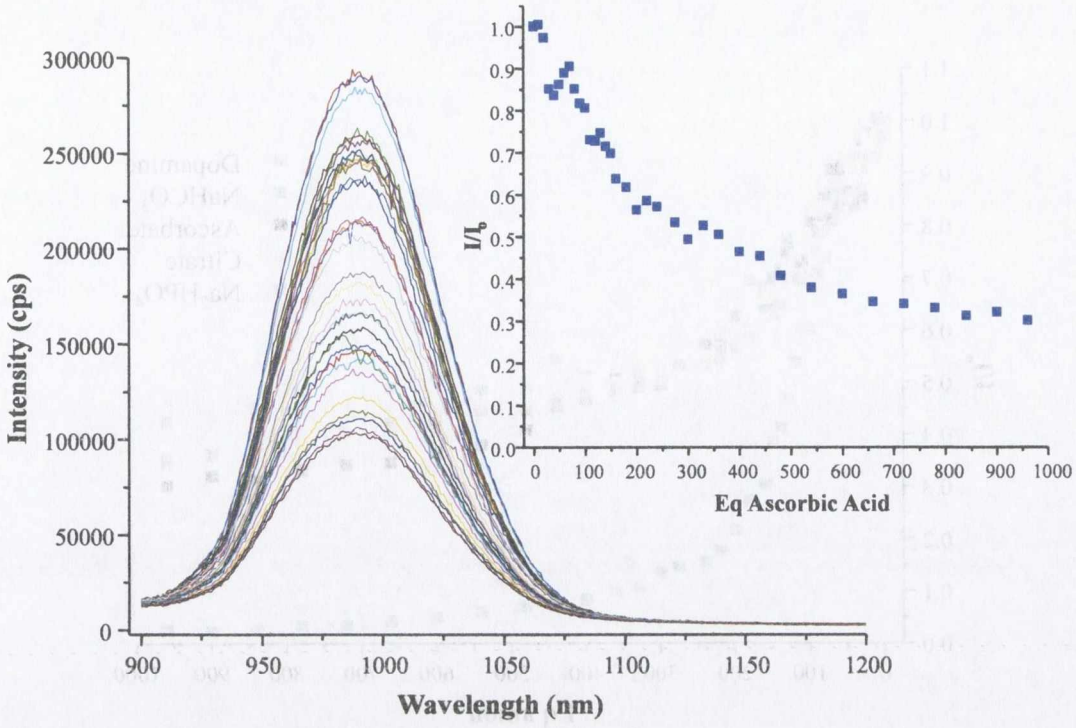


Figure 4.16: *Changes in the Yb(III) NIR emission of* ***AuNP-Yb·38-tta*** *(1×10^{-7} M) (λ_{ex} = 340 nm) as a function of equivalents of ascorbic acid added at pH 7.4 in 0.1 M HEPES. Inset: Changes in the normalised emission intensity (I/I_o) at 985 nm as a function of equivalents of ascorbic acid (5×10^{-6} M → 1×10^{-4} M).*

The sensing ability of **AuNP-Yb·38-tta** was also investigated towards other biologically relevant anions that are known to be found in high concentrations in biological media, such as carbonate, citrate and phosphate. The overall quenching effect on the Yb(III) emission by the respective anions and dopamine is illustrated in Figure 4.17. The UV-vis absorption spectra and NIR emission spectra are shown in Appendix A4.4-A4.9.

The UV-vis absorption spectrum of **AuNP-Yb·38-tta**, Appendix A4.4, A4.6, A4.8, displayed similar changes upon addition of carbonate, citrate and phosphate; a hypochromic shift of the absorbance band centred at 337 nm occurs with concomitant increase of the band centred at *ca.* 260 nm. Modulations of the Yb(III) emission that occurred upon addition of the anions under investigation were similar to those observed upon the addition of ascorbic acid; all experienced some degree of quenching of the NIR signal. In all cases the NIR emission appeared to be quenched by *ca.* 40% after the addition of *ca.* 200 equivalents of anion added, Figure 4.17. This is in comparison to a quenching of 80% for the same number of equivalents of dopamine. The similar behaviour observed for the range of analytes studies was somewhat unexpected and consequently, a stability study of the system will be investigated in the following Section to determine whether the quenching was in fact due to the presence of the analytes.

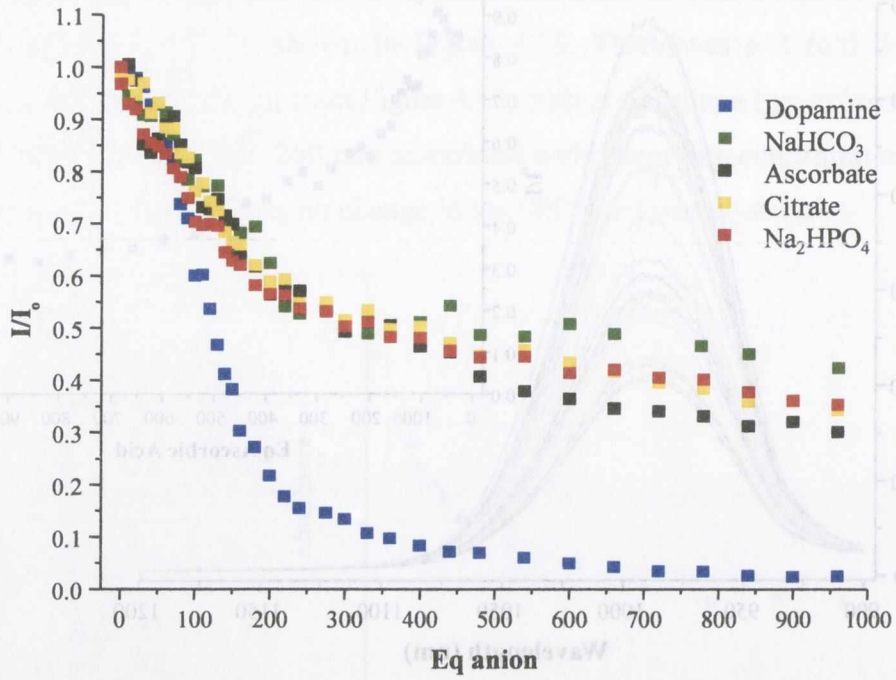


Figure 4.17: *Changes in the normalised emission intensity (I/I_o) at 985 nm as a function of equivalents of dopamine, ascorbic acid, carbonate, citrate and phosphate.*

4.7 Stability Study of AuNP-Yb·38-tta

When repeating some of the titrations it was observed that if a NIR emission scan of the sample was several times without the addition of any analyte, the Yb(III) emission would still experience some quenching. To further investigate this observation, it was decided to conduct a titration with the same number of additions as previous titrations however, adding increasing amounts of HEPES buffer to the solution instead of dopamine or any previously investigated analyte that may cause quenching of the NIR emission to occur. If **AuNP-Yb·38-tta** is fully photostable then no changes should occur to either the UV-vis absorption or NIR emission spectra.

As with previous titrations, aliquots of the buffer were added to the solution in the cell containing 0.1 M HEPES buffer and **AuNP-Yb·38-tta** and the absorption was measured followed by the NIR emission, with the changes observed described below. Significant changes were observed in the UV-vis absorption spectrum, shown in Figure 4.18. Most notably, the absorption band centred at 340 nm experienced a hypochromic shift, with a 35% decrease of the absorption maximum, inset Figure 4.18. The once strong absorption band with a defined maximum now appears as a slight shoulder. In comparison, only very minor changes occur at the absorption band centred at 260 nm, where in some of the previous titrations, the changes occurring at *ca.* 260 nm could be attributed to increasing concentrations of the analyte added. Furthermore, the SPR band remained relatively unchanged throughout the titration.

The fact that the UV-vis absorption spectrum was changing upon repeated excitation without the addition of any analyte indicates that photodegredation of the antenna must be occurring, leading us to conclude that the system chosen for the detection of dopamine, in the particular experimental conditions used, not photostable.

Simultaneously, by only adding HEPES buffer into the cell, a decrease in the Yb(III) NIR emission was observed, Figure 4.19. It was deduced that under repetitive excitation of the **tta** antenna at 340 nm using a Xenon lamp the **tta** antenna undergoes photodegradation. This in turn was detrimental to the sensitisation of the Yb(III) $^2F_{5/2}$ excited state and results in a 70% decrease in the NIR emission intensity, inset Figure 4.19. The photodegradation was only found to occur when using the Xenon lamp of the Fluorolog. Titrations carried out in Chapter 2 with **tta** and Eu(III) complexes using Cary Eclipse fluorescence spectrometers showed no such degradation of the **tta** antenna. To further confirm this a stability study was carried out on **Eu·38-tta**, Appendix A4.10 and no changes are observed in the Eu(III) emission upon continuous excitation into the **tta** antenna.

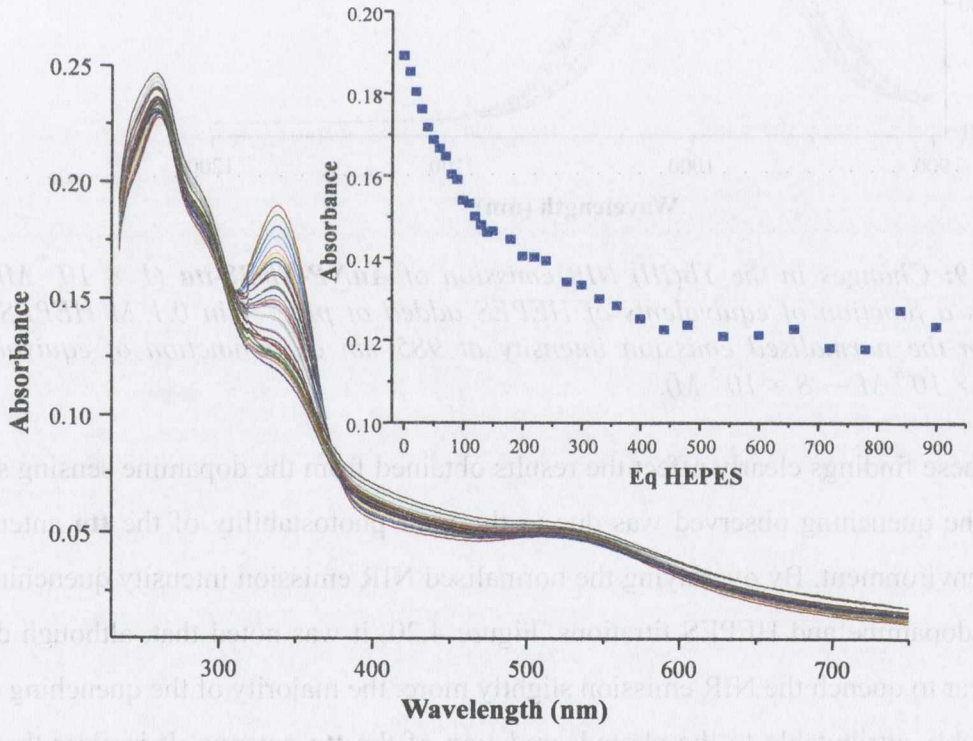


Figure 4.18: *Changes in the UV-vis absorption spectrum of* ***AuNP-Yb·38-tta*** *(1×10^{-7} M) as a function of equivalents of HEPES added at pH 7.4 in 0.1 M HEPES. Inset: Changes in the absorbance at 340 nm as a function of equivalents of HEPES.*

The same stability issue was observed on the complex **Yb·38-tta** unattached to the **AuNP** surface. The changes in the UV-vis absorption spectrum of **Yb·38-tta** upon titration with HEPES buffer is shown in Appendix A4.11. The absorption band centred at 340 nm experienced a hypochromic shift, with a 31% decrease in the absorption maximum, while in

the NIR emission spectrum, shown in Appendix A4.12, the decrease in Yb(III) emission intensity of *ca.* 35% was not to the same extent as that seen for **AuNP-Yb·38-tta**. Nevertheless, the changes still clearly illustrated that photodegredation of the **tta** antenna was occurring as a result of continuous excitation by the Xenon lamp.

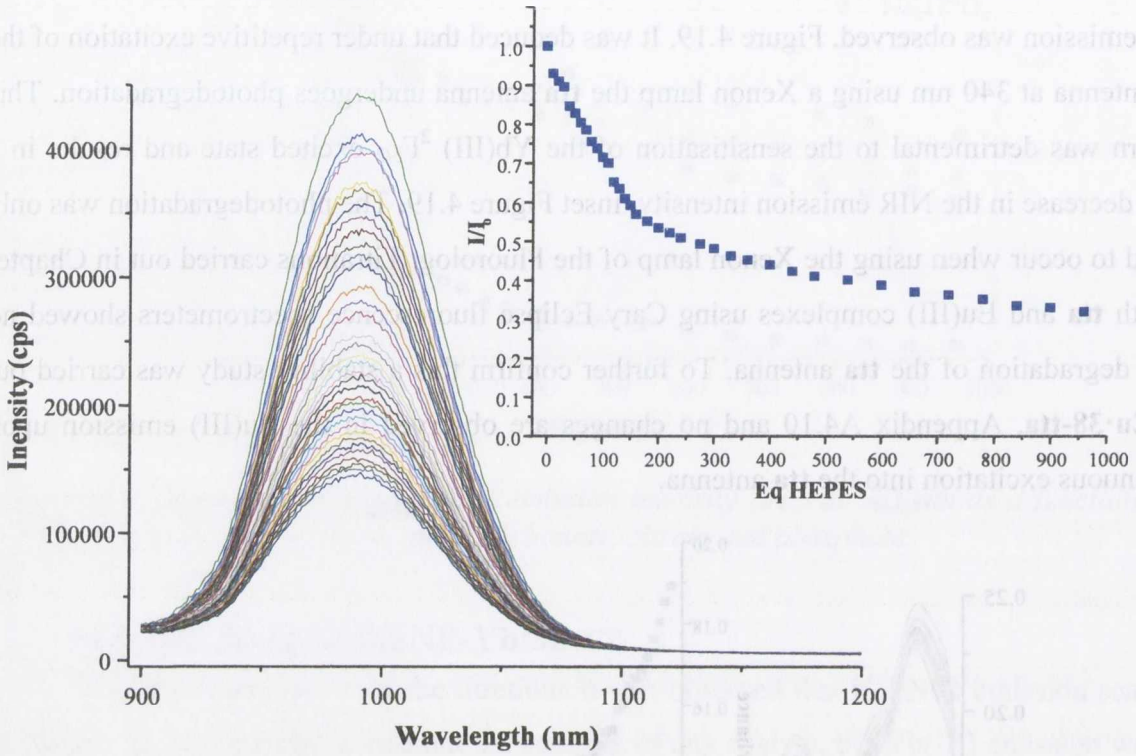


Figure 4.19: *Changes in the Yb(III) NIR emission of* ***AuNP-Yb·38-tta*** *(1×10^{-7} M) (λ_{ex} = 340 nm) as a function of equivalents of HEPES added at pH 7.4 in 0.1 M HEPES. Inset: Changes in the normalised emission intensity at 985 nm as a function of equivalents of HEPES (1×10^{-6} M → 8×10^{-5} M).*

These findings clearly affect the results obtained from the dopamine sensing studies as most of the quenching observed was due to the poor photostability of the **tta** antenna in an aqueous environment. By overlaying the normalised NIR emission intensity quenching results from the dopamine and HEPES titrations, Figure 4.20, it was noted that, although dopamine does appear to quench the NIR emission slightly more, the majority of the quenching observed was probably attributable to the photodegradation of the **tta** antenna. It is clear that **tta** was not a suitable antenna for the sensing of dopamine using NIR emitting Ln(III) such as Yb(III) and as such other suitable antennae will be investigated in the following section.

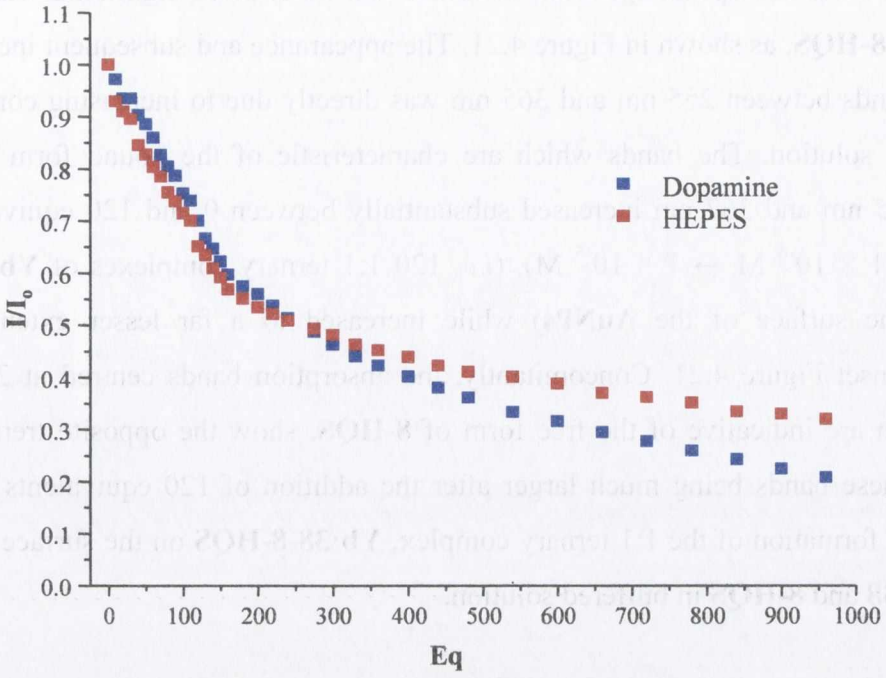
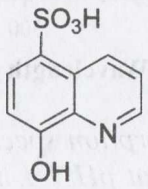


Figure 4.20: *Changes in the normalised emission intensity (I/I_o) at 985 nm as a function of equivalents of dopamine and HEPES.*

4.8 8-HQS as an Antenna for the Sensing of Dopamine using AuNP-Yb·38

8-hydroxyquinoline-5-sulfonic acid, **82**, (**8-HQS**) was next investigated as a suitable antenna for the sensing of dopamine using **AuNP-Yb·38**. This antenna has previously been used in Chapter 3 for the sensing of Zn(II) using a Yb(III) complex, therefore we already know that it is stable after continuous excitation using the Xenon lamp of the fluorolog. The **8-HQS** was chosen as it has been shown to bind strongly to Ln(III) ions and moreover, can efficiently sensitise their emission in the NIR range.[164-166]



82

4.8.1 Formation of AuNP-Yb·38-8-HQS

The formation of the ternary system **Yb·38-8-HQS** at the surface was studied by titrating a solution of **AuNP-Yb·38** with **8-HQS** in 0.1 M HEPES buffer at pH 7.4. The changes in the UV-vis absorption spectrum and the NIR emission were monitored throughout the titration.

The UV-vis absorption spectrum of **AuNP-Yb·38** showed significant changes upon titration with **8-HQS**, as shown in Figure 4.21. The appearance and subsequent increase in the absorption bands between 255 nm and 365 nm was directly due to increasing concentrations of **8-HQS** in solution. The bands which are characteristic of the bound form of **8-HQS**, centred at 255 nm and 367 nm increased substantially between 0 and 120 equivalents of **8-HQS** added (1×10^{-6} M → 1×10^{-5} M), (*i.e.* 120 1:1 ternary complexes of **Yb·38-8-HQS** formed on the surface of the **AuNPs**) while increased to a far lesser extent at higher equivalents, inset Figure 4.21. Concomitantly, the absorption bands centred at 240 nm and 306 nm which are indicative of the free form of **8-HQS**, show the opposite trend, with the increase of these bands being much larger after the addition of 120 equivalents of **8-HQS**, indicating the formation of the 1:1 ternary complex, **Yb·38-8-HQS** on the surface of **AuNPs**, between **Yb·38** and **8-HQS** in buffered solution.

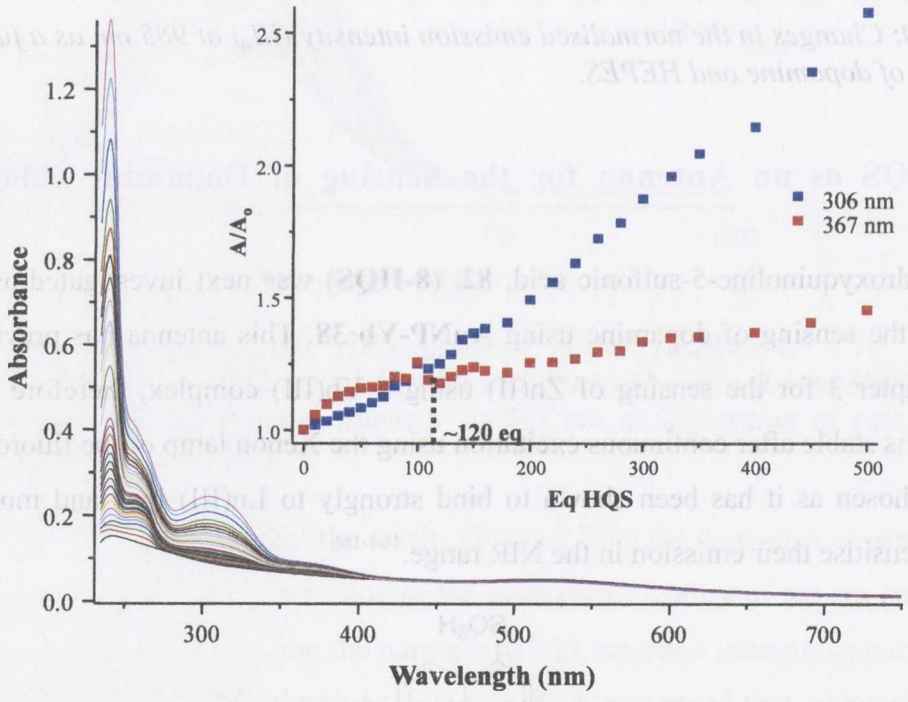


Figure 4.21: *Changes in the UV-vis absorption spectrum of* ***AuNP-Yb·38*** *(1×10^{-7} M) as a function of equivalents of* ***8-HQS*** *added at pH 7.4 in 0.1 M HEPES. Inset: Changes in the absorbance at 306 nm and 367 nm as a function of equivalents of* ***8-HQS****.*

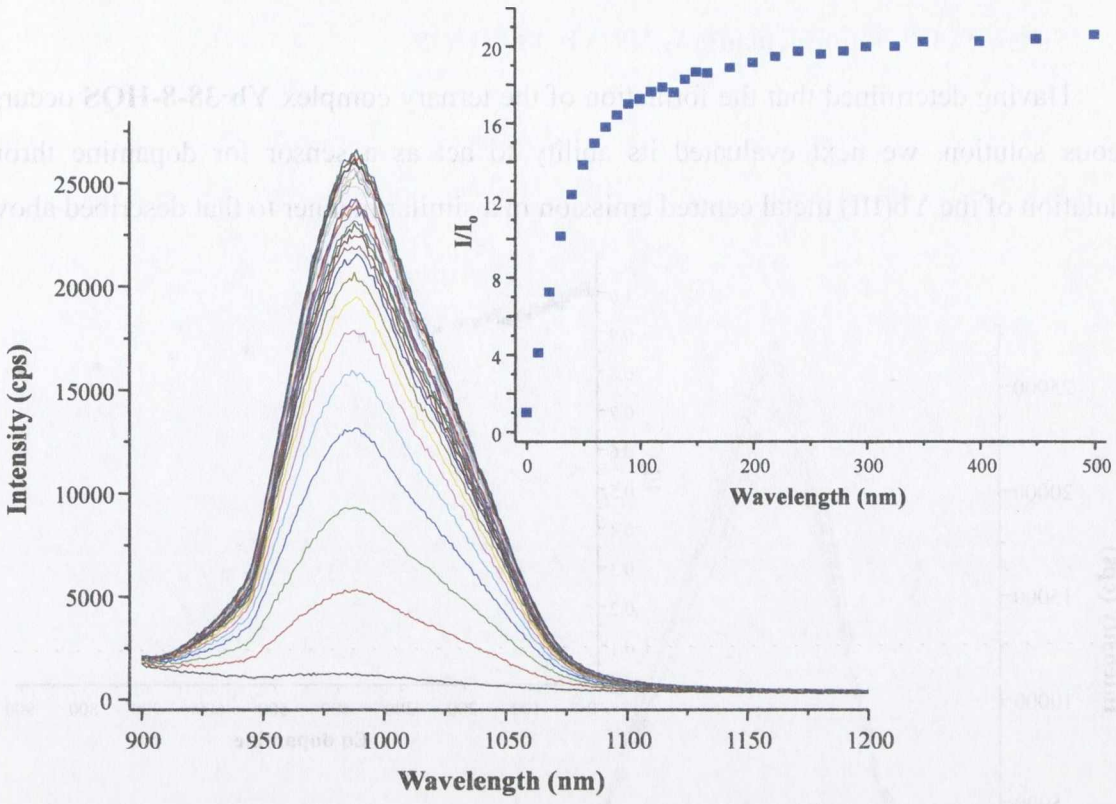


Figure 4.22: *Changes in the Yb(III) NIR emission of* ***AuNP-Yb·38*** *(1×10^{-7} M) (λ_{ex} = 360 nm) as a function of equivalents of* ***8-HQS*** *added at pH 7.4 in 0.1 M HEPES. Inset: Changes in the normalised emission intensity (I/I_o) at 985 nm as a function of equivalents of* ***8-HQS****.*

The formation of the ternary complex **Yb·38-8-HQS** *in situ* was followed by monitoring the Yb(III)-centred emission throughout the titration as **8-HQS** is known to be an efficient sensitiser for NIR-emitting Ln(III) ions.[195] Before the addition of **8-HQS**, the Yb(III) metal centred emission of **Yb·38** was found to be of very low intensity due to the lack of any incorporated chromophore and furthermore, by the presence of two metal bound water molecules. The addition of **8-HQS** resulted in characteristic Yb(III) NIR luminescence arising from the $^2F_{5/2} \rightarrow {}^2F_{7/2}$ transition upon excitation into the **8-HQS** antenna at 360 nm. The NIR was switched on, with a maximum observed at 985 nm. The emission intensity continued to increase up to the addition of *ca.* 120 equivalents of **8-HQS**, inset Figure 4.22, where it reached a plateau, indicating the formation of a 1:1 ternary complex between each of the **Yb·38** complexes on the surface and the **-8-HQS** antenna.

It was confirmed by an excitation spectrum that it was indeed the energy transfer from the **8-HQS** antenna that was causing sensitisation of the Yb(III) metal centre as it matched closely to that of the UV-vis absorption spectra, shown in Appendix A4.13. Moreover, the main band in the excitation spectrum at *ca.* 360 nm corresponds to that of the bound form of **8-HQS** and not that of the unbound form, verifying that any excess of **8-HQS** in solution was not contributing to the sensitisation process.

4.8.2 Sensing of Dopamine using AuNP-Yb·38-8-HQS

Having determined that the formation of the ternary complex **Yb·38-8-HQS** occurs in aqueous solution, we next evaluated its ability to act as a sensor for dopamine through modulation of the Yb(III) metal centred emission in a similar manner to that described above.

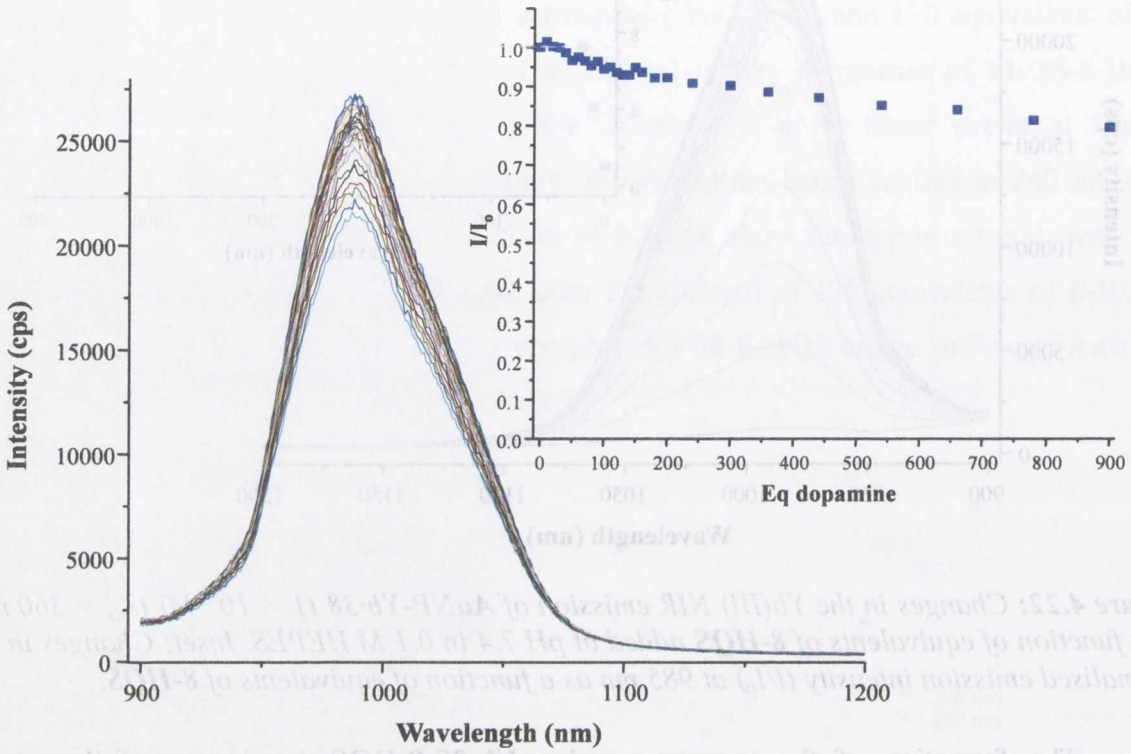


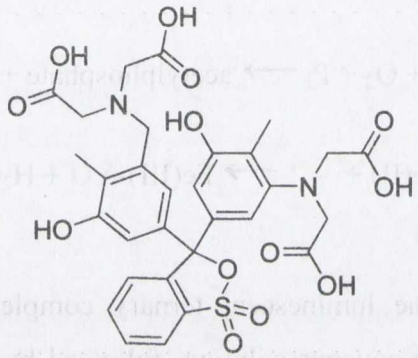
Figure 4.23: *Changes in the Yb(III) NIR emission of* ***AuNP-Yb·38-8-HQS*** *(1×10^{-7} M) (λ_{ex} = 360 nm) as a function of equivalents of dopamine added at pH 7.4 in 0.1 M HEPES. Inset: Changes in the normalised emission intensity (I/I_o) at 985 nm as a function of equivalents of dopamine.*

The changes observed in the UV-vis absorption spectrum of **AuNP-Yb·38-8-HQS** upon titration with dopamine are shown in Appendix A4.14. Only minor changes were observed with the only significant change being an increase in the absorption band centred at 280 nm which can be attributed to increasing concentrations of dopamine. The SPR band of the **AuNPs** at 523 nm also remains relatively unchanged throughout the titration, indicating that no aggregation of the **AuNPs** were taking place.

The NIR emission spectrum did not show significant changes in the $^2F_{5/2} \rightarrow {}^2F_{7/2}$ transition of the Yb(III) metal centre, Figure 4.23. As displayed in the inset in Figure 4.23, the addition of up to 900 equivalents of dopamine only resulted in a *ca.* 15% quenching of the NIR emission intensity of **AuNP-Yb·38-8-HQS**, which was not sufficient for this system to act as a dopamine sensor. Considering that we had not been able to find an appropriate antenna capable of efficiently sensitising the Yb(III) metal centre, sensing the presence of dopamine and at the same time, being photostable under Xenon lamp excitation, we therefore decided to investigate the antenna Xylenol orange, **91** (**XO**).

4.9 Xylenol Orange as a Potential Antenna

XO was chosen as a potential sensitising antenna for **Yb·38** and hence **AuNP-Yb·38**, as it has previously been shown to form stable complexes with NIR emitting Ln(III) such as Yb(III) by coordination to the NIR metal centre through some or all of its pendant carboxylate groups.[191,196] Furthermore, the UV-vis absorption spectrum of **XO** has a strong pH dependency, and the pH sensitivity of the resulting systems **Yb·38-XO** and **AuNP-Yb·38-XO** could be investigated for potential biological applications. Another benefit of using **XO** as the sensitising antenna is that NIR emission from the Yb(III) metal centre could be achieved *via* excitation within the visible range at *ca.* 580 nm, whereas the UV light needed to excite visible emitting Ln(III) probes may cause damage to biological molecules and the surrounding environment.[25]



91

The indicator Xylenol orange, **XO**, has found various uses in biological application such as the detection of thiol in blood plasma. Yan and co-workers investigated a Cu(II)-**XO** species capable of the selective detection of biological thiol containing species such as cysteine and glutathione and in addition, the recognition process gave rise to a rapid visual colour change from purple-red to yellow, clearly visible to the naked eye, as depicted in Figure 4.24.[197-199]

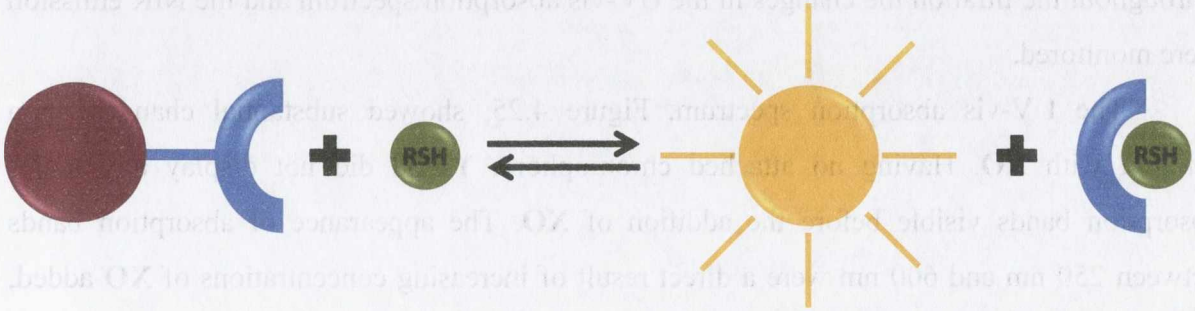


Figure 4.24: *Indicator displacement assays using Cu(II)-**XO** for the detection of thiols.*

Ishida *et al.*[200] developed a colourimetric method for the assay of ATP, using enzymatic cycling and Fe(III)-**XO** complex formation. Again, a visible colour change was observed, whereby a yellow colour indicates a low concentration of ATP and a purple colour indicates a concentration of ATP higher than the criterion of the test. The principle behind the colour change is that the pyruvate formed alongside ATP in the amplification reaction will produce hydrogen peroxide, which in turn will oxidise Fe(II) to Fe(III), shown in Equations 4.1-4.4. Fe(III) is capable of binding to **XO** with the newly formed Fe(III)-**XO** giving rise to the colour change from the unbound **XO**.

$$ATP + AMP \xrightarrow[PK]{AK} 2ADP \qquad \textbf{Equation 4.1}$$

$$ADP + PEP \longrightarrow ATP + pyruvate \qquad \textbf{Equation 4.2}$$

$$Pyruvate + O_2 + P_i \longrightarrow acetylphosphate + CO_2 + H_2O_2 \qquad \textbf{Equation 4.3}$$

$$H_2O_2 + Fe(II) + \textbf{XO} \longrightarrow Fe(III)\text{-}\textbf{XO} + H_2O \qquad \textbf{Equation 4.4}$$

The self-assembly of the luminescent ternary complexes **Yb·38-XO** and **AuNP-Yb·38-XO** were first studied in aqueous solution, followed by an investigation into the pH dependant properties of the NIR luminescent systems.

4.10 Formation and Photophysical Evaluation of Yb·38-XO and AuNP-Yb·38-XO

4.10.1 Formation of Yb·38-XO

The formation of the ternary system **Yb·38-XO** was firstly studied using the free complex. The titration of **Yb·38** with **XO** was carried out in 0.1 M HEPES buffer at pH 7.4. Throughout the titration the changes in the UV-vis absorption spectrum and the NIR emission were monitored.

The UV-vis absorption spectrum, Figure 4.25, showed substantial changes upon titration with **XO**. Having no attached chromophore, **Yb·38** did not display any major absorption bands visible before the addition of **XO**. The appearance of absorption bands between 250 nm and 600 nm were a direct result of increasing concentrations of **XO** added, with a maximum absorbance band occurring at 580 nm.

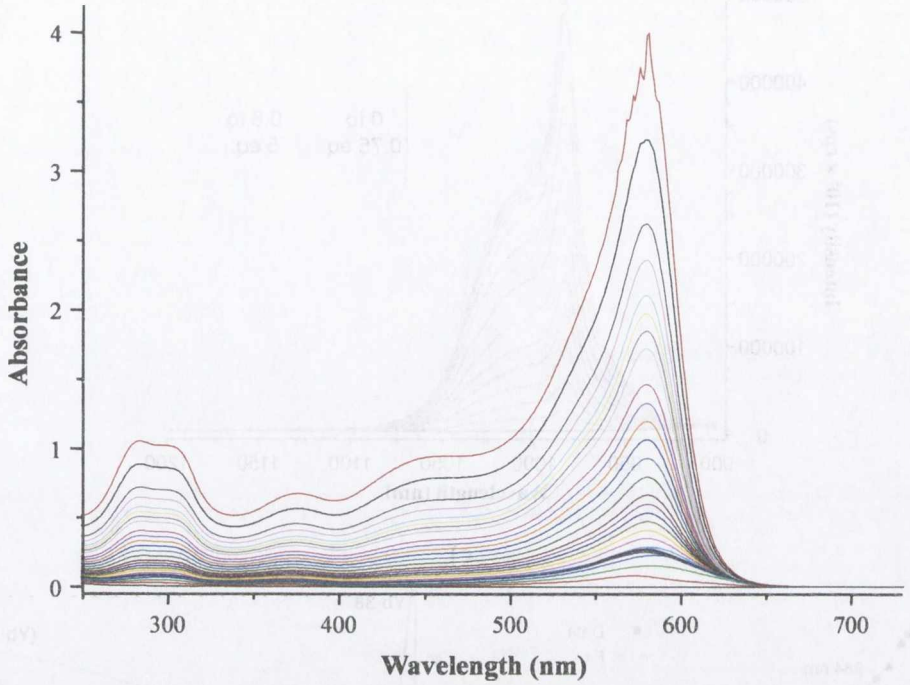


Figure 4.25: *Changes in the UV-vis absorption spectrum of* ***Yb·38*** *(1×10^{-5} M) as a function of equivalents of* ***XO*** *added at pH 7.4 in 0.1 M HEPES.*

Following the addition of **XO**, characteristic Yb(III) emission in the 900-1200 nm range, with a maximum at 985 nm and a slight shoulder at 1020 nm began to appear upon excitation at the visible wavelength of 580 nm, confirming that sensitised NIR emission had indeed occurred, Figure 4.26. The emission can be said to be "switched on" by the addition of **XO**, with the emission intensity being higher than that observed when the antenna **tta** was titrated against the same complex, indicating that **XO** was a more efficient sensitiser for **Yb·38** than **tta**.

The changes observed in the maximum at 985 nm were plotted against the equivalents of **XO** added, of which the increase in the NIR emission at 985 nm reached a maximum at the addition of 0.5 equivalents of **XO** before decreasing in intensity. This was in comparison to the **tta** titration, whereby a plateau was reached at *ca.* 1 equivalent of **tta**, as depicted in the inset in Figure 4.9. Unlike **tta**, the antenna **XO** possesses four carboxylic groups and was capable of binding to the Yb(III) metal centre *via* several different binding modes.

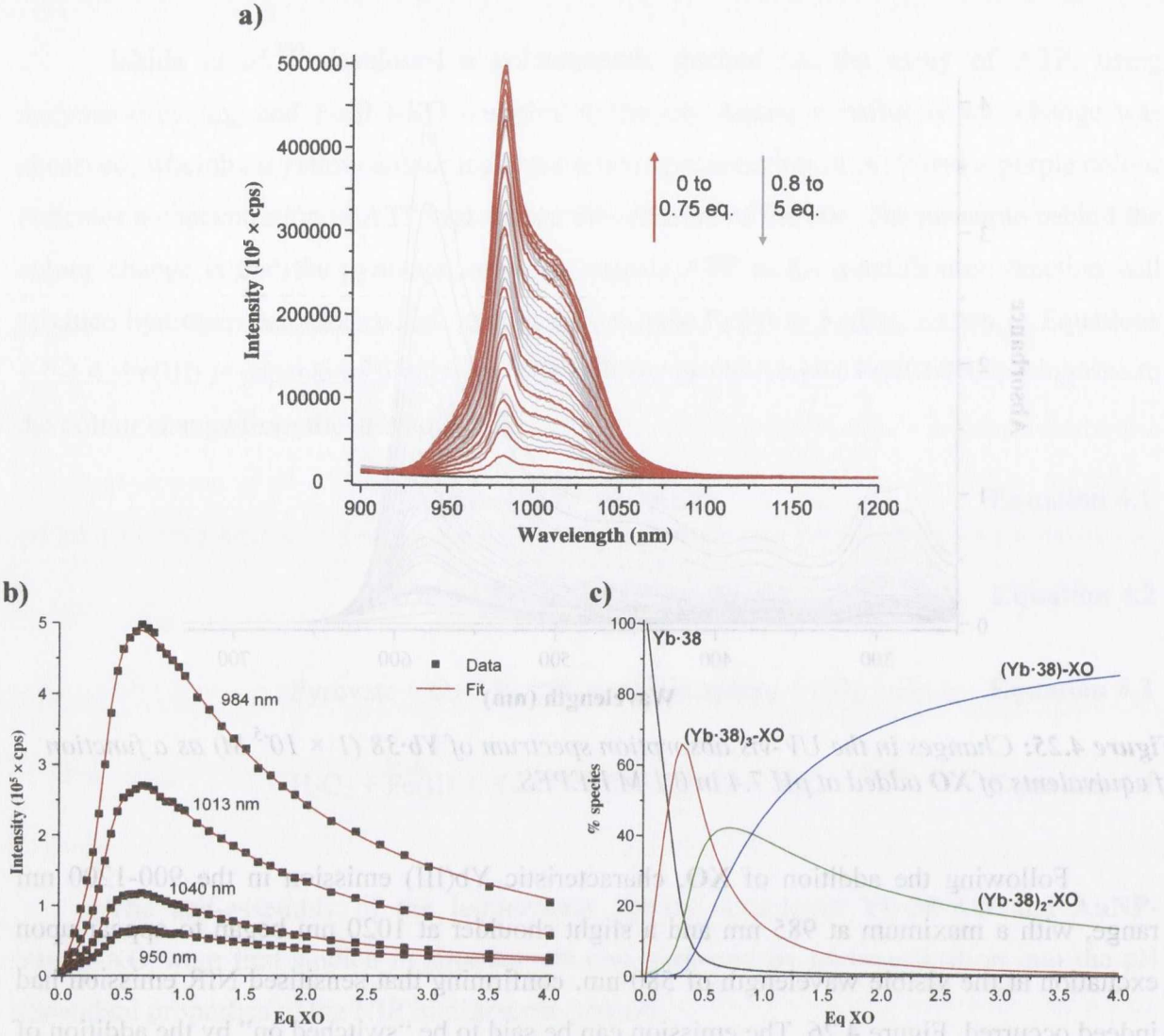


Figure 4.26: a) *The evolution of the Yb(III) NIR emission of* ***Yb·38*** *(1×10^{-5} M) (λ_{ex} = 580 nm) as a function of equivalents of* ***XO*** *added at pH 7.4 in 0.1 M HEPES.* ***b)*** *Experimental binding isotherms for the Yb(III) NIR emission of* ***Yb·38*** *upon titration with* ***XO*** *(λ_{ex} = 580 nm) in HEPES buffer and their corresponding fits using SPECFIT.* ***c)*** *Speciation-distribution diagram obtained from the fit.*

Non-linear least squares analysis of the data using SPECFIT (carried out by Dr. Steve Comby), Figure 4.26b and c showed the successive formation of 3:1, 2:1 and 1:1 **Yb·38:XO** species with log β of 19.7 ± 0.1, 13.48 ± 0.07 and 7.02 ± 0.05, respectively. The results from the titration suggest that one **XO** was binding to two **Yb·38** complexes in solution and that the latter species was the most emissive. Further addition of **XO** after 0.5 equivalents results in a decrease in Yb(III) emission intensity, possibly due to the formation of less emissive species in solution.

4.10.2 Formation of AuNP-Yb·38-XO

Having verified that **Yb·38** can form a ternary complex with **XO**, it was next investigated whether the same 2:1 **Yb·38**:**XO** ternary complex would be formed upon attachment of **Yb·38** to the surface of **AuNPs**. A titration was carried out on **AuNP-Yb·38**

adding increasing equivalents of **XO** in 0.1 M HEPES buffer at pH 7.4 and the UV-vis absorption spectrum and NIR emission were monitored throughout.

The UV-vis absorption spectrum showed similar changes to those observed for the complex **Yb·38** with the appearance and increase of absorption bands between 250 nm and 620 nm resulting from the increasing concentration of **XO** in solution, shown in Figure 4.27. Unlike previous antenna titrations on **AuNP-Yb·38**, the SPR band of the **AuNPs** was not visible and was masked by the intense absorption bands of **XO**.

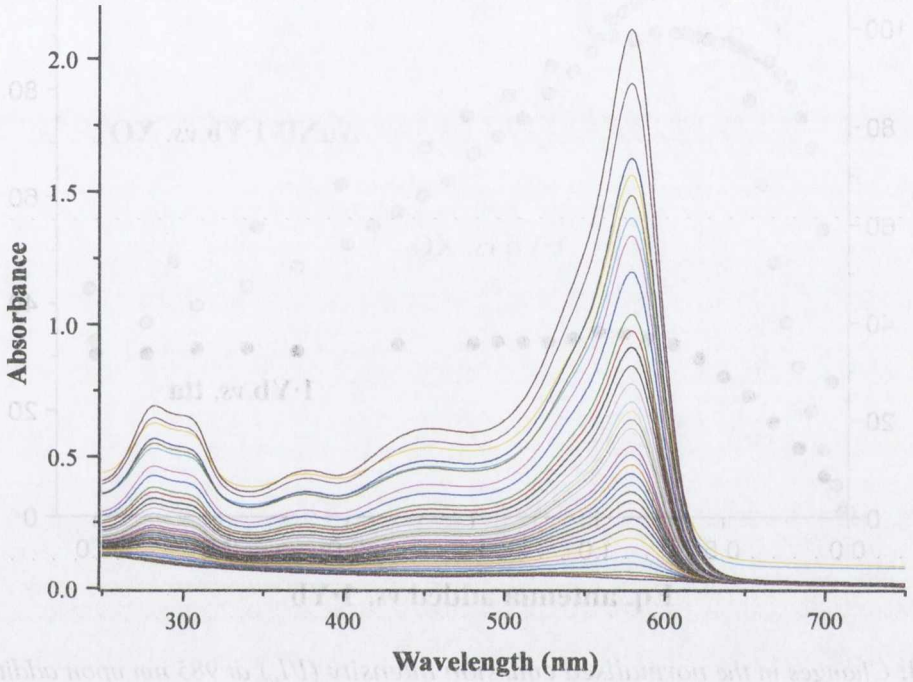


Figure 4.27: *Changes in the UV-vis absorption spectrum of* ***AuNP-Yb·38*** *(1×10^{-7} M) as a function of equivalents of* ***XO*** *(0→700 equivalents) (5×10^{-7} M → 5×10^{-5} M) added at pH 7.4 in 0.1 M HEPES.*

The NIR emission spectrum of **AuNP-Yb·38** was of very low intensity before the addition of **XO** as had been previously observed. The addition of **XO** resulted in characteristic Yb(III) NIR emission upon excitation into the **XO** antenna at the visible wavelength of 580 nm, Figure 4.28. The binding isotherm obtained from the titration is shown in Figure 4.28 and depicts a rapid emission enhancement within the addition of *ca.* 30 (± 10) equivalents of **XO**, followed by a slower enhancement between 30-60 equivalents after which it levels off until 120 equivalents and thereafter the emission is quenched. Given that it has been determined that there was *ca.* 120 **Yb·38** complexes per **AuNP**, it suggests that the **XO** was binding to the **Yb·38** complexes on the **AuNP** in a 4:1 (**Yb·38**:**XO**) ratio. This was not observed in the study of the complex alone, a possible explanation being that the **Yb·38** complexes attached to the **AuNP** surface are in closer proximity to each other than they would be in solution and therefore are in such a position that one **XO** molecule can access and bind

to four **Yb·38** complexes. In comparison to the unbound complex, **Yb·38**, only minor changes occurred in the Yb(III) emission intensity at higher equivalents (*ca.* 50-120) of **XO**, which demonstrates the formation of a self-assembly between **Yb·38** and **XO** on the gold surface, which was found to be stable of a period of several months.

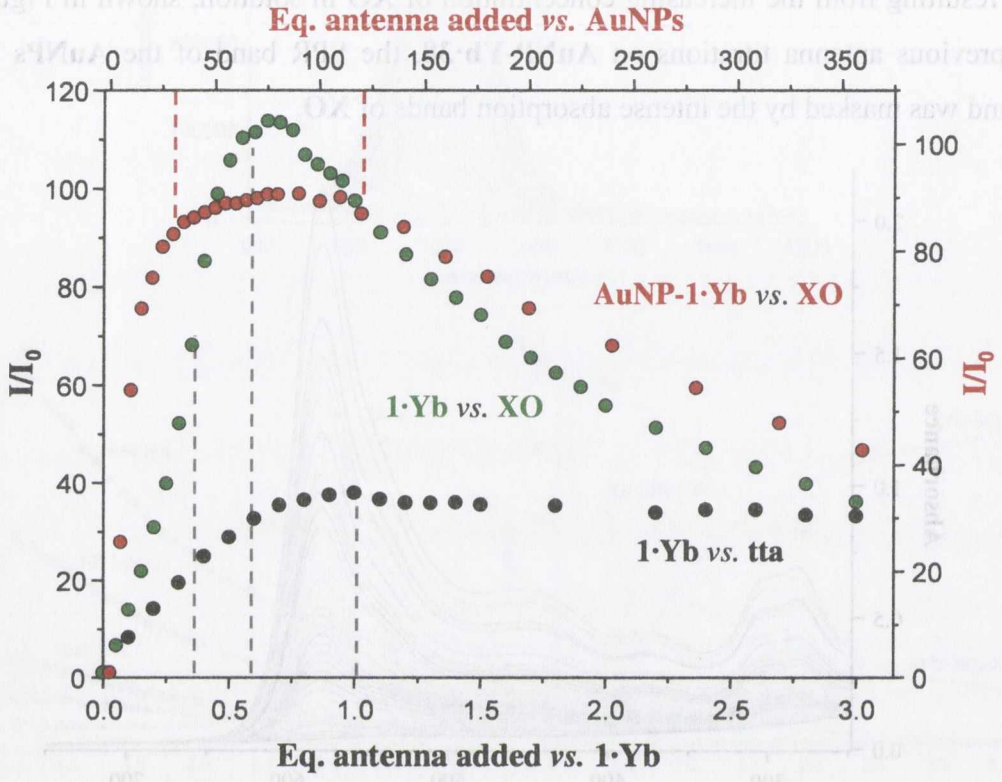


Figure 4.28: *Changes in the normalised emission intensity (I/I_0) at 985 nm upon addition of* ***tta*** *to* ***Yb·38*** *(black) and* ***XO*** *to* ***Yb·38*** *(green) or to* ***AuNP-Yb·38*** *(red, top-right scale).*

It was confirmed by an excitation spectrum that it was indeed the energy transfer from the **XO** antenna centred at *ca.* 580 nm that was efficiently sensitising the Yb(III) metal centre of **AuNP-Yb·38** as it matched closely to that of the UV-vis absorption spectra, shown in Appendix A4.15.

4.10.3 Determination of Quantum Yields for Yb·38 and AuNP-Yb·38

To quantify the Yb(III) emission from the ability of the **XO** antenna to sensitise the NIR-emitting Yb(III) ion, the quantum yields of **Yb·38-XO** and **AuNP-Yb·38-XO** complexes (prepared *in situ* in aqueous buffered solution) have been determined upon antenna excitation at 580 nm. The NIR emission quantum yields were found to be 0.20 ± 0.03% and 0.036 ± 0.005% for **Yb·38-XO** and **AuNP-Yb·38-XO**, respectively.

These values are sizeable compared to the published literature data,[192] particularly in aqueous solution, where the presence of proximate O-H oscillators often induces considerable quenching for ions having a small energy gap between their excited and ground states, which

is typically the case of NIR-emitting Ln(III) ions. Also, it was observed that the value for **AuNP-Yb·38-XO** was five times smaller than that of the unbound complex, signifying some quenching by the **AuNP** surface. Having established that **XO** was a suitable Yb(III) sensitiser and moreover, can form stable ternary complexes with **Yb·38**, both on and off the surface of **AuNPs**, the next stage was to evaluate the pH dependent properties of the ternary system and explore its applications as a consequence of its pH dependency.

4.11 pH Dependency of XO, Yb·38-XO and AuNP-Yb·38-XO

The antenna **XO** is also known as a pH indicator; where in pH 7.4 solution the chromophore absorbs with a maximum at 580 nm, being blue-shifted to 435 nm at pH 4.5, with striking purple to yellow colour changes that are clearly observed to the naked eye. Bearing this in mind, pH titrations were carried out on **XO**, **Yb·38-XO**, and **AuNP-Yb·38-XO** and compared over a pH range of pH 2-11 in 0.1 M NaCl solution to maintain a constant ionic strength.

4.11.1 pH Dependency of XO

The pH dependency of the absorption of **XO** was first investigated in order to be able to compare its pH behaviour independently, as the ternary system **Yb·38-XO** and finally as a ternary complex on the surface of **AuNPs**, **AuNP-Yb·38-XO**.

The changes in the ground state of **XO** as a function of pH are shown in Figure 4.29, and illustrates that the absorbance spectrum of **XO** was highly pH dependent. In acidic conditions, **XO** displayed an absorption maximum centred at 434 nm with a smaller band centred at 270 nm. The spectrum remained relatively unchanged until pH 5, where further basification to physiological pH gave rise to a substantial hypochromic shift in the absorbance band centred at 434 nm with the concomitant appearance of a strong absorption band centred at 580 nm. The band at 270 nm also experienced a slight bathochromic shift to 290 nm. Basification to pH 11 resulted in a further hyperchromic shift of the 580 nm absorbance band and complete disappearance of the 434 nm band. Pseudo isosbestic points were observed at 490 nm, 320 nm and 280 nm throughout the titration, signifying the presence of more than one species in solution.

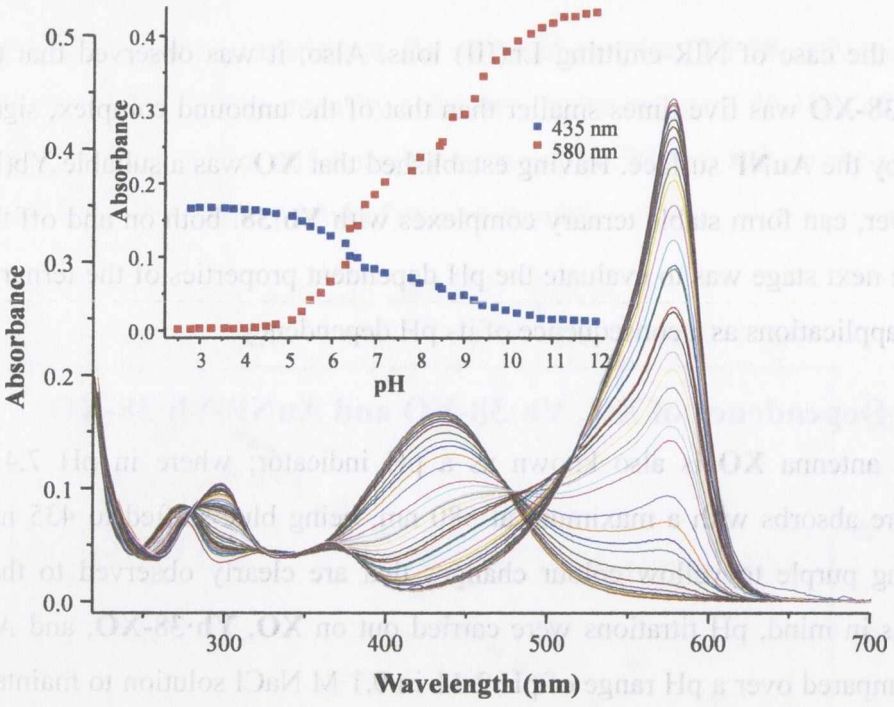


Figure 4.29: *Changes in the UV-vis absorption spectrum of* ***XO*** *(1×10^{-5} M) between pH 2-11 in 0.1 M NaCl. Inset: Changes in the absorbance at 435 nm and 580 nm as a function of pH.*

The changes at the main absorbance bands, with maximum centred at 435 nm and 580 nm, when plotted against pH, did not give rise to simple sigmoidal shape curves and as such could not be fit using Origin® to determine a pK_a value. The complicated curves obtained arise from the relatively large number of possible protonation and deprotonation sites that **XO** contains within its structure, such as the two tertiary amines and four carboxylic acid and two hydroxy groups. What can be ascertained from these curves is that the majority of changes, and hence the protonation/deprotonation events, take place between pH 5 and pH 10.

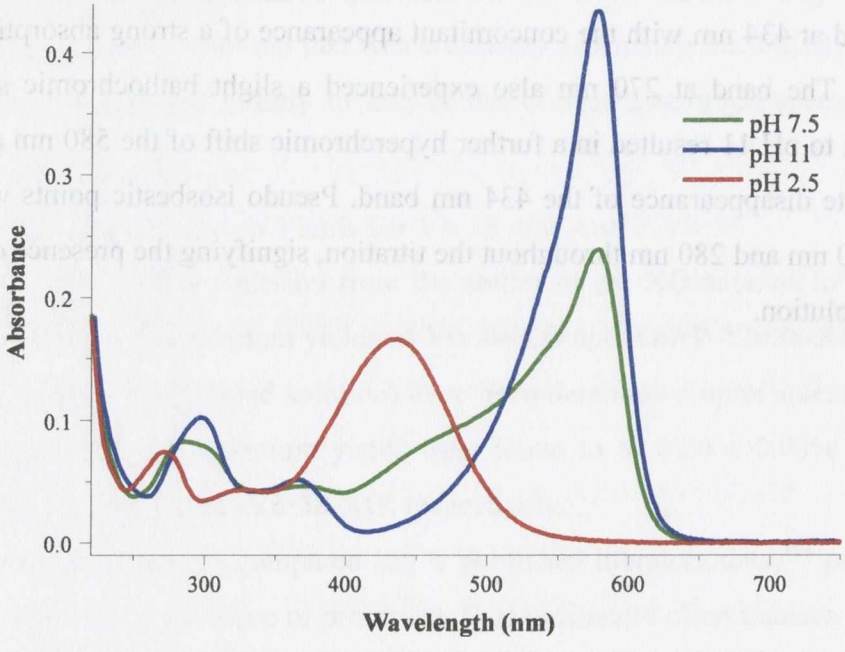


Figure 4.30: *The UV-vis absorption spectrum of* ***XO*** *(1×10^{-5} M) at pH 2.5, 7.5 and 11.*

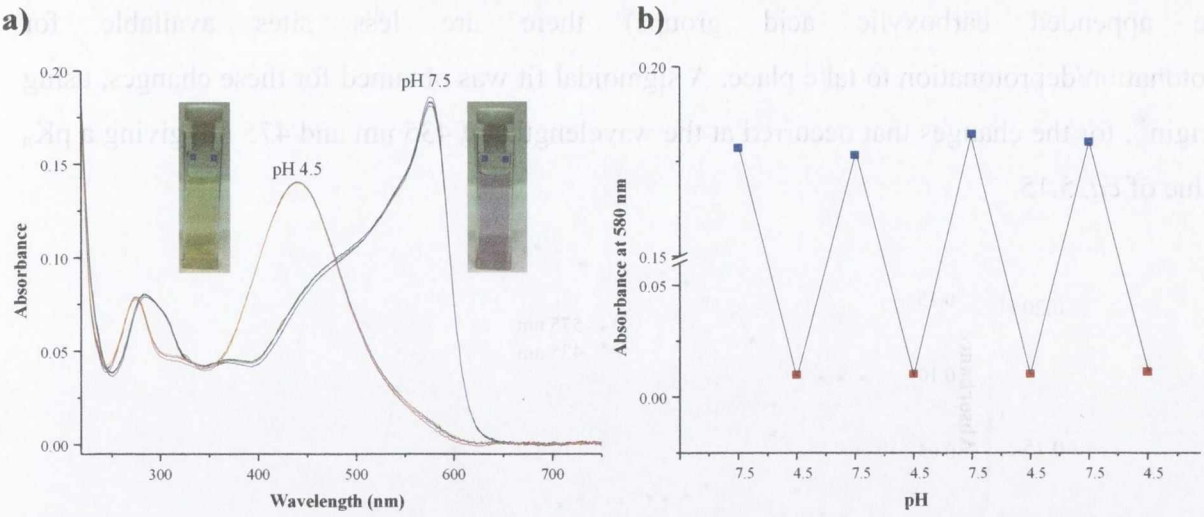


Figure 4.31: a) *Reversible changes in the UV-vis absorption spectrum of* ***XO*** *(1×10^{-5} M) and the corresponding colour change observed at pH 4.5 and 7.5.* ***b)*** *Reversible changes in the absorbance at 580 nm between pH 4.5 and 7.5.*

The reversibility of the pH dependency of the absorbance spectrum was also investigated by repeated cycles of adjusting the pH from pH 4.5 to pH 7.5. Each time the same spectrum was obtained when the pH was switched between pH 4.5 and pH 7.5, Figure 4.31, with simultaneous colour change from yellow to purple also occurring each time, inset in Figure 4.31a.

The changes in the singlet excited state, using an excitation wavelength of 435 nm, was also monitored as a function of pH and are shown in Appendix A4.16. The fluorescence emission of **XO** was found to be very weak over the entire pH range and as such was not monitored for the subsequent titrations involving **Yb·38-XO** and **AuNP-Yb·38-XO.**

4.11.2 pH Dependency of Yb·38-XO

The pH dependent behaviour of the ternary complex **Yb·38-XO** was next investigated, using a 2:1 solution of **Yb·38**:**XO** as it had previously been established that one **XO** molecule can bind to two **Yb·38** complexes. The changes in both the ground state and Yb(III) excited state were monitored between pH 2-11.

The changes in the UV-vis absorption spectrum were very similar to those observed for **XO** alone, Figure 4.32. At low pH the ternary system displays two absorbance bands, at 435 nm and a smaller one at 270 nm. Basification of the solution causes a large hypochromic shift of the band centred at 435 nm with concurrent hyperchromic shift of a strong new absorbance band centred at 575 nm. The plot of absorbance against pH for the two bands at 435 nm and 575 nm is shown in the inset in Figure 4.32 and indicates that the changes are occurring over a narrower pH window (pH 4.5-7) than seen for **XO** alone, Figure 4.29. One possible explanation for this is that upon **XO** binding to the Yb(III) metal centre (by some of

the appended carboxylic acid groups) there are less sites available for protonation/deprotonation to take place. A sigmoidal fit was obtained for these changes, using Origin®, for the changes that occurred at the wavelengths of 435 nm and 475 nm giving a pK_a value of *ca.* 5.15.

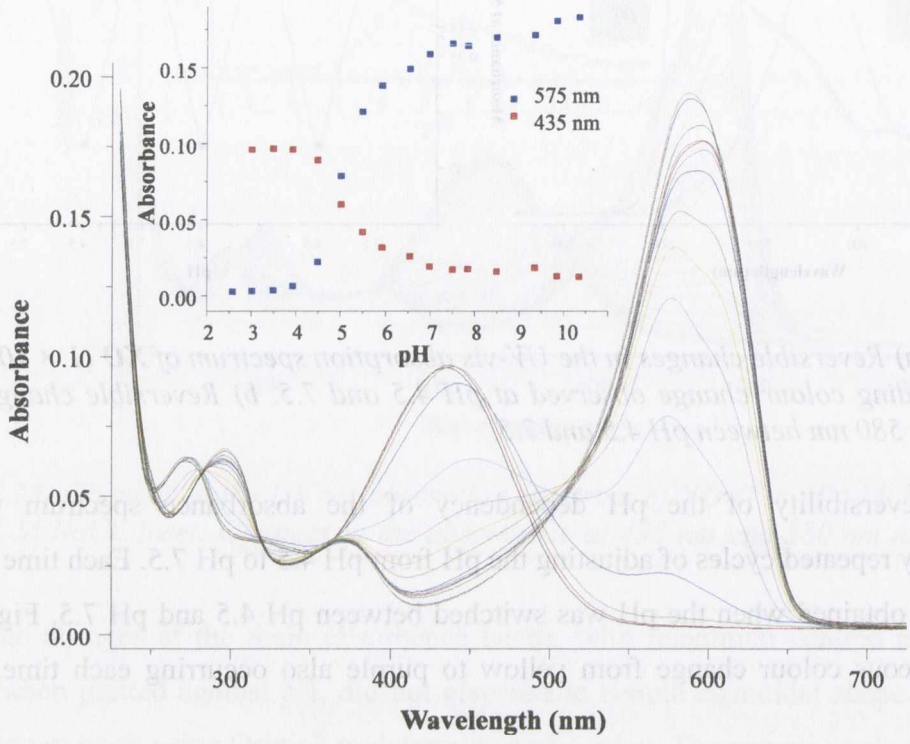


Figure 4.32: *Changes in the UV-vis absorption spectrum of* ***Yb·38-XO*** *(1×10^{-5} M) between pH 2-11 in 0.1 M NaCl. Inset: Changes in the absorbance at 435 nm and 575 nm as a function of pH.*

The NIR emission intensity arising from the energy transfer from **XO** to the Yb(III) metal centre was also examined as a function of pH between pH 2-11 upon excitation of the 2:1 **Yb·38**:**XO** ternary system at 580 nm, with the resulting spectra shown in Figure 4.33. In acidic pH below pH 4 very little or no NIR emission was observed and the Yb(III) emission can be described as being "switched off". It is possible that protonation of the carboxylic acid moieties at such low pH prevents the **XO** from binding to the Yb(III) metal centres and as such no sensitisation and hence no NIR emission, occurs. Increasing the pH from pH 4 to pH 7 by the addition of base to the solution gave rise to "switching on" of the Yb(III) emission, as the carboxylic acid moieties were no longer protonated and could now bind to the Yb(III) metal centre. Maximum emission intensity occurred at pH 7 with a *ca.* 30 fold increase in intensity observed when the pH was adjusted from pH 4 to 7. Further basification from pH 7 to 11 caused no significant changes in the emission intensity, and furthermore, it remained "switched on" in highly basic media, verifying the stability of the ternary complex at basic pH.

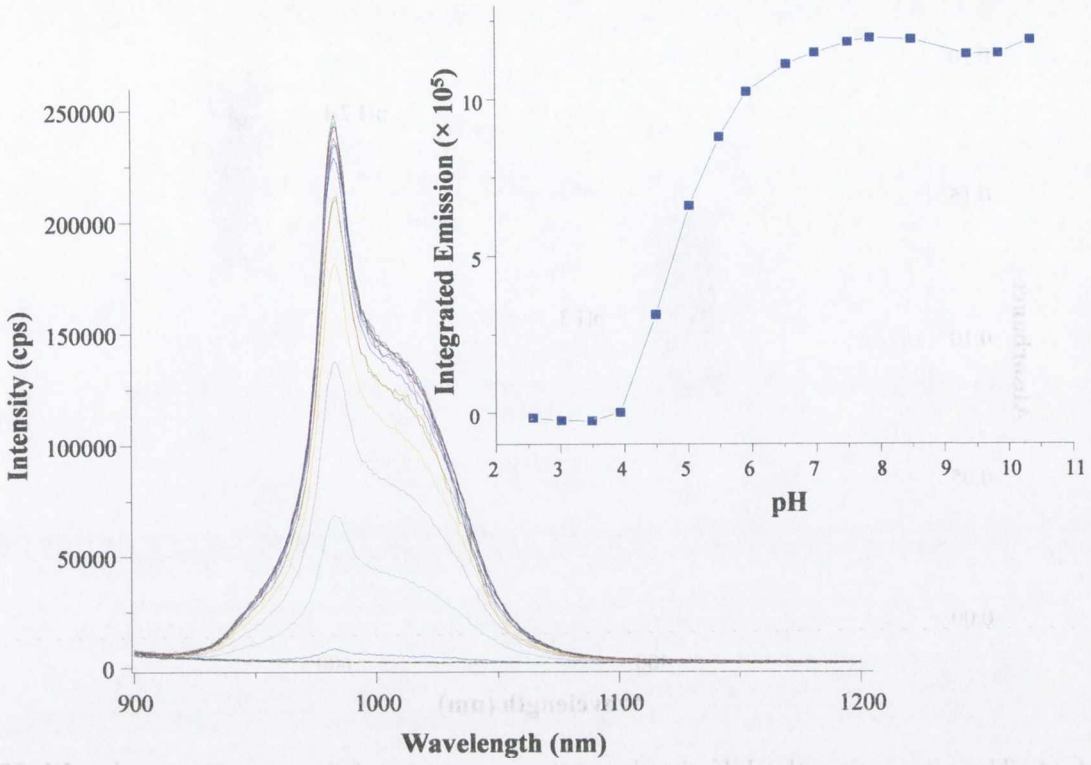


Figure 4.33: *The changes in the Yb(III) NIR emission of* ***Yb·38-XO*** *(ca. 1 × 10^{-5} M) (λ_{ex} = 580 nm) between pH 2-11 in 0.1 M NaCl. Inset: Changes in the integrated NIR emission as a function of pH.*

Having investigated the pH dependency of the ground and Yb(III) excited state of the ternary complex **Yb·38-XO**, the next step was to evaluate the reversibility of the changes at pH 3 and 7.4 and hence, if reversible "on/off switching" could be achieved.

The changes in the UV-vis absorption spectrum as the pH was adjusted from pH 3 to 7.4 are shown in Figure 4.34. In acidic pH the two main bands observed were centred at 435 nm and 270 nm. Changing the pH to 7.4 resulted in a somewhat different UV-vis absorption spectrum consisting of three bands with maxima centred at 290 nm, 370 nm and 580 nm, respectively. Altering the pH between pH 3 and 7.4 repeatedly resulted in the same spectrum being obtained at the respective pH value with coinciding colour change of the solution from yellow to blue, shown as inset. This colour change was different in comparison to the yellow to purple colour observed in the pH titration of the free **XO**.

The reversibility of the system was further investigated by monitoring the changes in the NIR emission of **Yb·38-XO**. As shown in Figure 4.35 the Yb(III) emission was at its maximum at pH 7.4 and was considerably quenched when acidified to pH 3 due to the possible dissociation of the ternary complex. Cycling the pH between pH 3 and 7.4 did not appear to be detrimental to the formation of the ternary complex as the NIR signal was "switched on" without the loss of measureable emission intensity each time the pH was readjusted to pH 7.4.

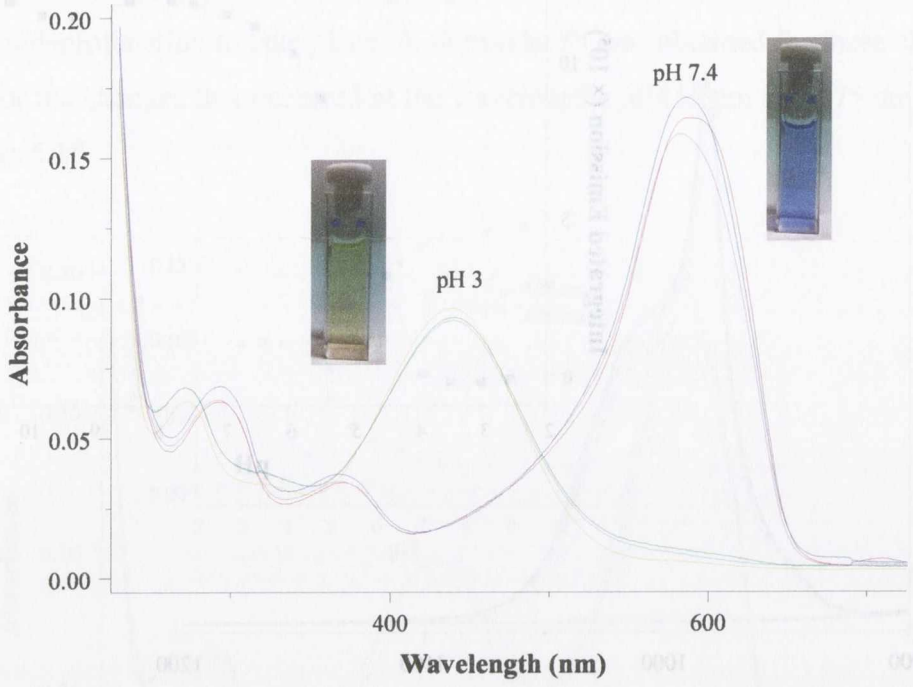


Figure 4.34: *The changes in the UV-vis absorption spectrum of the ternary complex* ***Yb·38-XO*** *(ca. 1 × 10^{-5} M) and the corresponding colour change observed at pH 3 and 7.4 upon repeatedly "switching" between these two pH values.*

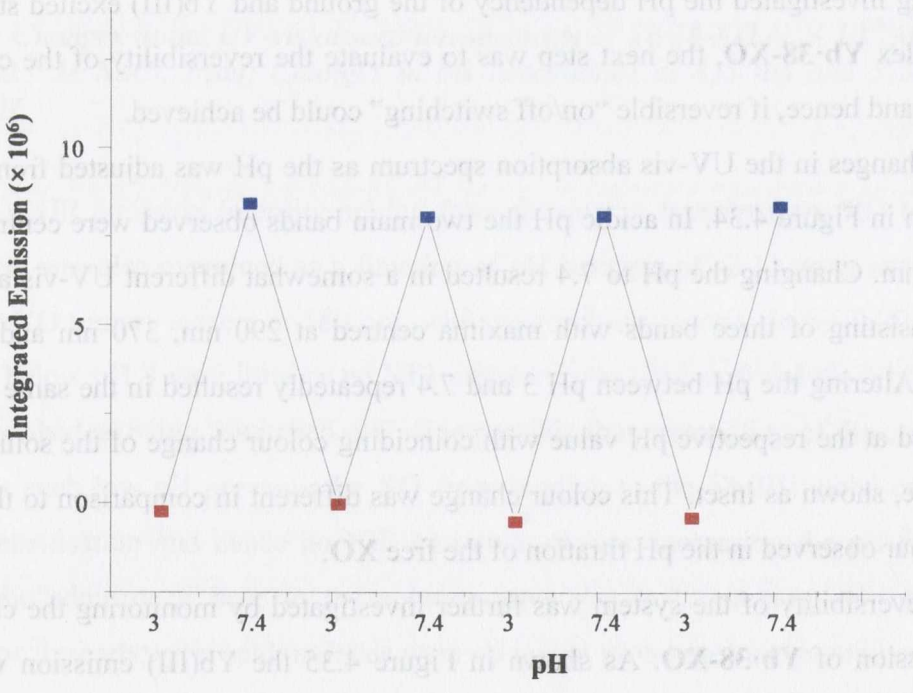


Figure 4.35: *Reversibility of the "on/off switching" behaviour of the Yb(III) centred emission of* ***Yb·38-XO*** *(ca. 1 × 10^{-5} M) at pH 7.4 and 3.*

4.11.3 pH Dependency of AuNP-Yb·38-XO

Having determined that the "on/off switching" of the NIR emission of the ternary complex **Yb·38-XO** can occur at pH 3 and 7.4, it was next investigated whether this pH behaviour would remain unchanged once **Yb·38** was bound to the surface of **AuNPs**, with subsequent formation of the ternary system by the addition of 30 equivalents of **XO** to **AuNP-Yb·38**. As above, the pH titration was carried out over the pH range 2-11 in 0.1 M NaCl solution, whereby the changes in both the absorption and the NIR emission of **AuNP-Yb·38-XO** were observed.

In acidic conditions the main absorbance band in the UV-vis absorption spectrum was centred at 430 nm with a slight shoulder observable at 300 nm. Upon basification of the solution results in a large hypochromic shift of the 430 nm band with concurrent appearance of a strong absorption band centred at 600 nm. This band was slightly red shifted by *ca.* 20 nm from that observed with **XO** and **Yb·38-XO** above. Furthermore, the effect on the SPR band of the **AuNPs** cannot be monitored as it was overlapped by the absorption bands of **XO**.

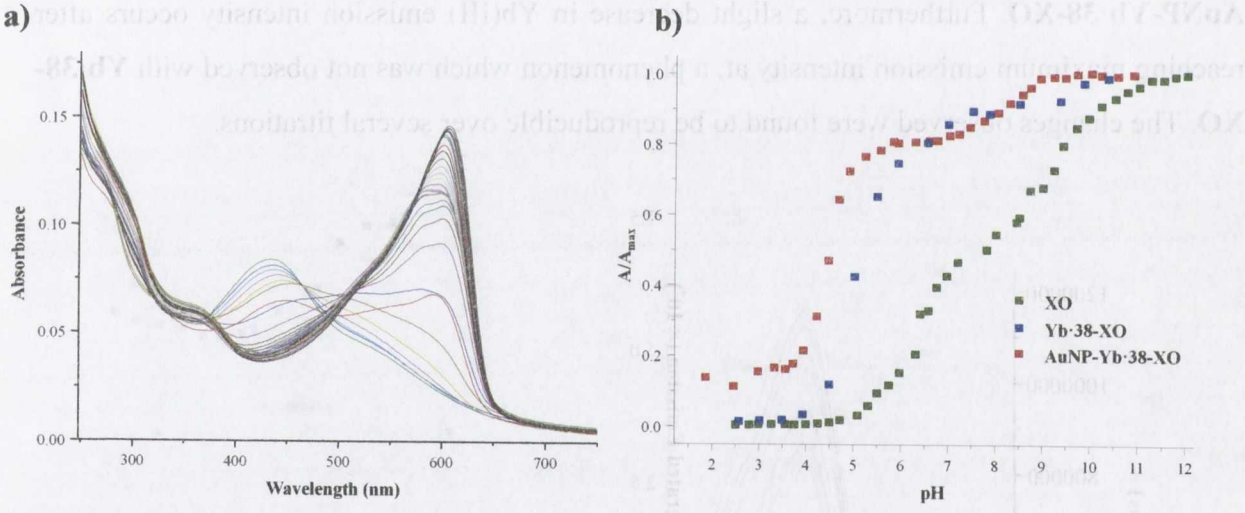


Figure 4.36: a) *Changes in the UV-vis absorption spectrum of* ***AuNP-Yb·38-XO*** *(1×10^{-7} M) between pH 2-11 in 0.1 M NaCl.* ***b)*** *Changes in the absorbance maximum of free* ***XO***, ***Yb·38-XO*** *and* ***AuNP-Yb·38-XO*** *as a function of pH; for the sake of comparison, absorbance's have been normalised by their maximum.*

In the UV-vis absorption spectrum the overall changes mirrored that seen for both **XO** alone and the ternary system **Yb·38-XO**, Figure 4.36. However, as shown in Figure 4.36b there are clear differences in the pH-profiles, where in the case of **AuNP-Yb·38-XO** the main changes occur within the pH range of 4-6. This was most likely due to the fact that upon binding to Yb(III), there are fewer available protonation sites in **XO**. This was confirmed by the results of previously discussed studies on **Yb·38-XO**, which showed similar pH dependent changes as shown for **AuNP-Yb·38-XO**.

It was also observed that the pK_a of **Yb·38-XO** and **AuNP-Yb·38-XO** appeared to be shifted to more acidic regions indicating direct coordination of **XO** to the Yb(III) metal centre occurred.

The changes observed in the Yb(III) emission spectrum were also examined as a function of pH and clearly demonstrate the formation of a highly pH dependent self-assembly on the surface of **AuNPs** upon excitation at 580 nm, with the Yb(III) emission being "switched off" in highly acidic pH (2-4) and "switched on" after pH 4, as illustrated in Figure 4.37. The main areas of change in the NIR emission in relation to pH can be described as occurring over 4 possible pH windows; between pH 2-4 the Yb(III) emission was "switched off" followed by a sharp increase in intensity between pH 4-5.5. The Yb(III) emission intensity then remains relatively constant from pH 6-10 and increases again from pH 10-11, Appendix A4.17. This behaviour was marginally different than that of the ternary system **Yb·38-XO** unattached to the **AuNP** surface. **Yb·38-XO** possesses a maximum emission intensity at pH 7 in comparison to a maximum obtained at the more acidic pH of 4.5-5.5 for **AuNP-Yb·38-XO**. Furthermore, a slight decrease in Yb(III) emission intensity occurs after reaching maximum emission intensity at, a phenomenon which was not observed with **Yb·38-XO**. The changes observed were found to be reproducible over several titrations.

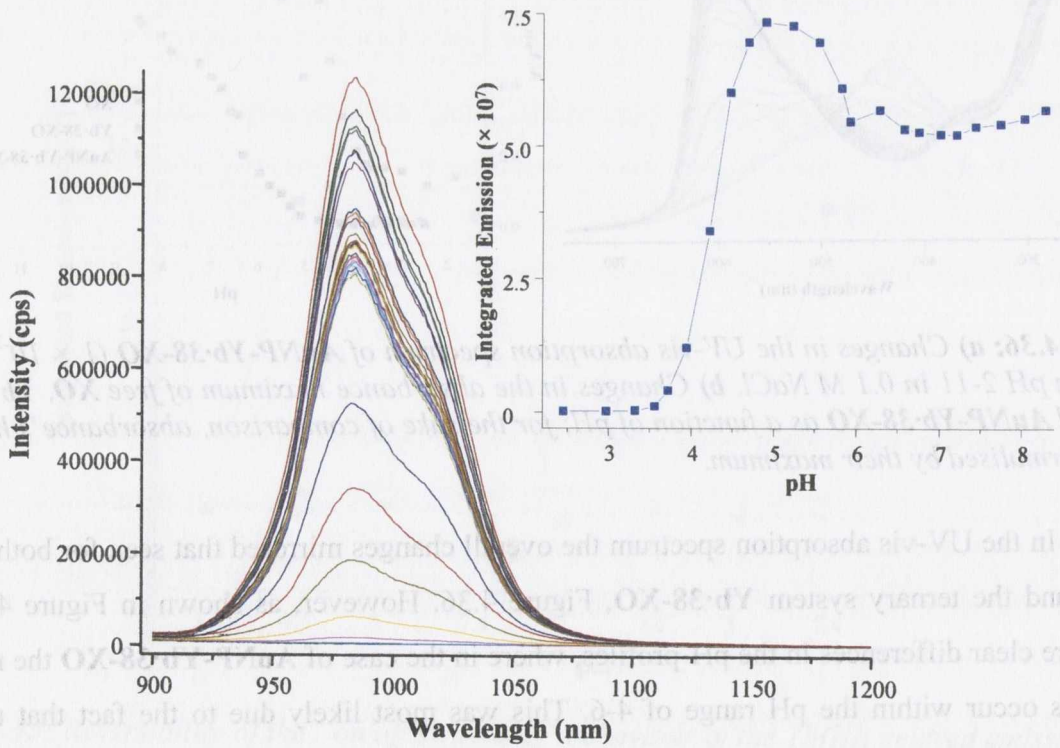


Figure 4.37: *The changes in the Yb(III) NIR emission of* ***AuNP-Yb·38-XO*** *(1×10^{-7} M) (λ_{ex} = 580 nm) between pH 2-11 in 0.1 M NaCl. Inset: Changes in the integrated NIR emission as a function of pH.*

It was clear from the modulations in the NIR emission intensity that changing the pH can greatly affect the ability of the antenna to efficiently populate the $^2F_{5/2}$ Yb(III) excited state and that attachment to the gold surface, while it does not affect the "on/off" behaviour, has an effect on the pH dependent properties of the Yb(III)-centred emission.

Having established the pH dependent properties of **AuNP-Yb·38-XO** and compared them to that of **Yb·38-XO** and free **XO**, it was necessary to determine the reversibility of the behaviour in the UV-vis absorption and more importantly, the "on/off" luminescence switching of the Yb(III) metal centre, in other words, to determine whether the ternary complex will remain stable after several pH cycles from neutral (pH 7.4) to acidic pH (pH 3).

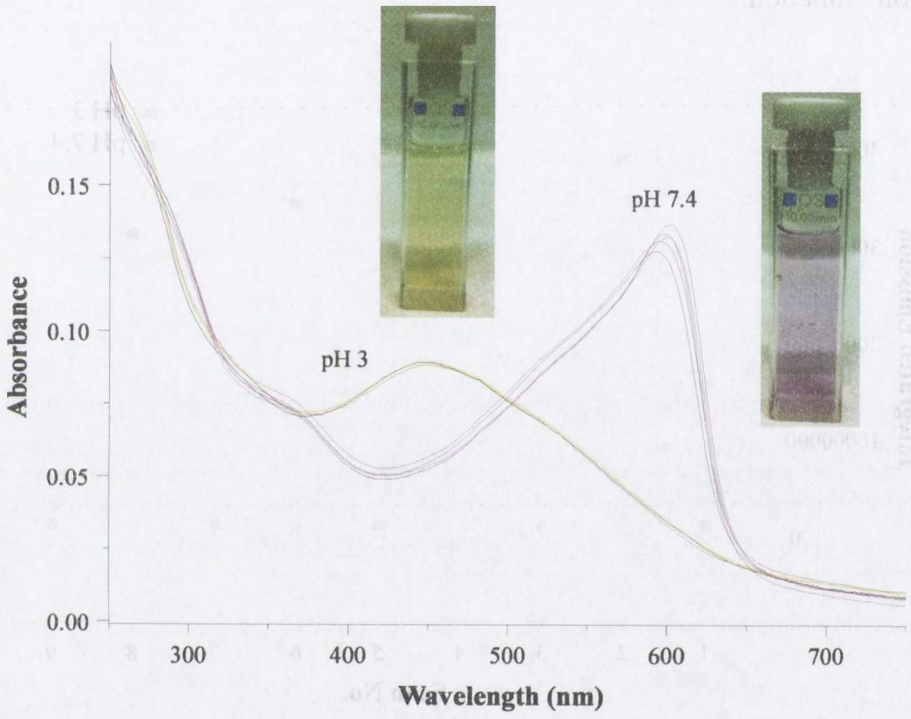


Figure 4.38: *Reversible changes observed in the UV-vis absorption spectrum of* ***AuNP-Yb·38-XO*** *(1×10^{-7} M) and the corresponding colour change observed at pH 3 and 7.4.*

As had previously been demonstrated for **XO** and **Yb·38-XO**, the changes in the absorbance of **AuNP-Yb·38-XO** were found to be fully reversible during repeated cycles of adjusting the pH from pH 3 to pH 7.4. Each time the same spectrum was obtained when the pH was adjusted back to either pH 3 or pH 7.4, Figure 4.38, with simultaneous colour change from yellow to blue also occurring each time, in comparison to the yellow to purple colour change observed in the case of unbound **XO**.

The reversibility of the **AuNP** system was further explored by examining the changes in the NIR emission arising from **AuNP-Yb·38-XO**. As shown in Figure 4.39 the Yb(III) emission output was "switched off" at acidic pH (pH 3). Basification to neutral pH of 7.4 gives rise to the "switching on" of the Yb(III)-centred luminescence upon excitation at 580 nm. Consequently, it was investigated whether the NIR emission could be repeatedly "switched on-off" as a function of pH. The results found for several cycles, recording the emission at pH 3 and 7.4 each time, are shown in Figure 4.39, demonstrating that the NIR signal was switched on less than 10% loss of emission intensity after the four complete cycles. Therefore, **AuNP-Yb·38-XO** can function as a supramolecular NIR luminescent pH switch with an "off-on" function.

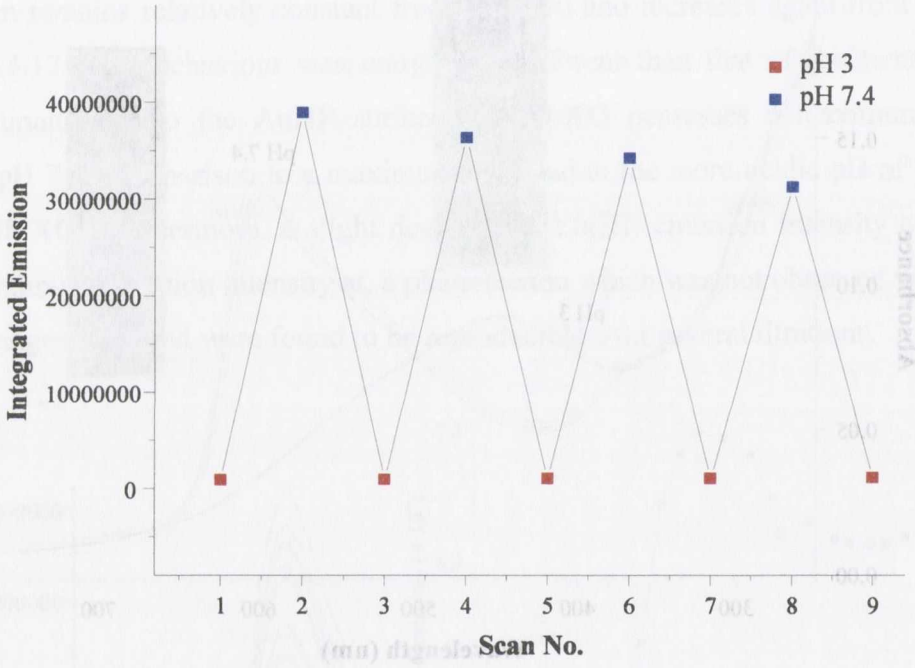


Figure 4.39: *Reversibility of the "on/off switching" behaviour of the Yb(III) centred emission of* ***AuNP-Yb·38-XO*** *(1×10^{-7} M) at pH 7.4 and 3.*

4.12 Aluminium Sensing

With the maximum Yb(III) emission intensity from **AuNP-Yb·38-XO** occurring at acidic pH (*ca.* 4.5), possible applications for this system would be the detection of aluminium at acidic pH so as to prevent the formation and precipitation of Al(III) hydroxide groups that would usually occur pHs higher than pH 5.5. Moreover, the three charges present on the Al(III) ion should cause the cation to interact strongly with the carboxylic acid moieties of **XO**.

Interest into the development of aluminium sensors has escalated substantially in recent times, as a result of increasing knowledge regarding the potential toxic effects of this element.[201] Al(III) is very abundant in nature and has long been recognised as a neurotoxic agent.[201] While normal day-to-day levels of Al(III) have not been known to cause cases of poisoning, there has been reports linking Al(III) exposure to certain neurological disorders such as Alzheimer's disease.[202] The Al(III) that we encounter on a daily basis is found in food and drinking water. In food, Al(III) appears to be bound to other substances and as such, is not capable of being absorbed into the bloodstream, however, studies have shown that the Al(III) present in water in μM concentrations can be absorbed, to a certain extent, by animals and humans.[203] Thus, very sensitive sensors are required with low detection limits. Bearing this in mind it was decided to examine the potential of the water soluble ternary system **AuNP-Yb·38-XO** to function as an Al(III) sensor.

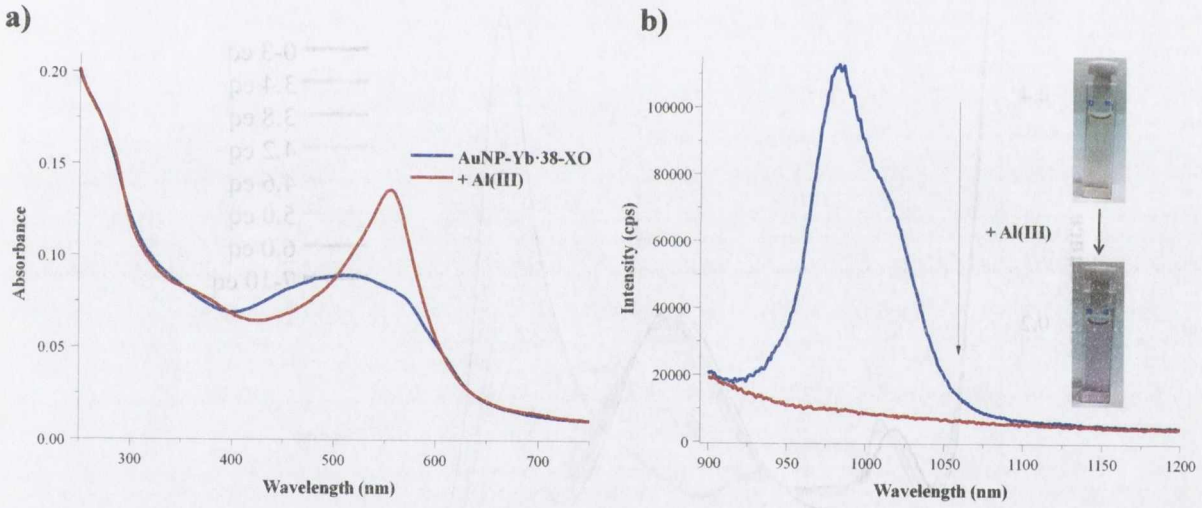


Figure 4.40: *Changes in the* ***a)*** *UV-vis absorption spectrum and* ***b)*** *NIR emission spectrum (λ_{ex} = 580 nm) of* ***AuNP-Yb·38-XO*** *upon addition of Al(III) with corresponding colour change.*

A screening test was carried out on a sample of **AuNP-Yb·38-XO** at pH 4.5 upon addition of $Al(ClO_4)_3$. Before the addition of Al(III), the Yb(III) emission of **AuNP-Yb·38-XO** was relatively high and the UV-vis absorption spectrum consisted of a main band with a maximum centred at *ca.* 500 nm, Figure 4.40. The addition of Al(III) caused complete quenching of the Yb(III) NIR emission and the UV-vis absorption transition centred at 500 nm was red shifted to 580 nm. From this quick test it was clear that the presence of Al(III) had a significant influence on the photophysical properties of **XO**, and therefore on the Yb(III)-centred emission of **AuNP-Yb·38-XO**.

In light of these findings, to test the sensing ability of **XO** towards Al(III), a titration was carried out on free **XO**, adding in increasing equivalents of $Al(ClO_4)_3$ in buffered solution at pH 4.7. The observed changes in the UV-vis absorption spectrum are shown in Figure 4.41. Before the addition of Al(III) two main transitions in the absorption spectrum were visible at 430 nm and 270 nm. The addition of up to three equivalents of Al(III) caused only minor changes to be observed; a small bathochromic shift by *ca.* 10 nm occurred in the absorption band centred at 430 nm with a band centred at 550 nm beginning to appear concomitantly. The next addition gave rise to more changes which appeared to cause some kinetic effect as the scan had to be repeated several times over the period of 30 minutes before the spectrum ceased to change. This phenomenon was repeated each time an addition of Al(III) was added until *ca.* 7 equivalents of Al(III) was added. At this stage the absorption spectrum was significantly altered to the initial spectrum, having absorption bands centred at 285 nm, 370 nm and 555 nm.

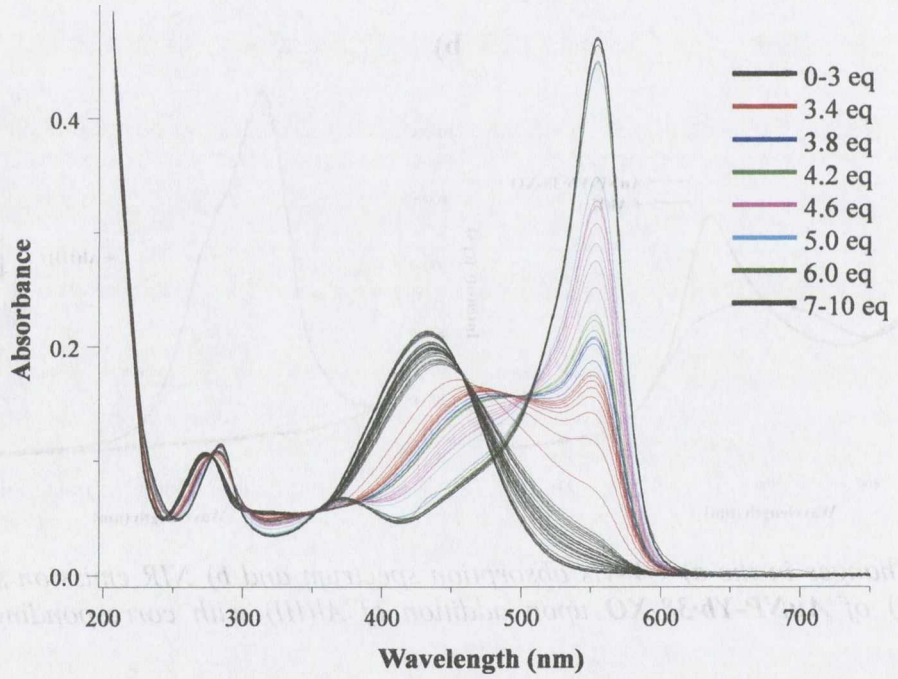


Figure 4.41: *Changes in the UV-vis absorption spectrum of* ***XO*** *(1×10^{-5} M) at pH 4.7 upon titration with Al(III).*

It was evident that there was very little changes between **XO** and Al(III) at the beginning of the titration from 0-3 equivalents of Al(III) added. This could be possibly due to the slow interaction between **XO** and Al(III) to form the 2:1 species $\mathbf{XO}_2$:Al. Increasing the equivalents of Al(III) could give rise to a shift in equilibrium towards the 1:1 **XO**:Al(III) species which could also account for the kinetic instability that was observed.[204] The number of possible species that exist between the pH range of 3.5-4.7 are depicted in Table 4.2.[204]

Table 4.2: *Binding constants of Al(III) with* ***XO*** *over a pH range.*[204]

Reaction	Species	Log K (σ_{fit})
$Al^{3-} + XO^{6-}$	Al-XO^{3-}	7.45 (0.015)
$H^{+} + Al\text{-}XO^{3-}$	Al-H-XO^{2-}	5.14 (0.015)
$H^{+} + Al\text{-}H\text{-}XO^{2-}$	Al-XO_2^{9-}	5.22 (0.038)

It can also be noted that the binding constants determined by Ghasemi and co-workers for the Al-**XO** species are relatively low (log K = *ca.* 6). Bearing all of these complications in mind it was decided not to further test the sensing ability of **AuNP-Yb·38-XO** towards Al(III), which would instead remain to function as an "on/off" pH sensitive NIR emissive switch.

4.13 Conclusion

The initial work described in this Chapter was concerned with the design and synthesis of a novel NIR emitting **AuNP** system. Yb(III) was chosen as the NIR emitting Ln(III) and incorporated into a cyclen based framework that was appended by three acetamide arms and twelve carbon alkyl chain terminated by a thiol group in order to facilitate adsorption of the Yb(III) complex, **Yb·38**, onto the surface of **AuNPs**. Successful synthesis of **Yb·38**, was followed by functionalisation of **AuNPs**, the formation of which was achieved by a modified Brust-Schiffrin method without the need for intermediate DMAP stabilised **AuNPs**. This involved direct functionalisation of the toluene solubilised **AuNPs** with an aqueous solution of **Yb·38** yielding the water soluble **AuNP** system **AuNP-Yb·38**. Analysis by TEM and DLS verified the presence of monodisperse **AuNPs** with an average diameter of 8 nm.

AuNP-Yb·38, possessing no antenna incorporated within its framework, combined with the presence of two metal bound water molecules, was photophysically silent and the incorporation of an external antenna was essential if Yb(III)-centred emission was to be obtained. The β-diketonate **tta** was chosen as the antenna and it has been shown to be suitable for the sensitisation of NIR emitting Ln(III) and can bind to the Ln(III) metal centre *via* the diketonate moiety.[192] Titrations of **tta** against both the complex **Yb·38**, and the **AuNP** system **AuNP-Yb·38** revealed the formation of a 1:1 ternary system of **Yb·38**:**tta**, both on and off the **AuNP** surface, where *ca.* 120 **Yb·38** complexes were found to occupy the gold surface.

Having determined that the formation of the ternary complex **Yb·38-tta** occurs in aqueous solution, both off and on the **AuNP** surface, the systems were evaluated for their ability to act as a NIR luminescent sensor for the biologically important neurotransmitter dopamine through modulation of the Yb(III) metal centred emission. It was found that the

addition of dopamine resulted in an almost complete quenching of the NIR signal. Moreover, selectivity over other biologically abundant anions such as ascorbate, citrate, carbonate and phosphate was achieved. However, it was discovered that the stability of the **tta** system in aqueous solution was problematic under continuous excitation by the Xenon lamp. A titration involving only the addition of HEPES buffer showed a similar decrease in emission intensity to that observed after the addition of dopamine, in other words, the majority of the quenching observed was attributed to the photodegradation of the **tta** antenna. From these findings it was clear that **tta** was not a suitable antenna for the sensing of dopamine using NIR emitting Yb(III) and as such other suitable antennae has been investigated in the following section.

The antenna **8-HQS** was briefly studied as a potential antenna. Although it was found to form photostable ternary complexes, **Yb·38-8-HQS**, on the **AuNP** surface, no significant changes were observed upon addition of dopamine.

The next antenna chosen was the colourimetric agent Xylenol orange. It has previously been shown to form stable complexes with Yb(III) *via* coordination to the NIR metal centre through its appended carboxylic acid groups.[191,196] Moreover, NIR emission from the Yb(III) metal centre could be achieved *via* excitation of **XO** in the visible range at *ca.* 580 nm. Formation of the self-assembly of **Yb·38** and **XO** at the **AuNP** surface was investigated as a function of pH as **XO** is a known pH indicator and depending on the dissociation of the protons in the structure, the spectrum of **AuNP-Yb·38-XO** varies with the pH of the solutions. Colourimetric changes were also observed where the **XO** solution was yellow at pH 3 and purple at pH 7.4.

To conclude, this Chapter describes the first example of a NIR emitting Yb(III)-based **AuNP** system **AuNP-Yb·38-XO** and furthermore, that the NIR emission can be reversibly and reproducibly switched "on" and "off" as a function of pH.

Chapter 5

Lanthanide Based Langmuir Blodgett Films

5. Introduction

Recent advances in supramolecular assemblies incorporating Ln(III) ions, in particular functional nanomaterials, have been aimed towards the development of systems capable of molecular recognition and sensing and extending to areas such as catalysis and optical devices.[38,205] As it has been discussed in previous Chapters, Ln(III) are desirable in the construction of supramolecular sensing systems owing to their unique photophysical properties such as their long lived excited states and sharp, line like emission bands.[20,206,207] The incorporation of luminescent Ln(III) complexes into biological or materials based applications often requires immobilisation onto solid substrates for practicality. The sensing of substrates using immobilised Ln(III) can be achieved by the adsorption of appropriate Ln(III) based complexes onto nanoparticles such as **AuNPs**,[117] as was discussed in Chapter 4 or alternatively onto flat surfaces such as flat gold films[125] or by forming thin film monolayers using Langmuir Blodgett (LB) techniques.[208] This Chapter aims to extend the use of LB films and Ln(III) chemistry by combining the areas of Ln(III) luminescent sensing and the formation of LB films and therefore a description of the LB technique will be given in the following sections.

The formation of a thin film by an array of different oils at an air-water interface was first reported by Irving Langmuir in 1917.[209] In his investigation he postulated that within the same molecule or structure, certain parts of it would be attracted to water while other parts would have an attraction towards oil. Moreover, he stated that the dispersion of oil on the surface of water was due to the existence of an "active group" within the molecule. By collaboration with Katherine Blodgett the applicability of the oil/water thin films was expanded to the attachment of these thin monolayers to solid substrates, which became known as Langmuir-Blodgett films.[210,211] Later, in the 1960's and 1970's, Hans Kuhn used LB methods to control the position and orientation of functional molecules within complex assemblies, a discovery which lead to extended interest in applications LB film chemistry over recent decades.[212] In the extensive study of Langmuir films that has ensued in recent decades, a number of factors have been established that are essential if a molecule is to successfully form a monolayer at an air-water interface.

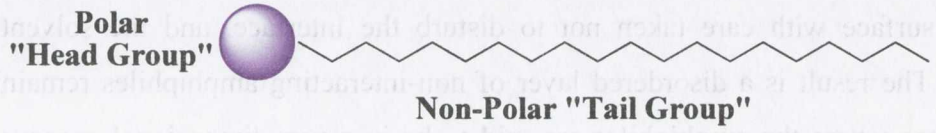


Figure 5.1: *Illustration of a molecule suitable for the formation of Langmuir films.*

As depicted in Figure 5.1, the molecule must contain a hydrophobic long alkyl chain (tail group) and an active hydrophilic "head group" capable of intermolecular interaction with the water subphase.[213] Chemical groups that are commonly encountered as head groups are those which possess a dipole moment >1 and include acid, alcohol, nitro and amine groups. These organic molecules, possessing both polar and non-polar counterparts (for example fatty acids) are known as surfactants or amphiphiles and will orient themselves at the surface interface of water in a manner which minimises their free energy.[213] The subsequent surface film formed is one molecule in thickness and is referred to as a monolayer. One component that needs to be taken into consideration in the design of Langmuir suitable molecules is the hydrophilic/hydrophobic ratio within the molecule as this will determine whether successful monolayer formation will occur.[213] For instance, a molecule possessing a large polar head group will need a larger tail group to compensate. Other factors such as temperature and alkyl chain length must also be taken into account when generating an ideal phase transition surface pressure-area isotherm as a monolayer's characteristics are highly dependent on these two parameters.

a) **b)**

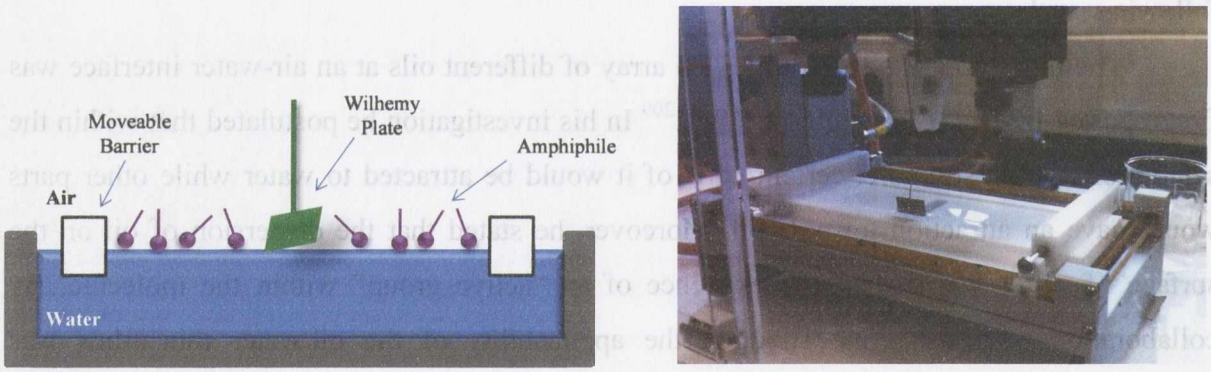


*Figure 5.2: **a)** Simplified illustration of a Langmuir trough containing movable barrier, amphiphile spread onto the surface and Wilhelmy plate. **b)** Langmuir trough used courtesy of Prof. Martin Albrecht (UCD) for all Langmuir studies carried out in this Chapter.*

The apparatus used for the formation of monolayers is known as a Langmuir trough and is illustrated above in Figure 5.2. To form a monolayer on the surface of water the amphiphile is dissolved in a water immiscible solution, usually $CHCl_3$ or hexane, at a concentration of *ca.* 2×10^{-4} M (0.5 mg per mL).[214] The solution (20 μL) is slowly added onto the water surface with care taken not to disturb the interface, and the solvent is left to evaporate. The result is a disordered layer of non-interacting amphiphiles remaining on the water surface where the amphiphiles are said to be in a two dimensional gaseous state (G). The moveable barriers of the Langmuir trough are then slowly compressed (6 mm/min) and

the amphiphiles on the water surface begin to undergo a series of phase transformations, which may be identified by monitoring the surface pressure (mN/m) as a function of the area ($Å^2$) occupied by these molecules. The surface pressure (π) of the water is monitored by means of a Wilhelmy Pt(II) plate and is defined as the difference in surface tension of the clean surface (γ_o) to the surface tension of the surface in the presence of the floating amphiphile monolayer (γ) ($\pi = \gamma_o - \gamma$).[213]

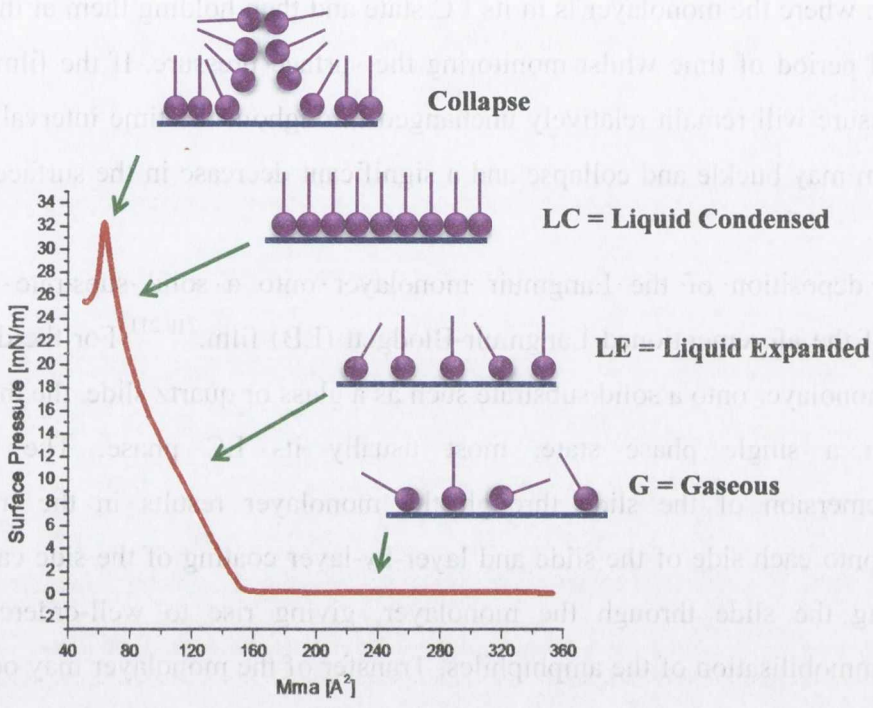


Figure 5.3: *Surface pressure-area isotherm indicating the different phase changes (gaseous (G), liquid expanded (LE), liquid condensed (LC) and collapse of an ideal Langmuir monolayer).*

Before compression, and indeed in the early stages of compression, the monolayer is in its gaseous phase (G), whereby there is sufficient spacing between amphiphiles on the water surface such that they exhibit little force on one another and the change in surface pressure is negligible. As compression of the barriers continues the hydrophobic hydrocarbon chains begin to orientate away from the water subphase and concomitantly, the hydrophilic head groups interact with the water subphase, giving rise to the liquid expanded phase (LE). The molecular area occupied by the monolayer is reduced and this occurrence is verified by an increase in the surface pressure-area isotherm, as shown in Figure 5.3. As the molecular area is increasingly reduced by further compression of the barriers, the liquid condensed (LC) phase of the monolayer may be observed. In this state, the ever decreasing area occupied by the monolayer causes the amphiphiles to become closely packed together; with the hydrocarbon chains all orientating away from the water surface and the polar head groups

interacting with the water surface. At this stage, the monolayer is one molecule thick and is referred to as a Langmuir monolayer, the area of which may be acquired by extrapolation of the surface pressure-area isotherm. If the barriers continue to move inward beyond this point, over compression of the LC state occurs, which results in the collapse or cracking of the film and can be identified by a sharp decrease in the surface pressure.

The stability of a monolayer, in its LC state, can be measured by adjusting the barriers to a position where the monolayer is in its LC state and then holding them at that position for an extended period of time whilst monitoring the surface pressure. If the film is stable, the surface pressure will remain relatively unchanged throughout the time interval. However, an unstable film may buckle and collapse and a significant decrease in the surface pressure will be observed.

The deposition of the Langmuir monolayer onto a solid substrate results in the formation of the aforementioned Langmuir-Blodgett (LB) film.[210,211] For the deposition of a Langmiur monolayer onto a solid substrate such as a glass or quartz slide, the monolayer must be held in a single phase state, most usually its LC phase. The slow vertical immersion/emersion of the slide through the monolayer results in the transfer of the monolayer onto each side of the slide and layer-by-layer coating of the side can be achieved by redipping the slide through the monolayer, giving rise to well-ordered and highly structured immobilisation of the amphiphiles. Transfer of the monolayer may occur by one of two ways depending on the hydrophobicity/hydrophilicity of the solid substrate. In the case of hydrophilic substrates, the slide is lowered below the water subphase before the formation of the monolayer.

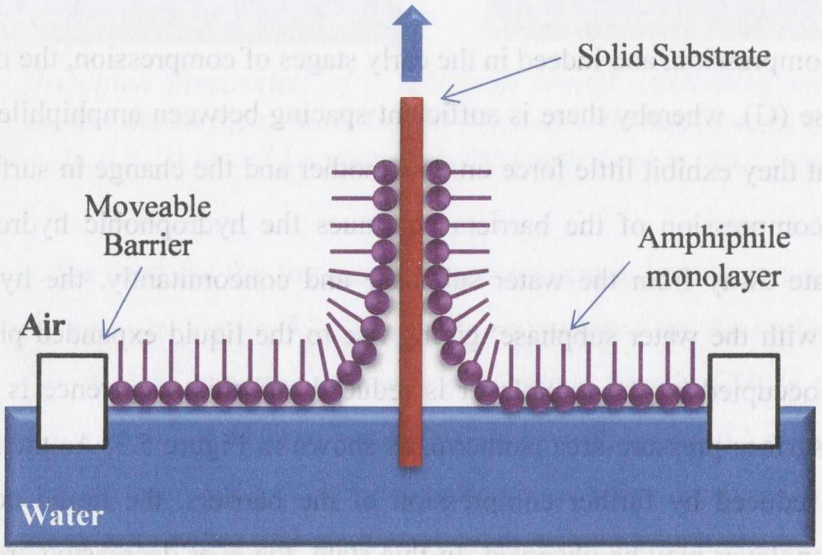


Figure 5.4: *Deposition of monolayer onto solid substrate as it is passed upward through the air-monolayer interface.*

Removal of the slide transpires by means of an upward stroke whereby the monolayer attaches *via* hydrophilic interactions between the polar head groups and slide, as shown in Figure 5.4. In contrast, hydrophobic coated slides remain suspended above the subphase/monolayer interface and a downward stroke of the slide results in attachment of the hydrophobic chains to the slide upon submersion. The type of deposition depicted above in Figure 5.4 is the most common form of monolayer deposition and is known as Y-type. In this case, the deposited monolayer stacks in a head-to-head and tail-to-tail pattern on each time it passed through the monolayer/air interface. Alternatively, transfer of the monolayer onto the substrate can occur only on insertion or removal of the substrate resulting in X-type (transfer of monolayer on downward stroke only) and Z-type (transfer of monolayer on upstroke only), as shown in Figure 5.5. The deposition mode is not strictly limited to these three types and the type of deposition may change as more and more layers are added to the substrate.

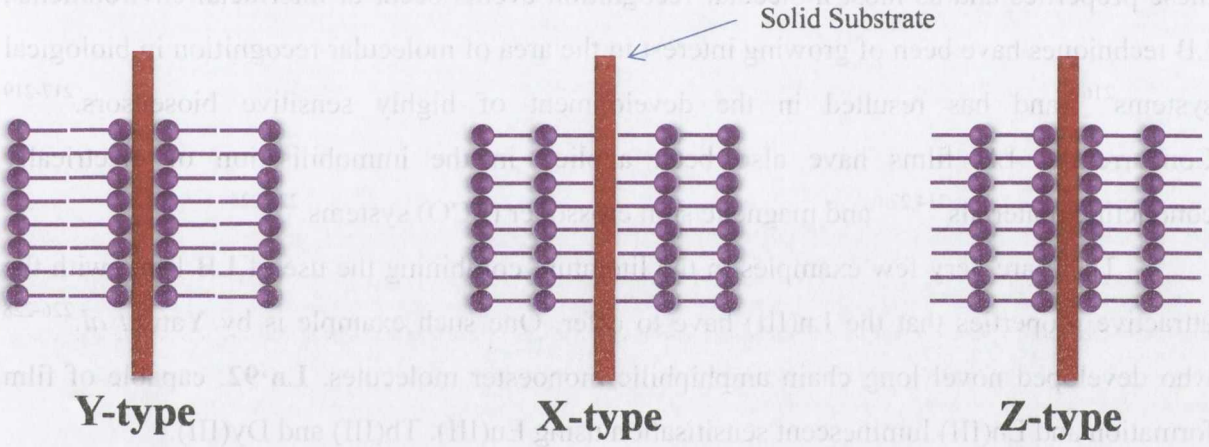


Figure 5.5: *Y-type, X-type and Z-type deposition of Langmuir monolayers/films onto a solid substrate resulting in LB films.*

Characterisation of the transfer of the monolayer from the water/air interface onto the solid substrate is achieved by measurement of the deposition ratio (τ), also known as the transfer ratio. This value is obtained from the area occupied by the monolayer on the water surface when held at a constant pressure (A_L) divided by the coated area of the solid substrate (A_S), as shown in Equation 5.1.[213] Ideally, the transer ratio should not fall outside the range of 0.95-1.05 to ensure high quaity transfer from interface to solid substrate. Any value not within this range implies poor film homogeneity.

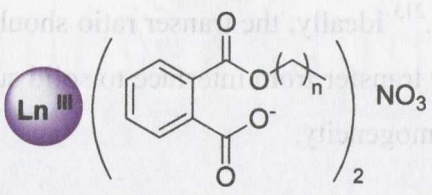
$$\tau = \frac{A_L}{A_S}$$ **Equation 5.1**

One final factor concerning successful monolayer transfer is the deposition speed; the rate at which the substrate is lowered/raised through the subphase. Lowering the substrate into the subphase can occur at higher speeds than raising it from the subphase without having much affect on the monolayer transfer. Upon withdrawl of the substrate it is essential that the substrate is not raised faster than the rate at which water drains from the solid. The average speed of the substrate is between 10 μm s^{-1} to a few mm s^{-1}. Furthermore, it is important to allow the film to dry in air before redipping to continue the deposition cycle.

Attachment of amphiphilic monolayers incorporating Ln(III) onto solid supports as LB films falls under the area of Ln(III) -based luminescent hybrid materials.[38,215] LB films possess advantages over other solid matrix immobilisation techniques, mainly the ability to process molecules in the form of thin films, the parameters of which can be accurately controlled, including layer number, deposition type and even molecule amount. Owing to these properties and as most molecular recognition events occur at interfacial environments, LB techniques have been of growing interest in the area of molecular recognition in biological systems[216] and has resulted in the development of highly sensitive biosensors.[217-219] Concurrently, LB films have also been applied in the immobilisation of electrically conducting materials[214,220] and magnetic spin crossover (SCO) systems.[221-225]

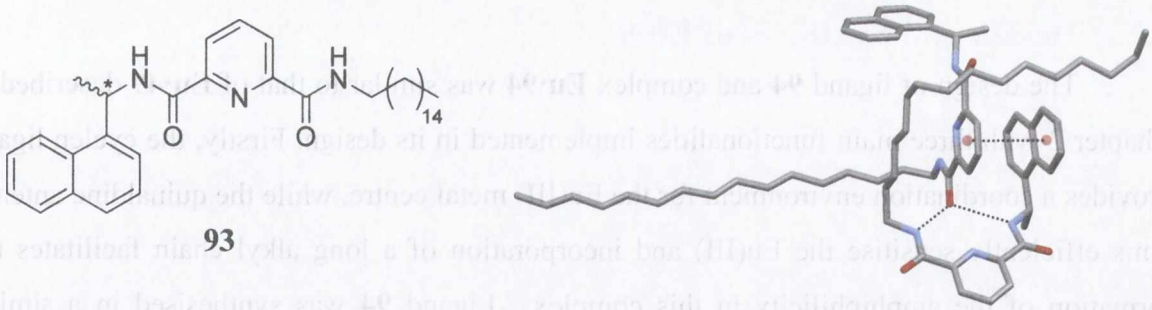
There are very few examples in the literature combining the use of LB films with the attractive properties that the Ln(III) have to offer. One such example is by Yan *et al.*[226-228] who developed novel long chain amphiphilic monoester molecules, **Ln·92**, capable of film formation and Ln(III) luminescent sensitisation using Eu(III), Tb(III) and Dy(III).

A total of nine Ln(III) complexes were synthesised and it was demonstrated that deposition of solutions of **Ln·92** in $CHCl_3$ onto a subphase of water with subsequent evaporation of the organic solvent resulted in the successful formation of LB films by the vertical deposition method using Z-type transfer. Luminescence measurements showed that the long chain phthalate ligands can sufficiently sensitise the Tb(III) and Dy(III) films, whereas the Eu(III) LB film did not give rise to detectable Eu(III) luminescence.



n = 15, 17, 19

Ln·92



93

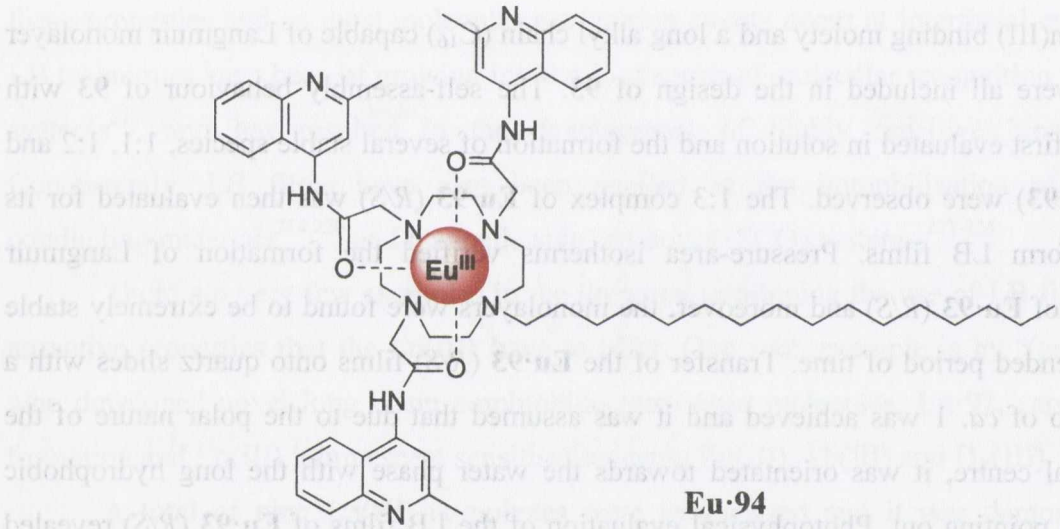
Figure 5.6: *Ligand **93**(R/S) and crystal structure showing perspective view of ligand **93**(S) illustrating dimeric nature of packing. Hydrogen atoms have been omitted for clarity.*

The Gunnlaugsson group reported Immobilised Chiral Luminescent Devices (ICLD's) by the formation of LB films possessing chiral Ln(III) complexes.[229] Both amphiphilic ligand enantiomers (*R/S*) of ligand **93** were synthesised, containing several important features. A suitable napthyl antenna for sensitisation of the Ln(III) Eu(III), Tb(III) and Sm(III), a terdentate Ln(III) binding moiety and a long alkyl chain (C_{16}) capable of Langmuir monolayer formation were all included in the design of **93**. The self-assembly behaviour of **93** with Eu(III) was first evaluated in solution and the formation of several stable species, 1:1, 1:2 and 1:3 (Eu(III):**93**) were observed. The 1:3 complex of **Eu·93** (*R/S*) was then evaluated for its ability to form LB films. Pressure-area isotherms verified the formation of Langmuir monolayers of **Eu·93** (*R/S*) and moreover, the monolayers were found to be extremely stable over an extended period of time. Transfer of the **Eu·93** (*R/S*) films onto quartz slides with a transfer ratio of *ca.* 1 was achieved and it was assumed that due to the polar nature of the Eu(III) metal centre, it was orientated towards the water phase with the long hydrophobic alkyl chains pointing out. Photophysical evaluation of the LB films of **Eu·93** (*R/S*) revealed identical spectra to that obtained of the solid complexes. The chirality of the monolayers was investigated and although the low concentrations of **Eu·93** (*R/S*) prevented a measurable circular dichroism (CD) spectra from being obtained, both enantiomers gave rise to sizeable Eu(III) centred circularly polarised luminescence (CPL) of equal and opposite signs for $\Delta J = 1$, 2, and 4 transitions. This was the first example of Ln(III) CPL emitting self-assemblies and the uses of these immobilised practical devices are being further explored.

As discussed in previous Chapters, Ln(III) complexes offer the potential to be functionalised to accommodate biological applications such as luminescent sensing and imaging of biologically relevant analytes or alternatively, for material based applications.[230] Consequently, by immobilising these systems their use as practical devices may be explored and as such this Chapter describes the synthesis and photophysical evaluation of Ln(III) based Langmuir monolayers and LB films and was carried out in collaboration with Dr. Jon Kitchen, TCD and Prof. Martin Albrecht, UCD.

5.1 Design and Synthesis of Eu·94

The design of ligand **94** and complex **Eu·94** was similar to that of **Eu·49** described in Chapter 2 with three main functionalities implemented in its design. Firstly, the cyclen ligand provides a coordination environment for the Eu(III) metal centre, while the quinaldine antenna arms efficiently sensitise the Eu(III) and incorporation of a long alkyl chain facilitates the formation of the amphiphilicity in this complex. Ligand **94** was synthesised in a similar manner to ligand **49** as discussed in Section 2.2; the cyclen ligand was monoalkylated with bromohexadecane to give **60c** in 78% yield, the ^{1}H NMR (400 MHz, $CDCl_3$) spectrum of which is shown in Figure 5.7 and corresponding ^{13}C NMR (150 MHz, $CDCl_3$) shown in Appendix A5.1. In the ^{1}H NMR spectrum the terminal CH_3 protons of the C_{16} chain resonate as a triplet at 0.87 ppm with most of the remaining CH_2 protons appearing as a large broad singlet at 1.25 ppm.



Eu·94

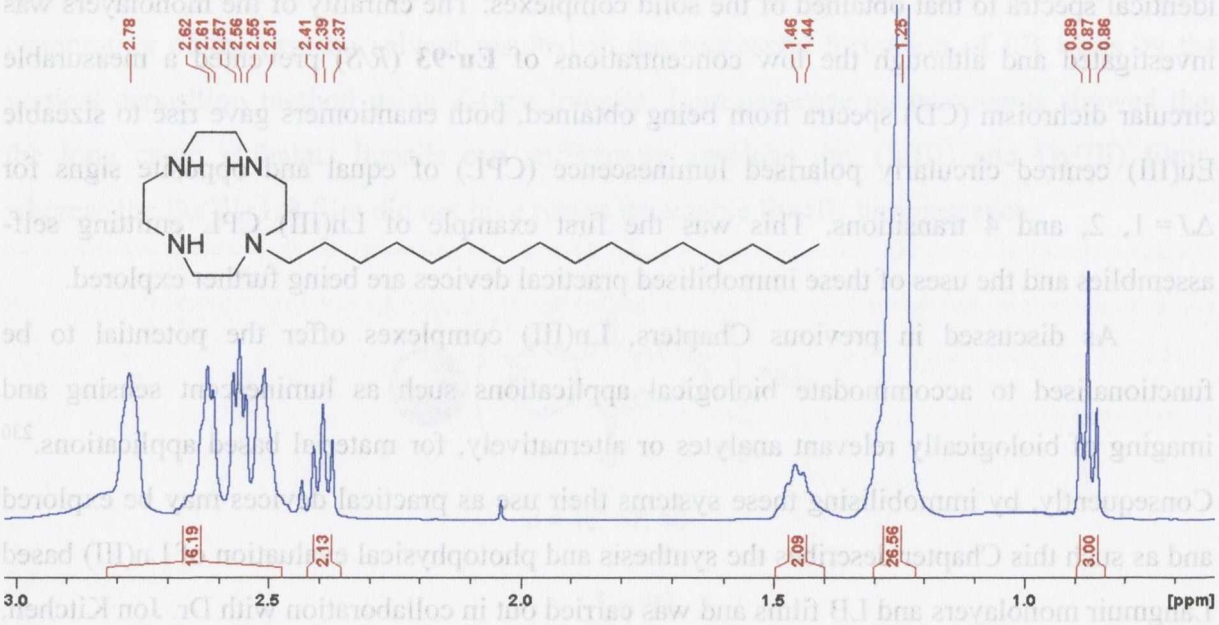


Figure 5.7: *The ^{1}H NMR spectrum (400 MHz, $CDCl_3$) of* ***60c****.*

This was followed by alkylation with three equivalents of the quinaldine antenna **52** in $CHCl_3$ in the presence of the base DIPEA. The reaction mixture was refluxed at 65°C for ten days to ensure maximum yield was achieved. Purification to remove any unreacted antenna and any unwanted side products was achieved by means of an acid-base extraction followed by precipitation of the product out of diethyl ether which gave **94** in 15% yield, the ^{1}H NMR (400 MHz, $CDCl_3$) of which is shown in Appendix A5.2. A multiplet of overlapping signals between 8.23 ppm and 7.42 ppm integrates to 15 and can be assigned to the aromatic protons of the quinaldine antenna. The proton resonances between the range of 3.51 ppm and 2.63 ppm comprise the 16 CH_2 protons of the cyclen along with some CH_2 protons of the alkyl chain, the majority of which can be found in the large broad singlet at 1.21 ppm.

The Eu(III) complex of **94** was obtained by reacting ligand **94** with one molar equivalent of $Eu(CF_3SO_3)_3$ in a small volume of methanol (*ca.* 5 mL) under microwave irradiation for 40 minutes. Precipitation of the product into a large volume ether afforded the complex **Eu·94** in 73% yield as a brown solid. The successful complexation of **94** was confirmed by ^{1}H NMR analysis (400 MHz, DMSO-d_6) (Appendix A5.3) which displayed the characteristic broadening and shifting of the proton signals and therefore verifying the incorporation of the Eu(III) ion within the macrocyclic cyclen cavity. Moreover, IR spectroscopy also established that complexation had occurred by the shift of *ca.* 20 wavenumbers of the carbonyl bond from 1647 cm^{-1} to 1630 cm^{-1} being observed in response to coordination of the Eu(III) metal centre to the carbonyl moieties of **94**.

5.1.1 Photophysical Characterisation of Eu·94

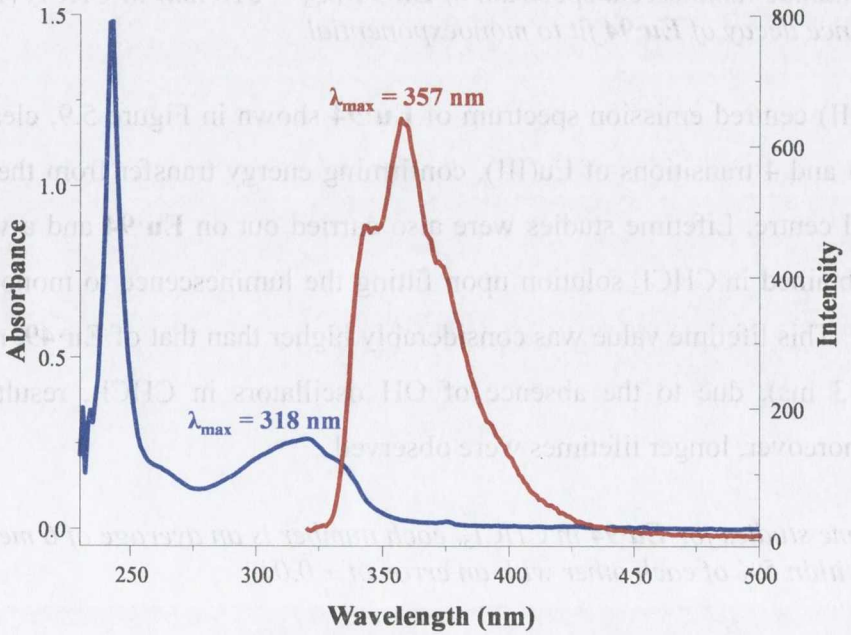


Figure 5.8: *The UV-vis absorption (-) and the fluorescence emission (-) (λ_{ex} = 318 nm) spectra of* ***Eu·94*** *in $CHCl_3$ (1 ×10^{-5} M).*

Before the attempted formation of Langmuir monolayers, the photophysical properties of **Eu·94** were evaluated with respect to the ground, singlet excited and Eu(III) excited states in solution.

The UV-vis absorption spectrum of **Eu·94** was recorded in $CHCl_3$ at a concentration of 1 $\times 10^{-5}$ M in a similar manner to that observed for the analogous Eu(III) complex **Eu·49** described in Chapter 2, the absorption maximum band was centred at 318 nm and assigned to the π-π^* transition, as shown in Figure 5.8. Excitation into this main band at 318 nm gave rise to the fluorescence emission spectrum also shown in Figure 5.8, possessing a λ_{max} at 357 nm with two minor shoulders at 343 nm and 373 nm.

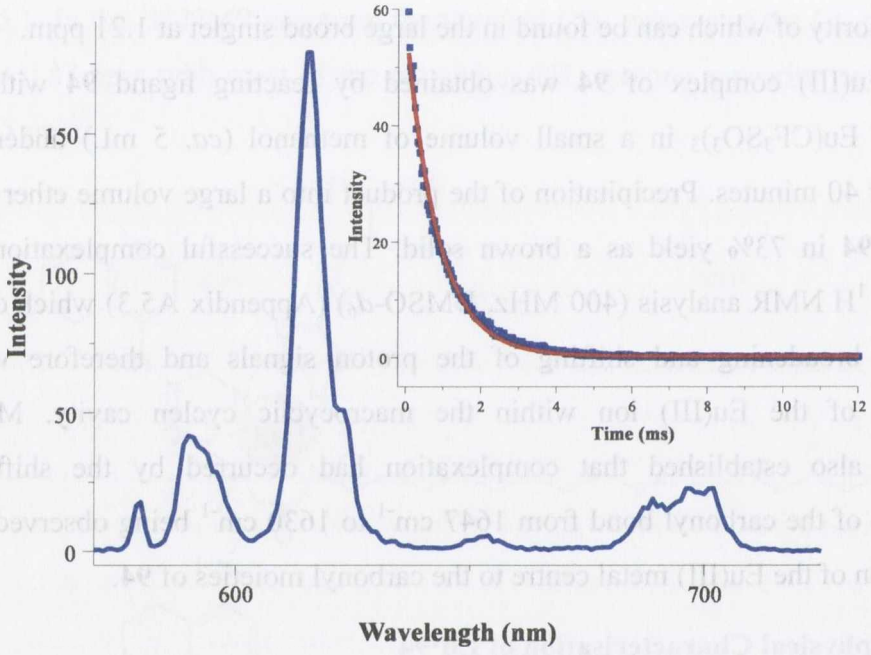


Figure 5.9: *Lanthanide luminescent spectrum of* ***Eu·94*** *(λ_{ex} = 318 nm) in $CHCl_3$ (1 $\times 10^{-5}$ M). Inset: Luminescence decay of* ***Eu·94*** *fit to monoexponential.*

The Eu(III) centred emission spectrum of **Eu·94** shown in Figure 5.9, clearly depicts the $J = 0$, 1, 2, 3 and 4 transitions of Eu(III), confirming energy transfer from the antenna to the Ln(III) metal centre. Lifetime studies were also carried out on **Eu·94** and a value of τ = 0.865 ms was obtained in $CHCl_3$ solution upon fitting the luminescence to monoexponential decay, Table 5.1. This lifetime value was considerably higher than that of **Eu·49**, measured in water (τ = 0.653 ms), due to the absence of OH oscillators in $CHCl_3$, resulting in less quenching and moreover, longer lifetimes were observed.

Table 5.1: *Lifetime studies for* ***Eu·94*** *in $CHCl_3$, each number is an average of 6 measurements all agreeing to within 5% of each other with an error of ± 0.01.*

	τ (ms)	k (ms^{-1})
Eu·94	0.86	1.15

5.1.2 Langmuir Monolayer Formation of Eu·94

The complex **Eu·94** was next assessed for its ability to form Langmuir monolayers at an air-water interface. The process was carried out in collaboration with Prof. Martin Albrecht, in the School of Chemistry, UCD. 20 μL of a solution of **Eu·94** in $CHCl_3$ (2.5×10^{-4} M) was carefully spread onto the surface of the water subphase at room temperature. The solvent was allowed to evaporate over a period of *ca.* 20 minutes before the barriers were closed at a rate of 6 mm min^{-1} while the surface pressure of the decreasing area was continuously monitored. The surface pressure-area isotherm graph obtained is shown in Figure 5.10.

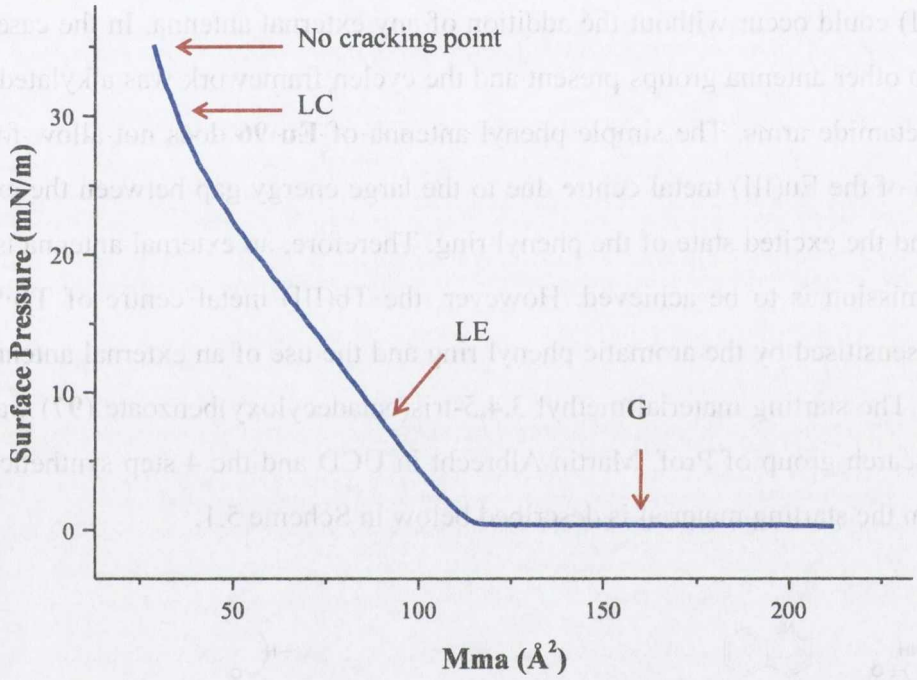
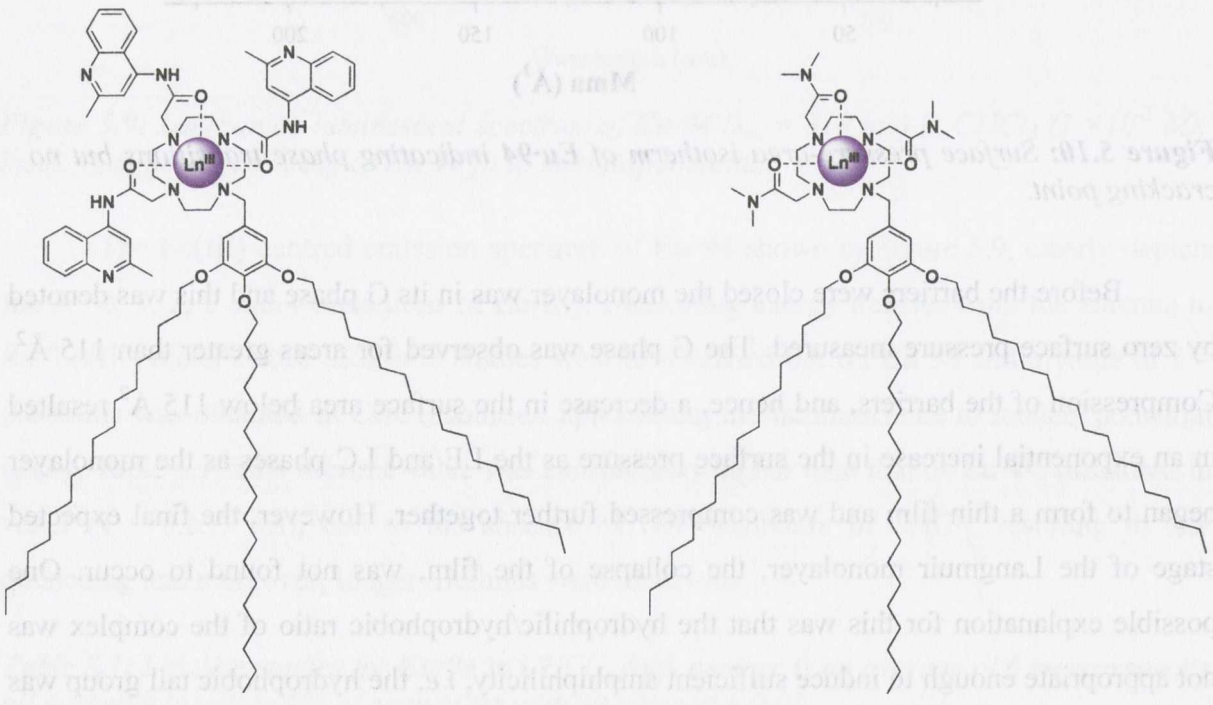


Figure 5.10: *Surface pressure-area isotherm of* ***Eu·94*** *indicating phase transitions but no cracking point.*

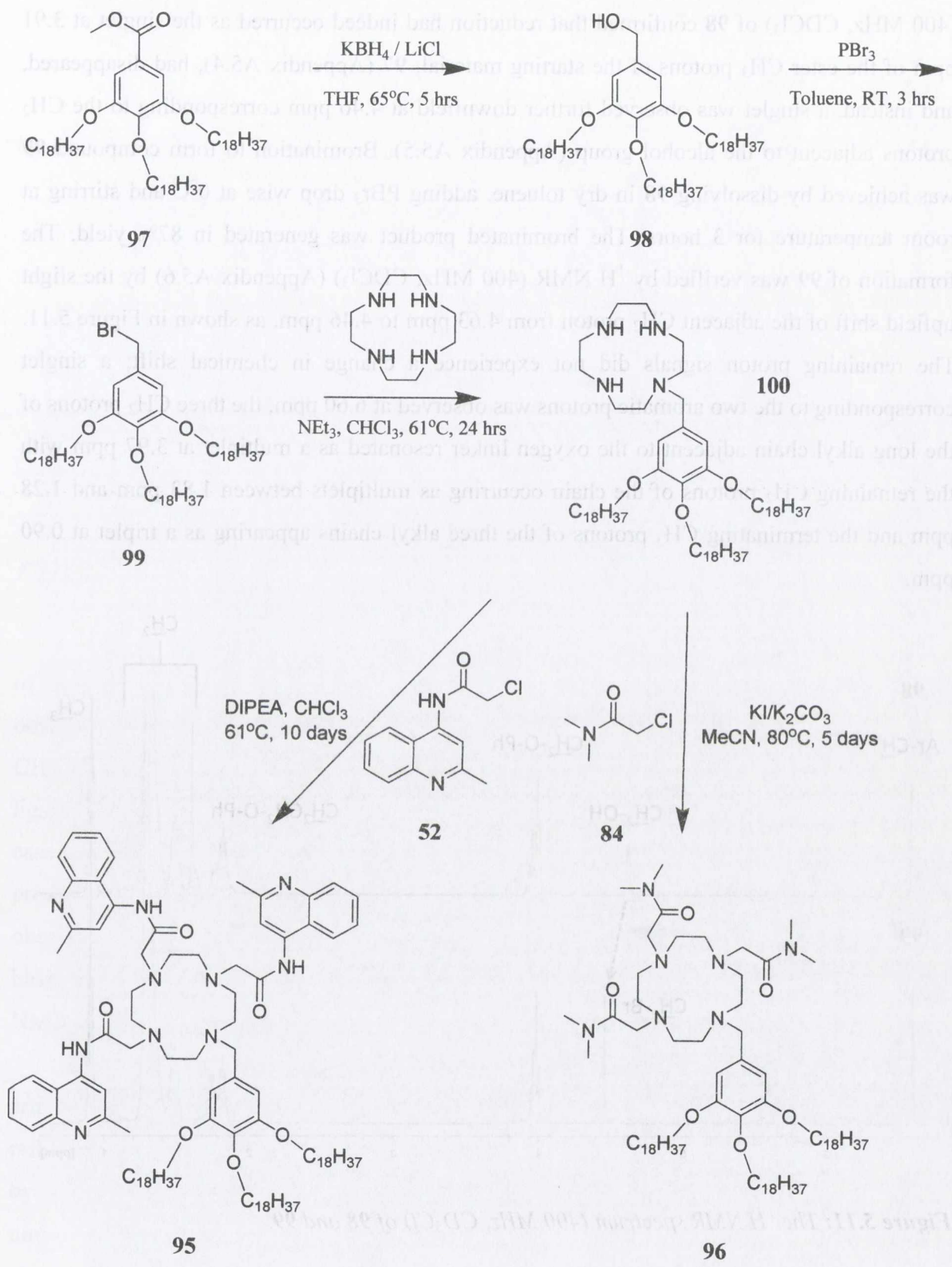
Before the barriers were closed the monolayer was in its G phase and this was denoted by zero surface pressure measured. The G phase was observed for areas greater than 115 $Å^2$. Compression of the barriers, and hence, a decrease in the surface area below 115 $Å^2$ resulted in an exponential increase in the surface pressure as the LE and LC phases as the monolayer began to form a thin film and was compressed further together. However, the final expected stage of the Langmuir monolayer, the collapse of the film, was not found to occur. One possible explanation for this was that the hydrophilic/hydrophobic ratio of the complex was not appropriate enough to induce sufficient amphiphilicity, *i.e.* the hydrophobic tail group was too small in relation to the hydrophilic head group. Bearing this in mind, new complex structures were designed and will be discussed in the following section.

5.2 Design and Synthesis of Ln·95/96

With the mono-chain systems being unsuccessful in the formation of LB films we moved to tri-chain systems, where the amphiphilicity of the cyclen systems was altered. Both **Ln·95** and **Ln·96** were designed so that the hydrophobic tail group was considerably larger than the previously studied **Eu·94**, which did not have a sufficient enough tail group to support the formation of Langmuir monolayers. The tail group consisted of three long alkyl (C_{18}) chains appended to a phenyl ring. The cyclen framework of **Ln·95** was functionalised with this hydrophobic tail group along with three quinaldine antennae surrounding the Eu(III) or Tb(III) metal ions. The incorporation of the quinaldine antenna was such that sensitisation of the Ln(III) could occur without the addition of any external antenna. In the case of **Ln·96**, there was no other antenna groups present and the cyclen framework was alkylated with three dimethyl acetamide arms. The simple phenyl antenna of **Eu·96** does not allow for adequate sensitisation of the Eu(III) metal centre due to the large energy gap between the excited state of Eu(III) and the excited state of the phenyl ring. Therefore, an external antenna is necessary if Eu(III) emission is to be achieved. However, the Tb(III) metal centre of **Tb·96** may be sufficiently sensitised by the aromatic phenyl ring and the use of an external antenna may not be required. The starting material methyl 3,4,5-tris(octadecyloxy)benzoate (**97**) was obtained from the research group of Prof. Martin Albrecht in UCD and the 4 step synthetic procedure towards from the starting material is described below in Scheme 5.1.



Ln·95 **Ln = Eu/Tb** **Ln·96**



Scheme 5.1: *Synthetic pathways of ligands* ***95*** *and* ***96****.*

The first step in the synthetic pathway involved the reduction of the ester group of **97** to the alcohol using LiCl and KBH_4 in THF. The combined reagents and starting material were refluxed in dry THF for 5 hours producing the alcohol, **98**, in 75% yield. The ^1H NMR

(400 MHz, $CDCl_3$) of **98** confirmed that reduction had indeed occurred as the singlet at 3.91 ppm of the ester CH_3 protons of the starting material, **97** (Appendix A5.4), had disappeared, and instead, a singlet was observed further downfield at 4.46 ppm corresponding to the CH_2 protons adjacent to the alcohol group (Appendix A5.5). Bromination to form compound **99** was achieved by dissolving **98** in dry toluene, adding PBr_3 drop wise at 0°C and stirring at room temperature for 3 hours. The brominated product was generated in 87% yield. The formation of **99** was verified by ^1H NMR (400 MHz, $CDCl_3$) (Appendix A5.6) by the slight upfield shift of the adjacent CH_2 proton from 4.63 ppm to 4.46 ppm, as shown in Figure 5.11. The remaining proton signals did not experience a change in chemical shift; a singlet corresponding to the two aromatic protons was observed at 6.60 ppm, the three CH_2 protons of the long alkyl chain adjacent to the oxygen linker resonated as a multiplet at 3.97 ppm with the remaining CH_2 protons of the chain occurring as multiplets between 1.83 ppm and 1.28 ppm and the terminating CH_3 protons of the three alkyl chains appearing as a triplet at 0.90 ppm.

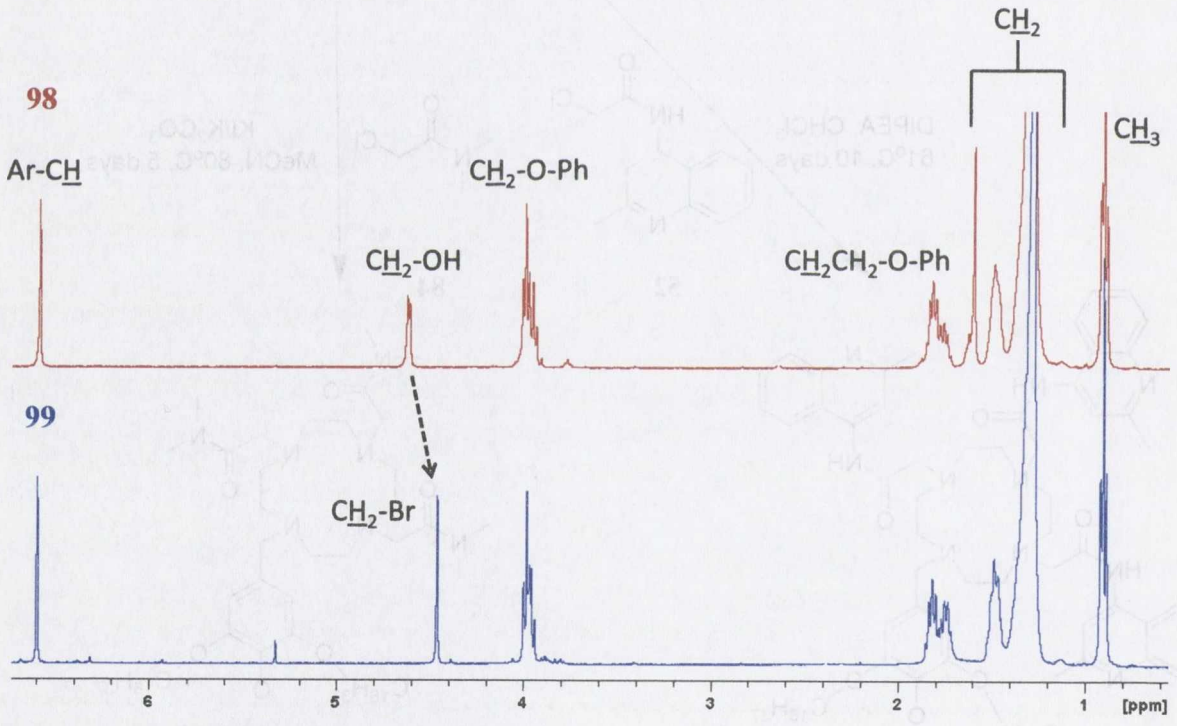


Figure 5.11: *The ^1H NMR spectrum (400 MHz, CD_3Cl) of **98** and **99**.*

The next step in the synthetic pathway was monoalkylation of cyclen using the brominated product **99** and a four-fold excess of cyclen in the presence of NEt_3.[169] This afforded the monoalkylated product **100** in 81% yield. The resulting ^1H NMR spectrum (400 MHz, $CDCl_3$) is shown in Figure 5.12.

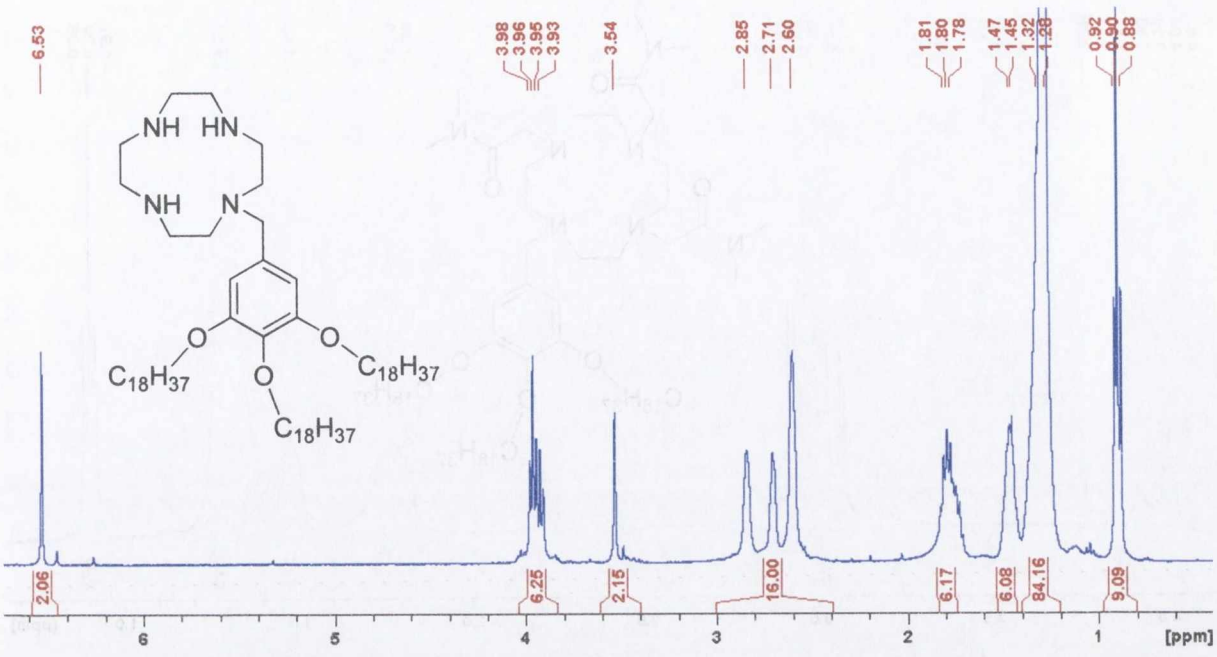


Figure 5.12: *The ^1H NMR spectrum (400 MHz, CD_3Cl) of* ***100****.*

The only major difference in the ^1H NMR spectrum was the appearance of a multiplet of signals between 2.85 ppm and 2.60 ppm belonging to the 16 CH_2 cyclen protons. The only other notable difference from the ^1H NMR spectrum was the significant upfield shift of the CH_2 protons adjacent to the cyclen from 4.46 ppm to 3.54 ppm. The final stage towards ligands **95** and **96** involved further alkylation of the cyclen with the appropriate arms. In the case of ligand **95**, compound **100** was alkylated with the quinaldine antenna group **52** in the presence of the base DIPEA. The reaction was refluxed for 10 days until the product was observed by mass spectrometry; 1684.2733 $[M + Na]^+$. Purification was achieved by an acid base work up followed by precipitation from diethyl ether to give **95** in 22% yield. The ^1H NMR (400 MHz, $CDCl_3$) is shown in Appendix A5.7.

Ligand **96** was synthesised by alkylating compound **100** with the dimethylacetamide arm **84** in the presence of potassium iodide and potassium carbonate. The reactants were refluxed in acetonitrile at 80°C for 5 days until formation of the desired product was observed by mass spectrometry; 1684.2731 $[M + Na]^+$. Purification to remove any excess arm or unwanted side products was achieved by alumina column chromatography using a gradient elution 100 to 80:20 CH_2Cl_2:CH_3OH. The desired product was obtained as a brown oil in 49% yield, the ^1H NMR (400 MHz, $CDCl_3$) is shown in Figure 5.13. The 9 CH_3 protons terminating the alkyl chains resonate as a triplet at 0.90 ppm while the cyclen 16 CH_2 protons are located within the multiplet between 3.06 ppm and 2.91 ppm.

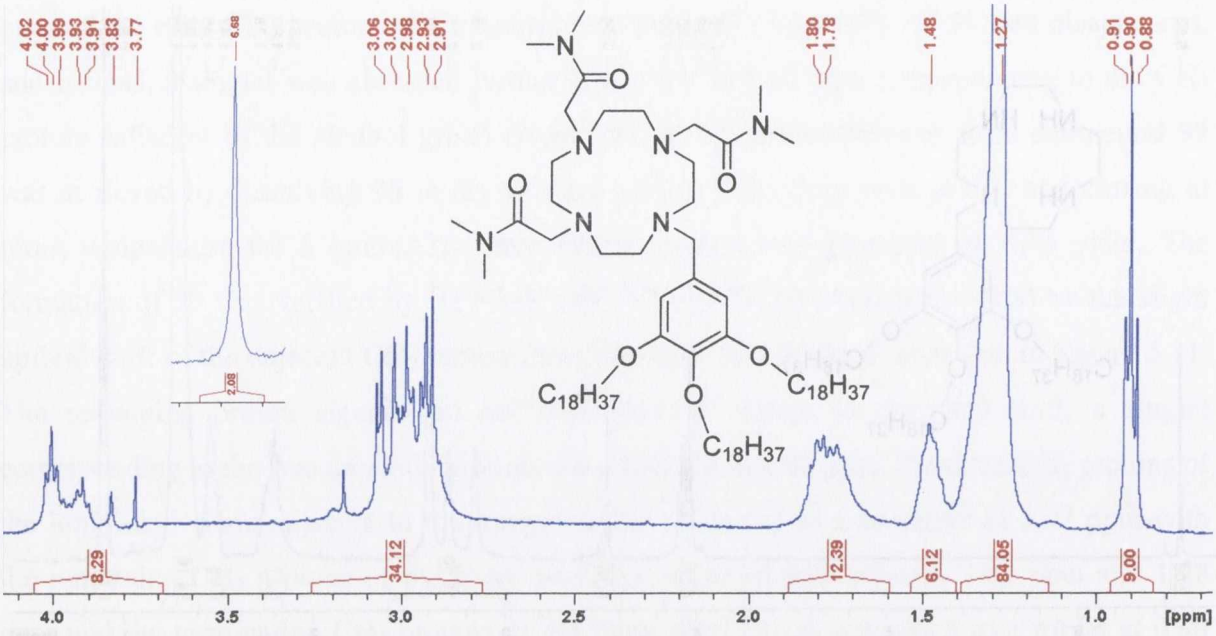
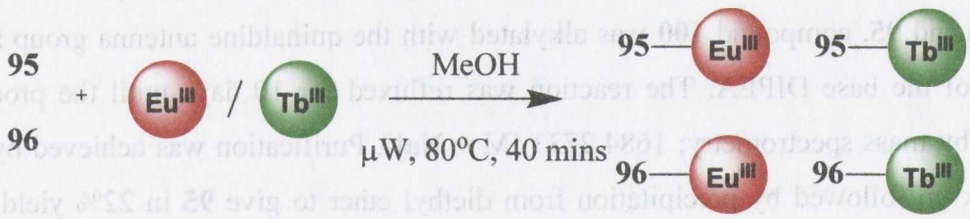


Figure 5.13: *The ^{1}H NMR spectrum (400 MHz, CD_3Cl) of ligand* ***96****.*

Having successfully synthesised and characterised both ligands the next step involved complexation with Eu(III) and Tb(III) to give **Eu·95**, **Tb·95**, **Eu·96** and **Tb·96**. All the complexations were carried out by reacting **95** and **96** with one molar equivalent of the relevant $Ln(CF_3SO_3)_3$ in a small volume of methanol (*ca.* 5 mL) under microwave irradiation for 40 minutes, as depicted in Scheme 5.2.



Scheme 5.2: *Synthetic pathway of* ***Eu·95****,* ***Tb·95****,* ***Eu·96*** *and* ***Tb·96****.*

The complexes were characterised by ^{1}H NMR, IR spectroscopy and mass spectrometry. The ^{1}H NMR (CD_3CN, 400 MHz) displays the characteristic broadening and shifting of peaks due to the paramagnetic nature of the Ln(III) ions and are shown in Appendix A5.8-11.

Table 5.2: *IR stretching frequency (cm^{-1}) of the carbonyl bands.*

	Ligand	Eu(III) complex	Tb(III) complex
95	1671	1643	1643
96	1667	1643	1643

IR spectroscopy also verified successful complexation of the Ln(III) to the cyclen macrocycle. The carbonyl bond of the ligands were found to have shifted by *ca.* 30 wavenumbers, as shown in Table 5.2, upon binding to the Ln(III) metal centre. Mass spectrometry was also employed to characterise the complexes, however, no successful hits for either complex **Eu·95** or **Tb·95** were obtained despite many attempts. A peak at m/z = 1624.0772 corresponding to a $[\mathbf{Eu{\cdot}96} + CF_3SO_3]^{2+}$ species in solution was found using MALDI-ToF analysis, with the expected isotopic distribution pattern associated with Eu(III) complexes also observed (Figure 5.14). Also, a peak at m/z = 1629.0778 corresponding to a $[\mathbf{Tb{\cdot}96} + CF_3SO_3]^{2+}$ species in solution was found using MALDI-ToF analysis and the expected isotopic distribution pattern related to Tb(III) was observed and is shown in Appendix A5.12.

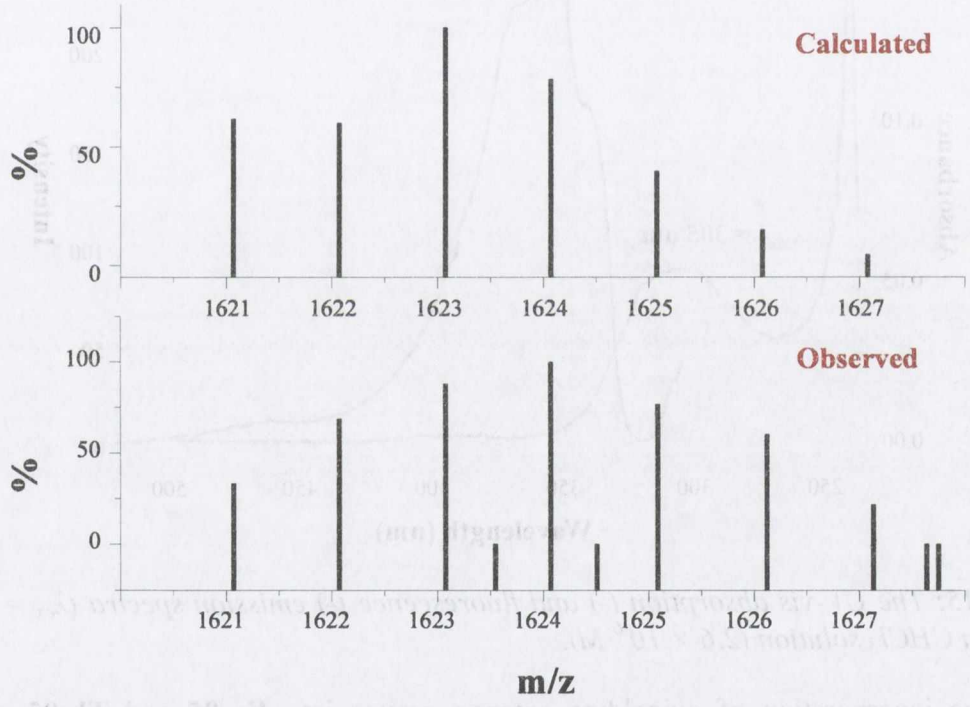


Figure 5.14: *The MALDI mass spectrum of* ***Eu·96*** *displaying the expected Eu(III) isotopic distribution pattern for the* $[\mathbf{Eu{\cdot}96} + CF_3SO_3]^{2+}$ *species.*

Before attempting to form Langmuir monolayers and LB films, the photophysical properties of the complexes **Eu·95**, **Tb·95**, **Eu·96** and **Tb·96** were first evaluated in solution, investigating the UV-vis absorption, fluorescence and phosphorescent properties of each complex in $CHCl_3$ solution, which was chosen as the solvent due to the fact that all solutions required for the formation of LB films must be immiscible with water and as such $CHCl_3$ was the solvent of choice.

5.3 Photophysical Characterisation of Eu·95 and Tb·95

The UV-vis absorption spectra of **Eu·95** and **Tb·95** were recorded in $CHCl_3$ solution at a concentration of 2.6×10^{-6} M. For both complexes the absorption maximum π-π^* transition band was centred at *ca.* 300 nm, as had been previously observed for the analogous complexes **Eu·49** and **Tb·49** (Chapter 2) containing the same quinaldine chromophore. Excitation into the main band gave rise to the fluorescence emission spectrum, possessing a λ_{max} at 355 nm with two minor shoulders at 340 nm and 370 nm. The UV-vis absorption and fluorescence emission spectra of **Eu·95** and **Tb·95** is shown in Figure 5.15 and Appendix A5.13, respectively.

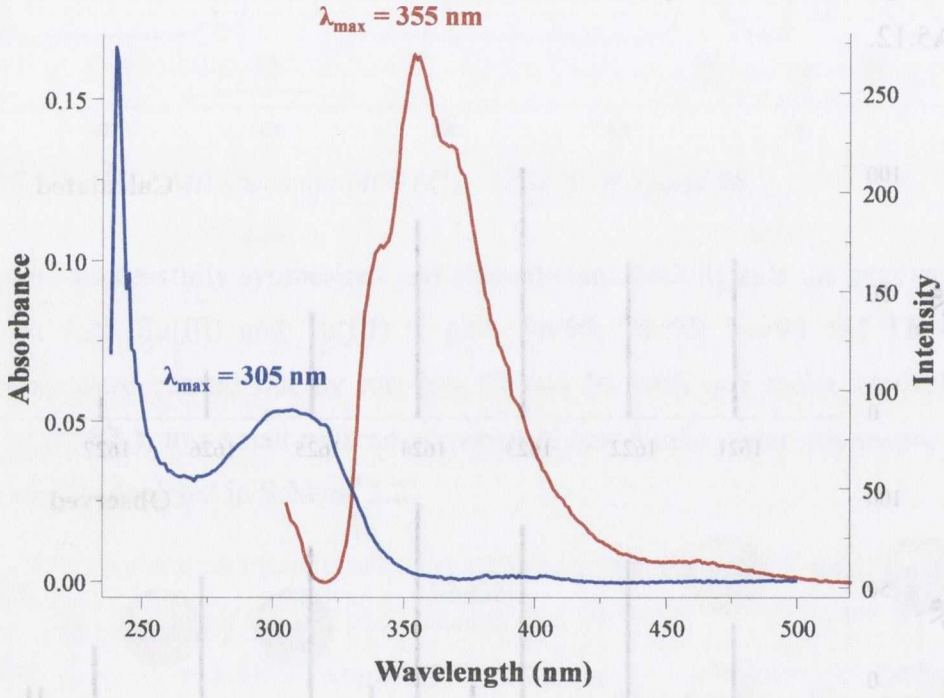


Figure 5.15: *The UV-vis absorption (-) and fluorescence (-) emission spectra (λ_{ex} = 305 nm) of* ***Tb·95*** *in $CHCl_3$ solution (2.6×10^{-6} M).*

The incorporation of quinaldine antenna groups into **Eu·95** and **Tb·95** envisaged indirect excitation of the Eu(III) and Tb(III) metal centres. Excitation of the antenna resulted in energy transfer, *via* the triplet state, to the $^5D_0$ state of Eu(III) and $^5D_4$ state of Tb(III), and hence, Ln(III) emission was observed. Figure 5.16 displays the characteristic Eu(III) and Tb(III) emission resulting from the transitions from the $^5D_0$ state to the ^7F_J state of the Eu(III) ion, where $J = 0$ (579 nm), 1 (591 nm), 2 (615 nm), 3 (651 nm), 4 (split; 687 nm and 699 nm) and the $^5D_4$ state to the ^7F_J of Tb(III) ion where $J = 6$ (488 nm), 5 (544 nm), 4 (586 nm) and 3 (621 nm). The same concentration and the same settings were used when investigating the photophysical properties of **Eu·95** and **Tb·95**, however, the Eu(III) emission was 4.5 fold more intense than the Tb(III) intensity.

This occurrence may result from the quinaldine antenna being a more suitable antenna to accommodate Eu(III) emission than Tb(III) emission. It may also be attributed to the susceptibility of the quinaldine antenna to quenching of its triplet state by molecular oxygen, culminating in quenched Tb(III) emission relative to the Eu(III) emission.

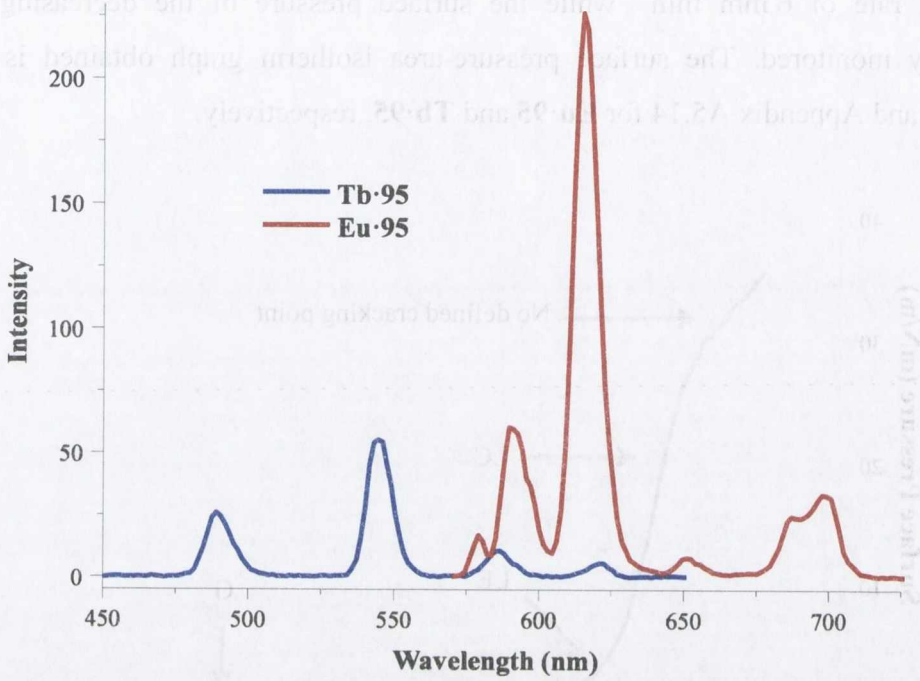


Figure 5.16: *Ln(III) luminescent spectra of* ***Tb·95*** *(-) and* ***Eu·95*** *(-) (λ_{ex} = 305 nm) in $CHCl_3$ solution (2.6×10^{-6} M).*

Lifetime studies were also carried out on **Eu·95** and **Tb·95** in $CHCl_3$ solution yielding values of τ = 0.68 ms and τ = 0.59 ms (Table 5.3), respectively, upon fitting the luminescence to monoexponential decay. Again, lifetime values were found to be higher in $CHCl_3$ solution than in aqueous solution due to the lack of OH oscillators in $CHCl_3$, resulting in less quenching and therefore, longer lifetime values were obtained.

Table 5.3: *Lifetime studies for* ***Eu·95*** *and* ***Tb·95*** *in $CHCl_3$, each number is an average of 6 measurements all agreeing to within 5% of each other with an error of ± 0.01.*

Complex	τ (ms)	k (ms^{-1})
Eu·95	0.68	1.46
Tb·95	0.59	1.68

Having established the photophysical properties of **Eu·95** and **Tb·95**, the ability of the complexes to from Langmuir films was next investigated.

5.4 Langmuir Monolayer Formation of Eu·95 and Tb·95

20 μL of a solution of **Eu·95** and **Tb·95** in $CHCl_3$ (2.6×10^{-4} M) was carefully dropped onto the surface of the water subphase of the Langmuir trough at room temperature. The solvent was allowed to evaporate over a period of *ca.* 20 minutes before the barriers were closed at a rate of 6 mm min^{-1} while the surface pressure of the decreasing area was continuously monitored. The surface pressure-area isotherm graph obtained is shown in Figure 5.17 and Appendix A5.14 for **Eu·95** and **Tb·95**, respectively.

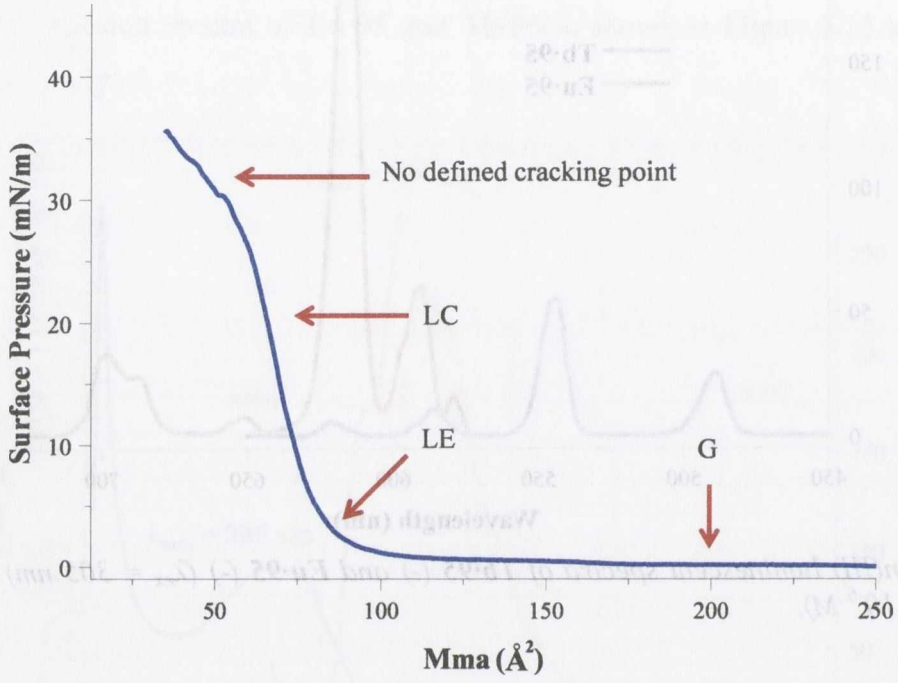


Figure 5.17: *Surface pressure-area isotherm of* ***Eu·95*** *indicating phase transitions but no defined collapsing point.*

Initially, when the barriers were fully open, the monolayer of **Eu·95** was in its G phase, displaying almost zero surface pressure. This G phase existed between a surface area of *ca.* 250 $Å^2$ to *ca.* 100 $Å^2$. Compression of the barriers beyond 200 $Å^2$ resulted in a very short LE state being observed immediately followed by a sharp transition to the LC state which stretched from 100-75 $Å^2$. An exponential increase in the surface pressure was observed increasing from 3-18 nM/m over a surface area change of only *ca.* 30 $Å^2$, indicating the formation of a thin film on the surface of the water subphase. The next expected phase was collapse of the thin film, which would be denoted by a sharp decrease in surface pressure. However, this decrease was not observed, instead the slope of the isotherm changed and appeared to "wobble" rather than drop off, indicating that collapse of the film was not occurring. The same trend was also observed in the surface pressure-area isotherm of **Tb·95**, Appendix A5.14. The collapse of a film is not the only possibility at smaller surface areas. It is possible that the strong polar head group of the complex caused the formation of micelles,

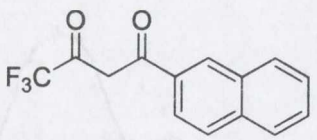
where the molecules are arranged in spheres, with the polar head groups on the outside and the long hydrophilic alkyl chains pointing towards the centre. Alternatively, the complexes may have been forming bilayers on top of the water subphase which would also account for the less steep increase observed in the isotherm towards smaller surface areas. Although the hydrophobicity of the complexes had been increased by the addition of three long alkyl chains, it appeared that the head group was still too polar and prevented the formation of ideal Langmuir monolayers.

Taking this into consideration, it was decided to redesign the complex incorporating smaller dimethyl acetamide arms instead of the larger quinaldine antenna in order to reduce the size of the head group. The following Section will discuss the photophysical properties of **Eu·96** and **Tb·96** before an investigation into their ability to form Langmuir monolayers and LB films.

5.5 Photophysical Characterisation of Eu·96 and Tb·96 in Solution

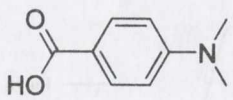
The only antenna incorporated into the design of **Eu·96** and **Tb·96** was a phenyl ring, which although it may sensitise the Tb(III) metal centre of **Tb·96**, is not known to efficiently sensitise Eu(III) and we would therefore expect very weak Eu(III) emission upon excitation into the phenyl ring of **Eu·96**. As such, it was decided to utilise the external antennae **nta** (**73**) and **DMAB** (**74**) to ensure that proficient sensitisation of the Eu(III) and Tb(III) metal centres of **Eu·96** and **Tb·96**, respectively, was achieved. These particular antennae were chosen as they have been shown to be capable of giving rise to significant Ln(III) emission in previous Chapters.

nta



73

DMAB



74

All solution studies were carried out in a $CHCl_3$ solution at a concentration of *ca.* 2.6×10^{-6} M with the exception of the UV-vis absorption scans, which were obtained in methanol solution as the noise of the $CHCl_3$ baseline towards the lower wavelengths was interfering with the main absorption band. The UV-vis absorption, fluorescence, phosphorescence, excitation and lifetimes of **Eu·96** and **Tb·96** were all recorded in the presence and absence of one equivalent of the external antennae **nta** (**Eu·96**) and **DMAB** (**Tb·96**).

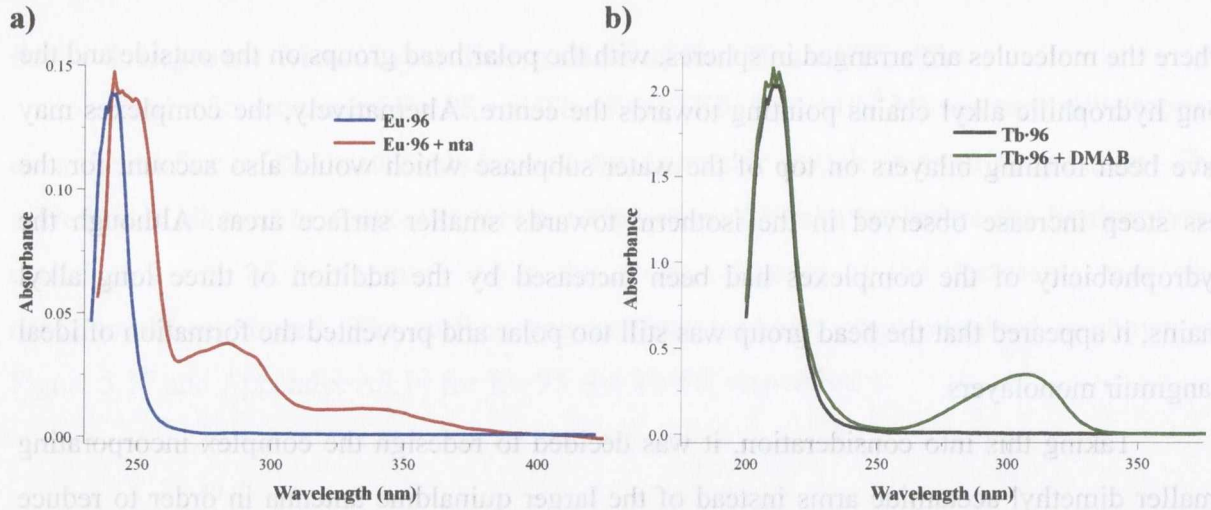


Figure 5.18: a) *The UV-vis absorption spectra of* ***Eu·96*** *in the absence (-) and presence (-) of one equivalent of the antenna* ***nta*** *in MeOH solution (2.6 × 10^{-6} M).* ***b)*** *UV-vis absorption spectra of* ***Tb·96*** *in the absence (-) and presence (-) of 1 equivalent of the antenna* ***DMAB*** *in MeOH solution (2.6 × 10^{-6} M).*

Figure 5.18 displays the UV-vis absorption spectra of **Eu·96** and **Tb·96** in the absence and presence of one equivalent of the external antennae **nta** and **DMAB**. For both complexes, in the absence of any antenna, the only significant absorption band was located between 230 nm and 250 nm and can be attributed to the π-π* transition of the phenyl ring of the ligand. Addition of the antennae resulted in significantly different spectra. The addition of **nta** to a solution of **Eu·96** (Figure 5.18a) resulted in a UV-vis absorption spectrum with bands centred at 250 nm, 280 nm and 330 nm, characteristic of the **nta** antenna. The UV-vis absorption spectrum of **Tb·96** in the presence of one equivalent of **DMAB** resulted in the appearance of a band centred at *ca.* 300 nm, representative of the **DMAB** antenna moiety.

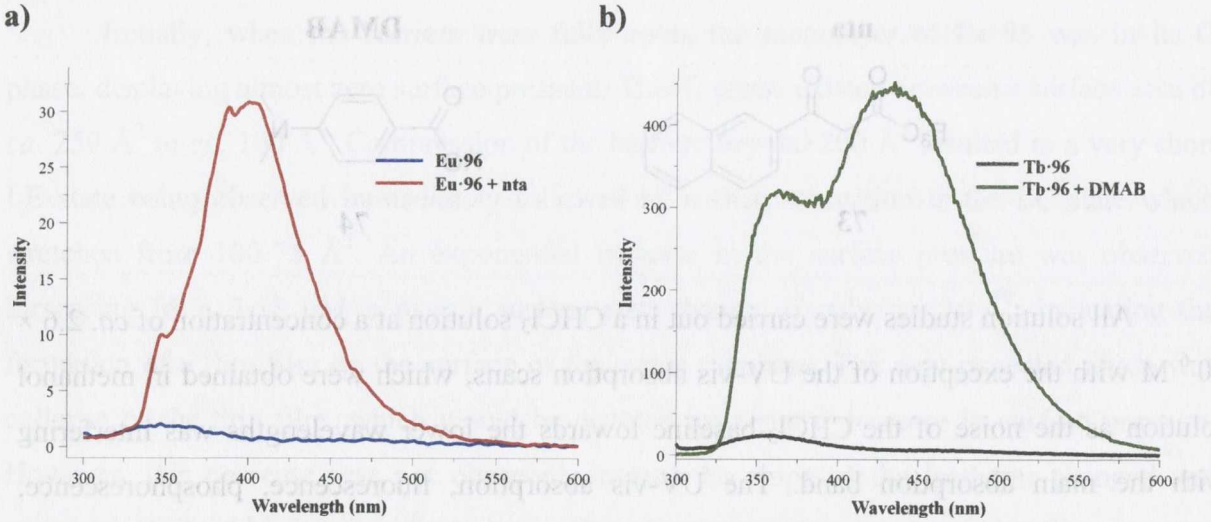


Figure 5.19: a) *The fluorescence spectra of* ***Eu·96*** *in the absence (-) and presence (-) of one equivalent of the antenna* ***nta*** *in $CHCl_3$ solution (λ_{ex} = 330 nm) (2.6 × 10^{-6} M).* ***b)*** *The fluorescence spectra of* ***Tb·96*** *in the absence (-) and presence (-) of 1 equivalent of the antenna* ***DMAB*** *in $CHCl_3$ solution (λ_{ex} = 300 nm) (2.6 × 10^{-6} M).*

Excitation into the main absorption band of each species **Eu·96** and **Tb·96**, **Eu·96-nta** and **Tb·96-DMAB** gave rise to the fluorescence emission spectrum shown in Figure 5.19. In the absence of any sensitising antenna in complexes **Eu·96** and **Tb·96**, only a very weak fluorescence emission was observed upon excitation at 240 nm. However, upon addition of the aforementioned antennae, significant fluorescence was recorded. Excitation into the 330 nm band of **Eu·96-nta** resulted in a fluorescence spectrum with a maximum centred at 400 nm (Figure 5.19a) while a λ_{ex} = 300 nm for **Tb·96-DMAB** gave rise to a fluorescence spectrum possessing a λ_{max} at 430 nm with a minor shoulder at 360 nm (Figure 5.19b).

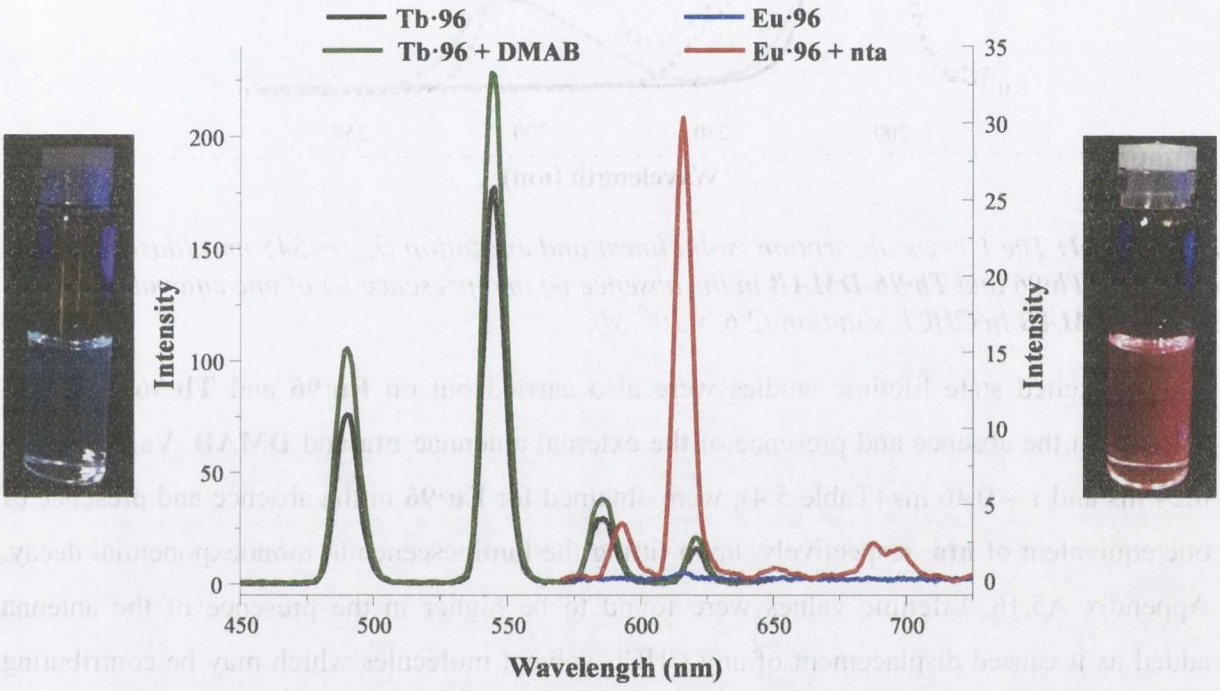


Figure 5.20: *Ln(III) luminescent spectra of* ***Tb·96*** *(-) and* ***Tb·96-DMAB*** *(-) (λ_{ex} = 300 nm) and* ***Eu·96*** *(-) and* ***Eu·96-nta*** *(-) (λ_{ex} = 330 nm) in $CHCl_3$ solution (2.6×10^{-6} M). Photos of phosphorescent solutions of* ***Tb·96-DMAB*** *(left) and* ***Eu·96-nta*** *(right).*

The Ln(III) luminescent spectra of the four different complexes were obtained and are shown in Figure 5.20. In the absence of **nta** the Eu(III) emission was so weak that it was undistinguishable from the baseline (λ_{ex} = 330 nm). However, the addition of **nta** results in sensitisation of the Eu(III) of **Eu·96**. This was verified by recording the excitation spectrum of **Eu·96** and **Eu·96-nta**, Appendix A5.15, which showed that the sensitisation of the Eu(III) metal centre was mainly occurring from the 330 nm UV-vis absorption band of **nta**.

Relatively strong Tb(III) metal centred emission was observed from **Tb·96** without the presence of an external antenna using a λ_{ex} = 300 nm. Addition of the antenna **DMAB** gave rise to a marginal increase in the Tb(III) emission. It was ascertained from the excitation spectrum that the increase in the Tb(III) emission arises from sensitisation from both the phenyl ring of **Tb·96** and **DMAB**, Figure 5.21.

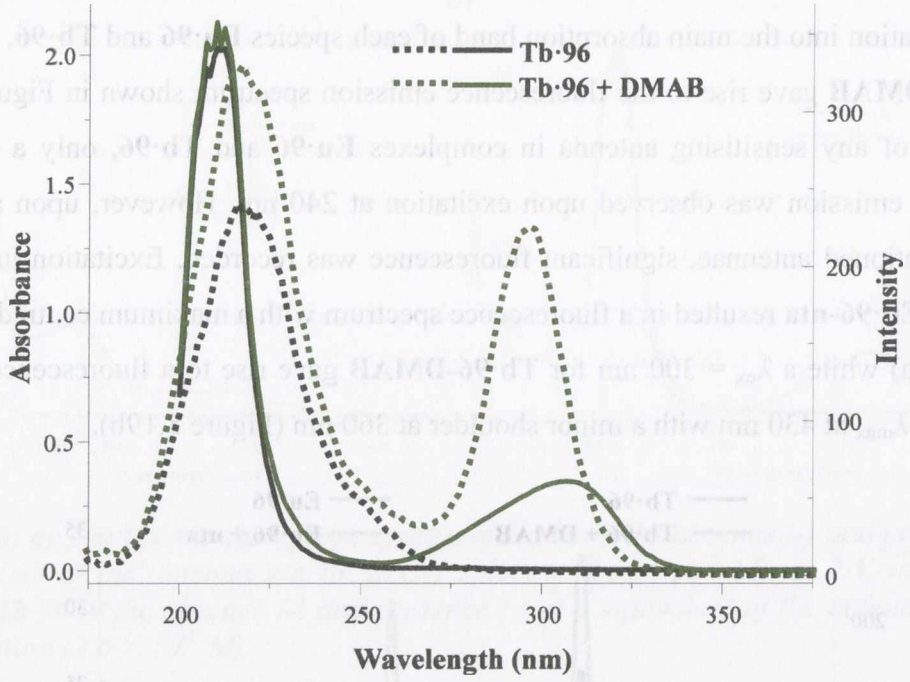


Figure 5.21: *The UV-vis absorption (solid lines) and excitation (λ_{em} = 545 nm) (dashed lines) spectra of* ***Tb·96*** *and* ***Tb·96-DMAB*** *in the absence (-) and presence (-) of one equivalent of the antenna* ***DMAB*** *in $CHCl_3$ solution (2.6×10^{-6} M).*

Excited state lifetime studies were also carried out on **Eu·96** and **Tb·96** in $CHCl_3$ solution in the absence and presence of the external antennae **nta** and **DMAB**. Values of τ = 0.24 ms and τ = 0.46 ms (Table 5.4), were obtained for **Eu·96** in the absence and presence of one equivalent of **nta**, respectively, upon fitting the luminescence to monoexponential decay, Appendix A5.16. Lifetime values were found to be higher in the presence of the antenna added as it caused displacement of any $CHCl_3$ solvent molecules which may be contributing to quenching of the Eu(III) luminescence. Moreover, the lifetime values were significantly lower than those obtained for **Eu·95**. One possible explanation for this could be that the bulky quinaldine groups of **Eu·95** shield the Eu(III) metal centre from some of the quenching by the solvent molecules. These groups are absent on **Eu·96** and allow for more quenching of the Eu(III) metal centre by solvent molecules.

Table 5.4: *Lifetime studies for* ***Eu·96*** *and* ***Tb·96*** *in $CHCl_3$ solution in the absence and presence of one equivalent of antennae each number is an average of 6 measurements all agreeing to within 5% of each other with an error of ± 0.01.*

Species	τ(ms)	k (ms^{-1})
Eu·96	0.24	4.17
+ nta	0.46	2.14
Tb·96	1.07	0.93
+ DMAB	1.27	0.78

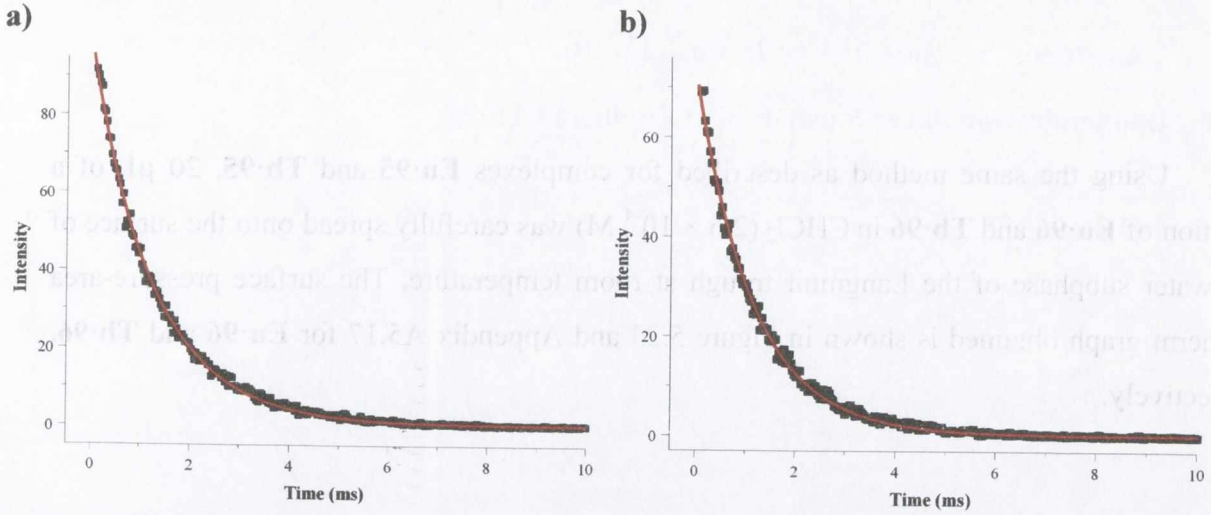


Figure 5.22: *Luminescence decay fit to monoexponential of* ***a) Tb·96*** *(λ_{ex} = 220 nm) and* ***b) Tb·96-DMAB*** *(λ_{ex} = 300 nm) in $CHCl_3$ solution.*

In contrast to the shorter excited state lifetimes observed for **Eu·96**, the lifetimes of **Tb·96**, as shown in Table 5.4, are significantly longer than those found for **Tb·95** and can also be fit to monoexponential decay, as shown in Figure 5.22. The longer lifetimes of **Tb·96** in comparison to **Tb·95** may be as a result of the absence of the quinaldine pendant antenna arms. Energy back transfer from the Tb(III) metal centre to the quinaldine antenna may occur in the case of **Tb·95**, leading to the shorter lifetimes being observed. The lifetimes of **Eu·96** were also measured in H_2O and D_2O in the presence and absence of one equivalent of **nta** antenna and consequently the q values were obtained, shown below in Table 5.5. It was determined that there were two metal bound water molecules for the complex **Eu·96** alone and that addition of antenna displaced these water molecules yielding a q value of 0.

Table 5.5: *Lifetime studies for* ***Eu·96*** *and* ***Eu·96-nta*** *at neutral pH, each number is an average of 6 measurements all agreeing to within 5% of each other with an error of ± 0.01.*

Species	τ_{H2O} (ms)	τ_{D2O} (ms)	k_{H2O} (ms^{-1})	k_{D2O} (ms^{-1})	q (±0.5)
Eu·96	0.23	0.37	4.42	2.66	1.86
+ nta	0.11	0.12	8.92	7.61	0.04

Having established the photophysical properties of **Eu·96** and **Tb·96** the ability of these complexes to form Langmuir monolayers on a water subphase and LB films was next investigated.

5.6 Langmuir Studies of Eu·96 and Tb·96

5.6.1 Langmuir Monolayer Formation of Eu·96 and Tb·96

Using the same method as described for complexes **Eu·95** and **Tb·95**, 20 μL of a solution of **Eu·96** and **Tb·96** in $CHCl_3$ (2.6×10^{-4} M) was carefully spread onto the surface of the water subphase of the Langmuir trough at room temperature. The surface pressure-area isotherm graph obtained is shown in Figure 5.23 and Appendix A5.17 for **Eu·96** and **Tb·96**, respectively.

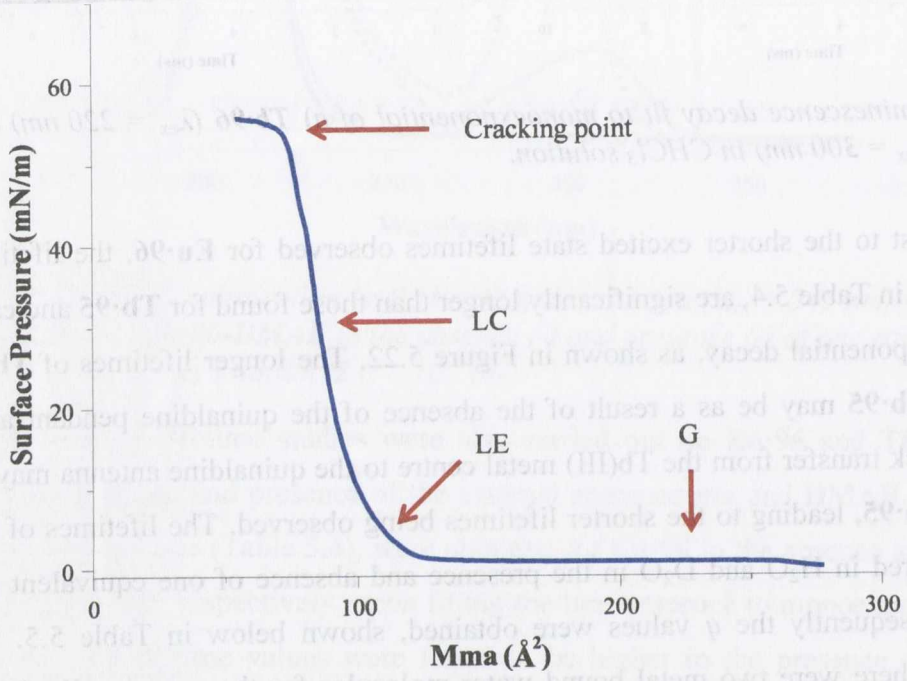


Figure 5.23: *Surface pressure-area isotherm of* ***Eu·96*** *indicating phase transitions and a cracking point.*

Decreasing the area by the gradual closing of the barriers results in the monolayer of **Eu·96** undergoing different phase transitions. Initially, the gaseous state was observed with the surface pressure remaining very close to zero (< 1 nM/m). Both **Eu·96** and **Tb·96** remained in the G phase at areas greater than 140 $Å^2$. At areas less than 140 $Å^2$ a substantial increase in the surface pressure was observed, indicating the beginnings of thin film formation through intermolecular organisational self-assembly. This was the monolayer in its LE phase, which existed over only a very short surface area of 130-95 $Å^2$. Further compression of the barriers prompted interfacial molecules to interact with one another very strongly and become more densely packed, forming the LC phase of the monolayer between 95-64 $Å^2$, referred to as the Langmuir monolayer. Collapse of the film occurred at a surface pressure of 55 mN/m, which corresponds to a surface area of 68 $Å^2$ per molecule for complex **Eu·96**. An area of *ca.* 22 $Å^2$ at film collapse denotes the cross sectional area of *ca.* one alkyl chain.[213] Therefore the

area observed, 68 $Å^2$, corresponds well to what we expect from the three alkyl chains of **Eu·96**. Based on this we can assume that in the LC state, the Eu(III) metal centre is orientated towards (and interacting with) the water phase with the long hydrophobic alkyl chains orientated perpendicular to the subphase plane, as depicted in Figure 5.24. The same trend was also observed in the surface pressure-area isotherm of **Tb·96**, where film collapse occurred at *ca.* 67 $Å^2$ (Appendix A5.17).

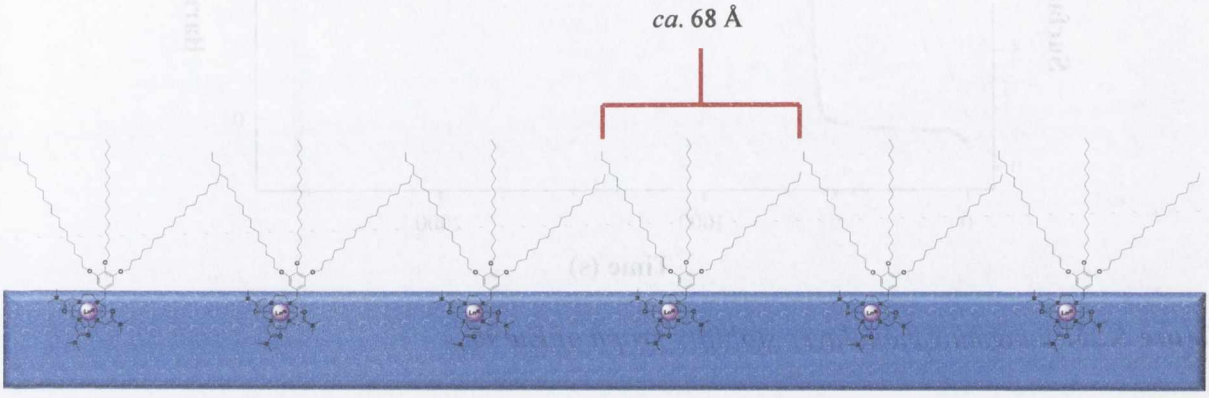


Figure 5.24: *Schematic representation of the Langmuir monolayer of* ***Ln·96*** *indicating the area occupancy of the three alkyl chains at the air water interface.*

5.6.2 Investigating the Stability of Monolayer of Eu·96 and Tb·96

In order to assess the stability of the Langmuir monolayers, measurements were carried out where the barriers were held at a fixed position for an extended period of time (over one hour) once the Langmuir film had reached the LC phase. Changes in the surface pressure were monitored over this time and the resulting plot from the stability study of **Eu·96** shown below in Figure 5.25 with that of **Tb·96** shown in Appendix A5.18. No significant decrease in the surface pressure was observed over this time, indicating that both Langmuir monolayers were relatively stable at the air water interface. An initial decrease was observed for both complexes before the pressure began to level off, possibly due to a certain amount of the monolayer forming micelles or the polar head group causing collapse of some molecules into the water subphase.

Having demonstrated successful Langmuir monolayer formation of **Eu·96** and **Tb·96** it was next decided to apply the Langmuir-Blodgett technique to immobilise the complexes onto a solid support and examine the photophysical properties of the LB films using absorption and steady-state spectroscopy.

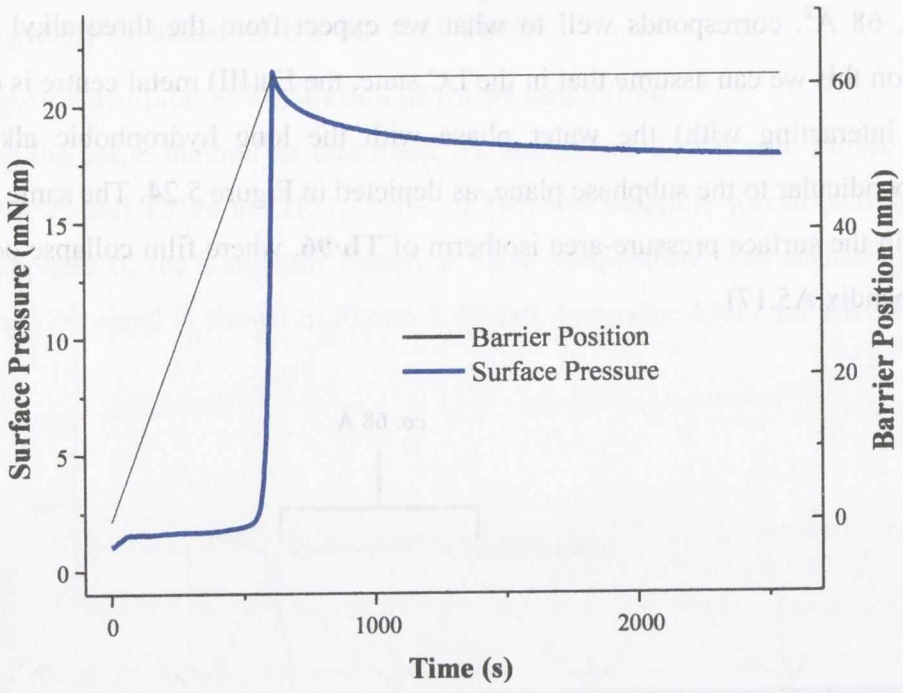


Figure 5.25: *Langmuir monolayer stability graph of* ***Eu·96****.*

5.6.3 LB Film Formation of Eu·96 and Tb·96

The dipping process utilised a quartz slide as the solid support for the deposition of the Langmuir film. Based on the isotherm measurements it was anticipated that deposition would occur through hydrophilic interactions between the polar head groups of the amphiphilic complexes and the hydrophilic surface of the untreated quartz slide. Because of this, dipping experiments occurred with the substrate submersed below the monolayer. Therefore, before formation of the monolayer the quartz slide (10 mm × 1 mm × 35 mm) was lowered and submerged to a depth of 10 mm below the water subphase surface. Having submerged the quartz slide, 20 μL of a solution of **Eu·96** and **Tb·96** in $CHCl_3$ (2.6×10^{-4} M) was carefully spread onto the surface of the water subphase of the Langmuir trough at room temperature, making sure that the surface pressure did not rise above 0.20 $Å^2$ during the spreading process. The solvent was allowed to evaporate over a period of 20 minutes. The barriers were slowly closed at a rate of 6 mm min^{-1} until a surface pressure of 30 mN m^{-1} was obtained. At this pressure the amphiphile was organised into its LE phase and allowed to stabilise for 20 minutes before emersion of the slide occurred by an upward stroke (at a speed of 5 mm min^{-1}) resulting in successful monolayer transfer.

Transfer of the monolayer from the water subphase surface to the quartz slide was monitored, as shown in Figure 5.26, with a transfer ratio of *ca.* 1 obtained for both **Eu·96** and **Tb·96** (Appendix A5.19) LB film deposition, indicating high quality transfer of the monolayer to the quartz slide with excellent order and uniformity.

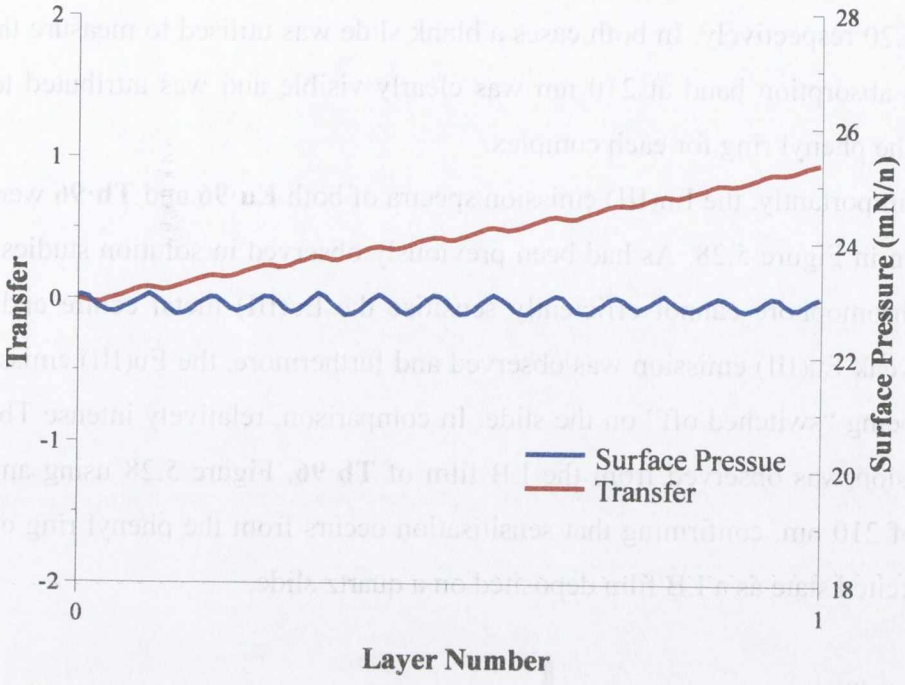


Figure 5.26: *Langmuir monolayer deposition graph of* ***Eu·96****.*

5.7 Photophysical Properties of Eu·96 and Tb·96 LB films

Having successfully formed LB films of **Eu·96** and **Tb·96**, their photophysical properties were next evaluated by recording their UV-vis absorption and phosphorescence spectra along with their lifetimes.

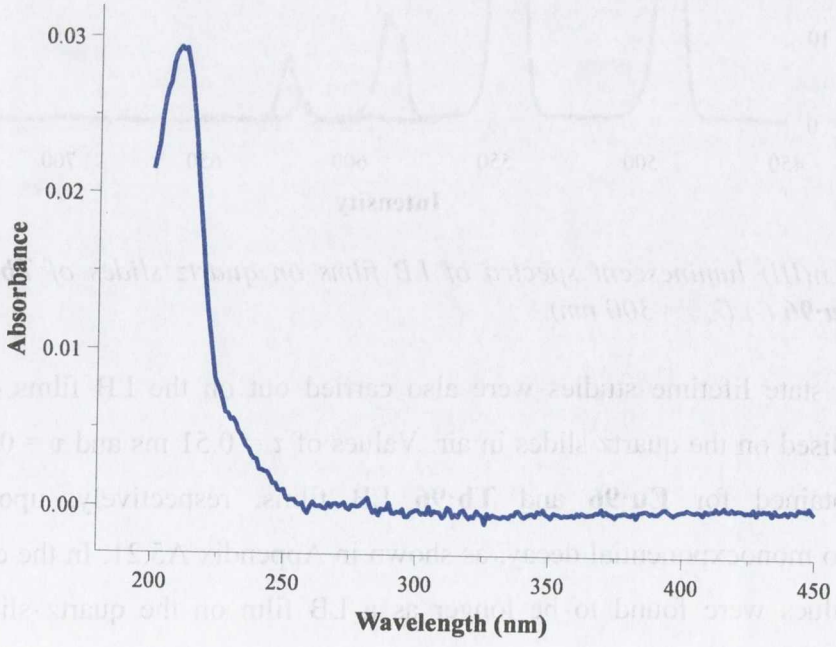


Figure 5.27: *The UV-vis absorption spectra of the LB film of* ***Eu·96*** *on a quartz slide.*

The UV-vis absorption spectra of **Eu·96** and **Tb·96** are shown in Figure 5.27 and Appendix A5.20 respectively. In both cases a blank slide was utilised to measure the baseline and the main absorption band at 210 nm was clearly visible and was attributed to the π-π* transition of the phenyl ring for each complex.

Most importantly, the Ln(III) emission spectra of both **Eu·96** and **Tb·96** were obtained and are shown in Figure 5.28. As had been previously observed in solution studies of **Eu·96**, the phenyl chromophore cannot efficiently sensitise the Eu(III) metal centre and therefore, only a very weak Eu(III) emission was observed and furthermore, the Eu(III) emission can be regarded as being "switched off" on the slide. In comparison, relatively intense Tb(III) metal centred emission was observed from the LB film of **Tb·96**, Figure 5.28 using an excitation wavelength of 210 nm, confirming that sensitisation occurs from the phenyl ring of **Tb·96** to the Tb(III) excited state as a LB film deposited on a quartz slide.

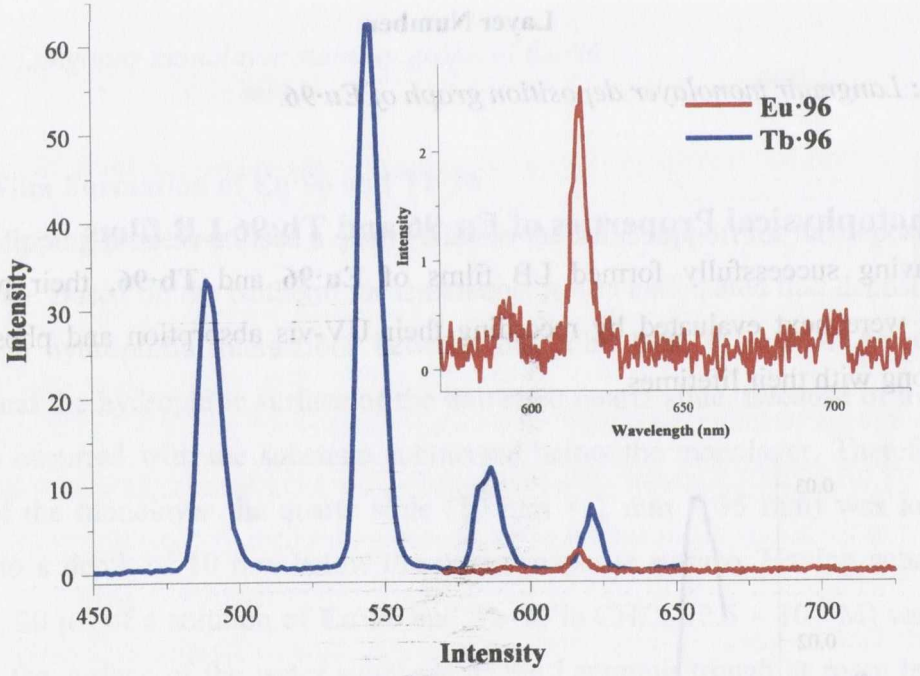


Figure 5.28: *Ln(III) luminescent spectra of LB films on quartz slides of* ***Tb·96*** *(-) (λ_{ex} = 210 nm) and* ***Eu·96*** *(-) (λ_{ex} = 300 nm).*

Excited state lifetime studies were also carried out on the LB films of **Eu·96** and **Tb·96** immobilised on the quartz slides in air. Values of τ = 0.51 ms and τ = 0.64 ms (Table 5.6), were obtained for **Eu·96** and **Tb·96** LB films, respectively, upon fitting the luminescence to monoexponential decay, as shown in Appendix A5.21. In the case of **Eu·96**, the lifetime values were found to be longer as a LB film on the quartz slide than those measured in $CHCl_3$ solution (τ = 0.24 ms). One possible explanation for this may be the fact that there may be no solvent molecules present on the slides, and therefore, quenching by solvent molecules of the Eu(III) metal centre cannot occur, resulting in the longer lifetimes

observed. The contrary was observed in the case of the **Tb·96** LB film, where the lifetimes are shorter as a LB film on quartz slides, Table 5.6, than those detected in $CHCl_3$ solution (τ = 1.07 ± 0.01 ms). This may be attributed to the quenching caused by oxygen which was more abundant on the quartz slide as it was open to the air than in $CHCl_3$ solution. Having fully photophysically characterised the LB films of **Eu·96** and **Tb·96** it was then decided to establish whether a LB film could be obtained of a 1:1 solution of **Eu·96:nta** and **Tb·96:DMAB**.

Table 5.6: *Lifetime studies for LB films on quartz slides of* ***Eu·96*** *and* ***Tb·96****, each number is an average of 6 measurements all agreeing to within 5% of each other with an error of ± 0.01.*

Species	τ(ms)	k (ms^{-1})
Eu·96	0.51	1.67
Tb·96	0.64	1.33

5.8 Langmuir Film Formation of Eu·96-nta and Tb·96-DMAB

Solutions of **Eu·96-nta** and **Tb·96-DMAB** were prepared in a 1:1 ratio of complex:antenna such that one antenna molecule would be bound to each complex in solution. These solutions were sent for mass spectrometry analysis, with a peak at m/z = 1740.1728 corresponding to a **[Eu·96-nta** – $H^+]^+$ species in solution was obtained using MALDI-ToF analysis, with the expected isotopic distribution pattern associated with Eu(III) complexes observed as shown in Figure 5.29. However, no hit was obtained for **Tb·96-DMAB**.

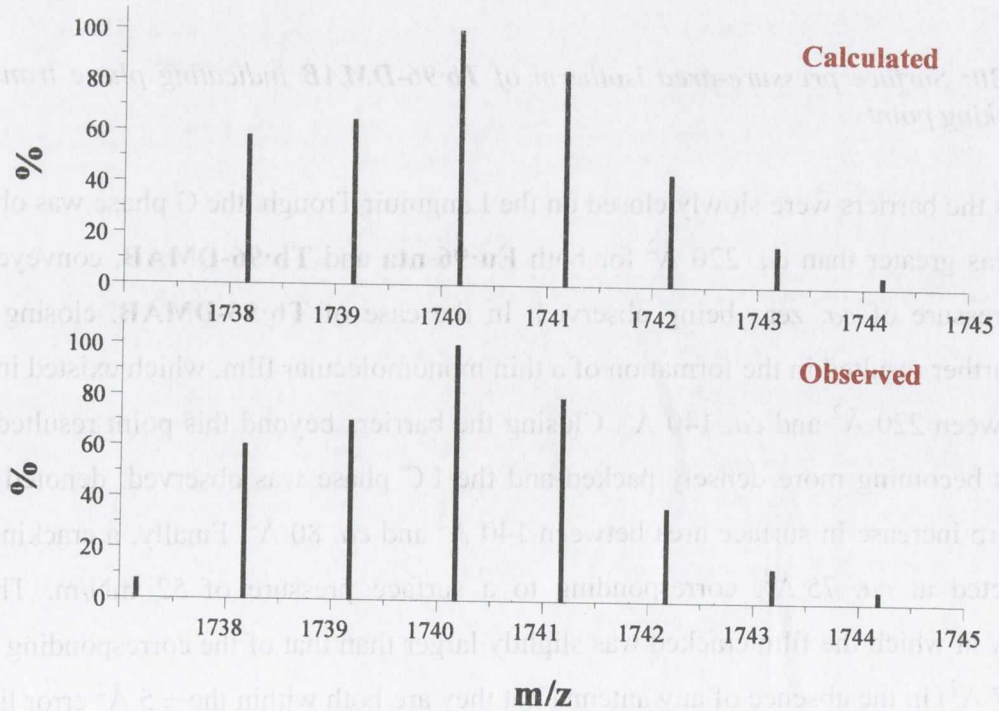


Figure 5.29: *The MALDI mass spectrum of* ***Eu·96-nta*** *displaying the expected Eu(III) isotopic distribution pattern for the [****Eu·96-nta*** *– $H^+]^+$ species.*

5.8.1 Langmuir Monolayer Formation of Eu·96-nta and Tb·96-DMAB

As previously described 20 μL of a solution of **Eu·96-nta** and **Tb·96-DMAB** in $CHCl_3$ (2.6×10^{-4} M) was carefully spread onto the surface of the water subphase of the Langmuir trough at room temperature. The organic solvent was allowed to evaporate off over 20 minutes before the barriers were slowly closed while the surface pressure of the decreasing area was continuously monitored. The resulting pressure-area isotherm graphs are shown in Appendix A5.17 and Figure 5.30 for **Eu·96-nta** and **Tb·96-DMAB**, respectively.

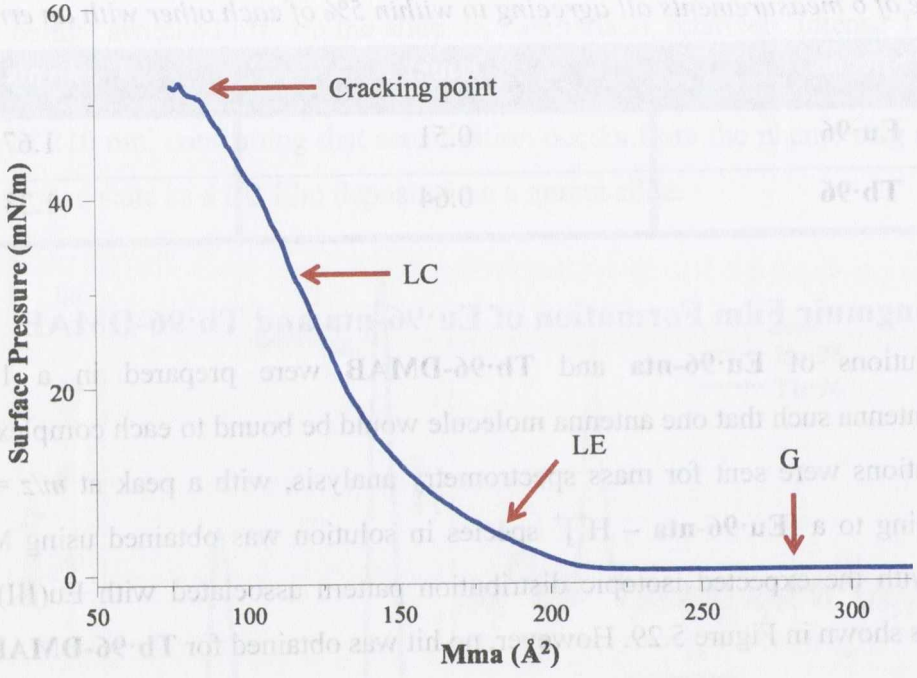


Figure 5.30: *Surface pressure-area isotherm of* ***Tb·96-DMAB*** *indicating phase transitions and a cracking point.*

As the barriers were slowly closed on the Langmuir Trough, the G phase was observed for all areas greater than *ca.* 220 Å^2 for both **Eu·96-nta** and **Tb·96-DMAB**, conveyed by a surface pressure of *ca.* zero being observed. In the case of **Tb·96-DMAB**, closing of the barriers further resulted in the formation of a thin monomolecular film, which existed in its LE phase between 220 Å^2 and *ca.* 140 Å^2. Closing the barriers beyond this point resulted in the molecules becoming more densely packed and the LC phase was observed, denoted by the rather sharp increase in surface area between 140 Å^2 and *ca.* 80 Å^2. Finally, a cracking point was detected at *ca.* 75 Å^2, corresponding to a surface pressure of 52 mN/m. The area occupancy at which the film cracked was slightly larger than that of the corresponding film of **Tb·96** (67 Å^2) in the absence of any antenna but they are both within the ± 5 Å^2 error limits of each other. We can also propose that the antenna is responsible for widening the area between

the amphiphilic **Tb·96** molecules, and hence, resulting in a larger cross sectional area occupied per molecule. A similar trend was observed for **Eu·96-nta** as shown in Appendix A5.22.

5.8.2 Stability of Monolayers of Eu·96-nta and Tb·96-DMAB

The stability of the Langmuir monolayers of **Eu·96-nta** and **Tb·96-DMAB** were next evaluated. A Langmuir monolayer film was formed on the Langmuir trough and the barriers were held at a fixed position once it had reached its LC phase. Alterations in the surface pressure were monitored over a relatively long time period, with the resulting plot of the stability measurements for **Eu·96-nta** and **Tb·96-DMAB** shown in Figure 5.31 and Appendix A5.23, respectively. The initial decrease in the surface pressure was significantly less than that observed in the stability study graphs of **Eu·96** and **Tb·96**. The films with the antenna attached appear to be more stable than their unsaturated complex counterparts. This may be attributed to the antenna groups taking away some of the polar nature of the head groups, making the amphiphilic molecules less likely to partake in the formation of micelles or collapse into the water subphase, and hence increasing the stability of the monolayer film. It was also noticed that at the stage that the film cracked, the water was pushed over the side of the Langmuir Trough, as shown below in Figure 5.31b. This denotes an extremely stable and flexible Langmuir monolayer that instead of completely collapsing will extend itself over the edges of the trough. This phenomenon was witnessed for both **Eu·96-nta** and **Tb·96-DMAB**.

Having demonstrated successful Langmuir monolayer formation of **Eu·96-nta** and **Tb·96-DMAB** the formation of LB films of the respective ternary complexes was next investigated.

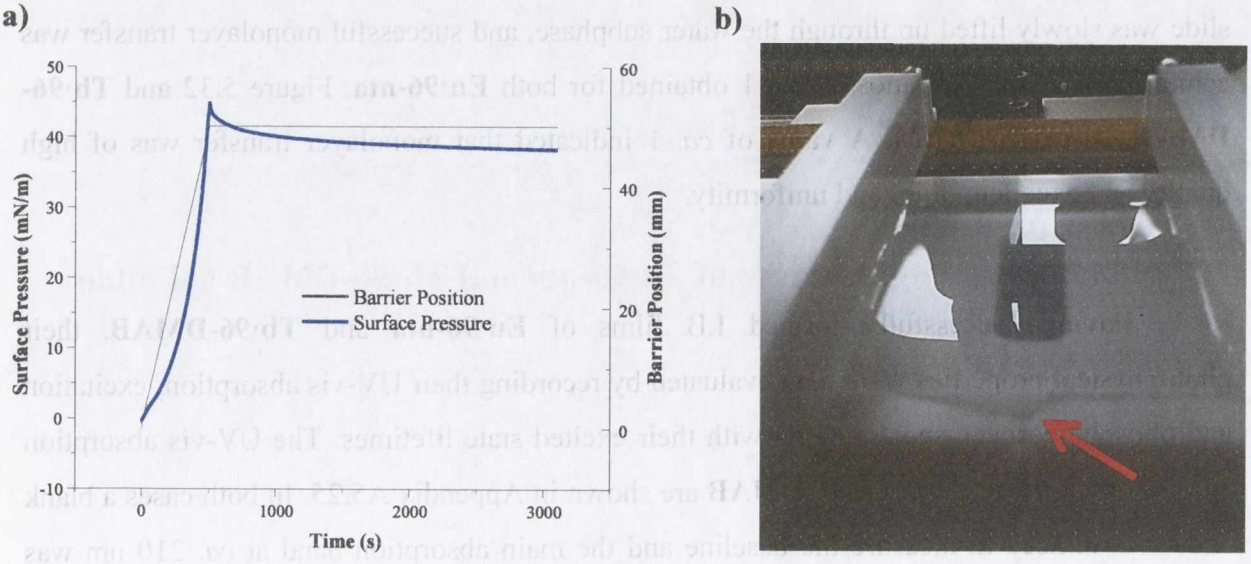


***Figure 5.31:** a) Langmuir monolayer stability graph of **Eu·96-nta**. b) Image of LB film of **Eu·96-nta** on Langmuir film showing film pushing off the side of the trough.*

5.8.3 LB Film Formation of Eu·96-nta and Tb·96-DMAB

The dipping process utilised was the same as that described for the LB film deposition of **Eu·96** and **Tb·96**. The quartz slide was submerged below the water subphase and 20 μL of solutions of **Eu·96-nta** and **Tb·96-DMAB** in $CHCl_3$ (2.6×10^{-4} M) were spread on the water subphase and the solvent allowed to evaporate for 20 minutes.

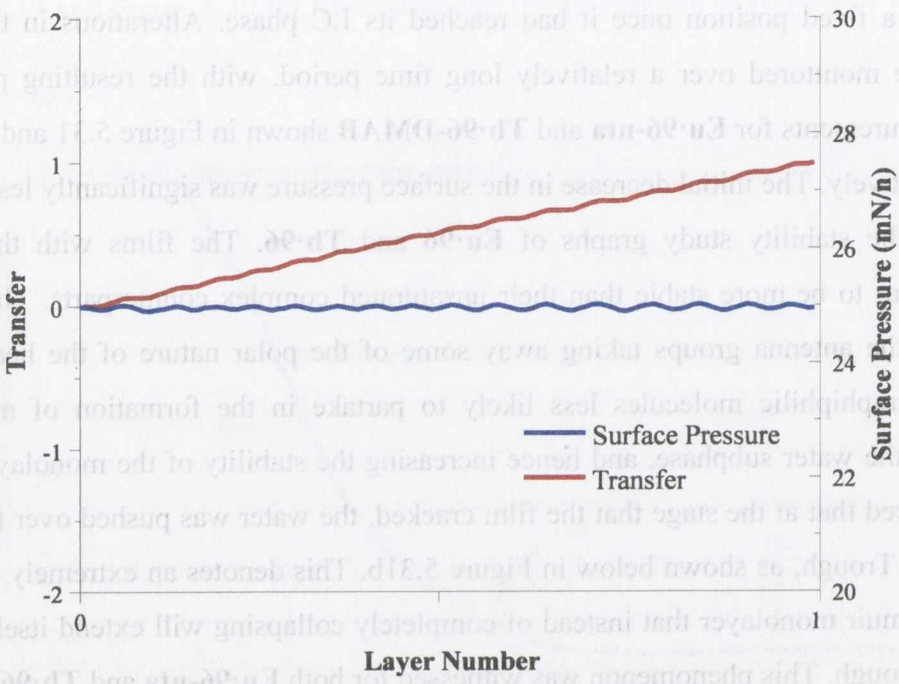


Figure 5.32: *Langmuir monolayer deposition graph of* ***Eu·96-nta****.*

The barriers were slowly closed until the molecules had arranged into the LE phase at a surface pressure of 25 mN m^{-1}. After allowing the monolayer to stabilise for 20 minutes the slide was slowly lifted up through the water subphase, and successful monolayer transfer was achieved with transfer ratios of *ca.* 1 obtained for both **Eu·96-nta**, Figure 5.32 and **Tb·96-DMAB**, Appendix A5.24. A value of *ca.* 1 indicated that monolayer transfer was of high quality and excellent order and uniformity.

5.9 Photophysical Properties of Eu·96-nta and Tb·96-DMAB LB Films

Having successfully formed LB films of **Eu·96-nta** and **Tb·96-DMAB**, their photophysical properties were next evaluated by recording their UV-vis absorption, excitation and phosphorescence spectra along with their excited state lifetimes. The UV-vis absorption spectra of **Eu·96-nta** and **Tb·96-DMAB** are shown in Appendix A5.25. In both cases a blank slide was utilised to measure the baseline and the main absorption band at *ca.* 210 nm was clearly visible and was attributed to the π-π^* transition of the phenyl ring for each complex. In the case of **Eu·96-nta** an additional absorption band centred at 330 nm was observed

corresponding to the **nta** antenna and for **Tb·96-DMAB** an absorption band centred at *ca.* 300 nm, characteristic of the **DMAB** antenna. The absorption spectra recorded were considerably weaker than any of the other spectra recorded. A baseline scan was recorded with a blank slide and although every effort was made to ensure the slide was cleaned thoroughly, the some bands of the UV-vis absorption spectra were barely visible.

The luminescence properties of the immobilised monolayers of **Eu·96-nta** and **Tb·96-DMAB** were also investigated, Figure 5.33. The Tb(III) emission arising from excitation into the **DMAB** antenna at 300 nm was recorded and found to be 2-fold greater than that of the LB film of **Tb·96** in the absence of the antenna attached (Appendix A5.26). A very faint green Tb(III) emission, that was visible to the naked eye was observed on the quartz slide under the UV lamp (but could not be picked up on camera). In contrast the Eu(III) emission of **Eu·96-nta** was very intense, and the red Eu(III) emission could be clearly observed by the naked eye under a UV lamp (see inset Figure 5.33). This was in contrast to the barely visible Eu(III) emission of the LB film of **Eu·96** (Figure 5.28). The Eu(III) emission was now "switched on" on the quartz slide.

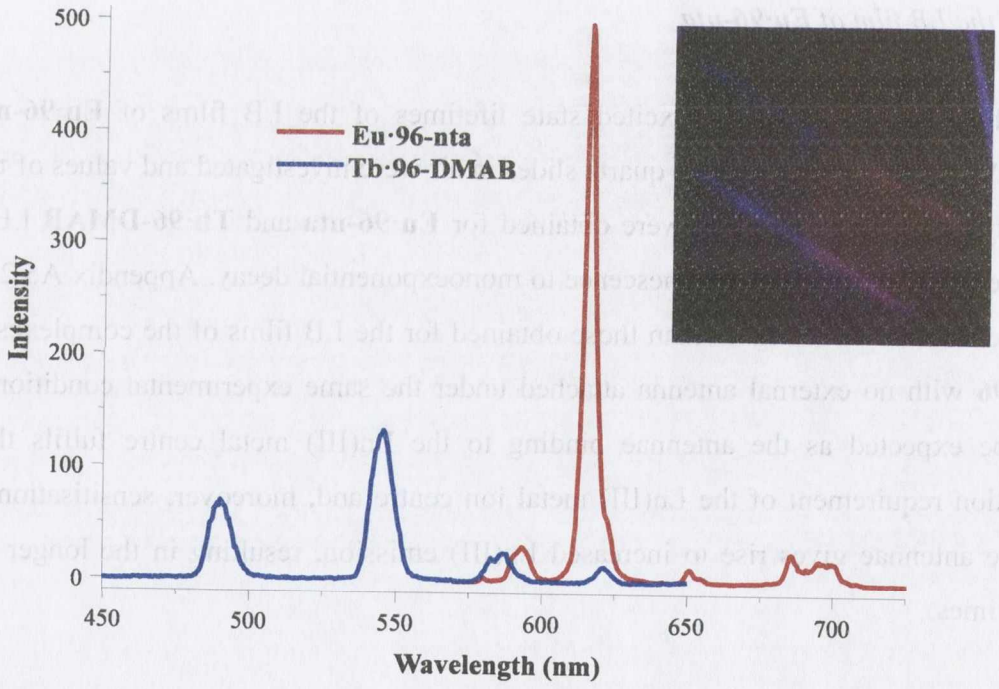


Figure 5.33: *Ln(III) luminescent spectra of LB films on quartz slides of* ***Tb·96-DMAB*** *(-) (λ_{ex} = 300 nm) and* ***Eu·96-nta*** *(-) (λ_{ex} = 330 nm). Inset: Eu(III) emission visible from LB film of* ***Eu·96-nta*** *on quartz slide.*

The excitation spectra for these samples were also recorded to ascertain that the sensitisation was occurring from the antenna. Figure 5.34 shows that the sensitisation of the Eu(III) metal centre of **Eu·96** was mainly transpiring from the 330 nm UV-vis absorption

band of **nta**. Similar results were obtained for the excitation spectra of **Tb·96**, Appendix A5.27.

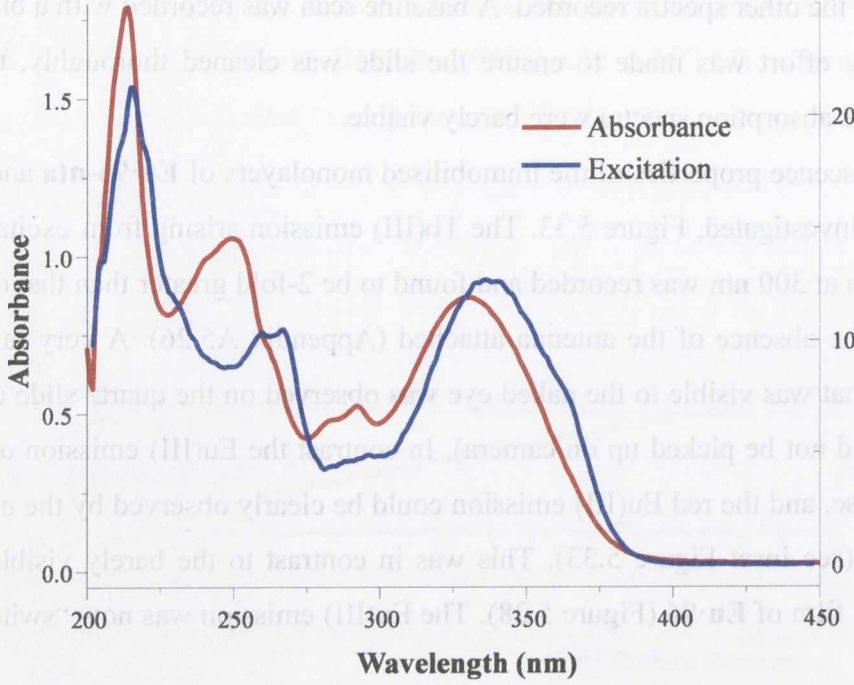


Figure 5.34: *The UV-vis absorption (-) of a solution of* ***nta*** *and excitation (λ_{em} = 545 nm) (-) spectra of the LB film of* ***Eu·96-nta****.*

The Eu(III) and Tb(III) excited state lifetimes of the LB films of **Eu·96-nta** and **Tb·96-DMAB** immobilised on the quartz slides in air were investigated and values of τ = 0.74 ms and τ = 1.23 ms (Table 5.6) were obtained for **Eu·96-nta** and **Tb·96-DMAB** LB films, respectively, upon fitting the luminescence to monoexponential decay, Appendix A5.28. Both values were found to be higher than those obtained for the LB films of the complexes **Eu·96** and **Tb·96** with no external antenna attached under the same experimental conditions. This was to be expected as the antennae binding to the Ln(III) metal centre fulfils the high coordination requirement of the Ln(III) metal ion centre and, moreover, sensitisation by the respective antennae gives rise to increased Ln(III) emission, resulting in the longer excited state lifetimes.

Table 5.7: *Lifetime studies for LB films on quartz slides of* ***Eu·96-nta*** *and* ***Tb·96-DMAB****, each number is an average of 6 measurements all agreeing to within 5% of each other with an error of ± 0.01.*

Species	τ(ms)	k (ms^{-1})
Eu·96-nta	0.74	1.34
Tb·96-DMAB	1.23	0.78

We have demonstrated in previous sections that the LB films of the Eu(III) and Tb(III) complexes of **96** can be formed in the presence and absence of antennae such as **nta** and **DMAB**, respectively. From the photophysical studies carried out on these LB films, it was evident that the Tb(III) emission was "switched on" in the absence of the antenna **DMAB** as the phenyl ring contained in the framework of ligand **96** was sufficient enough to sensitise the Tb(III) metal centre. This was not the case for **Eu·96**, where almost negligible Eu(III) emission was detected for the LB film on a quartz slide in the absence of **nta**, therefore the Eu(III) emission could be described as being "switched off" on the slide. The following section will describe the ability to "switch on" the Eu(III) emission of the LB film of **Eu·96**.

5.10 "Off/On" Eu(III) Emission from a LB Film of Eu·96.

A monolayer of **Eu·96** as a LB film on a quartz slide did not display significant Eu(III) emission when λ_{ex} = 330 nm was employed. The slide was immersed in an aqueous solution of **nta** (1×10^{-4} M) for one minute, as depicted in Figure 5.35, after which red Eu(III) emission was clearly visible under a UV lamp, and moreover, the characteristic Eu(III) spectrum was observed, Figure 5.36.

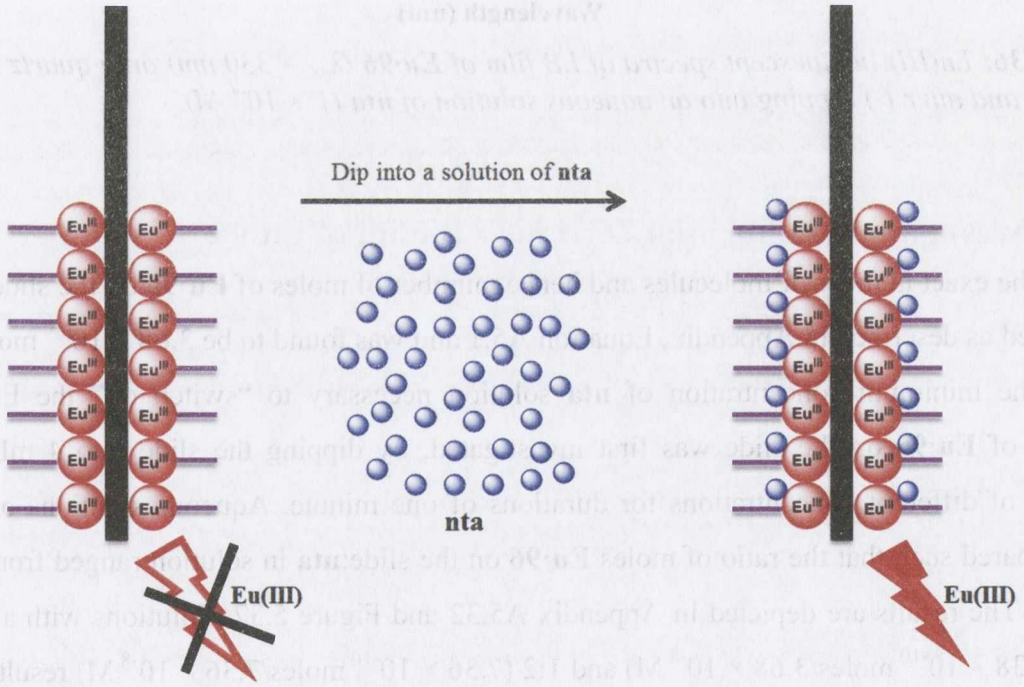


Figure 5.35: *Illustration of LB film of* ***Eu·96*** *on a quartz solid substrate dipped into an aqueous solution of* ***nta*** *(λ_{ex} = 330 nm).*

We have demonstrated that "off/on switching" of a Eu(III) complex as a LB film can be achieved by simply dipping the LB slide of **Eu·96** into an aqueous solution of **nta**. Even though it was determined that the amphiphilic molecules were orientated head first on the slide, the **nta** was still able to access and bind to the Eu(III) metal centre at the polar head end

of the molecule and allow for efficient Eu(III) sensitisation. The next step was to probe the limit of detection of **nta** by a LB film of **Eu·96**, in which the effect of slide immersion time and concentration of **nta** solution were investigated.

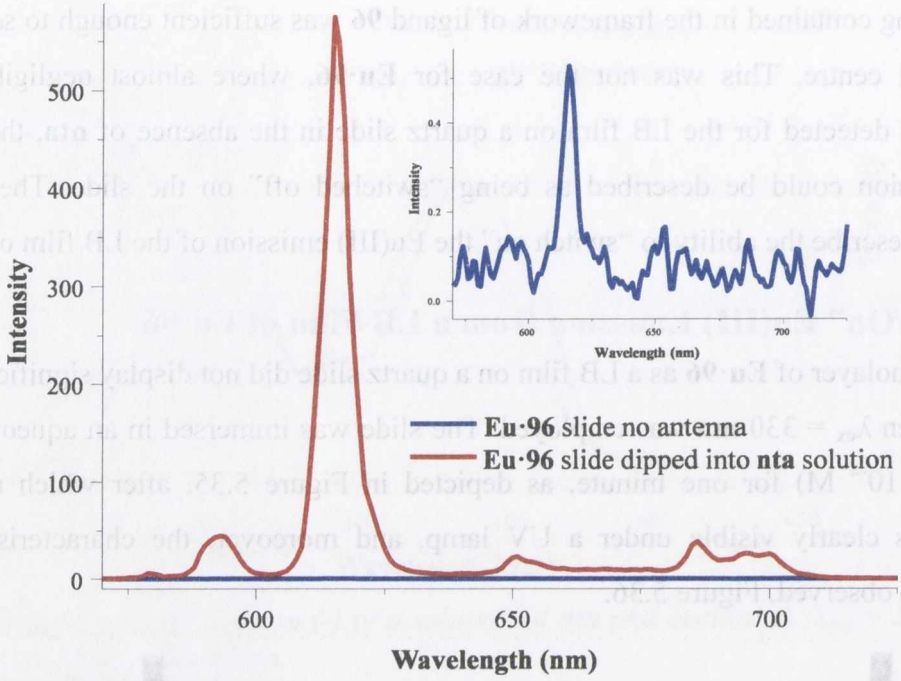


Figure 5.36: *Ln(III) luminescent spectra of LB film of* ***Eu·96*** *(λ_{ex} = 330 nm) on a quartz slide before (-) and after (-) dipping into an aqueous solution of* ***nta*** *(1 × 10^{-4} M).*

5.11 Investigation of Potential LOD for LB Film of Eu·96

The exact number of molecules and hence, number of moles of **Eu·96** on the slide was established as described in Appendix, Equation A5.1 and was found to be 3.68 × 10^{-10} moles.

The minimum concentration of **nta** solution necessary to "switch on" the Eu(III) emission of **Eu·96** on the slide was first investigated, by dipping the slide into 4 mL **nta** solutions of different concentrations for durations of one minute. Aqueous solutions of **nta** were prepared such that the ratio of moles **Eu·96** on the slide:**nta** in solution ranged from 1:1 to 1:100. The results are depicted in Appendix A5.32 and Figure 5.37. Solutions with a ratio of 1:1 (3.38 × 10^{-10} moles/3.68 × 10^{-8} M) and 1:2 (7.36 × 10^{-10} moles/7.36 × 10^{-8} M) resulted in only very minor increases in the Eu(III) emission (< 10%). However, using a 1:3 solution of **nta** (1.1 × 10^{-9} moles/1.1 × 10^{-7} M) resulted in a 4 fold increase in the Eu(III) emission from the slide that was significant enough to be described as "switched on" in comparison to the previous ratios.

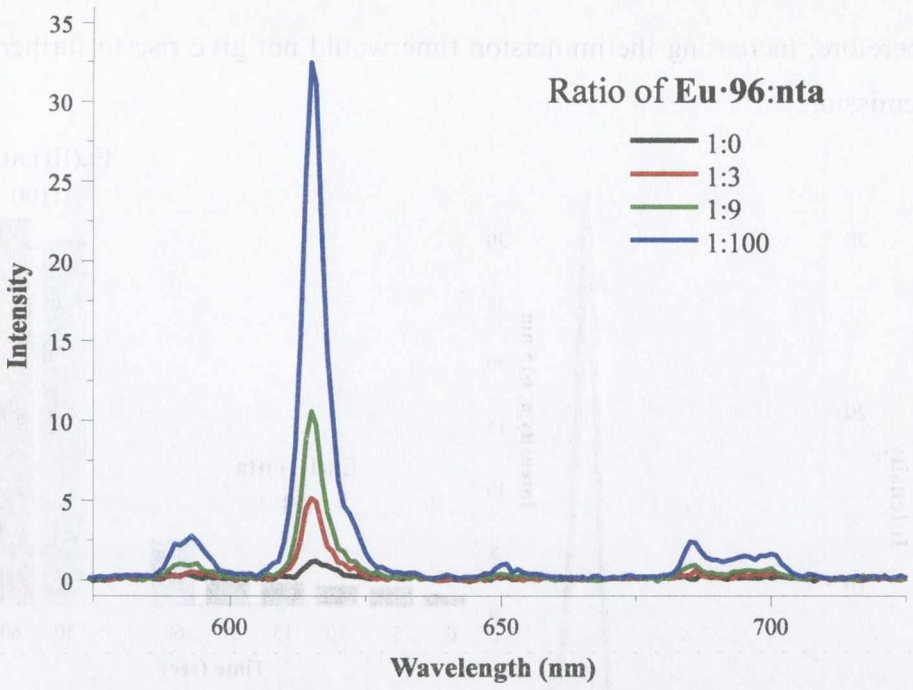


Figure 5.37: *LOD study of LB film of* ***Eu·96*** *using different concentrations of* ***nta*** *solution (λ_{ex} = 330 nm).*

It was determined that successful detection of **nta** in aqueous solution could be achieved at concentrations as low as 1.1×10^{-7} M. At concentrations lower than this the Eu(III) emission of the slide remained "switched off". Increasing the concentration of the **nta** solution from 1.1×10^{-7} M to 3.3×10^{-7} M causes further enhancements in the Eu(III) emission, where at a ratio of 1:100 the emission intensity had increased by over 2000%.

Next we investigated the effect that the immersion time of the slide within the **nta** solution had, the results of which are shown in Figure 5.38. Here, a slide of **Eu·96** was immersed into a 1.1×10^{-7} M solution of **nta** for 5, 10, 15, 30 and 60 seconds. Immersion up to 30 seconds did not give rise to any significant enhancement in the Eu(III) emission. However, a total immersion time of 60 seconds did give rise to a 4 fold increase in emission intensity. Using a more concentrated solution of **nta** 3.68×10^{-6} M (1:100 Eu(III):**nta**) allowed for a shorter immersion time of 30 seconds to achieve "switching on" of the Eu(III) emission.

In summary, these studies highlight the ability of a LB film of **Eu·96** to detect **nta** at concentrations as low as 1.1×10^{-7} M in aqueous solution with an immersion time of one minute. However, this immersion time was reduced to 30 seconds when a higher concentration of 3.68×10^{-6} M was used. Increasing the immersion time from 30 to 60 seconds using the concentration of 3.68×10^{-6} M (1:100 Eu(III):**nta**) did not result in any substantial increase in the Eu(III) emission from the slide. Due to the large excess of **nta** in solution in comparison to **Eu·96** on the slide it could be argued that in the short immersion time of 30 seconds an **nta** molecule had coordinated to each of the **Eu·96** molecules on the

slide and therefore, increasing the immersion time would not give rise to further increase in the Eu(III) emission.

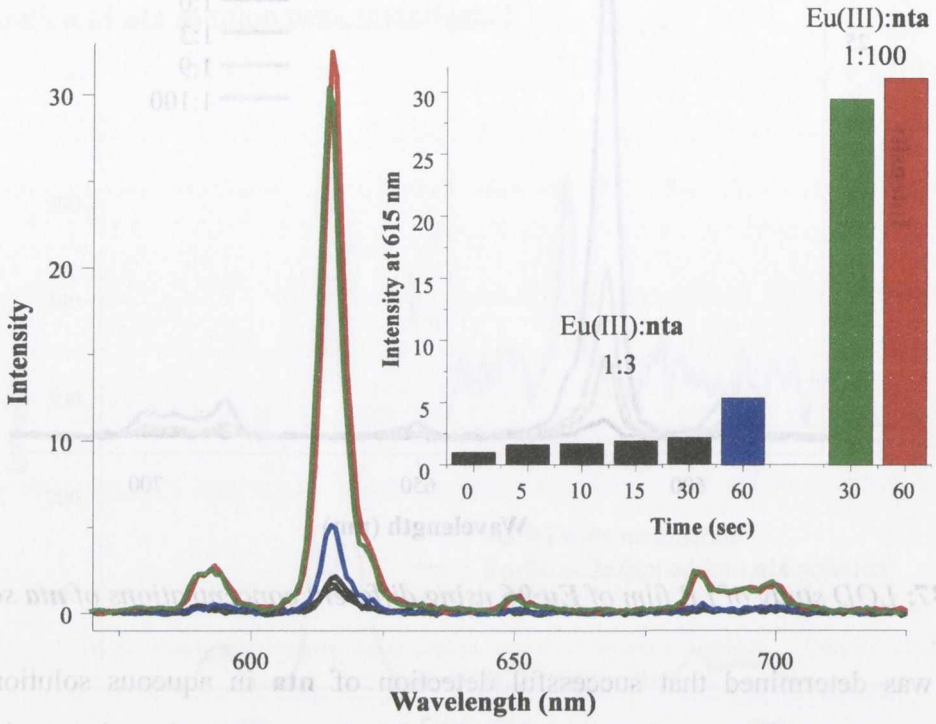


Figure 5.38: *LOD study of LB film of* ***Eu·96*** *using different immersion times (0-60 sec) of two concentrations of* ***nta*** *solution with ratios Eu(III):****nta*** *of 1:3 and 1:100 (λ_{ex} = 330 nm). Inset: Change in emission intensity at 615 nm as a function of immersion time in two different solutions.*

With a greater understanding of the potential LOD for a LB film of **Eu·96** the next stage involved investigating any change in Ln(III) emission of the LB films under a constant flow of water.

5.12 Flow Test of LB Films

In order to test the durability of the LB films of **Eu·96**, **Eu·96-nta**, **Tb·96** and **Tb·96-DMAB** on slides, simple, crude flow studies were carried out. These involved clamping a quartz slide coated with a LB film into a beaker, as depicted in Figure 5.39, into which a steady flow of tap water would pass through. The phosphorescence emission of the LB films were then measured at intervals under a constant flow of tap water in order to determine if the LB films would remain on the slide, and hence, if the Ln(III) luminescence from the film could be sustained, even with the constant flow of water between 15 minutes and 24 hours. The average water flow recorded was a rate of 75 mL / minute. The reason for this study was twofold, as tap water contains many impurities that may harm the film at the same time that the water has numerous potential analytes that might compete for any kind of recognition and as such this flow test could serve as a preliminary study for the potential use of these systems in a highly competitive environment.

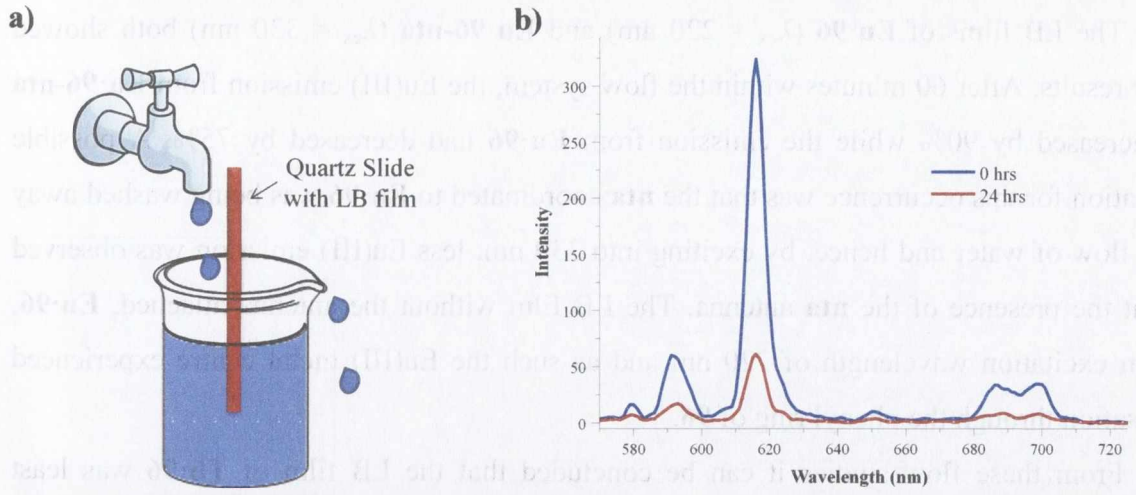


Figure 5.39: a) *Illustration of flow cell set up with quartz slide coated with LB film.* ***b)*** *Change in the Eu(III) emission of* ***Eu·96*** *(λ_{ex} = 220 nm) after 24 hours under the flow system.*

The results from the four different flow studies are illustrated below in Figure 5.40. The slide with a LB film of **Tb·96** with no antenna attached showed a substantial decrease in emission intensity at 545 nm upon excitation at 220 nm. After only 5 minutes within the flow system the emission intensity had decreased by 93% and after 2 hours the Tb(III) emission was barely measureable, Appendix A5.33. It was concluded that the LB film of **Tb·96** was almost completely removed by the flow of water under these conditions.

The same effect was not observed for **Tb·96-DMAB**, as after 5 minutes of water flow the Tb(III) emission intensity quenching was significantly less (*ca.* 50%). Also, the Tb(III) emission remained at a sizeable level thereafter, and was 10% of its original intensity even after being subjected to 24 hours under the flow system, Appendix A5.34.

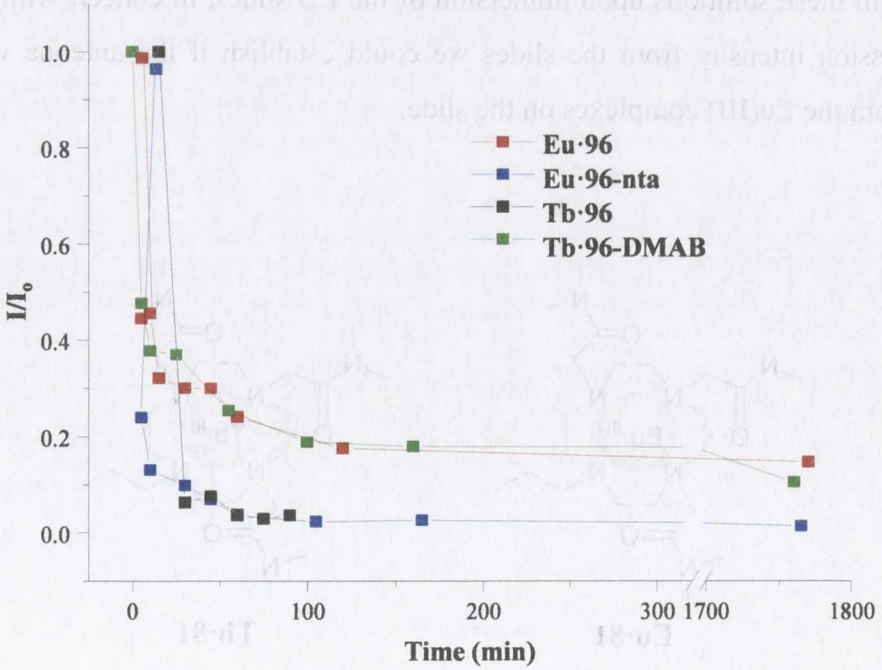


Figure 5.40: *Flow studies of LB film of* ***Eu·96****,* ***Eu·96-nta****,* ***Tb·96*** *and* ***Tb·96-DMAB*** *showing the changes in the normalised emission intensity (I/I_o) at 545 nm (Tb(III)) and 615 nm (Eu(III)) over time (0-24 hours).*

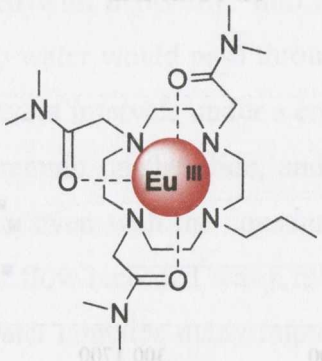
The LB films of **Eu·96** (λ_{ex} = 220 nm) and **Eu·96-nta** (λ_{ex} = 330 nm) both showed similar results. After 60 minutes within the flow system, the Eu(III) emission from **Eu·96-nta** had decreased by 90% while the emission from **Eu·96** had decreased by 75%. A possible explanation for this occurrence was that the **nta** coordinated to **Eu·96** was being washed away by the flow of water and hence, by exciting into 330 nm, less Eu(III) emission was observed without the presence of the **nta** antenna. The LB film without the antenna attached, **Eu·96**, used an excitation wavelength of 220 nm and as such the Eu(III) metal centre experienced sensitisation through the phenyl ring of **96**.

From these flow studies it can be concluded that the LB film of **Tb·96** was least durable of the films, and appeared to be almost completely removed from the slide within 2 hours under a constant flow of water. The LB film of **Eu·96** showed the highest Ln(III) emission remaining after 24 hours under the harsh flow system.

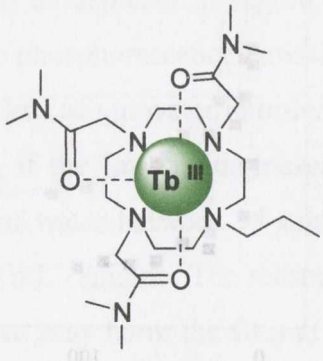
The studies described in the following section involved using aqueous solutions doped with Eu(III) and Tb(III) complexes in order to carry out "scavenger tests" on slides with a LB film of **Eu·96-nta**. The slides were immersed in the solutions of Eu(III) and Tb(III) complexes and the ability of the Ln(III) solutions to scavenge the antenna off the Eu(III) on the slide was examined.

5.13 Scavenger Tests on LB Films of Eu·96-nta

Compounds **Eu·81** and **Tb·81** were chosen to act as "scavengers" for the **nta** antenna on the LB film of **Eu·96-nta**. By monitoring whether an increase in Ln(III) emission was detected from these solutions upon immersion of the LB slides, in concert with a decrease in Eu(III) emission intensity from the slides we could establish if the antenna was becoming detached from the Eu(III) complexes on the slide.



Eu·81



Tb·81

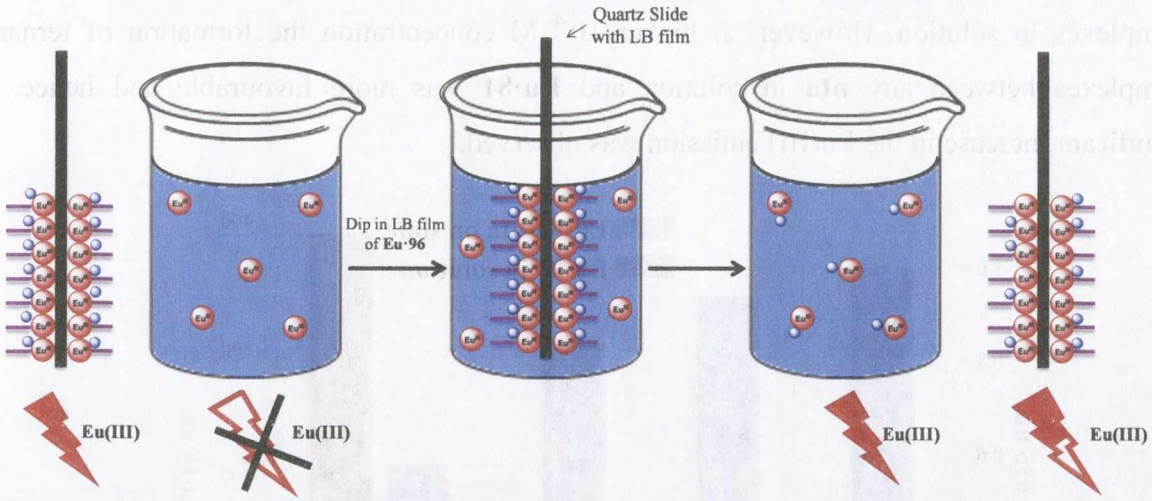


Figure 5.41: *Illustration of immersion of the emissive LB film of* ***Eu·96-nta*** *into a non-emissive solution of* ***Eu·81****.*

5.13.1 Eu(III) Scavenger Test

The solutions of **Eu·81** prepared for the scavenger tests were of different concentrations, such that the ratio of **Eu·96-nta** on the slide:**Eu·81** in solution was 1:100, 1:1000 and 1:10000. The Eu(III) emission of the solutions were measured before slide immersion (λ_{ex} = 330 nm) and the results showed that no detectable Eu(III) emission was observed. A slide possessing a LB film of **Eu·96-nta** was then immersed into the most dilute solution (1:100) and left sitting for one hour, after which time it was removed and the Eu(III) emission arising from both the slide and solution were remeasured.

After one hour immersion at 10^{-6} M concentrations of **Eu·81** (1:100 **Eu·96-nta**:**Eu·81)** the Eu(III) emission from the **Eu·96-nta** slide had decreased by only 7%, with a concomitant 12% increase in the Eu(III) emission arising from the **Eu·81** solution, Figure 5.42, Appendix A5.37 and A5.38. It was hypothesised that some of the **nta** had become dislodged from the Eu(III) metal centre of the **Eu·96** on the slide and instead were free to coordinate and excite the **Eu·81** molecules in solution. The slide was then re-immersed for one hour in a 10^{-5} M solution of **Eu·81** (1:1000 **Eu·96-nta**:**Eu·81)**. This lead to a further 10% decrease in the Eu(III) emission of the LB film and a further 15% increase in the emission from the **Eu·81** solution. Finally the slide was immersed in a 10^{-4} M solution of **Eu·81** (1:10000 **Eu·96-nta**:**Eu·81)**, which resulted in further changes in the Eu(III) emission from both the slide and solution, where the emission from the LB film had decreased by a total of 45% from the initial emission intensity and the Eu(III) emission output of **Eu·81** experienced a 390% increase. At the lower concentrations of **Eu·81** solution, even though the **nta** antenna had become dislodged from the **Eu·96** complexes on the slide the concentrations of **Eu·81** were still very low and thus the equilibrium may not have been fully shifted toward the formation of ternary

complexes in solution. However, at higher 10^{-4} M concentration the formation of ternary complexes between any **nta** in solution and **Eu·81** was more favourable and hence, a significant increase in the Eu(III) emission was observed.

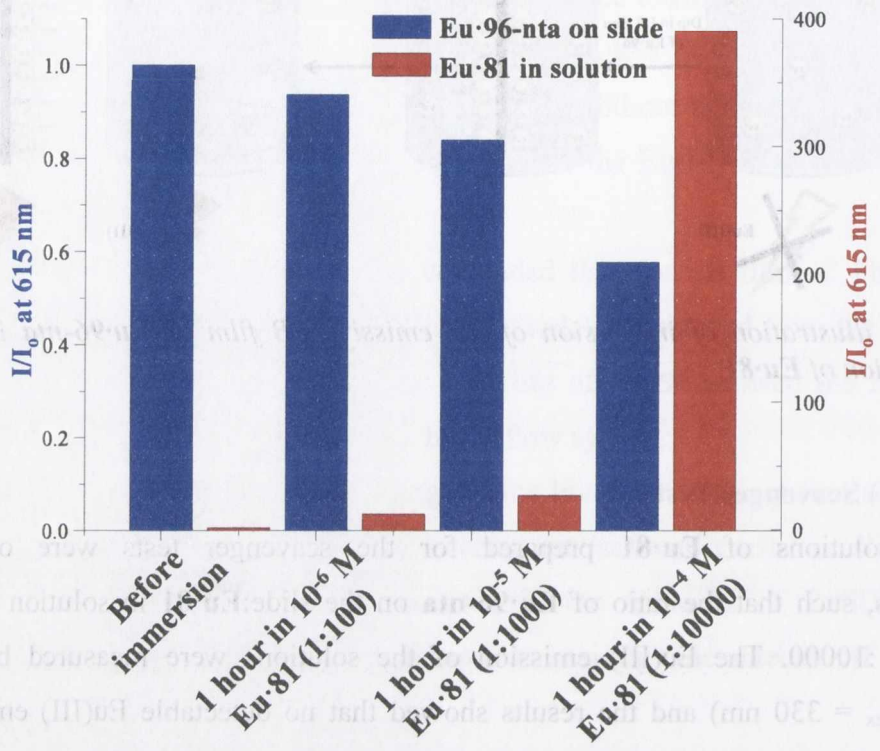


Figure 5.42: *Scavenger studies of LB film of* ***Eu·96-nta*** *immersed in solutions of* ***Eu·81*** *showing the changes in the normalised emission intensity (I/I_o) at 615 nm of both the LB film* ***Eu·96-nta*** *and the solution* ***Eu·81****.*

5.13.2 Tb(III) Scavenger Test

The same scavenger test was carried out on a LB film of **Eu·96-nta** using **Tb·81**. Again, three solutions of **Tb·81** with concentrations of 10^{-6} M, 10^{-5} M and 10^{-4} M, were prepared corresponding to ratios (**Eu·96-nta**:**Tb·81**) of 1:100, 1:1000 and 1:10000, respectively. The phosphorescence spectra (λ_{ex} = 220 nm and 330 nm) of the **Tb·81** solutions were recorded before immersion, and while there was no observable Tb(III) emission upon excitation at 330 nm, significant Tb(III) emission was detected using λ_{ex} = 220 nm. The **Eu·96-nta** slide was placed into a 10^{-6} M solution of **Tb·81** and continually scaned for one hour. It was then immersed in solutions of 10^{-5} M and 10^{-4} M **Tb·81** and left continually scanning. The changes in the Eu(III) and Tb(III) emission at 615 nm and 545 nm, respectively, were monitored and the results are shown in Figure 5.44 and Appendix A5.39.

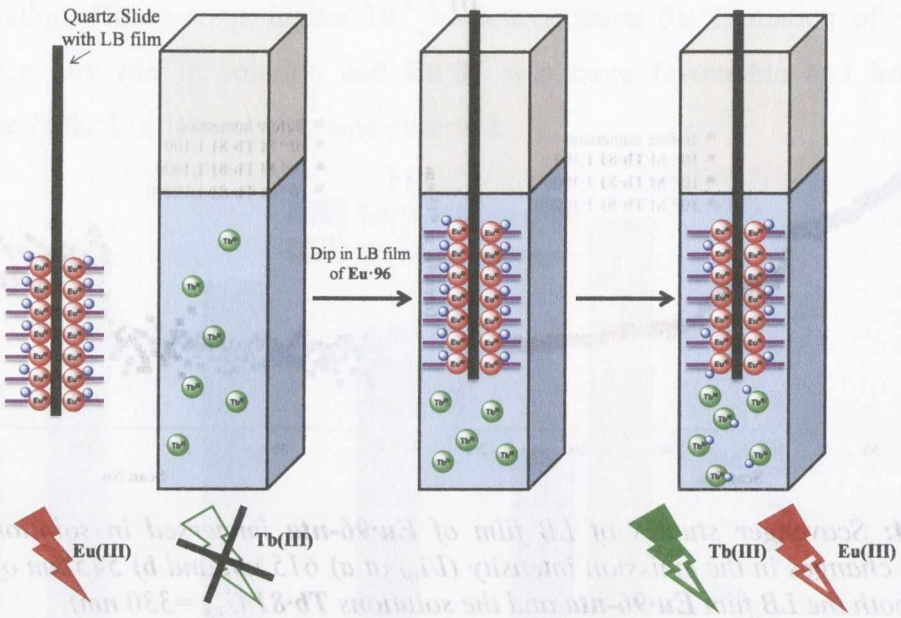


Figure 5.43: *Illustration of immersion of the emissive LB film of* ***Eu·96-nta*** *into a non-emissive solution of* ***Tb·81*** *in a fluorescence cell.*

The results from this investigation showed that there was a 28% decrease in the Eu(III) centred emission after one hour of immersion in a cuvette containing a 10^{-6} M solution of **Tb·81**. However, no increase in the Tb(III) centred emission was recorded. The slide was thus next immersed in a cell containing a 10^{-5} M solution of **Tb·81** and was left to scan over a period of one hour. A further 33% decrease in the emission of the Eu(III) was observed for **Eu·96-nta** (on the LB film). Again, no Tb(III) emission was detected. Finally, the slide was immersed in a 10^{-4} M solution of **Tb·81** in the cuvette so that the ratio of **Eu·96-nta** on the LB film:**Tb·81** was 1:10000. This gave rise to a 25% decrease in the Eu(III) emission intensity from the slide and furthermore, a 7 fold increase was observed in the Tb(III) emission. The ratio of **nta**:Tb(III) complexes in solution was high enough that the formation of **Tb·81-nta** ternary complexes was more favourable than in the previous dilutions of **Tb·81**. The antenna **nta** is not optimal for the sensitisation of Tb(III) complexes and the energy transfer to the Tb(III) metal centre from **nta** cannot occur due to the proximity of their triplet states. The increase in the Tb(III) emission that was observed is consistent with displacement of the metal bound water molecules from the Tb(III) metal centre in aqueous solution. The phosphorescence spectra of the **Eu·96-nta** slide and the **Tb·81** solution were recorded before and after immersion of the slide in the solution using the excitation wavelength of 220 nm, Figure 5.45.

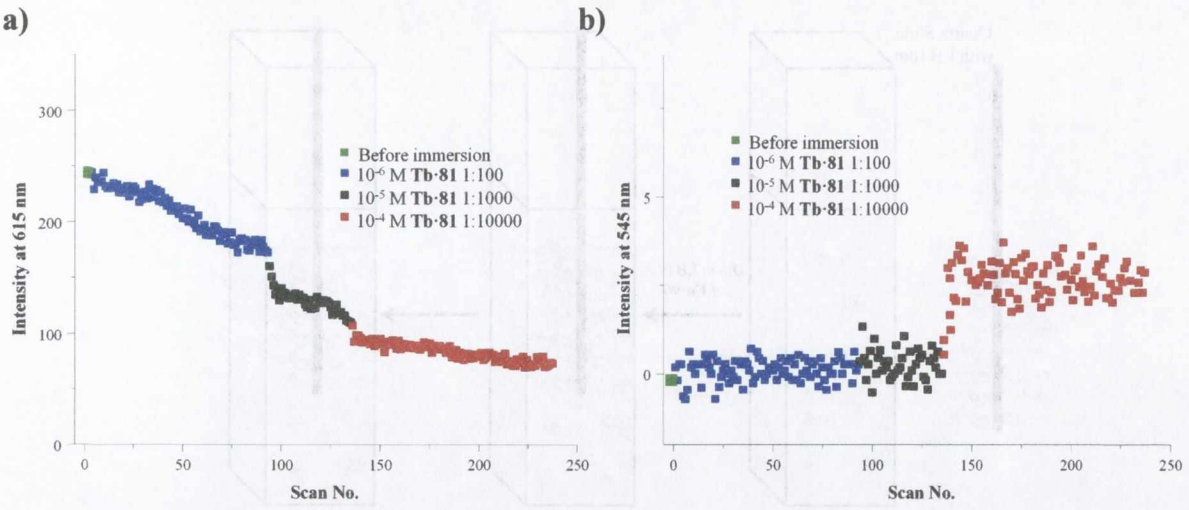


Figure 5.44: *Scavenger studies of LB film of* ***Eu·96-nta*** *immersed in solutions of* ***Tb·81*** *showing the changes in the emission intensity (I/I_o) at* ***a)*** *615 nm and* ***b)*** *545 nm of the cuvette containing both the LB film* ***Eu·96-nta*** *and the solutions* ***Tb·81*** *(λ_{ex} =330 nm).*

By using excitation at 220 nm and a high concentration of **Tb·81** (10^{-4} M), the Tb(III) emission was visible before immersion of the slide. However, after immersion a 2.5 fold enhancement was observed in the Tb(III) emission with a concomitant 2.5 fold decrease in the Eu(III) emission, reflecting the displacement of the **nta** antenna from **Eu·96** by **Tb·81** in solution and is consistent with the discussion above that the increase in the Tb(III) emission is due to the displacement of the metal bound water molecules from the metal centre, and not by sensitisation from **nta**.

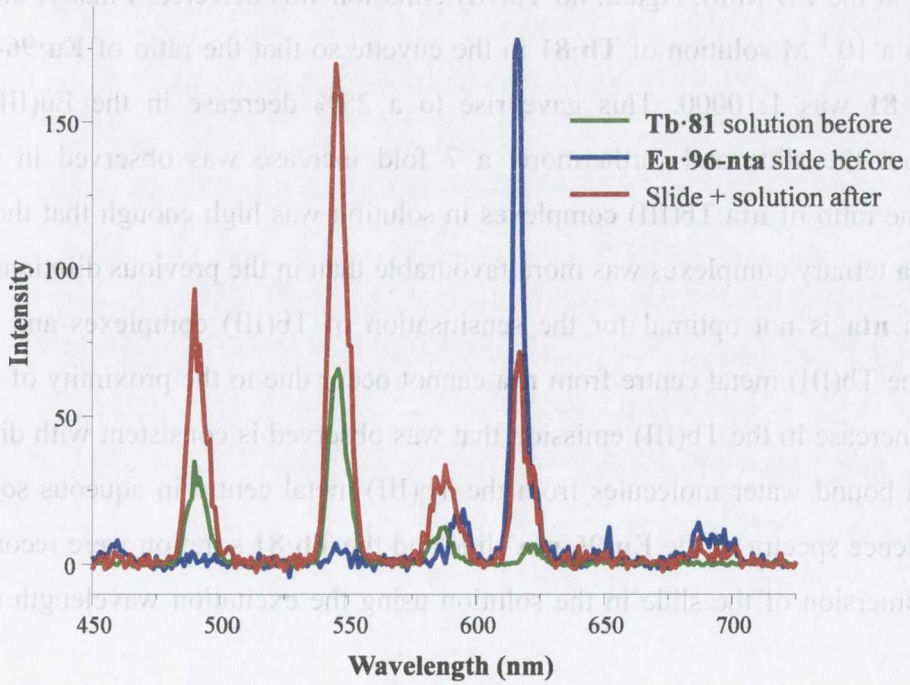


Figure 5.45: *Scavenger studies of LB film of* ***Eu·96-nta*** *immersed in 10^{-4} M solution of* ***Tb·81*** *showing the emission spectra recorded of the film and the slide before immersion and after (λ_{ex} =220 nm).*

The competitive binding described above show that by immersing slides of **Eu·96-nta** in solutions of **Eu·81** and **Tb·81** the **nta** can be displaced from **Eu·96** on the slide. In the case of **Eu·81** the Eu(III) emission was "switched on" by sensitisation of **Eu·81** by **nta** molecules in solution, however the Tb(III) emission is only increased due to displacement of the metal bound water molecules as no sensitisation of the Tb(III) occurs through **nta**.

5.14 Multilayer Deposition

In addition to forming monolayers on a solid support, it is also highly desirable to form multilayers, which would enhance emission signals, which is important in the fabrication of signalling devices.[224] The deposition of multilayers onto a solid support such as a quartz slide offers a versatile means of obtaining a hierarchical arrangement of molecules, with controlled intermolecular interactions. Both **Eu·96-nta** and **Eu·96** were examined for their ability to form multilayers.

5.14.1 Multilayer Deposition of Eu·96-nta

The multilayering experiment required a clean quartz slide to be lowered onto the top of the water subphase, but not lowered into the water as in previous experiments, before spreading 20 μL of the **Eu·96-nta** solution onto the surface. The solvent was allowed to evaporate off before the barriers were closed until the required pressure at which the monolayer was in its LE phase was reached, *ca.* 25 mN/m. Once the monolayer had stabilised the quartz slide was set up to go through a dipping experiment of ten cycles, consisting of five downward strokes and five upward strokes, beginning with a downward stroke through the monolayer and water subphase. The transfer ratio (TR) was recorded after each cycle, and the overall results of the multilayer deposition are shown below in Table 5.8.

Initial immersion of the slide through the monolayer into the water subphase resulted in a TR of *ca.* 0, indicating that no deposition onto the quartz substrate had occurred. However, subsequent emersion of the slide provided successful deposition of **Eu·96-nta** onto the quartz slide with a TR of *ca.* 1. The second downward stroke of the slide through the monolayer and water subphase also resulted in effective monolayer transfer with a TR of *ca.* 1 again being achieved. Re-emersion of the slide again gave rise to monolayer deposition with a TR of *ca.* 1. At this stage, after the first four deposition attempts, 3 layers of **Eu·96-nta** had been immobilised onto the solid support. The remaining deposition attempts, 5-10, followed a sequence of layer removal upon the downward stroke (TR *ca.* -1) and monolayer re-deposition upon the upward stroke such that after the 10 deposition attempts, three monolayers of **Eu·96-nta** remained on the quartz slide.

Table 5.8: *Multilayer deposition of* ***Eu·96-nta*** *onto quartz solid support showing transfer ratio after each deposition.*

Layer Number	*TR*	*Film ON/OFF*
1	0.062	-
2	1.073	ON
3	0.837	ON
4	0.885	ON
5	-0.936	OFF
6	0.939	ON
7	-1.021	OFF
8	0.957	ON
9	-0.965	OFF
10	0.915	ON

From these results it was concluded that a mixed deposition mode had occurred; deposition upon immersion and deposition upon emersion. This is the most common type of film deposition and is also referred to as Y-type deposition whereby the molecules are stacked onto the quartz slide in a head-to-head/tail-to-tail pattern as depicted in Figure 5.46.

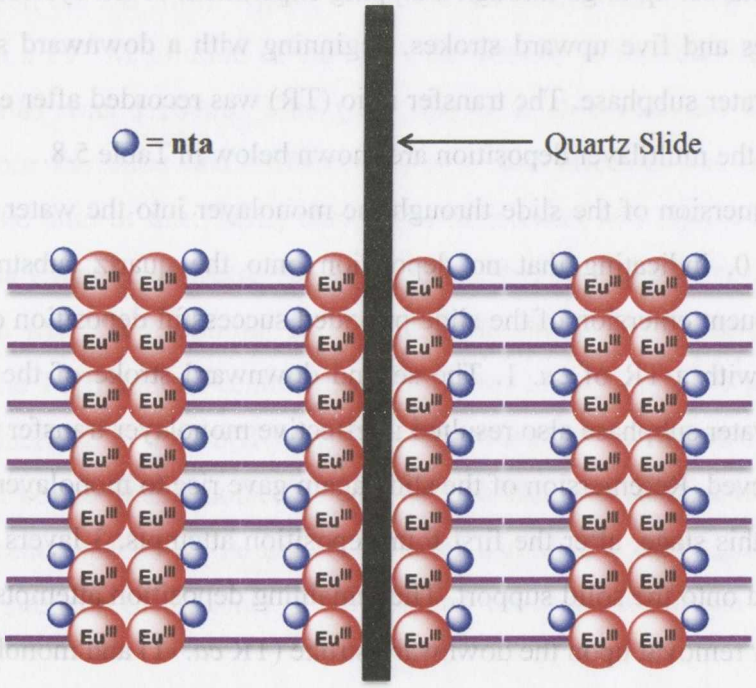


Figure 5.46: *Illustration of LB film multilayer of* ***Eu·96-nta*** *on a quartz solid substrate.*

The Eu(III) emission from the multilayered (ML) slide possessing three layers of **Eu·96-nta** was measured and compared to that of the slide with single deposition of **Eu·96-nta**. The same settings were employed and the resulting Eu(III) emission spectra are shown in Figure 5.47. It was discovered that the Eu(III) emission from the ML slide was *ca.* three times more intense than that of the single deposition, in keeping with the three fold increase in Eu(III) concentration on the ML slide.

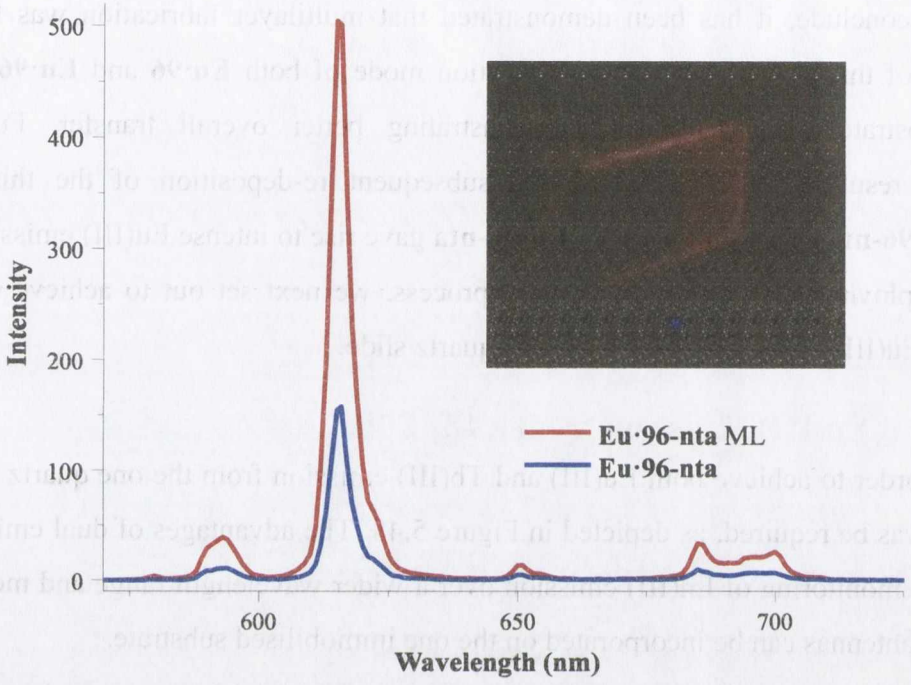


Figure 5.47: *Eu(III) emission from the multilayered LB film of* ***Eu·96-nta*** *(λ_{ex} = 330 nm) on a quartz slide. Inset: Eu(III) emission visible under a UV lamp from the multilayered LB film of* ***Eu·96-nta*** *on quartz slide.*

The Eu(III) emission of the ML of **Eu·96-nta** on the quartz slide is also clearly visible by the naked eye under a UV lamp, as shown in the inset in Figure 5.47, where red emission is observed from the ML film.

5.14.2 Multilayer Deposition of Eu·96

The same multilayering experiment was carried out on a monolayer of **Eu·96**. The transfer ratio was recorded after each cycle, and the overall results of the multilayer deposition are shown in Appendix, Table A5.1. As had been observed for **Eu·96-nta**, there was no deposition of **Eu·96-nta** on the quartz slide upon the initial downward stroke through the water subphase (TR *ca.* 0). Removal of the quartz slide from the water subphase did, however, give rise to deposition of a monolayer of **Eu·96-nta** on the slide (TR *ca.* 1). Subsequent re-immersion of the slide only gave rise to partial monolayer transfer with a TR of *ca.* 0.6. This partial transfer was in contrast to the effective monolayer transfer (TR *ca.* 1) of **Eu·96-nta** achieved on the second downward stroke, and can be attributed to the fact that the monolayer

of **Eu·96-nta** was found to be more stable than its non-ternary counterpart, **Eu·96-nta**, which in turn may affect the transfer ability of the monolayer. Re-emersion of the slide resulted once more in partial transfer of **Eu·96** being achieved, with a TR *ca.* 0.7. Hence, after two full cycles of dipping, one successful and two partial monolayer transfers have been achieved. Further dipping cycles followed the same trend as had been previously observed for **Eu·96-nta**; a layer was removed upon slide emersion and re-deposited upon re-emersion.

To conclude, it has been demonstrated that multilayer fabrication was limited to a maximum of three layers of Y-type deposition mode of both **Eu·96** and **Eu·96-nta** on the quartz substrate, with **Eu·96-nta** demonstrating better overall transfer. Further layer deposition resulted in the removal and subsequent re-deposition of the third layer of **Eu·96/Eu·96-nta**. The multilayers of **Eu·96-nta** gave rise to intense Eu(III) emission.

Employing the same multilayering process, we next set out to achieve dual Ln(III) emission (Eu(III) and Tb(III)) from the one quartz slide.

5.15 Dual Ln(III) Emission from a LB Film

In order to achieve both Eu(III) and Tb(III) emission from the one quartz slide, multi-dipping was be required, as depicted in Figure 5.48. The advantages of dual emission is that it enables monitoring of Ln(III) emission over a wider wavelength range and moreover, two different antennas can be incorporated on the one immobilised substrate.

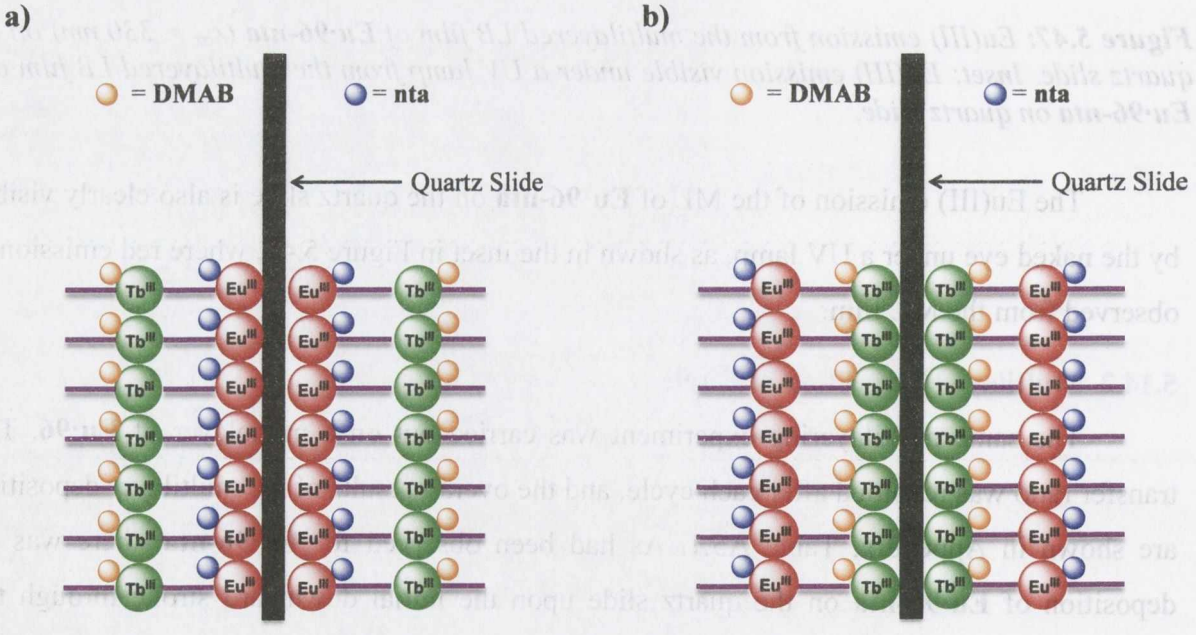


Figure 5.48: *Illustration of LB film multilayers of* ***Tb·96-DMAB*** *and* ***Eu·96-nta*** *on a quartz solid substrate.*

The slide that had previously been coated with a monolayer of a LB film of **Eu·96-nta** was then coated with a monolayer of a LB film of **Tb·96-DMAB**. The dipping procedure was

the same as previously described with the **Eu·96-nta** coated slide immersed under the water subphase of the trough before forming a monolayer film of **Tb·96-DMAB** on the surface. The slide was then slowly removed from the water by an upward stroke while monitoring the transfer of the monolayer after the **Tb·96-DMAB** film had been formed, Appendix A5.29. The transfer ratio was determined to be *ca.* 1. The same procedure was repeated coating the slide first with **Tb·96-DMAB** followed by **Eu·96-nta** and again both transfer ratios were determined to be *ca.* 1. Both slides were allowed to dry in the air before the Ln(III) luminescent spectrum of each was recorded at various excitation wavelengths.

The Ln(III) luminescent spectrum of the **Eu·96-nta-Tb·96-DMAB** slide shown in Figure 5.49 verified that dual Ln(III) emission, *i.e.* both Tb(III) and Eu(III) emission from 450 nm to 725 nm, can be obtained from the one slide using an excitation wavelength of 300 nm, suitable for the sensitisation of both Ln(III) metal centres by their respective antennae.

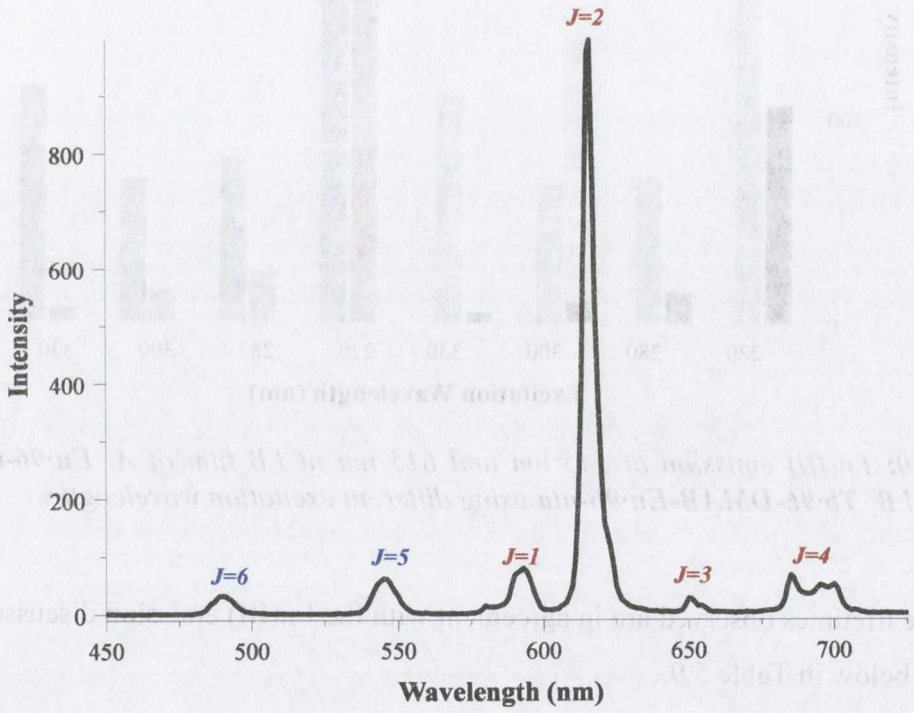


Figure 5.49: *Ln(III) luminescent spectra of LB film of* ***Tb·96-DMAB*** *and* ***Eu·96-nta*** *(λ_{ex} = 300 nm) showing the characteristic Tb(III) $^5D_4 \rightarrow {}^7F_J$ and Eu(III) $^5D_0 \rightarrow {}^7F_J$ transitions overlapping with one another.*

Both slides were excited at different wavelengths (220, 280, 300 and 330 nm) corresponding to the absorption bands of the antennae **nta** and **DMAB** with the results shown below in Figure 5.50 and Appendix A6.30-31. In the case of slide **A**, where the Tb(III) monolayer was the top layer, it was observed that at each of the aforementioned excitation

wavelengths the Eu(III) emission was more intense than that of the Tb(III) emission. This may be due to the quenching effect of oxygen on the Tb(III) emission as it is exposed to air.

For slide **B**, where the Eu(III) layer was on top of the Tb(III) monolayer the Eu(III) emission from **Eu·96-nta** was also more intense than that from **Tb·96-DMAB** as it is not effected by oxygen quenching to the same extent as **Tb·96-DMAB**. Moreover, the emission from the Tb(III) layer was stronger than that of slide **A**, being somewhat shielded from the air by the top Eu(III) monolayer.

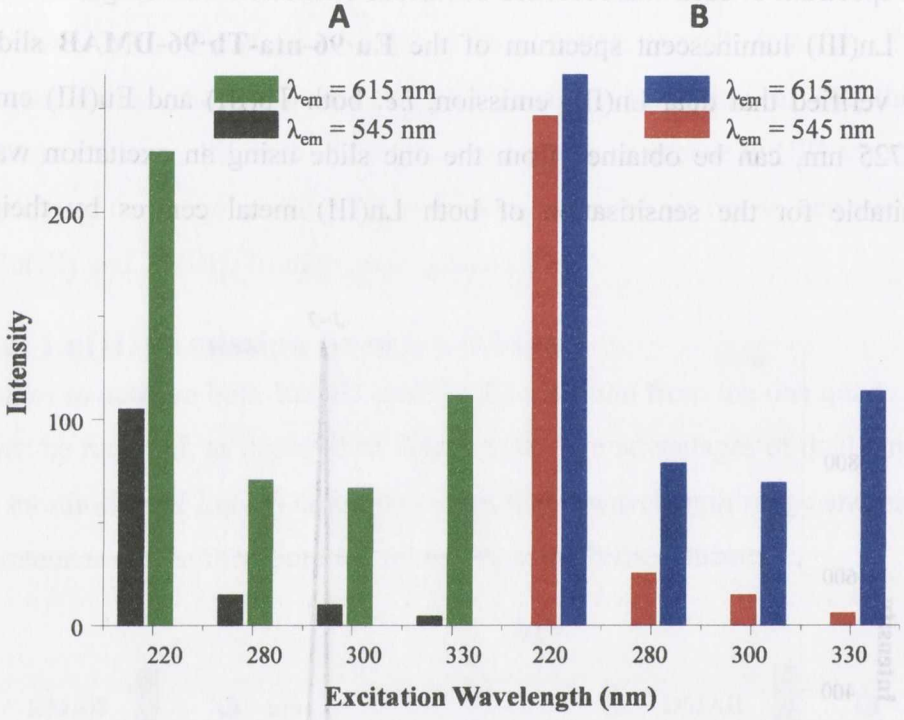


Figure 5.50: *Ln(III) emission at 545 nm and 615 nm of LB film of* ***A****,* ***Eu·96-nta-Tb·96-DMAB*** *and* ***B****,* ***Tb·96-DMAB-Eu·96-nta*** *using different excitation wavelengths.*

The lifetimes observed are in agreement with the Ln(III) emission discussed above and are shown below in Table 5.9.

Table 5.9: *Lifetime studies for multilayered LB films on quartz slides of* ***A*** *and* ***B****, each number is an average of 6 measurements all agreeing to within 5% of each other with an error of ± 0.01.*

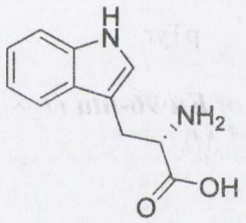
	τ(ms)		k (ms^{-1})	
Slide	545 nm	615 nm	545 nm	615 nm
A	1.32	0.74	0.76	1.36
B	1.41	0.81	0.71	0.73

In summary these results demonstrated the ability to achieve dual Ln(III) emission from a multilayered LB film deposited on a quartz slide, with the intensity of the Eu(III) and Tb(III) emission dependant on the excitation wavelength and whether the layer lies on the top or bottom of the slide.

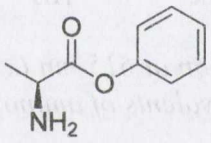
The ability of a LB film of **Eu·96-nta** to act as a sensor for amino acids by the modulation of the Eu(III) emission from the slide was next investigated in order to determine whether **Eu·96-nta** could distinguish tyrosine and phosphotyrosine from other amino acids.

5.16 Amino Acid Sensing using Eu·96-nta

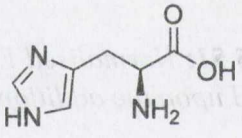
The amino acid tyrosine (Tyr) is essential in the body as it serves as a building block for several important neurotransmitters, including epinephrine, norepinephrine, and dopamine.[231] Although the phosphorylation of tyrosine to phosphotyrosine (pTyr) is a critical process within cellular regulation; its exact role is not fully understood and furthermore, pTyr only accounts for < 1% of the phosphorylated amino acids in the body.[232] Therefore, the selective and specific determination of pTyr over Tyr and other phosphorylated amino acids is essential.



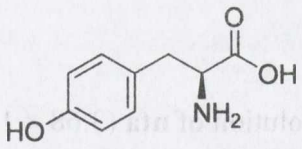
Trp



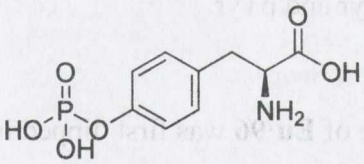
Phe



His



Tyr



pTyr

Solution studies were initially carried out to determine the effect of various amino acids on **Eu·96-nta**. It was envisaged that the amino acids would displace the **nta** antenna from the Eu(III) metal centre, hence modulating the Eu(III) emission. The amino acids investigated included tryptophan (Trp), phenylalanine (Phe), histidine (His), Tyr and pTyr.

5.16.1 Solution Studies

To a solution of **Eu·96-nta** (1×10^{-6} M) in MeOH, increasing concentrations of amino acid were added (1×10^{-6} M - 4×10^{-4} M) corresponding to 1 – 400 equivalents added. The normal concentration of amino acids in blood plasma is 10^{-4} M.[233] The results are depicted

below in Figure 5.51. The addition of up to 400 equivalents of Trp, Phe and His resulted in less than *ca.* 5% modulation in the Eu(III) emission. However, it was discovered that Tyr gave rise to *ca.* 50% quenching and furthermore, pTyr caused the Eu(III) emission to be completely "switched off".

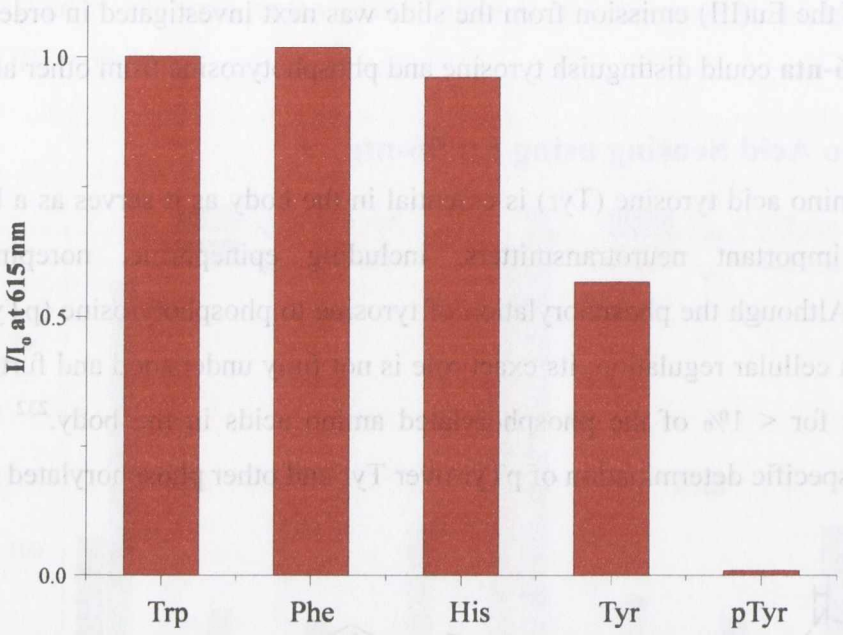


Figure 5.51: *Normalised Eu(III) emission at 615 nm (λ_{ex} = 330 nm) of* ***Eu·96-nta*** *(1×10^{-6} M) in MeOH upon the addition of 400 equivalents of amino acid (4×10^{-4} M).*

Based on the results from these solution studies, preliminary studies were carried out to investigate the ability of a LB film of **Eu·96-nta** to sense and distinguish between the amino acids Tyr and pTyr.

5.16.2 LB Film Studies

A slide of **Eu·96** was first dipped into an aqueous solution of **nta** (3.68×10^{-6} M). This switched the Eu(III) emission "on", Appendix A5.40. The slide was then immersed in solutions of amino acid of increasing concentrations for durations of one minute. The results obtained were in contrast to those observed in the solution studies and are shown in Figure 5.52 and Figure 5.53. Immersing the slide in up to 400 equivalents (1.84×10^{-5} M) of Tyr resulted in a *ca.* 60% decrease in Eu(III) emission whereas the same concentration of pTyr only gave rise to *ca.* 30% quenching. Analysis of the solutions after the slides were dipped showed that no Eu(III) emission was measurable, indicating that any reduction in the Eu(III) emission observed was a result of the Tyr/pTyr quenching the emission by displacing the **nta** antenna rather than **Eu·96**:**nta** being washed off the slide during the dipping process.

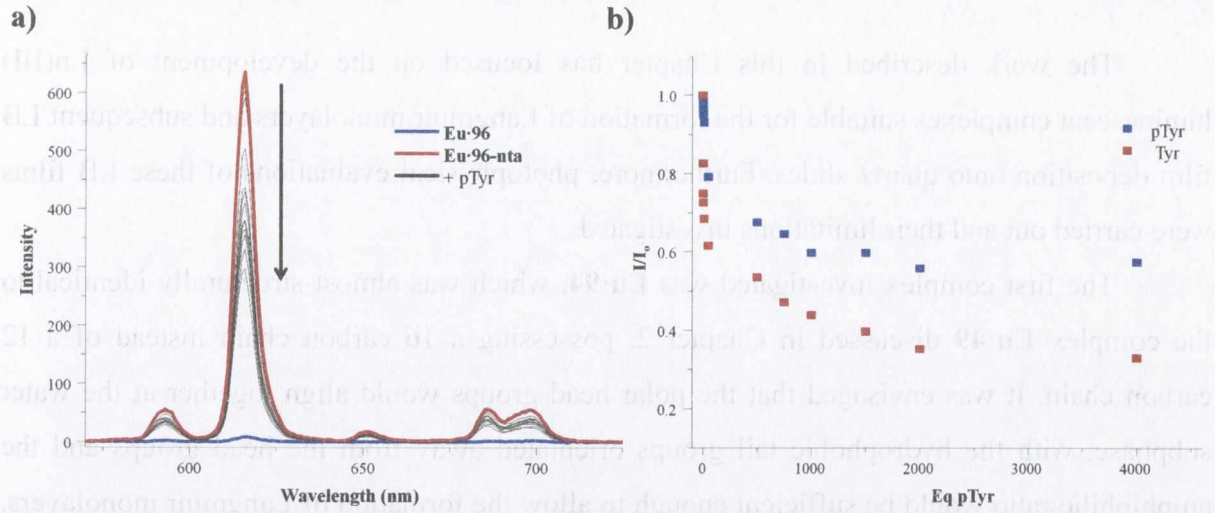


Figure 5.52: a) *Changes in the Eu(III) emission from a LB film of* ***Eu·96-nta*** *(λ_{ex} = 330 nm) upon dipping into increasing concentrations of pTyr in aqueous solution (0 – 3.68 × 10^{-2} M).* ***b)*** *Normalised Eu(III) emission at 615 nm (λ_{ex} = 330 nm) from a LB film of* ***Eu·96-nta*** *upon increasing concentrations of Tyr and pTyr (0 – 1.5 × 10^{-4} M).*

These results are preliminary and further studies are needed to explain the different behaviour observed between the solution and solid state studies. One possible explanation is that on the slide the **Eu·96** molecules are orientated head first, therefore the Eu(III) metal centre is not as accessible as it is in solution and so binding/displacement events of antenna molecules from the Eu(III) metal centre on the slide may not be the same as in solution.

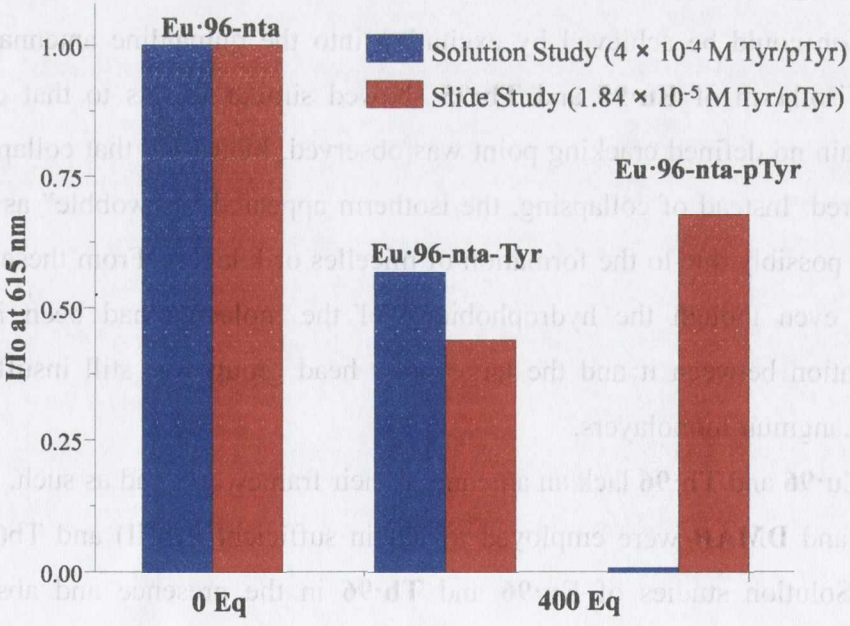


Figure 5.53: *Normalised Eu(III) emission at 615 nm (λ_{ex} = 330 nm) of* ***Eu·96-nta*** *in MeOH solution (1 × 10^{-6} M) and as a LB film (3.68 × 10^{-8} M) upon the addition of 400 equivalents of Tyr and pTyr.*

5.17 Conclusion

The work described in this Chapter has focused on the development of Ln(III) luminescent complexes suitable for the formation of Langmuir monolayers and subsequent LB film deposition onto quartz slides. Furthermore, photophysical evaluations of these LB films were carried out and their limitations investigated.

The first complex investigated was **Eu·94**, which was almost structurally identical to the complex **Eu·49** discussed in Chapter 2, possessing a 16 carbon chain instead of a 12 carbon chain. It was envisaged that the polar head groups would align together at the water subphase, with the hydrophobic tail groups orientated away from the head groups and the amphiphilic ratio would be sufficient enough to allow the formation of Langmuir monolayers. This however was not the case, as one of the characteristic phases that a Langmuir monolayer undergoes, the cracking point, was absent from the Langmuir isotherm of **Eu·94**. It was concluded that the polar head group of **Eu·49** was too large in comparison to the non-polar alkyl chain and therefore the hydrophilic/hydrophobic ratio of the complex was insufficient to induce the amphiphilicity required to form Langmuir monolayers.

Bearing this in mind complexes **Eu·95/96** and **Tb·95/96** were designed to overcome this problem. Both ligands **95** and **96** contained a hydrophobic tail group consisting of three long alkyl (C_{18}) chains appended to a phenyl ring. In the case of **95** the same quinaldine antenna arms were utilised whereas **96** employed the use of simple dimethyl acetamide arms within its structure. Solution studies of **Eu·95** and **Tb·95** demonstrated that Eu(III) and Tb(III) emission could be achieved by excitation into the quinaldine antenna. The surface pressure-area isotherm of **Eu·95** and **Tb·95** showed similar results to that obtained from **Eu·94** and again no defined cracking point was observed, indicating that collapse of the film had not occurred. Instead of collapsing, the isotherm appeared to "wobble" as smaller areas were reached, possibly due to the formation of micelles or bilayers. From these results it was apparent that even though the hydrophobicity of the molecule had been increased, the amphiphilic ration between it and the large polar head group was still insufficient for the formation of Langmuir monolayers.

Both **Eu·96** and **Tb·96** lack an antenna in their framework, and as such, the "external" antennae **nta** and **DMAB** were employed to obtain sufficient Eu(III) and Tb(III) emission, respectively. Solution studies of **Eu·96** and **Tb·96** in the presence and absence of their respective antennae demonstrated that Eu(III) emission was only observed in the presence of **nta** when excited at 330 nm. In contrast the Tb(III) excited state was efficiently populated by the phenyl ring in the absence of **DMAB**. All four surface pressure-area isotherms of **Eu·96**, **Tb·96**, **Eu·96-nta** and **Tb·96-DMAB** displayed the characteristic phase transitions of a

Langmuir monolayer; the G, LE, LC and finally, collapse of the film. Moreover, all monolayers were found to be stable over extended periods of time.

Having established successful monolayer formation, it was next investigated whether these Langmuir monolayers could be deposited onto quartz glass slides to generate LB films. Attachment of the species (**Eu·96**, **Tb·96**, **Eu·96-nta** and **Tb·96-DMAB**) onto the quartz slides was achieved *via* Y-type deposition with good transfer ratios of *ca.* 1. Photophysical evaluation of the LB films was in agreement with the solution studies. Films of **Tb·96** and **Tb·96-DMAB** both gave rise to substantial Tb(III) (λ_{ex} = 220 nm) emission, while Eu(III) (λ_{ex} = 330 nm) emission was only observed from the LB film of **Eu·96-nta** and not from **Eu·96**. However, it was discovered that the Eu(III) emission of **Eu·96** could be "switched on" by immersing the slide of **Eu·96** into an aqueous solution of **nta**.

The limit of detection studies on the ability of a LB film of **Eu·96** to sense **nta** were also investigated. The factors considered in the LOD study were the concentration of the **nta** solution and the immersion time of the slide in the solution. Concentrations ranging from 10^{-7} M to 10^{-4} M and immersion times as low as 5 seconds were examined. Overall, an immersion time of one minute was required using a concentration of 10^{-7} M, however, Eu(III) emission could be achieved from the slide after only a 30 seconds using a higher concentration of 10^{-6} M solution.

The next section dealt with the ability of LB films of **Eu·96**, **Tb·96**, **Eu·96-nta** and **Tb·96-DMAB** to withstand a constant flow of water over a period of 24 hours. It was established that the LB film of **Tb·96** was least stable, with a 93% decrease in Tb(III) emission being observed after only 2 hours. The remaining three films were more resistant to these conditions with Ln(III) emission intensities of between 10-20% still remaining after 24 hours under the flow system.

In addition to flow studies, "scavenger studies" were carried out on a LB film of **Eu·96-nta** to determine whether solutions of Eu(III) or Tb(III) could "scavenge" and bind to the **nta** antenna off **Eu·96** on the slide. Complexes **Eu·81** and **Tb·81** chosen to act as the scavenger solutions possessed no antenna and as such their Ln(III) emission was "switched off" (λ_{ex} = 330 nm). LB films of **Eu·96-nta** were immersed in 10^{-6}, 10^{-5} and 10^{-4} M solutions of **Eu·81** and **Tb·81** for durations of one hour. There was a significant "switching on" of the Ln(III) emission of the solutions when scavenger higher concentrations of 10^{-4} M were used. In the case of **Eu·81** this was attributed to the dislodged **nta** molecules sensitising the **Eu·81** in solution, whereas, the increase in the Tb(III) emission of **Tb·81** was due to displacement of the metal bound water molecules by the **nta**. Both instances require the formation of ternary

complexes **Eu·81-nta** and **Tb·81-nta** in solution, the equilibrium towards which may not have been favourable at lower concentrations of scavenger solutions.

Finally, multilayer deposition experiments were carried out to probe how many monolayers could be built up on the quartz substrate. Both **Eu·96-nta** and **Eu·96** were investigated and it was ascertained that a maximum of three layers could be achieved with any more attempted deposition resulting in the removal of a layer. The deposition style was determined to be Y-type deposition whereby the molecules are stacked onto the quartz slide in a head-to-head/tail-to-tail pattern.

The Eu(III) emission from the multilayer slide of **Eu·96-nta** was of such high intensity that it was clearly visible to the naked eye under a UV lamp and moreover, it was *ca.* 3 times more intense than that of a monolayer LB film of **Eu·96-nta**.

The multilayering technique was extended to achieve dual Ln(III) emission from the one slide. Two slides were prepared possessing a layer of **Eu·96-nta** and a layer of **Tb·96-DMAB**. Eu(III) and Tb(III) transitions were observed upon excitation using a range of wavelengths and the ratio of the Eu(III):Tb(III) could be altered depending on which excitation wavelength was used and also depending on the orientation of the Ln(III) layers.

Finally, preliminary studies were carried out to investigate the effect of amino acid on both solution and LB films of **Eu·96-nta**. The solution and solid state studies were in contradiction to one another. In solution the Eu(III) emission was completely "switched off" by the addition of 400 equivalents of pTyr and only partially quenched by Tyr. However, a LB film of **Eu·96-nta** showed *ca.* 30% more quenching with 400 equivalents of Tyr than pTyr. Further studies will be needed to give a more detailed explanation of this phenomenon.

Overall, the work detailed in this Chapter detailed the successful formation and subsequent photophysical evaluation of Langmuir monolayers and LB films on a solid quartz support of emissive Eu(III) and Tb(III) complexes.

Chapter 6

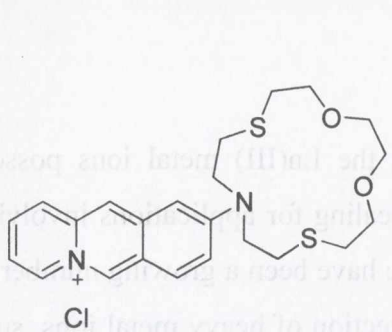
Attempted Mercury Sensor Synthesis

6. Introduction

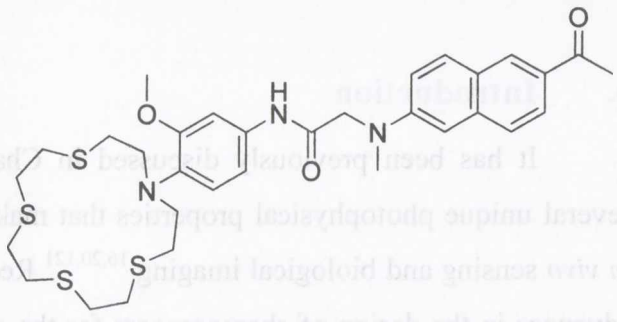
It has been previously discussed in Chapter 1 that the Ln(III) metal ions possess several unique photophysical properties that make them appealing for applications involving *in vivo* sensing and biological imaging.[16,20,121] Recently, there have been a growing number of advances in the design of chemosensors for the selective detection of heavy metal ions, such as mercury, based upon the incorporation of suitable antenna into the cyclen framework.[60,160,234] The antenna moiety must sufficiently sensitise the Ln(III) metal ion, whilst having additionally an incorporated receptor unit capable of binding to metal ions and hence, inducing an observable photophysical change in the Ln(III) emission properties.

There has been an increasing concern involving the overall health effects of chronic exposure to heavy metal ions present in the environment. It is therefore advantageous (in relation to environmental and biomedical monitoring) to develop sensors that have the ability to detect heavy metal ions such as mercury ions in aqueous solutions at extremely low concentrations. Mercury is an abundant transition metal that is widespread in the atmosphere, lithosphere and surface water.[58] It can exist in three forms; elemental, inorganic or ionic and organic, with the most toxic species being the inorganic divalent Hg(II) metal ion which can be found to be located in human tissue after conversion from other forms.[235] A major concern with Hg(II) is that owing to its solubility and stability in water it can undergo biomethylation to methyl mercury, its corresponding organic form, which can be found in in alarmingly high concentrations in specific fish.[235] This is one of the pathways in which mercury accumulates in the food chain and it is inevitable that consumption of mercury contaminated foods will occur by humans. Mercury has the ability to reach high levels in the central nervous system (CNS) by passing through the blood brain barrier, resulting in severe neurological disorders and neurotoxic effects.[236] Bearing in mind these hazardous health problems associated with mercury poisoning, the development of sensors which display selective and intense responses to mercury ions at low concentrations is an imperative area of research.

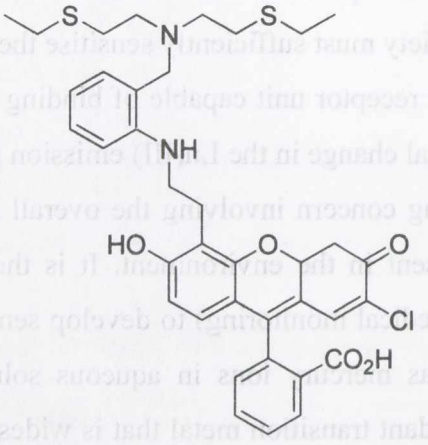
An examples of a fluorescent Hg(II) probes includes compound **101** designed by Ihmels and co-workers, which allows for the selective and ratiometric detection of Hg(II) ions in water utilising a macrocycle incorporating N, S and O atoms within its structure.[237] A similar macrocycle was incorporated into the framework of compound **102**, as demonstrated by Lim *et al.*[238] which was shown to estimate trace amounts of Hg(II) in fresh fish organs by means of a two-photon fluorescent probe. Alternatively, Lippard and co-workers devised the water soluble thiol derivatised fluorescein compound **103** containing an open form receptor capable of binding Hg(II).[239]



101

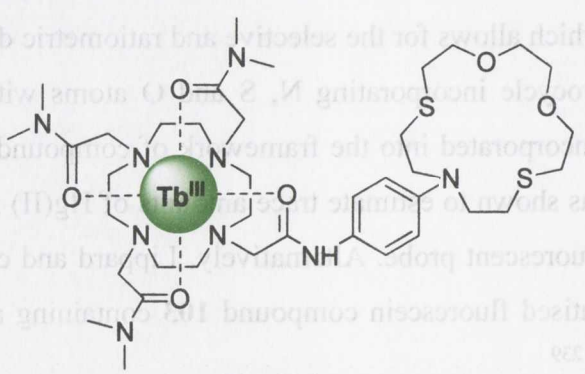


102



103

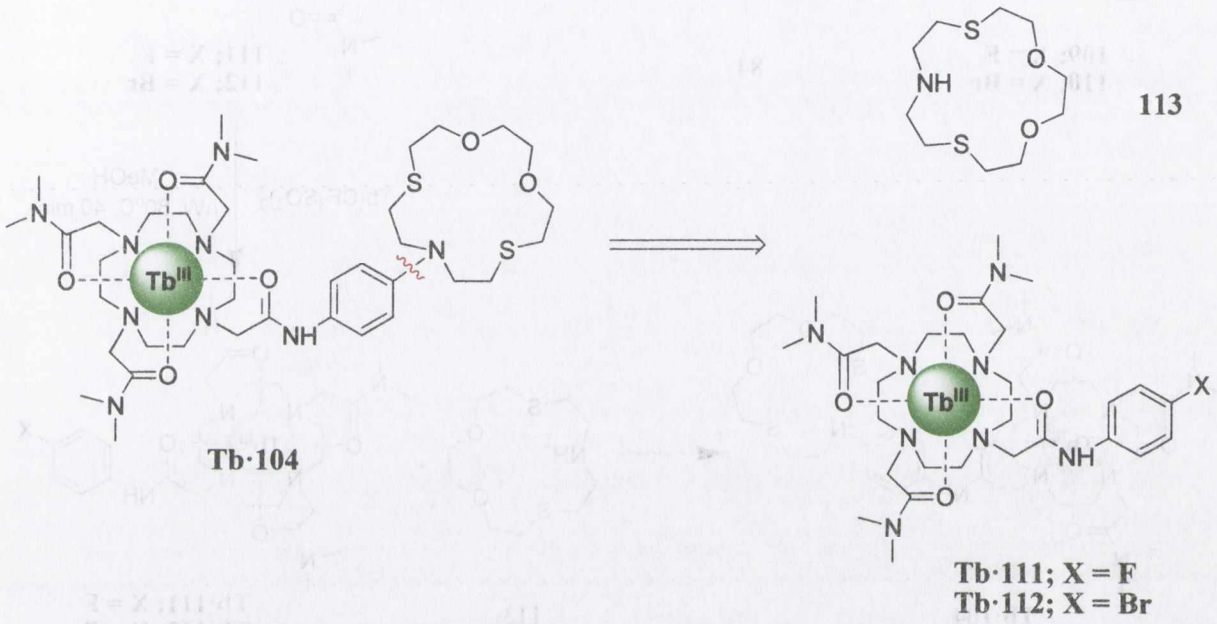
The aim of this project was to produce a Ln(III) luminescent Hg(II) sensor **Tb·104**, which could potentially selectively sense Hg(II) through modulation of the Tb(III) emission. Tb(III) was chosen as it is can be more efficiently sensitised through excitation into the phenyl ring than Eu(III). The macrocycle chosen has previously been demonstrated as a successful Hg(II) binder.[237] Consequently, it was envisaged that binding of Hg(II) within the macrocycle cavity would affect the photophysical properties of the aryl antenna, possibly by preventing photoinduced electron transfer (PET) from occurring from the macrocycle N to the phenyl ring and moreover, allowing sensitisation of the Tb(III) metal centre by the phenyl ring to be modulated. This Chapter discusses the attempted synthetic pathways towards the formation of complex **Tb·104**. While unfortunately the discussed product could not be formed, this work is on-going within the TG group.



Tb·104

6.1 Retrosynthetic and Synthetic Pathway towards Tb·104

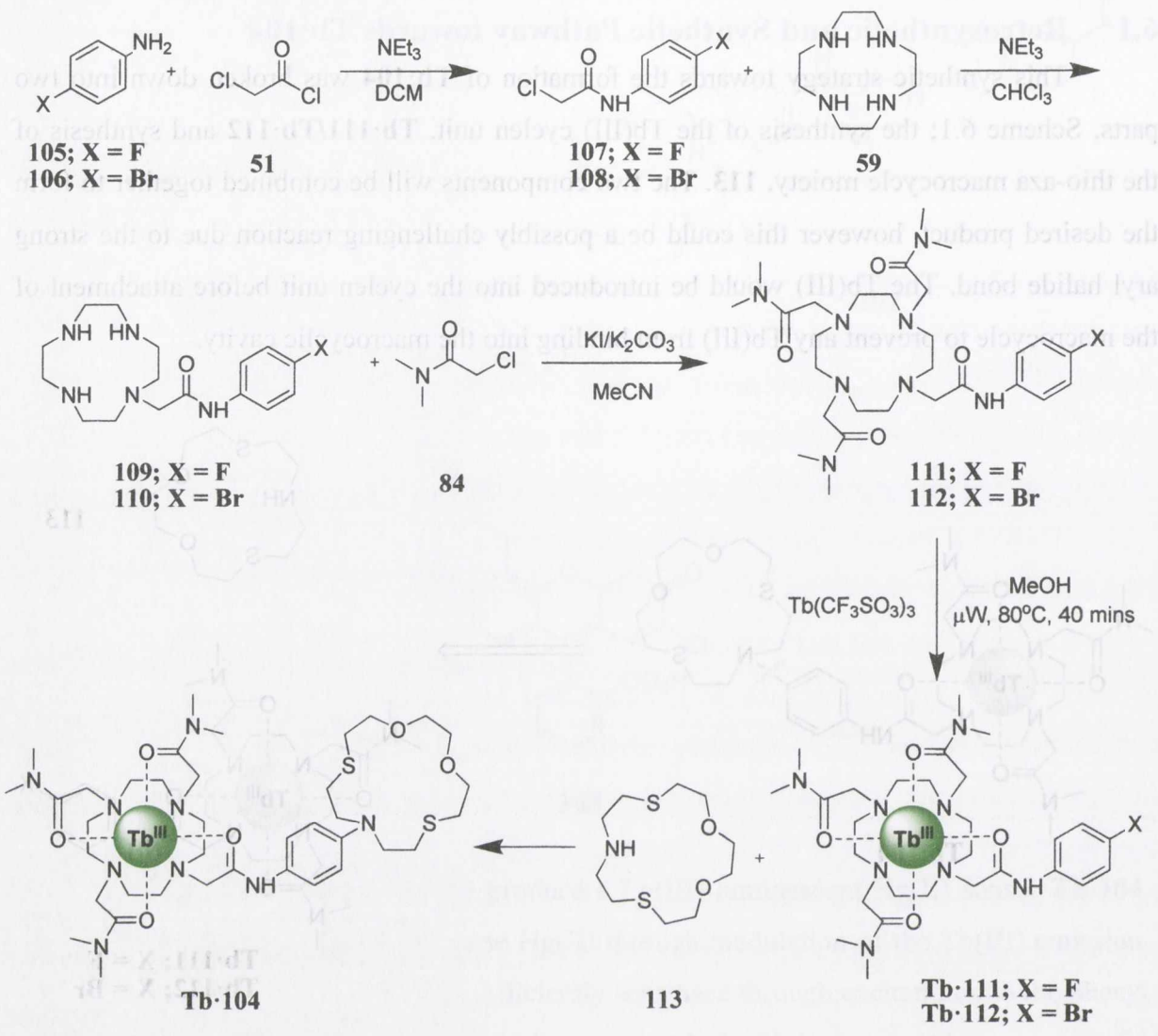
This synthetic strategy towards the formation of **Tb·104** was broken down into two parts, Scheme 6.1; the synthesis of the Tb(III) cyclen unit, **Tb·111/Tb·112** and synthesis of the thio-aza macrocycle moiety, **113**. The two components will be combined together to form the desired product, however this could be a possibly challenging reaction due to the strong aryl halide bond. The Tb(III) would be introduced into the cyclen unit before attachment of the macrocycle to prevent any Tb(III) from binding into the macrocyclic cavity.



Scheme 6.1 : *Retrosynthetic pathway for* ***Tb·104****.*

Both the fluorine and bromine analogues were synthesised and the synthesis will be discussed in parallel with the characterisation of the fluorine analogue and that of the bromine analogue shown in the Appendix.

The first step in the synthesis of **Tb·111/Tb·112** was the reaction of 4-fluoroaniline, **105**, or 4-bromoaniline, **106** with chloroacetyl chloride, **51**, in CH_2Cl_2 in the presence of NEt_3 generating **107** and **108** as brown and green solids, after recrystallisation from ethanol in 49% and 55% yield, respectively. Formation of the desired products was confirmed by ^1H NMR analysis (400 MHz, $CDCl_3$), Appendix A6.1, and A6.2.



Scheme 6.2: *Proposed synthesis of* ***Tb·104****.*

In the case of **106**, a broad singlet at 8.52 ppm was assigned to the amide NH and a singlet at 4.22 ppm corresponding to the two CH_2 protons. The next step involved the monoalkylation of cyclen with **107** or **108** using previously described procedures to give compounds **109** and **110** as brown oils in 42% and 63% yield, respectively, without the need for any further purification.[169] ^{1}H NMR analysis (400 MHz, $CDCl_3$) of **109**, Appendix A6.3, A6.4, showed the appearance of a multiplet of signals at 2.83 ppm consistent with the 16 CH_2 protons of the cyclen macrocycle. Alkylation of the remaining amine sites on the cyclen was next achieved under reflux in acetonitrile under an inert atmosphere by reacting 3.1 equivalents of 2-chloro-*N*,*N*-dimethylacetamide, **84**, with **109** or **110**, in the presence of K_2CO_3 and KI. After reaction for five days under these conditions the formation of **111** or **112** was observed by mass spectrometry; 579.3783 $[M + H^+]^+$ (**111**). Purification of the reaction mixture to remove any unreacted arm was achieved through column chromatography on

alumina eluting with CH_2Cl_2:MeOH using a gradient of 100:0 to 80:20. The ligands **111** and **112** were obtained as yellow and brown powders in 72% and 56% yield, respectively. Minor shifts were observed for the aromatic protons; however, the remaining protons of the cyclen and the dimethyl acetamide arms are undistinguishable from one another, appearing as a broad multiplet of 42 protons between 5.59 ppm and 2.52 ppm, Figure 6.1, Appendix A6.5.

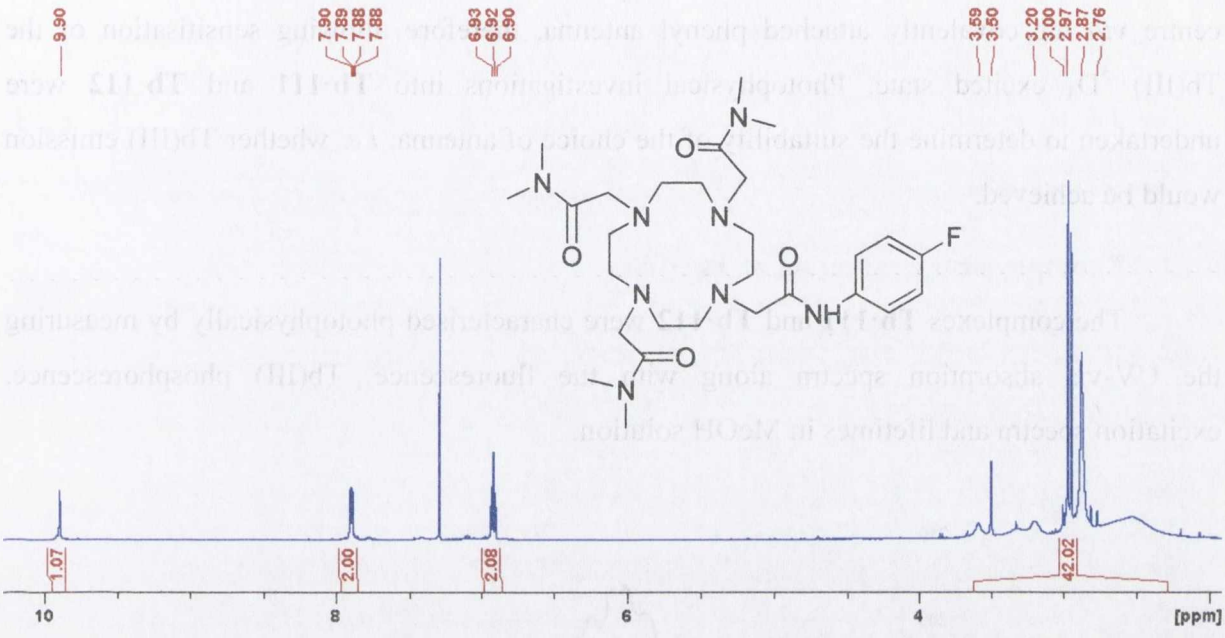


Figure 6.1: *The ^{1}H NMR spectrum (400 MHz, $CDCl_3$) of ligand **111**.*

The Tb(III) complexes of **111** and **112** were formed by microwave irradiation for 40 minutes in a small volume of methanol (*ca.* 5 mL) with one equivalent of $Tb(CF_3SO_3)_3$. The resulting solution was precipitated into a large volume of diethyl ether and the resulting precipitate was centrifuged to give rise to **Tb·111** and **Tb·112** as a brown powders in 66% and 96% yields, respectively. In the same manner as all the other Ln(III) based cyclen complexes described within this thesis, the ^{1}H NMR spectrum (400 MHz, MeOD) displayed the characteristic broadening and shifting of signals, verifying successful complexation of the Tb(III) ion within the macrocyclic cavity the ligands **111** and **112**. The complexation resulted in the ligand protons being shifted over a spectral range of *ca.* 500 ppm, the spectrum of which is shown in Appendix A6.6 to A6.8 and A6.9 to A6.10. Further proof of complexation of the Tb(III) metal ion in the cyclen cavity of the ligands was achieved through IR spectroscopy, where a shifting of the carbonyl bands of the acetamide pendant arms by *ca.* 20 cm^{-1} upon binding to the Ln centre for both **Tb·111** and **Tb·112**.

Table 6.1: *IR stretching frequency of the carbonyl bands in* ***111****,* ***112****,* ***Tb·111*** *and* ***Tb·112****.*

Compound	Ligand	Tb(III) Complex
111	1641	1620
112	1643	1618

The design of **Tb·111** and **Tb·112** anticipated indirect excitation of the Tb(III) metal centre *via* the covalently attached phenyl antenna, therefore allowing sensitisation of the Tb(III) $^5D_4$ excited state. Photophysical investigations into **Tb·111** and **Tb·112** were undertaken to determine the suitability of the choice of antenna, *i.e.* whether Tb(III) emission would be achieved.

6.1.1 Photophysical Evaluation of Tb·108

The complexes **Tb·111** and **Tb·112** were characterised photophysically by measuring the UV-vis absorption spectra along with the fluorescence, Tb(III) phosphorescence, excitation spectra and lifetimes in MeOH solution.

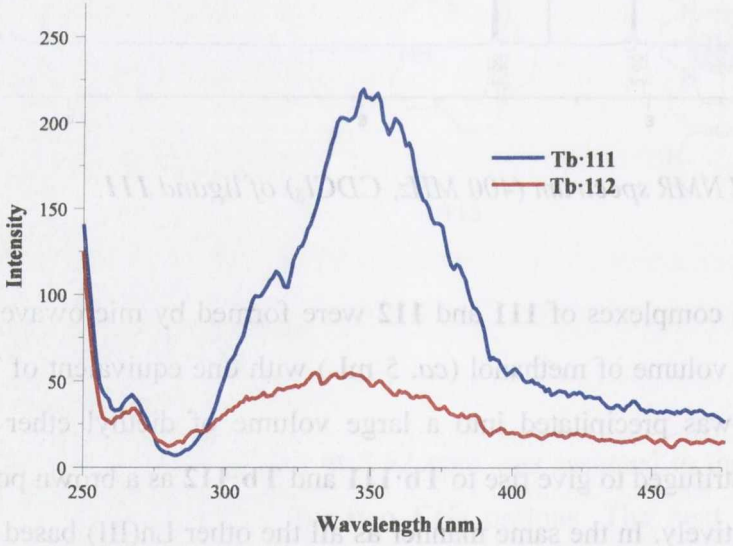


Figure 6.2: *The fluorescence emission spectra (λ_{ex} = 220 nm) of complexes* ***Tb·111*** *(-) and* ***Tb·112*** *(-) recorded in MeOH.*

The UV-vis absorption spectra of **Tb·111** and **Tb·112** were recorded in MeOH solutions and are shown in Appendix A6.11. Both spectra display a strong absorbance band at *ca.* 220 nm, and a slightly weaker one at *ca.* 250 nm, which are assigned to the π-π^* transitions of the phenyl ring. Excitation into the band at 220 nm gave rise to the fluorescence and phosphorescence spectra shown in Figure 6.2 and Figure 6.3, respectively. It was noticed that there was a significant decrease in the fluorescence emission in concert with an increase

in the Tb(III) centred emission as the halide was varied from F to Br. This is attributed to the heavy atom effect; an enhancement of the rate of a spin-forbidden process by the presence of an atom of high atomic number which is in close proximity to the chromophore.[240] The presence of Br increases the rate of intersystem crossing (ISC) by strengthening spin-orbit coupling which more efficiently populates the triplet state of the chromophore. Therefore, the obtained decrease in fluorescence emission can be explained by an increase in the probability of the competing ISC process from the triplet state of the chromophore to the Tb(III) excited state. Therefore, an increase in the phosphorescence of **Tb·112** was observed over that of **Tb·111**.

Excitation spectra were also recorded observing the emission at 545 nm, confirming that the energy transfer to the Tb(III) metal centre occurs from the phenyl chromophore, Appendix A6.12.

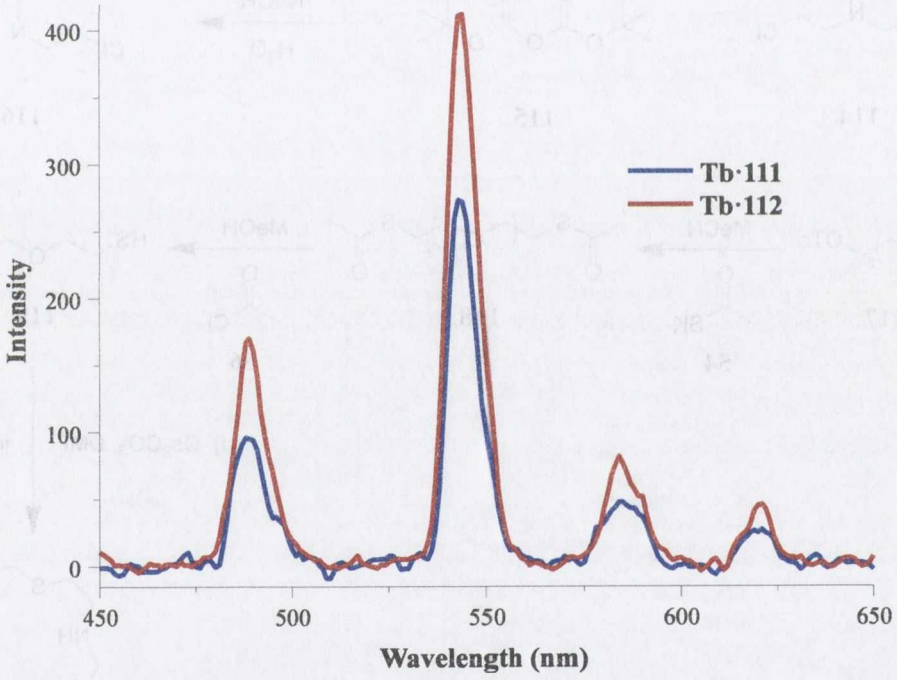


Figure 6.3: *The Tb(III) emission spectra (λ_{ex} = 220 nm) of complexes* ***Tb·111*** *(-) and* ***Tb·112*** *(-) recorded in MeOH.*

The lifetimes of both Tb(III) complexes were also obtained in MeOH solution. The excited state decays were best fit to monoexponential decay, Appendix A6.13 and the resulting lifetime values are given below in Table 6.1.

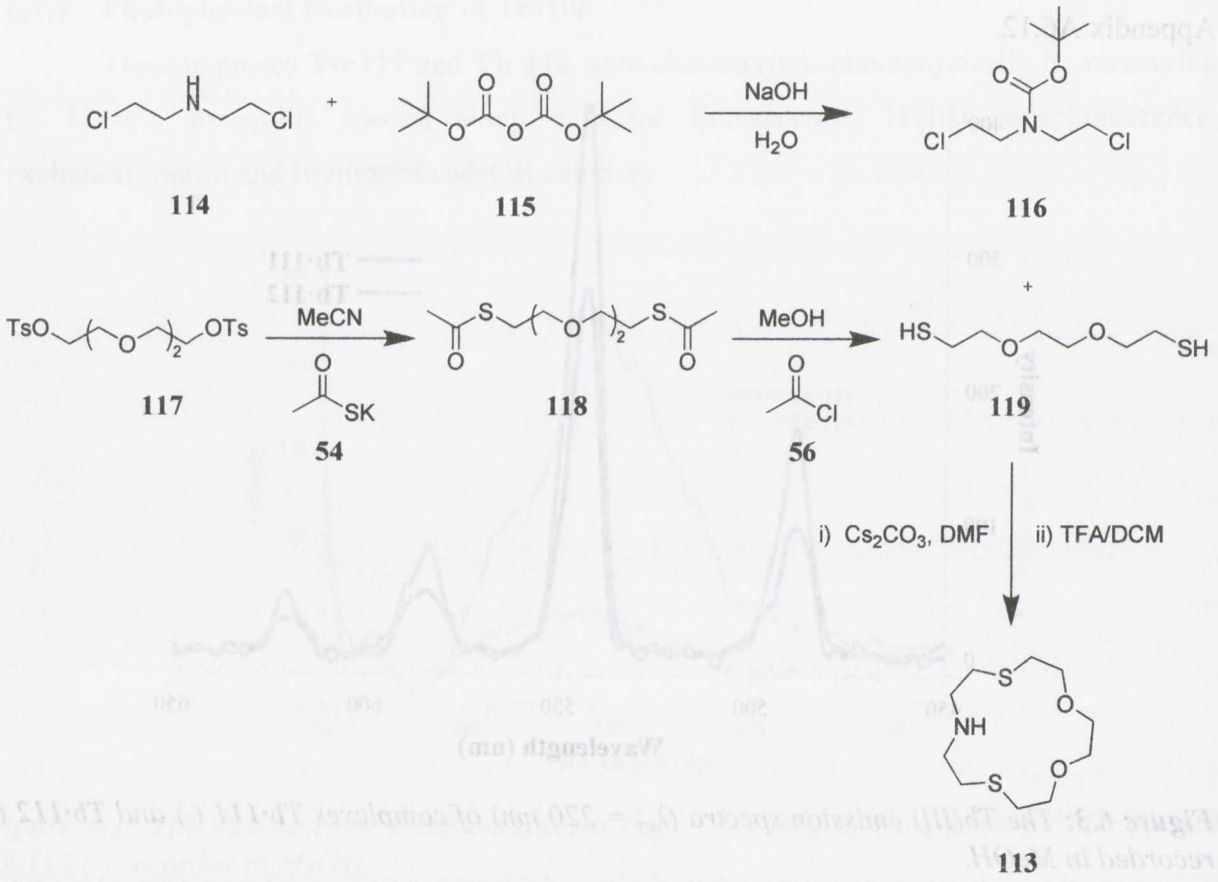
Table 6.2: *Lifetime studies for* ***Tb·111*** *and* ***Tb·112*** *in MeOH.*

	τ (ms)	k (ms^{-1})
Tb·111	0.373	2.684
Tb·112	0.558	1.791

Having synthesised and characterised the Tb(III) containing component of the target molecule, the next stage was to synthesise the macrocycle, **113**.

6.2 Synthesis of Macrocycle 113

The synthesis of the macrocycle was broken down into three separate stages; the synthesis of compound **116**, the synthesis of compound **119** and finally the reaction of **116** with **119** to form the desired compound **113**. Firstly, bis(2-chloroethyl) amine hydrochloride, **114**, was protected using di-*tert*-butyl carbonate, **115**. The protected compound **116** was verified by the appearance of a singlet in the ^{1}H NMR spectrum (400 MHz, $CDCl_3$) assigned to the *tert*-butyl groups of the protecting group. In a separate synthetic step, the tosylated chain, **117**, was substituted with a potassium thioacetate generating **118** in 76% yield.



114 115 116 117 54 118 56 119 113

Scheme 6.3: *Synthetic pathway towards compound 113.*

The ^{1}H NMR spectrum (400 MHz, $CDCl_3$) showed the absence of the aromatic tosyl peaks of the starting material and the appearance of a singlet at 2.35 ppm corresponding to the 6 protons of the terminal CH_3 groups. Deprotection of the acetate moiety was achieved by the addition of acetyl chloride, giving compound **119** in 83% yield. Compounds **116** and **119** were then reacted in a slow addition, high dilution synthetic method which involved dissolving Cs_2CO_3 in a large volume of dry DMF (*ca.* 100 mL) and heating it to 60°C. A separate

solution of DMF (*ca.* 100 mL) containing **116** and **119** was very slowly dropped into the Cs_2CO_3 containing solution overnight using a pressure equalised dropping funnel. Without further purification the compound was deprotected to remove to BOC groups by stirring the compound in a 50:50 solution of TFA: CH_2Cl_2 for 15 minutes. The final compound, **113**, was purified using silica flash chromatography eluting with CH_2Cl_2:MeOH, the ^1H NMR spectrum (400 MHz, $CDCl_3$) of which is shown below in Figure 6.4.

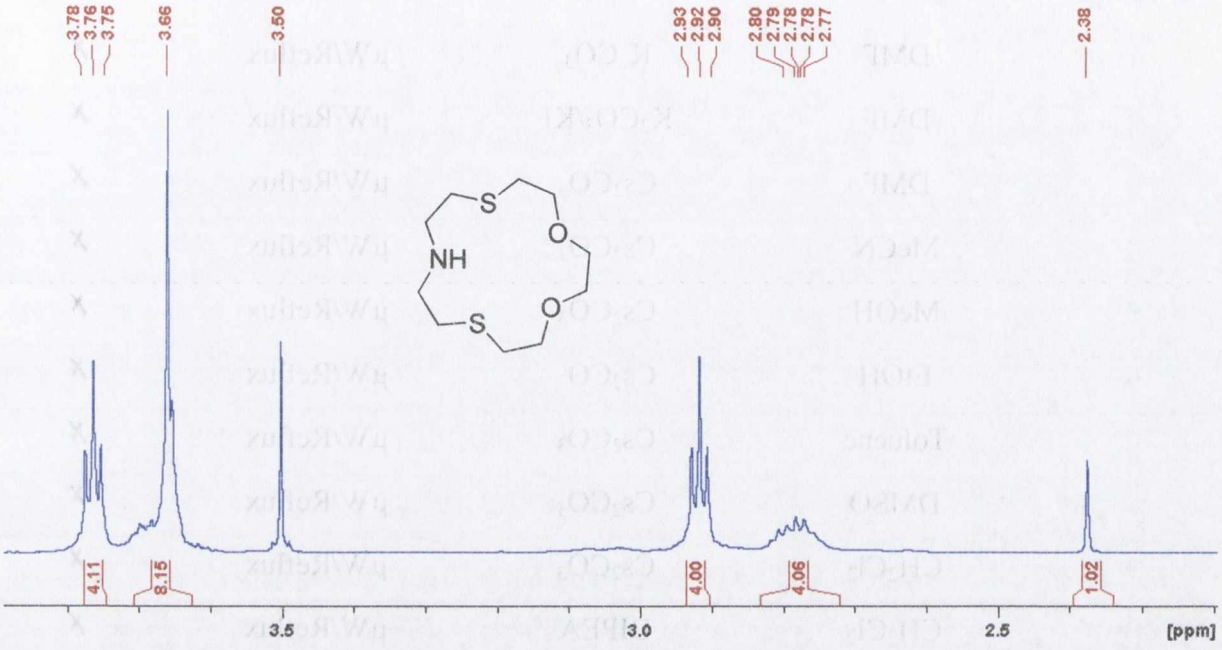


Figure 6.4: *The ^1H NMR spectrum (400 MHz, $CDCl_3$) of* ***113****.*

With both components successfully synthesised, all that remained was to react the two together to form the target compound **Tb·104**.

6.3 Attempted Synthesis of Tb·104

The first method attempted to react **113** with **Tb·111** or **Tb·112** involved dissolving both components in dry DMF in the presence of K_2CO_3 and refluxing overnight. Following removal of the base the desired product was not observed in mass spectrometry analysis; only starting material was observed. A number of other bases, solvents and reaction conditions were also implemented to obtain the desired product, which are detailed below in Table 6.3. All reactions were carried out using both **Tb·111** and **Tb·112**.

Despite every effort to achieve aromatic substitution of the macrocyclic ring **113** onto **Tb·111** or **Tb·112** using a number of different bases, solvents and reaction conditions, the desired product was not obtained

Aryl halides that do not contain an electron withdrawing group generally do not react with nucleophiles, unless extremely harsh reaction conditions are employed. Furthermore, the nucleophilic aromatic substitution that would occur, should the reaction conditions allow,

yields a highly unstable and unfavourable benzyne intermediate. From these reasons, it was apparent that reaction of **113** with **Tb·111** or **Tb·112** even under harsh conditions may not occur and so synthesis of this project was stopped due to time constraints.

Table 6.3: *Synthetic attempts for the formation of* ***Tb·104****.*

Attempt	Conditions			Product
	Solvent	Base		
1	DMF	K_2CO_3	μW/Reflux	✗
2	DMF	K_2CO_3/KI	μW/Reflux	✗
3	DMF	Cs_2CO_3	μW/Reflux	✗
4	MeCN	Cs_2CO_3	μW/Reflux	✗
5	MeOH	Cs_2CO_3	μW/Reflux	✗
6	EtOH	Cs_2CO_3	μW/Reflux	✗
7	Toluene	Cs_2CO_3	μW/Reflux	✗
8	DMSO	Cs_2CO_3	μW/Reflux	✗
9	CH_2Cl_2	Cs_2CO_3	μW/Reflux	✗
10	CH_2Cl_2	DIPEA	μW/Reflux	✗
11	$CHCl_3$	NEt_3	μW/Reflux	✗
12	-	-	Dry reaction	✗
13	DMF	K^tBuOH, Pd catalyst, triphenyl phosphine	μW/Reflux	✗

6.4 Conclusion

The purposes of this project was to synthesise and evaluate **Tb·104** as a Ln(III) luminescent sensor for the detection of Hg(II) at intracellular concentrations. The design of **Tb·104** envisaged binding of Hg(II) into the macrocycle component, **113**, and subsequent modulation of the Tb(III) emission. The complexes **Tb·111** and **Tb·112** were successfully synthesised and photophysically evaluated, demonstrating that Tb(III) emission could be achieved upon excitation into the attached phenyl chromophore. However, we were unable to achieve nucleophilic aromatic substitution of the macrocyclic ring, **113**, onto either **Tb·111** or **Tb·112** and redesign of the synthetic pathway may be a future project within the Gunnlaugsson group.

Future Work

The initial study discussed in Chapter 2 dealt with the design, synthesis and photophysical evaluation of novel cyclen based Ln(III) complexes, sensitisation of which was achieved through the incorporation of a quinaldine antenna unit into the cyclen framework. Moreover, the attachment of a long alkyl chain, terminated by a thiol group, was essential to this design in order to enable absorption onto the surface of **AuNPs**. Sensing studies were carried out on a wide range of biologically relevant analytes to modulate the Ln(III) emission output. Further studies are on-going within the Gunnlaugsson group with different cyclen complexes attached to AuNPs, including some complexes incorporating iminodiacetate pendant arms with the purpose of detecting Ca(II) on damaged bone samples.

The work carried out in Chapter 3 described the evaluation of a novel near-infrared (NIR) emissive Ln(III)-based zinc sensor that arises from the self-assembly in aqueous solution between the non-emissive unsaturated Yb(III) cyclen complex, **Yb·81**, and the sulfonated 8-hydroxyquinoline (**8-HQS**) antenna; a process that was shown to be fully reversible. Potential further studies onto the system could include incorporating the **8-HQS** antenna directly onto the cyclen unit and investigate how this could change the behaviour of the zinc sensing system.

Chapter 4 describes the first example of a NIR emitting Yb(III)-based **AuNP** system **AuNP-Yb·38-XO** and furthermore, that the NIR emission can be reversibly and reproducibly switched "on" and "off" as a function of pH. The Ln(III) emission output of the system on the **AuNPs** could be investigated by altering the chain length of the thiol chain attaching the Ln(III) complex to the **AuNP** surface and observing how the Ln(III) emission changes as a function of alkyl chain length. Furthermore the system could be reversed; the antenna could be attached to the **AuNP** surface and the Ln(III) cyclen complex added into the system to see if better Ln(III) emission would be observed as the Ln(III) would be further away from the quenching of the **AuNP** surface.

The work described in Chapter 5 focused on the development of Ln(III) luminescent complexes suitable for the formation of Langmuir monolayers and subsequent LB film deposition onto quartz slides. Furthermore, photophysical evaluations of these LB films were carried out and their limitations and sensing abilities were investigated. As only preliminary amino acid sensing studies were carried out on LB films of **Eu·96-nta**, further studies are needed to explain the different behaviour that was observed between the solution and solid state studies. One possible explanation is that on the slide the **Eu·96** molecules are orientated head first, therefore the Eu(III) metal centre is not as accessible as it is in solution and so binding/displacement events of antenna molecules from the Eu(III) metal centre on the slide

may not be the same as in solution. To further investigate this, the orientation of **Eu·96** could be reversed on the slide by hydrophobically coating the slide so that the **Eu·96** molecules would align with the tails pointing down to the slide and the heads pointing away from the slide surface and see how the behaviour compared to that of the solution studies. Furthermore, more in depth characterisation of the Lb films on the slides could be obtained by looking AFM or SEM images of the films to ensure all the films were of the same quality.

The final Chapter involved the synthesis and evaluation **Tb·104** as a Ln(III) luminescent sensor for the detection of Hg(II) at intracellular concentrations. The design of **Tb·104** envisaged binding of Hg(II) into the macrocycle component, and subsequent modulation of the Tb(III) emission. However, we were unable to achieve nucleophilic aromatic substitution of the macrocyclic ring, and redesign of the synthetic pathway may be a future project within the Gunnlaugsson group.

Chapter 7

Experimental

7.1 UV-vis Absorption and Luminescence Spectroscopy

All UV-vis absorption and luminescence spectra were recorded using a Varian CARY 50 spectrophotometer and a Varian Cary Eclipse spectrophotometer, respectively, equipped with a 1.0 cm path length quartz cell, respectively. All solvents used were of spectroscopic grade. The wavelength range for the UV-vis absorption scans was 200 nm to 800 nm with a scan rate of 600 nm min^{-1}. Baseline correction measurements were used for all spectra. All absorbance and fluorescence scans were measured in arbitrary units (A. U.) unless otherwise stated. The blank used in these measurements was different depending on the compound under study. The luminescence data was collected between 450 nm and 650 nm for the Tb(III) emission and between 550 and 750 nm for the Eu(III) emission. Fluorescence spectra in the near-infrared range were recorded on the Fluorolog FL 3-22 spectrophotometer from Horiba Jobin Yvon with double grating emission and excitation monochromators, and a R5509-73 photomultiplier. Light intensity was measured by a C9940-22 detector from Hamamatsu with a range from 800-1700 nm, cooled to 77K and coupled to a Jobin Yvon SpectrAcq v5.20 data acquisition system. All measurements were performed at 298K unless otherwise stated, which was kept constant by using a thermostated unit block, and in HEPES buffer at pH 7.4. Quantum yield (Q_{Ln}^{L}) of the **Yb·81-8-HQS** ternary complex (2×10^{-4} - 5×10^{-5} M) has been determined in Hepes buffer (pH 7.4), relative to the quantum yield of [$Yb(tta)_3phen$] (tta = thenoyltrifluoroacetylacetonate; phen = 1,10-phenanthroline) in toluene, Q_{Ln}^{L} = 1.10%,[173] at room temperature.

7.2 Characterisation of the Surface-Modified AuNPs

The size of the functionalised **AuNP** and their distribution in aqueous solution were determined by Transmission Electron Microscopy (TEM) and Dynamic Light Scattering (DLS), respectively. TEM analyses were carried out at the Centre for Microscopy and Analysis (CMA, Trinity College Dublin) using a JEOL 2100 microscope. DLS measurements were performed on 1-3 × 10^{-7} M solutions of **AuNP** in distilled water using a Zetasizer Nano Series (Malvern Instruments).

7.3 Langmuir Film Measurements

Surface pressure-area isotherms and time stability measurements were carried out at 25°C on a KSV MiniMicro Langmuir-Blodgett trough (KSV, Finland) in UCD with a surface area between 1700 and 8700 mm^2. Water was purified with a Milli-Q® Integral system (Millipore), and its resistivity was measured to be higher than 18 MΩcm. Chloroform (puriss. p.a. ≥ 99.8%, Sigma-Aldrich) was used as spreading solvent for all complexes studied. Typically drops (20 μL) of the surfactant solution (*ca.* 0.25 mM) were deposited using a

microsyringe onto the water subphase. After leaving the solvent to evaporate for 20 minutes, the barriers were compressed at 6 mm min^{-1} and the surface pressure was monitored using a platinum Wilhelmy plate.

7.4 General Synthetic Procedures

Procedure 1: Selective monoalkylation of cyclen[169]

The relevant alkyl halide (1 eq) was added to a freshly distilled $CHCl_3$ solution of cyclen (4 or 8 eq) and freshly distilled NEt_3 (1.2 or 2.4 eq). The resulting solution was refluxed at 65°C for 16 hours under inert atmosphere. After cooling to room temperature, the organic solution was washed three times with 20 mL of a 1 M NaOH solution to remove the excess cyclen and then three times with 10 mL of water, followed by drying over $MgSO_4$, filtering and removing the solvent under reduced pressure.

Procedure 2: Synthesis of lanthanide complexes using $Ln(CF_3SO_3)_3$

All lanthanide complexes found within were prepared using microwave irradiation. The relevant ligand with 1 molar equivalent of the appropriate lanthanide triflate in freshly distilled methanol (5 mL) for 40 minutes. After removal of solvent under reduced pressure vacuum, the complexes were isolated by dissolving them in a minimal amount of methanol and precipitating from swirling diethyl ether (200 mL). ^1H NMR spectra of the lanthanide complexes consisted of very broad signals and therefore were not fully characterised, *i.e.* integration of the signals was not possible. The paramagnetic properties of lanthanides prevent ^{13}C spectra from being obtained.

Procedure 3: AuNP synthesis

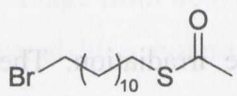
Au(III) chloride trihydrate (0.10 g) was dissolved in Millipore water (10 mL). Tetraoctylammonium bromide (TOAB) (0.36 g) was dissolved in toluene (25 mL). The two solutions were mixed and stirred together at room temperature for 10 minutes. Sodium borohydride ($NaBH_4$) (0.13 g) was dissolved in Millipore water (10 mL) and added dropwise to this solution. The resulting solution was mixture at room temperature for a further 2 hours, in which time the gold solution was reduced, causing the solution to change colour from yellow to red, and transferred into the toluene layer by the TOAB. After 2 hours the layers were separated and the toluene-**AuNP** layer was washed with water, 0.1 M HCl and 0.1 M NaOH. UV-vis absorption spectrum of the aqueous solution showed the appearance of the SPR band at 530 nm.

Procedure 4: Ln(III)-AuNP functionalisation

The toluene-**AuNP** solution (5 mL) was added to a *ca.* 1×10^{-4} M Ln(III) solution (water:DMSO 99:1) (5 mL) and the mixture was stirred vigorously at room temperature overnight. The initial pale yellow aqueous solution turned into a deep purple colour during the course of the reaction, confirming phase transfer of the **AuNPs** from the toluene layer to the aqueous layer. The layers were separated and the water layer was filtered through a micropipette to give a clear pink solution. Any unbound Ln(III) complex was removed using sephadex G15 column chromatography using water or NaCl (0.05 M) as the elutant. UV-vis absorption spectrum showed a red shifting in the SPR band compared to the non-surface modified system. TEM imagining and DLS showed monodisperse **AuNPs** with diameters ranging from 4 - 15 nm.

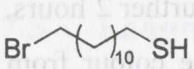
7.5 Experimental Details for Chapter 2

Thioacetic acid *S*-(12-bromododecyl) ester (55)[126]



Compound **55** was prepared by stirring 1, 12-dibromododecane (9.6 g, 29.3 mmol, 3.36 eq) and CH_3COSK (0.99 g, 8.71 mmol, 1 eq) at reflux in acetonitrile (200 mL) under an argon atmosphere for 3 days. The volume was reduced under a reduced pressure vacuum and redissolved in CH_2Cl_2 (100 mL), which was washed with water (3 × 25 mL). The organic layer was collected and dried over $MgSO_4$, filtered and the solvent removed under reduced pressure. Automatic flash chromatography using 95:5 hexane/ethyl acetate as eluant yielded **55** as a colourless oil in 37% yield (1.00 g, 3.1 mmol). HRMS (*m/z*) (ES^+) Calculated for $C_{14}H_{27}BrOSNa$ *m/z* = 345.0864 $[M + Na]^+$. Found *m/z* = 345.0864; ^1H NMR (400 MHz, $CDCl_3$) δ_H: 3.43 (2H, t, *J* = 7.0 Hz, $C\underline{H}_2Br$), 2.88 (2H, t, *J* = 7.5 Hz, $C\underline{H}_2S$), 2.35 (3H, s, $COC\underline{H}_3$), 1.87 (2H, qu, *J* = 7.0 Hz, $C\underline{H}_2CH_2Br$), 1.50 (2H, qu, *J* = 7.5 Hz, $C\underline{H}_2CH_2S$), 1.38 (16H, m, 8 × $C\underline{H}_2$); ^{13}C NMR (100 MHz, $CDCl_3$) δ_C: 33.66, 32.38, 30.31, 29.05, 28.99, 28.96, 28.71, 28.65, 28.36, 28.31, 27.73; IR υ_{max} (cm^{-1}): 2915 2850, 1685, 1469 1114, 959, 718.

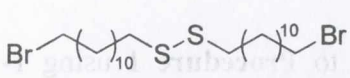
12-Bromododecane-1-thiol (57)[126]



Methanol (40 mL) was cooled to 0°C in an ice bath and acetyl chloride (5.45 g, 69.5 mmol, 25 eq) was added. To this solution **55** (0.90 g, 2.78 mmol, 1 eq) in 10 mL of methanol was added slowly to the reaction mixture with stirring using a pressure equalised dropping funnel. The reaction was stirred at room temperature overnight. The volume was reduced and 25 mL water was added. The product was extracted with CH_2Cl_2. The organic layers were combined, dried over $MgSO_4$, filtered and the solvent was removed under reduced pressure to give a white solid in 98% yield (0.77 g, 2.73 mmol).

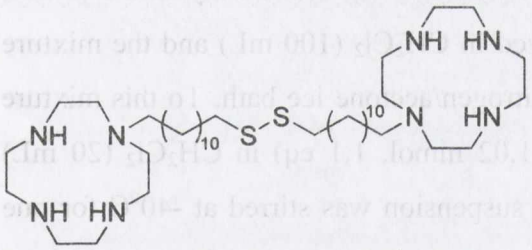
m.p. 35-37°C; ^{1}H NMR (400 MHz, $CDCl_3$) δ_H: 3.40 (2H, t, J = 7 Hz, $C\underline{H}_2Br$), 2.51 (2H, q, J = 7.3 Hz, $C\underline{H}_2SH$), 1.83 (2H, qu, J = 7.3 Hz, $C\underline{H}_2CH_2Br$), 1.60 (2H, q, J = 7.5 Hz, $C\underline{H}_2CH_2SH$), 1.35 (16H, m, 8 × $C\underline{H}_2$); ^{13}C NMR (100 MHz, $CDCl_3$) δ_C: 33.66, 33.59, 32.37, 29.04, 28.98, 28.60, 28.64, 28.35, 27.90, 27.72; IR υ_{max} (cm^{-1}): 2914, 2849, 2567, 1469, 1225, 716, 645.

1,2-Bis-(12-bromododecyl)disulfane (58)[126]



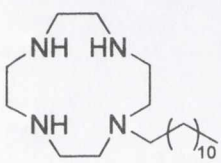
Compound **57** (0.42 g, 1.5 mmol, 1 eq) along with iodine (0.102 g, 0.45 mmol, 0.3 eq) was dissolved in CH_2Cl_2 (50 mL) and refluxed at 40°C overnight. The organic layer was washed with water (3 × 25 mL) and then dried over $MgSO_4$, filtered and the solvent removed under reduced pressure. The yellow solid obtained was recrystallised from hexane to give a white solid in 48% yield (0.40 g, 0.72 mmol). m.p. 48-50°C; ^{1}H NMR (400 MHz, $CDCl_3$) δ_H: 3.41 (4H, t, J = 7 Hz, 2 × $C\underline{H}_2Br$), 2.68 (4H, t, J = 7.5 Hz, 2 × $C\underline{H}_2S$), 1.85 (4H, qu, J = 7 Hz, 2 × $C\underline{H}_2CH_2Br$), 1.66 (4H, qu, J = 7.5 Hz, 2 × $C\underline{H}_2CH_2S$), 1.37 (32H, m, 16 × $C\underline{H}_2$); ^{13}C NMR (100 MHz, $CDCl_3$) δ_C: 39.20, 34.09, 32.84, 29.80, 29.54, 29.49, 29.43, 29.23, 29.10, 28.77, 28.53, 28.18; IR υ_{max} (cm^{-1}): 2917, 2848, 1470, 1271, 1220, 1035, 719, 649.

1,2-Bis[12-(1,4,7,10-tetraazacyclododecan-1-yl) dodecyl] disulfane (60)[169]



Compound **60** was synthesised according to **Procedure 1** using **58** (0.30 g, 0.54 mmol, 1 eq), cyclen (0.74 g, 4.32 mmol, 8 eq) and triethylamine (0.18 ml, 1.29 mmol, 2.4 eq). The product was isolated as a yellow oil in 77% yield (0.31 g, 0.41 mmol). HRMS (*m/z*) (ES^+) Calculated for $C_{40}H_{86}N_8S_2$ *m/z* = 743.6495 $[M + H]^+$. Found *m/z* = 743.6532; ^{1}H NMR (400 MHz, $CDCl_3$) δ_H: 7.06 (4H, br s, 4 × N$\underline{H}$), 6.59 (2H, br s, 2 × N$\underline{H}$), 2.71 (32H, m, cyclen H), 2.32 (4H, t, J = 7.2 Hz, 2 × $SC\underline{H}_2$), 1.59 (4H, qu, J = 7.2 Hz, 2 × $SCH_2C\underline{H}_2$), 1.29 (40H, m, 20 × $C\underline{H}_2$); ^{13}C NMR (100 MHz, $CDCl_3$) δ_C: 54.50, 50.96, 49.65, 46.87, 45.50, 45.19, 38.72, 29.23, 29.15, 29.10, 28.81, 28.78, 28.09, 27.00, 26.70; IR υ_{max} (cm^{-1}): 2917, 2848, 1471, 1461, 1271, 1220, 719, 650.

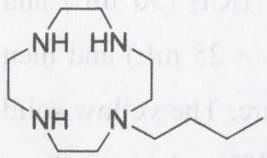
1-Dodecyl-1,4,7,10-tetraazacyclododecane (60a)[169]



Compound **60a** was synthesised according to **Procedure 1** using 1-bromododecane (0.36 g, 1.45 mmol, 1 eq), cyclen (1 g, 5.8 mmol, 4 eq) and triethylamine (0.175 g, 1.74 mmol, 1.2 eq). A colourless oil was obtained in 96% yield (0.47 g, 1.39 mmol). HRMS (*m/z*) (ES^+) Calculated for $C_{40}H_{86}N_8S_2$ *m/z*

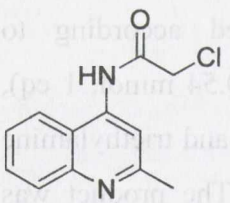
= 341.6495 $[M + H]^+$. Found *m/z* = 341.6532; ^{1}H NMR (400 MHz, $CDCl_3$) δ_H: 2.78-2.50 (16H, m, cyclen C$\underline{H}_2$), 2.39 (2H, t, *J* = 7.2 Hz, C$\underline{H}_2$), 1.23 (18H, m, 9 × C$\underline{H}_2$), 0.86 (3H, t, *J* = 7.0 Hz C$\underline{H}_2$); ^{13}C NMR (100 MHz, $CDCl_3$) δ_C: 54.50, 51.37, 46.83, 45.89, 45.00, 31.89, 29.66, 29.63, 29.53, 29.33, 27.46, 27.17, 22.65, 14.09; IR υ_{max} (cm^{-1}): 2920, 2850, 1642, 1533, 1458, 1406, 1345, 1283, 1027, 807.

1-Butyl-1,4,7,10-tetraazacyclododecane (60b)[169]



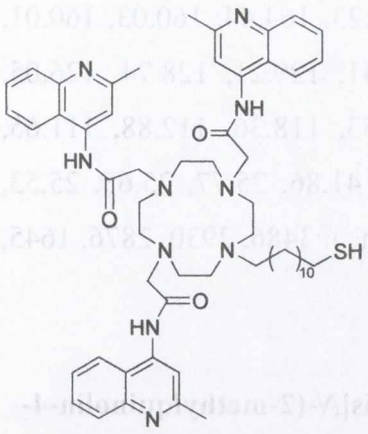
Compound **60b** was synthesised according to **Procedure 1** using 1-bromobutane (0.15 ml, 1.45 mmol, 1 eq), cyclen (1.00 g, 5.8 mmol, 4 eq) and triethylamine (0.24 ml, 1.74 mmol, 1.2 eq). A colourless oil was obtained in 96% yield (0.32 g, 1.40 mmol). HRMS (*m/z*) (ES^+) Calculated for $C_{12}H_{28}N_4$ *m/z* = 229.2392 $[M + H]^+$. Found *m/z* = 229.2402; ^{1}H NMR (400 MHz, $CDCl_3$) δ_H: 2.60 (16H, m, C$\underline{H}_2$), 2.41 (2H, t, *J* = 7 Hz, NC$\underline{H}_2$), 1.45 (2H, m, $NCH_2C\underline{H}_2$), 1.33 (2H, m, $NCH_2CH_2C\underline{H}_2$), 0.91 (3H, m, C$\underline{H}_3$); ^{13}C NMR (100 MHz, $CDCl_3$) δ_C: 53.68, 50.99, 46.23, 45.51, 44.56, 29.03, 20.15, 13.60; IR υ_{max} (cm^{-1}): 3012, 2910, 1654, 1448, 1378, 1224, 981, 789.

2-Chloro-*N*-2-methyl-quinolin-4-yl-acetamide (52)[242]



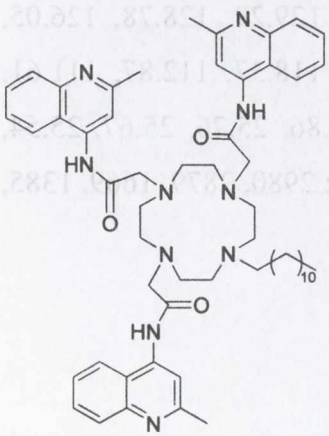
4-Aminoquinaldine (3.02 g, 19.11 mmol, 1 eq) and triethylamine (3 mL, 21.02 mmol, 1.1 eq) were dissolved in CH_2Cl_2 (100 mL) and the mixture was cooled to -40°C in a liquid nitrogen/acetone ice bath. To this mixture chloroacetyl chloride (1.8 mL, 21.02 mmol, 1.1 eq) in CH_2Cl_2 (20 mL) was added over a period of one hour. The resulting suspension was stirred at -40°C for one hour and then at room temperature overnight under an inert atmosphere. After an acid base extraction, the combined organic layers were dried over K_2CO_3, and the solvent removed under reduced pressure to give an off-white solid in 47% yield (2.15 g, 9.16 mmol). m.p. 148-150°C; HRMS (*m/z*) (ES^+) Calculated for $C_{12}H_{11}ClN_2O$ *m/z* = 235.0638 $[M + H]^+$. Found *m/z* = 235.0635; ^{1}H NMR (400 MHz, $CDCl_3$) δ_H: 9.23 (1H, br s, N$\underline{H}$), 8.23 (1H, s, Ar-$\underline{H}$), 8.12 (1H, d, *J* = 8.4 Hz, Ar-H), 7.83 (1H, d, *J* = 8.4 Hz, Ar-$\underline{H}$), 7.75 (1H, t, *J* = 7.2 Hz, Ar-$\underline{H}$), 7.60 (1H, t, *J* = 7.2 Hz, Ar-$\underline{H}$), 4.39 (2H, s $COC\underline{H}_2Cl$), 2.79 (3H, s, C$\underline{H}_3$); ^{13}C NMR (100 MHz, $CDCl_3$) δ_C: 164.33, 159.96, 129.99, 129.36, 126.29, 118.72, 118.36, 111.36, 43.45, 25.49; IR υ_{max} (cm^{-1}): 3255, 2920, 2850, 1673, 1620, 1538, 1351, 1218, 985, 764.

2,2',2''-(10-Dodecyl-1,4,7-tetraazacyclododecane-1,4,7-triyl) tris [*N*-(2-methylquinolin-4-yl) acetamide] (49)



Compound **60** (0.36 g, 0.49 mmol, 1 eq), **52** (0.71 g, 3.0 mmol, 6.2 eq) and diisopropylethylamine (0.53 mL, 3.0 mmol, 6.2 eq) were dissolved in 40 mL of $CHCl_3$ and refluxed for 10 days under an inert atmosphere. The reaction was monitored by mass spectrometry. Once the reaction was complete, sodium borohydride (0.04 g, 0.98 mmol, 2 eq) was added and the reaction mixture was stirred for a further 3 hours at room temperature. The product was isolated through an acid-base extraction process. The resulting neutral organic layer was dried over $MgSO_4$, filtered, and the solvent removed under reduced pressure. Further purification was achieved by precipitation from diethyl ether to give a brown solid in 14% yield (0.07 g, 0.07 mmol). m.p. 125-127°C; Calculated for $C_{56}H_{74}N_{10}O_3S.2CHCl_3.1Et_2O$: C, 58.17; H, 6.77; N, 10.94. Found C, 58.67; H, 6.40; N, 11.08; HRMS (*m/z*) (ES^+) Calculated for $C_{56}H_{74}N_{10}O_3S$ *m/z* = 966.5744 $[M + H]^+$. Found *m/z* = 966.5736; ^1H NMR (400 MHz, $CDCl_3$) δ_H: 10.08 (3H, br s, NH), 8.16-7.36 (15H, m, Ar-H), 3.37 (4H, m, 2 × CH_2), 3.17 (4H, m, 2 × CH_2), 2.95 (2H, m, CH_2), 2.64 (15H, m, 3 × CH_3, 3 × CH_2), 1.62 (4H, m, 2 × CH_2), 1.23 (28H, m, 14 × CH_2); ^{13}C NMR (100 MHz, $CDCl_3$) δ_C: 169.21, 159.79, 159.43, 148.01, 147.87, 139.35, 129.46, 129.22, 128.89, 128.78, 124.96, 124.86, 124.75, 118.45, 117.87, 111.63, 110.66, 60.73, 55.05, 53.25, 52.97, 52.34, 38.65, 29.01, 28.90, 28.74, 28.05, 27.13, 25.32, 25.15; IR υ_{max} (cm^{-1}): 3298, 2923, 2851, 1691, 1563, 1527, 1371, 1270, 1187, 1030, 759.

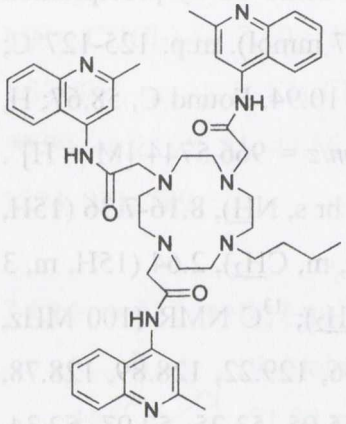
2,2',2''-(10-Dodecyl-1,4,7,10-tetraazacyclododecane-1,4,7-triyl) tris [*N*-(2-methylquinolin -4-yl) acetamide] (61)



Compound **60a** (0.49 g, 1.45 mmol, 1 eq), **52** (1.08 g, 4.64 mmol, 3.2 eq) and diisopropylethylamine (0.53 mL, 3.0 mmol, 6.2 eq) were dissolved in 40 mL of $CHCl_3$ and refluxed for 10 days under an inert atmosphere. The reaction was monitored by mass spectrometry. Once the reaction was complete, the product was isolated through the use of an acid-base extraction process. The resulting neutral organic layer was dried over $MgSO_4$, filtered, and the solvent removed under reduced pressure to give a brown oil in 9% yield (0.12 g, 0.13 mmol) HRMS (*m/z*) (ES^+) Calculated for $C_{56}H_{74}N_{10}O_3$ *m/z* = 935.6024 $[M + H]^+$. Found *m/z* = 935.5982; ^1H NMR (400 MHz, $CDCl_3$) δ_H: 9.36 (3H, br s, NH), 8.20

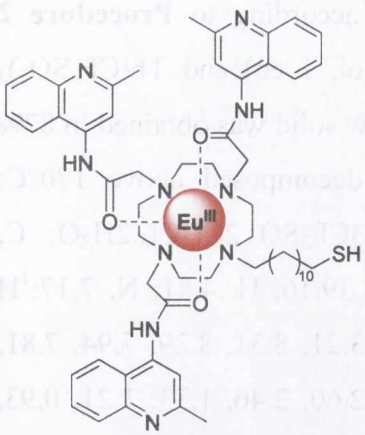
(3H, s, Ar-H), 8.12 (3H, m, Ar-H), 7.88 (3H, m Ar-H), 7.73 (3H, m, Ar-H), 7.58 (3H, m, Ar-H), 4.39 (6H, s, $COCH_2$), 2.77 (9H, s, 3 × CH_3), 1.97 (26H, m, 13 × CH_2), 1.24 (12H, m, 6 × CH_2), 0.87 (3H, m, CH_3); ^{13}C NMR (100 MHz, $CDCl_3$) δ_C: 170.23, 164.44, 160.03, 160.01, 159.33, 148.41, 148.26, 140.86, 139.79, 139.10, 129.72, 129.41, 129.21, 128.74, 126.05, 125.61, 125.47, 125.33, 122.03, 119.58, 119.28, 118.81, 118.53, 118.36, 112.88, 111.65, 110.77, 62.48, 57.93, 53.52, 53.11, 52.27, 50.07, 48.73, 43.44, 41.86, 25.77, 25.65, 25.53, 25.41, 24.52, 20.70, 20.24, 14.06, 13.91, 13.73, 13.61; IR υ_{max} (cm^{-1}): 3486, 2930, 2876, 1645, 1545, 1498, 1378, 1198, 1021, 987, 752.

2,2',2''-(10-Butyl-1,4,7,10-tetraazacyclododecane-1,4,7-triyl)tris[*N*-(2-methylquinolin-4-yl)acetamide] (62)



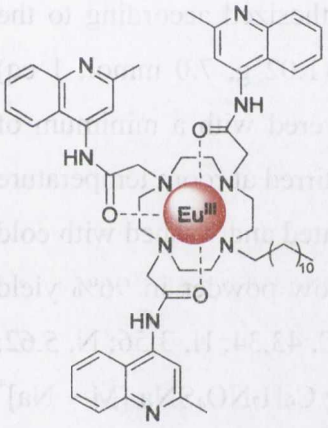
Compound **60b** (0.33 g, 1.46 mmol, 1 eq), **52** (1.07 g, 4.55 mmol, 3.1 eq) and diisopropylethylamine (0.53 mL, 3.0 mmol, 6.2 eq) were dissolved in 40 mL of $CHCl_3$ and refluxed at 65°C for 10 days under an inert atmosphere. The reaction was monitored by mass spectrometry. Once the reaction was complete, the solvent was removed to give a brown solid which was dissolved in a minimal amount of methanol (3 mL) and precipitated out of swirling diethyl ether (300 mL) to give a brown solid in 37% yield (0.44 g, 0.54 mmol). m.p. 129-131°C; Calculated for $C_{48}H_{58}N_{10}O_3.1.5CHCl_3.1.5H_2O$: C, 57.78; H, 6.61; N, 13.71. Found C, 57.93; H, 6.12; N, 13.61; HRMS (*m/z*) (ES^+) Calculated for $C_{48}H_{58}N_{10}O_3$ *m/z* = 823.4772 $[M + H]^+$. Found *m/z* = 823.4773; ^1H NMR (400 MHz, $CDCl_3$) δ_H: 10.30 (3H, br s, NH), 8.20-7.35 (15H, m, Ar-H), 4.08 (2H, m, CH_2), 3.05-2.19 (31H, m, 3 × CH_3, 11 × CH_2), 1.50 (2H, m, CH_2), 1.23 (2H, m, CH_2), 0.87 (3H, m, CH_3); ^{13}C NMR (100 MHz, $CDCl_3$) δ_C: 170.25, 164.43, 160.05, 160.02, 159.32, 148.46, 148.27, 140.84, 139.78, 139.15, 129.70, 129.44, 129.29, 128.78, 126.05, 125.65, 125.43, 125.33, 122.06, 119.54, 119.28, 118.88, 118.52, 118.37, 112.87, 111.61, 110.75, 62.49, 57.99, 53.55, 53.10, 52.24, 50.02, 48.75, 43.46, 41.86, 25.76, 25.67, 25.54, 25.48, 24.59, 20.74, 20.24, 14.02, 13.90, 13.79, 13.67; IR υ_{max} (cm^{-1}): 2980, 2879, 1669, 1385, 1125, 1167, 968, 795, 707.

Eu·49



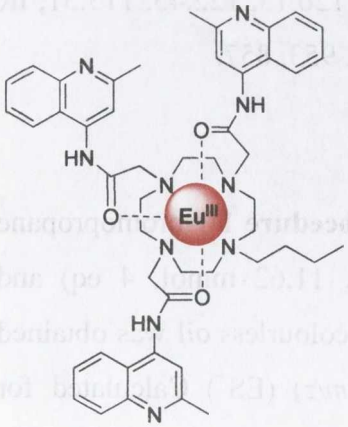
Complex **Eu·49** was synthesised according to **Procedure 2** using ligand **49** (0.05 g, 0.05 mmol, 1 eq) and $Eu(CF_3SO_3)_3$ (0.03 g, 0.05 mmol, 1 eq). A yellow solid was obtained in 90% yield (0.07 g, 0.05 mmol). m.p. decomposed above 170°C; Calculated for $C_{56}H_{74}N_{10}O_3S_1Eu.3CF_3SO_3.2.1CHCl_3.6.H_2O$: C, 38.09; H, 4.61; N, 6.78. Found C, 38.23; H, 4.31; N, 11.08; ^1H NMR (400 MHz, DMSO-d_6) δ_H: 13.74, 8.78, 8.02, 6.61, 6.16, 5.98, 5.75, 5.52, 3.45, 2.66, 2.50, 2.33, 1.58, 1.24, -0.06, -2.65, -4.81, -7.46, -8.24, -10.70, -15.61; IR υ_{max} (cm^{-1}): 3398, 3249, 3170, 2925, 1604, 1513, 1246, 1158, 1023, 819, 754.

Eu·61



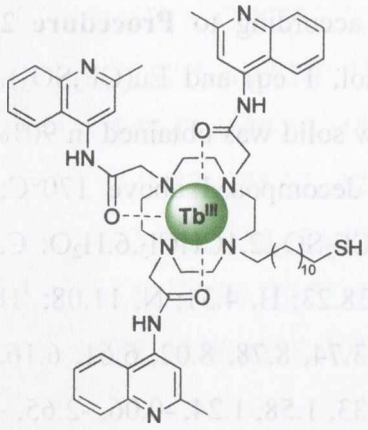
Complex **Eu·61** was synthesised according to **Procedure 2** using ligand **60** (0.04 g, 0.05 mmol, 1 eq) and $Eu(CF_3SO_3)_3$ (0.03 g, 0.05 mmol, 1 eq). A yellow solid was obtained in 86% yield (0.06 g, 0.04 mmol). m.p. decomposed above 165°C; Calculated for $C_{56}H_{74}N_{10}O_3Eu.3CF_3SO_3.4CHCl_3$: C, 37.59; H, 3.91; N, 6.96. Found C, 37.54; H, 3.99; N, 7.05; ^1H NMR (400 MHz, DMSO-d_6) δ_H: 8.30, 8.28, .94, 7.92, 7.80, 7.78, 7.68, 7.67, 6.67, 3.83, 3.75, 2.65, 1.42, 1.31, 1.20, 0.92, -0.27, -0.91, 1.95, 2.87; IR υ_{max} (cm^{-1}): 3358, 3243, 2926, 1603, 1510, 1238, 1158, 1027, 758.

Eu·62



Complex **Eu·62** was synthesised according to **Procedure 2** using ligand **62** (0.09 g, 0.11 mmol, 1eq) and $Eu(CF_3SO_3)_3$ (0.07 g, 0.11 mmol, 1 eq). A yellow solid was obtained in 73% yield (0.11 g, 0.07 mmol). m.p. decomposed above 130°C; Calculated for $C_{48}H_{58}N_{10}O_3Eu.3CF_3SO_3.2CHCl_3.2H_2O$: C, 37.49; H, 3.79; N, 8.24. Found C, 37.04; H, 4.14; N, 8.05; ^1H NMR (400 MHz, DMSO-d_6) δ_H: 13.39, 8.70, 8.37, 8.35, 7.90, 7.80, 7.78, 7.63, 6.59, .33, 1.08, 0.48, -4.49, -6.72, -8.41, -14.20, -15.96, 18.68, -21.59; IR υ_{max} (cm^{-1}): 2980, 1630, 1462, 1178, 1129, 1074, 1028, 797, 719.

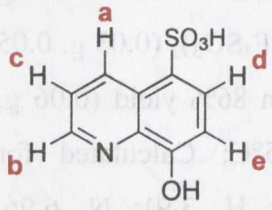
Tb·49



Complex **Tb·49** was synthesised according to **Procedure 2** using ligand **49** (0.02 g, 0.02 mmol, 1 eq) and $Tb(CF_3SO_3)_3$ (0.012 g, 0.02 mmol, 1 eq). A yellow solid was obtained in 87% yield (0.02 g, 0.05 mmol). m.p. decomposed above 170°C; Calculated for $C_{56}H_{74}N_{10}O_3S_1Tb.3CF_3SO_3.2CHCl_3.2H_2O$: C, 39.64; H, 4.36; N, 7.57. Found C, 39.16; H, 4.81; N, 7.17;^{1}H NMR (400 MHz, DMSO-d_6) δ_H: 13.21, 8.31, 8.29, 7.94, 7.81, 7.79, 7.67, 6.68, 5.05, 3.32, 2.92, 2.60, 2.46, 1.33, 1.21, 0.93, 0.12, -2.46; IR υ_{max} (cm^{-1}): 3384, 3257, 3110, 1608, 1523, 1223, 1145, 1022, 845, 718.

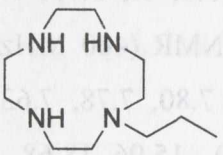
7.6 Experimental Details for Chapter 3

8-Hydroxyquinoline-5-sulfonic acid (8-HQS) (82)



8-Hydroxyquinoline-5-sulfonic acid was synthesized according to the literature procedure.[170] 8-Hydroxyquinoline (1.02 g, 7.0 mmol, 1 eq) was placed in a round bottom flask and covered with a minimum of oleum (H_2SO_4, SO_3 20%). The mixture was stirred at room temperature overnight and poured over ice, yielding a precipitate which was filtrated and washed with cold water. The solid collected was dried under vacuum to give a yellow powder in 96% yield (1.71 g, 6.7 mmol). Calculated for $C_9H_7NO_4S·0.8\ H_2O·0.1\ H_2SO_4$: C, 43.34; H, 3.56; N, 5.62; Found C, 43.16; H, 3.25; N, 5.58; HRMS (*m/z*) (ES^+) Calculated for $C_9H_7NO_4SNa$ $[M + Na]^+$ *m/z* = 247.9994, Found *m/z* = 247.9997; ^{1}H NMR (400 MHz, DMSO-d_6) δ_H: 12.11 (1H, s, OH), 9.77 (1H, d, *J* = 8.7 Hz, ArH$_a$), 9.09 (1H, d, *J* = 5.2 Hz, ArH$_b$), 8.15-8.11 (1H, dd, *J* = 5.2 Hz, ArH$_c$), 8.08 (1H, d, *J* = 5.2 Hz, ArH$_d$), 7.33 (1H, d, *J* = 8.0 Hz, ArH$_e$); ^{13}C NMR (100 MHz, $CDCl_3$) δ_C: 149.08, 145.26, 144.15, 135.47, 129.55, 128.26, 126.13, 122.45, 113.51; IR υ_{max} (cm^{-1}): 3103, 2012, 2564, 1625, 1552, 1309, 1224, 1181, 1041, 953, 857.

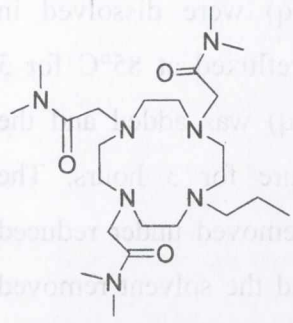
1-Propyl-1,4,7,10-tetraazacyclododecane (83)



Compound **83** was synthesised according to **Procedure 1** 1-bromopropane (0.26 mL, 2.90 mmol, 1.0 eq), cyclen (2 g, 11.62 mmol, 4 eq) and triethylamine (0.48 mL, 3.48 mmol, 1.2 eq). A colourless oil was obtained in 87% yield (0.54 g, 2.52 mmol). HRMS (*m/z*) (ES^+) Calculated for $C_{11}H_{27}N_4$ $[M+H]^+$ *m/z* = 215.2230. Found *m/z* = 215.2234; ^{1}H NMR (400 MHz, $CDCl_3$) δ_H: 2.69-2.35 (16H, m, cyclen CH$_2$), 2.28 (2H, t, *J* = 7 Hz, NCH$_2$), 1.40 (2H, m, NCH$_2$CH$_2$), 0.81

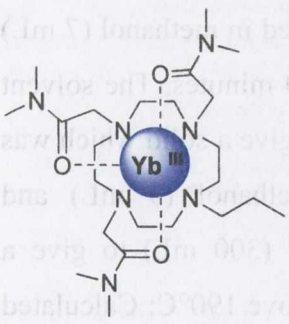
(3H, m, $NCH_2CH_2C\underline{H}_3$); ^{13}C NMR (100 MHz, $CDCl_3$) δ_C: 56.3, 51.5, 46.9, 46.1, 45.1, 20.4, 12.0; IR υ_{max} (cm^{-1}): 3385, 3234, 2808, 2416, 14658, 1541, 1405, 1345, 1283, 1009, 808.

2,2',2''-(10-Propyl-1,4,7,10-tetraazacyclododecane-1,4,7-triyl)tris(*N,N*-dimethylacetamide) (81)



Compound **83** (0.41 g, 1.89 mmol, 1.0 eq), 2-chloro-*N,N*-dimethylacetamide (0.71 g, 5.86 mmol, 3.1 eq), KI (1.01 g, 6.63 mmol, 3.5 eq) and K_2CO_3 (0.91 g, 6.63 mmol, 3.5 eq) were dissolved in acetonitrile (50 mL). The solution was refluxed at 83°C for 5 days. The solution was then filtered and the solvent was removed under reduced pressure. The resulting product was redissolved in $CHCl_3$, filtered and the solvent removed once more under reduced pressure. Purification was achieved by alumina column chromatography using a gradient elution 100 to 80:20 CH_2Cl_2:CH_3OH. The desired product was obtained as a colourless oil in 61% yield (0.54 g, 1.15 mmol). Calculated for $C_{23}H_{47}N_7O_3$. $1.7CHCl_3$: C, 44.12; H, 7.29; N, 14.57. Found C, 44.24; H, 7.36; N, 14.94; HRMS (*m/z*) (ES^+) Calculated for $C_{23}H_{48}N_7O_3$ $[M+H]^+$ *m/z* = 470.3813. Found *m/z* = 470.3818; ^1H NMR (400 MHz, $CDCl_3$) δ_H: 3.50-2.05 (42H, m, cyclen 8 × $C\underline{H}_2$, 6 × $C\underline{H}_3$, 4 × $C\underline{H}_2$), 1.42 (2H, m, $NCH_2C\underline{H}_2$), 0.83 (3H, t, *J* = 7.1 Hz, $NCH_2CH_2C\underline{H}_3$); ^{13}C NMR (100 MHz, $CDCl_3$) δ_C: 170.9, 170.5, 56.1, 55.4, 55.1, 50.2, 36.8, 36.6, 35.9, 35.5, 19.2, 11.8; IR υ_{max} (cm^{-1}): 2960, 2183, 1644, 1452, 1402, 1298, 1100, 997, 819.

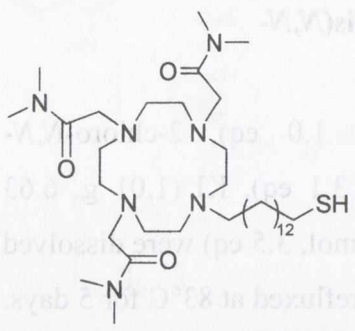
Yb·81



Complex **Yb·81** was synthesised according to **Procedure 2** using ligand **81** (0.112 g, 0.26 mmol, 1 eq) and $Yb(CF_3SO_3)_3$ (0.161 g, 0.26 mmol, 1 eq). A yellow solid was obtained in 81% yield (0.23 g, 0.21 mmol). m.p. decomposed above 180°C; Calculated for $C_{23}H_{47}N_7O_3Yb.2H_2O.3CHCl_3$: C, 24.31, H, 4.01, N, 7.08; Found C, 24.34, H, 3.72, N, 7.35; HRMS (*m/z*) (MALDI) Calculated for $C_{24}H_{46}N_7O_6S_1F_3Yb$ *m/z* = 791.2573 $[M-H+CF_3SO_3]^+$. Found *m/z* = 791.2571; ^1H-NMR (400MHz, CD_3OD) δ_H: 139.99, 118.06, 81.10, 39.64, 14.74, 3.00, 2.97, 1.18, 0.96, -4.12, -12.87, -22.19, -31.16, -60.56, -71.17, -93.88, -147.85; IR υ_{max} (cm^{-1}): 2940, 1624, 1506, 1251, 1184, 1028, 957, 826.

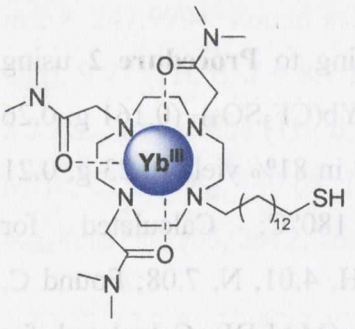
7.7 Experimental Details for Chapter 4

2,2',2''–(10-Propyl-1,4,7,10-tetraazacyclododecane-1,4,7-triyl)tris(*N*,*N*-dimethylacetamide) (38)



58 (1.00 g, 1.35 mmol, 1 eq), 2-chloro-*N*, *N*-dimethylacetamide (**84**) (1.01 g, 8.34 mmol, 6.2 eq), KI (1.24 g, 10.76 mmol, 8 eq) and K_2CO_3 (1.48 g, 10.76 mmol, 8 eq) were dissolved in acetonitrile (50 mL). The solution was refluxed at 85°C for 5 days. $NaBH_4$ (0.102 g, 2.69 mmol, 2 eq) was added and the solution was stirred at room temperature for 3 hours. The solution was then filtered to remove the salts and the solvent was removed under reduced pressure. The resulting product was redissolved in $CHCl_3$, filtered and the solvent removed under reduced pressure. Purification was achieved by alumina column chromatography using a gradient elution 100 to 80:20 CH_2Cl_2:CH_3OH. The desired product was obtained as an orange oil in 48% yield (0.40 g, 0.64 mmol). HRMS (*m/z*) (ES^+) Calculated for $C_{32}H_{65}N_7O_3S$ *m/z* = 627.4870 $[M]^+$. Found *m/z* = 627.4873; ^{1}H NMR (400MHz, $CDCl_3$) δ_H: 2.30-3.50 (42H, m, cyclen C$\underline{H}_2$, C$\underline{H}_2$CO, C$\underline{H}_3$), 1.68 (2H, m, C$\underline{H}_2$), 1.41 (6H, m, 3 × C$\underline{H}_2$), 1.24 (14H, m, 7 × C$\underline{H}_2$); ^{13}C NMR (100 MHZ, $CDCl_3$) δ_C: 170.50, 170.01, 162.70, 55.28, 55.01, 54.69, 54.34, 53.74, 50.64, 50.39, 49.71, 38.55, 37.85, 36.26, 36.15, 35.45, 35.14, 29.15, 29.05, 28.99, 28.71, 28.65, 27.97, 27.11, 25.13; IR υ_{max} (cm^{-1}): 3414, 2923, 2852, 1460, 1399, 1262, 1107, 726.

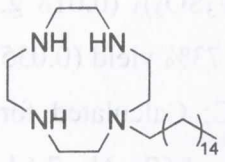
Yb·38



Compound **38** (0.027 g, 0.043 mmol, 1 eq) and $Yb(CF_3SO_3)_3$ (0.0269 g, 0.043 mmol, 1 eq) were dissolved in methanol (7 mL) and heated at 75°C in a microwave for 40 minutes. The solvent was evaporated under reduced pressure to give a solid which was dissolved in a minimal amount of methanol (3 mL) and precipitated out of swirling diethyl ether (300 mL) to give a yellow powder in 74% yield (0.40 g, 0.03 mmol). m.p. decomposed above 190°C; Calculated for $C_{32}H_{65}N_7O_3SYb.0.4\ CHCl_3$: C, 32.88, H, 5.02, N, 7.56, S, 9.88 Found C, 32.78, H, 5.08, N, 7.56, S, 9.89.^{1}H NMR (400MHz, CD_3CN) δ_H: 4.90, 3.49, 3.32, 3.03, 2.69, 1.69, 1.33, 1.19, -0.10, -0.70, -1.60, -2.66, -6.23, -9.02, -12.39, -14.27; IR υ_{max} (cm^{-1}): 1939, 1624, 1459, 1251, 1211, 1156, 1028, 957, 826.

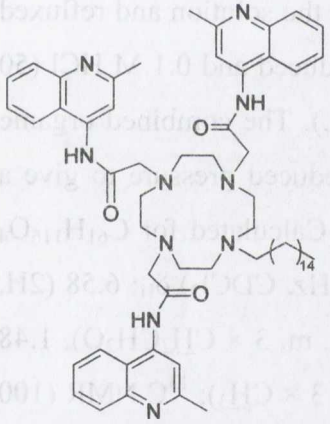
7.8 Experimental Details for Chapter 5

1-Hexadecyl-1,4,7,10-tetraazacyclododecane (60c)



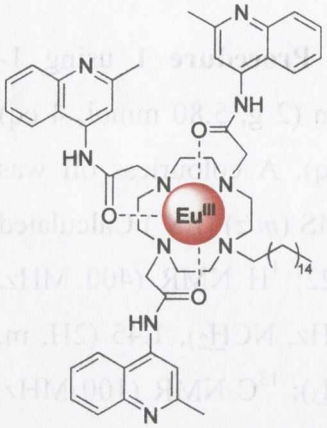
Compound **60c** was synthesised according to **Procedure 1** using 1-bromohexane (0.44 g, 1.45 mmol, 1.0 eq), cyclen (2 g, 5.80 mmol, 4 eq) and triethylamine (0.17 mL, 1.74 mmol, 1.2 eq). A colourless oil was obtained in 78% yield (0.45 g, 1.14 mmol). HRMS (*m/z*) (ES^+) Calculated for $C_{40}H_{86}N_8S_2$ *m/z* = 397.8455 $[M + H]^+$. Found *m/z* = 743.8522; ^1H NMR (400 MHz, $CDCl_3$) δ_H: 2.77-2.51 (16H, m, cyclen $C\underline{H}_2$), 2.39 (2H, t, *J* = 7.2 Hz, $NC\underline{H}_2$), 1.45 (2H, m, $NCH_2C\underline{H}_2$), 1.24 (26H, m, 13 × $C\underline{H}_2$) 0.81 (3H, t, *J* = 7.0 Hz, $C\underline{H}_3$); ^{13}C NMR (100 MHz, $CDCl_3$) δ_C: 54.00, 51.03, 46.51, 45.62, 44.64, 29.22, 29.18, 29.08, 28.89, 27.01, 26.84, 22.21, 13.65; IR υ_{max} (cm^{-1}): 3390-3224 (N-H stretch), 2959, 2931, 1639, 1467, 1451, 1349, 1221, 983, 767.

2,2',2''-(10-Hexadecyl-1,4,7,10-tetraazacyclododecane-1,4,7-triyl)tris[*N*-(2-methylquinolin-4-yl)acetamide] (94)



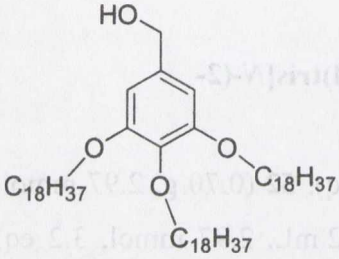
Compound **60c** (0.36 g, 0.89 mmol, 1 eq), **52** (0.70 g, 2.97 mmol, 3.2 eq) and diisopropylethylamine (0.52 mL, 2.97 mmol, 3.2 eq) were dissolved in 40 mL of $CHCl_3$ and refluxed at 65°C for 10 days under an inert atmosphere. The product was isolated through an acid-base extraction process. The resulting neutral organic layer was dried over $MgSO_4$, filtered, and the solvent removed under reduced pressure to give a brown oil in 15% yield (0.133 g, 0.134 mmol). HRMS (*m/z*) (ES^+) Calculated for $C_{60}H_{83}N_{10}O_3$ *m/z* = 991.6656 $[M + H]^+$. Found *m/z* = 991.6650; ^1H NMR (400 MHz, $CDCl_3$) δ_H: 8.23-7.42 (15H, m, Ar-$\underline{H}$), 3.51-2.63 (26H, br m, $C\underline{H}_2$), 1.85 (4H, m, 2 × $C\underline{H}_2$), 1.23 (31H, m, $C\underline{H}_2$ + $C\underline{H}_3$), 0.90 (3H, m, $C\underline{H}_3$); ^{13}C NMR (100 MHz, $CDCl_3$) δ_C: 168.5, 159.3, 149.2, 129.2, 128.4, 124.6, 123.6, 119.6, 106.3, 63.6, 58.6, 57.9, 55.8, 31.2, 29.6, 29.3, 28.4, 27.6, 26.9, 22.7, 20.8, 14.6; IR υ_{max} (cm^{-1}): 3490, 2945, 2189, 1647, 1500, 1347, 1178, 991, 765.

Eu·94



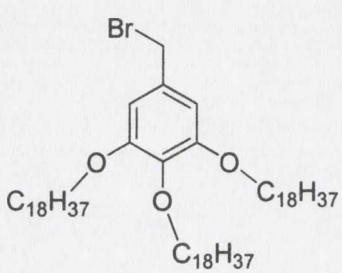
Complex **Eu·94** was synthesised according to **Procedure 2** using ligand **94** (0.029 g, 0.03 mmol, 1eq) and $Eu(CF_3SO_3)_3$ (0.018 g, 0.03 mmol, 1 eq). A brown solid was obtained in 73% yield (0.035 g, 0.022 mmol). m.p. decomposed above 140°C; Calculated for $C_{60}H_{82}N_{10}O_3Eu.3CF_3SO_3.2CHCl_3$: C, 42.63; H, 4.67; N, 7.64. Found C, 42.82; H, 4.31; N, 7.98; ^{1}H NMR (400 MHz, DMSO-d_6) δ_H: 8.296, 8.27, 8.11, 7.93, 7.78, 7.66, 7.58, 6.66, 6.179, 4.23, 4.04, 3.91, 3.58, 3.49, 2.79, 2.64, 2.20, 1.29, 0.90, -0.32. IR υ_{max} (cm^{-1}): 3346, 2980, 1630, 1622, 1237, 1138, 1005, 809.

[3,4,5-Tris(octadecyloxy)phenyl]methanol (98)



KBH_4 (4.77 g, 88.4 mmol, 50 eq) and LiCl (3.74 g, 88.4 mmol, 50 eq) were refluxed in dry THF (50 mL) for 2 hours. methyl 3,4,5-tris(octadecyloxy)benzoate (**97**) (1.64 g, 1.75 mmol, 1 eq) in THF (10 mL) was added dropwise to the solution and refluxed at 70°C for 5 hours. The solvent was reduced and 0.1 M HCl (50 mL) was added and the solution extracted with CH_2Cl_2 (3 × 50 mL). The combined organic extracts were dried over $MgSO_4$ and the solvent removed under reduced pressure to give a white solid in 75% yield (1.21 g, 1.32 mmol). HRMS (*m/z*) (ES^+) Calculated for $C_{61}H_{116}O_4$ *m/z* = 912.8874 $[M + H]^+$. Found *m/z* = 912.8885; ^{1}H NMR (400 MHz, $CDCl_3$) δ_H: 6.58 (2H, s, Ar-H), 4.61 (2H, m, CH_2OH), 3.98 (6H, m, 3 × CH_2O), 1.80 (6H, m, 3 × CH_2CH_2O), 1.48 (6H, m, 3 × $CH_2CH_2CH_2O$), 1.28 (84H, m, 42 × CH_2), 0.90 (9H, m, 3 × CH_3); ^{13}C NMR (100 MHz, $CDCl_3$) δ_C: 153.26, 137.62, 135.97, 105.35, 73.39, 69.09, 65.65, 31.89, 30.30, 29.68, 29.62, 29.59, 29.39, 29.33, 26.11, 26.07, 22.65, 14.07; IR υ_{max} (cm^{-1}): 3500, 2916, 2848, 1593, 1463, 1223, 1118, 719.

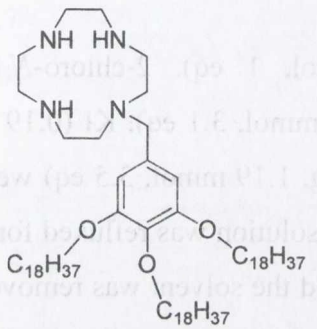
5-(Bromomethyl)-1,2,3-tris(octadecyloxy) benzene (99)



Compound **98** (0.20 g, 0.22 mmol, 3 eq) was dissolved in dry toluene (40 mL) and cooled to 0°C in an ice bath. Tribromophosphine (0.19 g, 0.73 mmol, 1 eq) was added dropwise. The solution was stirred at room temperature for 3 hours. The solvent was reduced and 0.1 M HCl (50 mL) was added and the solution extracted with CH_2Cl_2 (3 × 50 mL). The combined organic extracts were dried over $MgSO_4$ and the solvent removed under reduced pressure to give a white solid

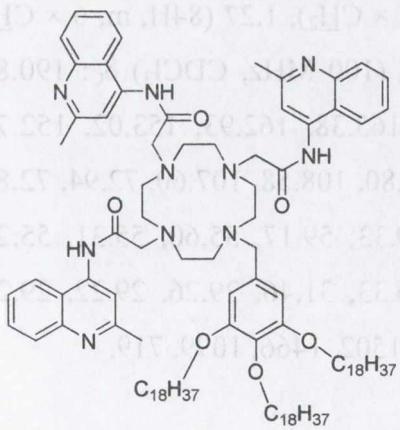
in 87% yield (0.187 g, 0.191 mmol). HRMS (*m/z*) (ES^+) Calculated for $C_{61}H_{115}O_3Br$ *m/z* = 974.8030 $[M^{\cdot}]^+$. Found *m/z* = 974.8061; ^1H NMR (400 MHz, $CDCl_3$) δ_H: 6.59 (2H, s, Ar-H), 4.46 (2H, s, CH_2Br), 3.98 (6H, m, 3 × CH_2O), 1.78 (6H, m, 3 × CH_2CH_2O), 1.48 (6H, m, 3 × $CH_2CH_2CH_2O$), 1.28 (84H, m, 42 × CH_2), 0.90 (9H, m, 3 × CH_3); ^{13}C NMR (100 MHz, $CDCl_3$) δ_C: 153.13, 132.46, 107.51, 73.42, 69.11, 34.58, 31.89, 30.29, 29.68, 29.63, 29.61, 29.57, 29.37, 29.33, 26.07, 26.05, 22.65, 14.07; IR υ_{max} (cm^{-1}): 2916, 2848, 1590, 1466, 1440, 1245, 1128, 1113, 720.

1-[3,4,5-Tris(octadecyloxy)benzyl]-1,4,7,10-tetraazacyclododecane (100)



Compound **100** was synthesised according to **Procedure 1** using **99** (0.18 g, 0.19 mmol, 1.0 eq), cyclen (0.13 g, 0.76 mmol, 4 eq) and triethylamine (0.03 mL, 0.23 mmol, 1.2 eq). A white waxy solid was obtained in 81% yield (0.16 g, 0.15 mmol). HRMS (*m/z*) (MALDI) Calculated for $C_{69}H_{135}N_4O_3$ $[M+H]^+$ *m/z* = 1068.0505. Found *m/z* = 1068.0534; ^1H NMR (400 MHz, $CDCl_3$) δ_H: 6.53 (2H, s, Ar-H) 3.96 (6H, m, 3 × CH_2O), 3.53 (2H, s, CH_2), 3.986 (6H, m, 3 × CH_2O), 2.84-2.60 (16H, m, cyclen CH_2), 1.79 (6H, m, 3 × CH_2CH_2O), 1.45 (6H, m, 3 × $CH_2CH_2CH_2O$), 1.30 (84H, m, 42 × CH_2), 0.90 (9H, m, 3 × CH_3);^{13}C NMR (100 MHz, $CDCl_3$) δ_C: 152.99, 134.16, 107.18, 73.42, 69.06, 51.22, 47.35, 46.56, 45.31, 31.94, 30.37, 29.74, 29.68, 29.50, 29.38, 26.18, 22.70, 14.13. IR υ_{max} (cm^{-1}): 3450, 2916, 2849, 1584, 1466, 1331, 1232, 1116, 720.

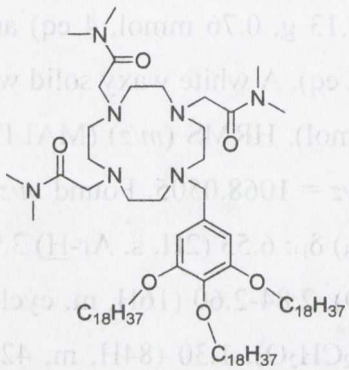
2,2',2''-{10-[3,4,5-Tris(octadecyloxy)benzyl]-1,4,7,10-tetraazacyclododecane-1,4,7-triyl}tris[*N*-(2-methylquinolin-4-yl)acetamide] (95)



Compound **100** (0.16 g, 0.15 mmol, 1 eq), **52** (0.11 g, 0.49 mmol, 3.3 eq) and diisopropylethylamine (0.09 mL, 0.49 mmol, 3.3 eq) were dissolved in 25 mL of $CHCl_3$ and refluxed for 10 days under an inert atmosphere. Once the reaction was complete, the product was isolated through an acid-base extraction process. The resulting neutral organic layer was dried over $MgSO_4$, filtered, and the solvent removed under reduced pressure to give a brown oil which was dissolved in a minimal amount of methanol (3 mL) and precipitated out of swirling diethyl ether (300 mL) to give a brown solid in 22% yield (0.06 g, 0.03 mmol). m.p. 76-78°C; Calculated for $C_{105}H_{164}N_{10}O_6.1CHCl_3.1H_2O$: C, 70.73; H, 9.35; N, 7.78. Found C, 70.89; H, 9.47; N, 7.57; HRMS (*m/z*) (MALDI) Calculated for $C_{105}H_{164}N_{10}O_6Na$ *m/z* = 1684.2733 [M +

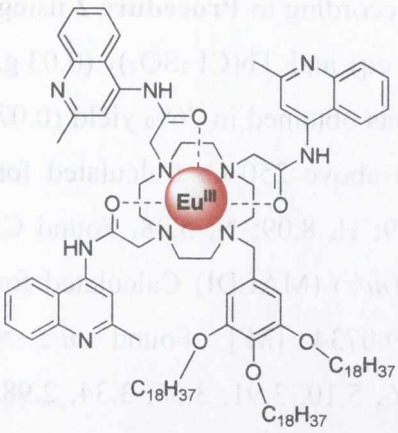
Na]$^+$. Found *m/z* = 1684.2731; ^{1}H NMR (400 MHz, $CDCl_3$) δ_H: 9.94 (1H, s, NH), 9.19 (1H, s, NH), 9.02 (1H, s, NH), 8.21-7.39 (15H, m, Ar-H), 6.34 (2H, s, Ar-H), 4.38 (2H, s, CH_2), 3.84-2.71 (29H, br m, CH_2 + CH_3), 1.75 (12H, m, CH_2), 1.27 (92H, m, CH_2), 0.90 (3H, m, CH_3); ^{13}C NMR (100 MHz, $CDCl_3$) δ_C: 169.74, 157.43, 152.63, 149.56, 137.38, 129.01, 124.52, 122.87, 119.79, 102.82, 104.45, 73.85, 69.12, 59.37, 57.89, 56.83, 33.39, 30.41, 29.70, 28.68, 27.89, 25.73, 23.54, 23.26, 22.76, 20.98, 15.59, 13.95, 13.72, 13.64; IR υ_{max} (cm^{-1}): 3430, 2916, 2849, 1671, 1564, 1529, 1466, 1116, 760.

2,2',2''-{10-[3,4,5-Tris(octadecyloxy)benzyl]-1,4,7,10-tetraazacyclododecane-1,4,7-triyl}tris(*N,N*-dimethylacetamide) (96)



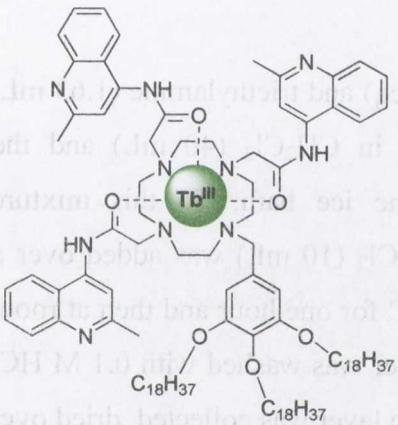
Compound **100** (0.36 g, 0.34 mmol, 1 eq), 2-chloro-*N,N*-dimethylacetamide (**84**) (0.12 g, 1.05 mmol, 3.1 eq), KI (0.19 g, 1.19 mmol, 3.5 eq) and K_2CO_3 (0.16 g, 1.19 mmol, 3.5 eq) were dissolved in acetonitrile (40 mL). The solution was refluxed for 5 days. The solution was then filtered and the solvent was removed under reduced pressure. The resulting product was redissolved in $CHCl_3$, filtered and the solvent removed once more under reduced pressure. Purification was achieved by alumina column chromatography using a gradient elution 100 to 80:20 CH_2Cl_2:CH_3OH. The desired product was obtained as a brown oil in 49% yield (0.23 g, 0.17 mmol). Calculated for $C_{81}H_{155}N_7O_6.3CHCl_3.2H_2O$: C, 58.74; H, 9.51; N, 5.71. Found C, 58.69; H, 9.60; N, 5.90; HRMS (*m/z*) (MALDI) Calculated for $C_{81}H_{155}N_7O_6Na$ *m/z* = 470.3813 [M + Na$^+$]. Found *m/z* = 470.3818; ^{1}H NMR (400 MHz, $CDCl_3$) δ_H: 6.68 (2H, s, Ar-H), 4.02-3.77 (8H, m, 3 × CH_2O, CH_2), 3.06-2.91 (34H, m, cyclen 8 × CH_2, 9 × CH_2), 1.80 (12H, m, 6 × CH_2), 1.48 (6H, m, 2 × CH_2), 1.27 (84H, m, 6 × CH_3, 33 × CH_2), 0.90 (9H, t, *J* = 7.0 Hz, 3 × CH_3); ^{13}C NMR (100 MHz, $CDCl_3$) δ_C: 190.89, 171.04, 170.51, 170.28, 170.03, 169.12, 168.09, 165.34, 163.38, 162.93, 153.02, 152.72, 152.58, 152.39, 137.71, 136.92, 135.96, 133.15, 131.73, 108.80, 108.58, 107.60, 72.94, 72.85, 72.59, 69.08, 68.86, 68.73, 68.53, 68.19, 61.48, 60.83, 59.33, 59.17, 55.60, 55.31, 55.25, 54.61, 52.41, 51.54, 51.13, 49.57, 48.84, 36.82, 36.43, 36.33, 31.46, 29.26, 29.22, 29.21, 29.06, 28.90, 22.22; IR υ_{max} (cm^{-1}): 3546, 2916, 2849, 1667, 1502, 1466, 1099, 719.

Eu·95



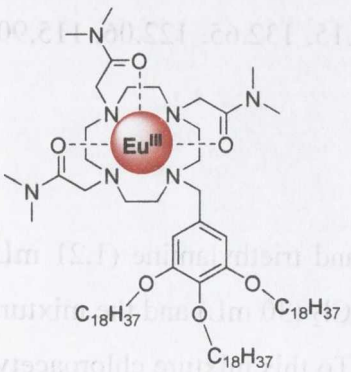
Complex **Eu·95** was synthesised according to **Procedure 2** using ligand **95** (0.05 g, 0.03 mmol, 1eq) and $Eu(CF_3SO_3)_3$ (0.02 g, 0.03 mmol, 1 eq). A brown solid was obtained in 69% yield (0.05 g, 0.02 mmol). m.p. decomposed above 250°C; Calculated for Calculated for $C_{105}H_{164}N_{10}O_6Eu.3CF_3SO_3.3Et_2O$: C, 58.00; H, 7.86; N, 5.63. Found C, 58.32; H, 8.21; N, 5.65; ^1H NMR (400 MHz, CD_3CN) δ_H: 8.00, 7.54, 6.45, 6.25, 3.90, 3.50, 3.49, 2.71, 1.73, 1.45, 1.27, 0.90, 0.09; IR υ_{max} (cm^{-1}): 3503, 2917, 2849, 1646, 1502, 1437, 1331, 1234, 1099, 720.

Tb·95



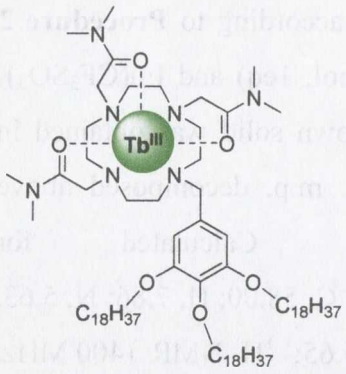
Complex **Tb·95** was synthesised according to **Procedure 2** using ligand **95** (0.05 g, 0.03 mmol, 1eq) and $Tb(CF_3SO_3)_3$ (0.02 g, 0.03 mmol, 1 eq). A brown solid was obtained in 88% yield (0.05 g, 0.03 mmol). m.p. decomposed above 250°C; Calculated for Calculated for $C_{105}H_{164}N_{10}O_6Tb.3CF_3SO_3.2CHCl_3$: C, 52.69; H, 6.67; N, 5.58. Found C, 52.34; H, 6.68; N, 5.59;^1H NMR (400 MHz, CD_3CN) δ_H: 11.07, 9.35, 8.32, 7.98, 7.47, 7.20, 6.73, 4.56, 4.13, 3.51, 2.97, 2.48, 1.93, 1.64, 1.47, 1.09, 0.29; IR υ_{max} (cm^{-1}): 3498, 2916, 2849, 1645, 1434, 1331, 1232, 1098, 720.

Eu·96



Complex **Eu·96** was synthesised according to **Procedure 2** using ligand **96** (0.05 g, 0.04 mmol, 1 eq) and $Eu(CF_3SO_3)_3$ (0.03 g, 0.04 mmol, 1 eq). A pale yellow solid was obtained in 80% yield (0.07 g, 0.04 mmol). m.p. decomposed above 250°C; Calculated for $C_{81}H_{155}N_7O_6Eu.3CF_3SO_3.2Et_2O$: C, 53.48; H, 8.65; N, 4.34. Found C, 53.26; H, 8.21; N, 3.92; HRMS (*m/z*) (MALDI) Calculated for $C_{82}H_{155}N_7O_9F_3SEu$ *m/z* = 1624.0772 [M]. Found *m/z* = 1624.0735; ^1H NMR (400 MHz, CD_3CN) δ_H: 17.00, 7.54, 7.28, 7.01, 6.17, 5.32, 4.56, 3.97, 3.56, 3.40, 3.34, 3.07, 2.99, 2.95, 2.92, 2.19, 2.07, 1.75, 1.27, 0.89, 0.08, -1.89, -8.94, -14.35, -19.46; IR υ_{max} (cm^{-1}): 3503, 2916, 2849, 1643, 1437, 1331, 1232, 1099, 720.

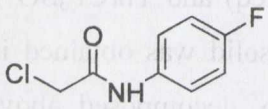
Tb·96



Complex **Tb·96** was synthesised according to **Procedure 2** using ligand **96** (0.05 g, 0.04 mmol, 1 eq) and $Tb(CF_3SO_3)_3$ (0.03 g, 0.04 mmol, 1 eq). A white solid was obtained in 76% yield (0.07 g, 0.03 mmol). m.p. decomposed above 250°C; Calculated for $C_{81}H_{155}N_7O_6Tb.3CF_3SO_3$: C, 52.29; H, 8.09; N, 5.08. Found C, 52.72; H, 7.85; N, 4.59; HRMS (*m/z*) (MALDI) Calculated for $C_{82}H_{154}N_7O_9F_3STb$ *m/z* = 1629.0734 [M$^+$]. Found *m/z* = 1629.0778; ^{1}H NMR (400 MHz, CD_3CN) δ_H: 9.70, 7.28, 6.46, 5.10, 3.91, 3.66, 3.34, 2.98, 2.85, 1.72, 1.45, 1.27, 1.02, 0.90, 0.09, -0.81, -2.50, -3.96; IR υ_{max} (cm^{-1}): 3545, 2919, 1647, 1436, 1331, 1234, 1099, 719.

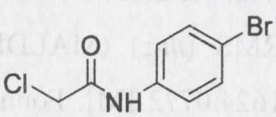
7.9 Experimental Details for Chapter 6

2-Chloro-*N*-(4-fluorophenyl)acetamide (107)



4-Fluoroaniline (1 mL, 13.76 mmol, 1 eq) and triethylamine (1.63 mL, 20.44 mmol, 1.5 eq) were dissolved in CH_2Cl_2 (40 mL) and the mixture cooled to 0°C in an acetone ice bath. To this mixture chloroacetyl chloride (5.74 mL, 21.02 mmol, 1.1 eq) in CH_2Cl_2 (10 mL) was added over a period of one hour. The resulting suspension was stirred at 0°C for one hour and then at room temperature overnight in an inert atmosphere. The organic layer was washed with 0.1 M HCl solution (20 mL) and Millipore water (2 × 20 mL). The organic layer was collected, dried over $MgSO_4$, filtered, and the solvent removed under reduced pressure followed by recrystallisation from methanol to give a brown solid in 49% yield (1.26 g, 6.71 mmol). HRMS (*m/z*) (ES$^-$) Calculated for C_8H_6NOClF *m/z* = 186.0122 [M - H]$^+$. Found *m/z* = 186.0122; ^{1}H NMR (400 MHz, $CDCl_3$) δ_H: 8.25 (1H, br s, N<u>H</u>), 7.54 (2H, m, Ar-<u>H</u>), 7.08 (2H, t, *J* = 8.6 Hz, Ar-<u>H</u>), 4.22 (2H, s, C<u>H</u>$_2$); ^{13}C NMR (100 MHz, $CDCl_3$) δ_C: 163.82, 161.15, 132.65, 122.06, 115.90, 42.82; IR υ_{max} (cm^{-1}): 3255, 1625, 1556, 1504, 1405, 1209, 829.

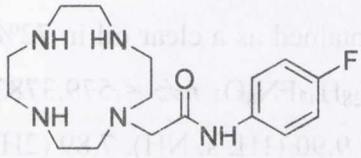
2-Chloro-*N*-(4-bromophenyl)acetamide (108)



4-Bromoaniline (1 g, 5.81 mmol, 1 eq) and triethylamine (1.21 mL, 8.71 mmol, 1.5 eq) were dissolved in CH_2Cl_2 (30 mL) and the mixture was cooled to 0°C in an acetone ice bath. To this mixture chloroacetyl chloride (0.60 mL, 7.55 mmol, 1.3 eq) in CH_2Cl_2 (10 mL) was added over a period of one hour. The resulting suspension was stirred at 0°C for one hour and then at room temperature overnight in an inert atmosphere. The organic layer was washed with 0.1 M HCl solution (20

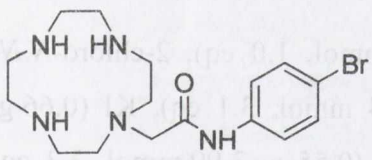
mL) and Millipore water (2 × 20 mL). The organic layer was collected, dried over $MgSO_4$, filtered, and the solvent removed under reduced pressure followed by recrystallisation from methanol to give a pale green solid in 55% yield (0.78 g, 3.17 mmol). HRMS (*m/z*) (ES^-) Calculated for $C_8H_6NOClBr$ *m/z* = 245.9321 $[M - H]^+$. Found *m/z* = 245.9321; ^1H NMR (400 MHz, $CDCl_3$) δ_H: 8.25 (1H, br s, NH), 7.49 (4H, s, Ar-H), 4.21 (2H, s, CH_2); ^{13}C NMR (100 MHz, $CDCl_3$) δ_C: 163.36, 135.27, 131.72, 121.16, 117.55, 42.39; IR υ_{max} (cm^{-1}): 3253, 3078, 1667, 1590, 1545, 1190, 820.

N-(4-Fluorophenyl)-2-(1,4,7,10-tetraazacyclododecan-1-yl)acetamide (109)



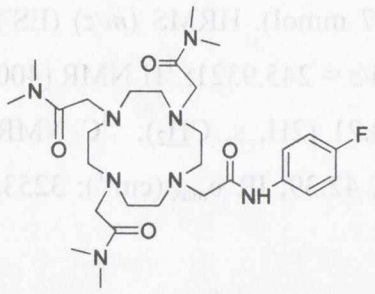
Compound **109** was synthesised according to **Procedure 1** using **107** (0.73 g, 3.92 mmol, 1 eq), cyclen (2.70 g, 15.68 mmol, 4 eq) and triethylamine (0.65 mL, 4.70 mmol, 1.2 eq). A brown oil was obtained in 42% yield (0.51 g, 1.64 mmol). HRMS (*m/z*) (ESI^+) Calculated for $C_{16}H_{27}FN_5O$ *m/z* = 324.2200 $[M + H^+]^+$. Found *m/z* = 324.2193; ^1H NMR (400 MHz, $CDCl_3$) δ_H: 10.19 (1H, s, NH), 7.71 (2H, m, Ar-H), 7.01 (2H. t, *J* = 8.7 Hz, Ar-H), 3.29 (2H, s, CH_2), 2.83 (16H, m, 8 × CH_2); ^{13}C NMR (100 MHz, $CDCl_3$) δ_C: 169.5, 134.0, 120.6, 120.5, 115.1, 114.9, 114.8, 59.2, 53.0, 46.7, 46.4, 45.3; IR υ_{max} (cm^{-1}): 3260, 3100, 1631, 1549, 1505, 1406, 1209, 1158, 830.

N-(4-Bromophenyl)-2-(1,4,7,10-tetraazacyclododecan-1-yl)acetamide (110)



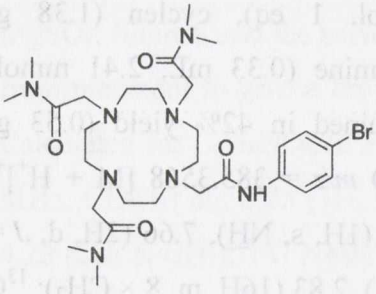
Compound **110** was synthesised according to **Procedure 1** using **108** (0.50 g, 2.01 mmol, 1 eq), cyclen (1.38 g, 8.04 mmol, 4 eq) and triethylamine (0.33 mL, 2.41 mmol, 1.2 eq). A yellow oil was obtained in 42% yield (0.53 g, 1.64 mmol). HRMS (*m/z*) (ESI^+) Calculated for $C_{16}H_{26}BrN_5O$ *m/z* = 385.3568 $[M + H^+]^+$. Found *m/z* =385.3723; ^1H NMR (400 MHz, $CDCl_3$) δ_H: 10.28 (1H, s, NH), 7.66 (2H, d, *J* = 9.1 Hz, Ar-H), 7.42 (2H. d, *J* = 9.1 Hz, Ar-H), 3.28 (2H, s, CH_2), 2.83 (16H, m, 8 × CH_2); ^{13}C NMR (100 MHz, $CDCl_3$) δ_C: 169.6, 131.8, 122.4, 121.6, 115.3, 115.0, 114.9, 59.6, 52.1, 47.2, 46.8, 45.1; IR υ_{max} (cm^{-1}): 3261, 3112, 1629, 1567, 1553, 1402, 1222, 1134, 820.

2,2',2''-{10-[2-(4-Fluorophenylamino)-2-oxoethyl]-1,4,7,10-tetraazacyclododecane-1,4,7-triyl}tris(*N,N*-dimethylacetamide) (111)



Compound **109** (0.30 g, 0.93 mmol, 1.0 eq), 2-chloro-*N,N*-dimethylacetamide (0.35 g, 2.87 mmol, 3.1 eq), KI (0.52 g, 3.06 mmol, 3.3 eq) and K_2CO_3 (0.42 g, 3.06 mmol, 3.3 eq) were dissolved in acetonitrile (30 mL). The solution was refluxed at 83°C for 5 days. The solution was then filtered and the solvent was removed under reduced pressure. The resulting product was redissolved in $CHCl_3$, filtered and the solvent removed once more under reduced pressure. Purification was achieved by alumina column chromatography using a gradient elution 100 to 80:20 CH_2Cl_2:CH_3OH. The desired product was obtained as a clear oil in 72% yield (0.34 g, 0.67 mmol). HRMS (*m/z*) (ES^+) Calculated for $C_{28}H_{47}FN_8O_4$ *m/z* = 579.3783 $[M+H]^+$. Found *m/z* = 579.3755; ^1H NMR (400 MHz, $CDCl_3$) δ_H: 9.90 (1H, s, NH), 7.89 (2H, m, Ar-H), 6.92 (2H, t, *J* = 8.6 Hz, Ar-H), 3.59-2.52 (42H, m, cyclen 8 × CH_2, 6 × CH_3, 4 × CH_2); ^{13}C NMR (100 MHz, $CDCl_3$) δ_C: 170.87, 170.71, 170.39, 159.57, 157.97, 135.13, 135.12, 121.43, 121.389, 114.75, 114.61, 58.15, 54.99, 54.92, 53.39, 50.75, 36.25, 36.10, 35.80, 35.63, 35.52; IR υ_{max} (cm^{-1}): 3440, 2820, 1641, 1508, 1404, 1209, 1102, 1004, 901, 838.

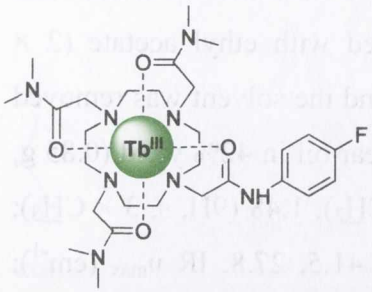
2,2',2''-{10-[2-(4-Fluorophenylamino)-2-oxoethyl]-1,4,7,10-tetraazacyclododecane-1,4,7-triyl}tris(*N,N*-dimethylacetamide) (112)



Compound **110** (0.46 g, 1.21 mmol, 1.0 eq), 2-chloro-*N,N*-dimethylacetamide (0.45 g, 3.74 mmol, 3.1 eq), KI (0.66 g, 3.99 mmol, 3.3 eq) and K_2CO_3 (0.55 g, 3.99 mmol, 3.3 eq) were dissolved in acetonitrile (40 mL). The solution was refluxed at 83°C for 5 days. The solution was then filtered and the solvent was removed under reduced pressure. The resulting product was redissolved in $CHCl_3$, filtered and the solvent removed once more under reduced pressure. Purification was achieved by alumina column chromatography using a gradient elution 100 to 80:20 CH_2Cl_2:CH_3OH. The desired product was obtained as a clear oil in 56% yield (0.44 g, 0.68 mmol). HRMS (*m/z*) (ES^+) Calculated for $C_{28}H_{47}BrN_8O_4$ *m/z* = 661.2801 $[M+Na]^+$. Found *m/z* = 661.2795; ^1H NMR (400 MHz, $CDCl_3$) δ_H: 10.18 (1H, s, NH), 7.86 (2H, d, *J* = 8.9 Hz, Ar-H), 7.33 (2H, d, *J* = 8.7 Hz, Ar-H), 3.61-2.54 (42H, m, cyclen 8 × CH_2, 6 × CH_3, 4 × CH_2); ^{13}C NMR (100 MHz, $CDCl_3$) δ_C: 170.91, 170.77, 170.74, 138.25, 133.00,

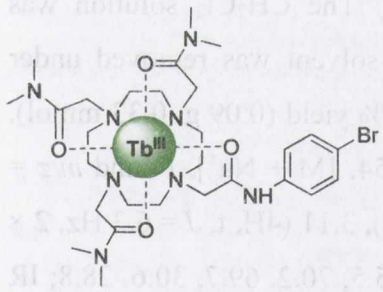
131.07, 129.804, 121.49, 115.65, 58.14, 55.07, 54.89, 51.71, 50.52, 36.34, 36.18, 35.66, 35.55; IR υ_{max} (cm^{-1}): 3448, 2819, 1643, 1488, 1297, 1101, 1004, 951.

Tb·111



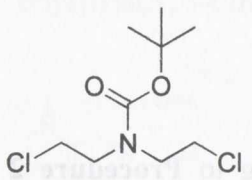
Complex **Tb·111** was synthesised according to **Procedure 2** using ligand **111** (0.18 g, 0.32 mmol, 1 eq) and $Tb(CF_3SO_3)_3$ (0.19 g, 0.32 mmol, 1 eq). A brown powder was obtained in 66% yield (0.30 g, 0.21 mmol). m.p. decomposed above 270°C; Calculated for $C_{28}H_{47}N_8O_8FTb.3CF_3SO_3.6CHCl_2$: C, 23.37; H, 2.81; N, 5.89. Found C, 22.93; H, 3.26; N, 6.00; HRMS (*m/z*) (MALDI) Calculated for $C_{29}H_{46}N_8O_7F_4STb$ *m/z* = 885.2400 $[M-H]^+$. Found *m/z* = 885.2419; ^1H NMR (400MHz, MeOD) δ_H: 306.01, 304.66, 304.42, 302.25, 266.11, 249.30, 209.68, 191.81, 158.37, 110.49, 75.36, 61.34, 55.44, 48.88, 43.40, 20.14, 16.87, 7.43, 4.91, 3.56, 3.33, 1.25, -0.69, -8.85, -47.78, -52.30, -71.66, -75.10, -78.35, -91.23, -93.98, -112.46, -116.39, -174.39, -180.88, -180.98; IR υ_{max} (cm^{-1}): 3403, 3397, 1620, 1507, 1238, 1168, 1026, 957, 825.

Tb·112



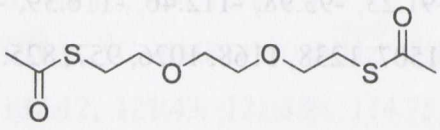
Complex **Tb·112** was synthesised according to **Procedure 2** using ligand **112** (0.13 g, 0.20 mmol, 1 eq) and $Tb(CF_3SO_3)_3$ (0.12 g, 0.205 mmol, 1 eq). A brown powder was obtained in 96% yield (0.24 g, 0.20 mmol). m.p. decomposed above 270°C; Calculated for $C_{28}H_{47}N_8O_8BrTb.3CF_3SO_3.4CHCl_2$: C, 24.39 ; H, 2.98; N, 6.50. Found C, 23.88; H, 3.19; N, 6.74; HRMS (*m/z*) (MALDI) Calculated for $C_{29}H_{46}N_8O_7F_3SBrTb$ *m/z* = 945.1599 $[M-H]^+$. Found *m/z* = 945.1602; ^{1} H NMR (400MHz, MeOD) δ_H: 377.44, 352.37, 348.49, 343,57, 320.67, 306.09, 304.94, 304.61, 303.54, 302.63, 264.56, 248.51, 211.45, 197.20, 165.15, 112.54, 97.92, 76.63, 51.08, 47.50, 42.63, 25.45, 22.05, 19.14, 12.27, 7.69, 3.84, 3.50, 2.43, 1,52, -8.83, -9.34, -46.10, -48.96, -53.67, -69.26, -72.25, -76.78, -83.36, -87.59, -92.59, -92.11, -93.88, -96.73, -110.87, -119.76, -168.94, -178.03, -185.50, -225.02, -296.14, -297.20, -297.70, -298.69, -299.54, -322.79, -374.34, -380.05, -400.95; IR υ_{max} (cm^{-1}): 3403, 1618, 1559, 1462, 1224, 1143, 1025, 956, 821.

Tert-butyl bis(2-chloroethyl)carbamate (116)[243]



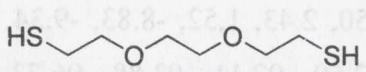
Bis(2-chloroethyl)amine hydrochloride (1.00 g, 8.06 mmol, 1 eq) was added to a solution of NaOH (1.29 g, 32.24 mmol, 4 eq) in water (15 mL) at 0°C. Di-*tert*-butyl dicarbonate (1.18 g, 8.14 mmol, 1.1 eq) was dissolved in water (10 mL) and added dropwise. The reaction mixture was stirred at room temperature overnight. The reaction was washed with ethyl acetate (2 × 20 mL). The combined organic extracts were dried over $MgSO_4$ and the solvent was removed under reduced pressure. The desired product was obtained as a clear oil in 42% yield (0.85 g, 3.53 mmol). ^{1}H NMR (400 MHz, $CDCl_3$) δ_H: 3.68 (8H, m, 4 × C$\underline{H}_2$), 1.48 (9H, s, 3 × C$\underline{H}_3$); ^{13}C NMR (100 MHz, $CDCl_3$) δ_C: 154.4, 80.2, 50.4, 50.2, 41.6, 41.5, 27.8. IR υ_{max} (cm^{-1}): 2947, 2720, 2437, 1750, 1695, 1431, 1156, 1070, 752.

_S,S'_-2,2'-[Ethane-1,2-diylbis(oxy)]bis(ethane-2,1-diyl) diethanethioate (118)



2,2'-(Ethane-1,2-diylbis(oxy))bis(ethane-2,1-diyl) bis(4-methylbenzenesulfonate) (0.20 g, 0.43 mmol, 1 eq) and potassium thioacetate (0.12 g, 0.87 mmol, 2 eq) were dissolved in MeCN (40 mL) and refluxed for 48 hours. The solvent was removed under reduced pressure and the product was redissolved in CH_2Cl_2. The CH_2Cl_2 solution was washed with water (2 × 20 mL) and dried over $MgSO_4$. The solvent was removed under reduced pressure giving the desired product as a brown oil in 76% yield (0.09 g, 0.33 mmol). HRMS (*m/z*) (ES^+) Calculated for $C_{10}H_{18}O_4NaS_2$ *m/z* = 289.0554, [M + Na^+]. Found *m/z* = 289.0544; ^{1}H NMR (400 MHz, $CDCl_3$) δ_H: 3.62 (8H, m, 4 × C$\underline{H}_2$), 3.11 (4H, t, *J* = 6.3 Hz, 2 × C$\underline{H}_2$), 2.35 (6H, s, 3 × C$\underline{H}_3$); ^{13}C NMR (100 MHz, $CDCl_3$) δ_C: 95.5, 70.2, 69.7, 30.6, 28.8; IR υ_{max} (cm^{-1}): 2920, 1787, 1567, 1456, 1271, 1099, 784.

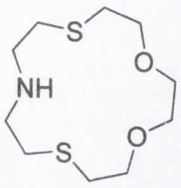
2,2'-[Ethane-1,2-diylbis(oxy)]diethanethiol (119)



Methanol (40 mL) was cooled to 0°C in an ice bath and acetyl chloride (4.83 g, 67.91 mmol, 25 eq) was added. The reaction mixture was allowed to cool to 0°C again. **118** (0.74 g, 2.72 mmol, 1 eq) was dissolved in methanol (10 mL) and added slowly to the reaction mixture with stirring using a pressure equalised dropping funnel. The reaction was stirred at room temperature overnight. The volume was reduced and 25 mL water was added. The product was extracted with CH_2Cl_2. The organic layers were combined, dried over $MgSO_4$, filtered and the solvent was removed under reduced pressure to give an orange oil in 83% yield (0.42 g, 2.27 mmol). HRMS (*m/z*) (ES^+) Calculated for $C_6H_{14}O_2NaS_2$ *m/z* = 205.0333, [M + Na^+]. Found *m/z* = 205.0333; ^{1}H

NMR (400 MHz, $CDCl_3$) δ_H: 3.58 (8H, m, 4 × OC<u>H</u>$_2$), 2.65 (4H, m, 2 × C<u>H</u>$_2$SH), 1.56 (1H, m, S<u>H</u>); ^{13}C NMR (100 MHz, $CDCl_3$) δ_C: 72.3, 69.6, 23.8; IR υ_{max} (cm^{-1}): 2863, 1735, 1597, 1450, 1355, 1256, 1173, 1095, 921, 774.

1,4-Dioxa-7,13-dithia-10-azacyclopentadecane (113)



Caesium carbonate (1.02 g, 3.11 mmol, 1.5 eq) was dissolved in DMF (100 mL) and heated to 60°C. **116** (0.50 g, 2.07 mmol, 1 eq) and **119** (0.378 g, 2.07 mmol, 1 eq) were dissolved in DMF (100 mL) and added dropwise very slowly overnight to the heated caesium carbonate solution in a pressure equalised dropping funnel under argon. The DMF was removed under reduced pressure. The product was redissolved in CH_2Cl_2 and washed with water (2 × 20 mL), dried over $MgSO_4$, filtered and the solvent was removed under reduced pressure. The protected macrocyclic product was confirmed by mass spec and without further purification. Deprotection of the BOC group was achieved by stirring the crude product in a 50:50 solution of CH_2Cl_2:TFA for 15 minutes at room temperature. The solvent was removed under reduced pressure to give a brown oil. Water was added (10 mL) and the pH was adjusted to pH 14 using NaOH (0.1 M). A waxy white solid precipitated out of solution and the brown oil remained undissolved. The white suspension separated leaving only the brown oil which was dissolved in CH_2Cl_2 and washed with water (2 × 20 mL), dried over $MgSO_4$, filtered and the solvent was removed under reduced pressure. Purification was achieved by alumina column chromatography using a gradient elution 100 to 80:20 CH_2Cl_2:CH_3OH. The desired product was obtained as a yellow oil in 2.5% yield (0.013 g, 0.005 mmol). HRMS (*m/z*) (ES^+) Calculated for $C_{10}H_{22}NO_2S_2$ *m/z* = 252.1092, [M + H^+]. Found *m/z* = 252.1092; ^{1}H NMR (400 MHz, $CDCl_3$) δ_H: 3.76 (4H, t, *J* = 4.4 Hz, C<u>H</u>$_2$), 3.66 (8H, m, C<u>H</u>$_2$), 2.92 (4H, t, *J* = 4.4 Hz, C<u>H</u>$_2$), 2.78 (4H, m, C<u>H</u>$_2$); ^{13}C NMR (100 MHz, $CDCl_3$) δ_C: 70.19, 69.52, 38.27, 50.80, 31.05; IR υ_{max} (cm^{-1}): 3380, 2919, 1657, 1469, 1099.

References

References

1. dos Santos, C. M. G.; Harte, A. J.; Quinn, S. J.; Gunnlaugsson, T. *Coord. Chem. Rev.* **2008**, *252*, 2512.
2. Beer, P. D.; Gale, P. A.; Smith, D. K., *Supramolecular Chemistry*. Oxford University Press: New York, 2003.
3. Freeman, R.; Li, Y.; Tel-Vered, R.; Sharon, E.; Elbaz, J.; Willner, I. *Analyst* **2009**, *134*, 653.
4. Balzani, V.; Bergamini, G.; Marchioni, F.; Ceroni, P. *Coord. Chem. Rev.* **2006**, *250*, 1254.
5. Massue, J.; Quinn, S. J.; Gunnlaugsson, T. *J. Am. Chem. Soc.* **2008**, *130*, 6900.
6. Zhong, H.; Zhang, Q.; Zhang, S. *Chem. Eur. J.* **2011**, *17*, 8388.
7. Daniel, M.-C.; Astruc, D. *Chem. Rev.* **2003**, *104*, 293.
8. Wang, Z.; Ma, L. *Coord. Chem. Rev.* **2009**, *253*, 1607.
9. de Silva, A. P.; Fox, D. B.; Huxley, A. J. M.; Moody, T. S. *Coord. Chem. Rev.* **2000**, *205*, 41.
10. www.shsu.edu/~chm_tgc/chemilumdir/JABLONSKI.
11. de Silva, A. P.; Fox, D. B.; Huxley, A. J. M.; Moody, T. S. *Coord. Chem. Rev.* **2000**, *205*, 41.
12. de Silva, A. P.; de Silva, S. A. *J. Chem. Soc., Chem. Commun.* **1986**, 1709.
13. Abebe, F. A.; Eribal, C. S.; Ramakrishna, G.; Sinn, E. *Tetrahedron Lett. 52*, 5554.
14. Gunnlaugsson, T.; Harte, A. J.; Leonard, J. P.; Nieuwenhuyzen, M. *Supramol. Chem.* **2003**, *15*, 505.
15. Bünzli, J.-C. G.; Choppin, G. R., *Lanthanide Probes in Life, Chemical and Earth Sciences: Theory and Practice*. Elsevier: Amsterdam, 1989.
16. Bünzli, J.-C. G.; Piguet, C. *Chem. Soc. Rev.* **2005**, *34*, 1048.
17. Gunnlaugsson, T.; Stomeo, F. *Org. & Biomol. Chem.* **2007**, *5*, 1999.
18. Faulkner, S.; Pope, S. J. A.; Burton-Pye, B. P. *Appl. Spectrosc. Rev.* **2005**, *40*, 1
19. Choppin, G. R.; Peterman, D. R. *Coord. Chem. Rev.* **1998**, *174*, 283.
20. Leonard, J.; Nolan, C.; Stomeo, F.; Gunnlaugsson, T. *Top. Curr. Chem.* **2007**, *281*, 1.
21. Bünzli, J.-C. G. *Acc. Chem. Res.* **2006**, *39*, 53.
22. de Silva, A. P.; Gunaratne, H. Q. N.; Gunnlaugsson, T.; Huxley, A. J. M.; McCoy, C. P.; Rademacher, J. T.; Rice, T. E. *Chem. Rev.* **1997**, *97*, 1515.
23. Gunnlaugsson, T.; Leonard, J. P. *Chem. Commun.* **2005**, 3114.
24. Heller, A.; Barkleit, A.; Bernhard, G.; Ackermann, J.-U. *Inorg. Chim. Acta* **2009**, *362*, 1215.
25. Pandya, S.; Yu, J.; Parker, D. *Dalton Trans.* **2006**, 2757.
26. Parker, D. *Coord. Chem. Rev.* **2000**, *205*, 109.
27. A. Beeby; D. Parker; Williams., J. A. G. *J. Chem. Soc., Perkin Trans. 2* **1996**, 1565
28. Sabbatini, N.; Guardigli, M.; Lehn, J.-M. *Coord. Chem. Rev.* **1993**, *123*, 201.
29. Forster, T. H. *Discuss. Faraday Soc.* **1959**, *27*, 7.
30. Dexter, D. L. *J. Chem. Phys.* **1953**, *215*, 836.
31. Binnemans, K. *Chem. Rev.* **2009**, *109*, 4283.
32. Beeby, A.; M. Clarkson, I.; S. Dickins, R.; Faulkner, S.; Parker, D.; Royle, L.; S. de Sousa, A.; A. Gareth Williams, J.; Woods, M. *J. Chem. Soc., Perkin Trans. 2* **1999**, 493.
33. Horrocks, W. D.; Sudnick, D. R. *Accounts Chem. Res.* **2002**, *14*, 384.
34. Bünzli, J.-C. G. *Chem. Rev.* **2010**, *110*, 2729.
35. Beeby, A.; Clarkson, I. M.; Dickins, R. S.; Faulkner, S.; Parker, D.; Royle, L.; Sousa, A. D.; Williams, J. A. G.; Woods, M. J. *J. Chem. Soc., Perkin Trans. 2* **1999**, 493.
36. Supkowski, R. M.; Horrocks Jr, W. D. *Inorg. Chim. Acta* **2002**, *340*, 44.

37. Caravan, P.; Ellison, J. J.; McMurry, T. J.; Lauffer, R. B. *Chem. Rev.* **1999**, *99*, 2293.
38. Binnemans, K. *Chem. Rev.* **2009**, *109*, 4283.
39. Sonya J, F. *Curr. Opin. Chem. Biol.* **2001**, *5*, 201.
40. Toth, E.; Burai, L.; Merbach, A. E. *Coord. Chem. Rev.* **2001**, *216-217*, 363.
41. Lukes, I.; Kotek, J.; VojtIsek, P.; Hermann, P. *Coord. Chem. Rev.* **2001**, *216-217*, 287.
42. Rodríguez-Rodríguez, A.; Esteban-Gómez, D.; de Blas, A.; Rodríguez-Blas, T.; Fekete, M.; Botta, M.; Tripier, R.; Platas-Iglesias, C. *Inorg. Chem.* **2012**, *51*, 2509.
43. Faulkner, S.; Burton-Pye, B. P. *Chem. Commun.* **2005**, 259.
44. Plush, S. E.; Clear, N. A.; Leonard, J. P.; Fanning, A.-M.; Gunnlaugsson, T. *Dalton Trans.* **2010**, *39*, 3644.
45. Spirlet, M. R.; Rebizant, J.; Desreux, J. F.; Loncin, M. F. *Inorg. Chem.* **1984**, *23*, 359.
46. Pease, A. R.; Jeppesen, J. O.; Stoddart, J. F.; Luo, Y.; Collier, C. P.; Heath, J. R. *Acc. Chem. Res.* **2001**, *34*, 433.
47. Rurack, K.; Resch-Genger, U. *Chem. Soc. Rev.* **2002**, *31*, 116.
48. Kataky, R.; Matthes, K. E.; Nicholson, P. E.; Parker, D.; Buschmann, H.-J. *J. Chem. Soc., Perkin Trans. 2* **1990**, 1425.
49. Kataky, R.; Parker, D.; Teasdale, A.; Hutchinson, J. P.; Buschmann, H.-J. *J. Chem. Soc., Perkin Trans. 2* **1992**, 1347.
50. Parker, D.; Williams, J. A. G. *J. Chem. Soc., Perkin Trans. 2* **1995**, 1305.
51. Georges, J. *Analyst* **1993**, *118*, 1481.
52. Yukruk, F.; Akkaya, E. U. *Tetrahedron Lett.* **2005**, *46*, 5931.
53. Pal, R.; Parker, D. *Org. Biomol. Chem.* **2008**, *6*, 1020.
54. McCoy, C. P.; Stomeo, F.; Plush, S. E.; Gunnlaugsson, T. *Chem. Mater.* **2006**, *18*, 4336.
55. Woods, M.; Sherry, A. D. *Inorg. Chem.* **2003**, *42*, 4401.
56. Pope, S. J. A.; Laye, R. H. *Dalton Trans.* **2006**, 3108.
57. Andrews, M.; Jones, J. E.; Harding, L. P.; Pope, S. J. A. *Chem. Commun.* **2011**, *47*, 206.
58. Selid, P.; Xu, H.; Collins, E. M.; Striped Face-Collins, M.; Zhao, J. X. *Sensors* **2009**, *9*, 5446.
59. Gunnlaugsson, T.; Leonard, J. P.; Senechal, K.; Harte, A. J. *Chem. Commun.* **2004**, 782.
60. McMahon, B. K.; Gunnlaugsson, T. *Tetrahedron Lett.* **2010**, *51*, 5406.
61. Gunnlaugsson, T.; Leonard, J. P. *Dalton Trans.* **2005**, 3204.
62. Kager, H.; Wadman, W. J.; Somjen, G. G. *J. Neurophysiol.* **2000**, *84*, 495.
63. Thibon, A.; Pierre, V. r. C. *J. Am. Chem. Soc.* **2008**, *131*, 434.
64. Thibon, A.; Pierre, V. *Anal. Bioanal. Chem.* **2009**, *394*, 107.
65. Weitz, E. A.; Pierre, V. C. *Chem. Commun.* **2011**, *47*, 541.
66. McMahon, B. K.; Gunnlaugsson, T. *J. Am. Chem. Soc.* **2012**, *134*, 10725.
67. Refsum, H.; Ueland, P. M.; Nygard, O.; Vollset, S. E. *Annu. Rev. Med.* **1998**, *49*, 31.
68. Perricone, C.; De Carolis, C.; Perricone, R. *Autoimmun. Rev.* **2009**, *8*, 697.
69. Dickins, R. S.; Aime, S.; Batsanov, A. S.; Beeby, A.; Botta, M.; Bruce, J. I.; Howard, J. A. K.; Love, C. S.; Parker, D.; Peacock, R. D.; Puschmann, H. *J. Am. Chem. Soc.* **2002**, *124*, 12697.
70. S. Dickins, R.; Gunnlaugsson, T.; Parker, D.; D. Peacock, R. *Chem. Commun.* **1998**, 1643.
71. Pope, S. J. A.; Burton-Pye, B. P.; Berridge, R.; Khan, T.; Skabara, P. J.; Faulkner, S. *Dalton Trans.* **2006**, 2907.
72. Shinoda, S.; Mizote, A.; Eiraku Masaki, M.; Yoneda, M.; Miyake, H.; Tsukube, H. *Inorg. Chem.* **2011**, *50*, 5876.
73. Santos, C. M. G. d.; Gunnlaugsson, T. *Dalton Trans.* **2009**, 4712.
74. Kotova, O.; Comby, S.; Gunnlaugsson, T. *Chem. Commun.* **2011**, *47*, 6810.

75. Fujiwara, M.; Tsukahara, S.; Watarai, H. *Phys. Chem. Chem. Phys.* **1999**, *1*, 2949.
76. Achterberg, E. P.; Holland, T. W.; Bowie, A. R.; Mantoura, R. F. C.; Worsfold, P. J. *Anal. Chim. Acta* **2001**, *442*, 1.
77. Law, G.-L.; Pal, R.; Palsson, L. O.; Parker, D.; Wong, K.-L. *Chem. Commun.* **2009**, 7321.
78. New, E. J.; Congreve, A.; Parker, D. *Chem. Sci.* **2010**, *1*, 111.
79. Dias, D. M.; Teixeira, J. M. C.; Kuprov, I.; New, E. J.; Parker, D.; Geraldes, C. F. G. C. *Org. Biomol. Chem.* **2011**, *9*, 5047.
80. Poole, R. A.; Bobba, G.; Cann, M. J.; Frias, J. C.; Parker, D.; Peacock, R. D. *Org. Biomol. Chem.* **2005**, *3*, 1013.
81. Pal, R.; Parker, D.; Costello, L. C. *Org. Biomol. Chem.* **2009**, *7*, 1525.
82. Pal, R.; Beeby, A.; Parker, D. *J. Pharm. Biomed. Anal.* **2011**, *56*, 352.
83. Costello, L.; Franklin, R. *Mol. Cancer* **2006**, *5*, 17.
84. Law, G.-L.; Man, C.; Parker, D.; Walton, J. W. *Chem. Commun.* **2010**, *46*, 2391.
85. Smith, D. G.; Law, G.-l.; Murray, B. S.; Pal, R.; Parker, D.; Wong, K.-L. *Chem. Commun.* **2011**, *47*, 7347.
86. McMahon, B.; Mauer, P.; McCoy, C. P.; Lee, C. T.; Gunnlaugsson, T. *J. Am. Chem. Soc.* **2009**.
87. Nagarajan, R.; Hatton, T. A., *Nanoparticles: building blocks for nanotechnology*. American Chemical Society: Washington D. C., 2008.
88. www.webexhibits.org/causesofcolor/9.html.
89. Faraday, M. *Philos. Trans. R Soc.* **1857**, 145.
90. Turkevich, J. *Faraday Soc.* **1951**, 55.
91. Frens, J. *Nature: Phys. Sci.* **1973**, 20.
92. Sherry, L. J.; Jin, R.; Mirkin, C. A.; Schatz, G. C.; Van Duyne, R. P. *Nano Lett.* **2006**, *6*, 2060.
93. Lewis, D. J.; Day, T. M.; MacPherson, J. V.; Pikramenou, Z. *Chem. Commun.* **2006**, 1433.
94. Sperling, R. A.; Rivera Gil, P.; Zhang, F.; Zanella, M.; Parak, W. J. *Chem. Soc. Rev.* **2008**, *37*, 1896.
95. Turkevich, J.; Stevenson, P. C.; Hillier, J. *Discuss. Faraday Soc.* **1951**, *11*, 55.
96. Gittins, D. I.; Caruso, F. *Angew. Chem., Int. Ed.* **2001**, *40*, 3001.
97. L. N. Lewis, *Chem. Rev.* **1993**, *93*, 2693.
98. Yockell-Lelièvre, H.; Gingras, D.; Vallée, R.; Ritcey, A. M. *J. Phys. Chem. C* **2009**, *113*, 21293.
99. Sharma, R.; Holland, G. P.; Solomon, V. C.; Zimmermann, H.; Schiffenhaus, S.; Amin, S. A.; Buttry, D. A.; Yarger, J. L. *J. Phys. Chem. C* **2009**, *113*, 16387.
100. Park, J.-H.; Ganbold, E. O.; Uuriintuya, D.; Lee, K.; Joo, S.-W. *Chem. Commun.* **2009**, 7354.
101. Kundu, S.; Wang, K.; Liang, H. *J. Phys. Chem. C* **2009**, *113*, 5157.
102. Jans, H.; Liu, X.; Austin, L.; Maes, G.; Huo, Q. *Anal. Chem.* **2009**, *81*, 9425.
103. Woehrle, G. H.; Brown, L. O.; Hutchison, J. E. *J. Am. Chem. Soc.* **2005**, *127*, 2172.
104. Wilson, R. *Chem. Soc. Rev.* **2008**, *37*, 2028.
105. Murphy, C. J.; Gole, A. M.; Stone, J. W.; Sisco, P. N.; Alkilany, A. M.; Goldsmith, E. C.; Baxter, S. C. *Acc. Chem. Res.* **2008**, *41*, 1721.
106. Li, B.; Du, Y.; Dong, S. *Anal. Chim. Acta* **2009**, *644*, 78.
107. Comby, S.; Gunnlaugsson, T. *ACS Nano* **2011**, *5*, 7184.
108. Elmes, R. B. P.; Orange, K. N.; Cloonan, S. M.; Williams, D. C.; Gunnlaugsson, T. *J. Am.Chem. Soc.* **2011**, *133*, 15862.
109. Lin, S.-Y.; Wu, S.-H.; Chen, C.-H. *Angew. Chem. Int. Ed.* **2006**, *45*, 4948.
110. Li, D.; Wieckowska, A.; Willner, I. *Angew. Chem. Int. Ed.* **2008**, *47*, 3927.
111. Cao, X.; Ye, Y.; Liu, S. *Anal. Biochem.* **2011**, *417*, 1.

112. Ghosh, P.; Yang, X.; Arvizo, R.; Zhu, Z.-J.; Agasti, S. S.; Mo, Z.; Rotello, V. M. *J. Am. Chem. Soc.* **2010**, *132*, 2642.
113. Ghosh, P. S.; Han, G.; Erdogan, B.; Rosado, O.; Krovi, S. A.; Rotello, V. M. *Chem. Biol. Drug Des.* **2007**, *70*, 13.
114. Pichon, C.; Gonçalves, C.; Midoux, P. *Adv. Drug Delivery Rev.* **2001**, *53*, 75.
115. Miranda, O. R.; Li, X.; Garcia-Gonzalez, L.; Zhu, Z.-J.; Yan, B.; Bunz, U. H. F.; Rotello, V. M. *J. Am. Chem. Soc.* **2011**, *133*, 9650.
116. Brecher, M. E.; Hay, S. N. *Clin. Microbiol. Rev.* **2005**, *18*, 195.
117. Massue, J.; Quinn, S. J.; Gunnlaugsson, T. *J. Am. Chem. Soc.* **2008**, *130*, 6900.
118. Bonnet, C. S.; Massue, J.; Quinn, S. J.; Gunnlaugsson, T. *Org. & Biomol. Chem.* **2009**, *7*, 3074.
119. Kevin P, W. *Coord. Chem. Rev.* **1997**, *166*, 35.
120. Wolbers, M. P. O.; van Veggel, F. C. J. M.; Snellink-Ruel, B. H. M.; Hofstraat, J. W.; Geurt, F. A. J.; Reinhoudt, D. N. *J. Chem. Soc., Perkin Trans. 2* **1998**, 2141.
121. Parker, D.; Dickins, R. S.; Puschmann, H.; Crossland, C.; Howard, J. A. K. *Chem. Rev.* **2002**, *102*, 1977.
122. Nishiyabu, R.; Aime, C.; Gondo, R.; Kaneko, K.; Kimizuka, N. *Chem. Commun.* **2010**, *46*, 4333.
123. Gunnlaugsson, T.; Mac Donaill, D. A.; Parker, D. *J. Am. Chem. Soc.* **2001**, *123*, 12866.
124. Gunnlaugsson, T.; McCoy, C. P.; Stomeo, F. *Tetrahedron Lett.* **2004**, *45*, 8403.
125. Murray, N. S.; Jarvis, S. P.; Gunnlaugsson, T. *Chem. Commun.* **2009**, 4959.
126. Yokokawa, S.; Tamada, K.; Ito, E.; Hara, M. *J. Phys. Chem. B* **2003**, *107*, 3544.
127. Massue, J.; Plush, S. E.; Bonnet, C. S.; Moore, D. A.; Gunnlaugsson, T. *Tetrahedron Lett.* **2007**, *48*, 8052.
128. Akitt, J. W., *NMR and chemistry: an introduction to modern NMR spectroscopy*. 4th ed.; Stanley Thornes: 2000.
129. Horrocks, W. D.; Sudnick, D. R. *Acc. Chem. Res.* **1981**, *14*, 384.
130. Jaffe, H. H.; Orchin, M., *Theory and Applications of Ultraviolet Spectroscopy*. Wiley: New York, 1962.
131. Bonnet, C. S.; Gunnlaugsson, T. *New J. Chem.* **2009**, *33*, 1025.
132. Leonard, J. P.; Santos, C. M. G. d.; Plush, S. E.; McCabe, T.; Gunnlaugsson, T. *Chem. Commun.* **2007**, 129.
133. Plush, S. E.; Gunnlaugsson, T. *Org. Lett.* **2007**, *9*, 1919.
134. Harte, A. J.; Jensen, P.; Plush, S. E.; Kruger, P. E.; Gunnlaugsson, T. *Inorg. Chem.* **2006**, *45*, 9465.
135. Moudam, O.; Rowan, B. C.; Alamiry, M.; Richardson, P.; Richards, B. S.; Jones, A. C.; Robertson, N. *Chem. Commun.* **2009**, 6649.
136. Boisselier, E.; Astruc, D. *Chem. Soc. Rev.* **2009**, *38*, 1759.
137. Brust, M.; Walker, M.; Bethell, D.; Schifrin, D. J.; Whyman, R. *Chem. Commun.* **1994**, 801.
138. Kim, K.-H.; Kim, J.-U.; Cha, S.-H.; Lee, J.-C. *J. Am. Chem. Soc.* **2009**, *131*, 7482.
139. Berne, B. J.; Pecora, R., *Dynamic Light Scattering: with applications to chemistry, biology and physics*. Dover Publications: Mineola, N.Y., 2000.
140. Link, S.; El-Sayed, M. A. *J. Phys. Chem. B* **1999**, *103*, 8410.
141. Nagarajan, R.; Hatton, T. A., *Nanoparticles: building blocks for nanotechnology*. American Chemical Society: Washington D. C., 2008.
142. Molloy, J. K. TCD, 2010.
143. Que, E. L.; Domaille, D. W.; Chang, C. J. *Chem. Rev.* **2008**, *108*, 1517.
144. Kelleher, S. L.; McCormick, N. H.; Velasquez, V.; Lopez, V. *Adv. Nutr.* **2011**, *2*, 101.
145. Frederickson, C. J.; Koh, J. Y.; Bush, A. I. *Nat. Rev. Neurosci.* **2005**, *6*, 449.
146. Rink, L. *Proc. Nutr. Soc.* **2000**, *59*, 541.

147. Fukada, T.; Yamasaki, S.; Nishida, K.; Murakami, M.; Hirano, T. *J. Biol. Inorg. Chem.* **2011**, *16*, 1123.
148. Burdette, S. C.; Lippard, S. J. *Coord. Chem. Rev.* **2001**, *216–217*, 333.
149. Sensi, S. L.; Paoletti, P.; Koh, J. Y.; Aizenman, E.; Bush, A. I.; Hershfinkel, M. *J.Neurosci.* **2011**, *31*, 16076.
150. Fraker, P. J.; King, L. E. *Annu. Rev. Nutr.* **2004**, *24*, 277.
151. Opazo, C.; Luza, S.; Villemagne, V. L.; Volitakis, I.; Rowe, C.; Barnham, K. J.; Strozyk, D.; Masters, C. L.; Cherny, R. A.; Bush, A. I. *Aging Cell* **2006**, *5*, 69.
152. Nolan, E. M.; Lippard, S. J. *Acc. Chem. Res.* **2008**, *42*, 193.
153. Bazzicalupi, C.; Bencini, A.; Biagini, S.; Faggi, E.; Farruggia, G.; Andreani, G.; Gratteri, P.; Prodi, L.; Spepi, A.; Valtancoli, B. *Dalton Trans.* **2010**, *39*, 7080.
154. Koutaka, H.; Kosuge, J. I.; Fukasaku, N.; Hirano, T.; Kikuchi, K.; Urano, Y.; Kojima, H.; Nagano, T. *Chem. Pharm. Bull.* **2004**, *52*, 700.
155. Gunnlaugsson, T.; Lee, T. C.; Parkesh, R. *Org. Lett.* **2003**, *5*, 4065.
156. Wang, H.; Wu, H.; Xue, L.; Shi, Y.; Li, X. *Org. Biomol. Chem.* **2011**, *9*, 5436.
157. Zhao, Q.; Li, F.; Huang, C. *Chem. Soc. Rev.* **2010**, *39*, 3007.
158. Ho, M.-L.; Hwang, F.-M.; Chen, P.-N.; Hu, Y.-H.; Cheng, Y.-M.; Chen, K.-S.; Lee, G.-H.; Chi, Y.; Chou, P.-T. *Org. Biomol. Chem.* **2006**, *4*, 98.
159. Li, M.-J.; Chu, B. W.-K.; Zhu, N.; Yam, V. W.-W. *Inorg. Chem.* **2007**, *46*, 720.
160. Reany, O.; Gunnlaugsson, T.; Parker, D. *J. Chem. Soc., Perkin Trans. 2* **2000**, 1819.
161. Imbert, D.; Comby, S.; Chauvin, A. S.; Bünzli, J. C. G. *Chem. Commun.* **2005**, 1432.
162. Nonat, A. M.; Allain, C.; Faulkner, S.; Gunnlaugsson, T. *Inorg. Chem.* **2010**, *49*, 8449.
163. Bünzli, J.-C. G.; Comby, S.; Chauvin, A.-S.; Vandevyver, C. D. B. *J. Rare Earths* **2007**, *25*, 257.
164. Comby, S.; Gumy, F.; Bünzli, J. C. G.; Saraidarov, T.; Reisfeld, R. *Chem. Phys. Lett.* **2006**, *432*, 128.
165. Comby, S.; Imbert, D.; Chauvin, A. S.; Bünzli, J. C. G. *Inorg. Chem.* **2006**, *45*, 732.
166. Comby, S.; Imbert, D.; Vandevyver, C. D. B.; Bünzli, J. C. G. *Chem. Eur. J.* **2007**, *13*, 936.
167. McRae, R.; Bagchi, P.; Sumalekshmy, S.; Fahrni, C. J. *Chem. Rev.* **2009**, *109*, 4780.
168. Watanabe, S.; Frantz, W.; Trottier, D. *Anal. Biochem.* **1963**, *5*, 345.
169. Massue, J.; Plush, S. E.; Bonnet, C. S.; Moore, D. A.; Gunnlaugsson, T. *Tetrahedron Lett.* **2007**, *48*, 8052.
170. Claus, A.; Posselt, M. *J. Prakt. Chem.* **1890**, *41*, 32.
171. Martell, A. E.; Smith, R. M., *Critical Stability Constants*. Plenum Press: New York, 1974.
172. Faulkner, S.; Beeby, A.; Carri,, M. C.; Dadabhoy, A.; Kenwright, A. M.; Sammes, P. G. *Inorg. Chem. Commun.* **2001**, *4*, 187.
173. Meshkova, S. B.; Topilova, Z. M.; Bolshoi, D. V.; Beltyukova, S. V.; Tsvirko, M. P.; Venchikov, V. Y. *Acta Phys. Pol. A* **1999**, *95*, 983.
174. Comby, S.; Bünzli, J. C. G., *Lanthanide Near-Infrared Luminescence in Molecular Probes and Devices*. Elsevier Science B.V.: Amsterdam, 2007; p 217.
175. Valeur, B., *Molecular Fluorescence - An Introduction: Principles and Applications*. Wiley-VCH Verlag GmbH: 2000; p 1.
176. Hanaoka, K.; Kikuchi, K.; Kojima, H.; Urano, Y.; Nagano, T. *Angew. Chem. Int. Ed.* **2003**, *42*, 2996.
177. Basu, S.; Dasgupta, P. S. *J. Neuroimmunol.* **2000**, *102*, 113.
178. Carlsson, M. L.; Carlsson, A.; Nilsson, M. *Curr. Med. Chem.* **2004**, *11*, 267.
179. Boneberg, E.-M.; von Seydlitz, E.; Pröpster, K.; Watzl, H.; Rockstroh, B.; Illges, H. *J. Neuroimmunol.* **2006**, *173*, 180.
180. Tainaka, K.; Sakaguchi, R.; Hayashi, H.; Nakano, S.; Liew, F. F.; Morii, T. *Sensors* **2010**, *10*, 1355.

181. Ates, M.; Yilmaz, K.; Shahryari, A.; Omanovic, S.; Sarac, A. S. *Sensors* **2008**, *8*, 1628.
182. Celebanska, A.; Tomaszewska, D.; Lesniewski, A.; Opallo, M. *Biosens. Bioelectron.* **2011**, *26*, 4417.
183. Hui-Fang, C.; Yu-Han, C.; Yu-Long, S.; Kuan, Z.; Wei-De, Z. *Nanotechnology* **2010**, *21*, 215601.
184. Liew, F. F.; Hasegawa, T.; Fukuda, M.; Nakata, E.; Morii, T. *Bioorg. Med. Chem.* **2011**, *19*, 4473.
185. Wang, H. Y.; Hui, Q. S.; Xu, L. X.; Jiang, J. G.; Sun, Y. *Anal. Chim. Acta* **2003**, *497*, 93.
186. Wang, F.; Banerjee, D.; Liu, Y.; Chen, X.; Liu, X. *Analyst* **2010**, *135*, 1839.
187. Zhang, Q. Y.; Huang, X. Y. *Prog. Mat. Sci.* **2010**, *55*, 353.
188. Bünzli, J. C. G.; Eliseeva, S. V. *J. Rare Earths* **2010**, *28*, 824.
189. Wang, M.; Mi, C.-C.; Wang, W.-X.; Liu, C.-H.; Wu, Y.-F.; Xu, Z.-R.; Mao, C.-B.; Xu, S.-K. *ACS Nano* **2009**, *3*, 1580.
190. Niedbala, R. S.; Feindt, H.; Kardos, K.; Vail, T.; Burton, J.; Bielska, B.; Li, S.; Milunic, D.; Bourdelle, P.; Vallejo, R. *Anal. Biochem.* **2001**, *293*, 22.
191. Korovin, Y.; Rusakova, N. *J. Fluoresc.* **2002**, *12*, 159
192. Comby, S.; Bünzli, J. C. G. *Handbook on the Physics and Chemistry of Rare Earths* **2007**, *32*, 217.
193. Sun, C.-L.; Chang, C.-T.; Lee, H.-H.; Zhou, J.; Wang, J.; Sham, T.-K.; Pong, W.-F. *ACS Nano* **2011**, *5*, 7788.
194. Wang, C.; Yuan, R.; Chai, Y.; Zhang, Y.; Hu, F.; Zhang, M. *Biosens. Bioelectron.* **2011**, *30*, 315.
195. Gillin, W. P.; Curry, R. J. *Appl. Phys. Lett.* **1999**, *74*, 798.
196. Rusakova, N. V.; Meshkova, S. B. *J. Anal. Chem. USSR (Engl.Transl.)* **1990**, *45*, 1371.
197. Huo, F. J.; Yang, Y. T.; Su, J.; Sun, Y. Q.; Yin, C. X.; Yan, X. X. *Analyst* **2011**, *136*, 1892.
198. Lee, T. C.; Mohsin, S.; Taylor, D.; Parkesh, R.; Gunnlaugsson, T.; O'Brien, F. J.; Giehl, M.; Gowin, W. *J. Anat.* **2003**, *203*, 161.
199. Rochat, S. B.; Severin, K. *J. Comb. Chem.* **2010**, *12*, 595.
200. Ishida, A.; Yamada, Y.; Kamidate, T. *Anal. Bioanal. Chem.* **2008**, *392*, 987.
201. Zatta, P.; Lucchini, R.; van Rensburg, S. J.; Taylor, A. *Brain Res. Bull.* **2003**, *62*, 15.
202. Campbell, A.; Becaria, A.; Lahiri, D. K.; Sharman, K.; Bondy, S. C. *J. Neurosci. Res.* **2004**, *75*, 565.
203. Veríssimo, M. I. S.; Gomes, M. T. S. R. *Anal. Chim. Acta* **2008**, *617*, 162.
204. Gholivand, M. B.; Bamdad, F.; Ghasemi, J. *Talanta* **1998**, *46*, 875.
205. Eliseeva, S. V.; Bünzli, J. C. G. *Chem. Soc. Rev.* **2010**, *39*, 189.
206. Hamacek, J.; Besnard, C.; Penhouet, T.; Morgantini, P.-Y. *Chem. Eur. J.* **2011**, *17*, 6753.
207. Chauvin, A.-S.; Comby, S.; Song, B.; Vandevyver, C. D. B.; Bünzli, J.-C. G. *Chem. Eur. J.* **2008**, *14*, 1726.
208. Kitchen, J. A.; White, N. G.; Gandolfi, C.; Albrecht, M.; Jameson, G. N. L.; Tallon, J. L.; Brooker, S. *Chem. Commun.* **2010**, *46*, 6464.
209. Langmuir, I. *J. Am. Chem. Soc.* **1917**, *39*, 1848.
210. Blodgett, K. B. *J. Am. Chem. Soc.* **1934**, *56*, 495.
211. Blodgett, K. B.; Langmuir, I. *Phys. Rev.* **1937**, *51*, 964.
212. Kuhn, H.; D., M.; Bucher, H., *Physical Methods of Chemistry*. John Wiley and Sons: 1972; Vol. 1, Part IIIB.
213. Petty, M. C., *Langmuir Blodgett Films: An Introduction*. Cambridge University Press: Cambridge, 1996.

214. Talham, D. R. *Chem. Rev.* **2004**, *104*, 5479.
215. Clemente-León, M.; Coronado, E.; Soriano-Portillo, A.; Mingotaud, C.; Dominguez-Vera, J. M. *Adv. Colloid Interface Sci.* **2005**, *116*, 193.
216. Ariga, K.; Hill, J.; Endo, H. Int. *J. Mol. Sci.* **2007**, *8*, 864.
217. Davis, F.; Higson, S. P. J. *Biosens. Bioelectron.* **2005**, *21*, 1.
218. Gidalevitz, D.; Huang, Z.; Rice, S. A. *Biophys. J.* **1999**, *76*, 2797.
219. Matharu, Z.; Bandodkar, A. J.; Gupta, V.; Malhotra, B. D. *Chem. Soc. Rev.* **2012**, *41*, 1363.
220. Bryce, M. R.; Petty, M. C. *Nature* **1995**, *374*, 771.
221. Gandolfi, C.; Cotting, T.; Martinho, P. N.; Sereda, O.; Neels, A.; Morgan, G. G.; Albrecht, M. *Dalton Trans.* **2011**, *40*, 1855.
222. Brooker, S.; Kitchen, J. *Dalton Trans.* **2009**, 7331.
223. Armand, F.; Badoux, C.; Bonville, P.; Ruaudel-Teixier, A.; Kahn, O. *Langmuir* **1995**, *11*, 3467.
224. Gandolfi, C.; Miyashita, N.; Kurth, D. G.; Martinho, P. N.; Morgan, G. G.; Albrecht, M. *Dalton Trans.* **2010**, *39*, 4508.
225. Gandolfi, C.; Moitzi, C.; Schurtenberger, P.; Morgan, G. G.; Albrecht, M. *J. Am. Chem. Soc.* **2008**, *130*, 14434.
226. Yan, B.; Xu, B. *J. Fluoresc.* **2009**, *19*, 663.
227. Xu, B.; Yan, B. *Colloids Surf., A* **2008**, *329*, 7.
228. Yan, B.; Xu, B. *Appl. Surf. Sci.* **2008**, *254*, 7237.
229. Kitchen, J. A.; Barry, D. E.; Mercs, L.; Albrecht, M.; Peacock, R. D.; Gunnlaugsson, T. *Angew. Chem. Int. Ed.* **2012**, *51*, 704.
230. Eliseeva, S. V.; Bünzli, J. C. G. *Chem. Soc. Rev.* **2009**, *39*, 189.
231. http://www.umm.edu/altmed/articles/tyrosine-000329.htm.
232. Akiba, H.; Sumaoka, J.; Komiyama, M. *ChemBioChem* **2009**, *10*, 1773.
233. http://www.nlm.nih.gov/medlineplus/ency/article/003361.htm.
234. Gunnlaugsson, T.; Leonard, J. P. *Chem. Commun.* **2003**, 2424.
235. Houston, M. C. *J. Clin. Hypertens.* **2011**, *13*, 621.
236. Farina, M.; Rocha, J. B. T.; Aschner, M. *Life Sci.* **2011**, *89*, 555.
237. Tian, M.; Ihmels, H. *Chem. Commun.* **2009**, 3175.
238. Lim, C. S.; Kang, D. W.; Tian, Y. S.; Han, J. H.; Hwang, H. L.; Cho, B. R. *Chem. Commun.* **2010**, *46*, 2388.
239. Nolan, E. M.; Racine, M. E.; Lippard, S. *J. Inorg. Chem.* **2006**, *45*, 2742.
240. N. Berberan Santos, M. *Phys. Chem. Commun.* **2000**, *3*, 18.
241. Vogel, A. I.; Tatchell, A. R.; Furnis, B. S.; Hannaford, A. J.; Smith, P. W. G., Vogel's Textbook of Practical Organic Chemisrty. 5th ed.; Prentice Hall: New York, 1996.
242. Stomeo, F. TCD, 2006.
243. Glenny, M. W.; van de Water, L. G. A.; Vere, J. M.; Blake, A. J.; Wilson, C.; Driessen, W. L.; Reedijk, J.; Schröder, M. *Polyhedron* **2006**, *25*, 599.

Appendices

Appendix 2

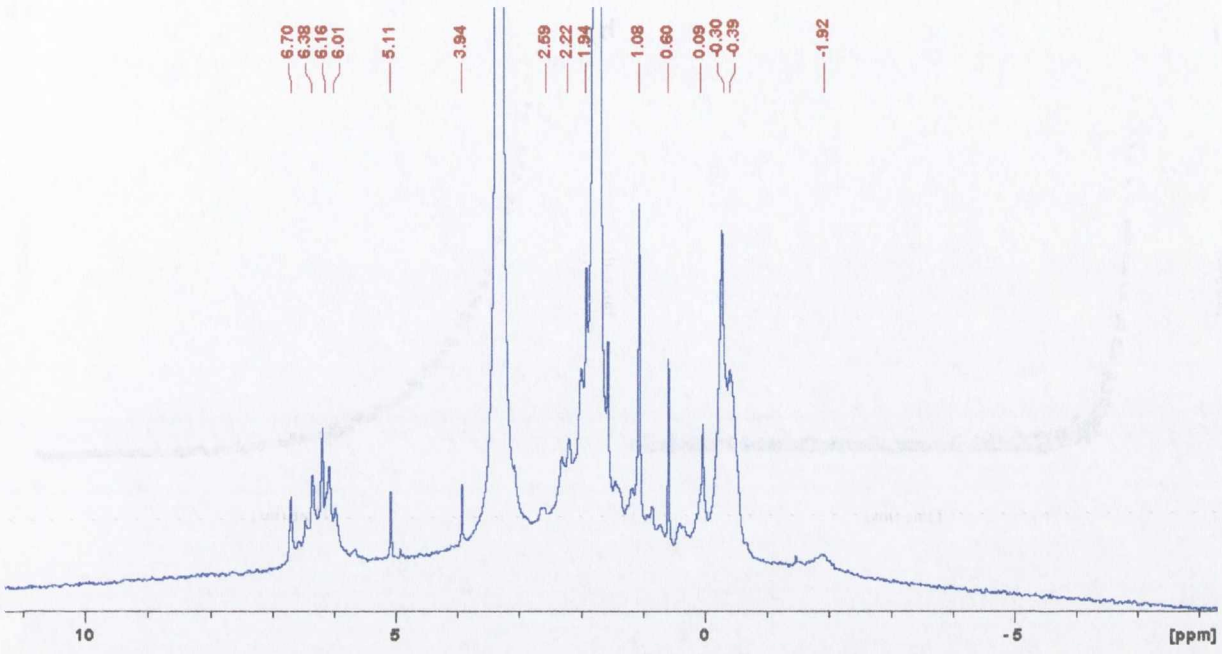


Figure A2.1: *The ^{1}H NMR spectrum (400 MHz DMSO-d_6) of* ***Tb·49****.*

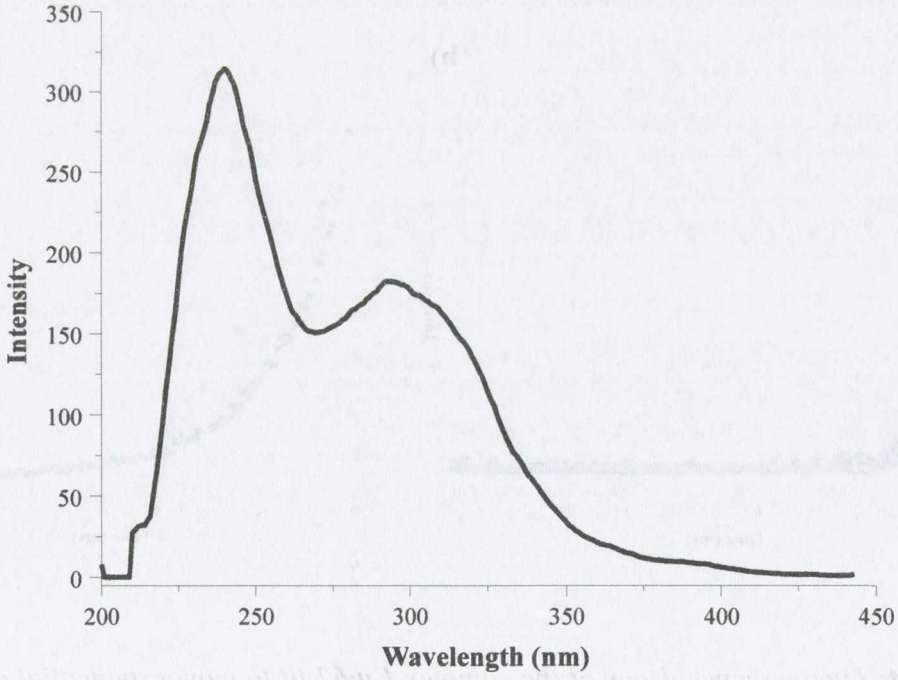


Figure A2.2: *Excitation spectrum of* ***Eu·49*** *in a mixed DMSO:H_2O (1:99 v/v) solution.*

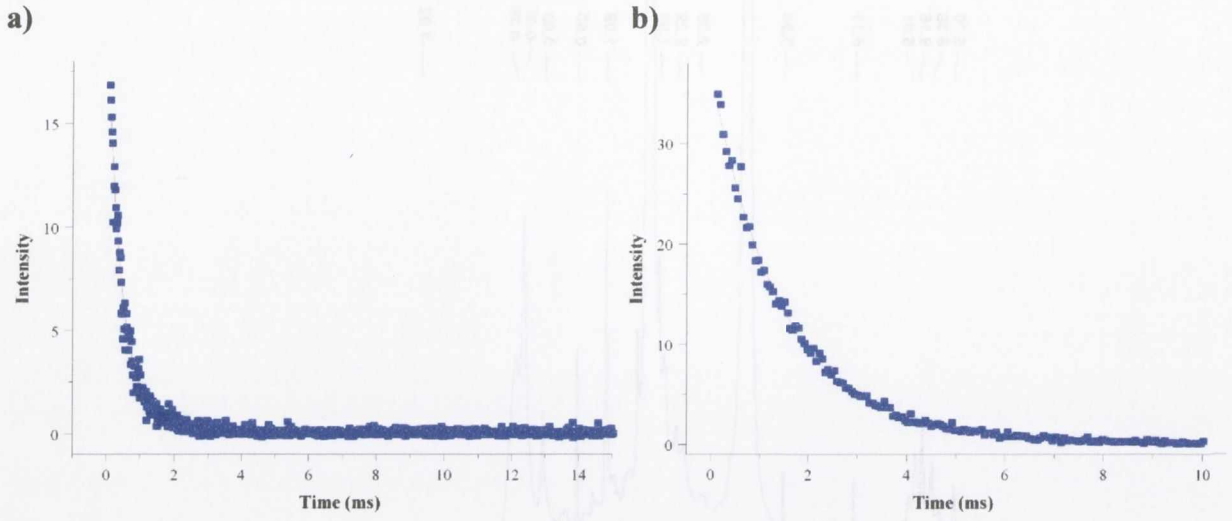


Figure A2.3: *Luminescence decay of the complex* ***Eu·61*** *fit to monoexponential decay in a* ***a)*** *mixed DMSO:H_2O (1:99 v/v) solution and* ***b)*** *mixed DMSO-d_6:D_2O(1:99 v/v) solution.*

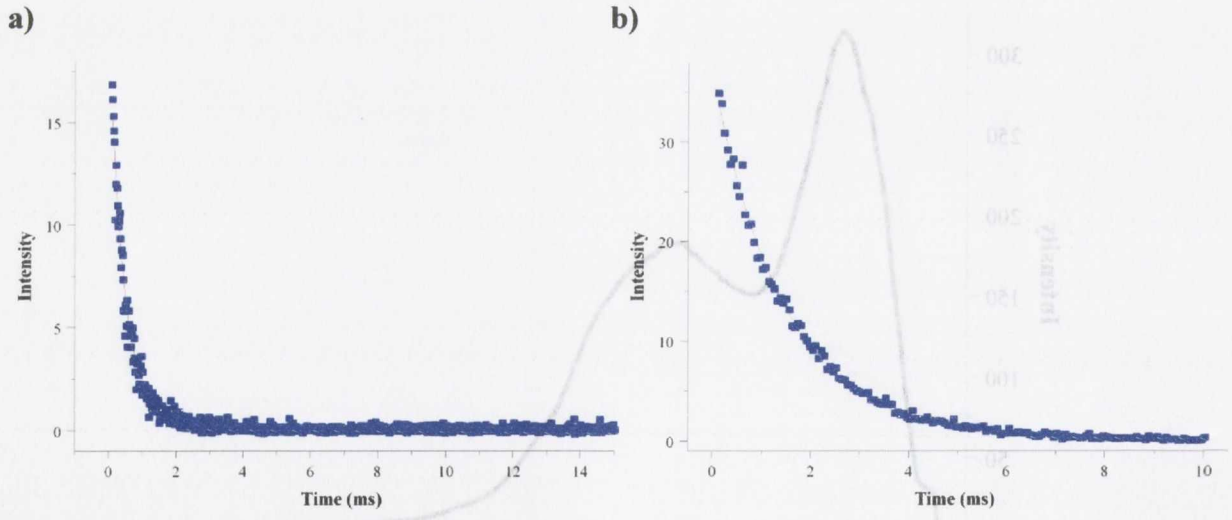


Figure A2.4: *Luminescence decay of the complex* ***Eu·62*** *fit to monoexponential decay in a* ***a)*** *mixed DMSO:H_2O (1:99 v/v) solution and* ***b)*** *mixed DMSO-d_6:D_2O(1:99 v/v) solution.*

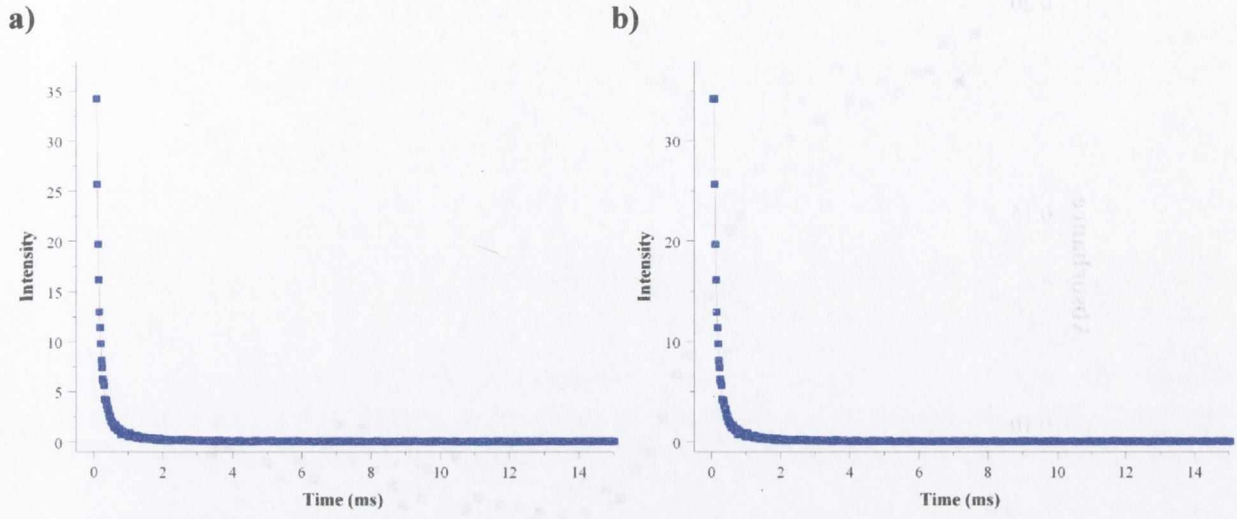


Figure A2.5: *Luminescence decay of an aerated solution of the complex* ***Tb·49*** *fit to double exponential decay in a* ***a)*** *mixed DMSO:H_2O (1:99 v/v) solution and* ***b)*** *mixed DMSO-d_6:D_2O(1:99 v/v) solution.*

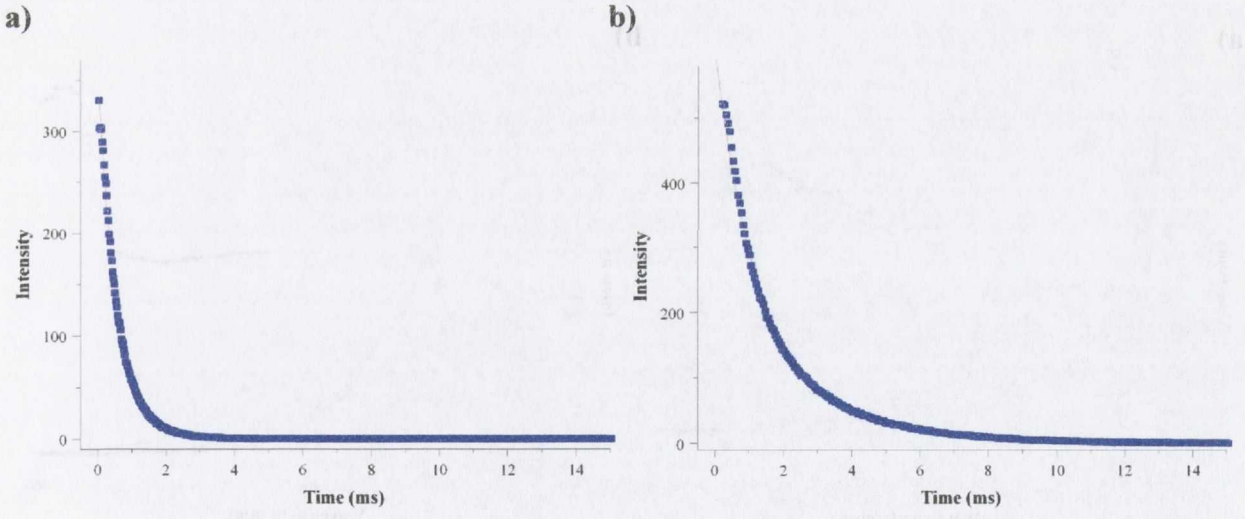


Figure A2.6: *Luminescence decay of a degassed solution of the complex* ***Tb·49*** *fit to monoexponential decay in a* ***a)*** *mixed DMSO:H_2O (1:99 v/v) solution and* ***b)*** *mixed DMSO-d_6:D_2O(1:99 v/v) solution.*

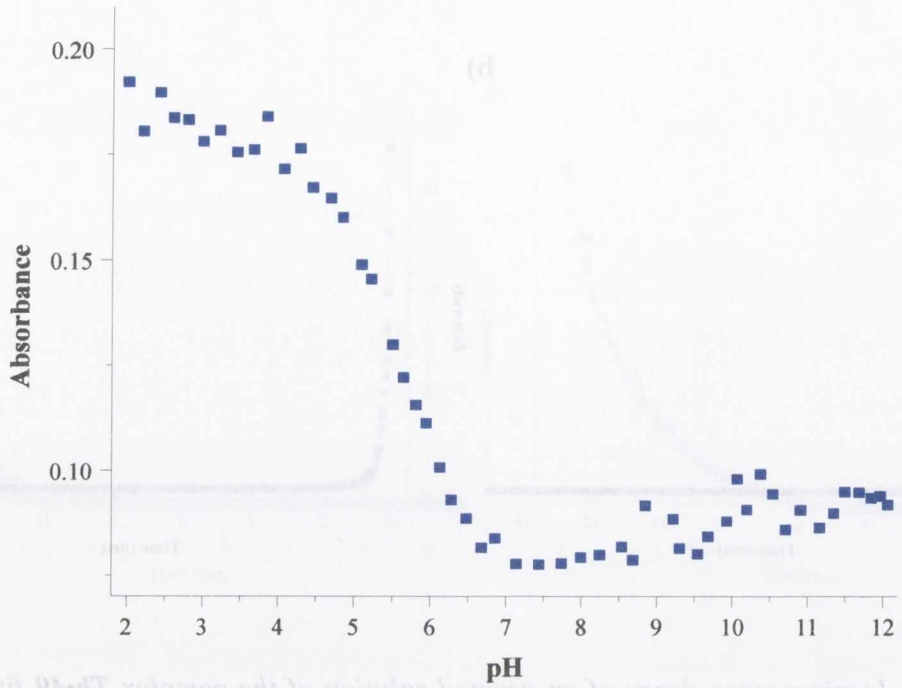


Figure A2.7: *Changes in the absorbance at 315 nm of ligand* ***49*** *as a function of pH in a mixed DMSO:H_2O (1:99 v/v) solution [I = 0.1 M TEAP].*

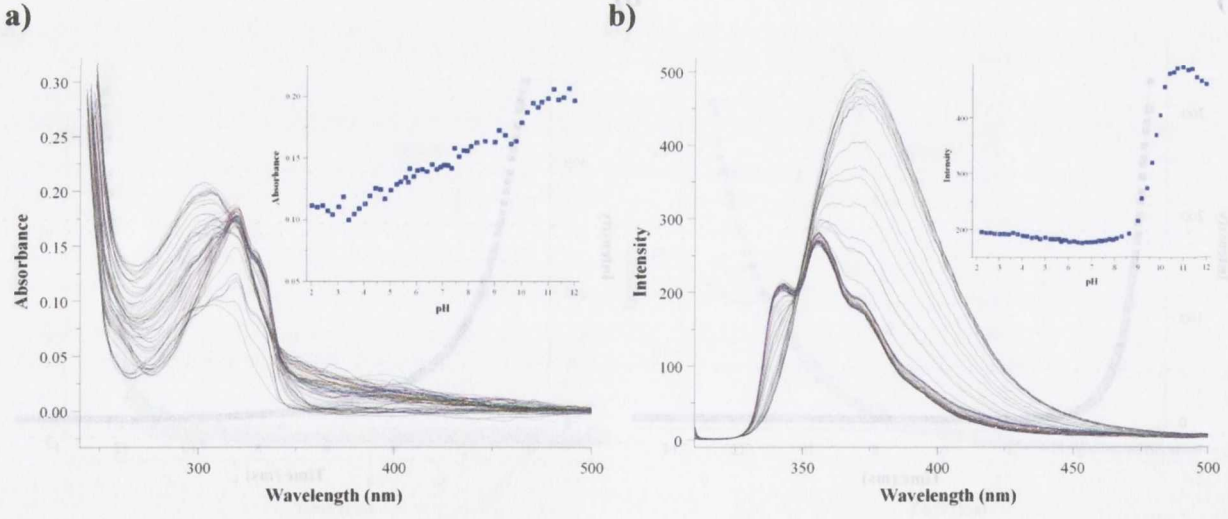


Figure A2.8: ***a)*** *Changes in the UV-vis absorption spectra of* ***Tb·49*** *as a function of pH in a mixed DMSO:H_2O (1:99 v/v) solution [I = 0.1 M TEAP]. Inset: Changes in the absorbance at 300 nm as a function of pH.* ***b)*** *Changes in the fluorescence emission spectra of* ***Tb·49*** *as a function of pH in a mixed DMSO:H_2O (1:99 v/v) solution [I = 0.1 M TEAP]. Inset: Changes in the fluorescence at 370 nm as a function of pH.*

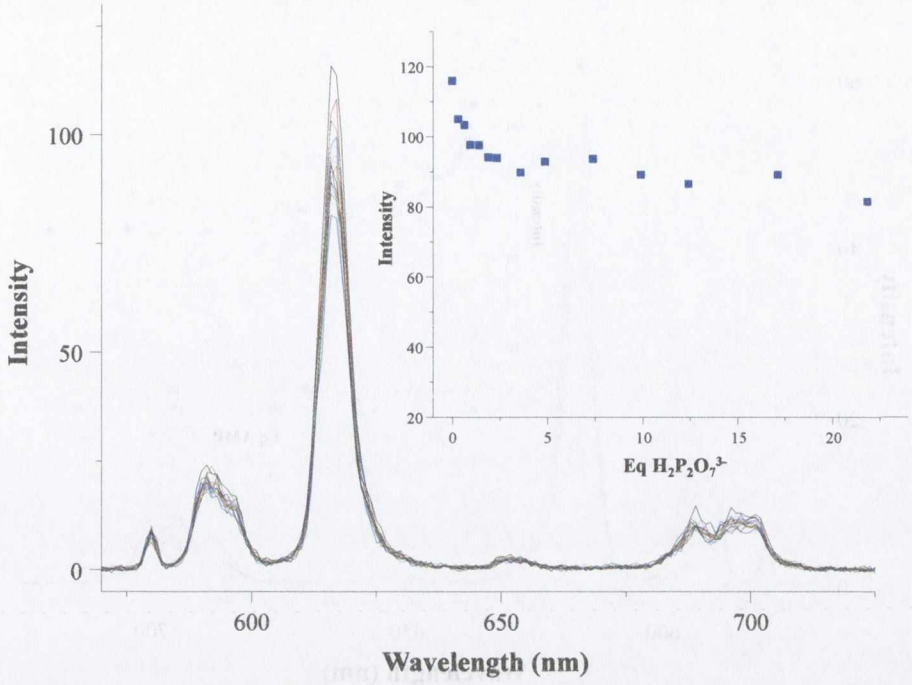


Figure A2.9: *The Eu(III) luminescence response (λ_{ex} = 318 nm) of* ***Eu·49*** *as a function of equivalents of $H_2P_2O_7^{3-}$ at pH 7.4 in 0.1 M HEPES. Inset: Changes in the phosphorescence at 615 nm upon the addition of $H_2P_2O_7^{3-}$ (0-25 equivalents).*

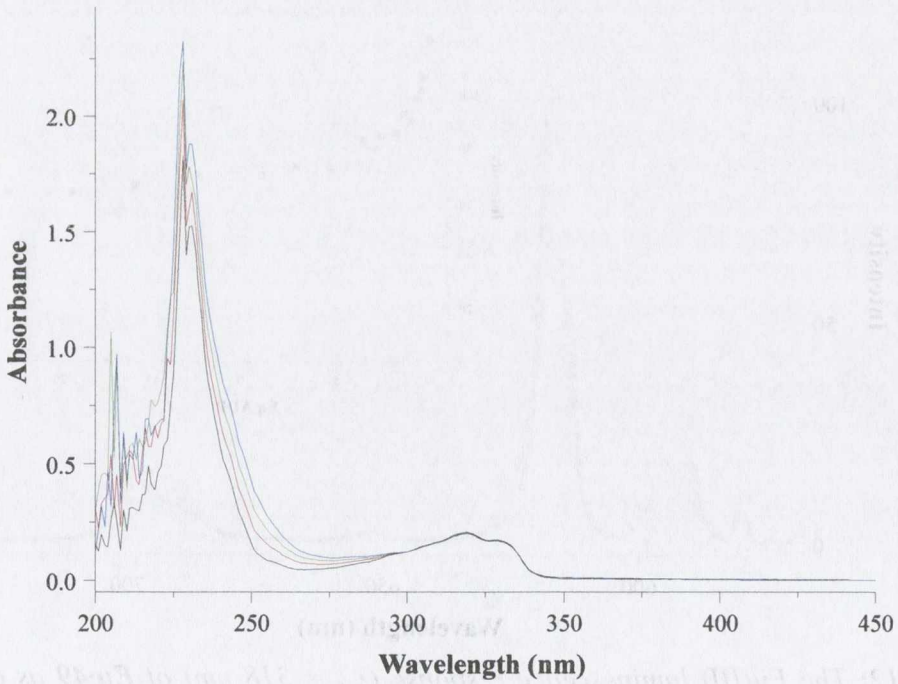


Figure A2.10: *Changes in the UV-vis absorption spectra of* ***Eu·49*** *(1×10^{-5} M) as a function of equivalents of terephthalic acid at pH 7.4 in 0.1 M HEPES*

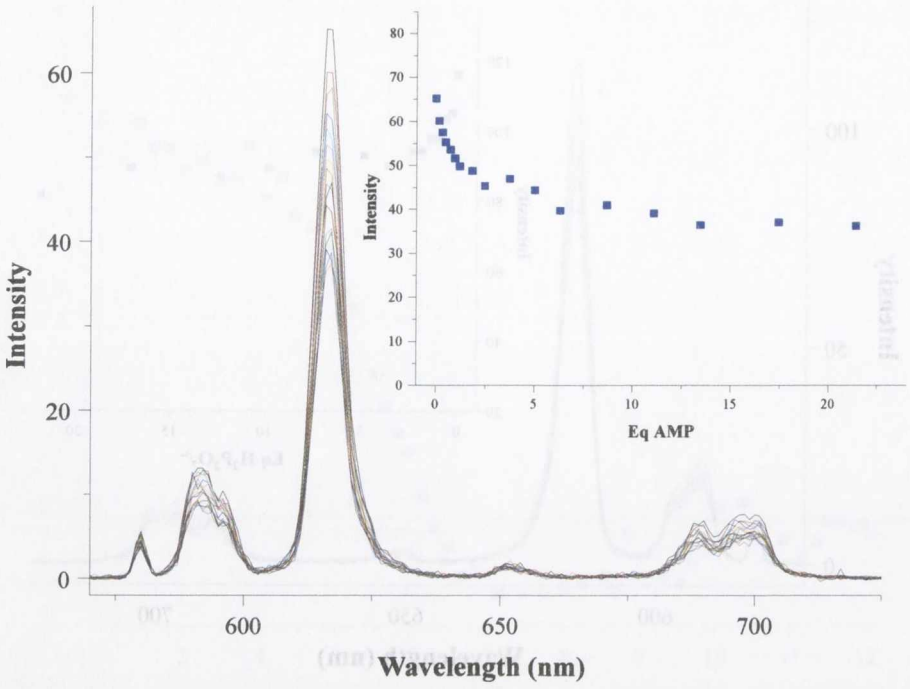


Figure A2.11: *The Eu(III) luminescence response (λ_{ex} = 318 nm) of* ***Eu·49*** *as a function of equivalents of AMP at pH 7.4 in 0.1 M HEPES. Inset: Changes in the phosphorescence at 615 nm upon the addition of AMP (0-25 equivalents).*

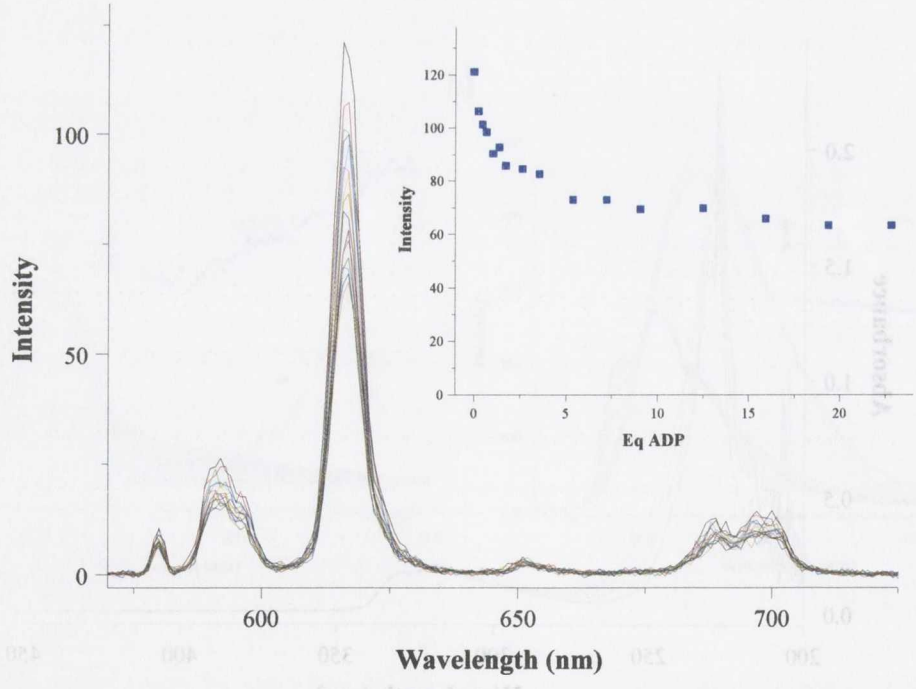


Figure A2.12: *The Eu(III) luminescence response (λ_{ex} = 318 nm) of* ***Eu·49*** *as a function of equivalents of ADP at pH 7.4 in 0.1 M HEPES. Inset: Changes in the phosphorescence at 615 nm upon the addition of ADP (0-25 equivalents).*

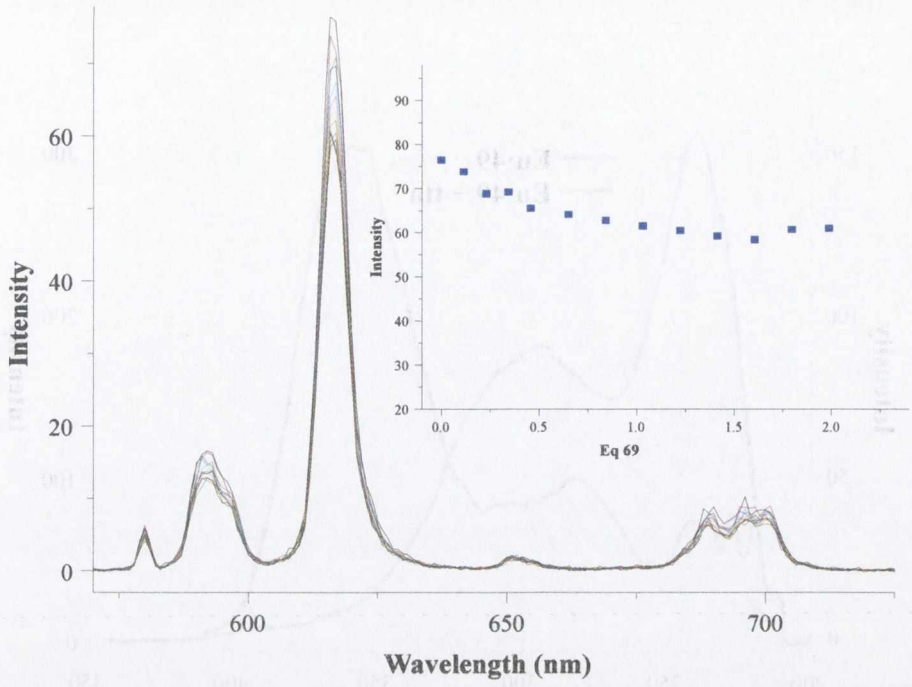


Figure A2.13: *The Eu(III) luminescence response (λ_{ex} = 318 nm) of* ***Eu·49*** *as a function of equivalents of Malonic Acid (**69**) at pH 7.4 in 0.1 M HEPES. Inset: Changes in the phosphorescence at 615 nm upon the addition of Malonic Acid (0-2.5 equivalents).*

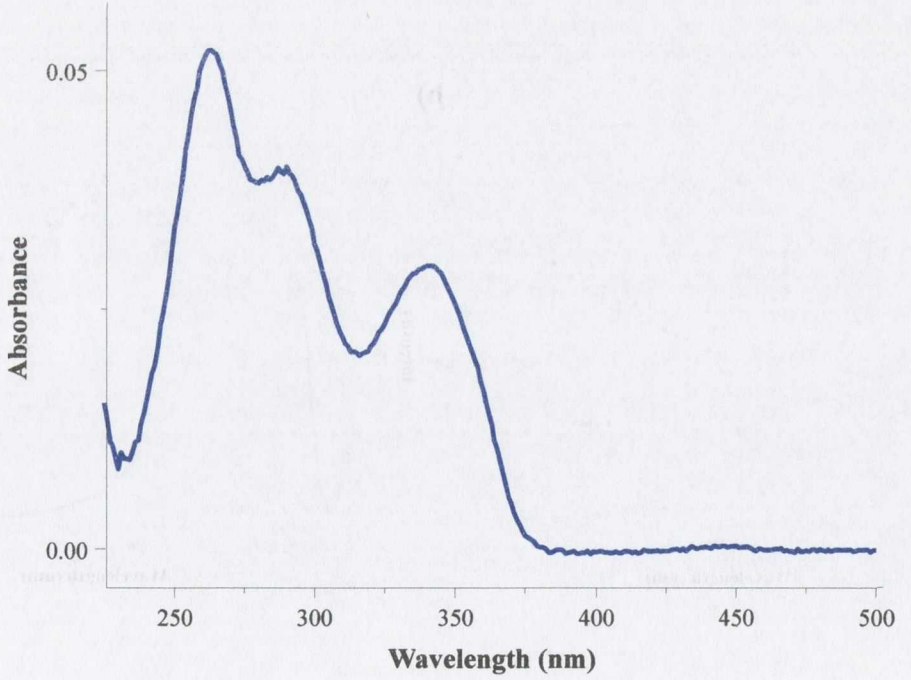


Figure A2.14: *UV-vis absorption spectrum of* ***tta****.*

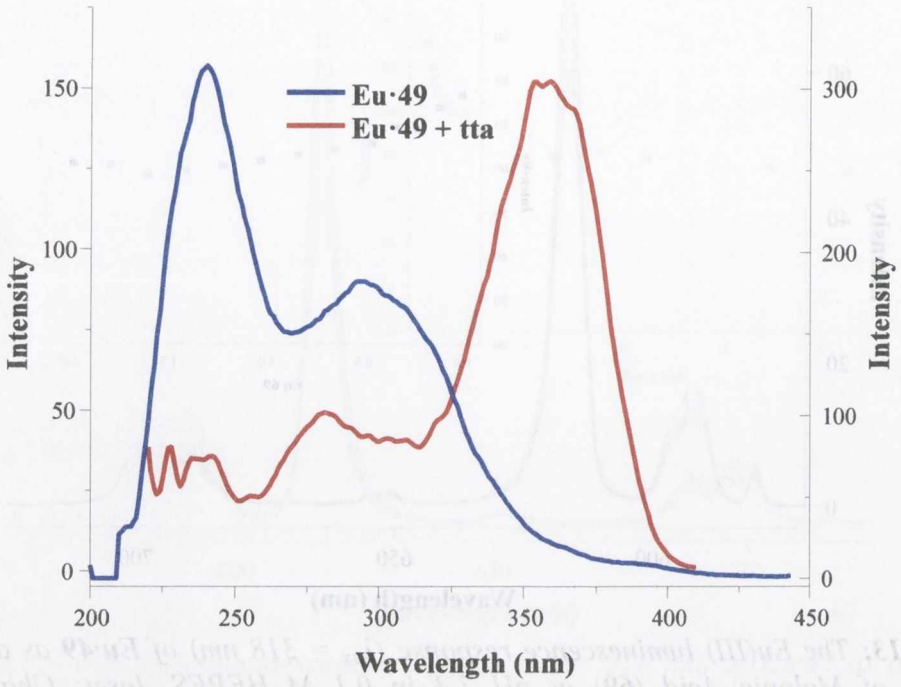


Figure A2.15: *Excitation spectra (λ_{em} = 615 nm) of* ***Eu·49*** *before and after the addition of* ***tta****.*

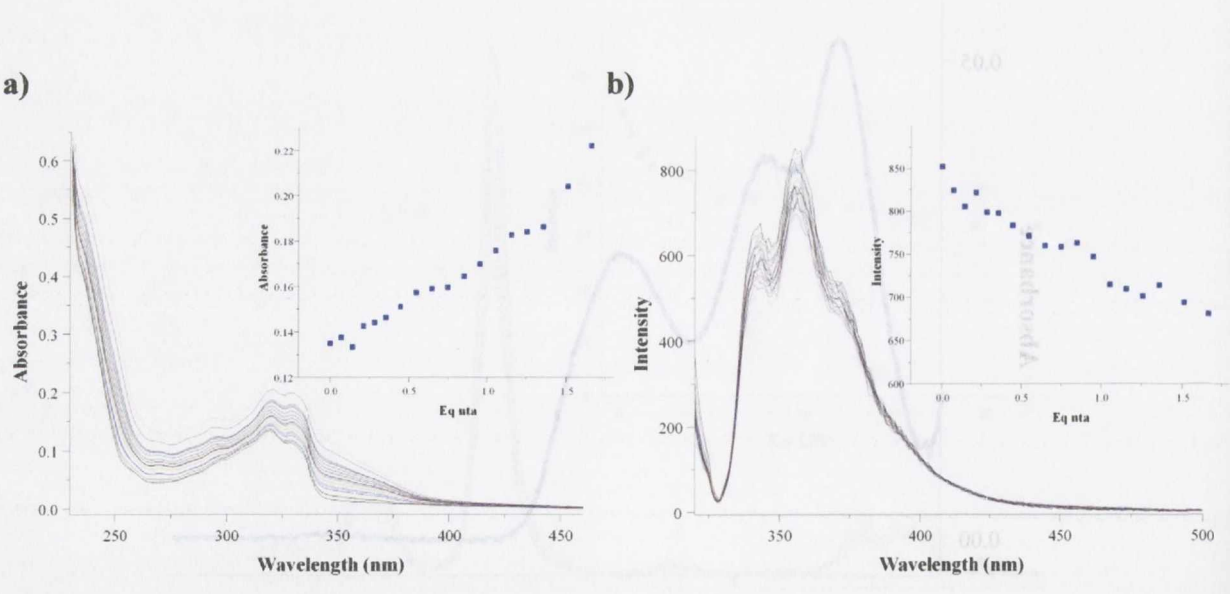


Figure A2.16: *Changes in the* ***a)*** *UV-vis absorption spectra and* ***b)*** *fluorescence spectra (λ_{ex} = 318 nm) of* ***Eu·49*** *(1×10^{-5} M) as a function of equivalents of* ***nta*** *at pH 7.4 in 0.1 M HEPES. Insets: Changes in the* ***a)*** *absorbance at 318 nm and* ***b)*** *fluorescence at 355 nm upon the addition of* ***nta*** *(0-3 equivalents).*

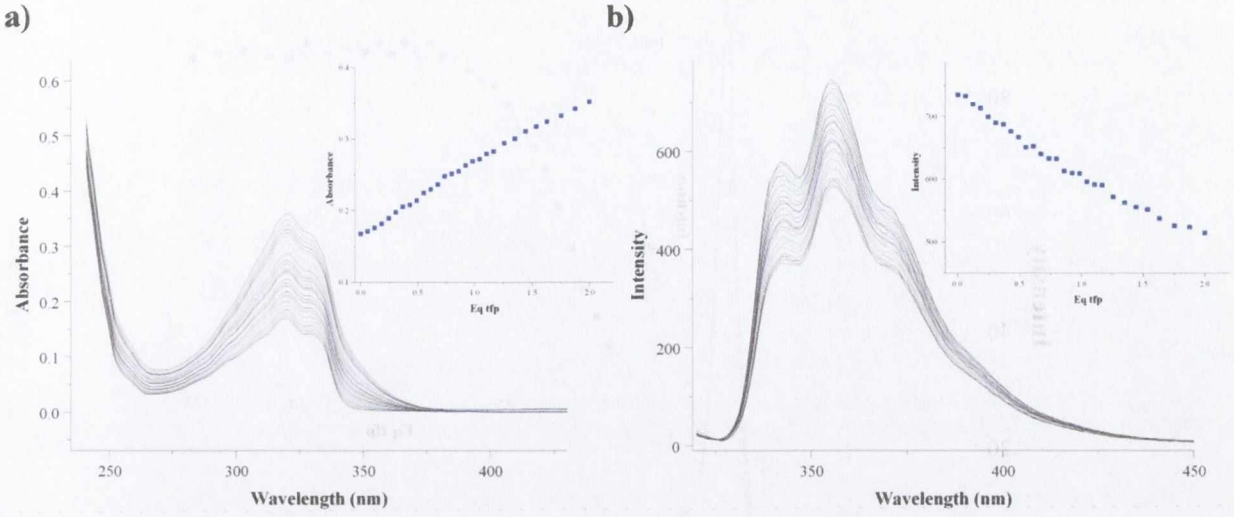


Figure A2.17: *Changes in the* ***a)*** *UV-vis absorption spectra and* ***b)*** *fluorescence spectra (λ_{ex} = 318 nm) of* ***Eu·49*** *(1×10^{-5} M) as a function of equivalents of* ***tfp*** *at pH 7.4 in 0.1 M HEPES. Insets: Changes in the* ***a)*** *absorbance at 318 nm and* ***b)*** *fluorescence at 355 nm upon the addition of* ***tfp*** *(0-3 equivalents).*

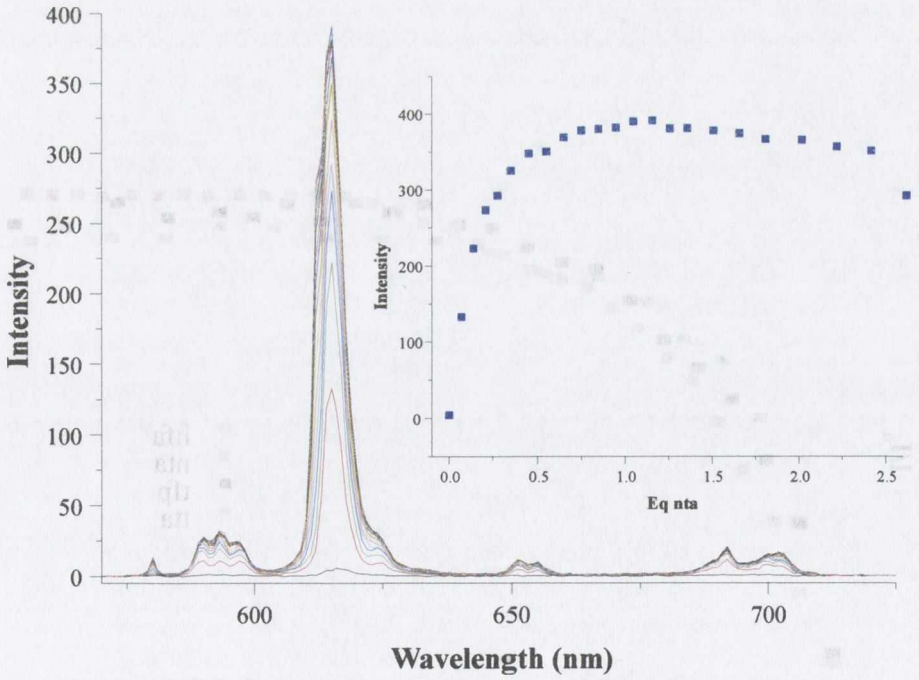


Figure A2.18: *The Eu(III) luminescence response (λ_{ex} = 318 nm) of* ***Eu·49*** *as a function of equivalents of* ***nta*** *at pH 7.4 in 0.1 M HEPES. Inset: Changes in the phosphorescence at 615 nm upon the addition of* ***nta*** *(0-2.5 equivalents).*

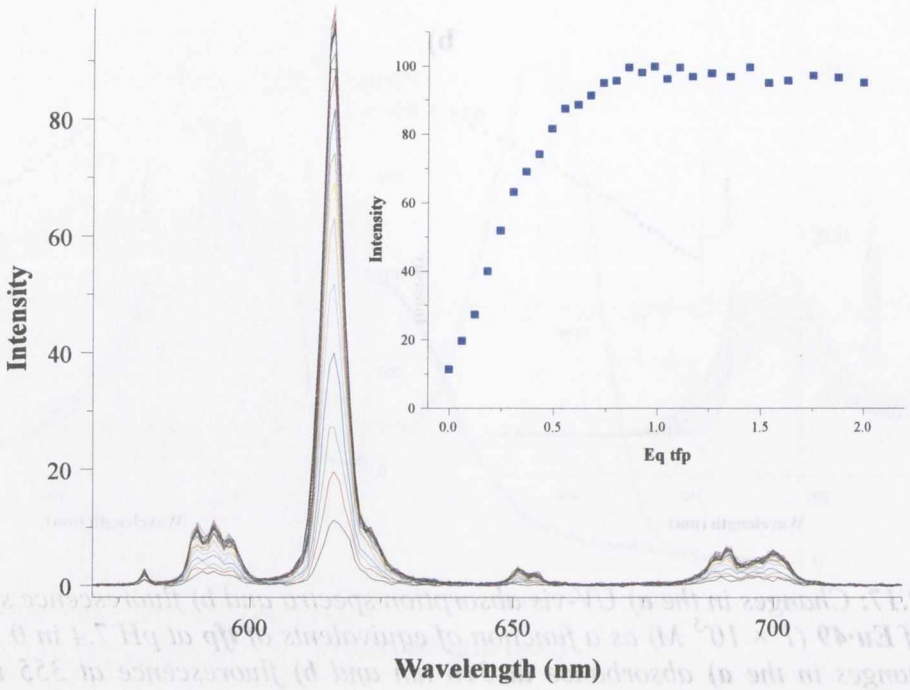


Figure A2.19: *The Eu(III) luminescence response (λ_{ex} = 318 nm of **Eu·49** as a function of equivalents of **tfp** at pH 7.4 in 0.1 M HEPES. Inset: Changes in the phosphorescence at 615 nm upon the addition of **tfp** (0-2.5 equivalents).*

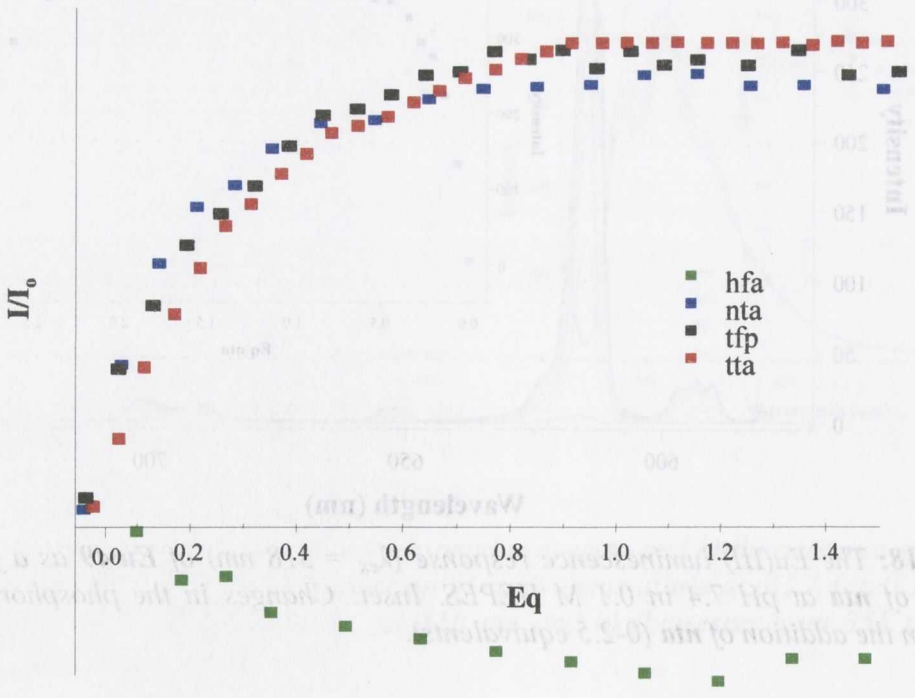


Figure A2.20: *Changes in the phosphorescence at 615 nm upon the addition of **nta**, **tfp**, **tta** and **hfa** (0-1.5 equivalents).*

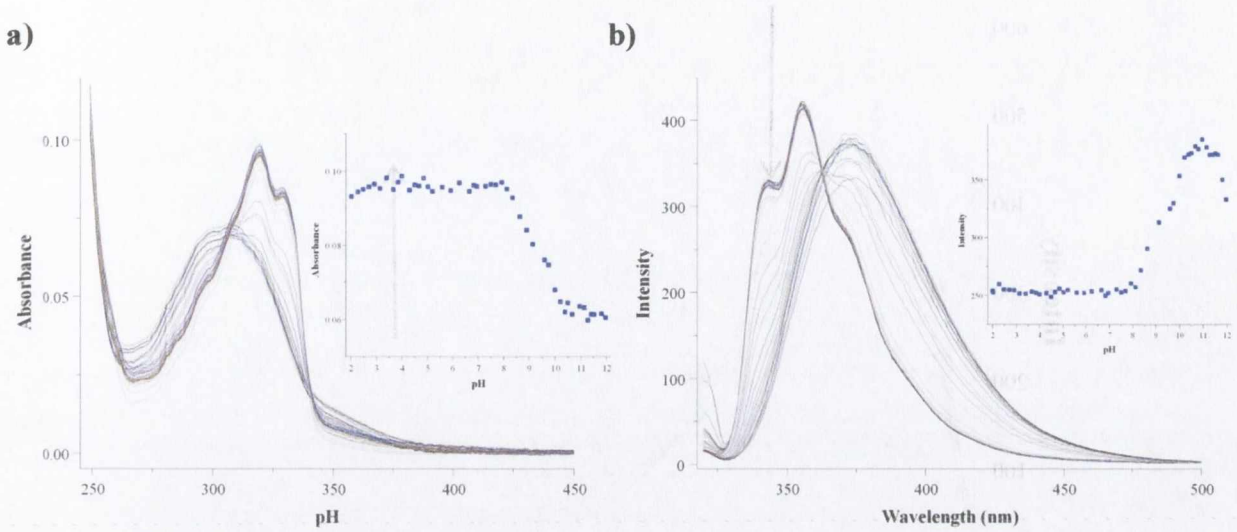


Figure A2.21: a) *Changes in the UV-vis absorption spectra of* ***Eu·49-nta*** *as a function of pH in a mixed DMSO:H_2O (1:99 v/v) solution [I = 0.1 M TEAP]. Inset: Changes in the absorbance at 318 nm as a function of pH.* ***b)*** *Changes in the fluorescence emission spectra of* ***Eu·49-nta*** *as a function of pH in a mixed DMSO:H_2O (1:99 v/v) solution [I = 0.1 M TEAP]. Inset: Changes in the fluorescence at 370 nm as a function of pH.*

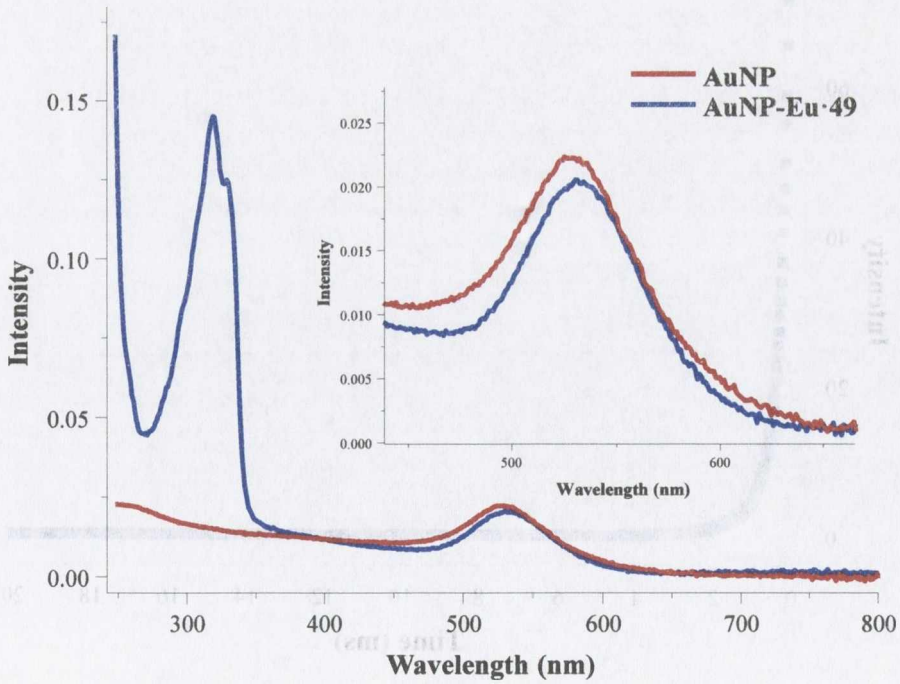


Figure A2.22: *Shift of the SPR band in the UV-vis absorption spectrum by ca. 10 nm upon functionalisation of the citric acid method* ***AuNPs*** *with* ***Eu·49****.*

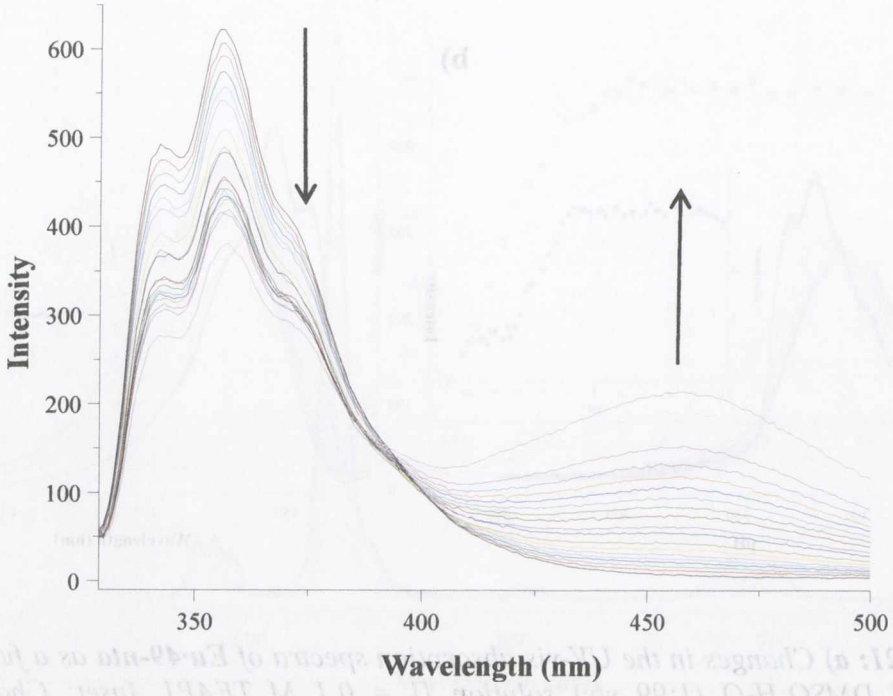


Figure A2.23: *The fluorescence response (λ_{ex} = 318 nm) of* ***AuNP-Eu·49*** *as a function of equivalents of* ***nta*** *at pH 7.4 in 0.1 M HEPES.*

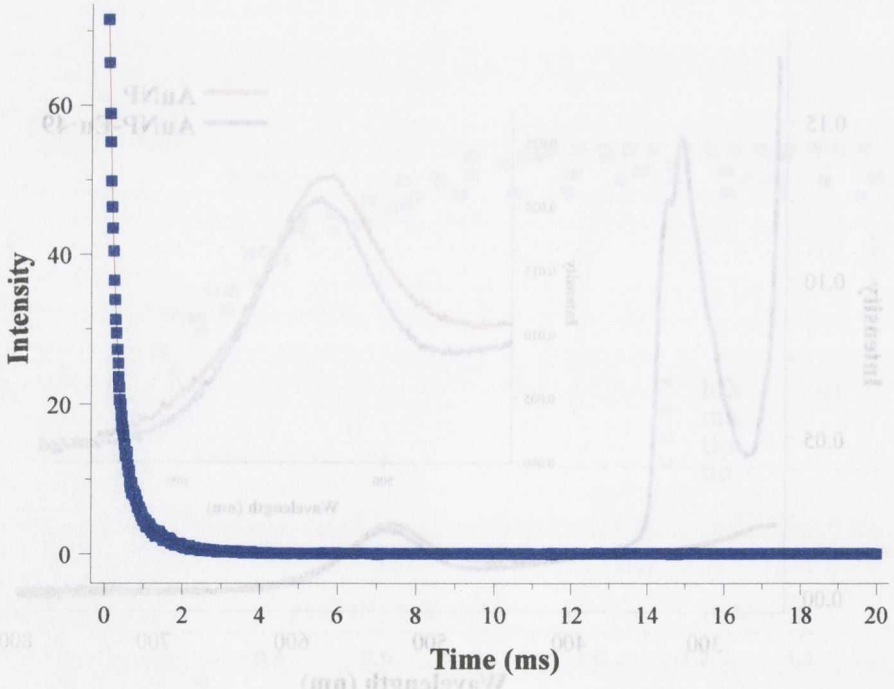


Figure A2.24: *Luminescence decay of the complex* ***AuNP-Eu·49-nta*** *fit to monoexponential decay.*

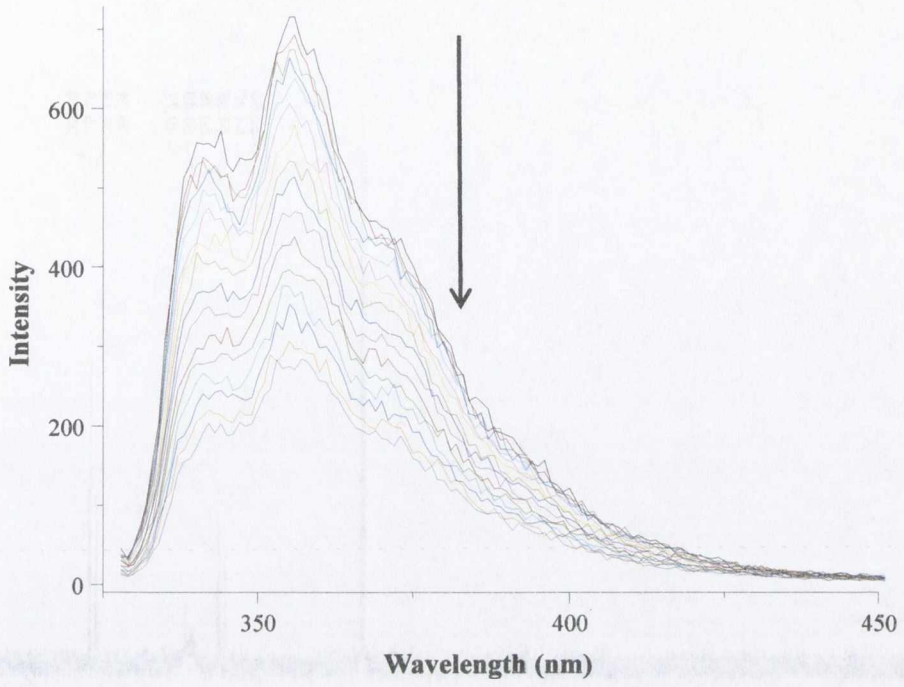


Figure A2.25: *The fluorescence response (λ_{ex} = 318 nm) of* ***AuNP-Tb·49*** *as a function of equivalents of* ***DMAB*** *at pH 7.4 in 0.1 M HEPES.*

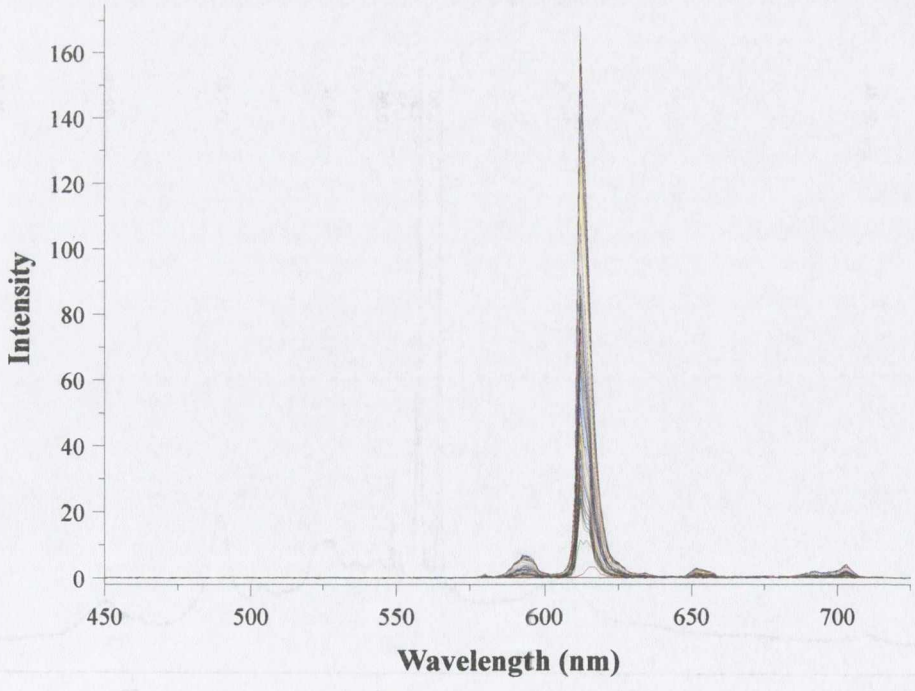


Figure A2.26: *The Tb(III) and Eu(III) luminescence response (λ_{ex} = 318 nm) of* ***AuNP-Eu·49/Tb·49*** *(1×10^{-7} M) as a function of equivalents of* ***nta*** *and* ***DMAB*** *at pH 7.4 in 0.1 M HEPES.*

Appendix 3

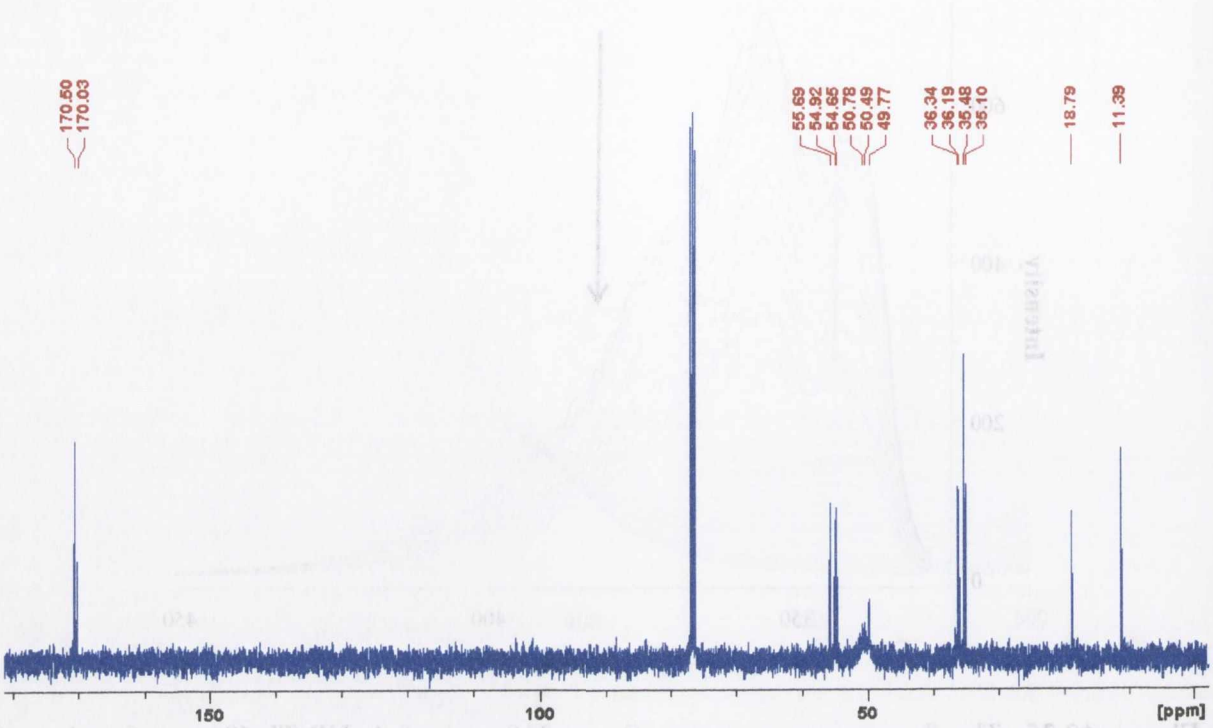


Figure A3.1: *The ^{13}C NMR spectrum (100 MHz, $CDCl_3$) of ligand* ***81****.*

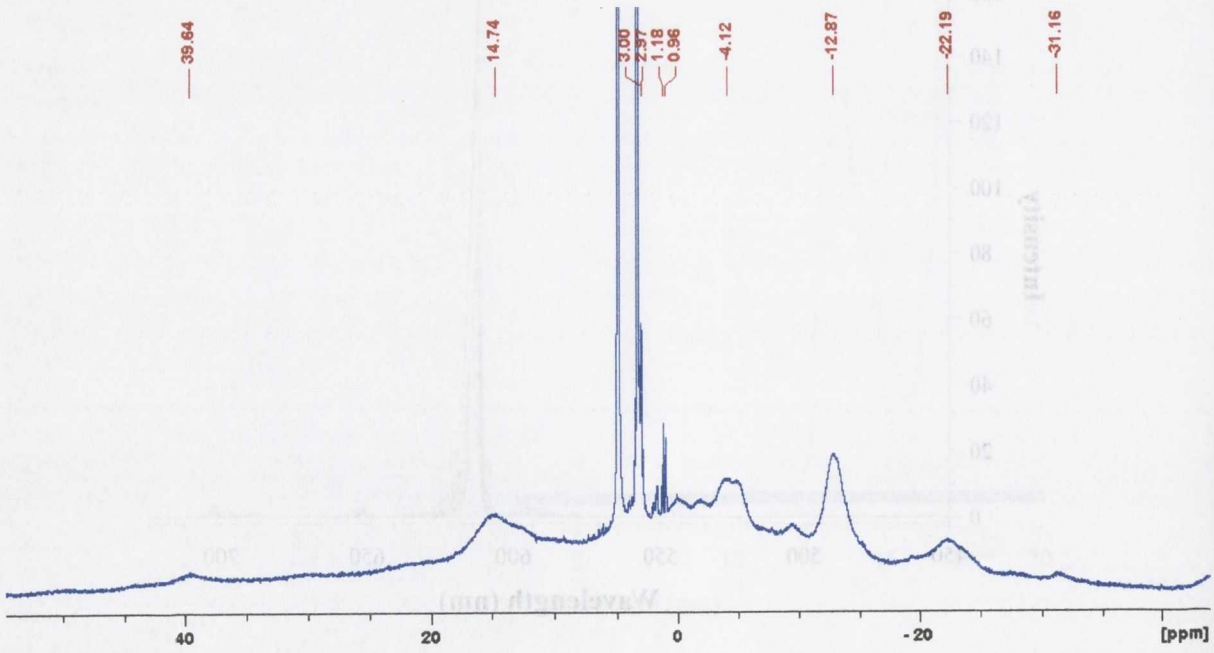


Figure A3.2a: *The ^{1}H NMR spectrum (400 MHz, CD_3OD) of complex* ***Yb·81****.*

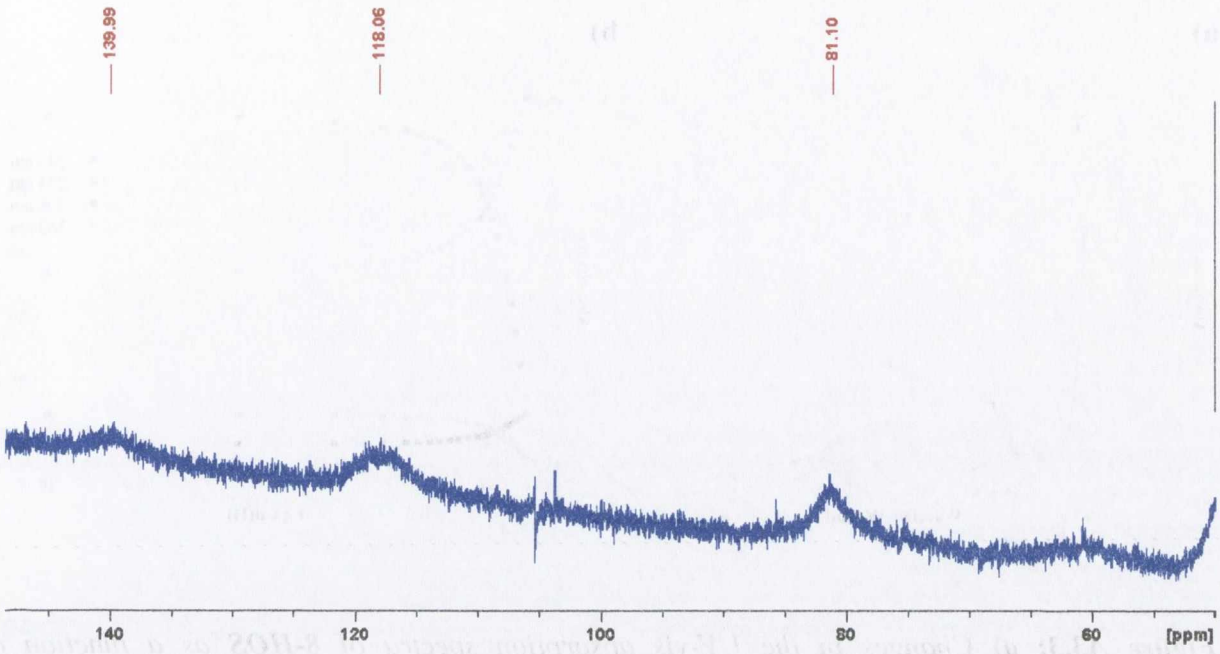


Figure A3.2b: *The remainder of the ^{1}H NMR spectrum (400 MHz, CD_3OD) of complex* ***Yb·81.***

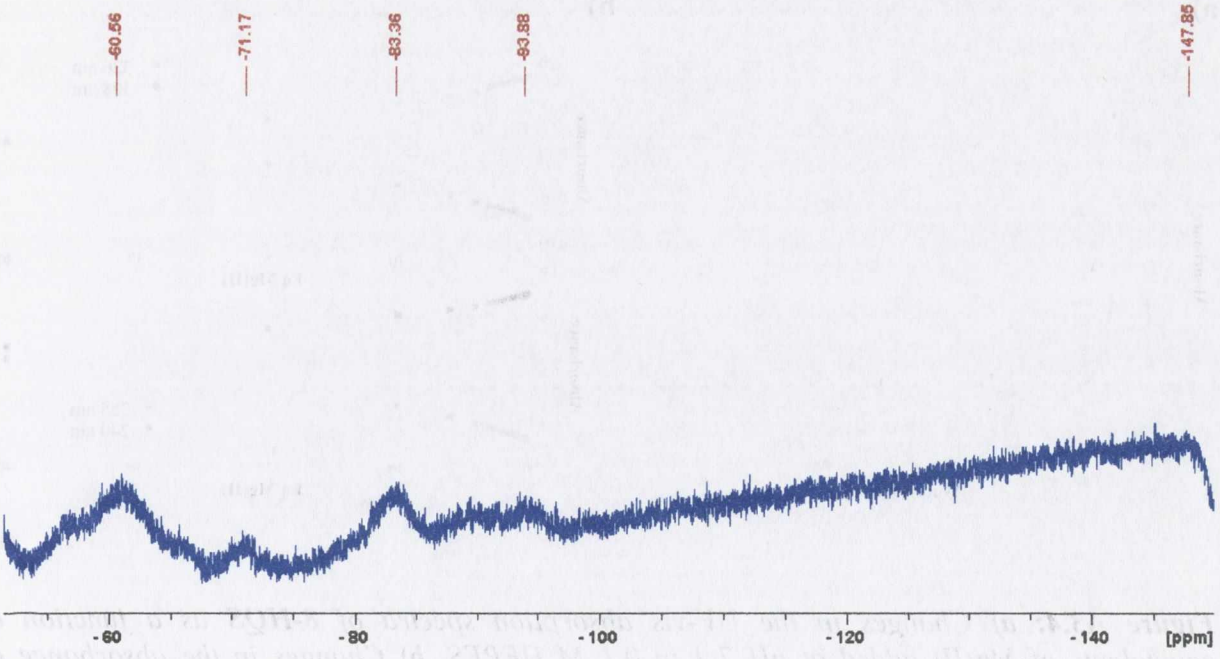


Figure A3.2c: *The remainder of the ^{1}H NMR spectrum (400 MHz, CD_3OD) of complex* ***Yb·81.***

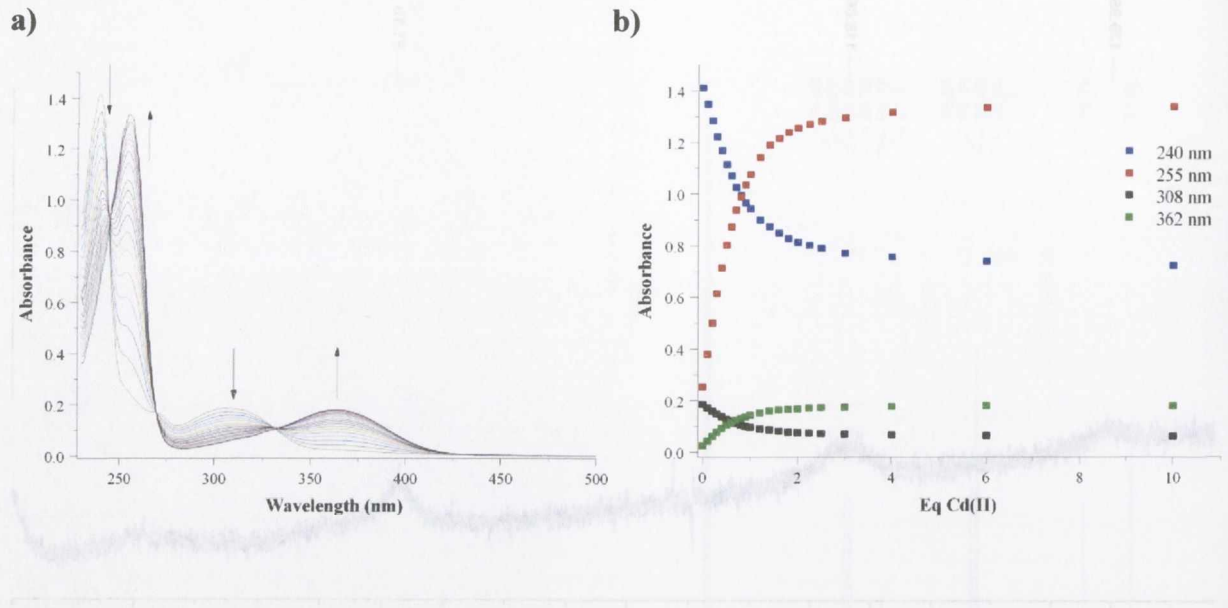


Figure A3.3: ***a)*** *Changes in the UV-vis absorption spectra of* ***8-HQS*** *as a function of equivalents of Cd(II) added at pH 7.4 in 0.1 M HEPES.* ***b)*** *Changes in the absorbance at 240 nm, 255 nm, 308 nm and 362 nm upon the addition of Cd(II).*

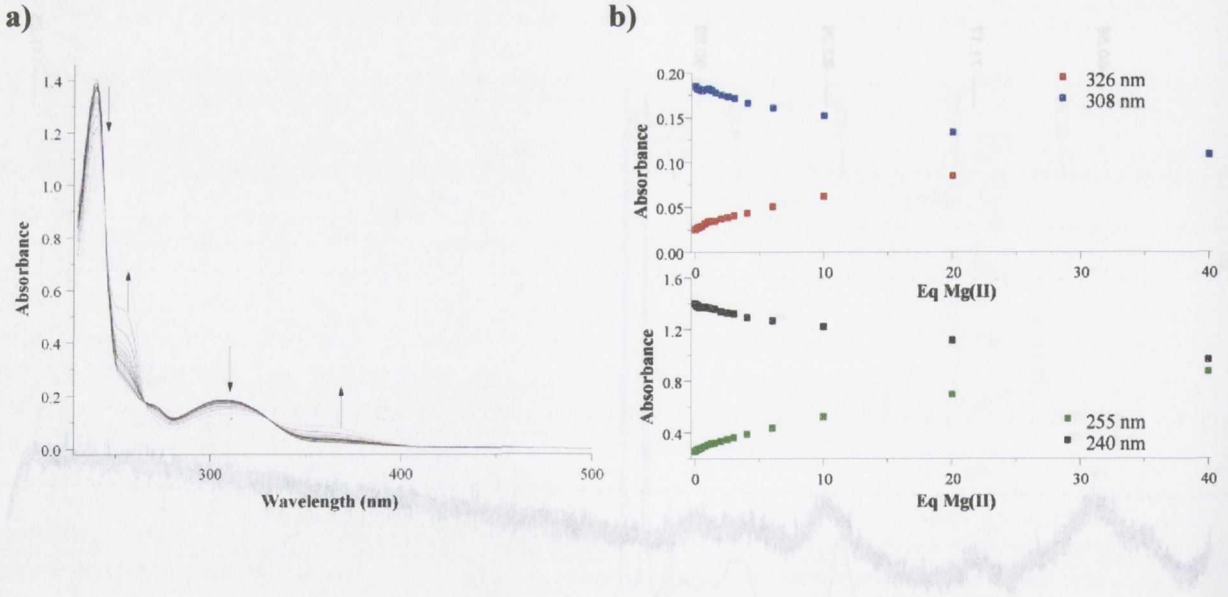


Figure A3.4: ***a)*** *Changes in the UV-vis absorption spectra of* ***8-HQS*** *as a function of equivalents of Mg(II) added at pH 7.4 in 0.1 M HEPES.* ***b)*** *Changes in the absorbance at 240 nm, 255 nm, 308 nm and 362 nm upon the addition of Mg(II).*

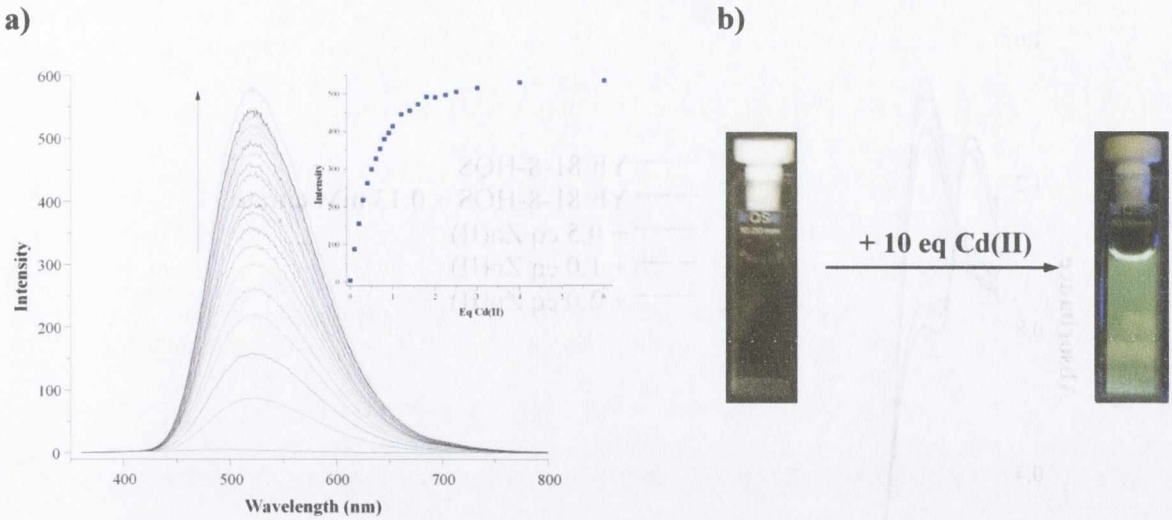


Figure A3.5: a) *Changes in the fluorescence spectrum of* ***8-HQS*** *as a function of equivalents of Cd(II) added at pH 7.4 in 0.1 M HEPES. Inset: Changes in the fluorescence at 523 nm upon the addition of Cd(II).* ***b)*** *Fluorescence response of* ***8-HQS*** *in the presence of Cd(II) under a UV-visible lamp (λ_{ex} = 365 nm).*

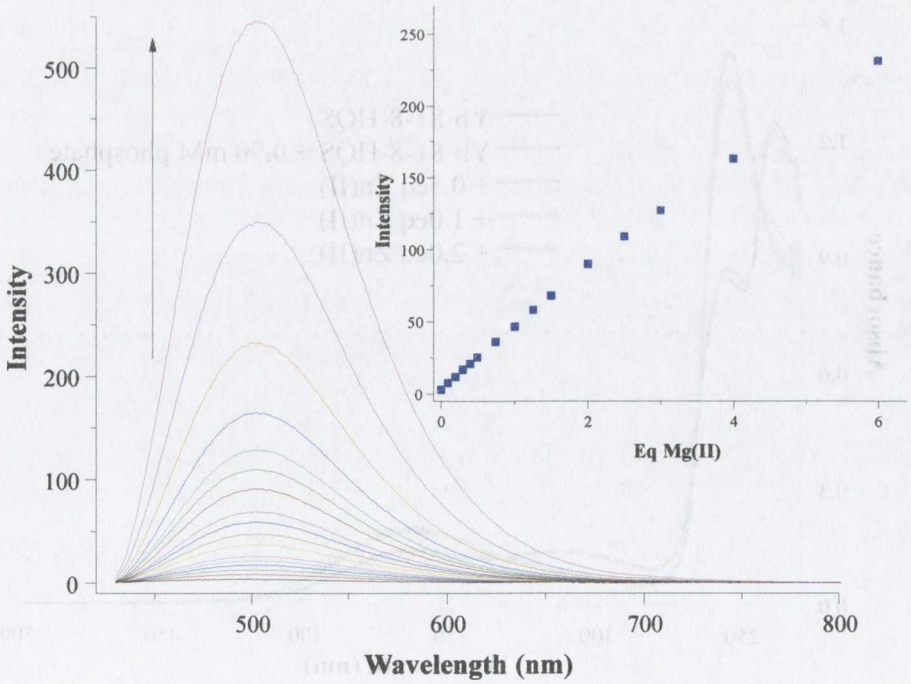


Figure A3.6: *Changes in the fluorescence spectrum of* ***8-HQS*** *as a function of equivalents of Mg(II) added at pH 7.4 in 0.1 M HEPES. Inset: Changes in the fluorescence at 500 nm upon the addition of Mg(II).*

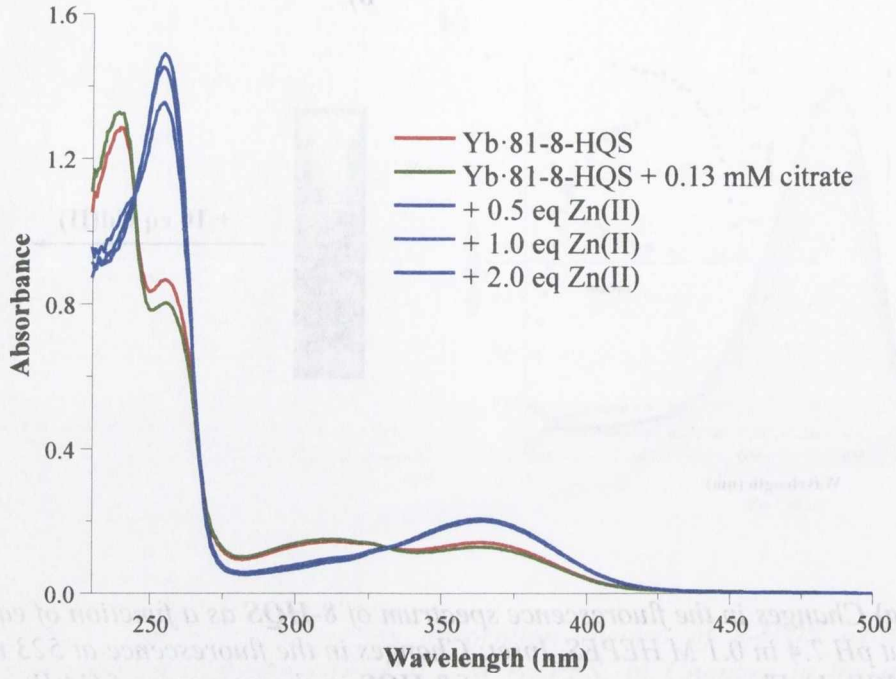


Figure A3.7: *Changes in the UV-vis absorption spectrum of* ***Yb·81-8-HQS*** *upon the addition of 0.13 mM citrate followed by 0.5, 1.0 and 2.0 equivalents of Zn(II) at pH 7.4 in 0.1 M HEPES.*

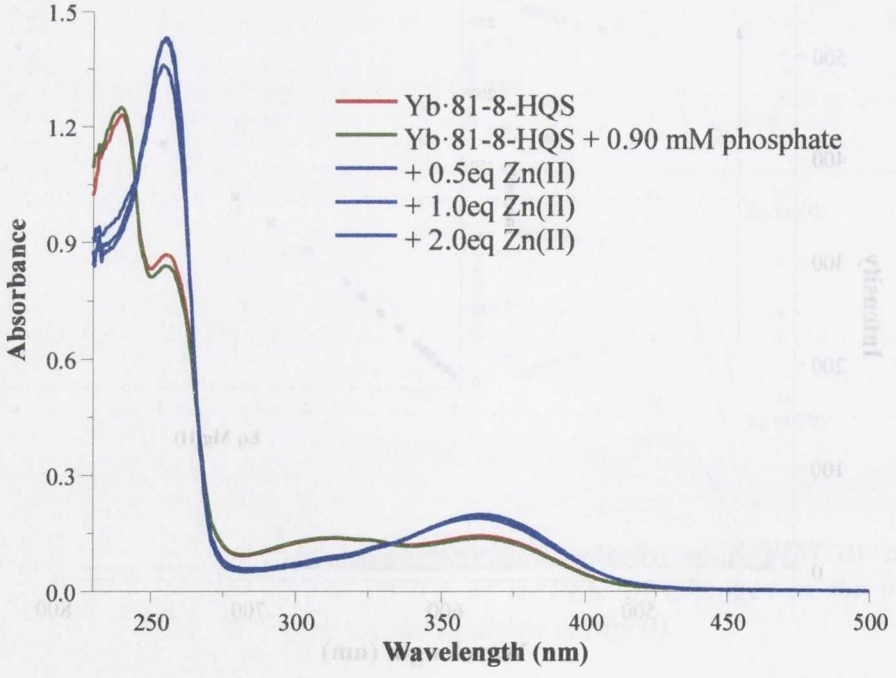


Figure A3.8: *Changes in the UV-vis absorption spectrum of* ***Yb·81-8-HQS*** *upon the addition of 0.13 mM phosphate followed by 0.5, 1.0 and 2.0 equivalents of Zn(II) at pH 7.4 in 0.1 M HEPES.*

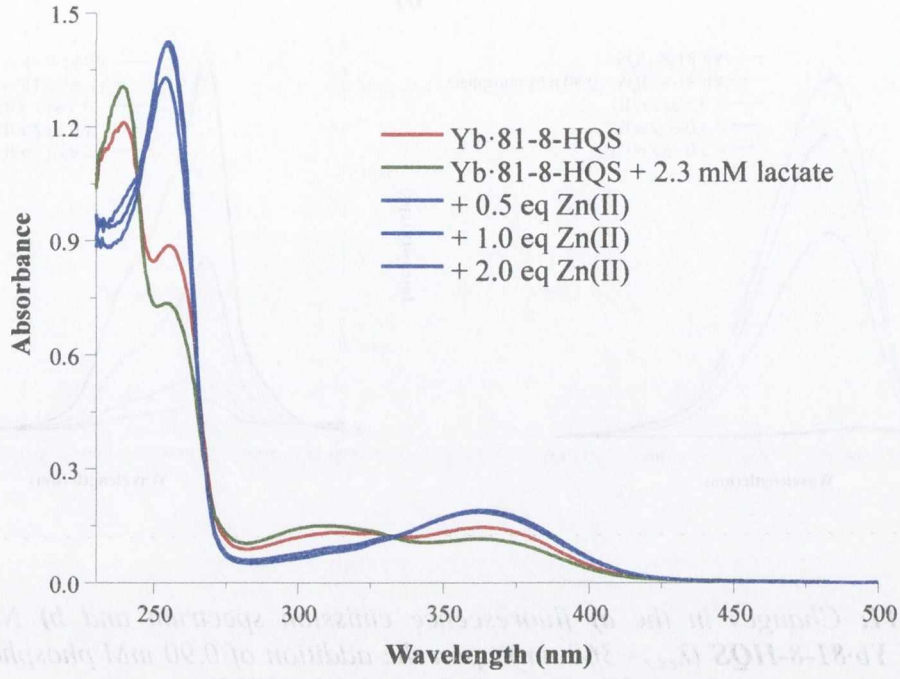


Figure A3.9: *Changes in the UV-vis absorption spectrum of* ***Yb·81-8-HQS*** *upon the addition of 2.3 mM lactate followed by 0.5, 1.0 and 2.0 equivalents of Zn(II) at pH 7.4 in 0.1 M HEPES.*

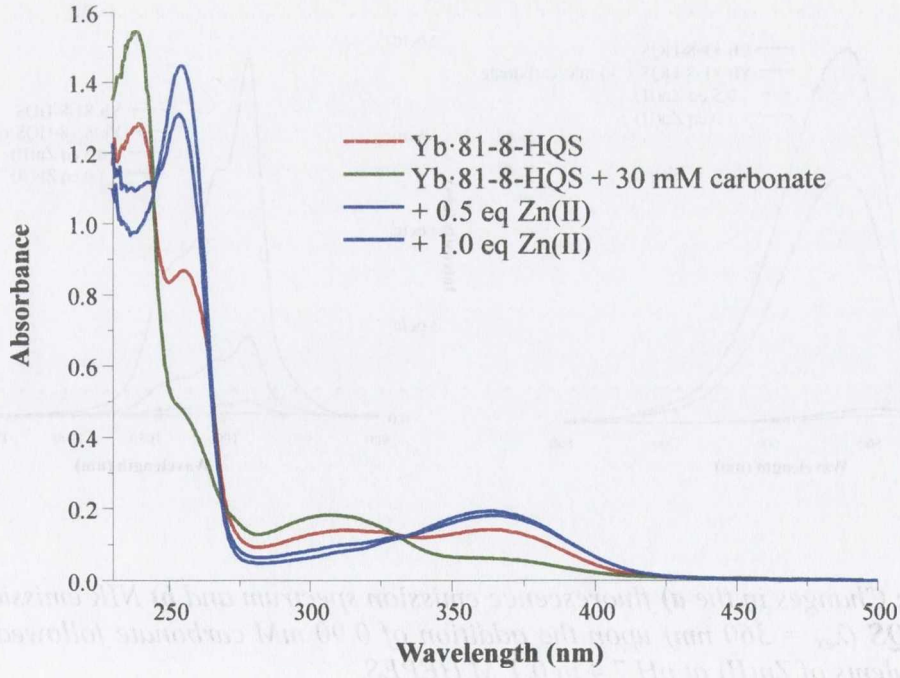


Figure A3.10: *Changes in the UV-vis absorption spectrum of* ***Yb·81-8-HQS*** *upon the addition of 30 mM carbonate followed by 0.5 and 1.0 equivalents of Zn(II) at pH 7.4 in 0.1 M HEPES.*

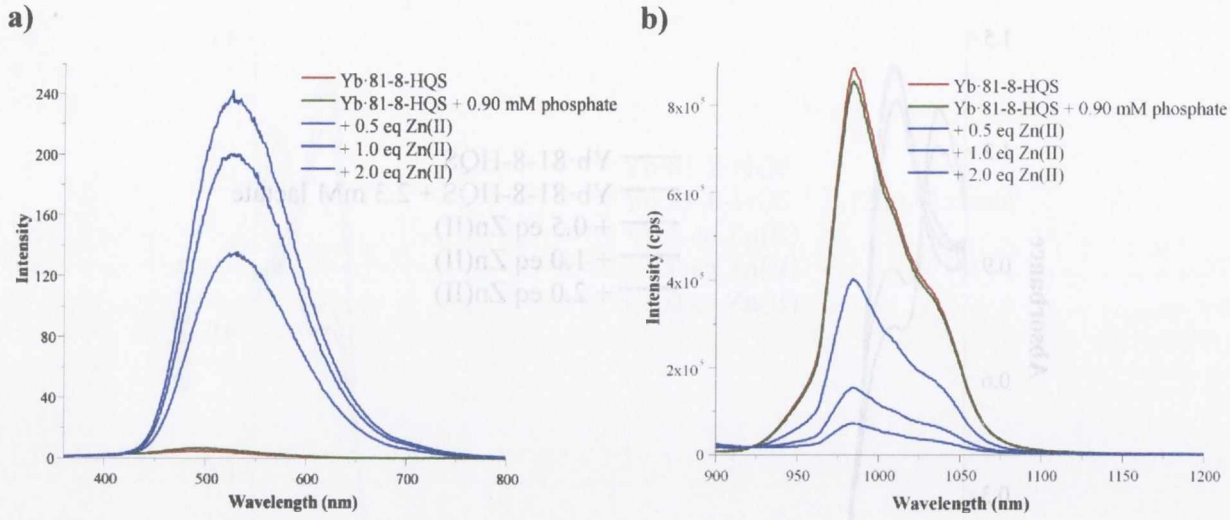


Figure A3.11: *Changes in the* ***a)*** *fluorescence emission spectrum and* ***b)*** *NIR emission spectrum of* ***Yb·81-8-HQS*** *(λ_{ex} = 360 nm) upon the addition of 0.90 mM phosphate followed by 0.5, 1.0 and 2.0 equivalents of Zn(II) at pH 7.4 in 0.1 M HEPES.*

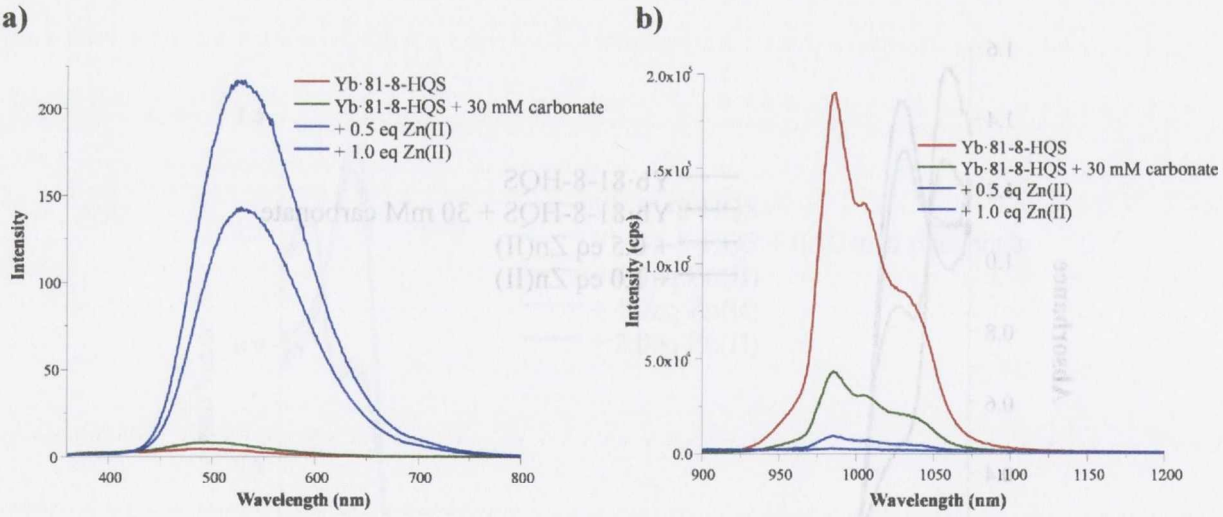


Figure A3.12: *Changes in the* ***a)*** *fluorescence emission spectrum and* ***b)*** *NIR emission spectrum of* ***Yb·81-8-HQS*** *(λ_{ex} = 360 nm) upon the addition of 0.90 mM carbonate followed by 0.5, 1.0 and 2.0 equivalents of Zn(II) at pH 7.4 in 0.1 M HEPES.*

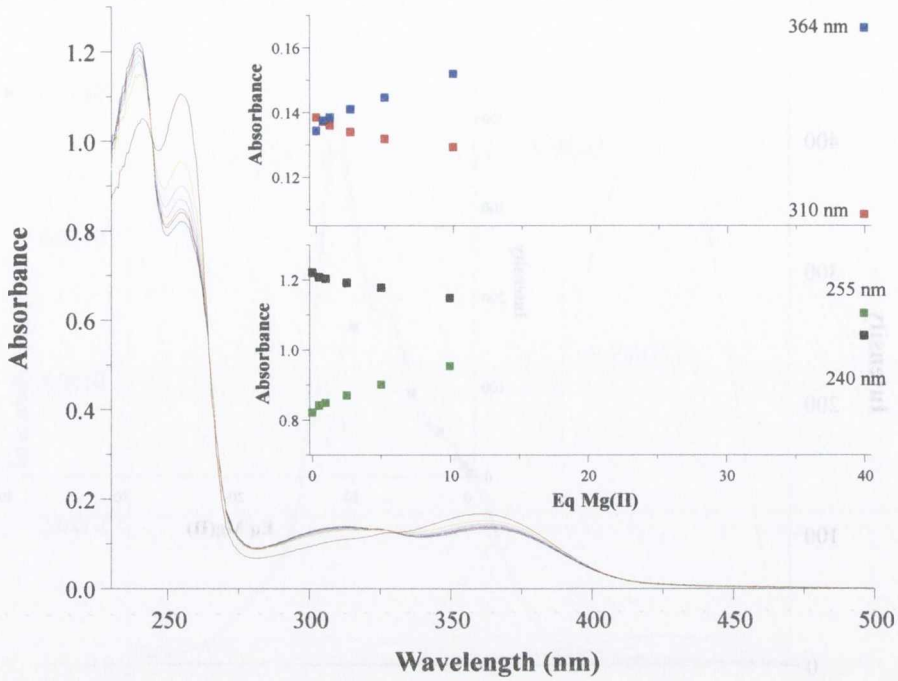


Figure A3.13: *Changes in the UV-vis absorption spectrum and of* ***Yb·81-8-HQS*** *upon the addition of Mg(II) at pH 7.4 in 0.1 M HEPES. Inset: Changes in the absorbance at 240 nm, 255 nm, 310 nm and 364 nm as a function of equivalents of Mg(II).*

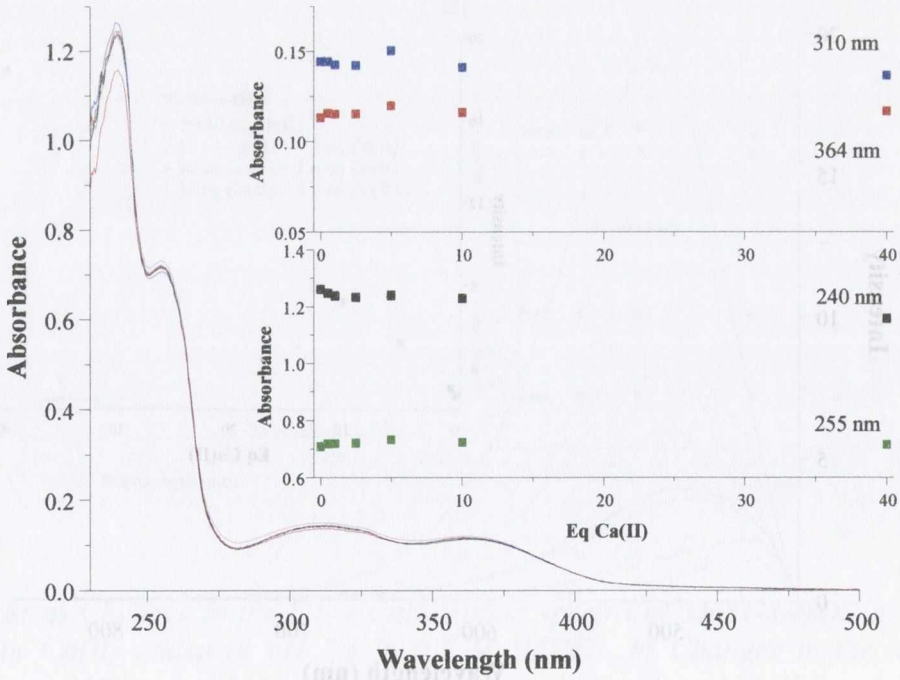


Figure A3.14: *Changes in the UV-vis absorption spectrum and of* ***Yb·81-8-HQS*** *upon the addition of Ca(II) at pH 7.4 in 0.1 M HEPES. . Inset: Changes in the absorbance at 240 nm, 255 nm, 310 nm and 364 nm as a function of equivalents of Ca(II).*

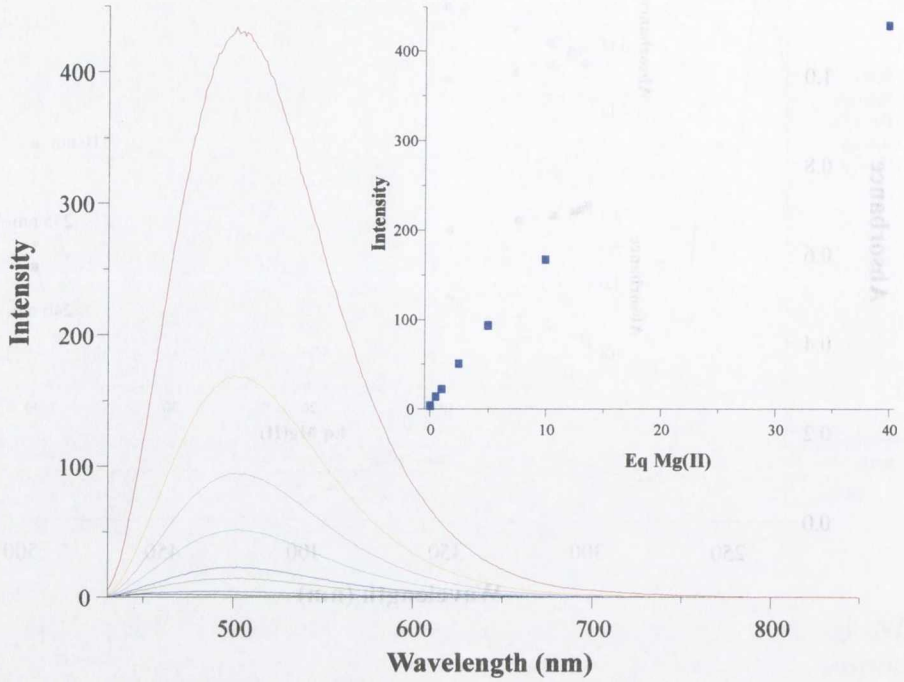


Figure A3.15: *Changes in the fluorescence emission spectrum of* ***Yb·81-8-HQS*** *(λ_{ex} = 360 nm) upon the addition of Mg(II) at pH 7.4 in 0.1 M HEPES. Insets: Changes in the fluorescence at 527 nm upon the addition of Mg(II).*

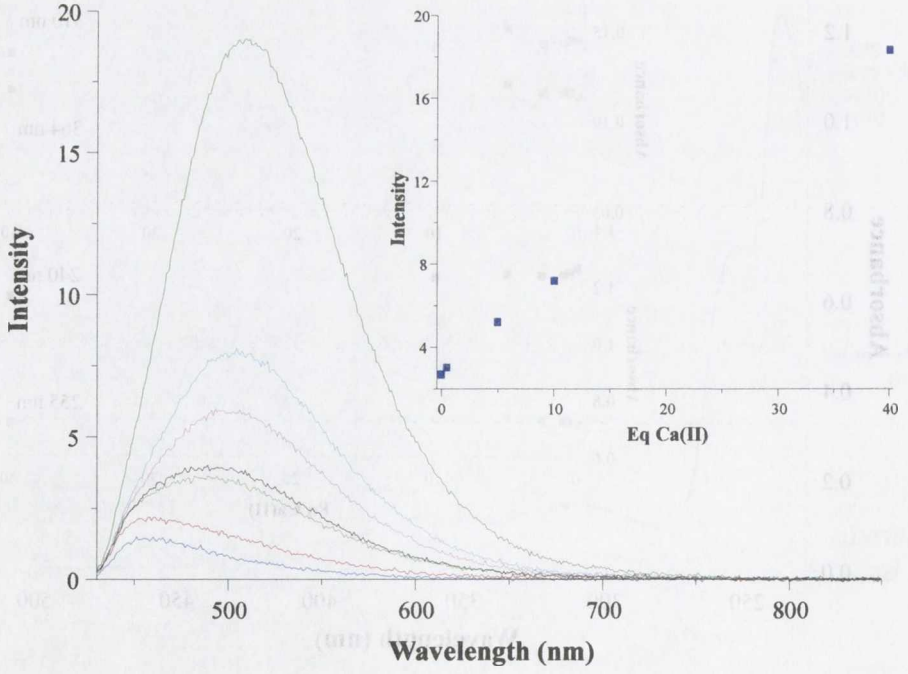


Figure A3.16: *Changes in the fluorescence emission spectrum of* ***Yb·81-8-HQS*** *(λ_{ex} = 360 nm) upon the addition of Ca(II) at pH 7.4 in 0.1 M HEPES. Insets: Changes in the fluorescence at 509 nm upon the addition of Ca(II).*

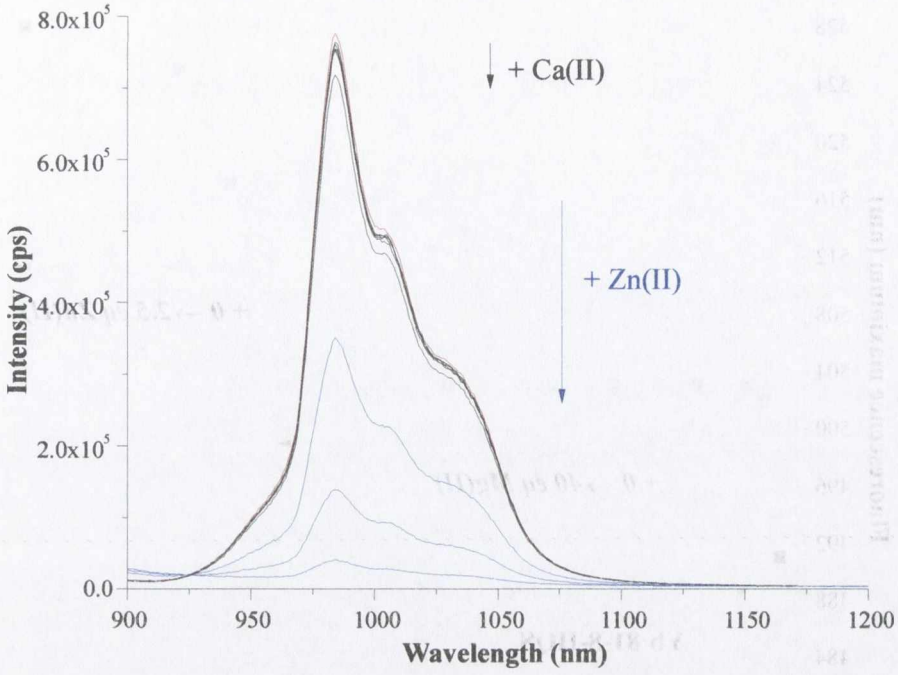


Figure A3.17: *NIR emission spectrum (λ_{ex} = 360 nm) of* ***Yb·81-8-HQS*** *(5×10^{-5} M) upon the addition of Ca(II) followed by Zn(II) at pH 7.4 in 0.1 M HEPES.*

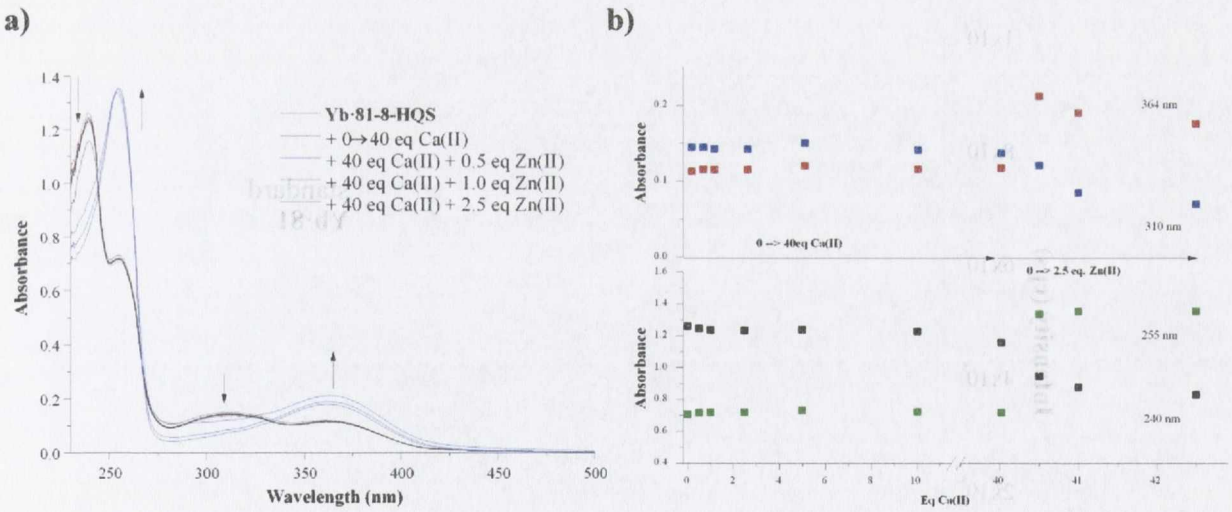


Figure A3.18: ***a)*** *Changes in the UV-vis absorption spectra of* ***Yb·81-8-HQS*** *as a function of equivalents of Ca(II) added at pH 7.4 in 0.1 M HEPES.* ***b)*** *Changes in the absorbance at 240 nm, 255 nm, 310 nm and 364 nm upon the addition of Ca(II) and Zn(II).*

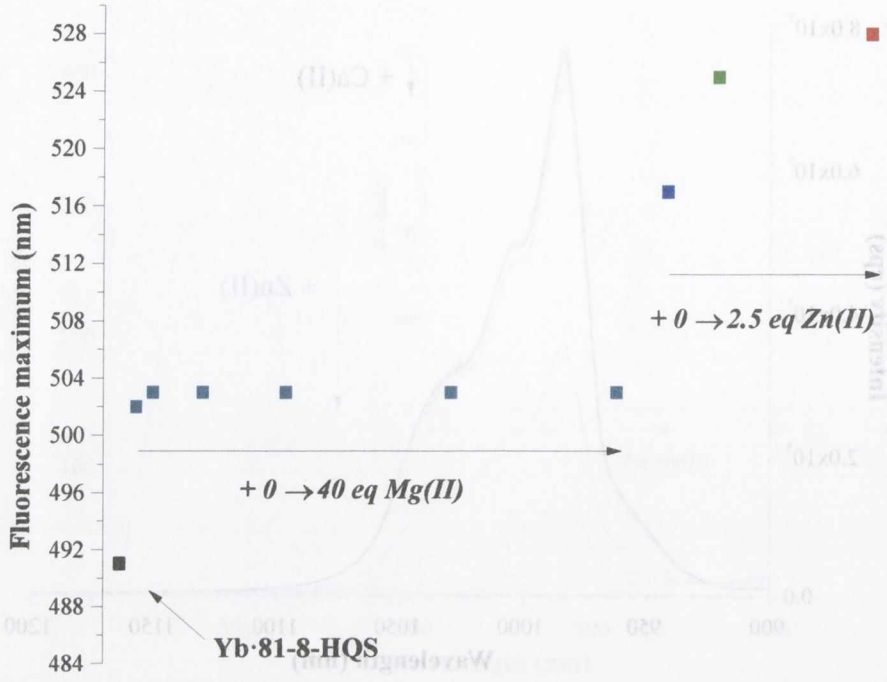


Figure A3.19: *Changes in the fluorescence maximum upon the addition of Ca(II) and Zn(II).*

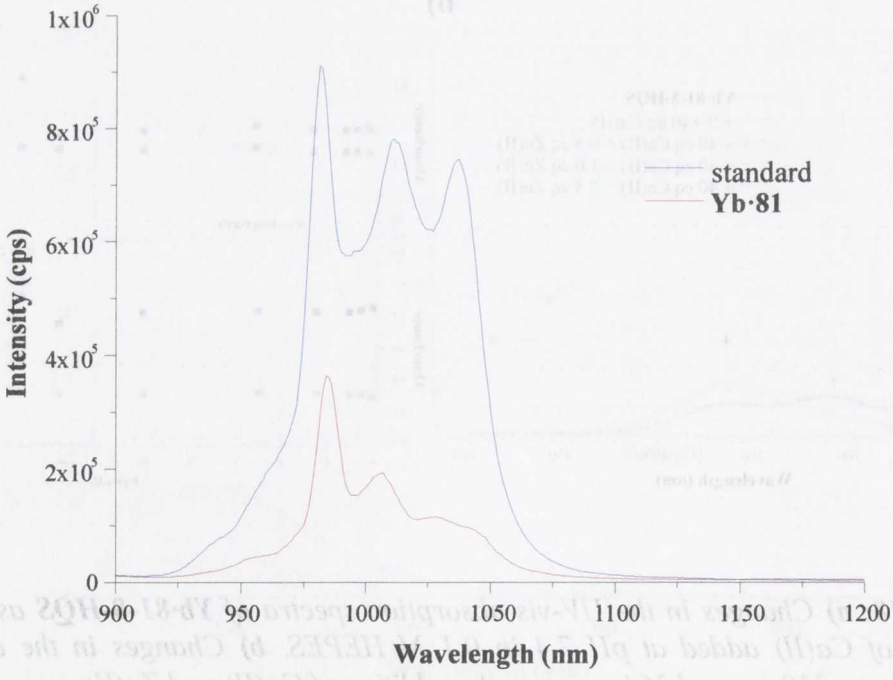


Figure A3.20: *NIR Yb(III) emission of standard and* ***Yb·81****,* λ_{ex} *= 339 nm.*

Appendix 4

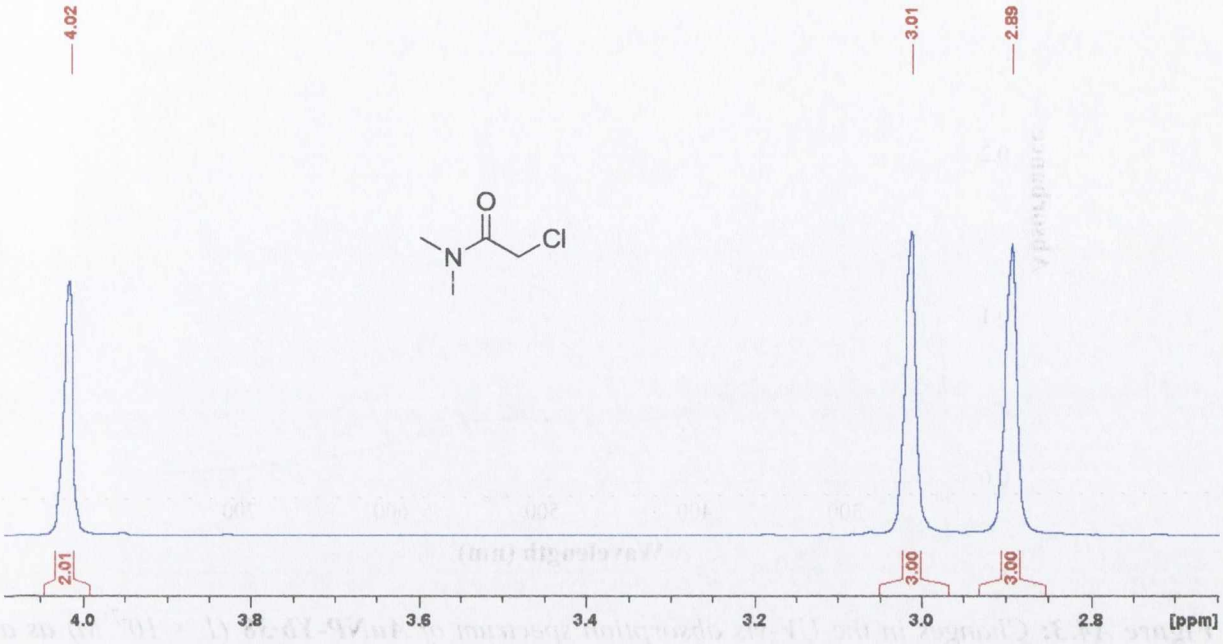


Figure A4.1: *The ^{1}H NMR spectrum (400 MHz, $CDCl_3$) of* ***84****.*

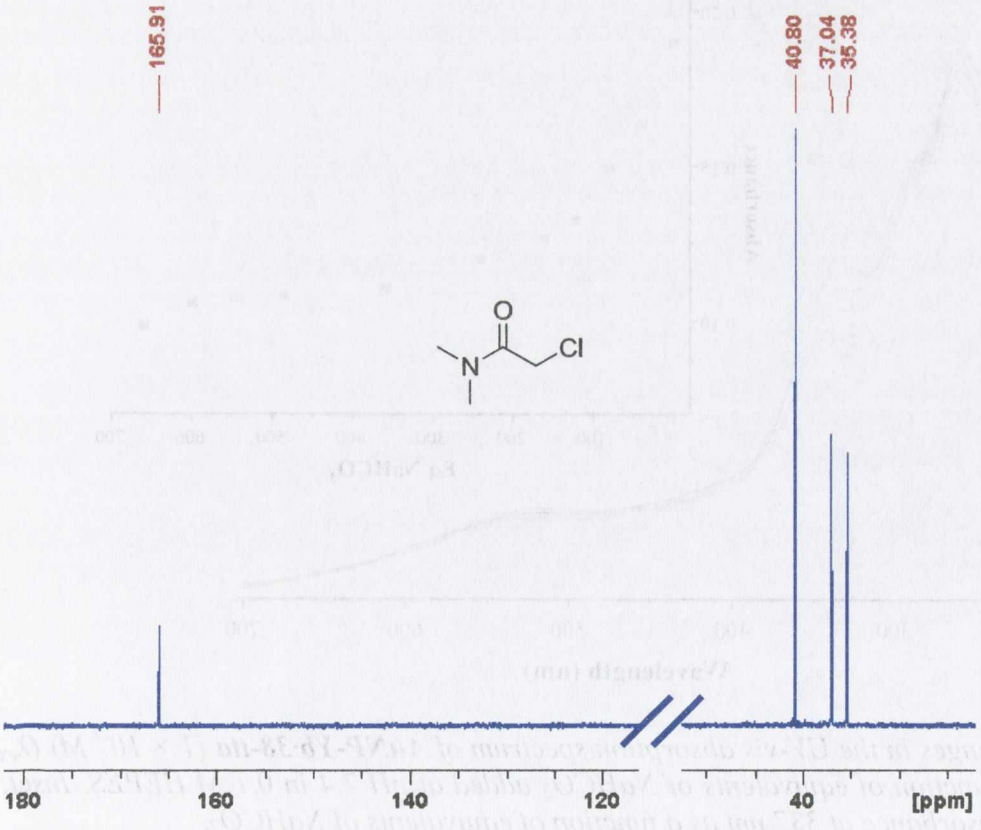


Figure A4.2: *The ^{13}C NMR spectrum (100 MHz, $CDCl_3$) of* ***84****.*

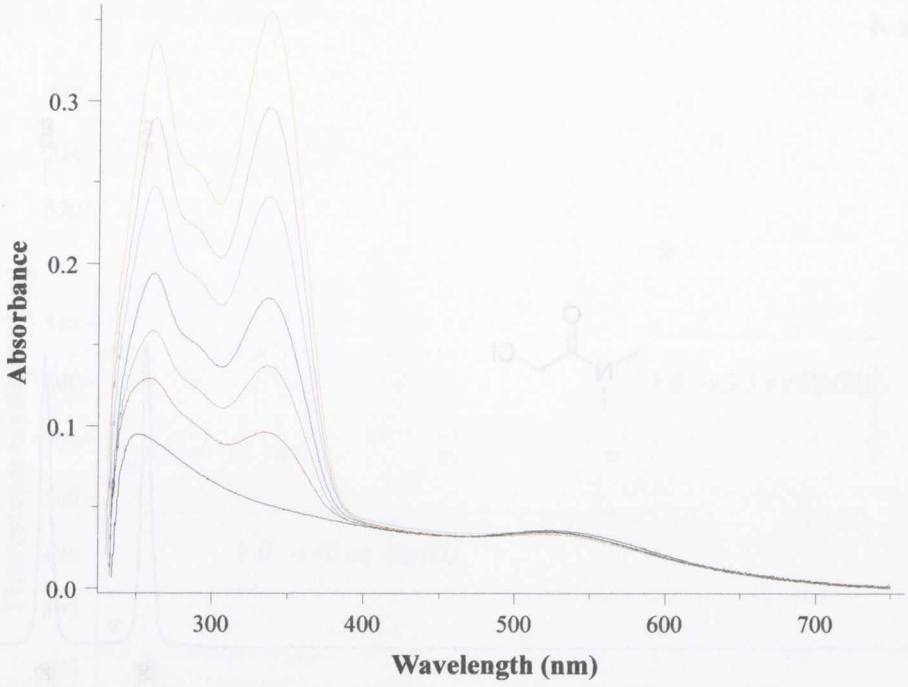


Figure A4.3: *Changes in the UV-vis absorption spectrum of* ***AuNP-Yb·38*** *(1×10^{-7} M) as a function of equivalents of* ***tta*** *added at pH 7.4 in 0.1 M HEPES.*

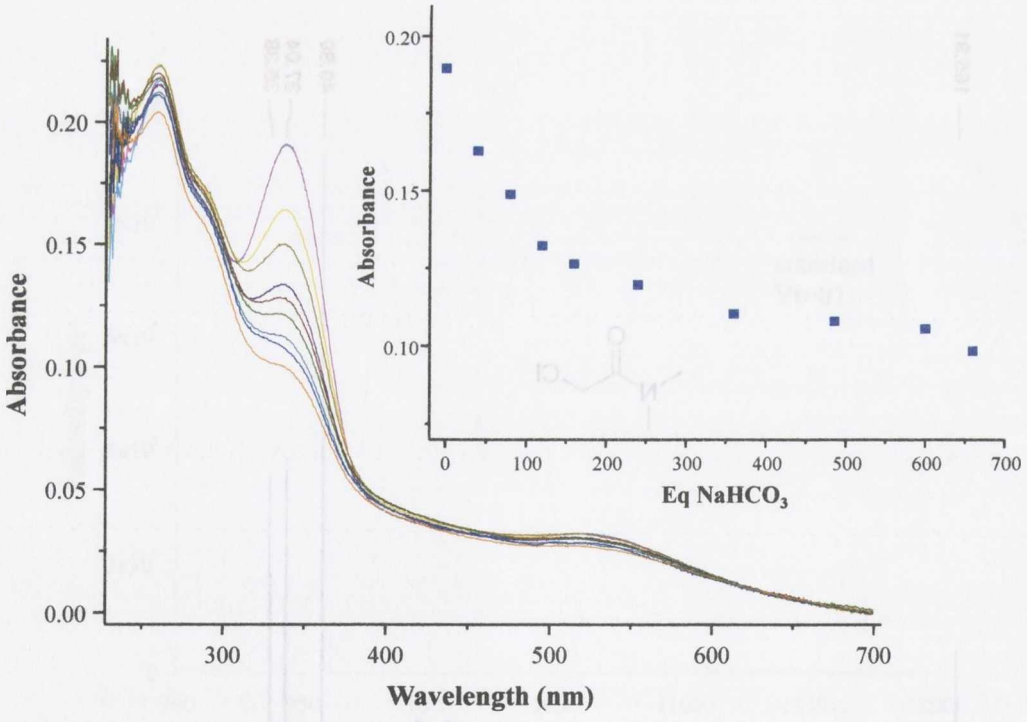


Figure A4.4: *Changes in the UV-vis absorption spectrum of* ***AuNP-Yb·38-tta*** *(1×10^{-7} M) (λ_{ex} = 340 nm) as a function of equivalents of $NaHCO_3$ added at pH 7.4 in 0.1 M HEPES. Inset: Changes in the absorbance at 337 nm as a function of equivalents of $NaHCO_3$.*

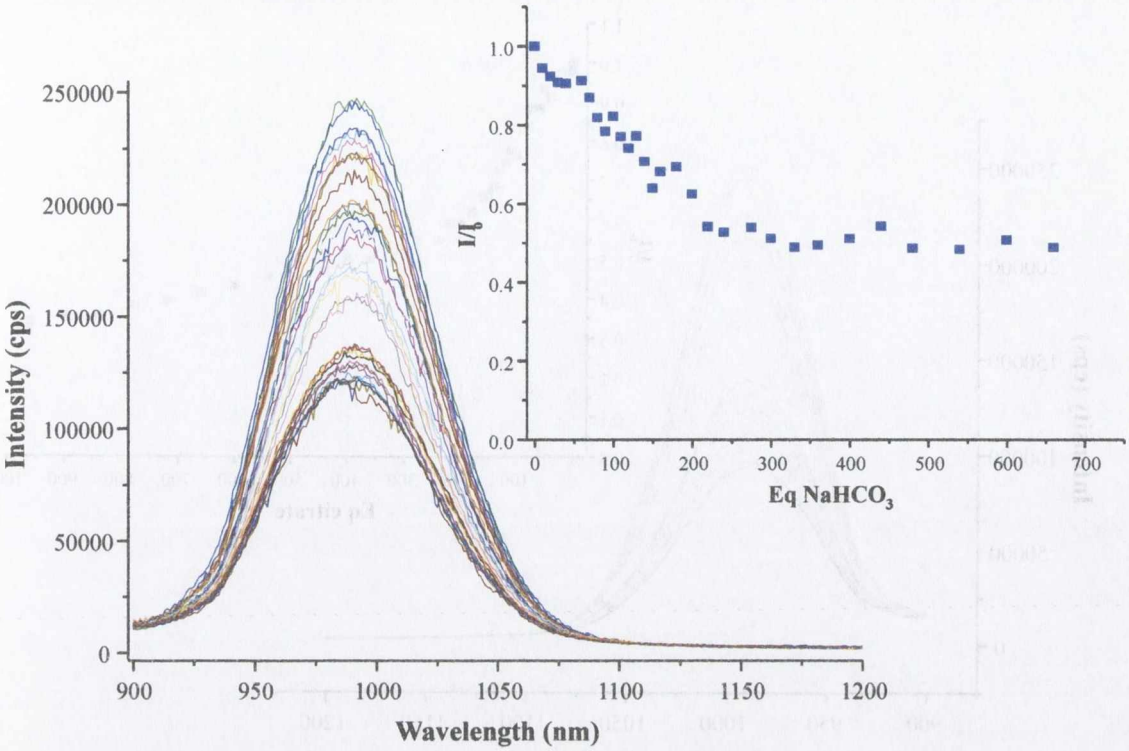


Figure A4.5: *Changes in the Yb(III) NIR emission of* ***AuNP-Yb·38-tta*** *(1×10^{-7} M) (λ_{ex} = 340 nm) as a function of equivalents of $NaHCO_3$ added at pH 7.4 in 0.1 M HEPES. Inset: Changes in the normalised emission intensity (I/I_o) at 985 nm as a function of equivalents of $NaHCO_3$.*

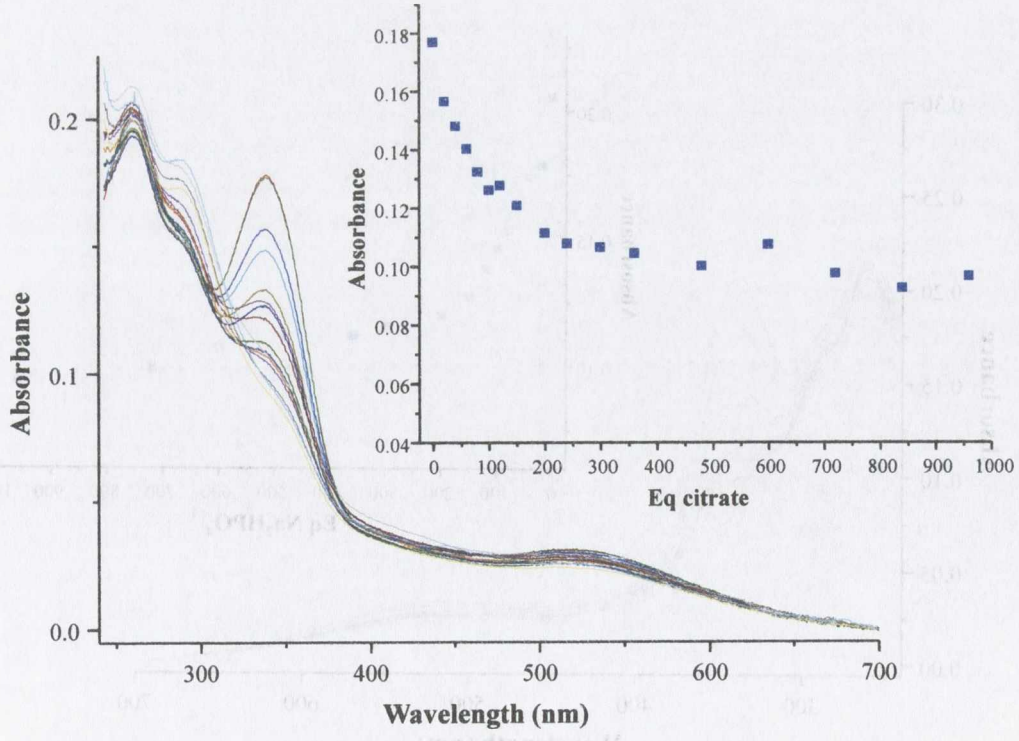


Figure A4.6: *Changes in the UV-vis absorption spectrum of* ***AuNP-Yb·38-tta*** *(1×10^{-7} M) as a function of equivalents of citrate added at pH 7.4 in 0.1 M HEPES. Inset: Changes in the absorbance at 337 nm as a function of equivalents of citrate.*

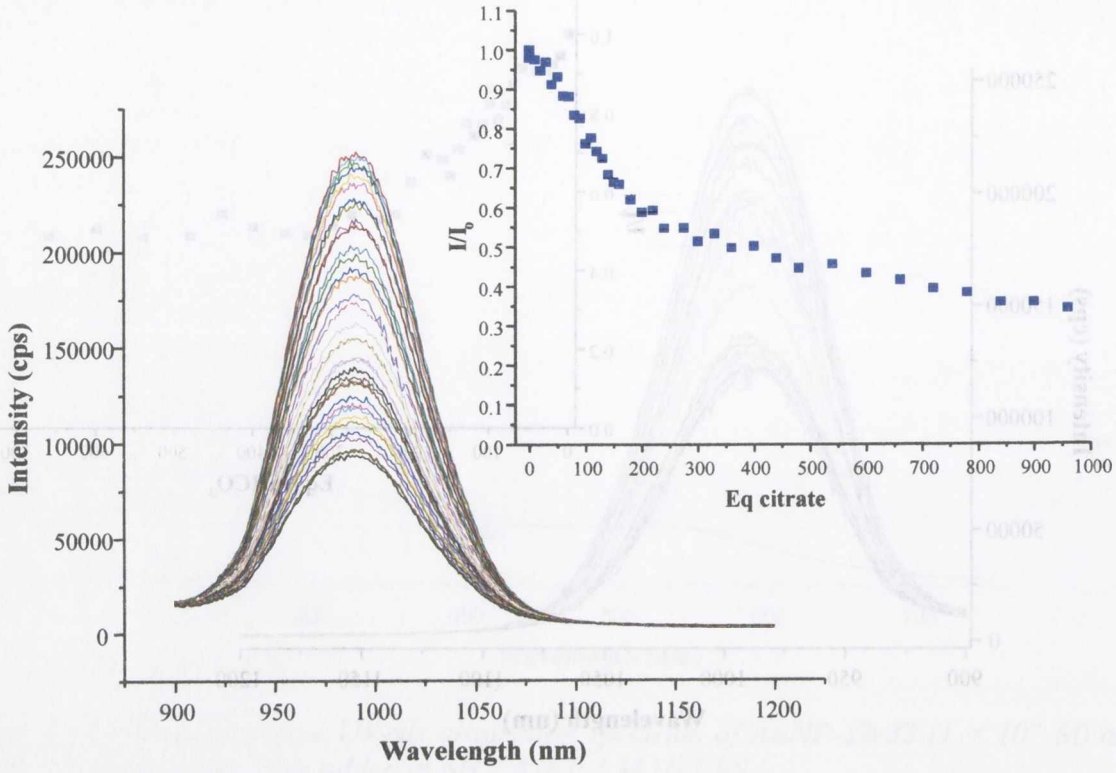


Figure A4.7: *Changes in the Yb(III) NIR emission of* ***AuNP-Yb·38-tta*** *(1 × 10^{-7} M) (λ_{ex} = 340 nm) as a function of equivalents of citrate added at pH 7.4 in 0.1 M HEPES. Inset: Changes in the normalised emission intensity (I/I_o) at 985 nm as a function of equivalents of citrate.*

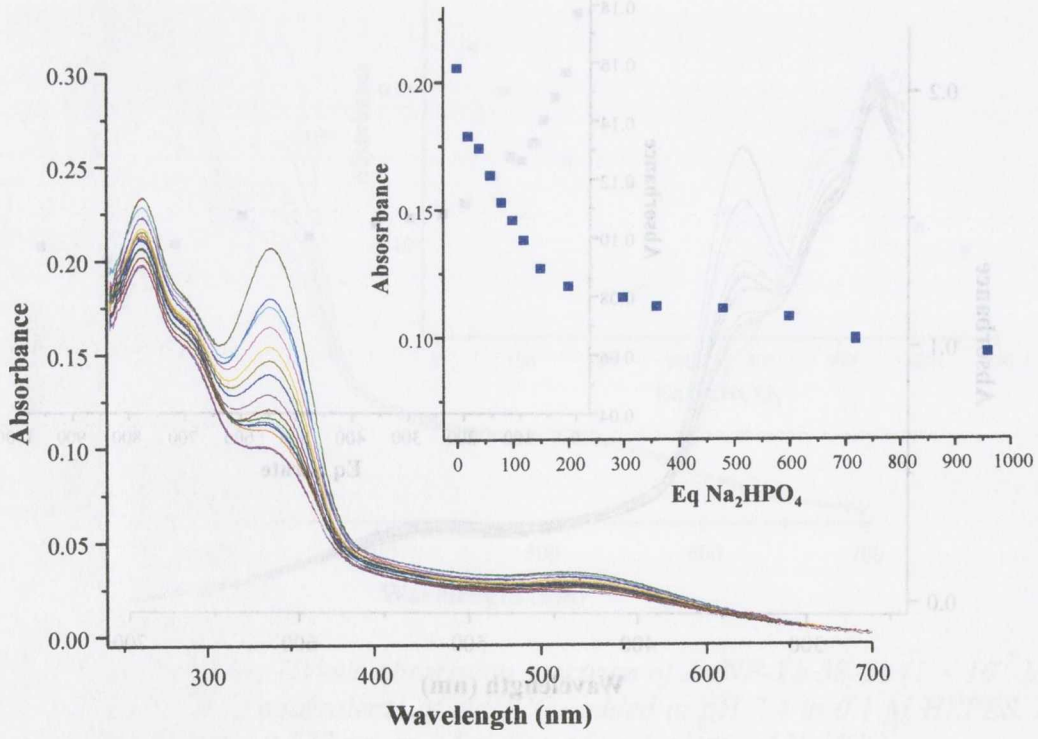


Figure A4.8: *Changes in the UV-vis absorption spectrum of* ***AuNP-Yb·38-tta*** *(1 × 10^{-7} M) as a function of equivalents of Na_2HPO_4 added at pH 7.4 in 0.1 M HEPES. Inset: Changes in the absorbance at 337 nm as a function of equivalents of Na_2HPO_4.*

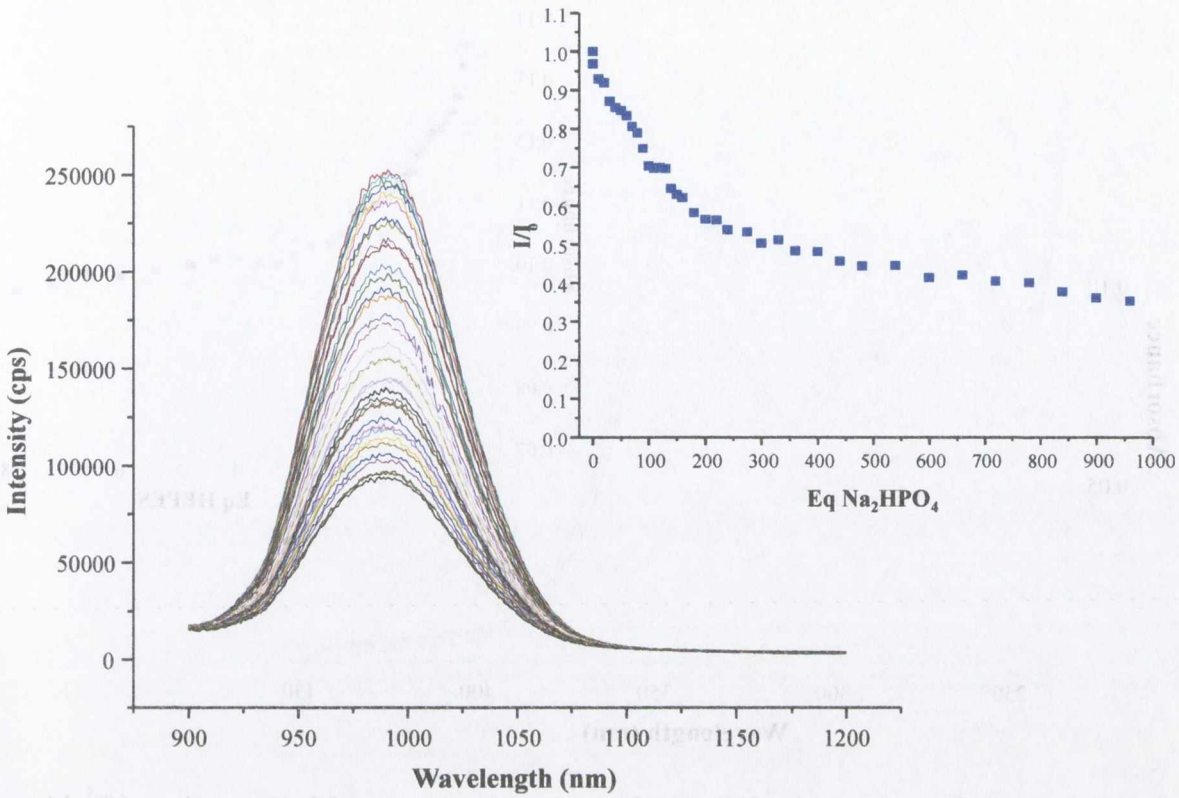


Figure A4.9: *Changes in the Yb(III) NIR emission of* ***AuNP-Yb·38-tta*** *(1×10^{-7} M) (λ_{ex} = 340 nm) as a function of equivalents of Na_2HPO_4 added at pH 7.4 in 0.1 M HEPES. Inset: Changes in the normalised emission intensity (I/I_o) at 985 nm as a function of equivalents of Na_2HPO_4.*

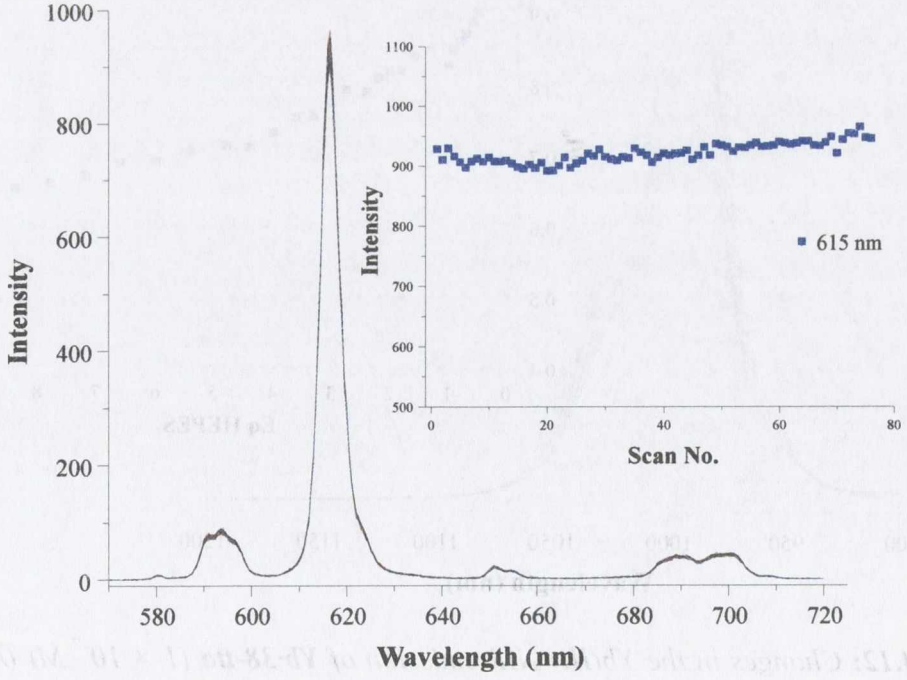


Figure A4.10: *Changes in the Eu(III) emission of* ***Eu·38-tta*** *(1×10^{-5} M) (λ_{ex} = 340 nm) over continual excitation. Inset: Changes in the emission intensity at 615 nm as a function of scans.*

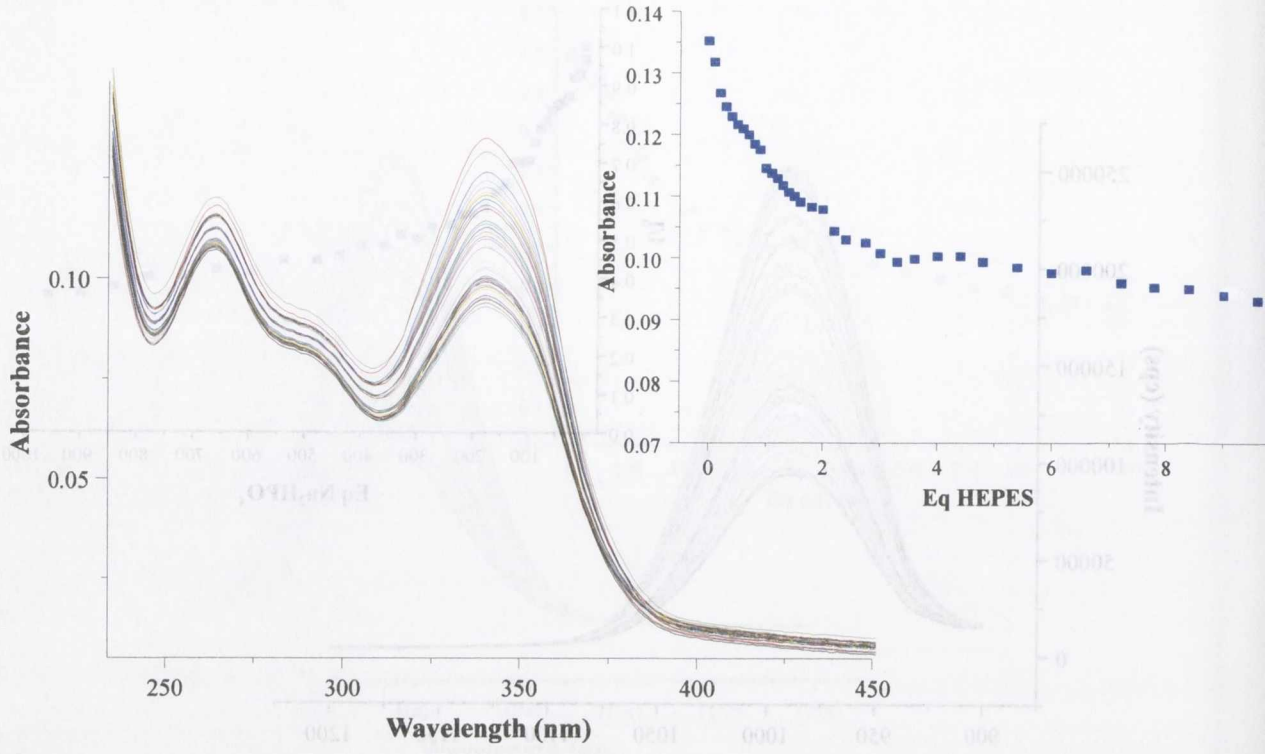


Figure A4.11: *Changes in the UV-vis absorption spectrum of* ***Yb·38-tta*** *(1×10^{-5} M) as a function of equivalents of HEPES added at pH 7.4 in 0.1 M HEPES. Inset: Changes in the absorbance at 340 nm as a function of equivalents of HEPES.*

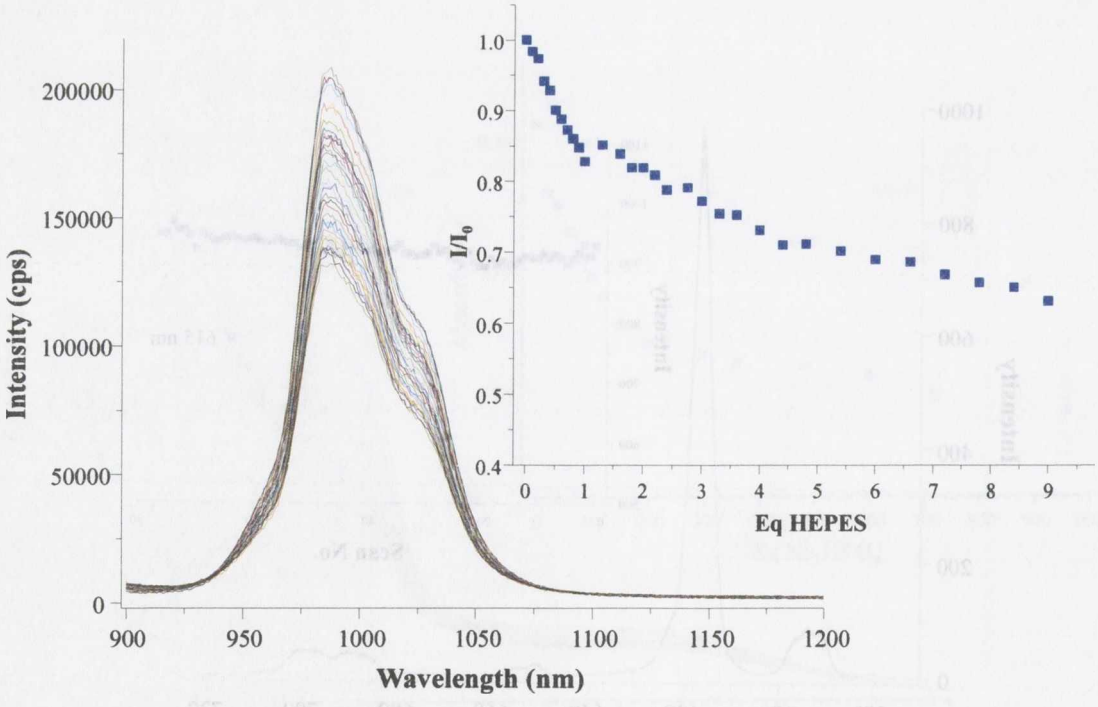


Figure A4.12: *Changes in the Yb(III) NIR emission of* ***Yb·38-tta*** *(1×10^{-7} M) (λ_{ex} = 340 nm) as a function of equivalents of HEPES added at pH 7.4 in 0.1 M HEPES. Inset: Changes in the normalised emission intensity (I/I_o) at 985 nm as a function of equivalents of HEPES.*

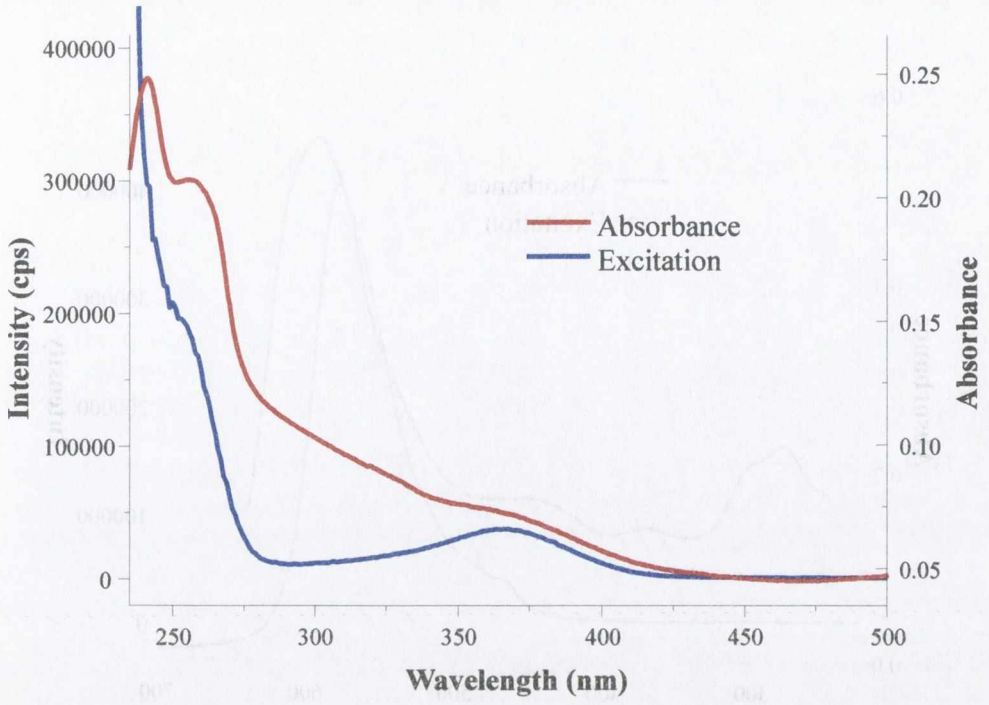


Figure A4.13: *Absorption and excitation (λ_{em} = 985 nm) spectra of* ***AuNP-Yb·38-8-HQS*** *at pH 7.4 in 0.1 M HEPES.*

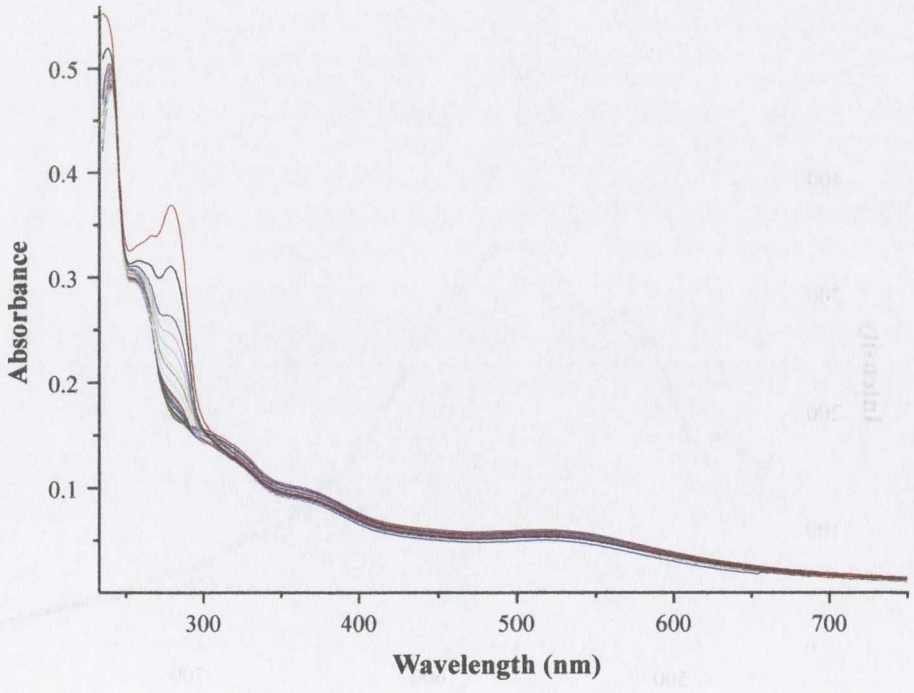


Figure A4.14: *Changes in the UV-vis absorption spectrum of* ***AuNP-Yb·38-8-HQS*** *(1×10^{-7} M) as a function of equivalents of dopamine added at pH 7.4 in 0.1 M HEPES.*

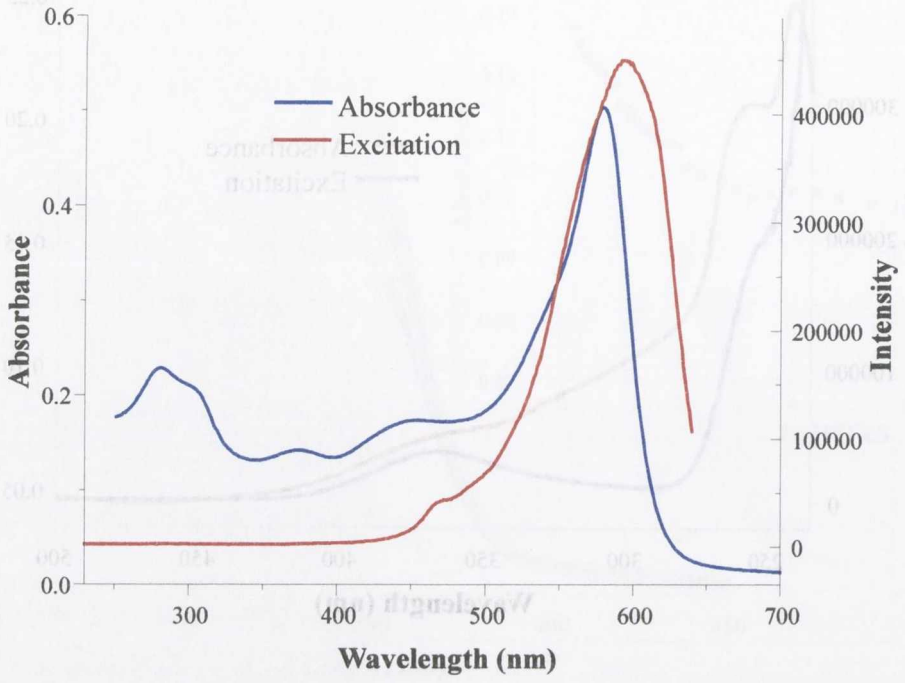


Figure A4.15: *Absorption and excitation (λ_{em} = 985 nm) spectra of* ***AuNP-Yb·38-XO*** *at pH 7.4 in 0.1 M HEPES.*

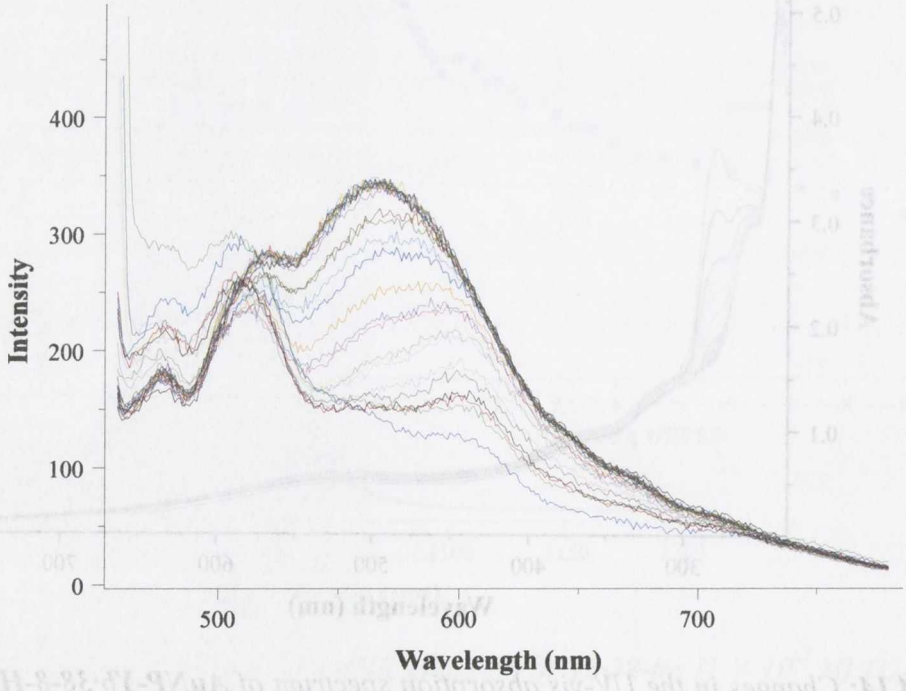


Figure A4.16: *Changes in the fluorescence spectrum of* ***XO*** *(ca. 1 × 10^{-5} M) (λ_{ex} = 435 nm) between pH 2-11 in 0.1 M NaCl.*

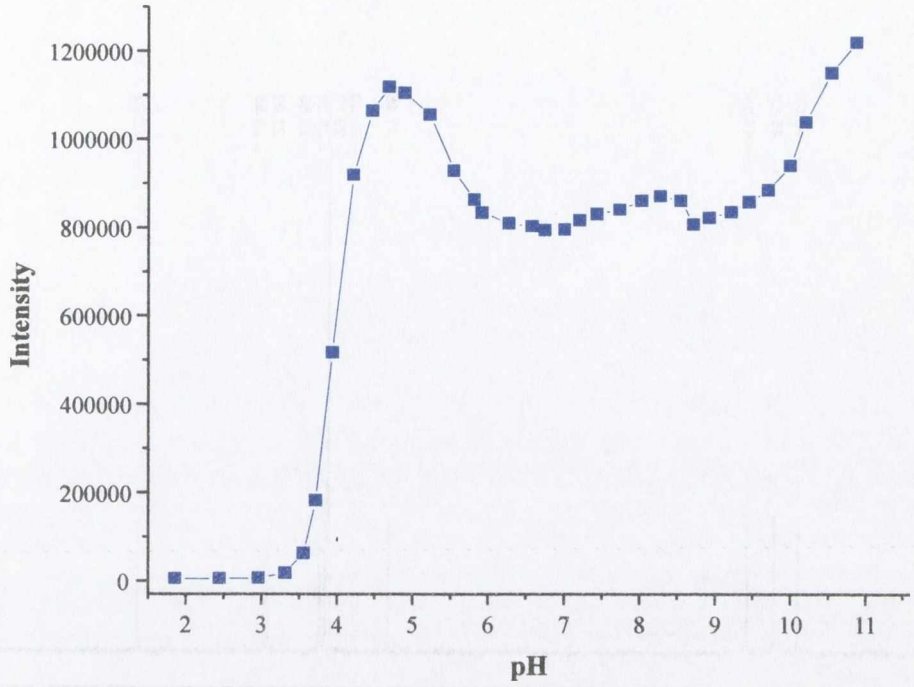


Figure A4.17: *Changes in the NIR emission intensity of* ***AuNP-Yb·38-XO*** *at 985 nm as a function of pH.*

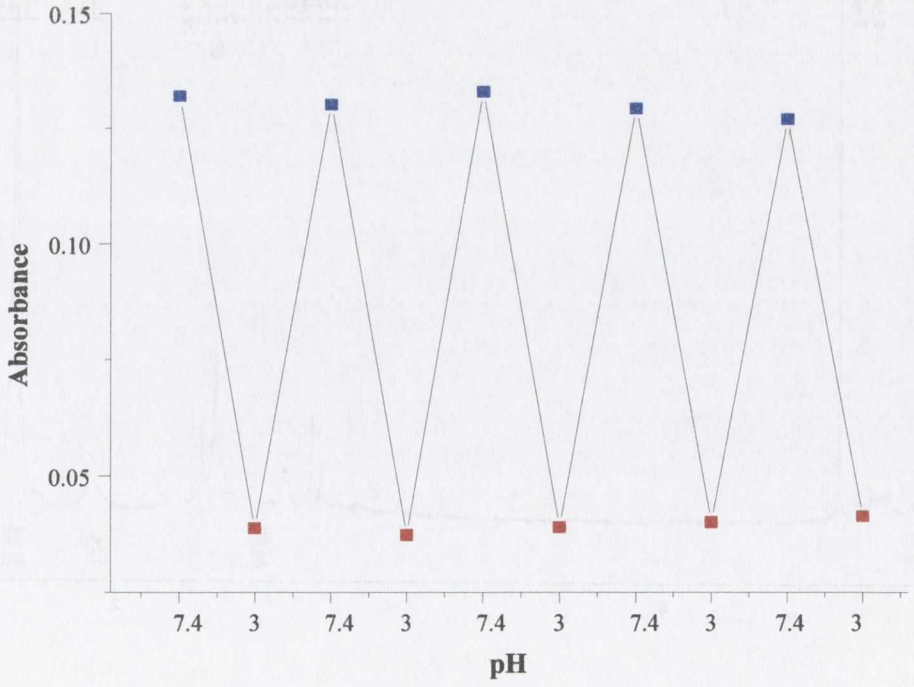


Figure A4.18: *Reversible changes in the absorbance of* ***AuNP-Yb·38-XO*** *at 580 nm between pH 3 and 7.4.*

Appendix 5

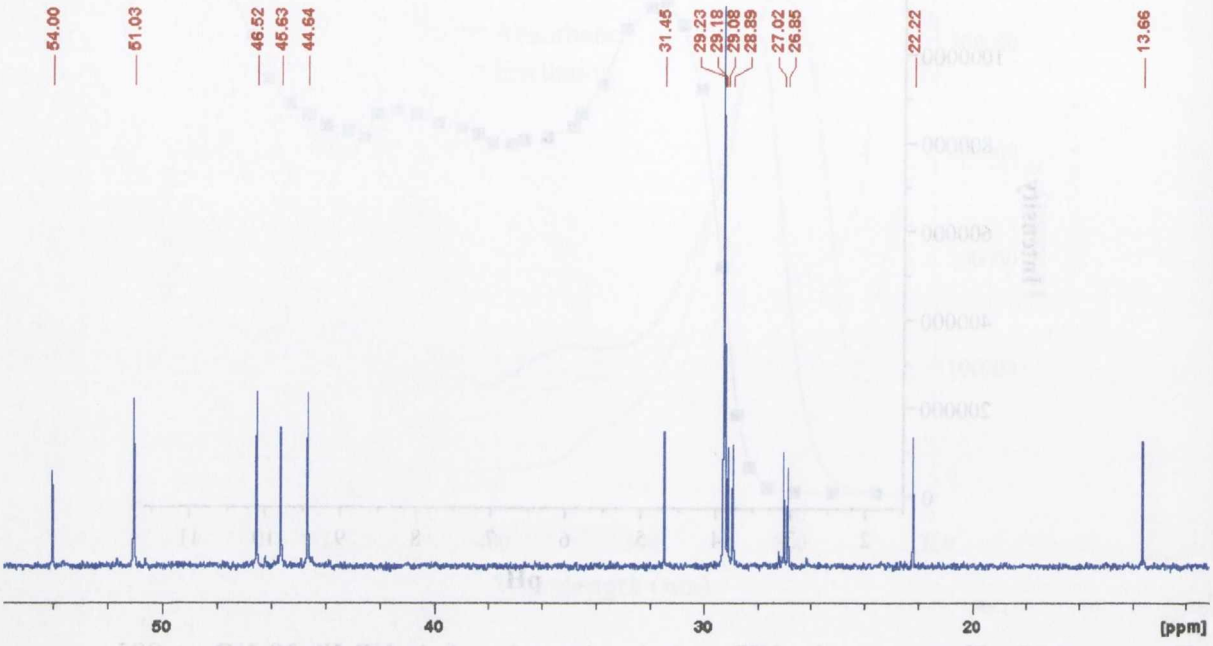


Figure A5.1: *The ^{13}C NMR spectrum (150 MHz, $CDCl_3$) of* ***60c****.*

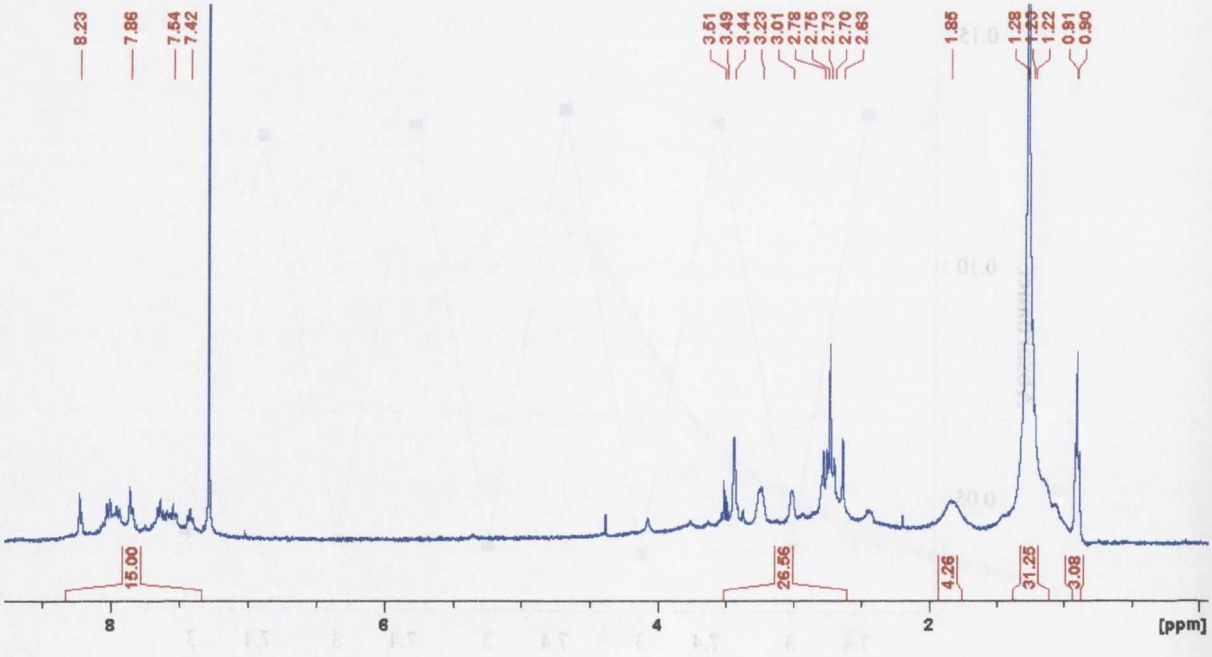


Figure A5.2: *The ^{1}H NMR spectrum (400 MHz, $CDCl_3$) of ligand* ***94****.*

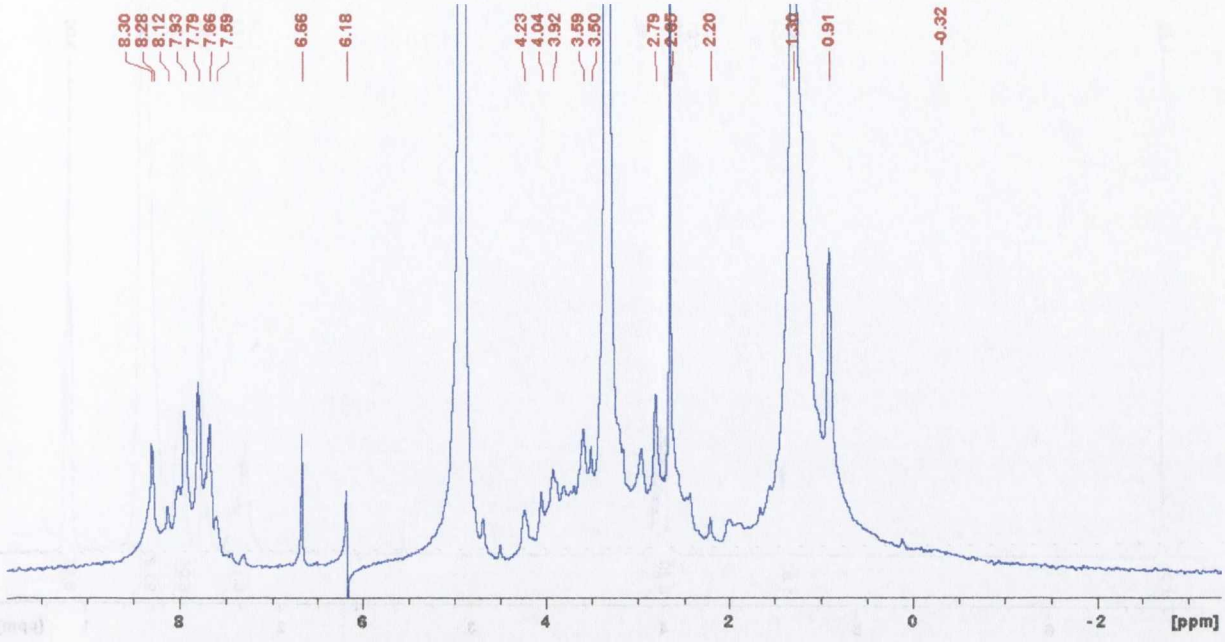


Figure A5.3: *The ^{1}H NMR spectrum (400 MHz, CD_3CN) of complex* ***Eu·94****.*

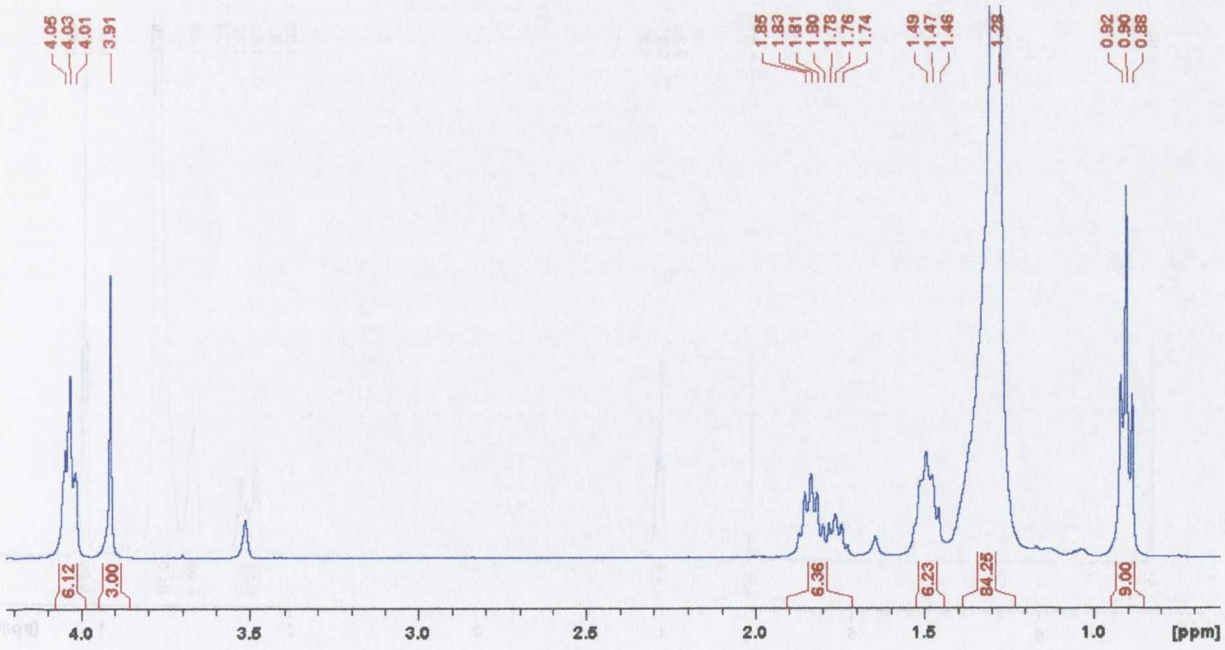


Figure A5.4: *The ^{1}H NMR spectrum (400 MHz, CD_3Cl) of* ***97****.*

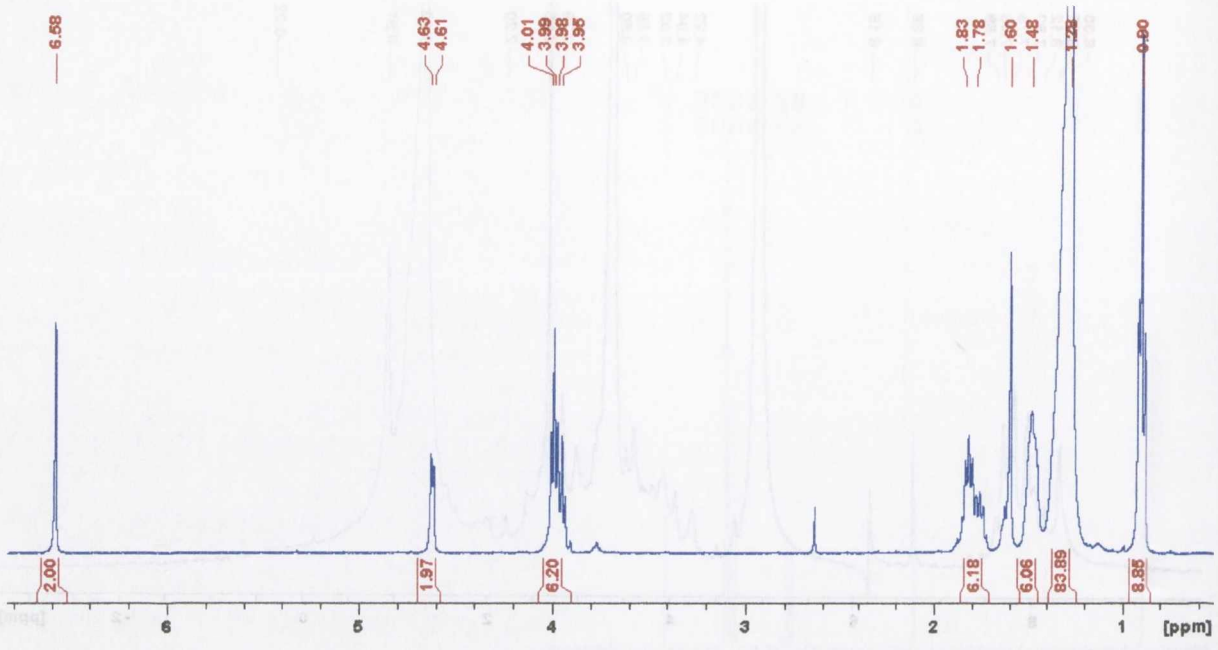


Figure A5.5: *The ^{1}H NMR spectrum (400 MHz, CD_3Cl) of* ***98****.*

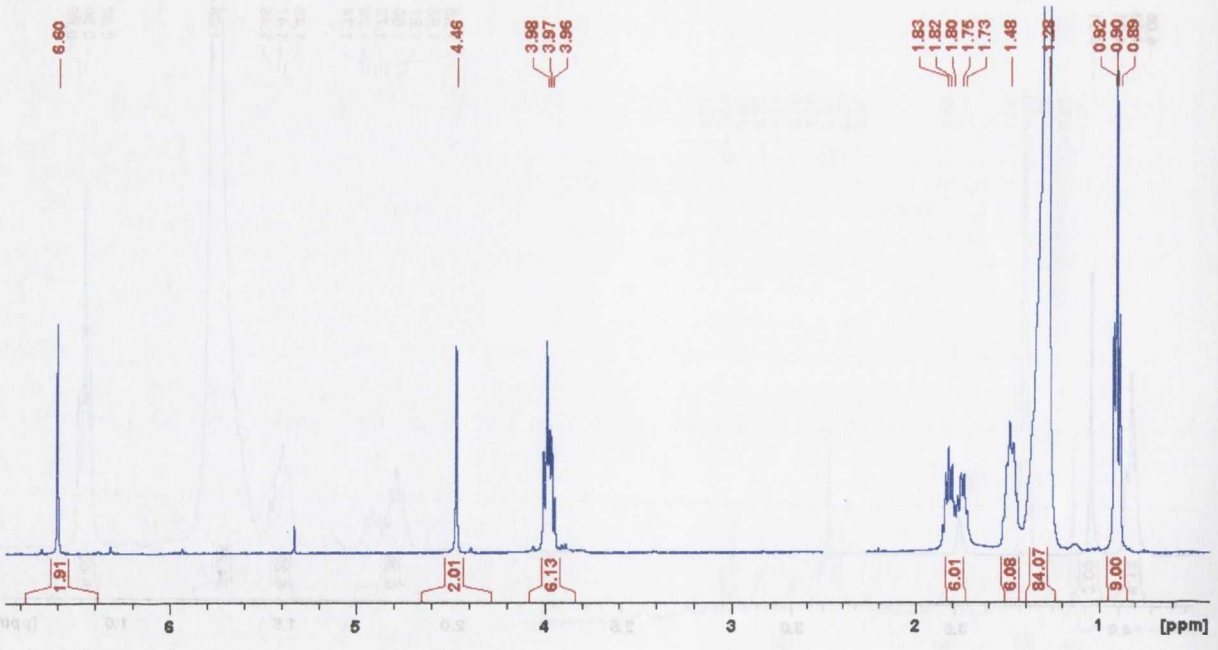


Figure A5.6: *The ^{1}H NMR spectrum (400 MHz, CD_3Cl) of* ***99****.*

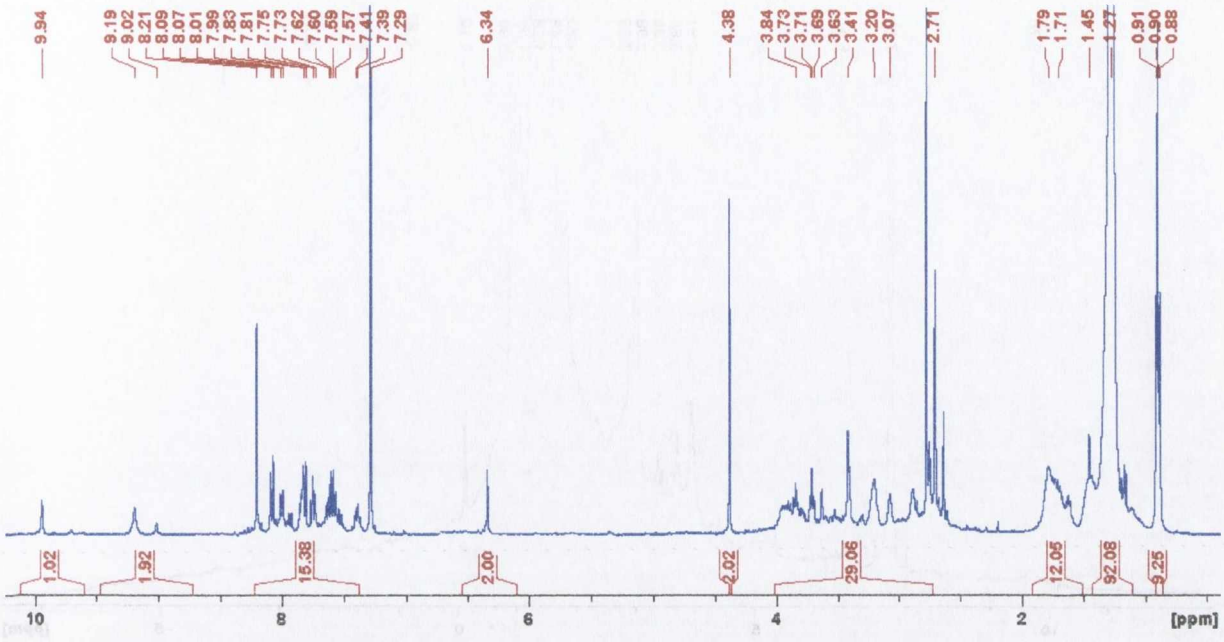


Figure A5.7: *The ^{1}H NMR spectrum (400 MHz, CD_3Cl) of ligand* ***95****.*

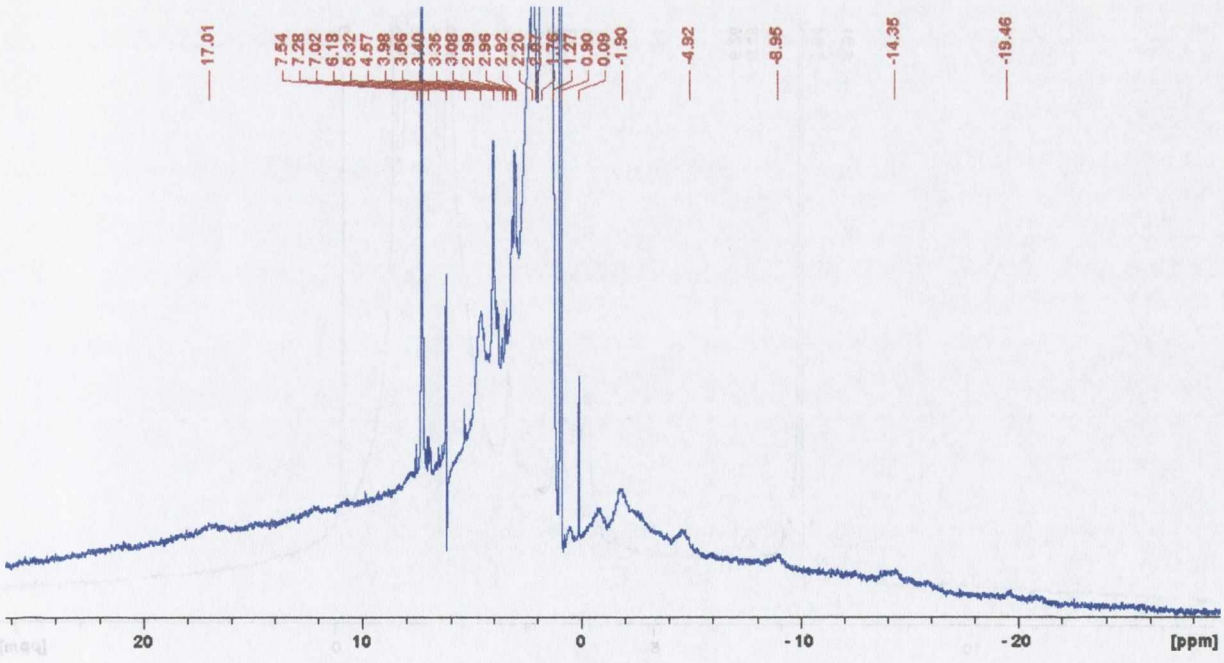


Figure A5.8: *The ^{1}H NMR spectrum (400 MHz, CD_3CN) of complex* ***Eu·95****.*

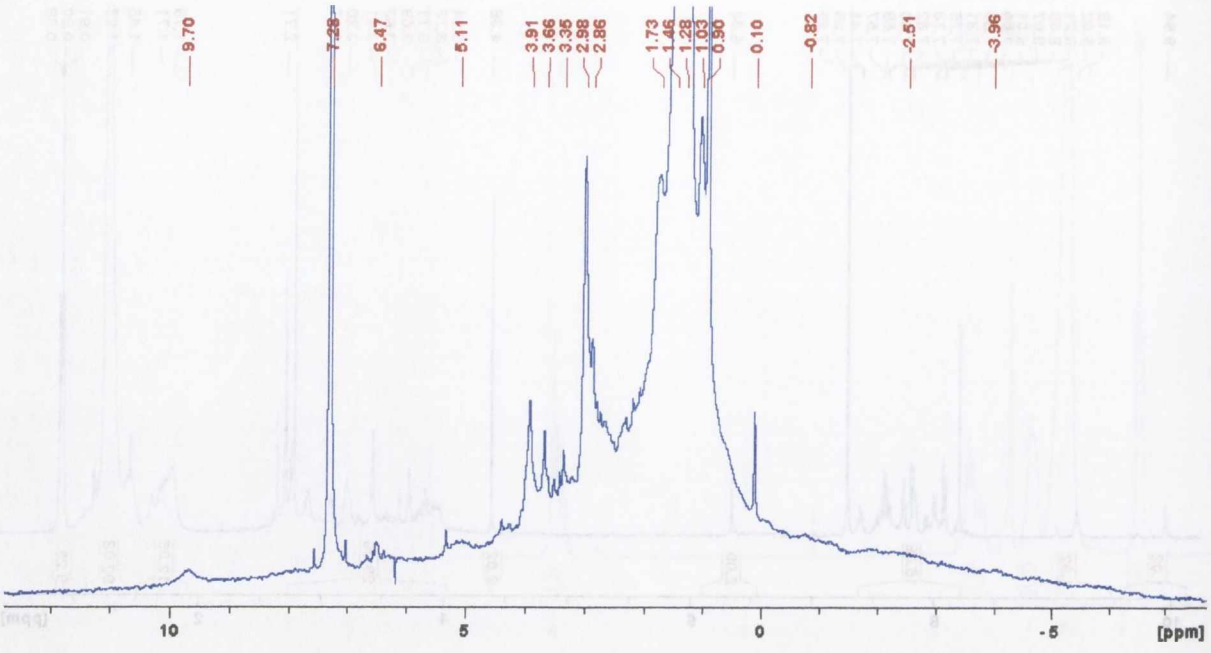


Figure A5.9: *The ^{1}H NMR spectrum (400 MHz, CD_3CN) of complex* ***Tb·95****.*

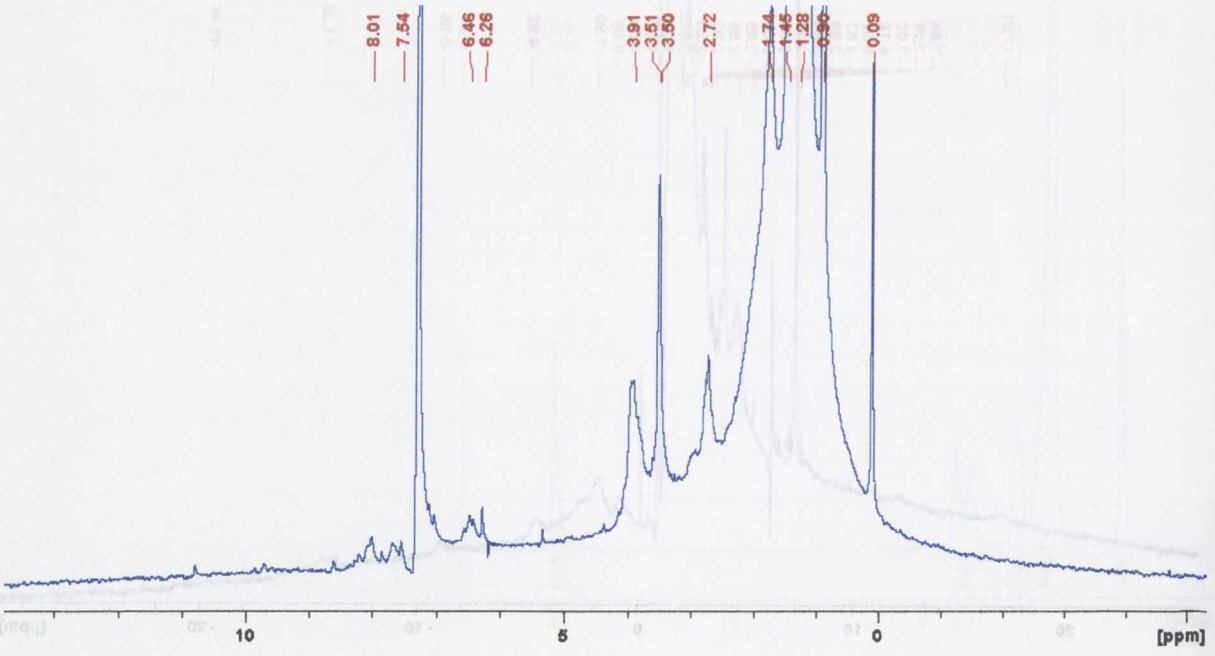


Figure A5.10: *The ^{1}H NMR spectrum (400 MHz, CD_3CN) of complex* ***Eu·96****.*

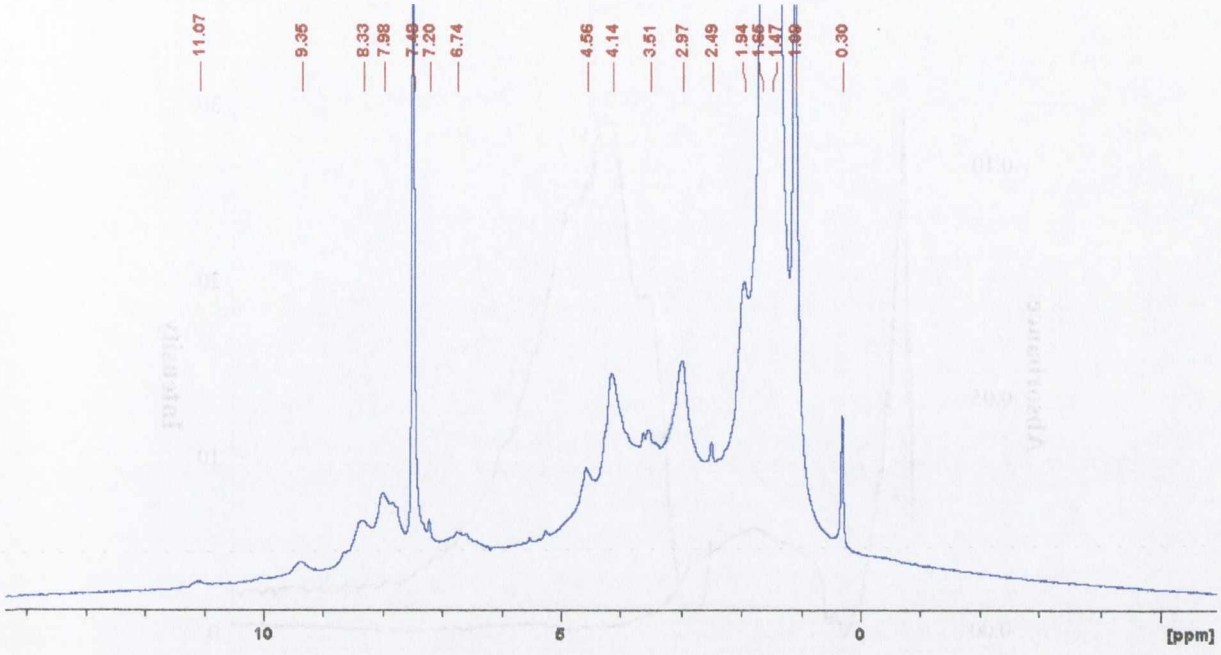


Figure A5.11: *The ^{1}H NMR spectrum (400 MHz, CD_3CN) of complex* ***Tb·96****.*

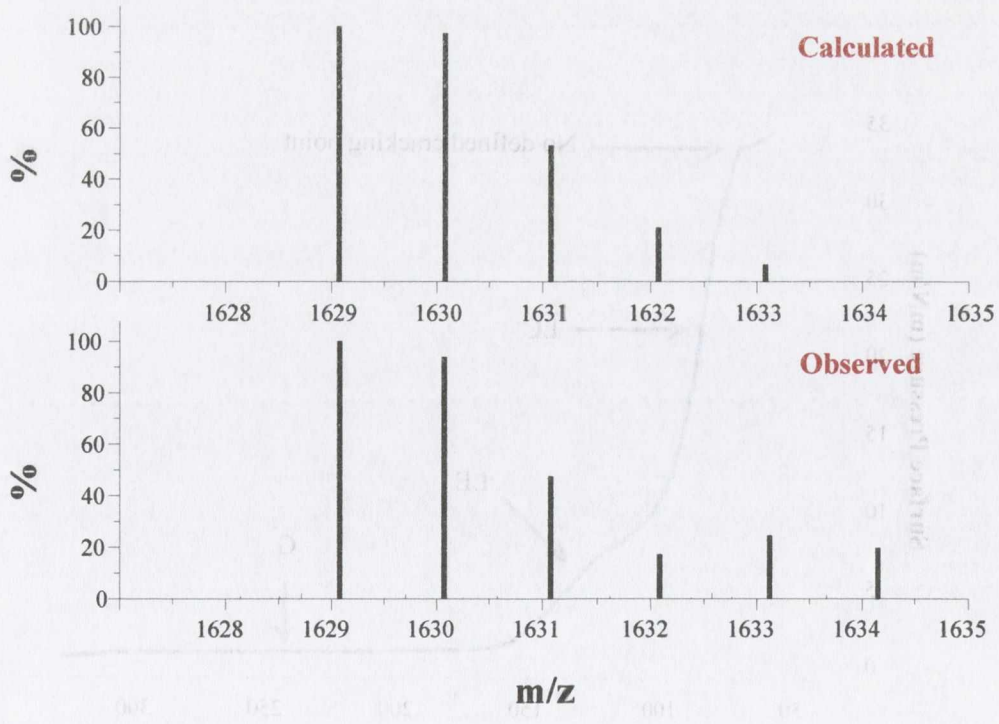


Figure A5.12: *The MALDI mass spectrum of* ***Tb·95*** *displaying the expected Tb(III) isotopic distribution pattern for the [****Tb·95*** *+ CF_3SO_3]$^{2+}$ species.*

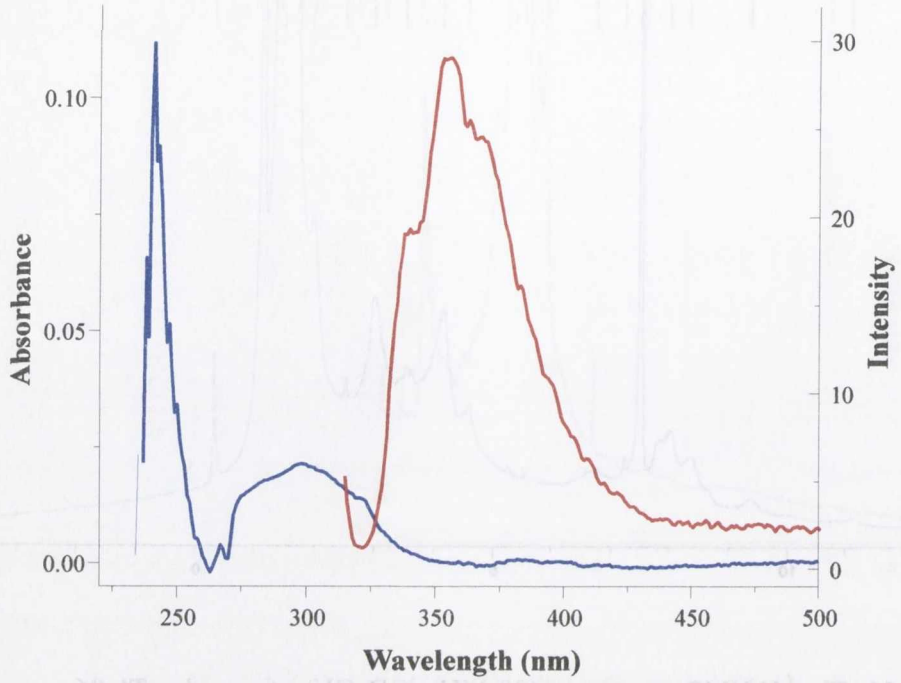


Figure A5.13: *The UV-vis absorption (-) and fluorescence (-) emission spectra (λ_{ex} = 305 nm) of* ***Eu·95*** *in $CHCl_3$ solution (2.6×10^{-6} M).*

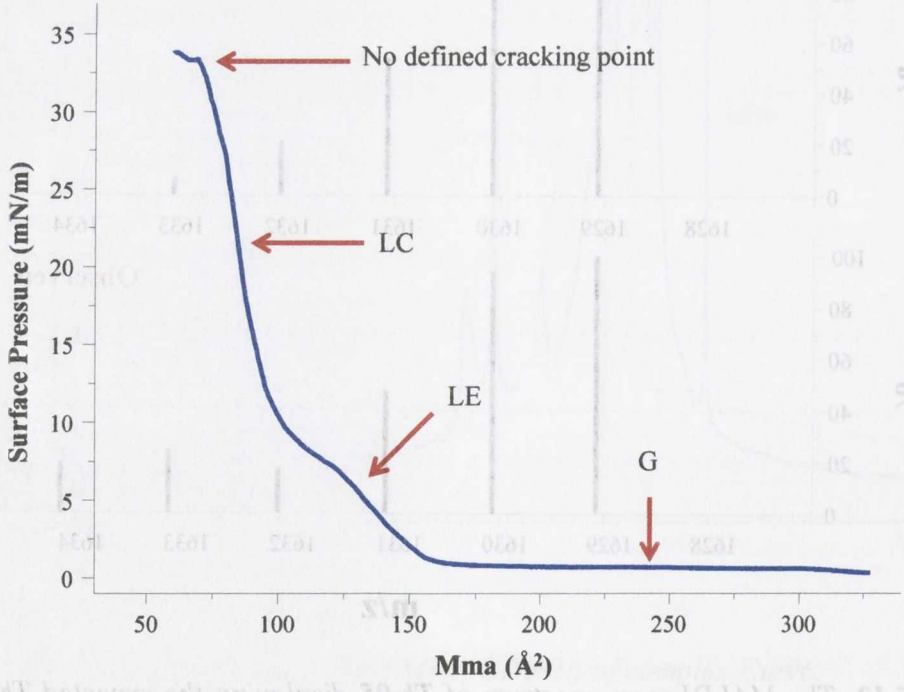


Figure A5.14: *Surface pressure-area isotherm of* ***Tb·95*** *indicating phase transitions but no defined collapsing point.*

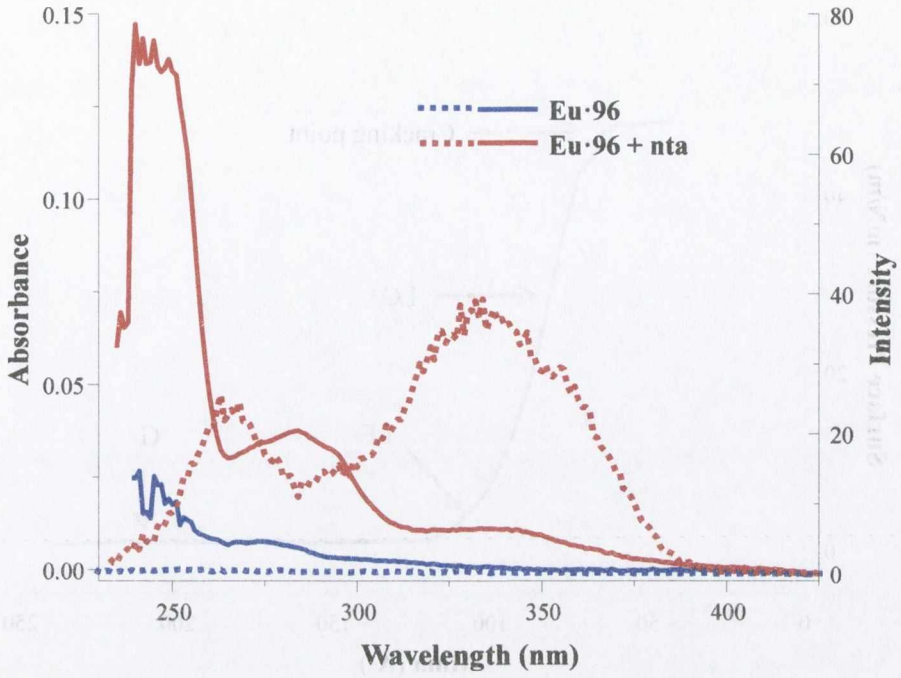


Figure A5.15: *The UV-vis absorption (solid lines) and excitation spectra (λ_{em} = 615 nm) (dashed lines) of* ***Eu·96*** *in the absence (-) and presence (-) of one equivalent of the antenna* ***nta*** *$CHCl_3$ solution (2.6×10^{-6} M).*

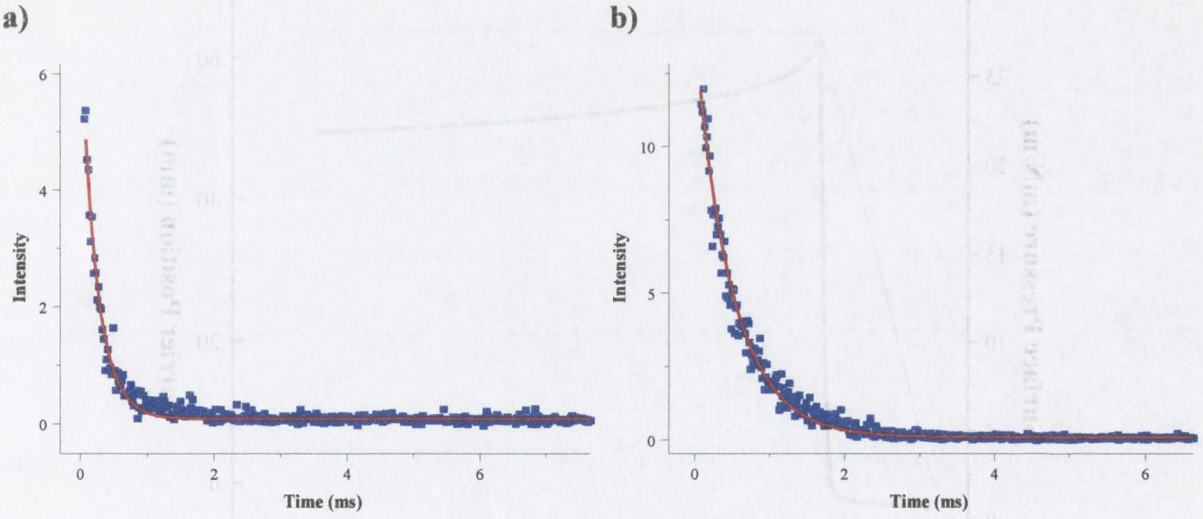


Figure A5. 16: *Luminescence decay fit to monoexponential of* ***a) Eu·96*** *and* ***b) Eu·96-nta*** *in $CHCl_3$ solution (λ_{ex} = 330 nm).*

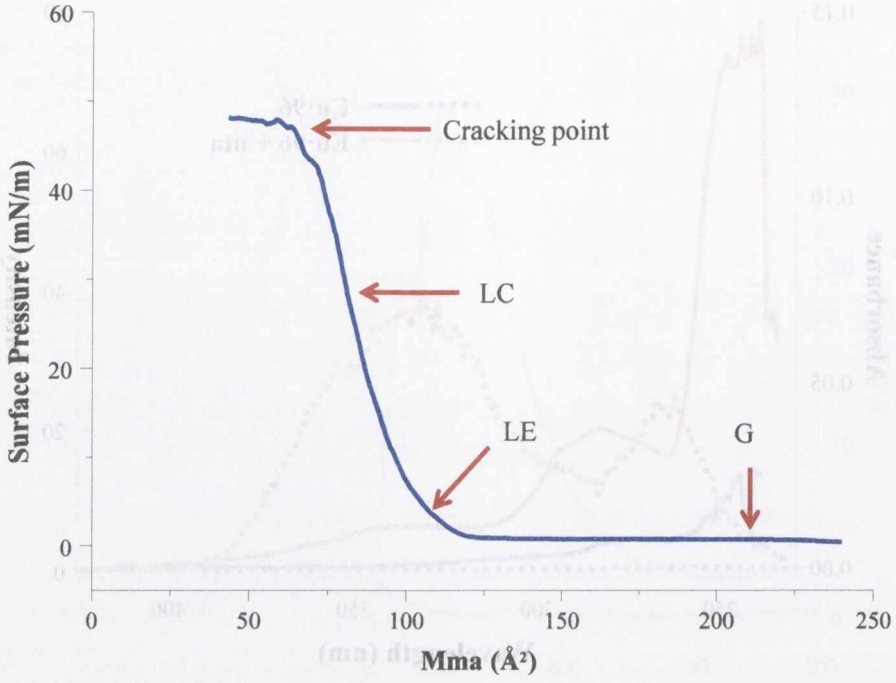


Figure A5. 17: *Surface pressure-area isotherm of* ***Tb·96*** *indicating phase transitions and a cracking point.*

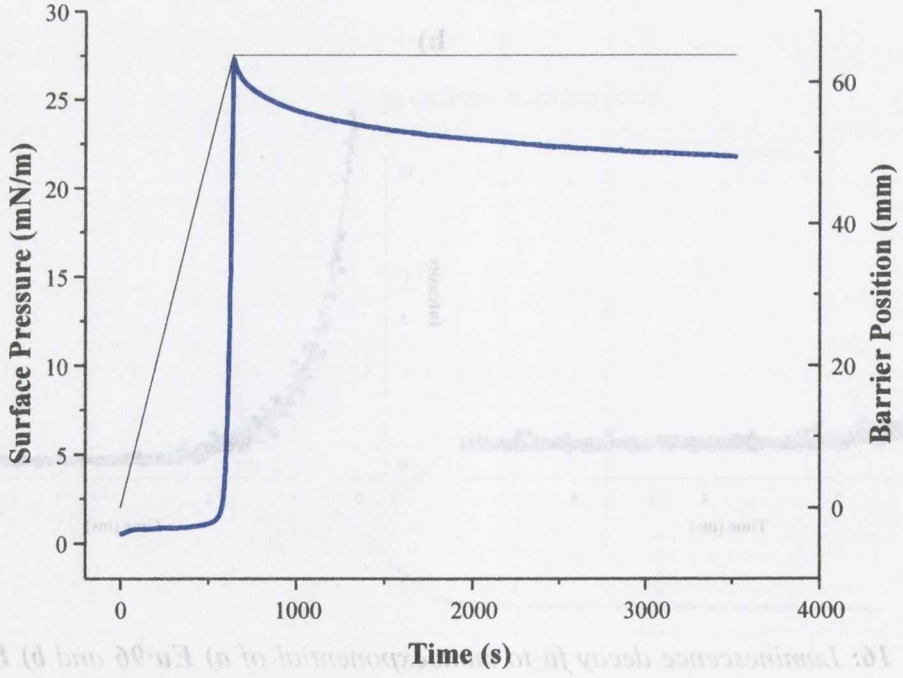


Figure A5. 18: *Langmuir monolayer stability graph of* ***Tb·96****.*

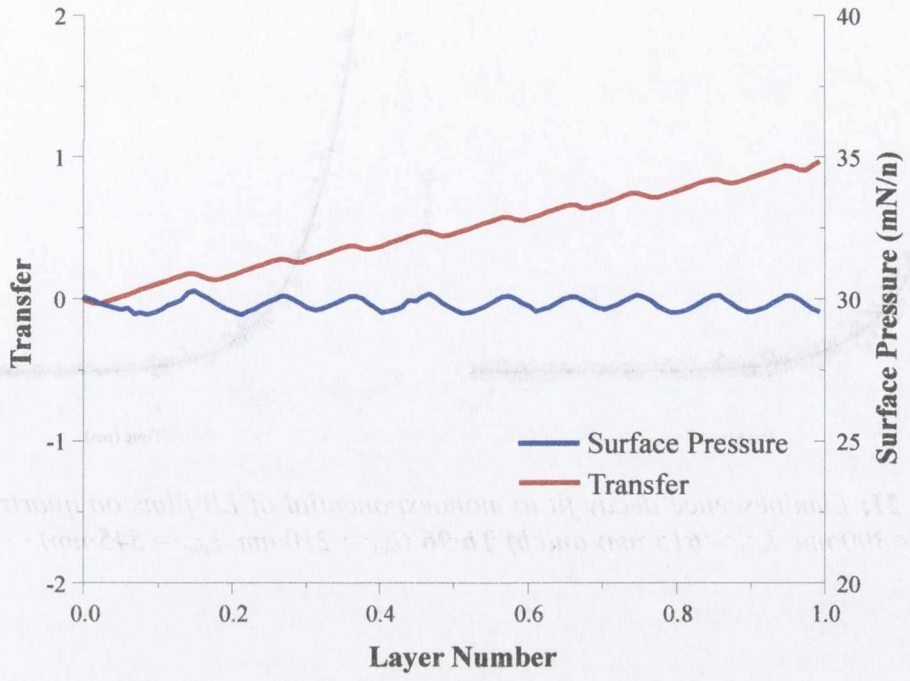


Figure A5. 19: *Langmuir monolayer deposition graph of* ***Tb·96****.*

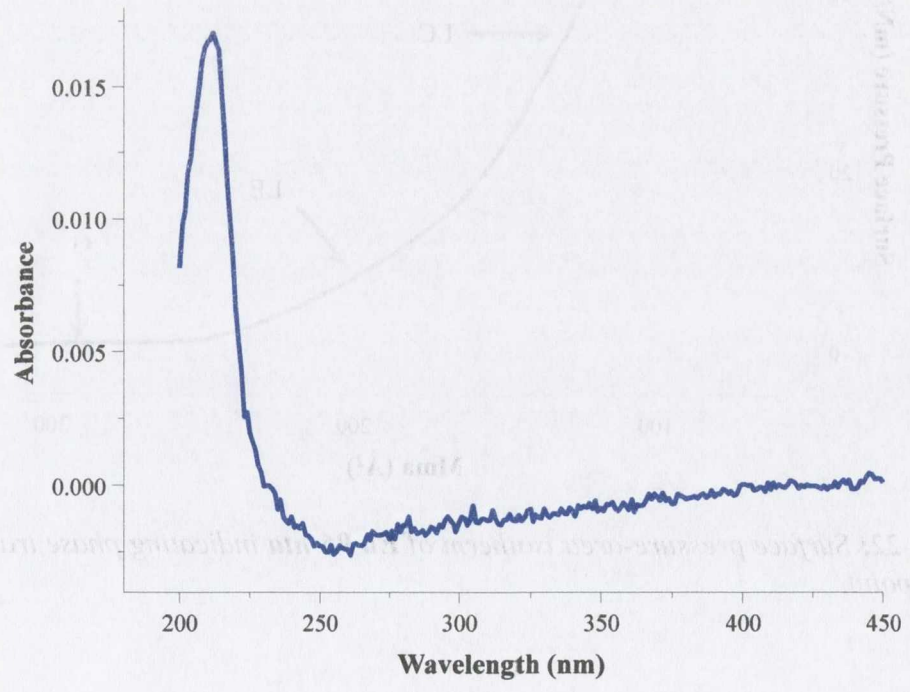


Figure A5. 20: *The UV-vis absorption spectra of the LB film of* ***Tb·96*** *on a quartz slide.*

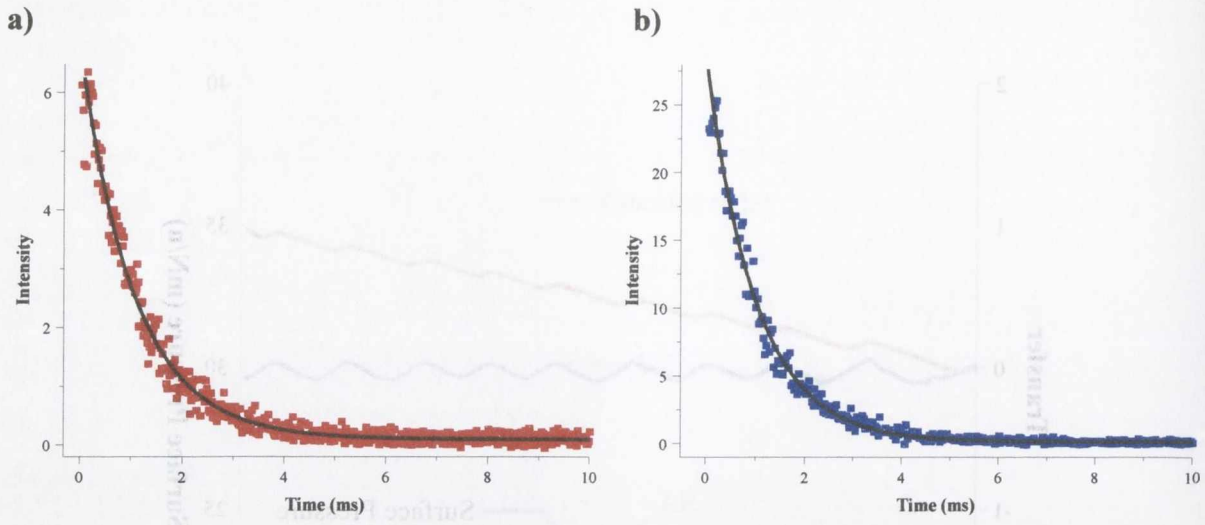


Figure A5. 21: *Luminescence decay fit to monoexponential of LB films on quartz slides of* ***a) Eu·96*** *(λ_{ex} = 300 nm, λ_{em} = 615 nm) and* ***b) Tb·96*** *(λ_{ex} = 210 nm, λ_{em} = 545 nm).*

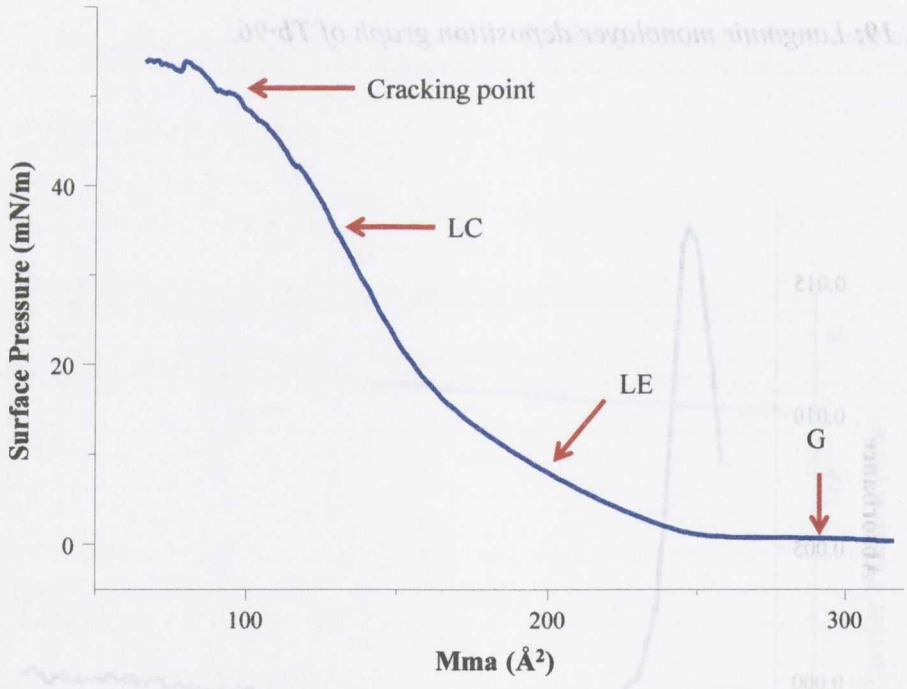


Figure A5. 22: *Surface pressure-area isotherm of* ***Eu·96-nta*** *indicating phase transitions and a cracking point.*

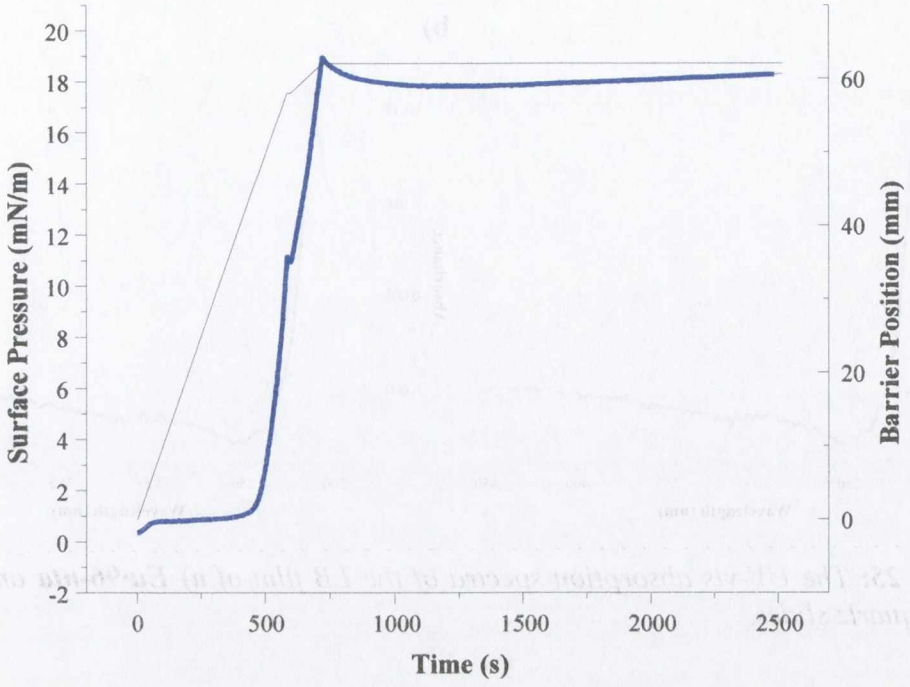


Figure A5. 23: *Langmuir monolayer stability graph of* ***Tb·96-DMAB****.*

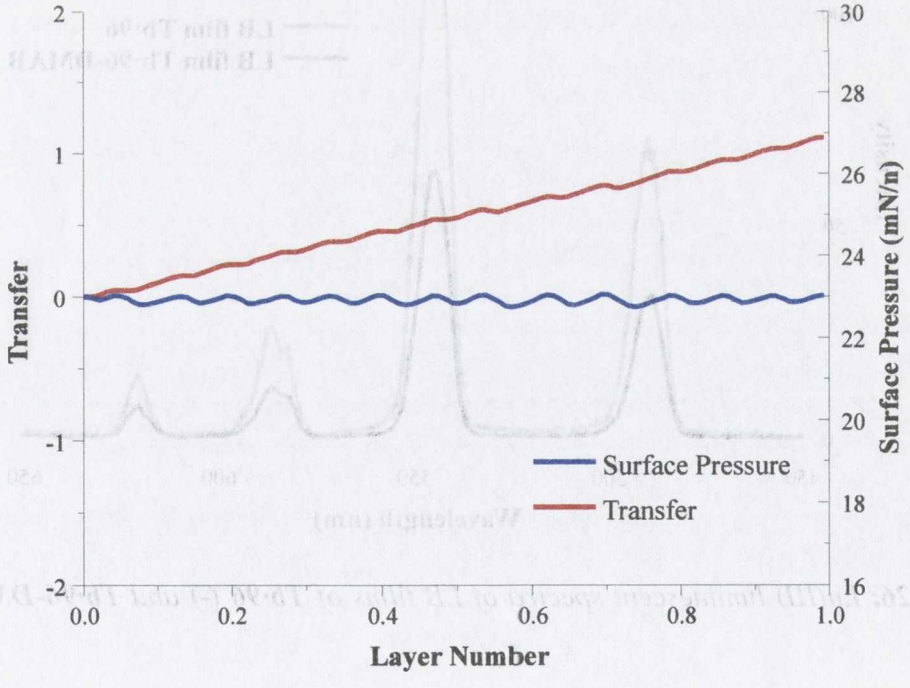


Figure A5. 24: *Langmuir monolayer deposition graph of* ***Tb·96-DMAB****.*

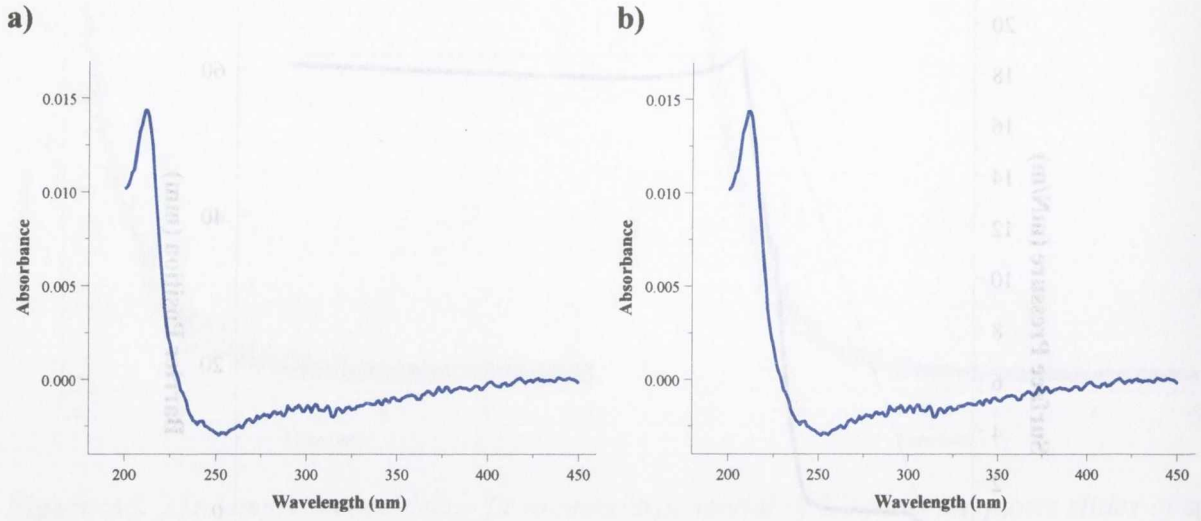


Figure A5. 25: *The UV-vis absorption spectra of the LB film of* ***a) Eu·96-nta*** *and* ***b) Tb·96-DMAB*** *on quartz slides.*

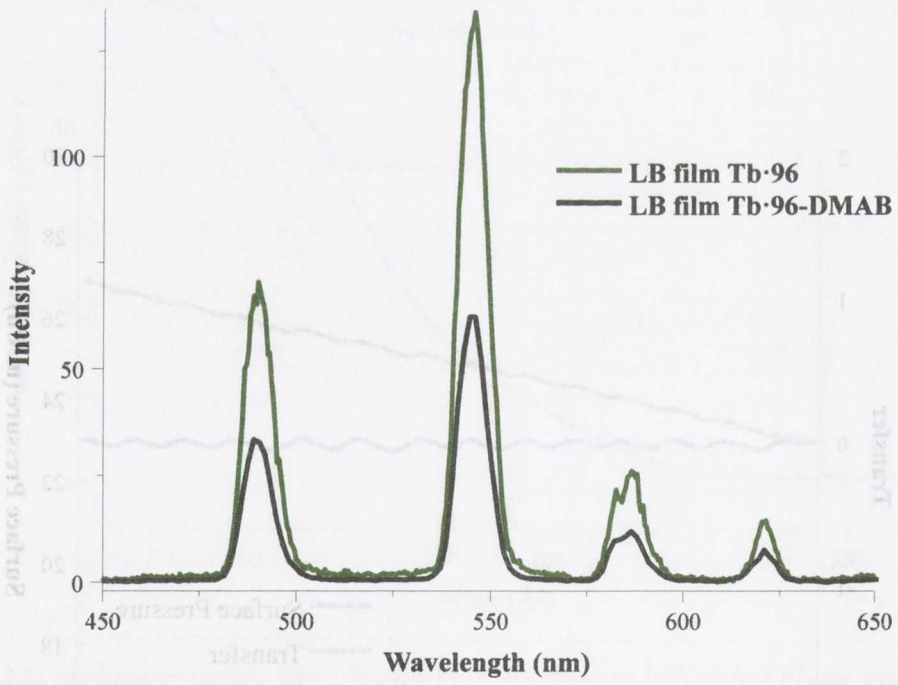


Figure A5.26: *Ln(III) luminescent spectra of LB films of* ***Tb·96*** *(-) and* ***Tb·96-DMAB*** *(-) (λ_{ex} = 220 nm).*

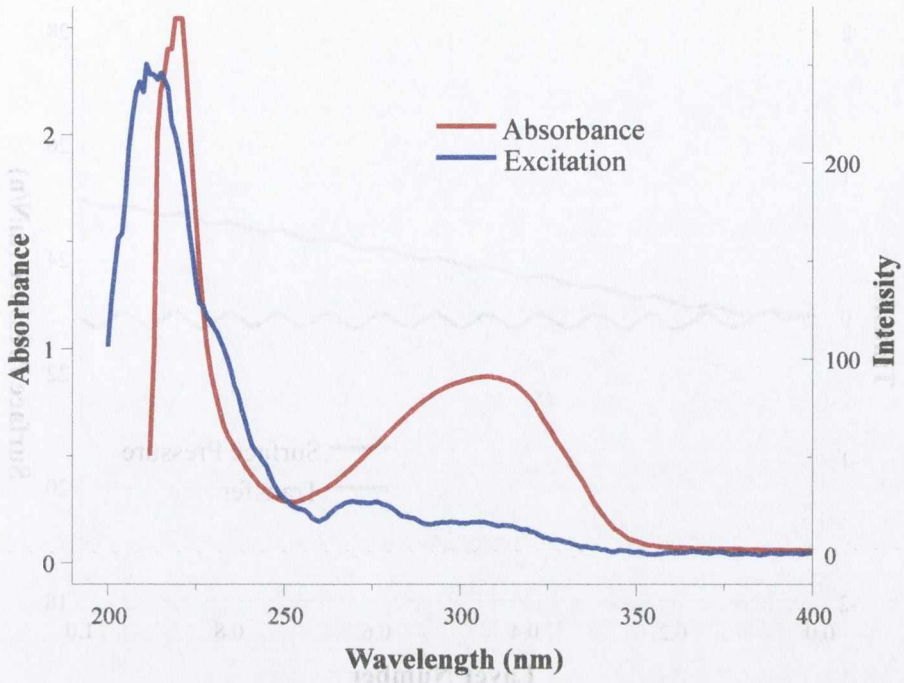


Figure A5.27: *The UV-vis absorption (-) of a solution of* ***DMAB*** *and excitation (λ_{em} = 545 nm) (-) spectra of the LB film of* ***Tb·96-DMAB****.*

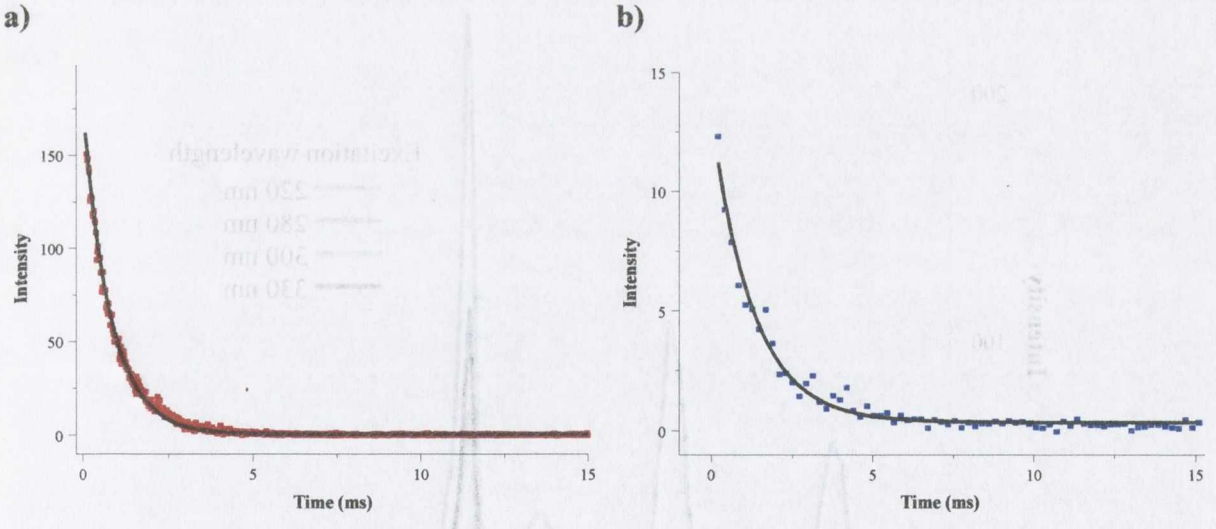


Figure A5.28: *Luminescence decay fit to monoexponential of LB films on quartz slides of* ***a) Eu·96-nta*** *(λ_{ex} = 330 nm, λ_{em} = 615 nm) and* ***b) Tb·96-DMAB*** *(λ_{ex} = 220 nm, λ_{em} = 545 nm).*

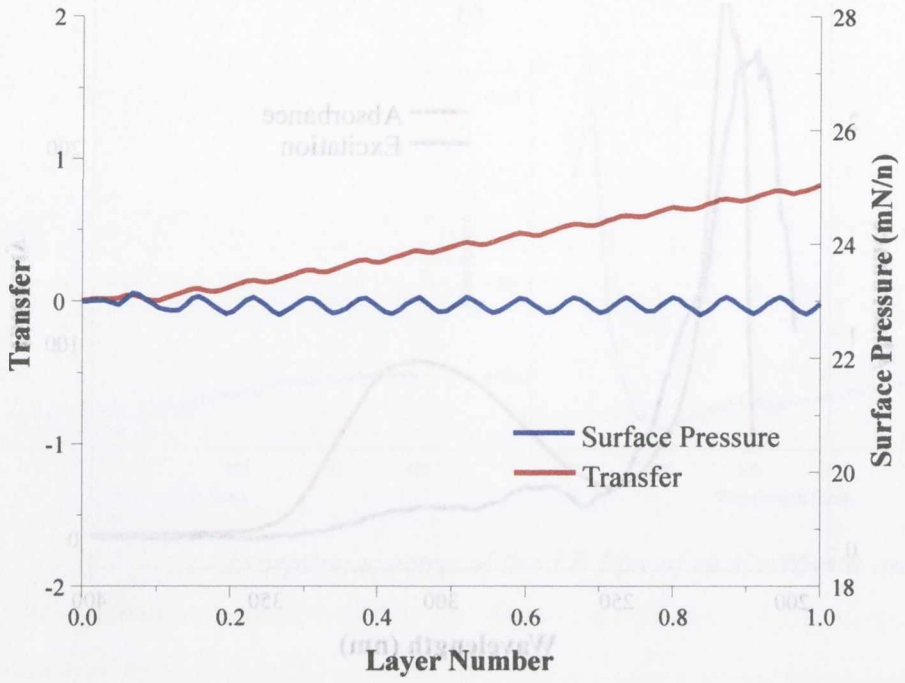


Figure A5.29: *Langmuir monolayer deposition graph of* ***Eu·96-nta*** *on top of a monolayer of* ***Tb·96-DMAB*** *on a quartz slide.*

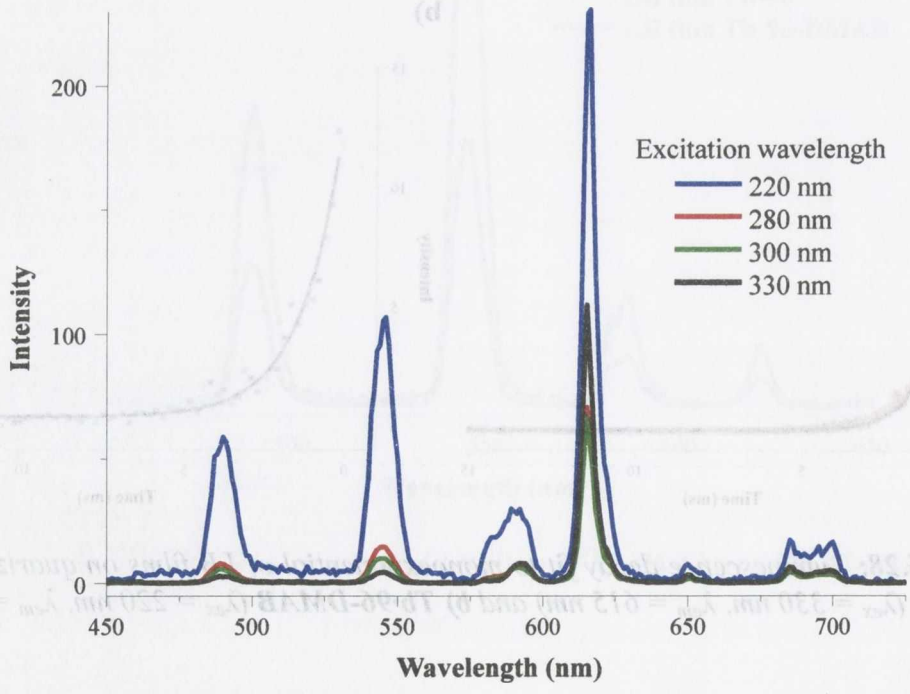


Figure A5.30: *Ln(III) luminescent spectra of LB film of* ***Eu·96-nta-Tb·96-DMAB*** *using different excitation wavelengths.*

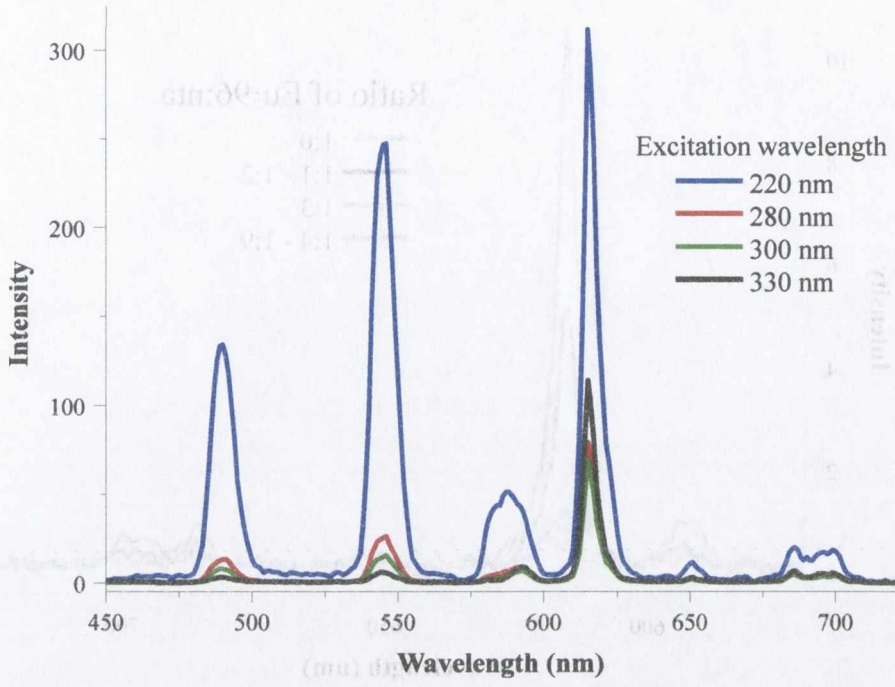


Figure A5.31: *Ln(III) luminescent spectra of LB film of* ***Tb·96-DMAB-Eu·96-nta*** *using different excitation wavelengths.*

Want to know concentration/number of moles of **Eu·96** on a slide.

From isotherm the surface pressure at which slide is dipped is 23 mN/m and corresponds to an area of 90.23 $Å^2$.

Area of 1 **Eu·96** = 90.23 $Å^2$

1 Å = 10^{-10} m

1 $Å^2$ = 10^{-20} m^2

1 $Å^2$ = 10^{-14} mm^2

90.23 $Å^2$ = 90.23 × 10^{-14} mm^2

Total area covered on slide = 100 mm^2

100 mm^2/90.23 × 10^{-14} mm^2 = 1.108 × 10^{14} molecules

Two sides of slide covered

(1.108 × 10^{14}) × 2 = 2.216 × 10^{14} molecules

Conc = Number molecules/Avogadro's number

Conc **Eu·96** on slide = 2.216 × 10^{14}/6.022 × 10^{23}

= $\underline{3.68 \times 10^{-10}\ \text{moles}}$

Equation A5.1: *Determining the concentration of a LB film of* ***Eu·96****.*

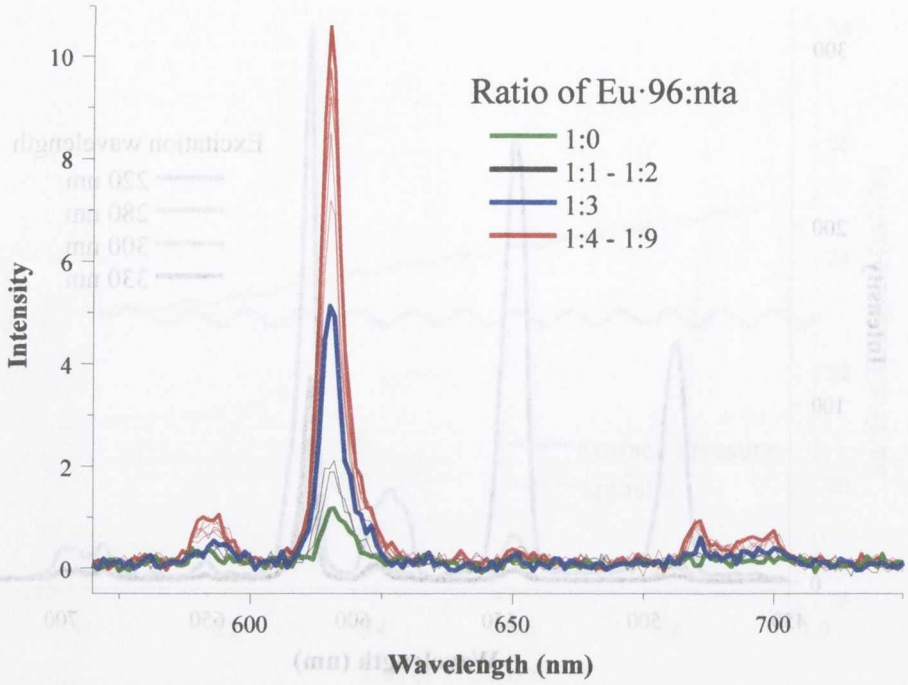


Figure A5.32: *LOD study of LB film of* ***Eu·96*** *using different concentrations of* ***nta*** *solution (λ_{ex} = 330 nm).*

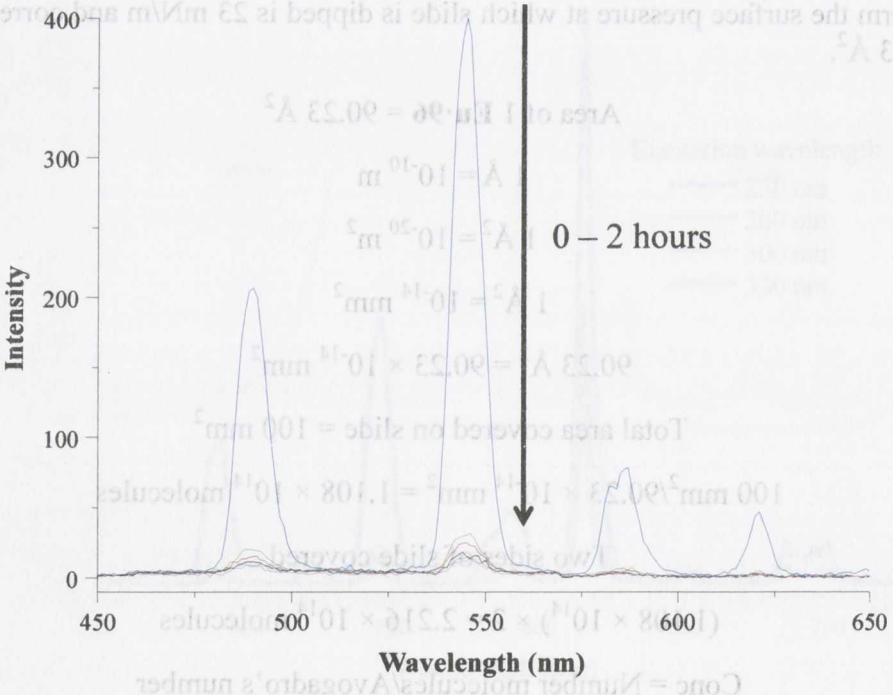


Figure A5.33: *Flow study of LB film of* ***Tb·96*** *(λ_{ex} = 220 nm) over 2 hours.*

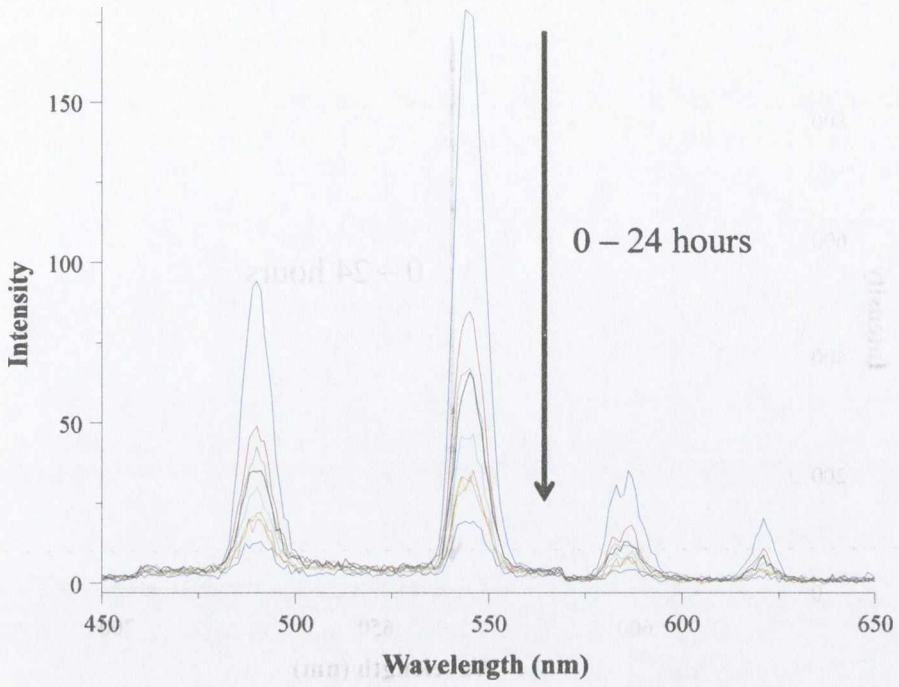


Figure A5.34: *Flow study of LB film of* ***Tb·96-DMAB*** *(λ_{ex} = 220 nm) over 24 hours.*

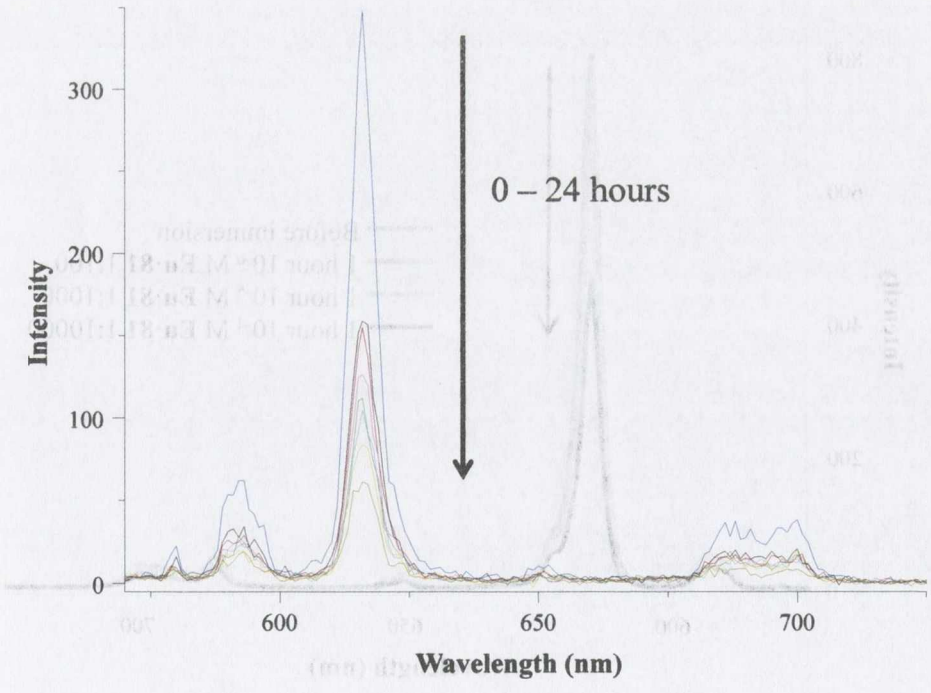


Figure A5.35: *Flow study of LB film of* ***Eu·96*** *(λ_{ex} = 220 nm) over 24 hours.*

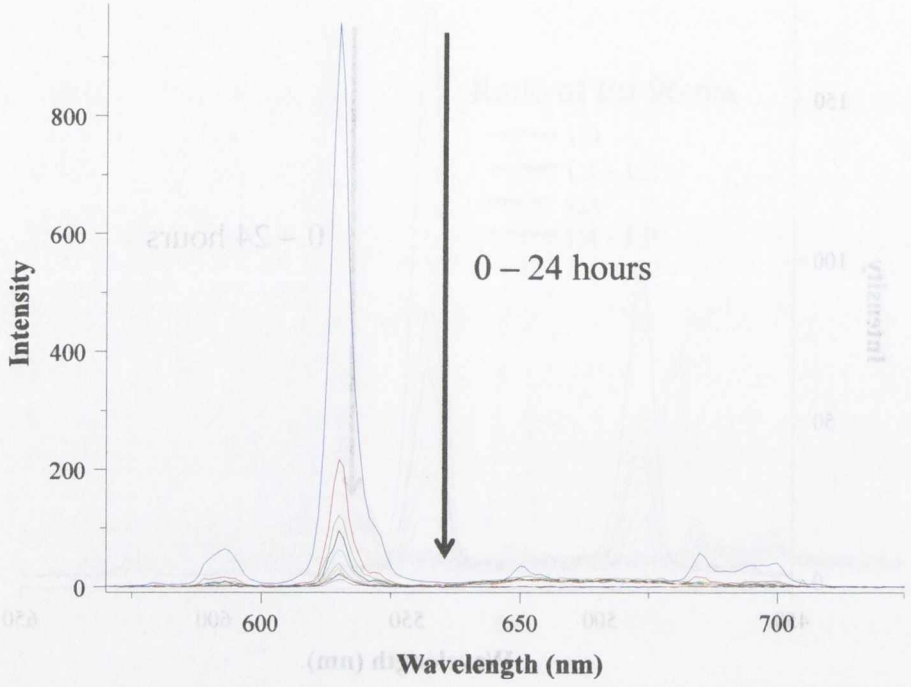


Figure A5.36: *Flow study of LB film of* ***Eu·96-nta*** *(λ_{ex} = 330 nm) over 24 hours.*

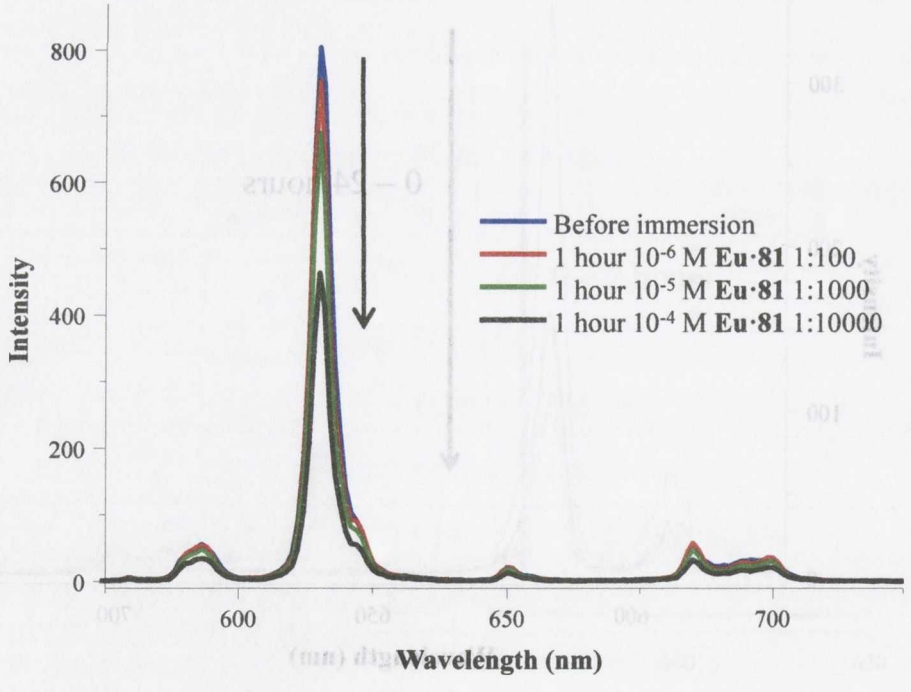


Figure A5.37: *Scavenger test Eu(III) emission of LB film of* ***Eu·96-nta*** *(λ_{ex} = 330 nm) showing decrease in Eu(III) emission upon immersion in solutions of* ***Eu·81****.*

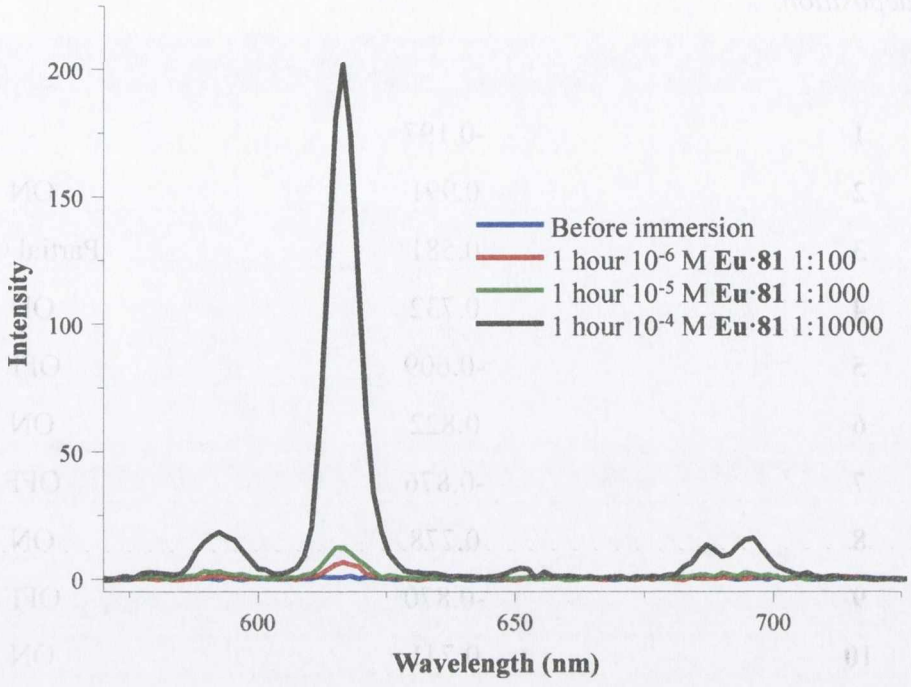


Figure A5.38: *Scavenger test Eu(III) emission of solution of* ***Eu·81*** *(λ_{ex} = 330 nm) showing increase in Eu(III) emission upon immersion of LB film of* ***Eu·96-nta****.*

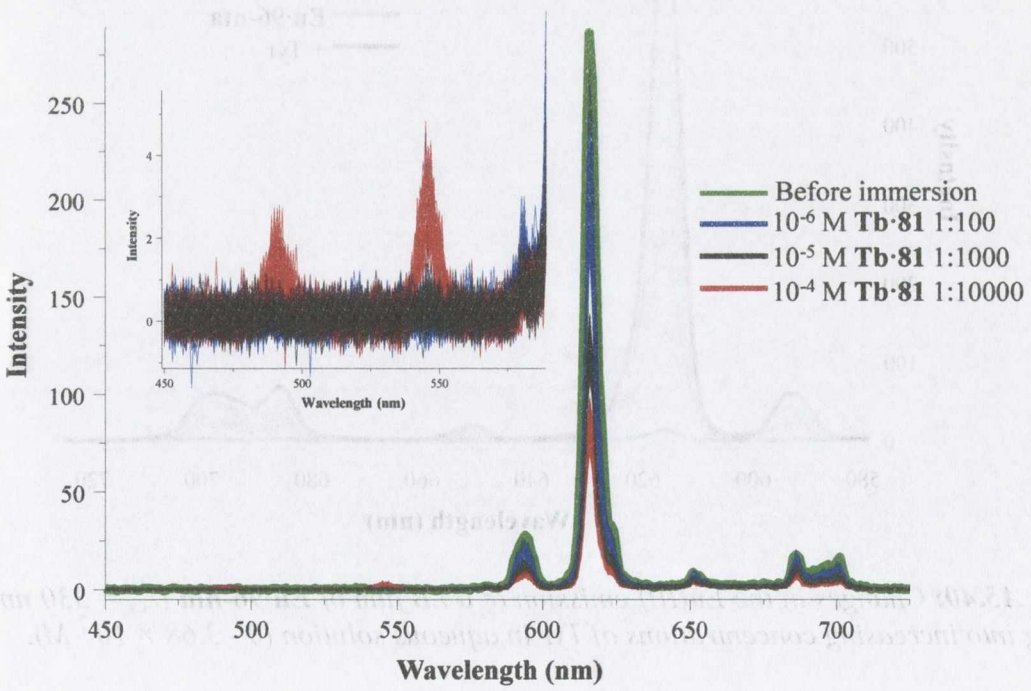


Figure A5.39: *Scavenger test Eu(III) and Tb(III) emission of solution of the cuvette containing both the LB film* ***Eu·96-nta*** *and the solutions of* ***Tb·81*** *(λ_{ex} = 330 nm).*

Table A5.1: *Multilayer deposition of* ***Eu·96*** *onto quartz solid support showing transfer ratio after each deposition.*

Layer Number	TR	Film ON/OFF
1	-0.197	-
2	0.991	ON
3	0.581	Partial ON
4	0.732	ON
5	-0.609	OFF
6	0.822	ON
7	-0.876	OFF
8	0.778	ON
9	-0.870	OFF
10	0.741	ON

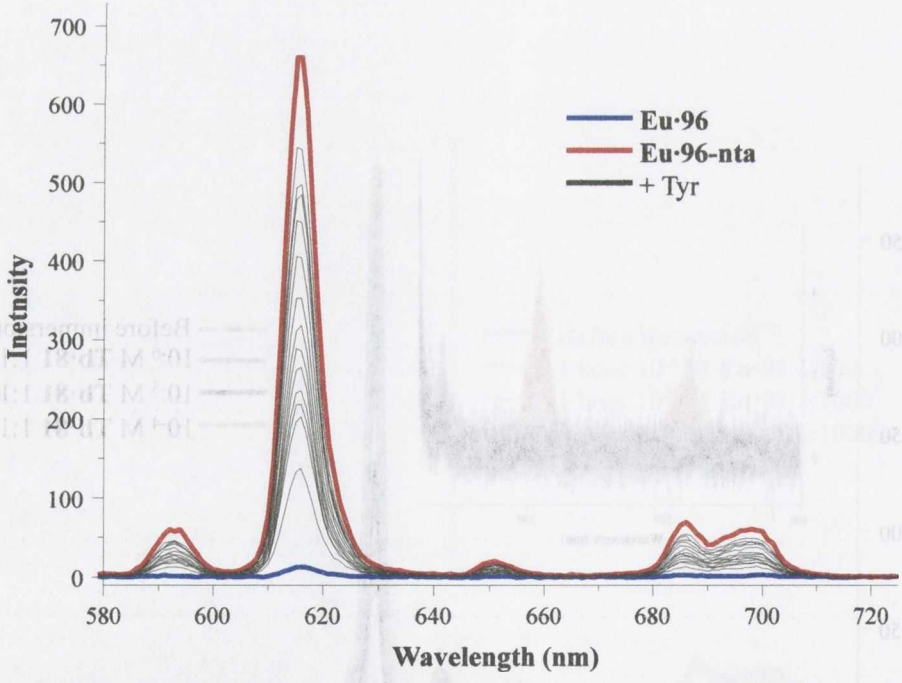


Figure A5.40: *Changes in the Eu(III) emission of a LB film of* ***Eu·96-nta*** *(λ_{ex} = 330 nm) upon dipping into increasing concentrations of Tyr in aqueous solution (0 - 3.68 × 10^{-2} M).*

Appendix 6

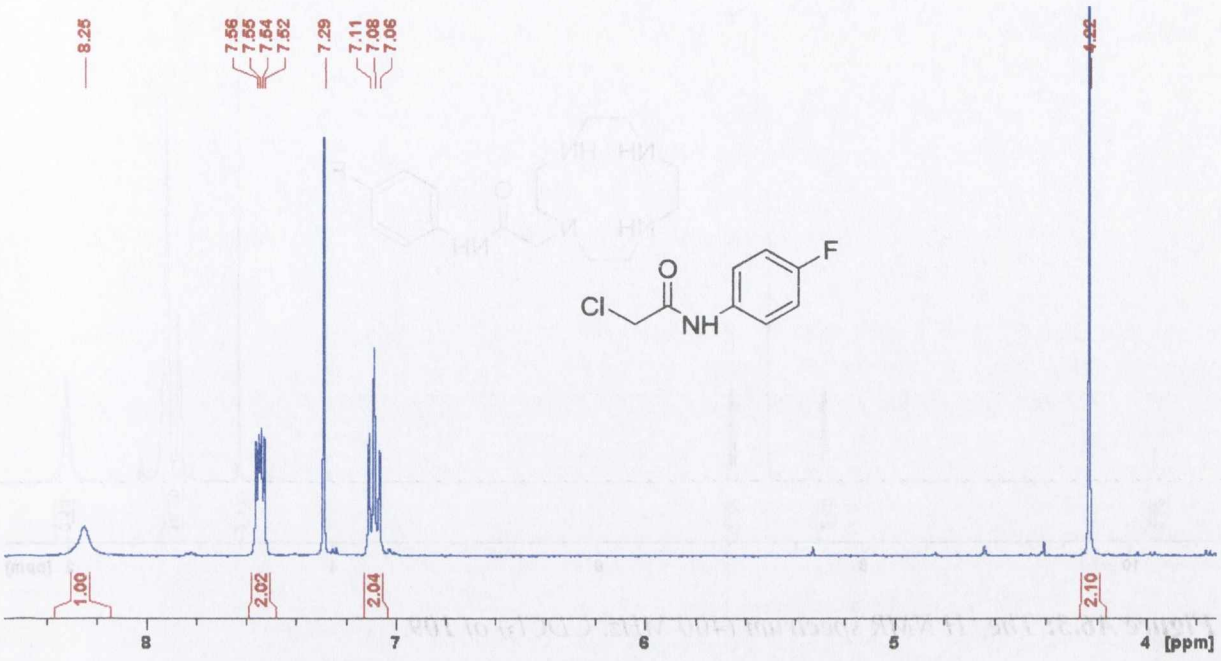


Figure A6.1: *The ^{1}H NMR spectrum (400 MHz, $CDCl_3$) of* ***107****.*

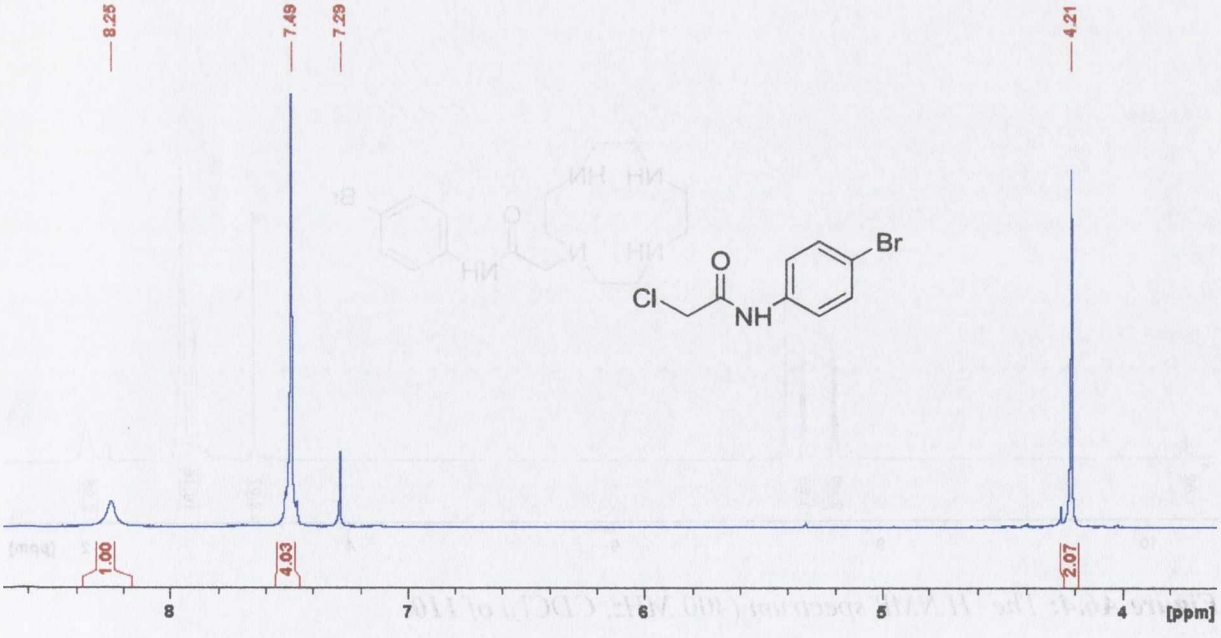


Figure A6.2: *The ^{1}H NMR spectrum (400 MHz, $CDCl_3$) of* ***108****.*

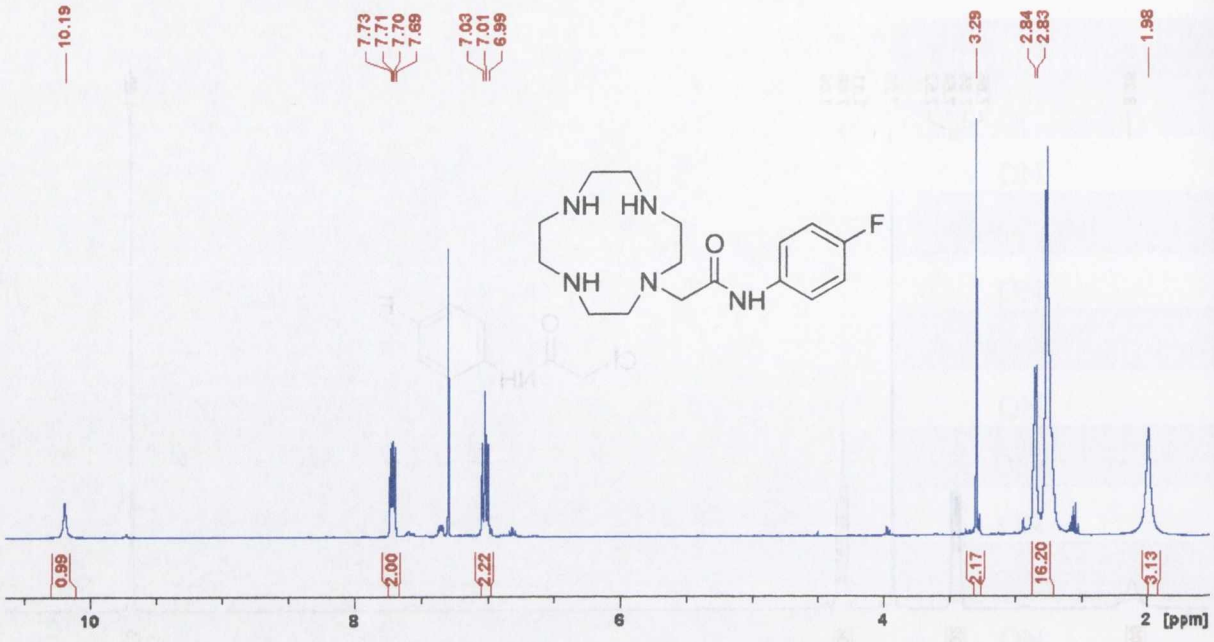


Figure A6.3: *The ^{1}H NMR spectrum (400 MHz, $CDCl_3$) of* ***109****.*

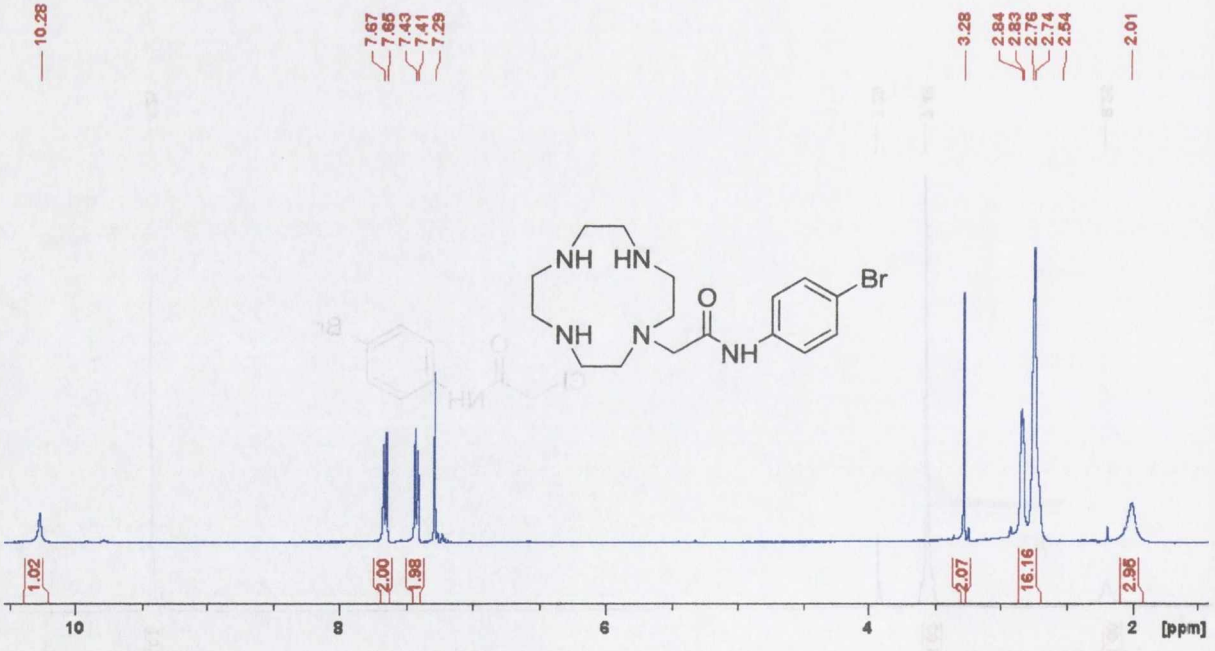


Figure A6.4: *The ^{1}H NMR spectrum (400 MHz, $CDCl_3$) of* ***110****.*

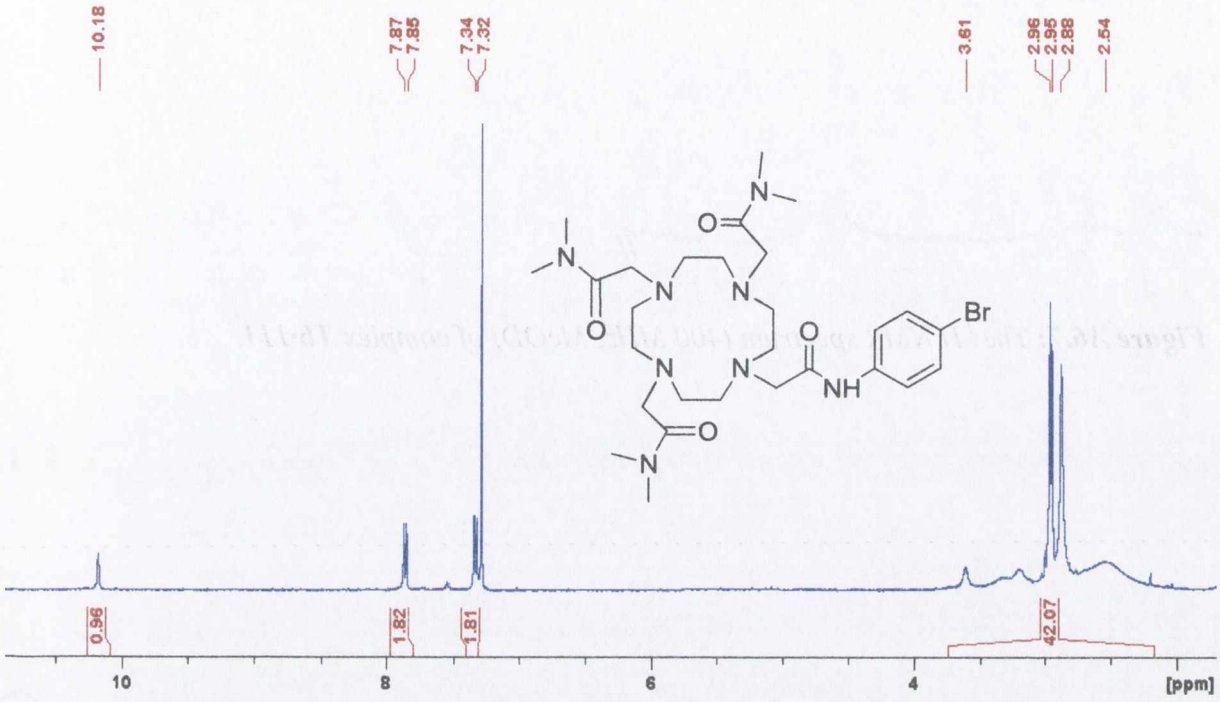


Figure A6.5: *The ^{1}H NMR spectrum (400 MHz, $CDCl_3$) of ligand* ***112****.*

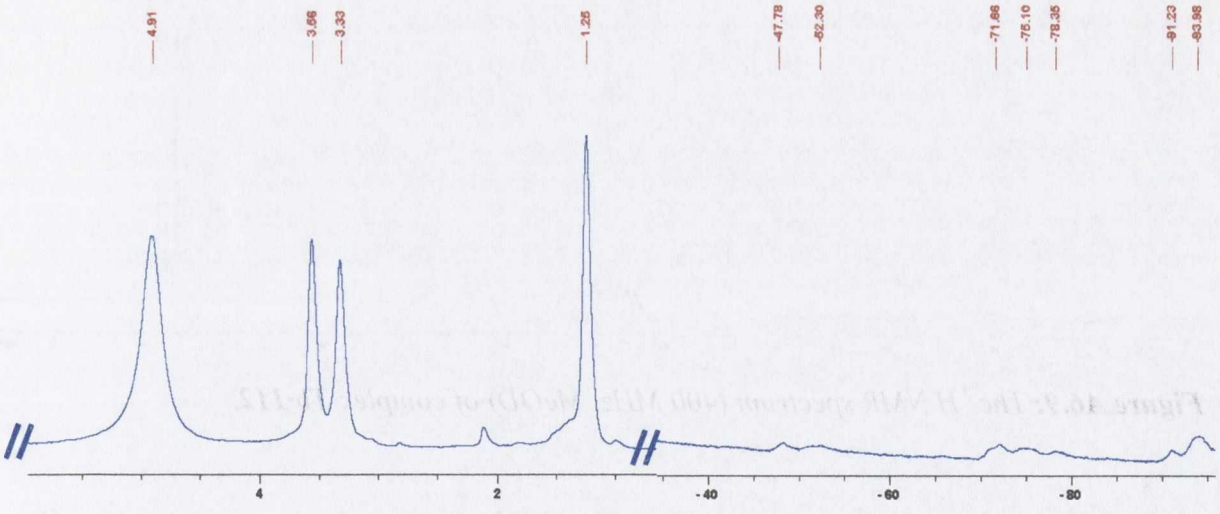


Figure A6.6: *The ^{1}H NMR spectrum (400 MHz, MeOD) of complex* ***Tb·111****.*

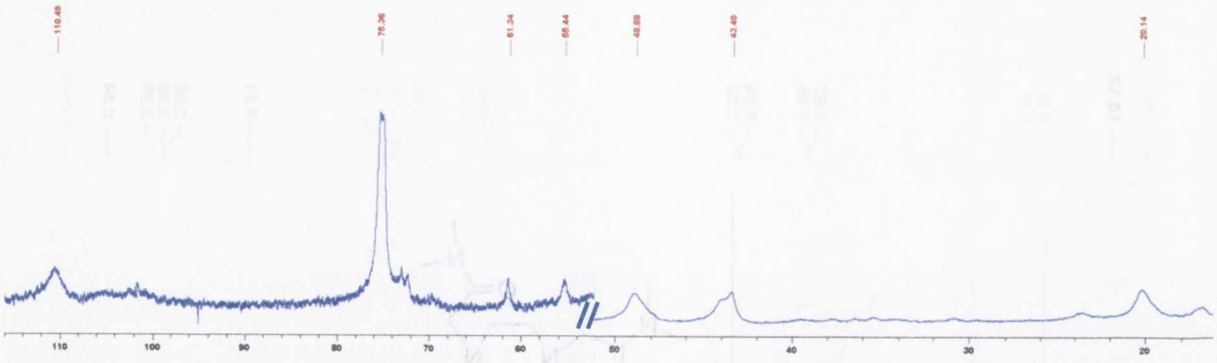


Figure A6.7: *The ^{1}H NMR spectrum (400 MHz, MeOD) of complex* ***Tb·111****.*

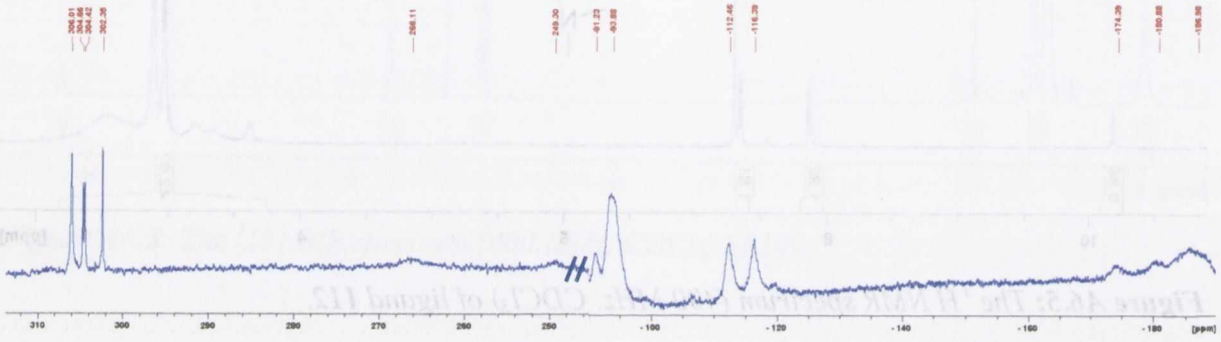


Figure A6.8: *The ^{1}H NMR spectrum (400 MHz, MeOD) of complex* ***Tb·111****.*

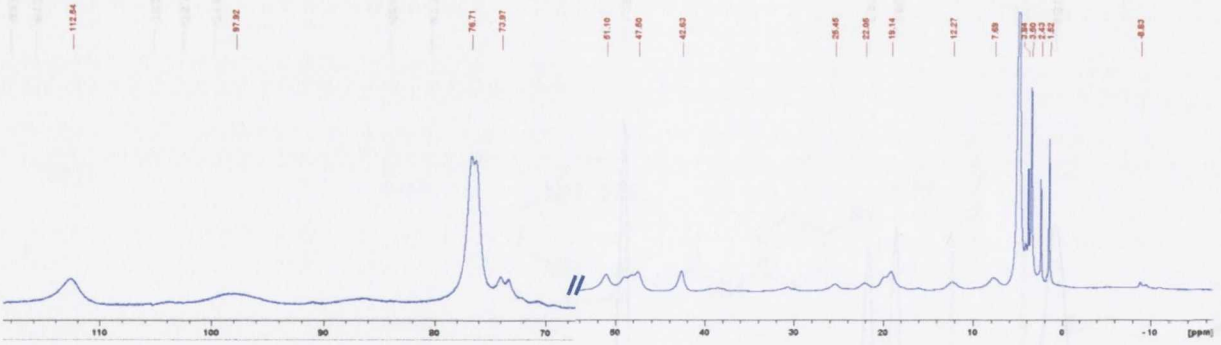


Figure A6.9: *The ^{1}H NMR spectrum (400 MHz, MeOD) of complex* ***Tb·112****.*

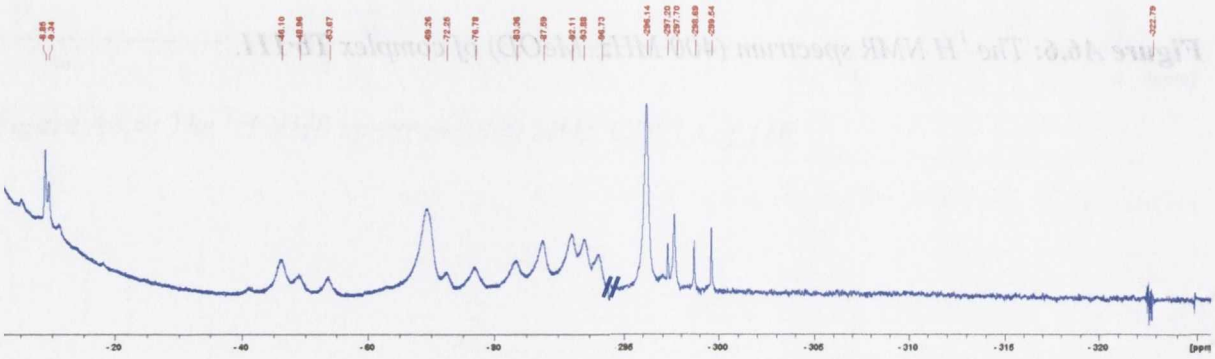


Figure A6.10: *The ^{1}H NMR spectrum (400 MHz, MeOD) of complex* ***Tb·112****.*

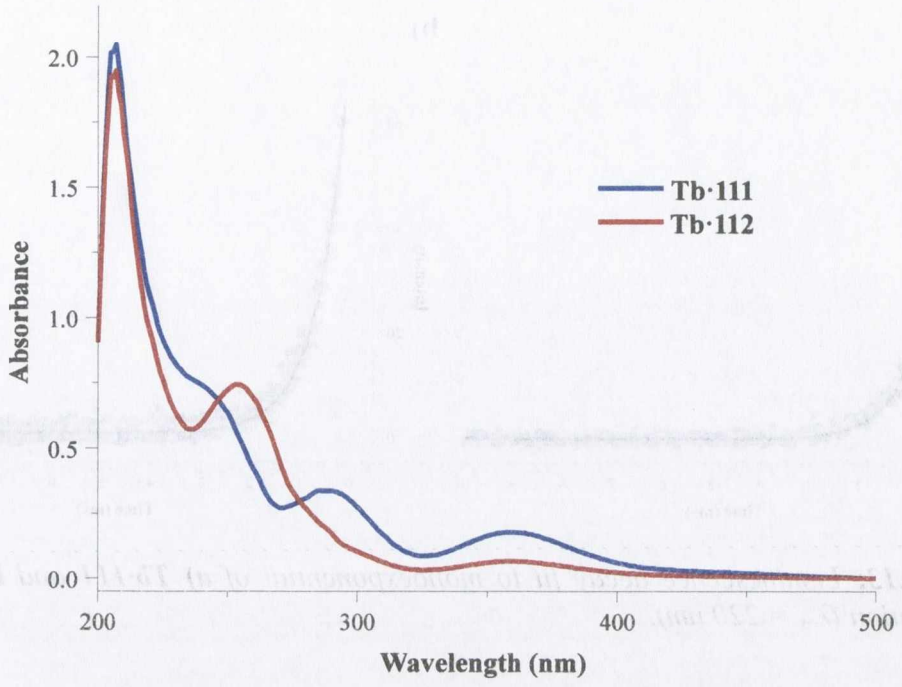


Figure A6.11: *The UV-vis absorption spectra of complexes* ***Tb·111*** *(-) and* ***Tb·112*** *(-) recorded in MeOH.*

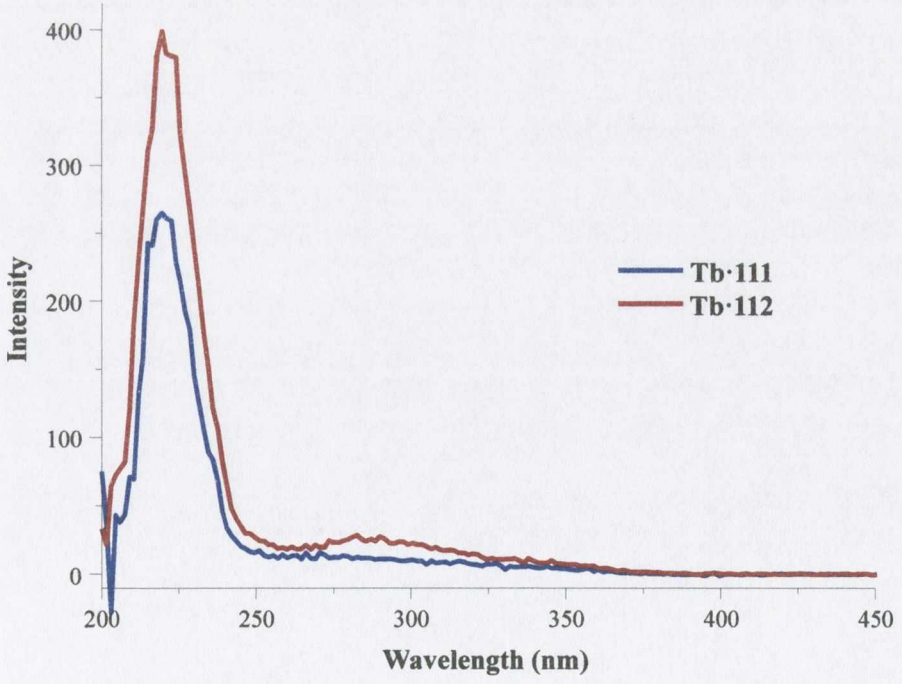


Figure A6.12: *Excitation spectra (λ_{em} = 545 nm) of complexes* ***Tb·111*** *(-) and* ***Tb·112*** *(-) recorded in MeOH.*

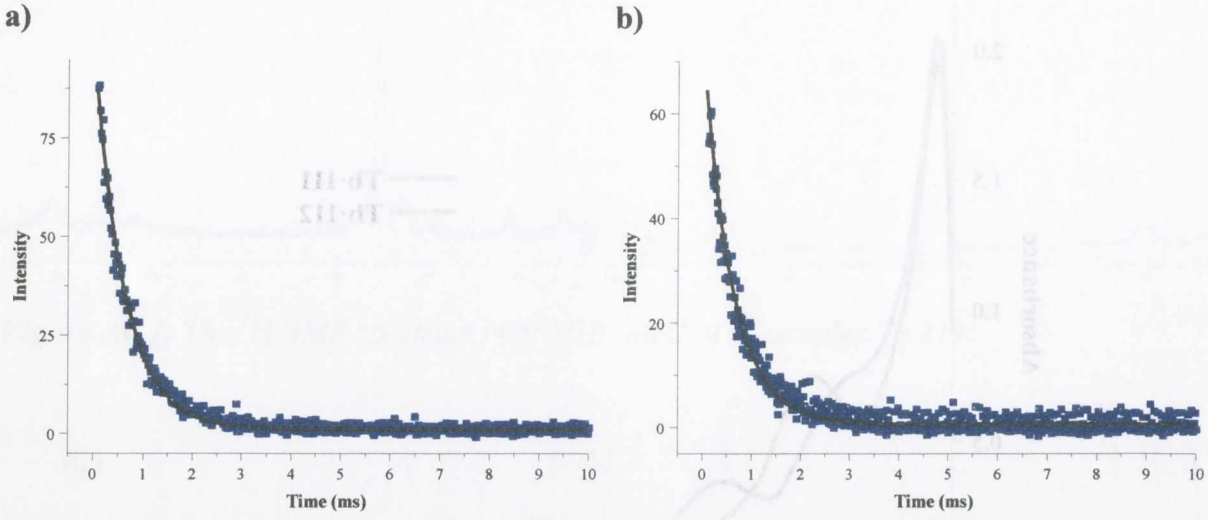


Figure A6.13: *Luminescence decay fit to monoexponential of* ***a) Tb·111*** *and* ***b) Tb·112*** *in MeOH solution (λ_{ex} = 220 nm).*

Publications